Oxidative Medicine and Cellular Longevity

Role of ROS-Induced NLRP3 Inflammasome Activation in Chronic Diseases and Conditions

Lead Guest Editor: Tao Zheng
Guest Editors: Fang Bian, Juyi Li, and Francesca Danesi

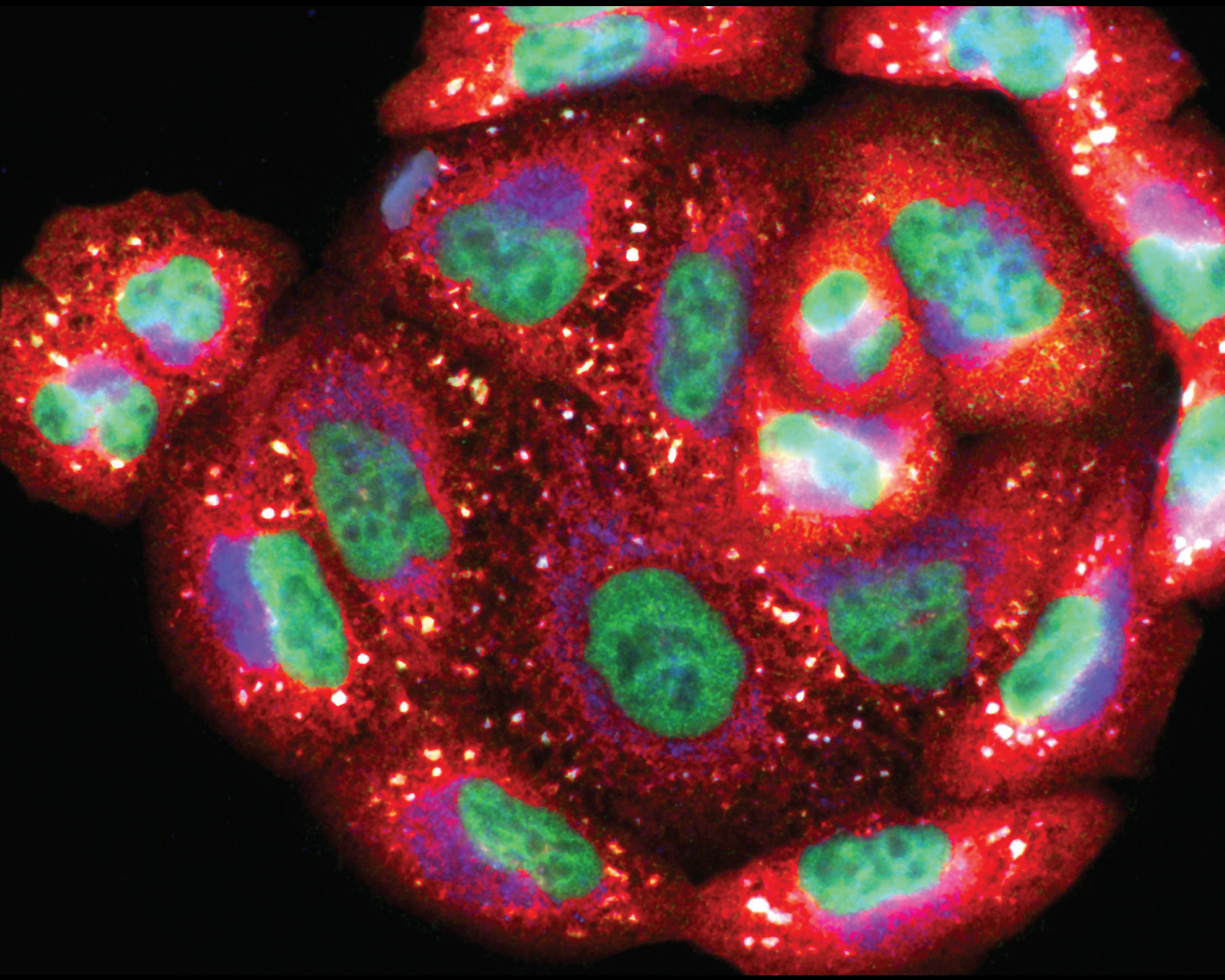

Role of ROS-Induced NLRP3 Inflammasome Activation in Chronic Diseases and Conditions

Oxidative Medicine and Cellular Longevity

Role of ROS-Induced NLRP3 Inflammasome Activation in Chronic Diseases and Conditions

Lead Guest Editor: Tao Zheng
Guest Editors: Fang Bian, Juyi Li, and Francesca Danesi

Chief Editor

Jeannette Vasquez-Vivar, USA

Associate Editors

Amjad Islam Aqib, Pakistan
Angel Catalá, Argentina
Cinzia Domenicotti, Italy
Janusz Gebicki, Australia
Aldrin V. Gomes, USA
Vladimir Jakovljevic, Serbia
Thomas Kietzmann, Finland
Juan C. Mayo, Spain
Ryuichi Morishita, Japan
Claudia Penna, Italy
Sachchida Nand Rai, India
Paola Rizzo, Italy
Mithun Sinha, USA
Daniele Vergara, Italy
Victor M. Victor, Spain

Academic Editors

Ammar AL-Farga, Saudi Arabia
Mohd Adnan, Saudi Arabia
Ivanov Alexander, Russia
Fabio Altieri, Italy
Daniel Dias Rufino Arcanjo, Brazil
Peter Backx, Canada
Amira Badr, Egypt
Damian Bailey, United Kingdom
Rengasamy Balakrishnan, Republic of Korea
Jiaolin Bao, China
Ji C. Bihl, USA
Hareram Birla, India
Abdelhakim Bouyahya, Morocco
Ralf Braun, Austria
Laura Bravo, Spain
Matt Brody, USA
Amadou Camara, USA
Marcio Carocho, Portugal
Peter Celec, Slovakia
Giselle Cerchiaro, Brazil
Arpita Chatterjee, USA
Shao-Yu Chen, USA
Yujie Chen, China
Deepak Chhangani, USA
Ferdinando Chiaradonna, Italy
Zhao Zhong Chong, USA
Fabio Ciccarone, Italy
Alin Ciobica, Romania
Ana Cipak Gasparovic, Croatia
Giuseppe Cirillo, Italy
Maria R. Ciriolo, Italy
Massimo Collino, Italy
Manuela Corte-Real, Portugal
Manuela Curcio, Italy
Domenico D'Arca, Italy
Francesca Danesi, Italy
Claudio De Lucia, USA
Damião De Sousa, Brazil
Enrico Desideri , Italy
Francesca Diomede, Italy
Raul Dominguez-Perles, Spain
Joël R. Drevet, France
Grégory Durand, France
Alessandra Durazzo, Italy
Javier Egea, Spain
Pablo A. Evelson, Argentina
Mohd Farhan, USA
Ioannis G. Fatouros, Greece
Gianna Ferretti, Italy
Swaran J. S. Flora, India
Maurizio Forte, Italy
Teresa I. Fortoul, Mexico
Anna Fracassi , USA
Rodrigo Franco, USA
Juan Gambini, Spain
Gerardo García-Rivas, Mexico
Husam Ghanim, USA
Jayeeta Ghose, USA
Rajeshwary Ghosh, USA
Lucia Gimeno-Mallench , Spain
Anna M. Giudetti, Italy
Daniela Giustarini, Italy
José Rodrigo Godoy, USA
Saeid Golbidi, Canada
Guohua Gong, China
Tilman Grune, Germany
Solomon Habtemariam, United Kingdom
Eva-Maria Hanschmann, Germany
Md Saquib Hasnain, India
Md Hassan, India

Contents

Hindawi
Oxidative Medicine and Cellular Longevity
Volume 2022, Article ID 1652244, 26 pages
https://doi.org/10.1155/2022/1652244

Research Article

Corilagin Restrains NLRP3 Inflammasome Activation and Pyroptosis through the ROS/TXNIP/NLRP3 Pathway to Prevent Inflammation

Tianyu Luo,[1,2] Xiaoyi Zhou,[1,2] Minyan Qin,[1,2] Yuqing Lin,[1,2] Jiefen Lin,[2] Guangpei Chen,[1] Aijun Liu,[1,2] Dongyun Ouyang,[3] Dongfeng Chen ,[1,2] and Hao Pan [1,2,4]

[1]*Department of Human Anatomy, School of Basic Medical Sciences, Guangzhou University of Chinese Medicine, Guangzhou, Guangdong, China*
[2]*Research Center for Integrative Medicine, School of Basic Medical Sciences, Guangzhou University of Chinese Medicine, Guangzhou, Guangdong, China*
[3]*Department of Immunobiology, College of Life Science and Technology, Jinan University, Guangzhou, Guangdong, China*
[4]*Dongguan Institute of Guangzhou University of Chinese Medicine, Dongguan, Guangdong, China*

Correspondence should be addressed to Dongfeng Chen; chen888@gzucm.edu.cn and Hao Pan; hao.pan25@foxmail.com

Received 16 February 2022; Revised 22 June 2022; Accepted 24 September 2022; Published 17 October 2022

Academic Editor: Tao Zheng

Corilagin, a gallotannin, shows excellent antioxidant and anti-inflammatory effects. The NLRP3 inflammasome dysfunction has been implicated in a variety of inflammation diseases. However, it remains unclear how corilagin regulates the NLRP3 inflammasome to relieve gouty arthritis. In this study, bone marrow-derived macrophages (BMDMs) were pretreated with lipopolysaccharide (LPS) and then incubated with NLRP3 inflammasome agonists, such as adenine nucleoside triphosphate (ATP), nigericin, and monosodium urate (MSU) crystals. The MSU crystals were intra-articular injected to induce acute gouty arthritis. Here we showed that corilagin reduced lactate dehydrogenase (LDH) secretion and the proportion of propidium iodide- (PI-)stained cells. Corilagin suppressed the expression of N-terminal of the pyroptosis executive protein gasdermin D (GSDMD-NT). Corilagin restricted caspase-1 p20 and interleukin (IL)-1β release. Meanwhile, corilagin attenuated ASC oligomerization and speck formation. Our findings confirmed that corilagin diminished NLRP3 inflammasome activation and macrophage pyroptosis. We further discovered that corilagin limited the mitochondrial reactive oxygen species (ROS) production and prevented the interaction between TXNIP and NLRP3, but ROS activator imiquimod could antagonize the inhibitory function of corilagin on NLRP3 inflammasome and macrophage pyroptosis. Additionally, corilagin ameliorated MSU crystals induced joint swelling, inhibited IL-1β production, and abated macrophage and neutrophil migration into the joint capsule. Collectively, these results demonstrated that corilagin suppressed the ROS/TXNIP/NLRP3 pathway to repress inflammasome activation and pyroptosis and suggest its potential antioxidative role in alleviating NLRP3-dependent gouty arthritis.

1. Introduction

Corilagin ($C_{27}H_{22}O_{18}$), a natural polyphenol tannic acid compound, is the main active component of *Phyllanthus urinaria*, *Phyllanthus emblica*, *Geranium*, and other medicinal plants [1]. Recent pharmacological researches have demonstrated that corilagin displays various biological activities, such as antioxidation [2] and anti-inflammation [3] activities. For example, corilagin can inhibit calcium oxalate crystal-evoked oxidative stress, inflammation, apoptosis, and relieve kidney stones in rats [4]. Corilagin enhances the survival rate of septic mice by inhibiting the expression of proinflammatory cytokines such as IL-1β, IL-6, and TNF-α [5]. Nevertheless, the mechanism of corilagin on anti-inflammation has not been fully elucidated.

The NLR family pyrin domain-containing protein 3 (NLRP3) inflammasome is deeply involved in the regulation of inflammation-related diseases [6]. The NLRP3 inflammasome is mainly a multimeric cytosolic protein complex composed of NLRP3, the adaptor protein apoptosis-associated speck-like protein containing a CARD (ASC) and the effector protease caspase-1. The classical activation of NLRP3 inflammasome comprises two steps. First, cells are primed via pattern recognition receptors, e.g., Toll-like receptor (TLR) 4 or tumor necrosis factor receptor (TNFR)), which activate the NF-κB signaling to initiate *NLRP3* and *IL-1β* genes transcription [7]. Second, the NLRP3 inflammasome, composed of the NLRP3, ASC, and caspase-1, is activated by pathogen-associated molecular patterns (PAMPs) or damage-associated molecular patterns (DAMPs), e.g., ATP, nigericin, and MSU crystals. Subsequently, precursor (pro)-caspase-1 is cleaved into its active form (p10 and p20 subunits), which splits pro-IL-1β (31 kDa) to produce mature IL-1β (17 kDa) [7]. Gasdermin D (GSDMD) was also cleaved to obtain an N-terminal fragment (GSDMD-NT), which is an effector protein to induce pyroptosis and release cytokines [8]. Inflammation can eliminate foreign bodies and promote tissue repair, while sustained uncontrolled inflammation can engender tissue damage.

The NLRP3 can be activated by diverse molecules or cellular events, including mitochondrial dysfunction and mitochondrial DNA, ROS, ion flux, and lysosomal damage [9]. Upon the second signal stimulation, mitochondrial morphology changes and generates ROS. Excessive ROS causes thioredoxin (TRX) to dissociate from thioredoxin-interacting protein (TXNIP), and activated TXNIP combines with NLRP3 to promote inflammasome activation [10, 11]. The topical immunomodulator imiquimod induces NLRP3 activation by triggering ROS and mitochondrial complex I dysfunction [12]. However, it is unclear whether corilagin manages ROS generation to interfere with NLRP3 inflammasome activation.

Purine metabolism disorder causes urate accumulation to form MSU crystals, which can drive NLRP3 inflammasome oligomerization and IL-1β release and triggers acute gouty arthritis flares [13]. The NLRP3 senses MSU crystals mainly through the following two pathways. MSU crystals increase intracellular ROS production, which promotes TXNIP dissociation from TRX, thereby promoting NLRP3 inflammasome assembly. In addition, MSU crystals facilitate IL-1β secretion, which stimulates nonhematopoietic cells to generate IL-6 and chemokines to recruit neutrophils, resulting in inflammation and joint tissue damage [7, 14, 15]. Small molecular compounds derived from plants show promising potential in antigouty arthritis. Our previous research revealed that compounds derived from traditional Chinese medicine display potential therapeutic effects on NLRP3-dependent gouty arthritis [16, 17]. However, whether corilagin targets NLRP3 to treat gouty arthritis is unknown.

Here, we show that corilagin suppressed ASC polymerization, caspase-1 activation, mature IL-1β release, and macrophage pyroptosis. Importantly, corilagin blocked ROS-induced interaction between TXNIP and NLRP3. ROS activator imiquimod abrogated the function of corilagin in inhibiting NLRP3 inflammasome activation and macrophage pyroptosis. In addition, corilagin prevented joint swelling, reduced IL-1β and caspase-1 (p20) expression, and inhibited neutrophils and macrophages aggregation in the MSU crystals-caused arthritis mice. Our results illustrate that corilagin restricts ROS/TXNIP/NLRP3 pathway to diminish macrophage pyroptosis and proinflammatory cytokines release, thereby alleviating NLRP3-dependent gouty arthritis.

2. Materials and Methods

2.1. Mice. 8-10 weeks-old C57BL/6 J male mice were came from the Laboratory Animal Center of Guangzhou University of Chinese Medicine. NLRP3-deficient ($NLRP3^{-/-}$) mice, C57BL/6 J background, were kindly provided by Dr. Dongyun Ouyang of Jinan University, Guangzhou, China. All mice were maintained at a temperature- and humidity-controlled facility and fed in pathogen-free conditions. All animal studies were conducted by following the strict guidelines defined by the Institutional Animal Care and Use Committees of Guangzhou University of Chinese Medicine.

2.2. Reagents Resource. Corilagin (B20672) was acquired from Yuanye Bio-Technology (Shanghai, China). 20 mg corilagin was dissolved in 315 μl DMSO to obtain a concentration of 100 mM, and then aliquoted 50 μl into 6 centrifuge tubes and stored at -20°C. Adenosine triphosphate (ATP, A6419), fetal bovine serum (FBS, S8318), Hoechst 33342 (B2261), lipopolysaccharide (LPS, L4391), and propidium iodide (PI, P4170) were acquired from Sigma–Aldrich (St. Louis, MO, USA). Colchicine (T0320), H2DCFDA (T15458), and Imiquimod (T0134) were bought from TargetMol (Boston, MA, USA). Nigericin (tlrl-nig) and MSU crystals (tlrl-msu) were bought from InvivoGen (San Diego, CA, USA). MitoSOX™ Red (M36008), MitoTracker® Deep Red FM (M22426), and streptomycin/penicillin (15140122) were obtained from Thermo Fisher Scientific (CA, USA). The cell lysis buffer for western blot and IP (P0013), Enhanced Mitochondrial Membrane Potential Assay Kit with JC-1 (C2003S), Hematoxylin and Eosin (H&E) Staining Kit (C0105), and Lactate Dehydrogenase (LDH) Cytotoxicity Assay Kit (C0017) were purchased from Beyotime Biotechnology (Haimen, China). The BCA Protein Assay Kit (FD2001) and one-step gel preparation kit (FD341) were purchased from Fude Biological Technology (Hangzhou, China). Mouse TNF-α (EMC102a) and IL-1β (EMC001b) ELISA kits were purchased from Neobioscience Technology Co., Ltd. (Shenzhen, China). Histostain TM-Plus Kits (SP-0022) were from Bioss (Beijing, China). DAB Chromogenic Kit (G1212) was acquired from Servicebio Technology (Wuhan, China). Mayer's hematoxylin solution (G1080) was from Solarbio Science and Technology (Beijing, China). An ECL kit (picogram) (KF001) was obtained from Affinity Biosciences (Cincinnati, USA). Protein G agarose beads (#37478) and Protein A agarose beads (#9863) were obtained from Cell Signaling Technology (Danvers, MA). The antibody sources are shown in Table 1.

Table 1: The source and identifier of antibodies used in this study.

Antibodies	Source	Identifier
Anti-NLRP3	Cell signaling technology	Cat# 15101
Anti-ASC	Cell signaling technology	Cat# 67824
Anti-TXNIP	Cell signaling technology	Cat# 14715
Anti-Phospho (p)-IκBα	Cell signaling technology	Cat# 2859
Anti-Phospho (p)-NF-κB p65	Cell signaling technology	Cat# 3033
Anti-IκBα	Cell signaling technology	Cat# 4814
Anti-NF-κB p65	Cell signaling technology	Cat# 8242
Normal rabbit IgG	Cell signaling technology	Cat# 2729
Anti-rabbit IgG (Alexa Fluor® 488 conjugate)	Cell signaling technology	Cat# 4412
Anti-mouse IgG (Alexa Fluor® 555 conjugate)	Cell signaling technology	Cat# 4409
Anti-β actin antibody	Abcam	Cat# ab8227
Anti-GAPDH antibody	Abcam	Cat# ab181602
Anti-GSDMD antibody	Abcam	Cat# ab209845
Anti-NEK7 antibody	Abcam	Cat# ab133514
Anti-IL-1β antibody	Abcam	Cat# ab9722
Anti-α-tubulin antibody	Proteintech	Cat# 11224-1-AP
Anti-NLRP3 mouse mAb	Adipogen life sciences	Cat# AG-20B-0014-C100
Anti-caspase-1 (p20)	Adipogen life sciences	Cat# AG-20B 0042
Anti-caspase-1 antibody	Novus biologicals	Cat# NB100-56565
Ly-6G antibody	Thermo fisher scientific	Cat# 14-5931-82
F4/80 antibody	Thermo fisher scientific	Cat# 14-4801-82

2.3. Cell Culture and Stimulation. L929 cells were incubated in high glucose DMEM supplemented with 10% FBS and 100 U/ml penicillin–streptomycin. The L929 cells culture medium was collected after the liquid was slightly yellow. The abundant M-CSF in the supernatant of L929 cells could induce mouse bone marrow-derived macrophages (BMDMs). In our previous studies, we established a mature method to generate BMDMs [16]. Briefly, bone marrow cells were collected and gently blown to disperse into a suspension. Then red blood cells were lysed, and the remaining bone marrow cells were incubated in high glucose DMEM containing 20% L929 cell-conditioned medium, 10% FBS, and 100 U/ml penicillin–streptomycin for 7 days. The culture medium was changed every two days to obtain BMDMs. Cells were seeded at 1×10^6 cells/ml in 12-well or 6-well plates overnight. The next day, macrophages were stimulated with LPS (0.5 μg/ml) for 4 hours followed by challenge with NLRP3 activators ATP (3 mM) and nigericin (10 μM) for 1 hour or MSU (300 μg/ml) for 6 hours. Cell culture medium and cell lysates were gathered for subsequent experiments.

2.4. Cell Death Detection. After stimulation, PI (2 μg/ml) and Hoechst 33342 (5 μg/ml) were loaded onto the cell culture plate and incubated at room temperature for 10 min. Immediately after staining, a BIO-RAD ZOE™ Fluorescent Cell Imager was used to take images of multiple cell fields. Multiple cell fields were randomly selected and photographed to count the frequency (%) of PI-positive cells.

LDH release was detected by LDH cytotoxicity assay kit to analyze cell death. 120 μl cell supernatant and 60 μl prepared LDH reagent were loaded to a 96-well plate, and then incubated on a horizontal shaker in the dark for 30 minutes. A PerkinElmer EnSpire was employed to measure the absorbance at 490 nm.

2.5. Enzyme-Linked Immunosorbent Assay (ELISA). According to the manual of the ELISA manufacturer, mouse IL-1β and TNF-α ELISA kits were used to determine cytokine by macrophages. In brief, the supernatant or standard sample was loaded to the precoated plate and maintained at 37°C for 90 min. Then the plate was washed with a washing solution five times. Biotinylated antibody working solution was loaded and reacted at 37°C for 1 hour in a dark place. Wash the plate five times. The enzyme conjugate working solution was loaded to the samples and maintained at 37°C for 30 min. Next, chromogenic substrate (TMB) was loaded to the plate and maintained at 37°C for 15 min. Finally, the reaction was blocked by the stop solution. Samples were quantified in a PerkinElmer EnSpire to capture absorbance at 450 nm. The cytokine concentration of each sample was analyzed with ELISACalc software using a standard curve method.

2.6. Immunofluorescence and Confocal Microscopy. Macrophage or joint tissue was fixed in 4% paraformaldehyde, followed by permeabilization with 0.5% Triton X-100, and blocked in 1× PBS supplemented with 3% normal goat serum. The samples were maintained in primary antibodies

at 4°C overnight, and then combined with secondary alexa antibodies from Cell Signaling Technology for 1 h. Cell nuclei were counterstained with Hoechst 33342. Zeiss LSM 800 confocal laser scanning microscope was employed to capture fluorescent images.

2.7. Western Blotting. To concentrate cell supernatants for immunoblotting, 800 μl of cell supernatant, an equal volume of methanol and 1/4 volume of chloroform were mixed and vortexed for 1 min. The mixtures were centrifuged at 12000 rpm at 4°C for 10 min. Supernatants were removed, and the remaining pellet was resuspended in 35 μl 1× sample loading buffer. Macrophages were lysed by RIPA buffer supplemented with the protease and phosphatase inhibitor cocktail. Whole protein density was measured by a BCA Protein Assay Kit. Concentrated supernatants and cell lysates were denatured under 95°C for 5 min. The denatured protein samples were separated by SDS–PAGE and transferred onto the PVDF membrane. The next day, the PVDF membrane was blocked in 5% nonfat milk in 1× TBST at room temperature for 1 h. The samples were maintained in the primary antibodies at 4°C overnight, followed by incubation with the secondary antibodies at room temperature for 1 h. The PVDF membrane was detected using a picogram ECL kit (Affinity, KF001). Protein visualization occurred on a Tanon 4600 imaging system (Tanon, Shanghai, China).

2.8. ASC Oligomerization and Speck Formation Assay. Macrophages were treated as described above. Cells were fixed in 4% paraformaldehyde at room temperature for 15 min, followed by permeabilization with ice-cold methanol. Then macrophages were incubated with anti-ASC antibody with a final dilution of 1 : 300 at 4°C overnight and Alexa Fluor 488 goat anti-rabbit IgG antibody for 1 h. Cell nuclei were counterstained with Hoechst 33342. ASC specks images were captured under a Zeiss Axio observer 3 fluorescence microscope.

LPS-primed BMDMs were treated with ATP or nigericin as stated above. Then, macrophages were lysed in ice-cold PBS supplemented with 0.5% Triton-X 100 and a protease inhibitor cocktail for 30 min. Cell lysates were centrifuged at 6,000 × g at 4°C for 15 min. The remaining pellets were washed twice with PBS and resuspended in 200 μl PBS. Disuccinimidyl suberate (2 mM) was loaded onto the pellets and maintained at room temperature for 30 min to cross-link. The samples were centrifuged at 6,000 × g at 4°C for 15 min. 30 μl loading buffer was added to the cross-linked pellets and subsequently boiled for 5 min. The sample was run on a gel and immunoblotted using an anti-ASC antibody.

2.9. Coimmunoprecipitation (Co-IP). BMDMs were lysed in ice-cold cell lysis buffer for western blotting and IP. Cell lysates were transferred into microcentrifuge tubes and centrifuged at 12000 rpm at 4°C for 15 min. The protein concentration of each sample was determined using a BCA Protein Assay Kit. Cell lysate samples were dispensed and precleared on Protein A/G agarose beads with mild rotation at 4°C for 30 min. The sample was maintained in anti-TXNIP antibody or IgG antibody on a rotational cell mixer at 4°C overnight. The next day, protein A/G agarose beads were added to the immune complexes and gently rotated at 4°C for 2 h. The samples were then centrifuged. The beads were washed with cell lysis buffer five times. The proteins of each sample were eluted from washed beads by boiling for 5 min in 3× SDS loading buffer and analyzed by SDS–PAGE.

2.10. MitoSOX and MitoTracker Staining. LPS-primed macrophages were stimulated with the NLRP3 inflammasome activators. MitoSOX was used to detect mitochondrial ROS (mtROS). MitoTracker was employed to assess mitochondrial morphology. MitoTracker (200 nM) or MitoSOX red (5 μM) was loaded and incubated for 30 min before the stimulation was complete. BMDMs were washed with PBS three times and counterstained with Hoechst 33342. Cells' fluorescent images were observed and took photographed through a Zeiss LSM 800 confocal laser scanning microscope.

2.11. Mitochondrial Morphology Analysis. Open Fiji-ImageJ (NIH) and click Plugins to install MiNA macros. Images from the Zeiss LSM 800 were loaded into FIJI for mitochondria morphology analysis. The binary image was converted into a skeleton representing the features in the original image by using "skeletonize". Next, the mean branch length and the number of individuals were determined by using the "Analysis Skeleton" plug-in.

2.12. Mitochondrial Membrane Potential Assay with JC-1 Kit. After treating the cells as described above, aspirate the old medium. Cells were loaded with JC-1 working solution and maintained in a cell incubator at 37°C for 20 minutes in the dark. Aspirate the supernatant and wash with JC-1 staining buffer twice. The mitochondrial membrane potential is high in healthy cells, and JC-1 exists as aggregates with bright red fluorescence. When the mitochondrial membrane potential decreased, the number of JC-1 monomers increased and showed green fluorescence. Then the cell fluorescence images were observed and captured using a laser scanning microscope.

2.13. MSU-Induced Gouty Arthritis in Mice. A knee joint gouty arthritis mice model was established according to our previous studies [16, 17]. Corilagin (20 mg/kg) or colchicine (1 mg/kg) was intraperitoneally injected into the right knee joint of C57BL/6 J mice colchicine treated group was a positive control. After one hour, 0.5 mg MSU crystals resuspended in 20 μl of sterile PBS were injected into the knee joint of each mouse. We determined the joint diameter using an electronic caliper at the indicated time of up to 24 hours. The knee joints were isolated and incubated in Opti-MEM supplemented with 100 U/ml penicillin–streptomycin for 1 h. The joint culture medium was collected for cytokine measurement. The harvested knee joint was fixed and decalcified for histological staining.

2.14. Histological Evaluation and Immunohistochemistry. The knee joint was embedded in paraffin. Then the joint tissue was sectioned and stained with hematoxylin and eosin (H&E) to determine morphological injury and inflammation. In addition, joint sections were deparaffinized, rehydrated, and unmasked with antigen in citrate buffer at 60°C overnight. The joint sections were incubated with 3% hydrogen peroxide,

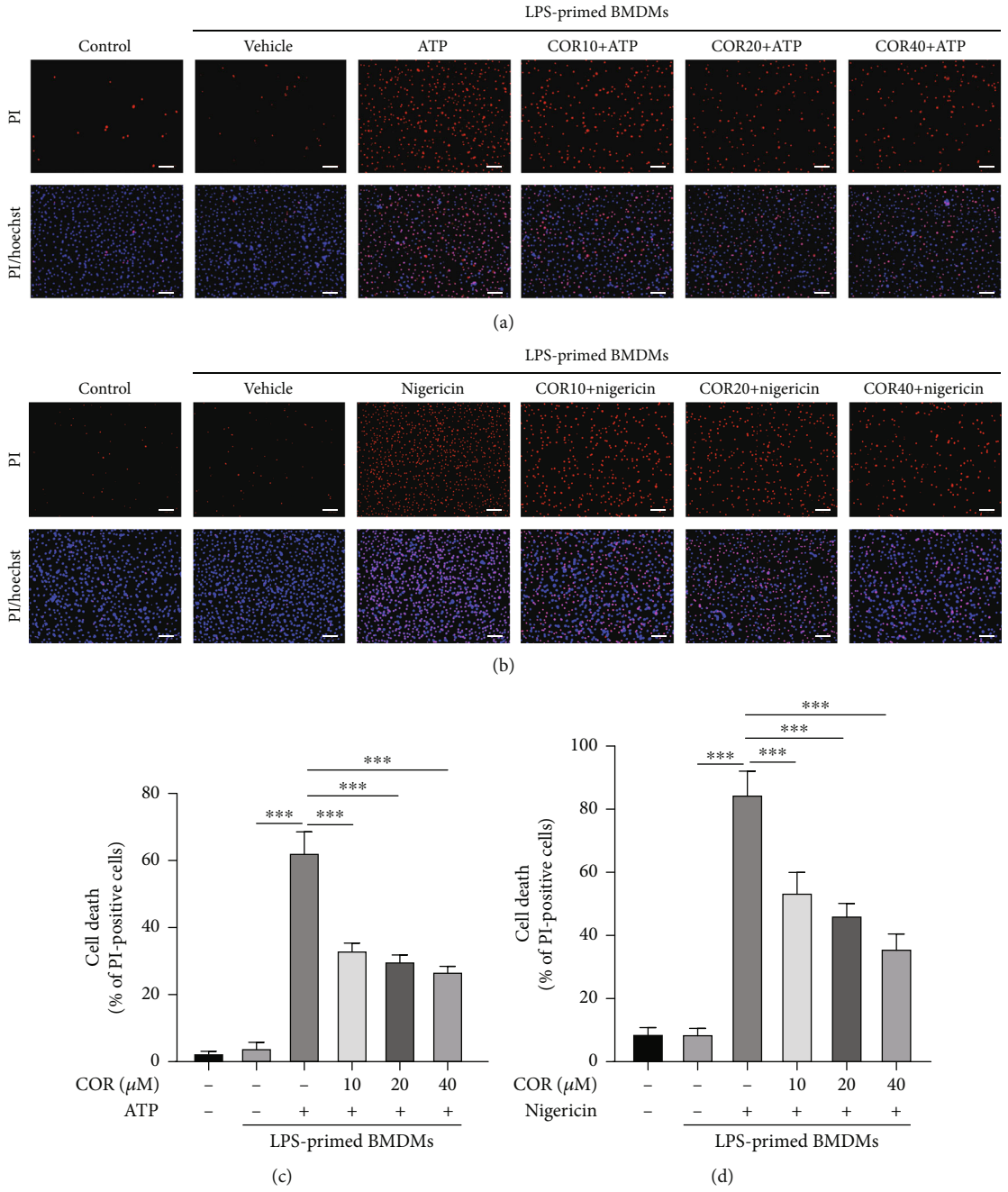

Figure 1: Continued.

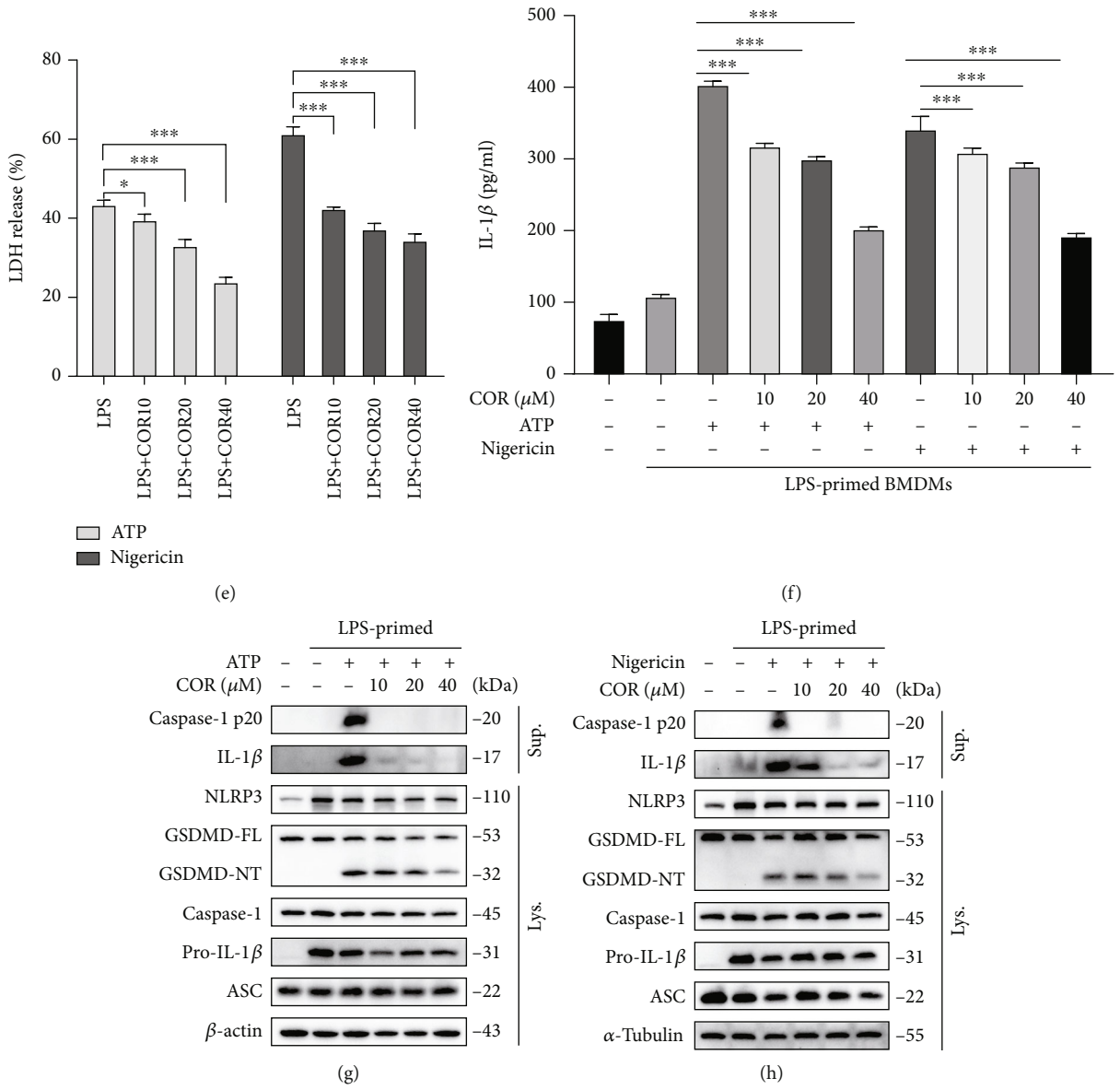

Figure 1: Corilagin inhibits NLRP3 inflammasome activation and pyroptosis in BMDMs. (a–h) BMDMs were primed with LPS (0.5 μg/ml) for 4 h and then stimulated with ATP (3 mM) or nigericin (10 μM) for 1 h with or without corilagin. (a–d) Cells were stained with PI (2 μg/ml) and Hoechst 33342 (5 μg/ml) for 10 min, and the percentage of PI-positive (red) cells relative to total cells (Hoechst 33342, blue) was analyzed ($n = 6$). Scale bar, 100 μm. (e) Cell supernatant was collected to detect LDH release. (f) ELISA determined IL-1β level in supernatants. (g and h) Western blotting was used to detect protein expression in the culture supernatant (Sup.) and cell lysate (Lys.). COR: corilagin. $^{*}P < 0.05$, $^{**}P < 0.01$, $^{***}P < 0.001$.

followed by permeabilization with 0.1% Triton X-100 in PBS. After washing, the joint sections were maintained in 3% sheep serum at room temperature for 1 h. The joint sections were incubated with an antibody specific for F4/80 (macrophage marker) or myeloperoxidase (Ly-6G, neutrophil marker). NLRP3 inflammasome components of the joint were immunostained with caspase-1 p20 or IL-1β antibodies at 4°C overnight. Joint sections were maintained in HRP-conjugated secondary antibody and then reacted with DAB. Then the cell nuclei were counterstained with hematoxylin. Immunohistochemistry images were taken pictures by a Zeiss Axio observer 3 microscope. Moreover, the joint sections were maintained in alexa secondary antibody at 37°C for 1 h. Hoechst 33342 was used to stain cell nuclei. The fluorescence pictures were captured through a Zeiss LSM 800 confocal laser scanning microscope.

2.15. Statistical Analysis. The data are represented as the mean ± standard deviation (SD) or mean ± standard error of the mean (SEM). The statistical analysis method and the significance levels are also displayed in the respective figure legends. Either Student's t-test (two-tailed, unpaired) or one-way ANOVA was employed to analyze raw data, followed by either Tukey's or Dunnett's correction test using

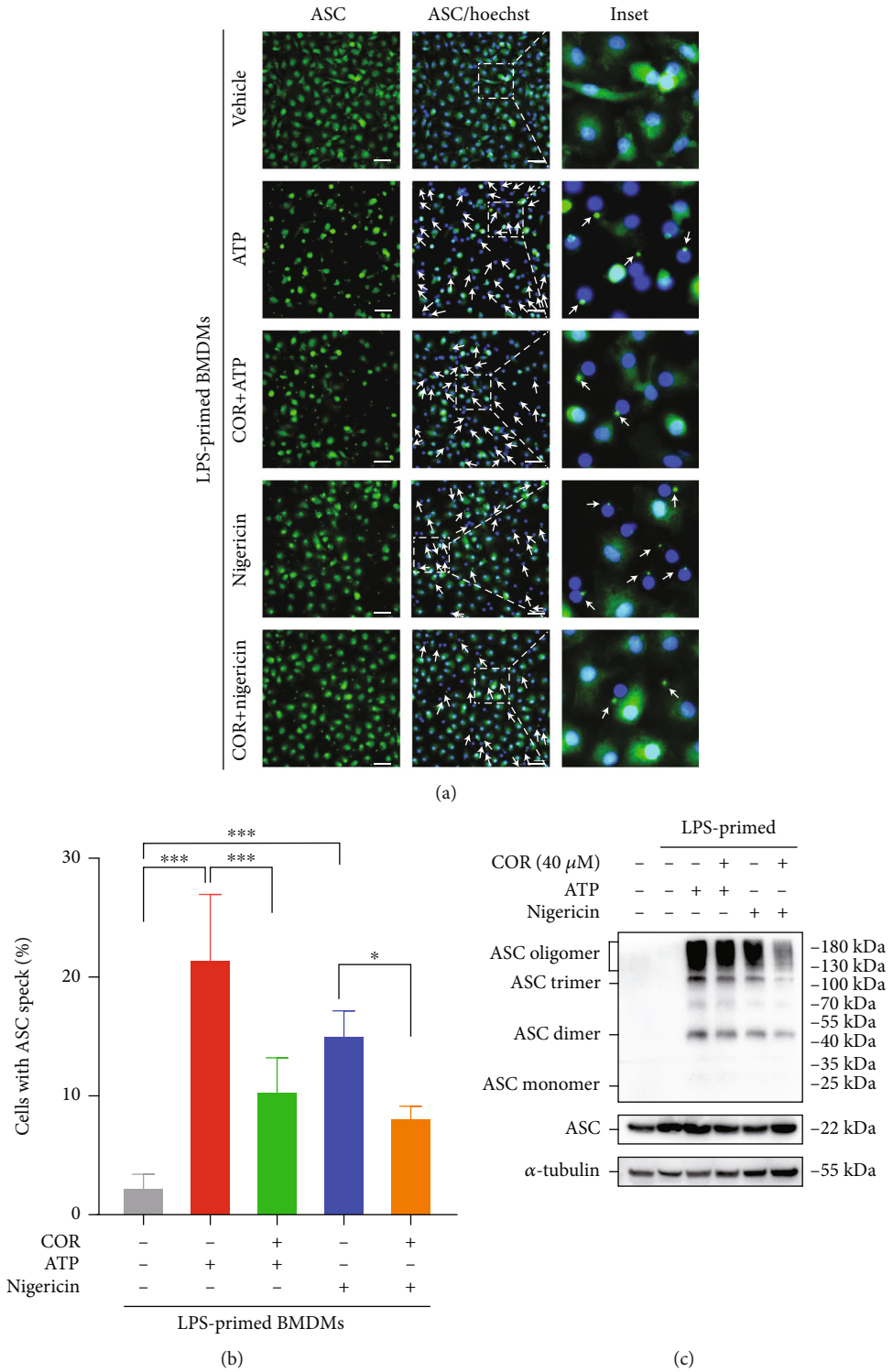

Figure 2: Corilagin prevents ASC aggregation in BMDMs. (a–c) BMDMs were primed with LPS (0.5 μg/ml) for 4 hours and then incubated with ATP (3 mM) or nigericin (10 μM) for 1 hour with or without corilagin (40 μM). (a) Representative image of cell immunofluorescence stained for ASC (green). Scale bar, 20 μm. (b) Percentages of cells shown in (a) with ASC specks ($n = 5$). (c) Western blotting was applied to analyze ASC oligomerization in ATP- or nigericin-treated BMDMs. α-Tubulin is the loading control. COR: corilagin. $^{*}P < 0.05$, $^{***}P < 0.001$.

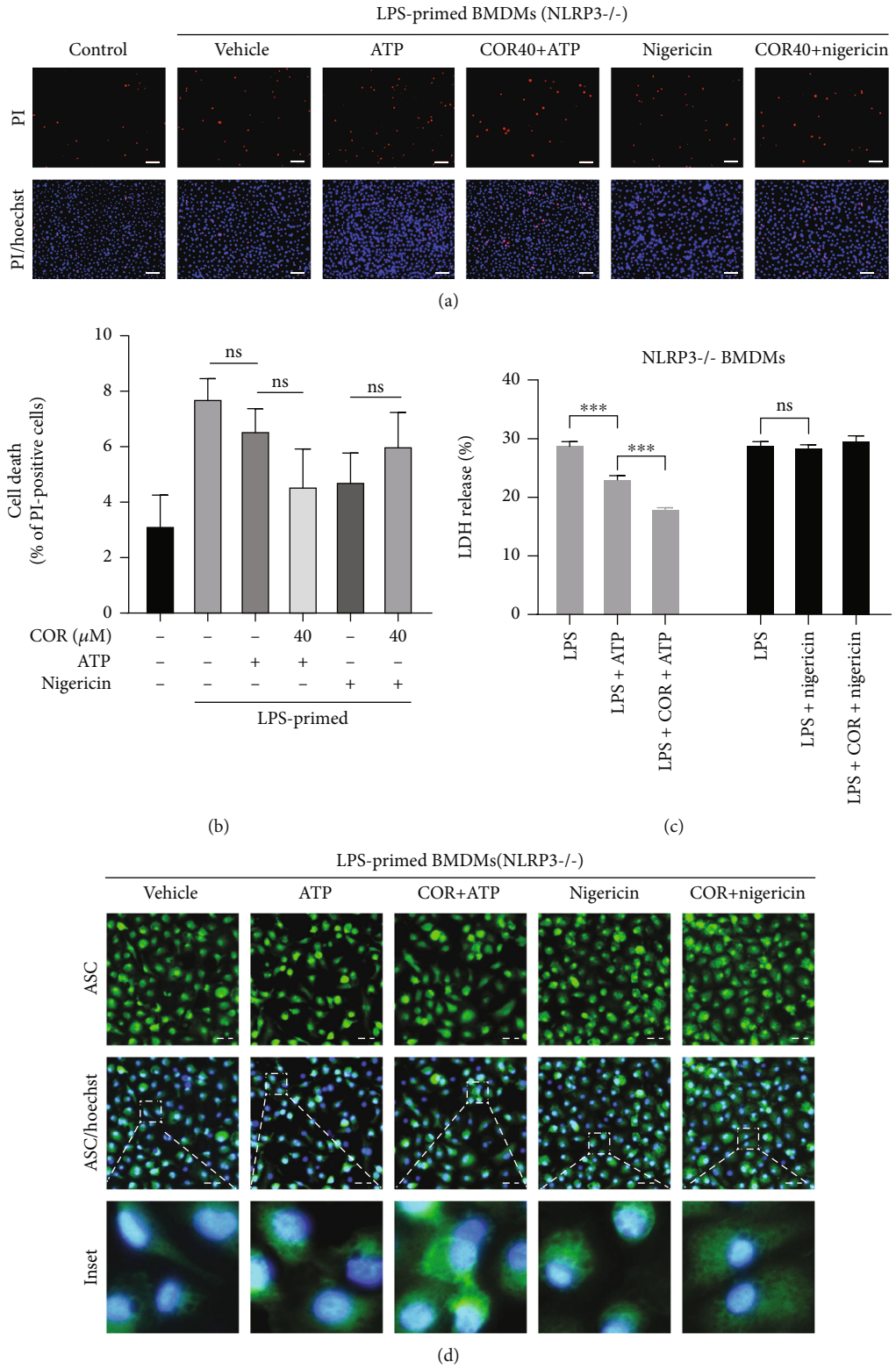

Figure 3: Continued.

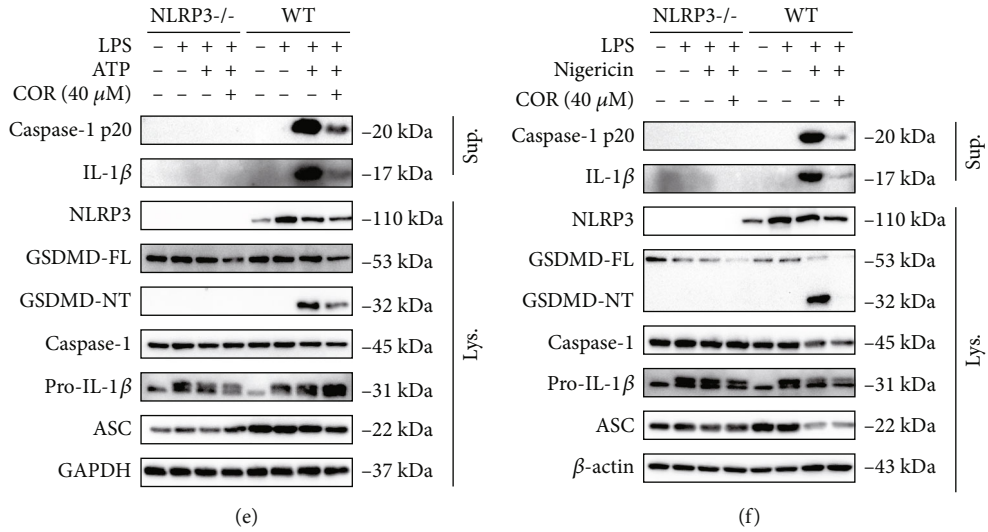

Figure 3: Corilagin restrains inflammasome activation and pyroptosis in an NLRP3-dependent manner. (a–d) NLRP3$^{-/-}$ BMDMs and WT BMDMs were pretreated with LPS (0.5 μg/ml) for 4 hours and then stimulated with ATP (3 mM) or nigericin (10 μM) in the presence of corilagin for 1 hour. (a) NLRP3$^{-/-}$ BMDMs were stained with PI and Hoechst 33342 for 10 min. Scale bar, 100 μm. (b) The percentage of PI-positive (red) cells relative to total cells (Hoechst 33342, blue) was analyzed ($n = 5$). (c) The LDH release in the supernatant was detected. (d) The distribution of ASC in BMDMs was observed by immunofluorescence. Scale bar, 20 μm. (e and f) Western blotting was used to analyze the proteins in the supernatant concentrate and cell lysate. COR: corilagin; WT: wild type. $^{***}P < 0.001$.

GraphPad Prism 8 (GraphPad Software Inc, La Jolla, CA). P value less than 0.05 was considered significant.

3. Results

3.1. Corilagin Blocks NLRP3 Inflammasome Activation and Pyroptosis. Corilagin exerts anti-inflammatory activity mainly by abating proinflammatory cytokines expression, but the mechanism is uncertain. NLRP3 inflammasome activation and pyroptosis contribute to promoting the maturation of inflammatory cytokines such as IL-1β. LPS-primed BMDMs were stimulated with classical NLRP3 inflammasome activators (ATP and nigericin) in the presence of corilagin. The proportion of cell death was analyzed by propidium iodide (PI) staining and LDH release detection. ELISA determined the density of IL-1β in culture supernatants. In addition, immunoblotting was performed to detect caspase-1 p20 (20 kDa) and mature IL-1β (17 kDa) in the supernatant to identify inflammasome activation and the expression of the NLRP3 inflammasome component and pyroptosis executive protein GSDMD in the cell lysate.

The results showed that corilagin dose-dependently reduced ATP- and nigericin-caused mortality in LPS-primed BMDMs (Figures 1(a)–1(d)) and limited LDH and IL-1β release in the supernatant (Figures 1(e) and 1(f)). Western blot results showed that LPS stimulated NLRP3 and pro-IL-1β expression, whereas corilagin did not influence NLRP3, pro-IL-1β, ASC, or caspase-1 expression in LPS-primed and NLRP3-activated cells. Corilagin significantly inhibited ATP- and nigericin-induced release of caspase-1 p20 and mature IL-1β (17 kDa) into the culture supernatant and decreased GSDMD-NT expression (Figures 1(g) and 1(h)). LPS binds to TLR4 to activate the NF-κB pathway and gene transcription. BMDMs were pretreated with corilagin before LPS stimulation, followed by challenge with or without nigericin. The immunoblotting results showed that corilagin did not inhibit LPS-activated phospho (p)-P65 and p-IκB and could not abolish LPS-induced IκB degradation (Figure S1). The result indicated that corilagin could not inhibit TLR4/NF-κB pathway. Collectively, we conclude that corilagin specifically obstructs NLRP3 inflammasome activation and macrophage pyroptosis, thereby reducing IL-1β release.

3.2. Corilagin Suppresses ASC Oligomerization and Speck Formation. NLRP3 inflammasome is a multiprotein complex. ASC acts as a linker between NLRP3 and caspase-1 and participates in caspase-1 activation. NLRP3 activation is accompanied by ASC protein oligomerization, and ASC specks are a significant marker of NLRP3 inflammasome aggregation. ATP and nigericin were added to stimulate LPS-primed macrophages for NLRP3 inflammasome activation. Immunofluorescence results displayed that ASC specks were increased and irregularly distributed in the positive group, and corilagin significantly blocked ASC speck formation (Figures 2(a) and 2(b)). Furthermore, ASC oligomerization was detected by chemical cross-linking and western blotting. The results showed that corilagin inhibited ATP- and nigericin-caused ASC oligomerization in LPS-stimulated BMDMs (Figure 2(c)). Altogether, these results indicate that corilagin can reduce ASC speck formation by blocking ASC oligomerization, which reveals its potential to restrict NLRP3 inflammasome assembly and activation.

3.3. Corilagin Prevents Inflammasome Activation Dependent on NLRP3. To further prove the specificity of corilagin in restricting the NLRP3 inflammasome, bone marrow cells

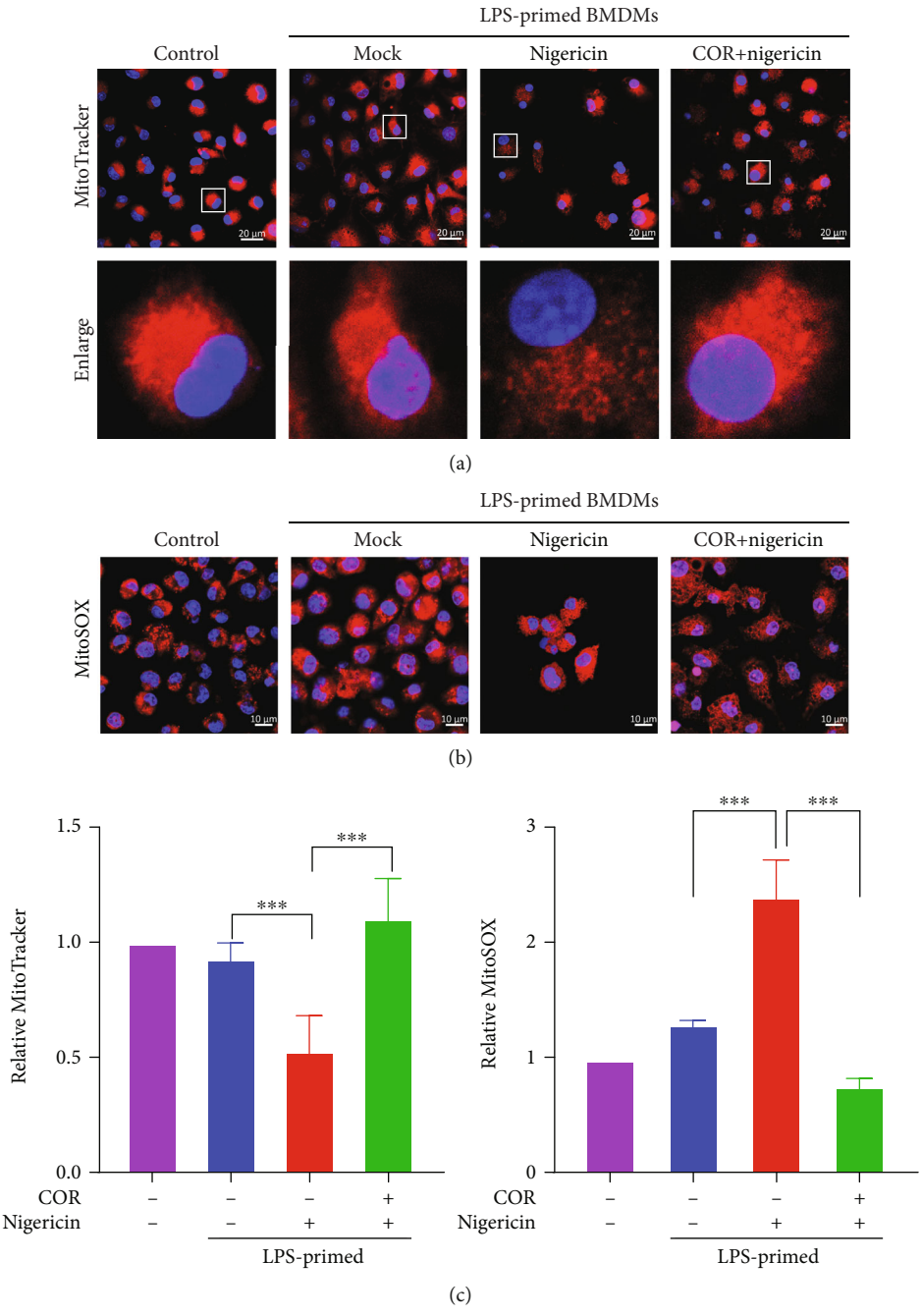

Figure 4: Continued.

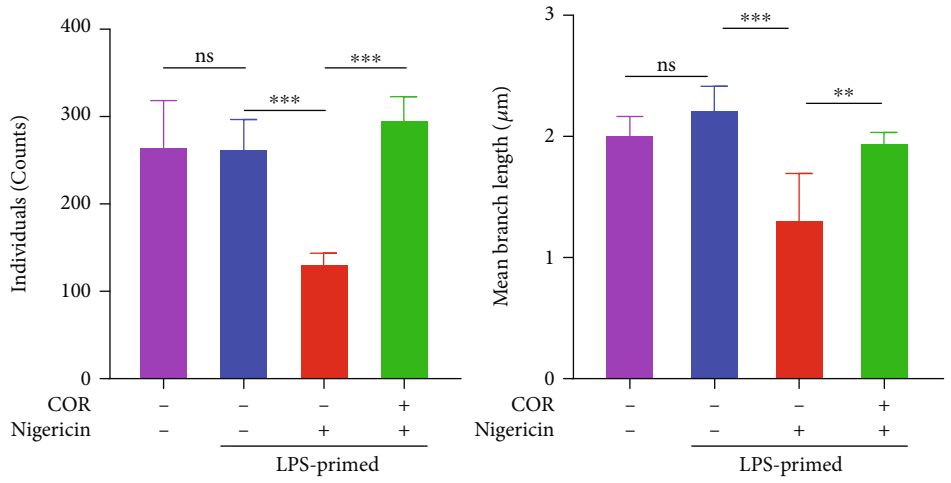

(d)

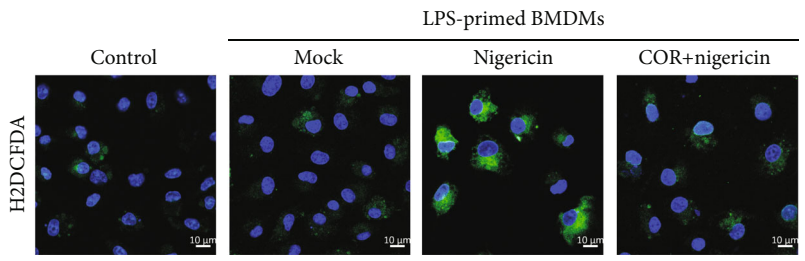

(e)

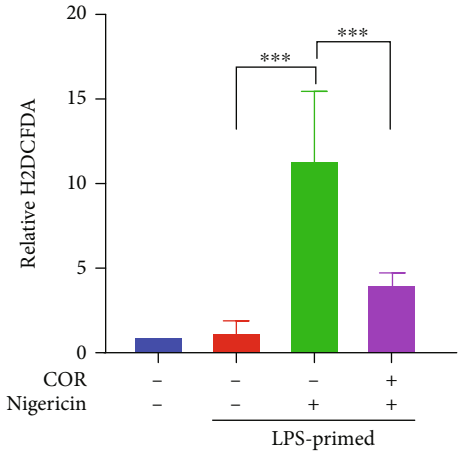

(f)

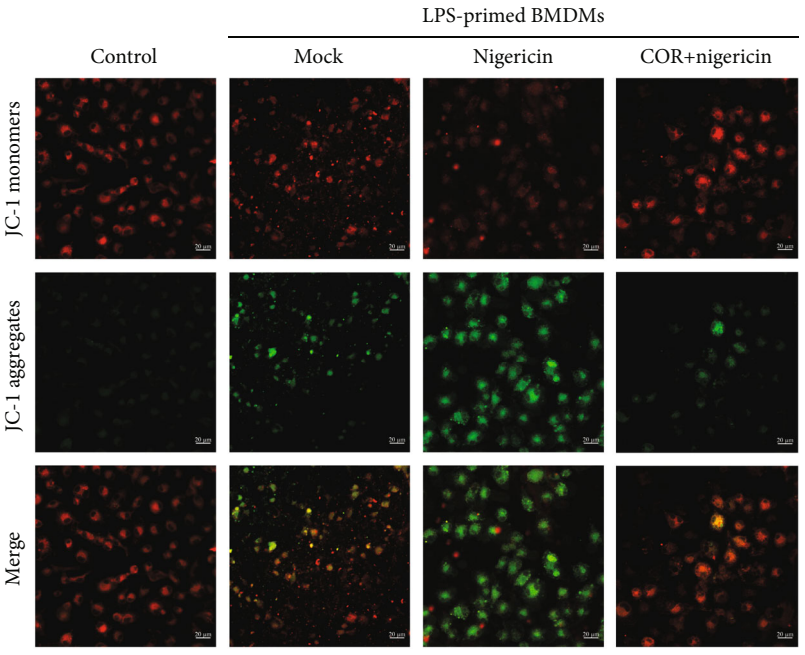

(g)

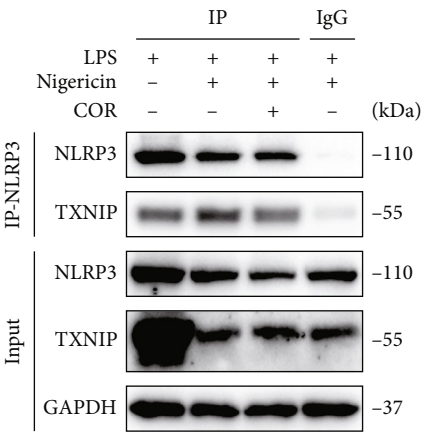

(h)

Figure 4: Continued.

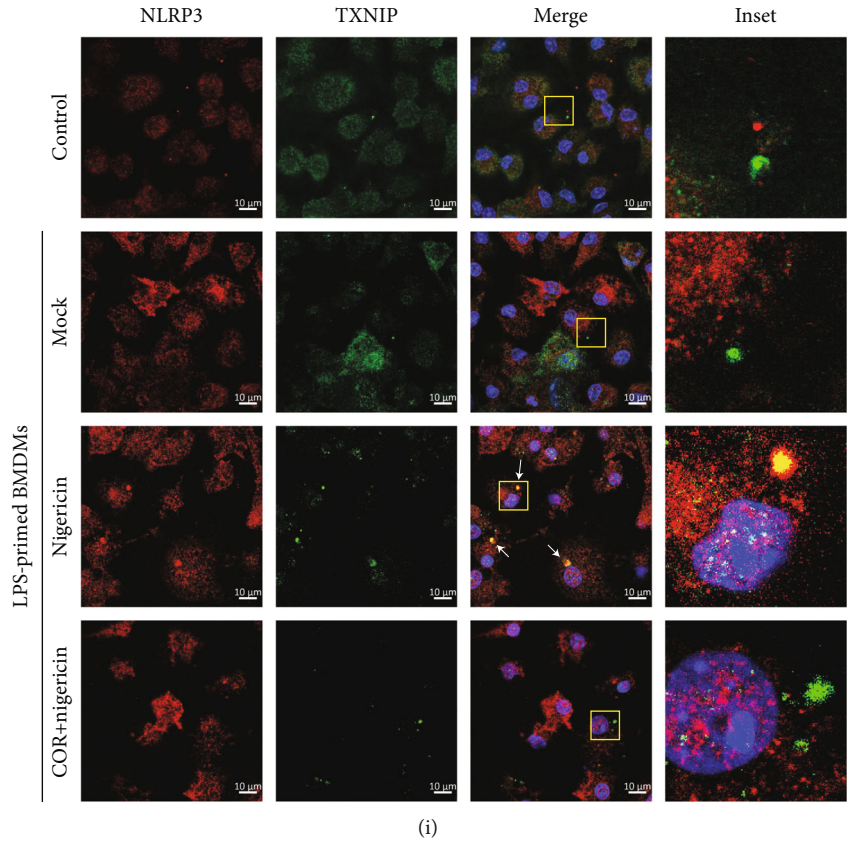

(i)

Figure 4: Corilagin decreases the production of mtROS and the NLRP3-TXNIP interaction. (a–i) LPS-primed BMDMs were incubated with or without corilagin (40 μM) for 30 min, and then stimulated with nigericin for 1 h. (a–c) MitoTracker or MitoSOX reagent stained cells for 30 min before the stimulation was complete. A confocal microscope randomly photographed multiple cell regions. (c) Quantification of representative images shown in (a and b). The quantitative statistics of mitochondrial individuals and mean branch length in (a) were represented in (d) (n =5). (e) Cellular ROS level was detected by H2DCFDA, and the relative fluorescence intensity was shown in (f). Scale bar, 10 μm. (g) Cells stained with JC-1 and captured by confocal microscopy. Scale bar, 20 μm. (h) Coimmunoprecipitation analysis of the interaction between TXNIP and NLRP3. (i) Representative fluorescent images of BMDM costained for TXNIP and NLRP3. Scale bar, 10 μm. COR: corilagin. $^{***}P < 0.001$.

from NLRP3-deficient (NLRP3$^{-/-}$) mice and wild-type (WT) mice were isolated and induced to obtain BMDMs. NLRP3 inflammasome activation was then induced with LPS and ATP or nigericin. PI staining results displayed that few cells died in NLRP3$^{-/-}$ BMDMs, and corilagin showed no noticeable antipyroptosis effect (Figures 3(a) and 3(b)). LDH release was inhibited by corilagin in ATP-activated cells but not nigericin-stimulated cells (Figure 3(c)). In addition, ASC specks were not observed in NLRP3$^{-/-}$ BMDMs (Figure 3(d)). ATP and nigericin could not trigger the generation of caspase-1 p20, mature IL-1β, and GSDMD-NT (Figures 3(e) and 3(f)). Almost no secreted IL-1β was detected in the supernatant of NLRP3$^{-/-}$ BMDMs (Figure S2). In summary, these results demonstrate that corilagin prevents NLRP3-dependent inflammasome activation and pyroptosis.

3.4. Corilagin Diminishes ROS Generation and the Interaction between TXNIP and NLRP3. Mitochondrial morphology changes cause increasing mitochondrial reactive oxygen species (mtROS). Excessive ROS induces TXNIP binding to NLRP3 and activates NLRP3 inflammasome [11]. To explore the mechanism of how corilagin inhibited NLRP3 inflammasome activation, we employed MitoTracker to identify mitochondria and MitoSOX Red to stain mtROS. Furthermore, H2DCFDA and JC-1 were used to detect intracellular ROS and mitochondrial membrane potential, respectively. Next, the interaction between TXNIP and NLRP3 was determined by Co-IP assay and immunofluorescence. Our results showed that nigericin significantly induced a fragmented mitochondrial morphology as indicated by a decrease in mitochondrial individuals and mean branch length, while corilagin restored mitochondrial morphology phenotype (Figures 4(a) and 4(d)). Consistently, corilagin reduced the production of mtROS (Figures 4(b) and 4(c)) and intracellular ROS (Figures 4(e) and 4(f)). Besides, corilagin prevented the loss of mitochondrial membrane potential in nigericin-stimulated BMDMs (Figure 4(g)). The study has proved that serine/threonine kinase NEK7 binds to NLRP3 and promotes NLRP3 inflammasome activation [18]. However, the Co-IP results showed that corilagin did not affect the interaction between NEK7 and NLRP3 (Figure S3). Furthermore, we examined the interaction between TXNIP and NLRP3 by immunofluorescence and Co-IP. As shown in

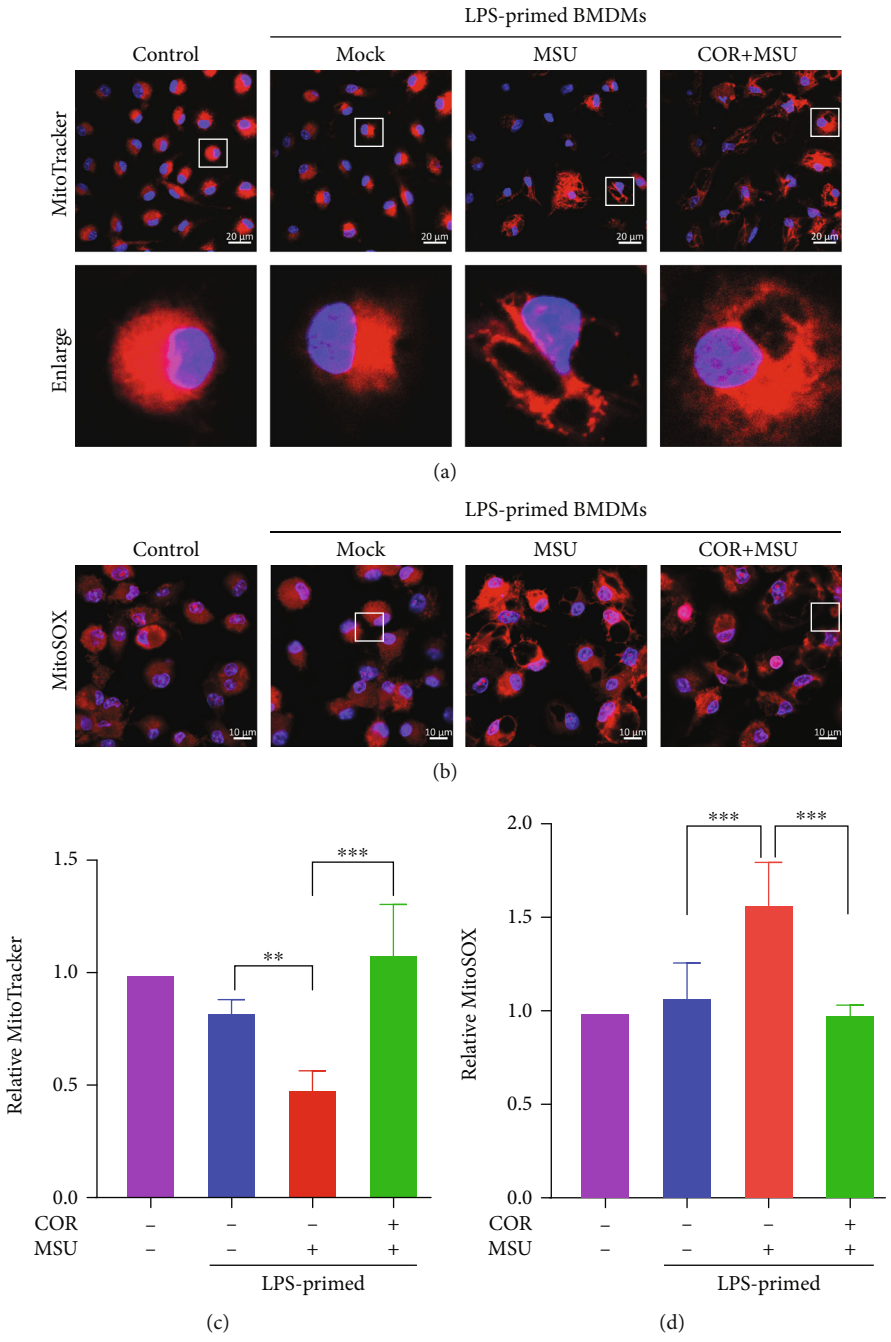

Figure 5: Continued.

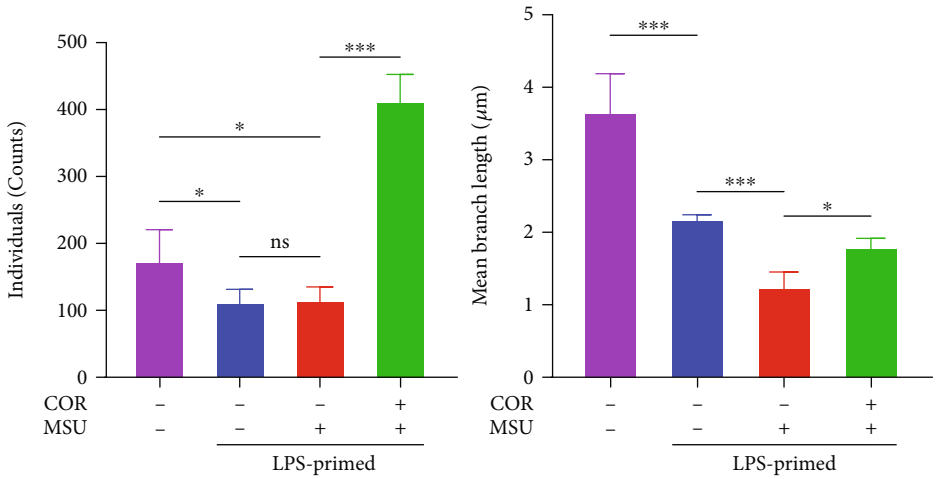

(e)

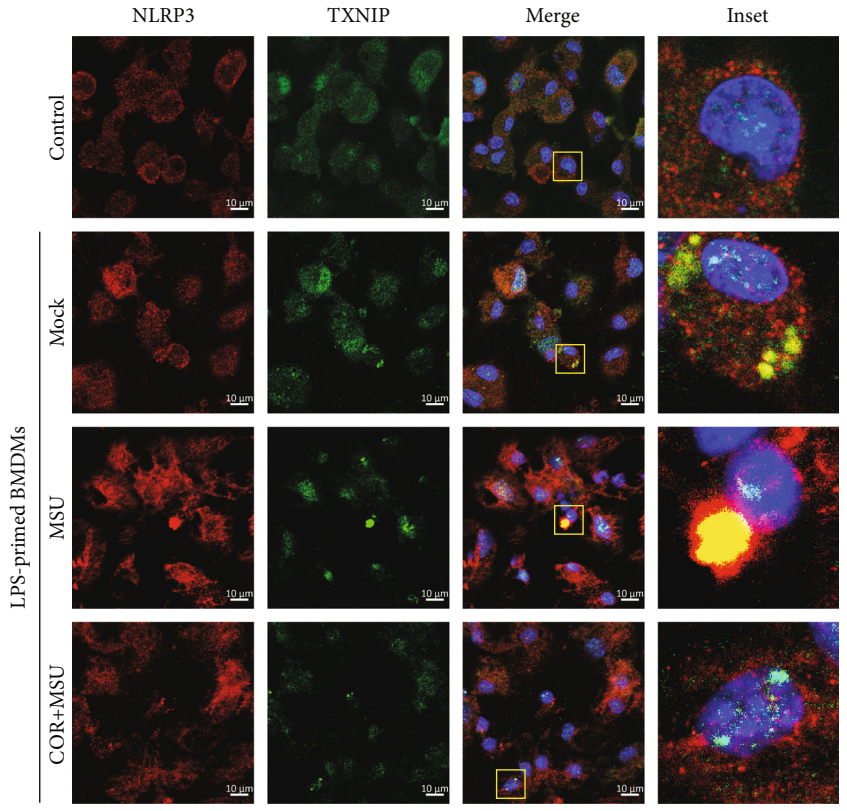

(f)

Figure 5: Continued.

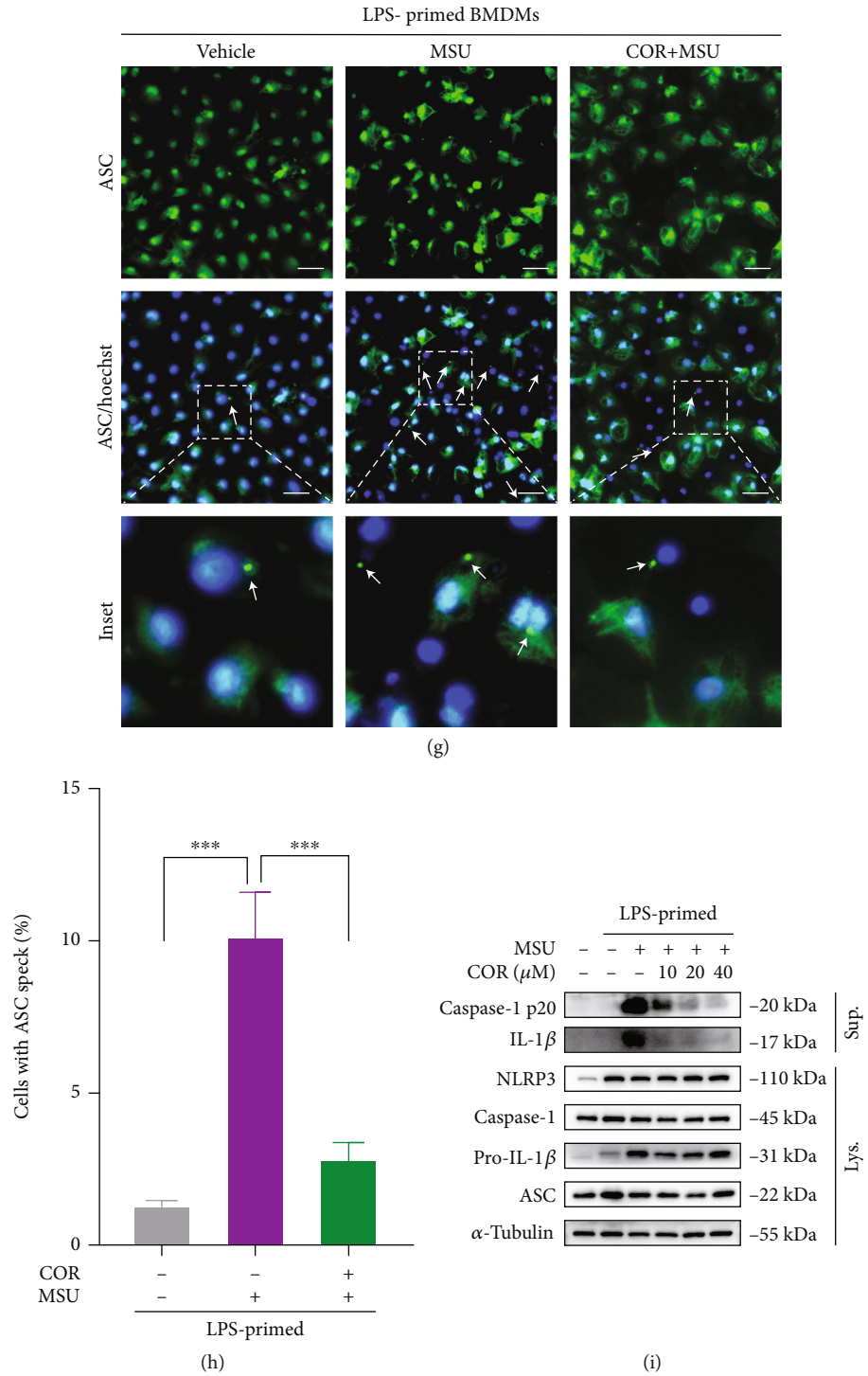

Figure 5: Corilagin inhibits MSU-induced activation of the ROS-TXNIP-NLRP3 pathway. (a–h) LPS-primed BMDMs were treated with corilagin (40 μM) for 30 min followed by stimulation with MSU (300 μg/ml) for 6 h. (a and b) The cells were stained with MitoTracker or MitoSOX for 30 min, and fluorescence images were taken by the confocal microscope. Statistical analysis of cell fluorescence intensity was shown in (c and d) ($n = 5$). (e) Histograms show the mitochondrial individuals and mean branch length in (a). (f) Immunofluorescence staining of TXNIP (green) and NLRP3 (red). Scale bar, 10 μm. (g) Immunofluorescence analysis of the subcellular distribution of ASC specks (white arrow indicator). Scale bar, 20 μm. Quantitative analysis of the percentage of ASC specks displayed in (h). (i) NLRP3 inflammasome components were analyzed by western blot. COR: corilagin. $^{**}P < 0.01$, $^{***}P < 0.001$.

Figured 4(h) and 4(i), nigericin caused the colocalization of TXNIP and NLRP3, but corilagin abolished the interaction between TXNIP and NLRP3.

To further identify whether corilagin modulates inflammasome by the ROS-TXNIP-NLRP3 pathway in MSU-stimulated BMDMs. Immunofluorescence results also

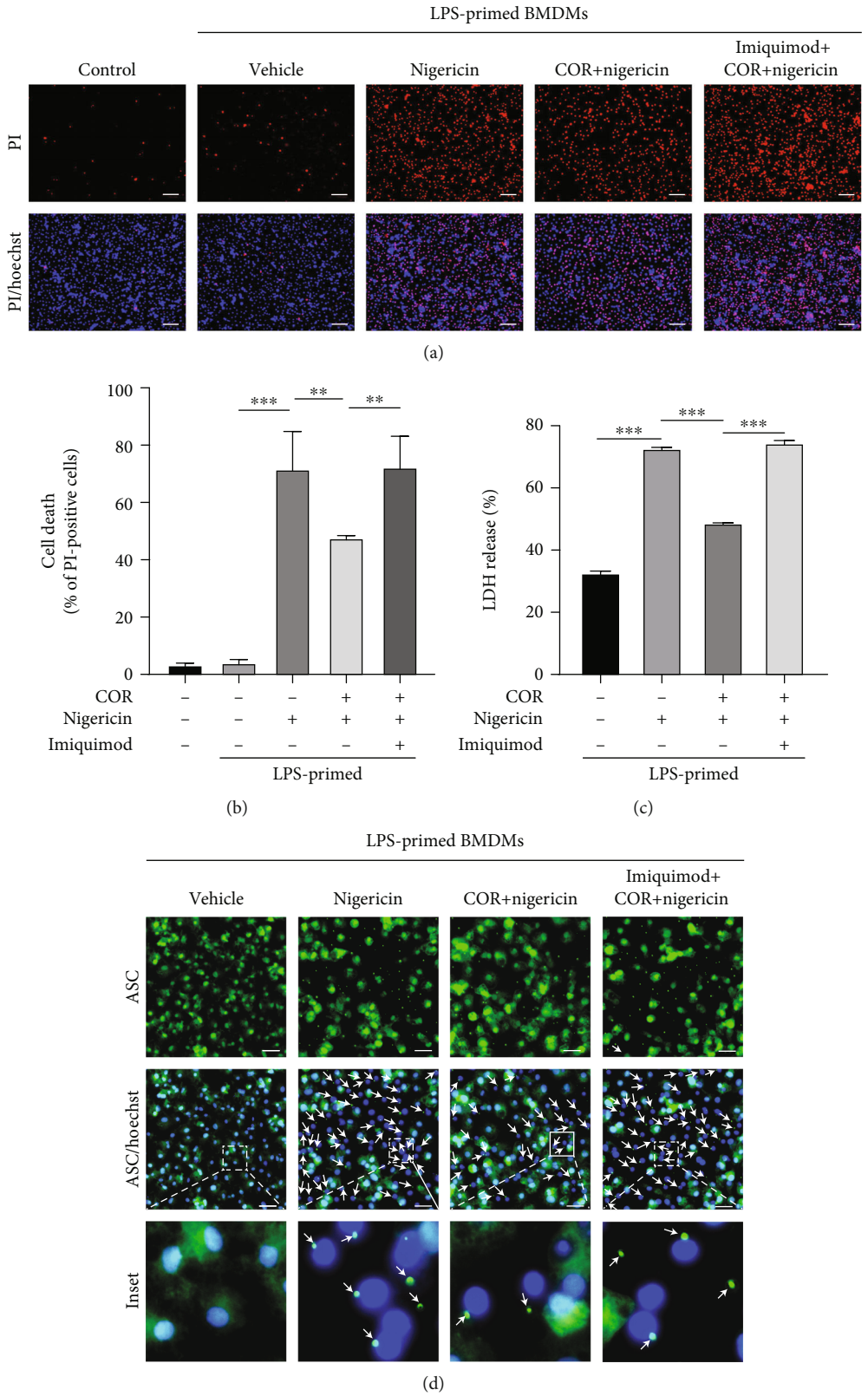

Figure 6: Continued.

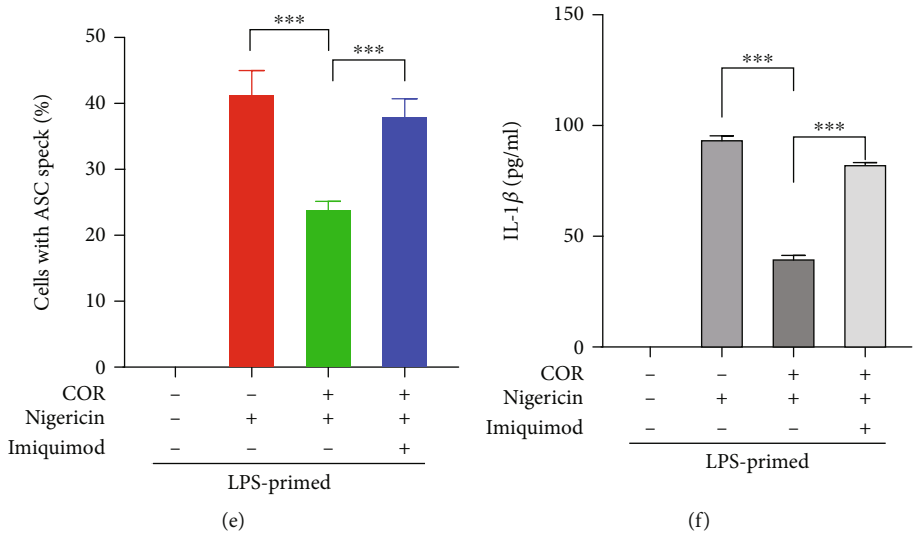

(e) (f)

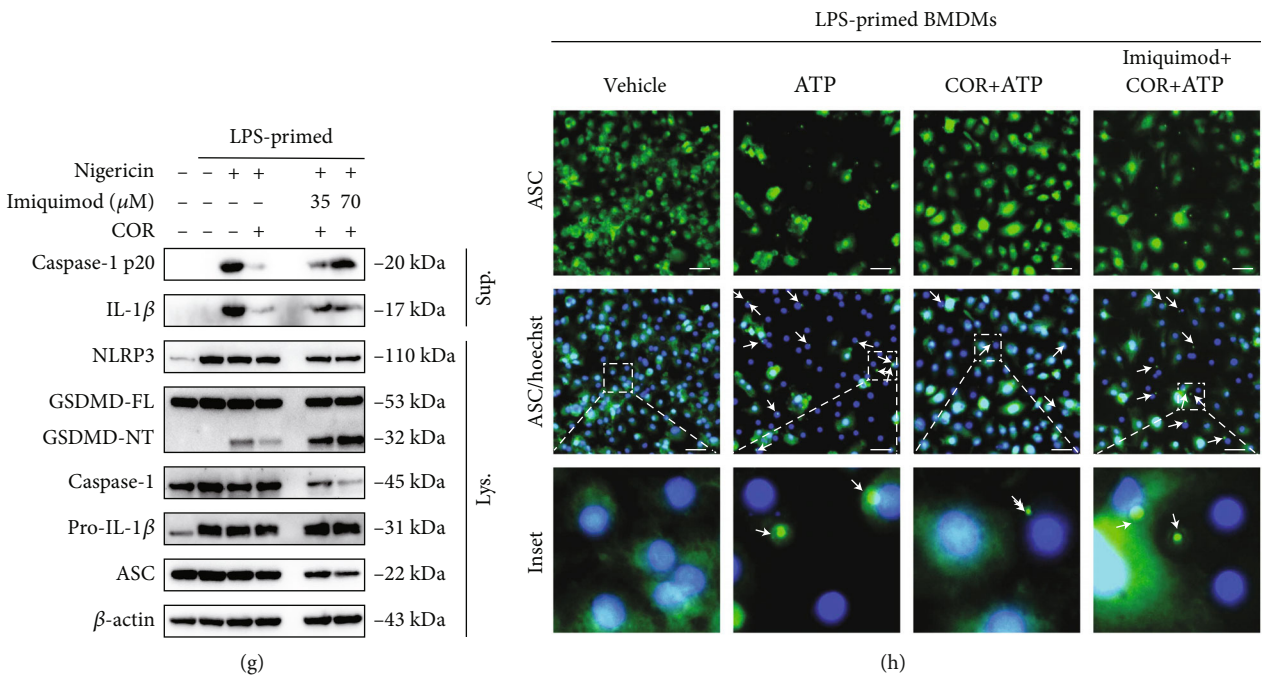

(g) (h)

Figure 6: Continued.

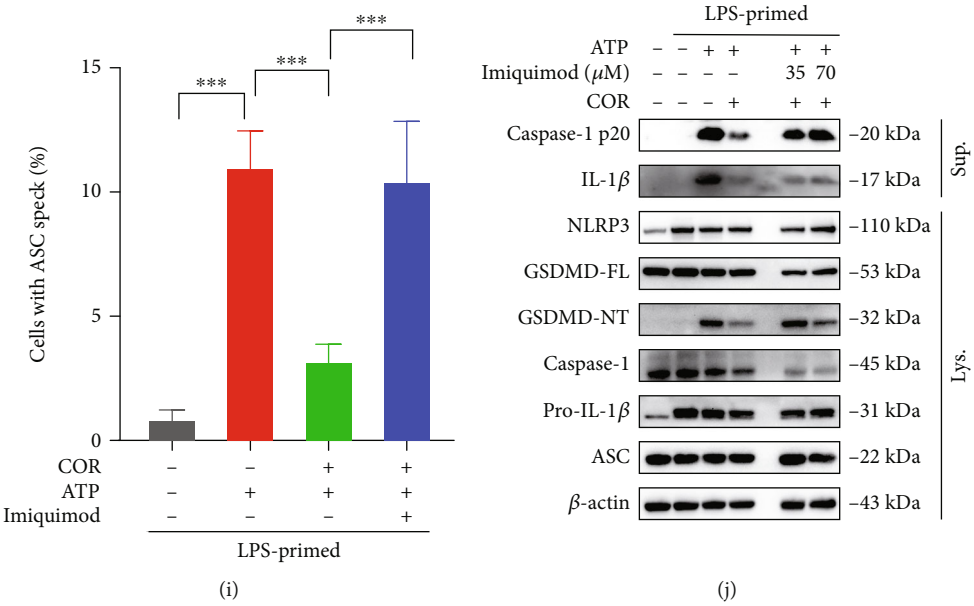

Figure 6: Imiquimod resists the inhibitory effect of corilagin on NLRP3 inflammasome activation and pyroptosis. (a–f, h and i) LPS-primed BMDMs were incubated with imiquimod (70 μM) for 30 min, treated with corilagin (40 μM) for 30 min, and then stimulated with nigericin or ATP for 1 h. (a) Representative images of cell death (PI positive) are shown in BMDMs staining with Hoechst 33342 and PI. Scale bar, 100 μm. (b) Quantification of cell death in (a). (c) Analysis of culture supernatant levels of LDH. (d and h) Representative immunofluorescence images of BMDMs stained for ASC. White arrows indicate ASC speck. Scale bar, 20 μm. (e and i) Quantification of the ASC specks in (d and h) ($n = 6$). (f) IL-1β level was assayed by ELISA kit. (g and j) Immunoblot analysis of pro- and activated (p20) caspase-1, pro- and mature IL-1β, GSDMD, NLRP3, and ASC. β-Actin was used as the internal control.

showed that corilagin inhibited MSU-induced mitochondria fragmentation to restore mitochondrial morphology phenotype (Figures 5(a), 5(c), and 5(e)) and reduced MSU-stimulated mtROS generation (Figures 5(b) and 5(d)) and NLRP3-TXNIP interaction (Figure 5(f)). In addition, corilagin prevented MSU-induced ASC speck formation (Figures 5(g) and 5(h)) and decreased the production of caspase-1 p20 and mature IL-1β in the culture medium (Figure 5(i)). Collectively, these results demonstrate that corilagin restrains TXNIP-NLRP3 interaction by inhibiting mitochondrial morphology changes and mtROS generation to prevent NLRP3 inflammasome activation.

3.5. Corilagin Inhibits Inflammasome Activation and Pyroptosis Depending on the ROS/TXNIP/NLRP3 Pathway. A variety of molecules regulate the NLRP3 inflammasome, in which the PKA signal inhibits the inflammasome by increasing the phosphorylation of NLRP3 at Ser/Thr residues [19, 20]. Nrf2 blocks NLRP3 inflammasome activation by promoting antioxidant activity [21]. We adopted the PKA inhibitor H89 and the Nrf2 inhibitor ML385, and the results showed that these two inhibitors did not counteract the effect of corilagin (Figure S4). Imiquimod can induce decreased mitochondrial respiratory activity and dynamic imbalance [22]. Imiquimod can activate the NLRP3 inflammasome by inducing ROS generation [12]. Since corilagin is a potential antioxidant, we employed imiquimod to determine whether corilagin inhibits the NLRP3 inflammasome by modulating ROS production.

Our data showed that imiquimod reversed the effect of corilagin in decreasing pyroptosis and LDH release in nigericin-stimulated BMDMs (Figures 6(a)–6(c)). Additionally, corilagin reduced ASC specks in ATP- or nigericin-stimulated BMDMs, while imiquimod restored ASC speck formation (Figures 6(d), 6(e), 6(h), and 6(i)). Imiquimod also restored IL-1β expression upon corilagin incubation in LPS- and nigericin-treated cells (Figure 6(f)). Moreover, corilagin restrained caspase-1 p20, mature IL-1β, and GSDMD-NT production, while imiquimod antagonized the function of corilagin. (Figures 6(g) and 6(j)). Overall, we conclude that imiquimod resists the inhibitory function of corilagin on NLRP3 inflammasome activation and macrophage pyroptosis.

Imiquimod can significantly increase the production of mitochondrial ROS [23]. However, whether imiquimod neutralizes the effect of corilagin via the mitochondrial ROS pathway remains unknown. Upon nigericin or MSU stimulation, LPS-primed macrophages were incubated with or without imiquimod, followed by treated with corilagin. MitoTracker fluorescence images showed that corilagin protected macrophages from nigericin- and MSU-induced mitochondrial morphology changes, while imiquimod antagonized the effect of corilagin and exacerbated mitochondrial morphology fragmentation (Figures 7(a), 7(c), 7(d), and 7(f)). MitoSOX fluorescence images showed that corilagin could reduce mtROS levels, while imiquimod enhanced mtROS generation in the presence of corilagin (Figures 7(b), 7(c), 7(e), and 7(f)). Immunoprecipitation results revealed that corilagin inhibited MSU-induced TXNIP binding to NLRP3, while imiquimod promoted the TXNIP-NLRP3 interaction (Figure 7(g)). These results demonstrate that imiquimod abrogates the effect of

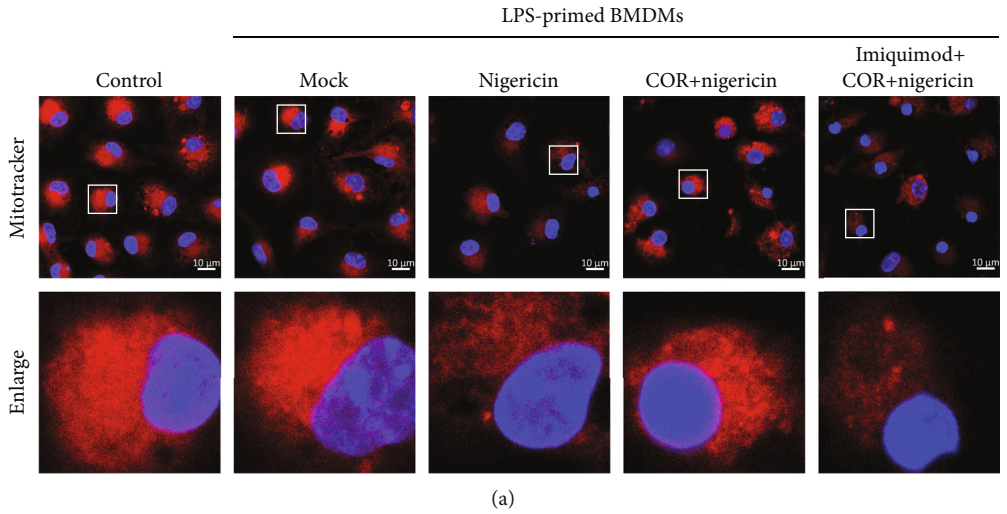

(a)

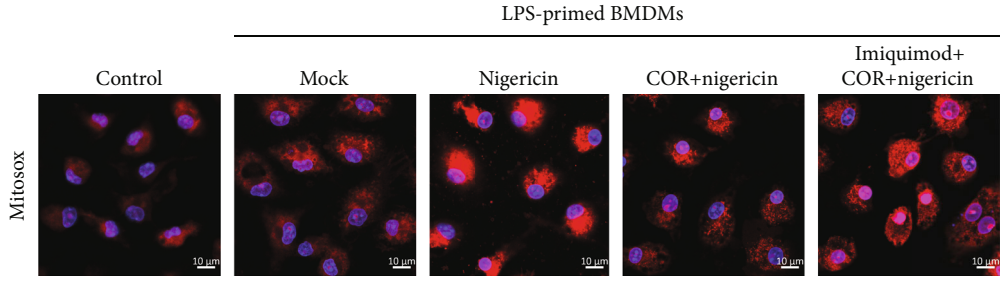

(b)

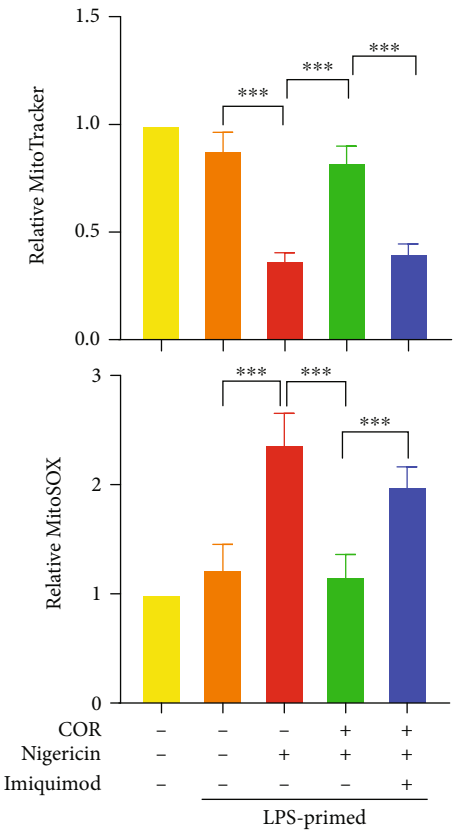

(c)

Figure 7: Continued.

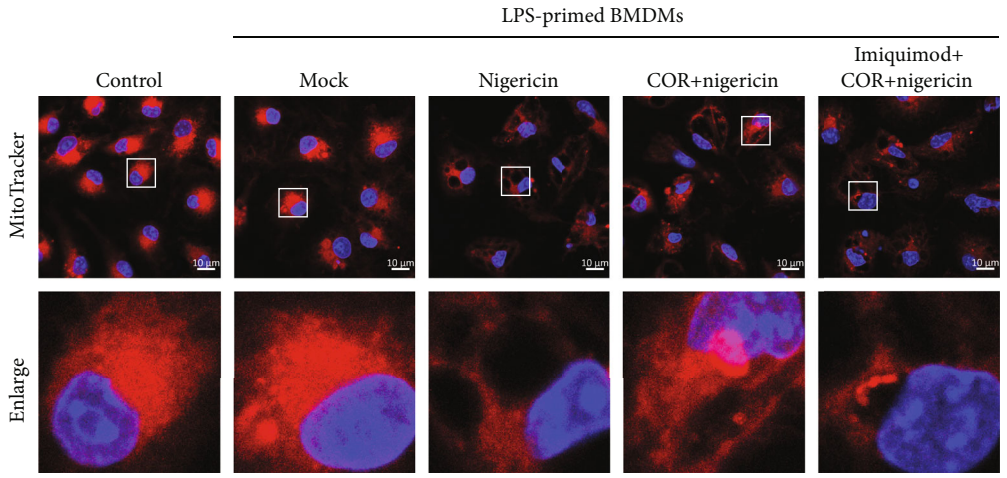

(d)

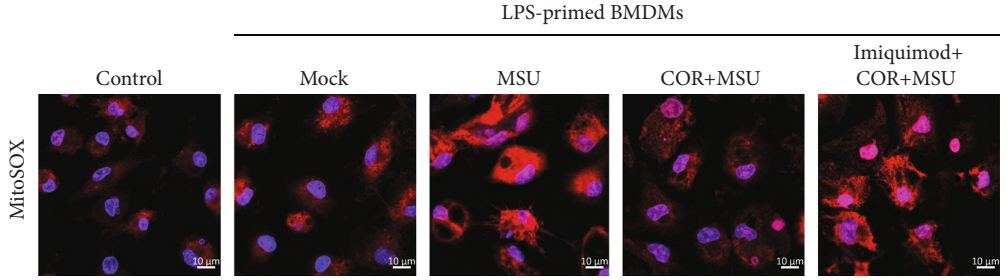

(e)

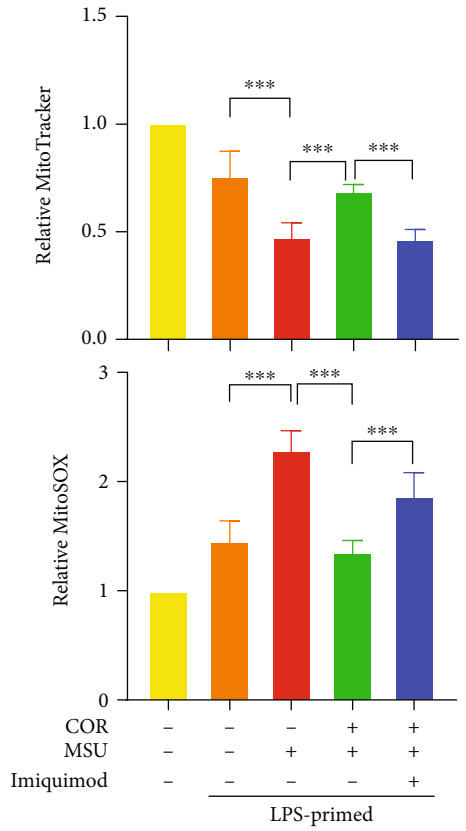

(f)

Figure 7: Continued.

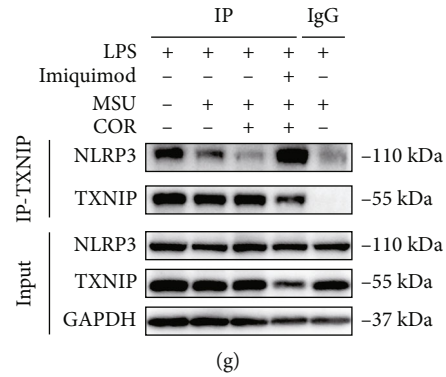

(g)

Figure 7: Imiquimod counteracts the effect of corilagin by activating the ROS/TXNIP/NLRP3 pathway. (a–g) LPS-primed BMDMs were treated with corilagin (40 μM) in the presence or absence of imiquimod (70 μM), and then stimulated with MSU. (a and b, d and e) BMDMs were stained with MitoTracker or MitoSOX for 30 min. Fluorescence images were taken by the confocal laser scanning microscope. Scale bar, 10 μm. (c and f) The relative fluorescence intensity of MitoTracker or MitoSOX was analyzed and normalized to the control ($n = 5$). (g) Immunoprecipitation analysis of the interaction between TXNIP and NLRP3. COR: corilagin. $^{***}P < 0.001$.

corilagin on reducing mitochondrial morphology changes and mtROS generation, further confirming that corilagin inhibits inflammasome activation partly through the ROS/TXNIP/NLRP3 pathway.

3.6. Corilagin Ameliorates Monosodium Urate Crystals-Induced Gouty Arthritis. MSU crystals can motivate the activation of NLRP3 inflammasome, which triggers the gout flare. We have demonstrated that corilagin can effectively inhibit MSU-stimulated NLRP3 inflammasome activation *in vitro*. Therefore, MSU crystals-caused gouty arthritis were employed to explore the anti-inflammation activity of corilagin *in vivo,* and colchicine was taken as the positive control. The results reveal that corilagin alleviates MSU crystals-caused knee swelling in mice (Figure 8(a)). ELISA was applied to detect inflammatory cytokines in the culture supernatant of the isolated knee joint. We found that both corilagin and colchicine could reduce IL-1β and TNF-α generation (Figures 8(b) and 8(c)). We also observed that corilagin and colchicine restrained MSU-induced inflammatory cell infiltration (Figure 8(d)). Immunohistochemical results showed that corilagin and colchicine decreased the production of IL-1β and caspase-1 p20 in the joint tissue (Figure 8(e)).

To further determine which inflammatory cells gather, the joint tissue was stained with Ly-6G (neutrophil marker) antibody or F4/80 (macrophage marker) antibody. The immunofluorescence image results showed that MSU attracted the neutrophils and macrophages aggregation in the joint, but corilagin and colchicine reduced the accumulation of these inflammatory cells (Figure 8(f)). Collectively, we conclude that corilagin alleviates MSU crystals-caused gouty arthritis by restraining NLRP3 inflammasome activation, inflammatory cytokines expression, and immune cell infiltration.

4. Discussion

Colchicine, NSAIDs, or glucocorticoids are often used as first-line drugs to treat gout flares, but several patients have poor tolerance or contraindications to these common anti-inflammatory therapies. Here, we find that corilagin, a compound derived from traditional Chinese medicine, alleviates MSU-induced acute gouty arthritis by preventing NLRP3 inflammasome and reducing IL-1β production and immune cell infiltration, and no significant adverse reactions were observed. We provide evidence that corilagin inhibits the interaction between TXNIP and NLRP3 by reducing mitochondrial morphology changes and ROS generation. Ultimately, corilagin suppresses NLRP3 inflammasome activation and the subsequent release of mature IL-1β.

Corilagin has been demonstrated to prevent inflammation by inhibiting the production of proinflammatory cytokines such as IL-1β and TNF-α [24]. In addition, corilagin exerts its potent antioxidant effect by decreasing ROS expression [25–27]. Consistent with the previous studies, we find that corilagin significantly prevents inflammasome activation and IL-1β expression (Figures 1, 2, and 5), and this effect depended on NLRP3 (Figure 3). Excessive mitochondrial ROS promotes TXNIP binding to NLRP3 and thus induces NLRP3 inflammasome activation [10, 11]. We show herein that corilagin limits mitochondria morphology changes, reduces mtROS generation, and prevents the interaction between TXNIP and NLRP3. (Figures 4 and 5). These findings suggest that corilagin suppresses NLRP3 inflammasome activation through the ROS/TXNIP/NLRP3 pathway. Lian et al. also confirmed that ROS/TXNIP/NLRP3 is a critical priming signaling pathway for periodontitis [28]. Metformin has been shown to inhibit TXNIP expression and the interaction between TXNIP and NLRP3 and decrease caspase-1 and GSDMD-NT expression, thereby protecting barrier function from intestinal ischemia-reperfusion injury and abating oxidative stress and inflammation [29]. These results reveal that targeting the ROS/TXNIP/NLRP3 pathway could be a potential anti-inflammation strategy. Imiquimod, a ROS activator, can reverse the inhibitory function of corilagin on the NLRP3 inflammasome and macrophage pyroptosis (Figure 6). Furthermore, imiquimod promotes the binding of TXNIP to NLRP3 by inducing mitochondrial

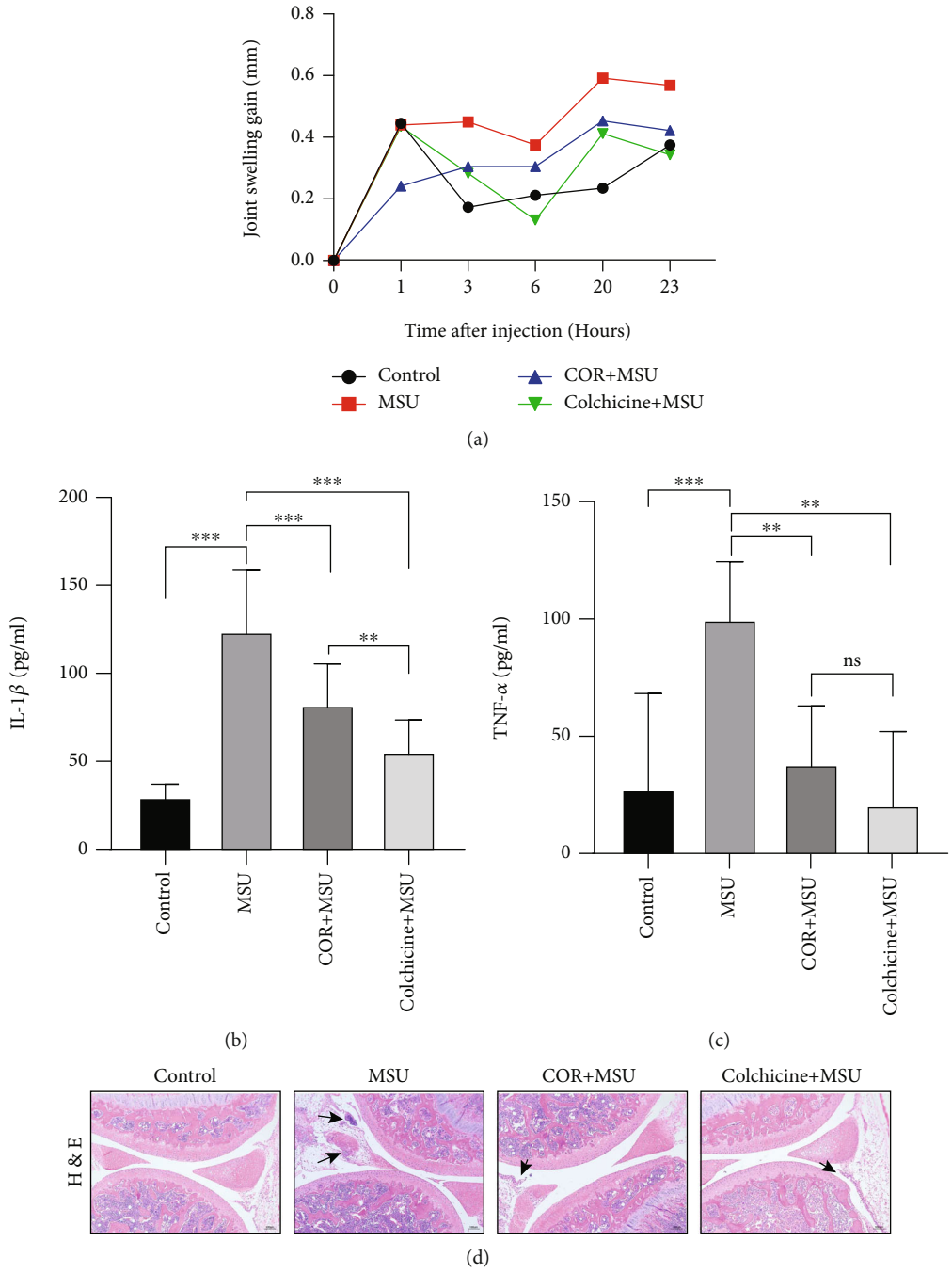

Figure 8: Continued.

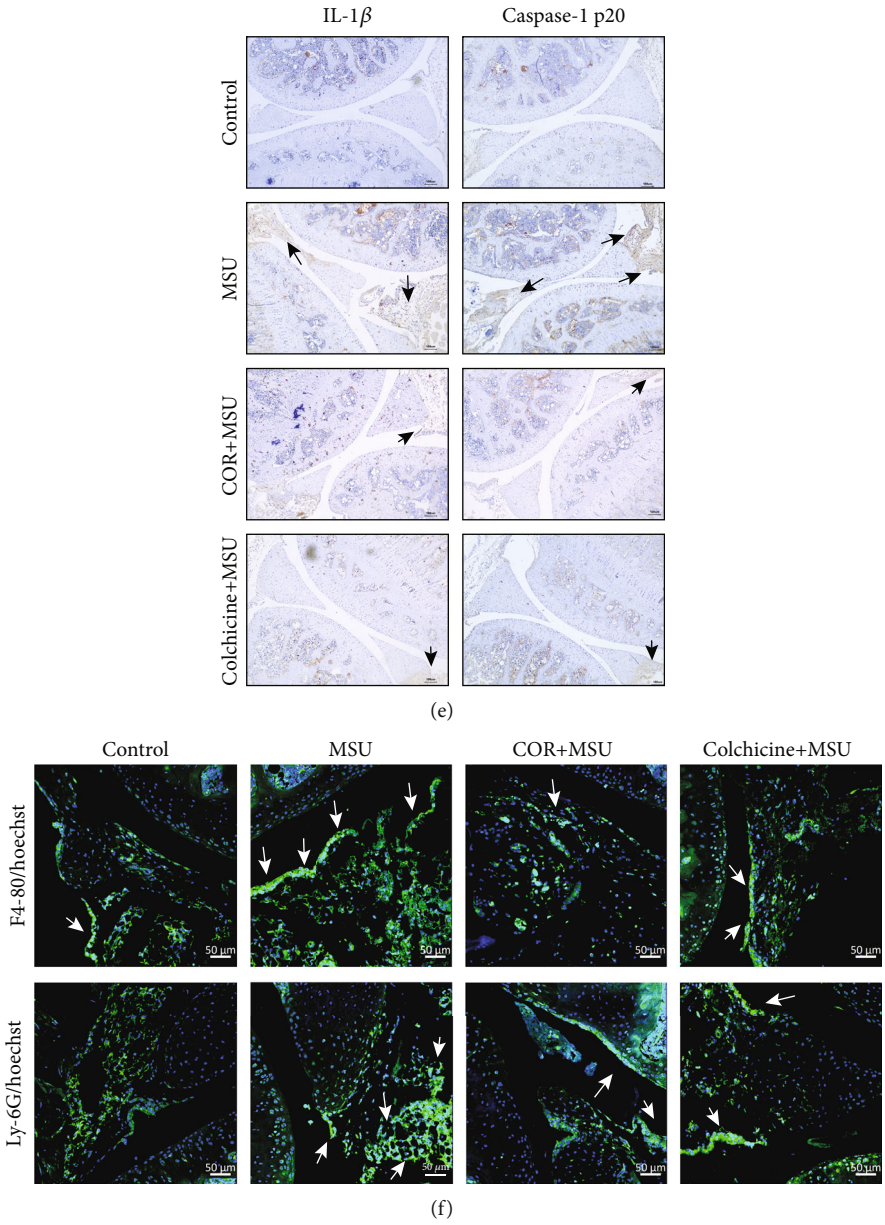

Figure 8: Corilagin relieves MSU-induced arthritis in C57BL/6 J mice. (a–g) C57BL/6 J mice were intraperitoneal injection with corilagin (20 mg/kg) or colchicine (1 mg/kg), and then MSU crystals were injected into the knee joint for 24 h. (a) Joint swelling was measured at different times. (b and c) Levels of IL-1β and TNF-α were detected by ELISA kits ($n = 6$). (d) H&E staining of knee joint section. Black arrows indicate cell infiltration. Scale bar, 100 μm. (e) Immunohistochemistry analysis for IL-1β and caspase-1 p20. Scale bar, 100 μm. (f) Immunofluorescence staining of F4/80 and Ly-6G in joint sections. Scale bar, 50 μm. $^{***}P < 0.001$.

morphology changes and ROS production (Figure 7). Our results preliminarily proved that corilagin limited NLRP3 inflammasome activation and the macrophage pyroptosis through antioxidant effects.

Multiple molecules and pathways regulate the NLRP3 inflammasome. NEK7, a serine/threonine kinase is an integral part of the NLRP3 inflammasome. NEK7 binds to the inflammasome by binding to the LRR domain of NLRP3, which is necessary for the activation of the NLRP3 inflammasome [18]. However, the Co-IP analysis results revealed that corilagin did not prevent the interaction between NEK7 and NLRP3 (Figure S3). In addition, our previous studies have proved that wedelolactone increases Ser/Thr phosphorylation of NLRP3 by enhancing the PKA signal, thereby impeding NLRP3 inflammasome activation and macrophage pyroptosis. Meanwhile, the PKA inhibitor H89 can reverse the function of wedelolactone [16]. Gallic acid enhances Nrf2 signaling and reduces mtROS production to limit NLRP3 inflammasome activation, while the Nrf2 inhibitor ML385 antagonizes the effect of gallic acid [17]. Cells were treated with H89 and ML385 during stimulation. However, these two inhibitors could not

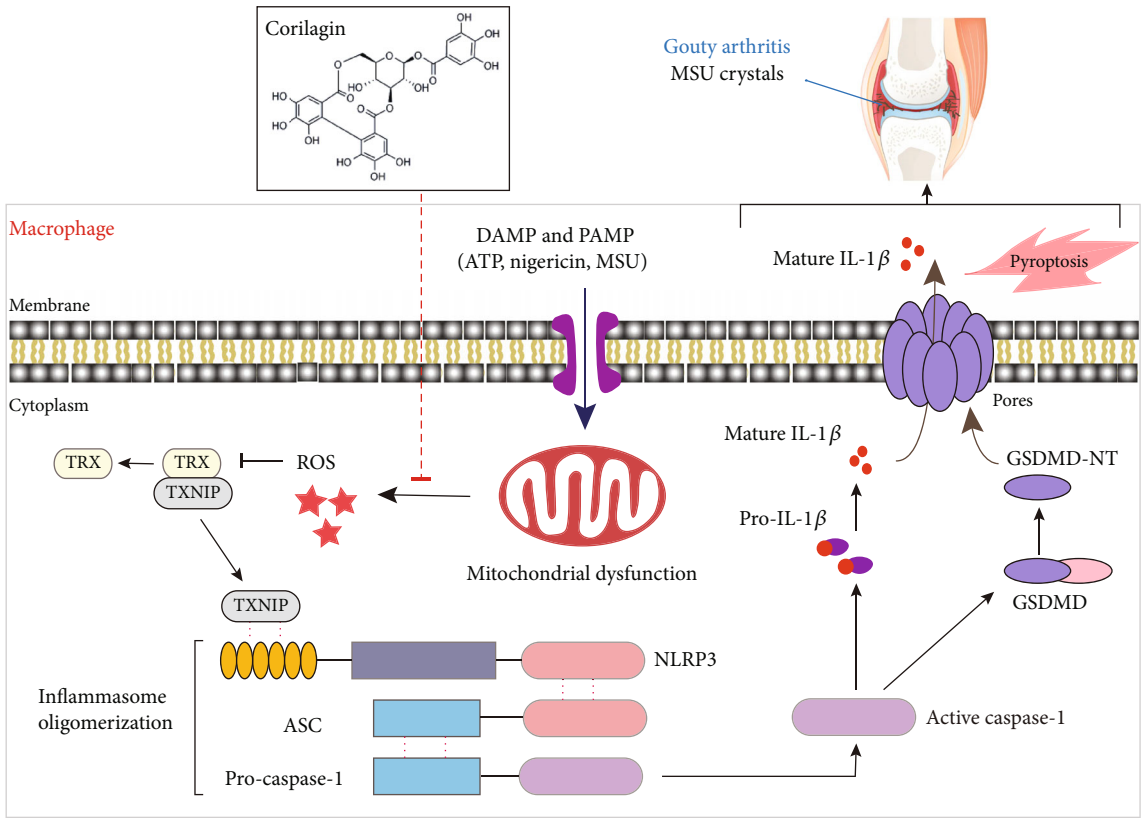

Figure 9: The proposed mechanism. Corilagin restrains NLRP3 inflammasome activation and IL-1β secretion to prevent MSU-induced inflammation.

counteract the effect of corilagin (Figure S4). The results conclude that corilagin obstructs NLRP3 inflammasome independent of the PKA or Nrf2 pathway.

Colchicine, a microtubule-depolymerizing agent used in the prevention and treatment of acute gout attacks, reduces the MSU crystals-induced painful inflammatory response in joints [13]. However, colchicine often causes gastrointestinal and other adverse reactions. The *in vivo* results suggest that the gastrointestinal reactions of corilagin are significantly lower than in colchicine treated group. Corilagin reduces immune cell infiltration and inflammatory symptoms in MSU-induced acute gouty arthritis (Figure 8). Corilagin mainly inhibits the infiltration of macrophages and neutrophils by blocking NLRP3 activation and IL-1β release. Although corilagin treats gouty arthritis by obstructing the NLRP3 inflammasome, the *in vivo* function of corilagin in mediating the ROS/TXNIP/NLRP3 pathway remains unclear. In addition, it is also unclear whether corilagin can lower serum uric acid. Corilagin displays extensive pharmacological activities in cells and mice models. One study indicated that corilagin (100 μM) displayed no cytotoxicity to human normal cells (LO2, BEAS-2B, and HEK293). Moreover, oral administration of corilagin (300 mg/kg) showed no apparent toxicity or detrimental effects, mice body weight and organ weight also did not change significantly [30]. However, there are fewer clinical trials of corilagin *in vivo*. Therefore, the safety and clinical transformation of corilagin in humans deserve further study.

In summary, we confirm that corilagin inhibits the NLRP3 inflammasome and pyroptosis by protecting mitochondrial integrity, reducing mitochondrial ROS production, and preventing the interaction between TXNIP and NLRP3. In addition, we have proved that corilagin can reduce inflammatory cytokines expression and immune cell infiltration during acute gouty arthritis flares (Figure 9). These results provide a reliable pharmacological basis for preclinical studies. As one of the active ingredients of natural medicine, the safety of corilagin is also guaranteed. Therefore, corilagin possesses excellent potential to treat NLRP3-dependent inflammatory diseases such as gout, diabetes, sepsis, and cancer.

Data Availability

All data supporting the findings of this study were shown in this manuscript and its supplementary materials.

Conflicts of Interest

All authors declare that they have no competing financial interests.

Authors' Contributions

Tianyu Luo and Xiaoyi Zhou performed almost all the experiments and analyzed the data. Minyan Qin, Yuqing

Lin, and Jiefen Lin assisted in some animal experiments. Guangpei Chen, Dongyun Ouyang, and Aijun Liu contributed essential reagents and discussed the results. Dongfeng Chen and Hao Pan designed the project and wrote the article. Tianyu Luo and Xiaoyi Zhou contributed equally to this work.

Acknowledgments

This research was supported by the Administration of Traditional Chinese Medicine of Guangdong Province (20221124), the National Natural Science Foundation of China (82004026), Guangdong Basic and Applied Basic Research Foundation (2019A1515110613), the Science and Technology Program of Guangzhou (202102020540), and the Natural Science Foundation of Guangdong Province (2017A030312009).

Supplementary Materials

Figure S1: Corilagin does not inhibit TLR4/NF-κB signaling pathway. Figure S2: NLRP3$^{-/-}$ BMDMs do not secrete IL-1β. Figure S3: Corilagin does not affect the binding of NKE7 and NLRP3. Figure S4: Corilagin inhibits NLRP3 inflammasome activation independent of PKA or Nrf2 signaling. *(Supplementary Materials)*

References

[1] X. Li, Y. Deng, Z. Zheng et al., "Corilagin, a promising medicinal herbal agent," *Biomedicine & Pharmacotherapy*, vol. 99, pp. 43–50, 2018.

[2] N. Wu, Y. Zu, Y. Fu et al., "Antioxidant activities and xanthine oxidase inhibitory effects of extracts and main polyphenolic compounds obtained from Geranium sibiricum L," *Journal of Agricultural and Food Chemistry*, vol. 58, no. 8, pp. 4737–4743, 2010.

[3] L. Zhao, S. L. Zhang, J. Y. Tao et al., "Preliminary exploration on anti-inflammatory mechanism of corilagin (beta-1- *O* -galloyl-3,6-(*R*)-hexahydroxydiphenoyl-d-glucose) *in vitro*," *International Immunopharmacology*, vol. 8, no. 7, pp. 1059–1064, 2008.

[4] H. Yuan, J. Zhang, X. Yin et al., "The protective role of corilagin on renal calcium oxalate crystal-induced oxidative stress, inflammatory response, and apoptosis via PPAR-γ and PI3K/Akt pathway in rats," *Biotechnology and Applied Biochemistry*, vol. 68, no. 6, pp. 1323–1331, 2020.

[5] H. R. Li, J. Liu, S. L. Zhang et al., "Corilagin ameliorates the extreme inflammatory status in sepsis through TLR4 signaling pathways," *BMC Complementary and Alternative Medicine*, vol. 17, no. 1, p. 18, 2017.

[6] B. R. Sharma and T. D. Kanneganti, "NLRP3 inflammasome in cancer and metabolic diseases," *Nature Immunology*, vol. 22, no. 5, pp. 550–559, 2021.

[7] Y. He, H. Hara, and G. Núñez, "Mechanism and regulation of NLRP3 inflammasome activation," *Trends in Biochemical Sciences*, vol. 41, no. 12, pp. 1012–1021, 2016.

[8] W. T. He, H. Wan, L. Hu et al., "Gasdermin D is an executor of pyroptosis and required for interleukin-1β secretion," *Cell Research*, vol. 25, no. 12, pp. 1285–1298, 2015.

[9] R. C. Coll, C. L. Holley, and K. Schroder, "Mitochondrial DNA synthesis fuels NLRP3 inflammasome," *Cell Research*, vol. 28, no. 11, pp. 1046-1047, 2018.

[10] K. E. Lawlor and J. E. Vince, "Ambiguities in NLRP3 inflammasome regulation: is there a role for mitochondria?," *Biochimica et Biophysica Acta*, vol. 1840, no. 4, pp. 1433–1440, 2014.

[11] J. Tschopp and K. Schroder, "NLRP3 inflammasome activation: the convergence of multiple signalling pathways on ROS production?," *Nature Reviews. Immunology*, vol. 10, no. 3, pp. 210–215, 2010.

[12] C. J. Gross, R. Mishra, K. S. Schneider et al., "K^+ efflux-independent NLRP3 inflammasome activation by small molecules targeting mitochondria," *Immunity*, vol. 45, no. 4, pp. 761–773, 2016.

[13] N. Dalbeth, H. K. Choi, L. A. B. Joosten et al., "Gout," *Disease Primers*, vol. 5, no. 1, 2019.

[14] R. Zhou, A. Tardivel, B. Thorens, I. Choi, and J. Tschopp, "Thioredoxin-interacting protein links oxidative stress to inflammasome activation," *Nature Immunology*, vol. 11, no. 2, pp. 136–140, 2010.

[15] E. Yoshihara, S. Masaki, Y. Matsuo, Z. Chen, H. Tian, and J. Yodoi, "Thioredoxin/TXNIP: redoxisome, as a redox switch for the pathogenesis of diseases," *Frontiers in Immunology*, vol. 4, p. 514, 2014.

[16] H. Pan, Y. Lin, J. Dou et al., "Wedelolactone facilitates Ser/Thr phosphorylation of NLRP3 dependent on PKA signalling to block inflammasome activation and pyroptosis," *Cell Proliferation*, vol. 53, no. 9, article e12868, 2020.

[17] Y. Lin, T. Luo, A. Weng et al., "Gallic acid alleviates gouty arthritis by inhibiting NLRP3 inflammasome activation and pyroptosis through enhancing Nrf2 signaling," *Frontiers in Immunology*, vol. 11, article 580593, 2020.

[18] H. Shi, Y. Wang, X. Li et al., "NLRP3 activation and mitosis are mutually exclusive events coordinated by NEK7, a new inflammasome component," *Nature Immunology*, vol. 17, no. 3, pp. 250–258, 2016.

[19] L. Mortimer, F. Moreau, J. A. MacDonald, and K. Chadee, "NLRP3 inflammasome inhibition is disrupted in a group of auto-inflammatory disease CAPS mutations," *Nature Immunology*, vol. 17, no. 10, pp. 1176–1186, 2016.

[20] C. Guo, S. Xie, Z. Chi et al., "Bile acids control inflammation and metabolic disorder through inhibition of NLRP3 inflammasome," *Immunity*, vol. 45, no. 4, pp. 802–816, 2016.

[21] P. Hennig, M. Garstkiewicz, S. Grossi, M. Di Filippo, L. E. French, and H. D. Beer, "The crosstalk between Nrf2 and inflammasomes," *International Journal of Molecular Sciences*, vol. 19, no. 2, p. 562, 2018.

[22] K. C. Chuang, C. R. Chang, S. H. Chang et al., "Imiquimod-induced ROS production disrupts the balance of mitochondrial dynamics and increases mitophagy in skin cancer cells," *Journal of Dermatological Science*, vol. 98, no. 3, pp. 152–162, 2020.

[23] H. J. Lee, S. J. Kang, Y. Woo, T. W. Hahn, H. J. Ko, and Y. J. Jung, "TLR7 stimulation with imiquimod induces selective autophagy and controls mycobacterium tuberculosis growth in mouse macrophages," *Frontiers in Microbiology*, vol. 11, p. 1684, 2020.

[24] Y. J. Guo, L. Zhao, X. F. Li et al., "Effect of corilagin on anti-inflammation in HSV-1 encephalitis and HSV-1 infected microglias," *European Journal of Pharmacology*, vol. 635, no. 1-3, pp. 79–86, 2010.

[25] S. Kinoshita, Y. Inoue, S. Nakama, T. Ichiba, and Y. Aniya, "Antioxidant and hepatoprotective actions of medicinal herb, *Terminalia catappa* L. from Okinawa Island and its tannin corilagin," *Phytomedicine*, vol. 14, no. 11, pp. 755–762, 2007.

[26] J. Xu, G. Zhang, Y. Tong, J. Yuan, Y. Li, and G. Song, "Corilagin induces apoptosis, autophagy and ROS generation in gastric cancer cells in vitro," *International Journal of Molecular Medicine*, vol. 43, no. 2, pp. 967–979, 2019.

[27] H. Lv, L. Hong, Y. Tian, C. Yin, C. Zhu, and H. Feng, "Corilagin alleviates acetaminophen-induced hepatotoxicity via enhancing the AMPK/GSK3β-Nrf2 signaling pathway," *Cell Communication and Signaling: CCS*, vol. 17, no. 1, 2019.

[28] D. Lian, L. Dai, Z. Xie et al., "Periodontal ligament fibroblasts migration injury via ROS/TXNIP/Nlrp3 inflammasome pathway with *Porphyromonas gingivalis* lipopolysaccharide," *Molecular Immunology*, vol. 103, pp. 209–219, 2018.

[29] Y. Jia, R. Cui, C. Wang et al., "Metformin protects against intestinal ischemia-reperfusion injury and cell pyroptosis via TXNIP-NLRP3-GSDMD pathway," *Redox Biology*, vol. 32, article 101534, 2020.

[30] L. J. Yang, R. H. Chen, S. Hamdoun et al., "Corilagin prevents SARS-CoV-2 infection by targeting RBD-ACE2 binding," *Phytomedicine*, vol. 87, article 153591, 2021.

Hindawi
Oxidative Medicine and Cellular Longevity
Volume 2022, Article ID 9251835, 15 pages
https://doi.org/10.1155/2022/9251835

Research Article

HSPB8 Overexpression Ameliorates Cognitive Impairment in Diabetic Mice via Inhibiting NLRP3 Inflammation Activation

Yanmin Chang,[1] Yanqing Wu,[1] Xingjun Jiang,[1] Jiahui Zhu,[1] Cailin Wang,[1] Rong Ma,[2] and Gang Li[1]

[1]*Department of Neurology, Union Hospital, Tongji Medical College, Huazhong University of Science and Technology, Wuhan, China*
[2]*Department of Pharmacology, Tongji Medical College, Huazhong University of Science and Technology, Wuhan, China*

Correspondence should be addressed to Rong Ma; marong1109@163.com and Gang Li; gangli2008@hotmail.com

Received 9 March 2022; Revised 20 June 2022; Accepted 19 July 2022; Published 1 August 2022

Academic Editor: Tao Zheng

Type 2 diabetes mellitus (T2DM) is associated with an elevated risk of cognitive impairment. And the underlying mechanism remains unillustrated. HSPB8 is a member of the small heat shock protein family. In this study, we found that the expression of HSPB8 was upregulated in the hippocampus of high – fat diet (HFD) + streptozotocin (STZ) – induced diabetic mice and N2a cells exposed to high glucose. Overexpression of HSPB8 relieved cognitive decline in DM mice. Mechanically, HSPB8 overexpression in the hippocampus of diabetic mice inhibited NOD-like receptor protein 3 (NLRP3) inflammasome activation via dephosphorylating mitochondrial fission-associated protein dynamin-related protein 1 (DRP1) at the phosphorylated site Ser616 (p-Drp1S616). Furthermore, HSPB8 overexpression increased mitochondrial membrane potential (MMP) and reduced oxidative stress. These results indicate a protective effect of HSPB8 in the hippocampus of diabetic mice and N2a cells exposed to high glucose. Overexpression of HSPB8 might be a useful strategy for treating T2DM-related cognitive decline.

1. Introduction

Diabetes mellitus is a common metabolic disorder that can cause multiple comorbidities, such as nephropathy, cardiovascular disease, and retinopathy [1]. Additionally, people with type 2 diabetes mellitus perform poorly on learning and memory tests [2]. Due to the diabetes pandemic and the concomitant rise in the aging population worldwide, diabetes-related cognitive dysfunction substantially affects society and seriously affects patients' quality of life and has received significant attention [3]. But the potential mechanisms underlying Type 2 diabetes mellitus (T2DM) related cognitive decline remain elusive. Therefore, it is urgent to clarify the pathogenesis of diabetes-related cognitive decline and find effective prevention and treatment strategies.

HSPB8, Heat shock protein 22 (HSP22), known as H11 kinase, E21G1, is a member of the small HSP family of proteins containing an α-crystalline domain and has been demonstrated to have a protective effect against various conditions including oxidative stress, aging, cancer, and apoptosis [4–7]. Notably, HSPB8 could regulate mitochondrial biogenesis and prevent excessive mitochondrial fission [5].

Mitochondria are dynamic organelles providing necessary energy for cells. The morphology of these organelles can make adaptive changes according to the needs of the cells and undergo continuous fusion and fission. Mitochondrial fusion and fission defects would cause mitochondrial dysfunction [8–10]. Mitochondrial fusion is mainly mediated by the fusion proteins Mfn1, Mfn2, and OPA1 [11, 12]. The central player in mitochondrial fission is DRP1 [13]. The activity of DRP1 is mediated by phosphorylation of two critical phosphorylation sites, serine 616 (active form) and serine 637 (inactive form) [8, 10, 14, 15]. Due to the vital role of mitochondria homeostasis in the T2DM-related

cognitive decline, it is vital to explore whether overexpression of HSPB8 could ameliorate mitochondrial dysfunction in the brains of the T2DM mouse model.

In the current study, we used mice treated with a high-fat diet and streptozotocin to mimic T2DM. The results showed upregulated expression of HSPB8 in the hippocampus of diabetic mice and N2a cells exposed to high glucose. Overexpressing HSPB8 in the hippocampi inhibited NLRP3 inflammasome activation via dephosphorylating DRP1 at the phosphorylated site Ser616 (p-Drp1S616), reduced oxidative stress, and ultimately relieved cognitive impairments. This study suggests that HSPB8 could be a promising therapeutic target for T2DM-related cognitive decline.

2. Materials and Methods

2.1. Animals. Male C57BL/6 mice (7-week-old) were purchased from Beijing Vital River Laboratory Animal Technology Co., Ltd. These mice were randomly divided into four groups ($n = 20$ per group). Two groups of mice were fed with high-fat diet (HFD) (60 kcal% fat). Then, at 20 weeks old, mice were treated with streptozotocin (STZ) (100 mg/kg) by intraperitoneal (i.p.) injection. One week later, we detected blood glucose levels with fasting 12 h. Mice with the features (polyphagia, polydipsia, and polyuria) and blood glucose levels exceeding 11.1 mmol/L were thought to be T2DM. At 28^{th} week, the virus was injected into the hippocampus. One group of mice received virus AAV-HSPB8-EGFP (group: DM + HSPB8). Another group received the control virus AAV-EGFP (group: DM). Another two groups of mice were treated with normal diet. Then, mice received a single dose of citrate buffer vehicle (pH 4.5). One group of mice received virus AAV-HSPB8-EGFP(group: WT + HSPB8). Another group received the control virus AAV-EGFP (group: WT). All animals were housed in a specific pathogen-free environment at 22°C, with 12 h light-dark cycles. Mice were allowed to move for food and water freely. Animal experiments were performed according to protocols approved by the animal ethics committee of Tongji Medical College, Huazhong University of Science and Technology.

2.2. Stereotactic Injection. Adeno-associated virus was coded for HSPB8 with enhanced green fluorescent protein EGFP. AAV-HSPB8-EGFP (1×10^{13} vg/mL) and the control AAV-EGFP (1×10^{13} vg/mL) were obtained from OBiO Biologic Technology Co., Ltd. (Shanghai, China). Mouse was fixed on stereotaxic apparatus after anesthesia with isoflurane. Animals were bilaterally injected with 1 μL of virus into the hippocampus (AP-1.9 mm; ML ± 1.5 mm; DV-1.9 mm) at an injection rate of 100 nl/min. Before being removed, the needle was allowed to remain for an additional 10 min. Behavioral tests were performed 4 weeks after virus injection.

2.3. Novel Object Recognition (NOR). According to the previous report [16], a novel object recognition test was performed in a box ($50 \times 50 \times 50$ cm). First, mouse was put in the box to adapt to the environment for 5 min in an empty box 24 h before testing. Two identical objects (A and B) were put at two different corners during the training phase. Mice were placed in the center of the bottom and allowed to explore for 5 min freely. Time to explore each object was recorded. Twenty-four hours later, the testing phase began. A differently new object C was used to take the place of object A. And mice were placed in the box to explore for another 5 min. Time to explore object B and object C was recorded. The recognition index was calculated as (object C exploration time)/(object A exploration time + object C exploration time).

2.4. Morris Water Maze (MWM). Morris water maze test was carried out to evaluate spatial learning and memory. A circular pool (120 cm diameter) filled with water was divided into 4 quadrants. 1.5 cm beneath the water surface, a platform (10 cm diameter) was placed in a fixed position at the center of the target quadrant. The mice were trained to find the platform for five consecutive days. Mice were put into water from four different quadrants daily for 60 s or till the platform was found and then they were allowed to rest on the platform for 20 s. Latencies loading to the platform were recorded. After 24 h of the last training, a probe test was conducted. In the probe test, the platform was removed and the number of times the mice crossed through the platform position, and the time stayed at the target quadrant and the locus of the movement was recorded (60 s of test duration). All data were recorded by using Chengdu Taimeng Software Co. Ltd. (China).

2.5. Western Blotting. Protein samples from all groups were lysed with RIPA lysis buffer. Via centrifugation at 12,000 g for 15 min at 4°C, the supernatant was obtained. Protein concentration was decided by the BCA Protein Assay kit (Beyotime, Shanghai, China). After SDS acrylamide gel electrophoresis, the proteins were subjected to transfer onto nitrocellulose membranes (Amersham Biosciences, Germany). Following by blocking with 5% BSA at 25°C for 1 h, the membranes were incubated with primary antibodies overnight at 4°C. Primary antibodies used were listed in Table 1. After that, the membranes were subjected to incubation with the corresponding secondary antibody for 1 h at room temperature. Finally, the proteins were visualized by Odyssey Infrared Imaging System (Licor biosciences, Lincoln, NE, USA) and ECL Imaging System (610007-8Q, Clinx Science Instruments Co., Ltd.). The quantitative analysis of proteins was performed by using ImageJ software.

2.6. Golgi Staining. Golgi staining was conducted using FD Rapid GolgiStainTM kit (FD NeuroTechnologies, USA). Hippocampus from all groups was immersed in solutions A and B at room temperature for 4 weeks. After that, brains were transferred into solution C in the dark for a week. Brain tissues were sliced at a thickness of 100 μm. The slices were stained in a mixture of solution D and solution E for 10 min. Following dehydrating with ethanol and clearing with xylene, the sections were mounted on slides.

2.7. Immunofluorescence. Brains were paraffin-embedded, and slices (5 μm thickness) were used for immunofluorescence analysis. After removing paraffin with xylene, slices

Table 1: Antibodies used in this study.

Antibody	Host	Dilution (WB)	Dilution (IF)	Company
Anti-HSPB8	Rabbit	1 : 500	1 : 50	Abcam
Anti-β-actin	Mouse	1 : 4000		Proteintech
Anti-NLRP3	Rabbit	1 : 1000		Abcam
Anti-Caspase1	Rabbit	1 : 1000		Proteintech
Anti-IL-1β	Rabbit	1 : 1000		Proteintech
Anti-ASC	Mouse	1 : 1000		Santa Cruz
Anti-MFN1	Rabbit	1 : 1000		Cell Signaling Technology
Anti-MFN2	Rabbit	1 : 1000		Cell Signaling Technology
Anti-OPA1	Rabbit	1 : 1000		ABclonal
Anti-DRP1	Rabbit	1 : 1000		ABclonal
Anti-(pDrp1S616)	Rabbit	1 : 1000	1 : 50	ABclonal
Anti- SOD1	Rabbit	1 : 1000		Proteintech
Anti-catalase	Rabbit	1 : 1000		ABclonal

were subjected to rehydrated through incubation in gradient ethanol. Followed by antigen repairing in sodium citrate, the slices were then going through membrane rupturing with 0.5% Triton X-100 and blocking in 5% BSA at room temperature. After that, sections were incubated with primary antibodies at 4°C overnight. The primary antibodies were as follows: after 3 times washing with PBS, sections were incubated with fluorescent secondary antibodies (Alexa Fluor 488 and 594). DAPI was needed for the staining of nuclei for 10 min at 25°C. Finally, immunofluorescence images were observed with a microscope (SV120, OLYMPUS).

2.8. Quantitative Real-Time PCR. Total RNA was extracted from hippocampi of all groups using Trizol reagent (TaKaRa). The reverse transcription and amplification were performed according to manufacturer's instruction (TaKaRa). RT-PCR was conducted on a StepOne Plus Real-Time PCR Detection System (Applied Biosystems). The expression level of the target gene was normalized to β-actin mRNA expression level and calculated by the $2\Delta\Delta$Ct method for relative expression analysis. Primers employed in this study were listed in Table 2.

2.9. Transmission Electron Microscopy. Hippocampi were separated and fixed in 2.5% glutaraldehyde at 4°C. Then, tissues were postfixed with 1% osmium tetroxide for 2 h. After that, samples were subjected to dehydrate in graded ethanol and followed by embedding in epoxy resin. The tissues were cut into ultrathin sections (50 nm). After staining with uranyl acetate for 20 min and lead citrate for 5 min, slices were observed with a transmission electron microscope (Thermo Fisher Scientific).

2.10. SOD, CAT, and MDA Assays. To detect superoxide dismutase (SOD), catalase (CAT), and malondialdehyde (MDA), mice were anesthetized and decapitated. Hippocampus was rapidly removed and homogenized. After centrifugation, the supernatant was collected to evaluate the levels of MDA (Beyotime, Haimen, China) and activities of SOD (Nanjing Jiancheng Bioengineering Institute, Nanjing, China) and CAT with assay kits (Nanjing Jiancheng Bioengineering Institute, Nanjing, China) following the manufacturer's directions.

Table 2

Gene	Forward primer (5′ to 3′)	Reverse primer (5′ to 3′)
HSPB8	ATGAAGAGAAGC AGCAGGAAGGTG	TGGTTGTCTTGA GGAAGCTCGTTG
β-Actin	GGCTGTATTCCC CTCCATCG	CCAGTTGGTAAC AATGCCATGT

2.11. Cell Culture, Treatments, and Transfection. Mouse N2a neuroblastoma cells were obtained from Professor Gongping Liu from Tongji Medical College, Huazhong University of Science and Technology. Cells were cultured in Dulbecco's modified Eagle's medium (containing 25 mM glucose, NG group) supplemented with 10% FBS, streptomycin/penicillin (1%). When cells were approximately 70–80% confluent, they were exposed to high glucose condition (HG group). In the present study, 100 mM concentration of glucose was used as high glucose condition [17]. For transfection experiments, N2a cells were plated onto 12-well plates, and HSPB8-EGFP plasmids (OBiO Biologic Technology, Shanghai) and shRNA(HSPB8)-EGFP (OBiO Biologic Technology, Shanghai) were transfected using NEOFECTTM DNA transfection reagent (NEOFECT, Beijing). All cells were maintained in a humidified incubator at 37°C under 5% CO_2 containing atmosphere.

2.12. Assessment of Mitochondrial Membrane Potential by JC-1. The mitochondrial membrane potential (MMP) was measured by JC-1 dye (Beyotime, Haimen, China). N2A cells were incubated with cell culture medium mixed with JC-1 staining working solution and mixed well. After incubation at 37°C for 20 minutes, the supernatant was removed

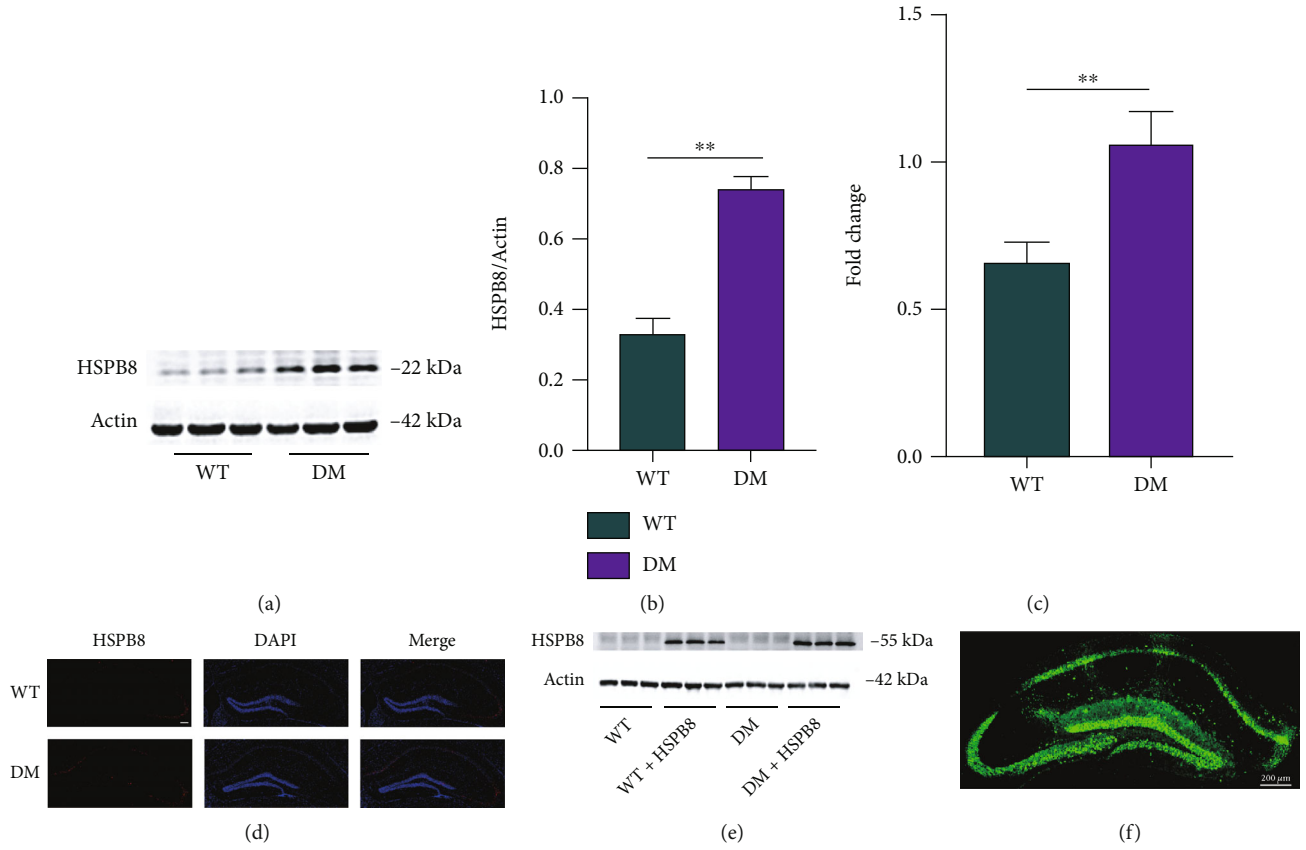

Figure 1: Upregulation of HSPB8 in the hippocampus of DM mice. (a, b) Representative western blot images and quantitative analyses of HSPB8 in the hippocampus of WT and DM mice ($n = 5$ mice per group). **, $p < 0.01$. (c) mRNA levels of HSPB8 in the hippocampus of WT and DM mice were detected by PCR. **, $p < 0.01$. (d) Representative immunofluorescence staining images of HSPB8 (red) in the hippocampus of WT and DM mice. Nuclei were counterstained with DAPI (blue). Scale bar = 200 μm. (e) Upregulation of HSPB8 was confirmed by western blotting and (f) immunofluorescent staining when injected virus in the hippocampus ($n = 5$ mice per group).

and washed cells twice with JC-1 staining buffer. Then, add 2 mL fresh medium to the well.

Finally, cells were observed under confocal microscope (Leica, Germany). The ratio of red and green fluorescence was analyzed.

2.13. Statistical Analysis. Data were expressed as the Mean ± SEM. Statistical analysis was performed using GraphPad Prism 9. Comparisons were evaluated using unpaired Student's *t*-test, one-way ANOVA, or two-way repeated measures ANOVA followed by Tukey's post hoc test. Differences with $p < 0.05$ were considered as statistical significance.

3. Results

3.1. Increased HSPB8 Protein Expression in the Hippocampus of DM Mice. We measured the protein (Figures 1(a) and 1(b)) and mRNA levels (Figure 1(c)) of HSPB8 in the hippocampus of WT and DM mice. Upregulation of HSPB8 was detected in DM mice. These findings were validated by immunofluorescence staining (Figure 1(d)). Overexpression of HSPB8 was shown by western blotting and immunofluorescence in the virus-injected hippocampus (Figure 1(e) and 1(f)).

3.2. HSPB8 Overexpression Relieves Cognitive Dysfunction in DM Mice. To explore the role of HSPB8 overexpression in learning and memory abilities, we conducted the Morris water maze (MWM) and novel object recognition (NOR) tests. In the MWM test, DM mice showed longer latency to reach the platform during the training stage, indicating memory deficits than WT mice. However, HSPB8 overexpression attenuated the spatial learning deficits, as shown by the downregulated escape latency at the 4th and 5th day during the training phase (Figure 2(a)). On the 7th day, by removing the platform, we found that HSPB8 overexpression ameliorated the DM mice's memory deficits as they spent less time arriving platform placed previously (Figure 2(b)), increased time stayed in the target quadrant (Figure 2(c)), and the times across the target quadrant (Figure 2(e)). A representative swimming trace was shown (Figure 2(d)). No significant difference in swimming speed was detected (Figure 2(f)), indicating no motor dysfunction among the four groups. Furthermore, NOR was performed, and DM mice spent less time with the novel object compared with WT mice, which indicated cognitive impairment. While HSPB8 overexpression ameliorated this performance, showing upregulated time spent with the new novel object at 24 h in DM mice (Figure 2(g)).

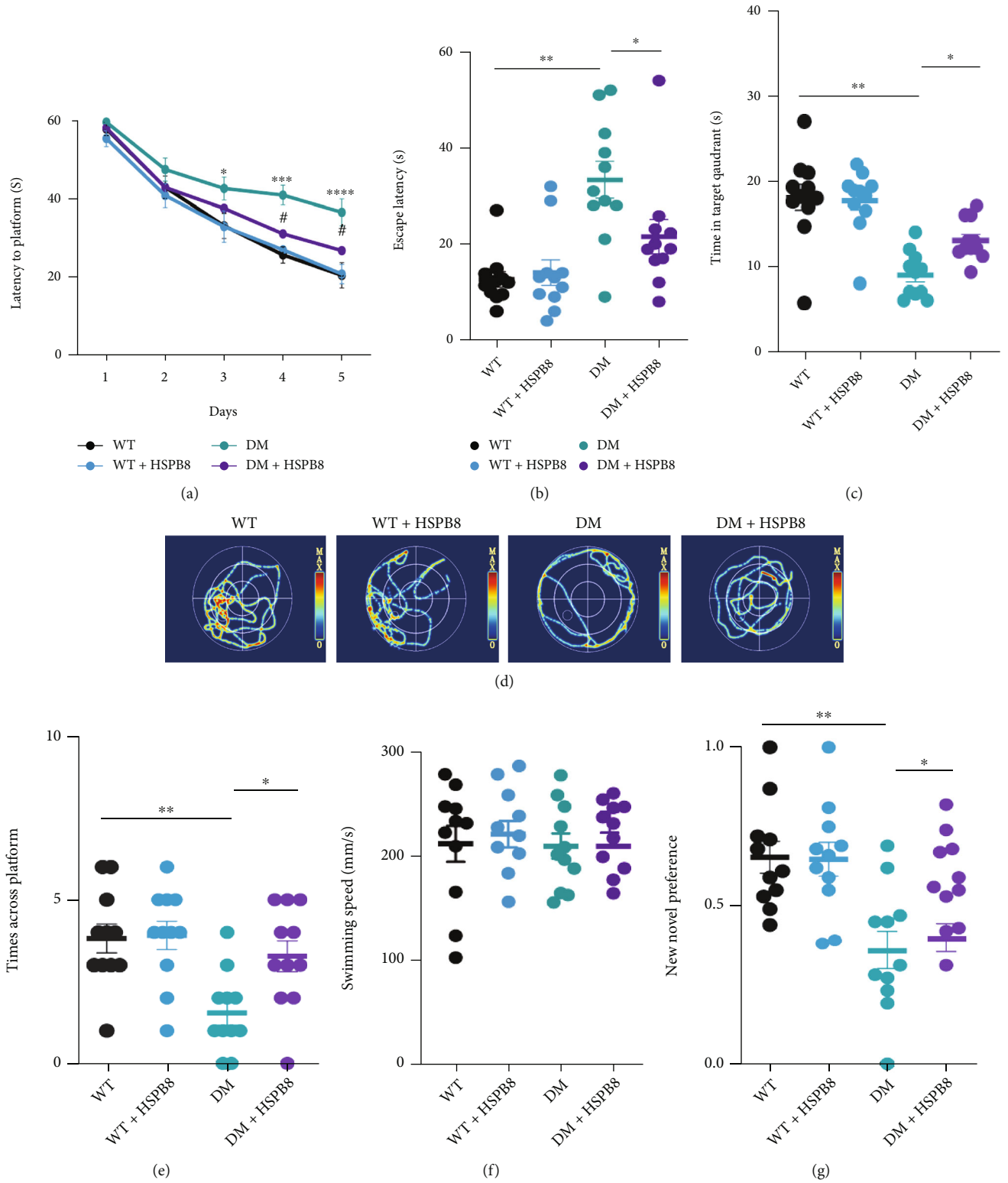

Figure 2: Overexpression of HSPB8 relieved cognitive dysfunction in DM mice. (a) Latency to the platform during training stage in Morris water maze (MWM), $n = 11$ mice/group, two-way repeated-measures ANOVA test followed by Tukey's post hoc test, *, $p < 0.05$, ***, $p < 0.001$, ****, $p < 0.0001$, WT group vs. DM group; $^{\#}p < 0.05$, DM group vs. DM + HSPB8 group. (b–f) The cognitive ability was detected by MWM. (b) Escape latency, (c) time in the target quadrant, (d) the representative swimming path of the mice during the MWM probe test, (e) and times across the platform. (f) There was no significant difference in swimming speed among the four groups. ($n = 10 - 13$ mice/group). *, $p < 0.05$, **, $p < 0.01$. (g) Recognition index during training and test in new object recognition (NOR) ($n = 10$ mice/group). *, $p < 0.05$, **, $p < 0.01$.

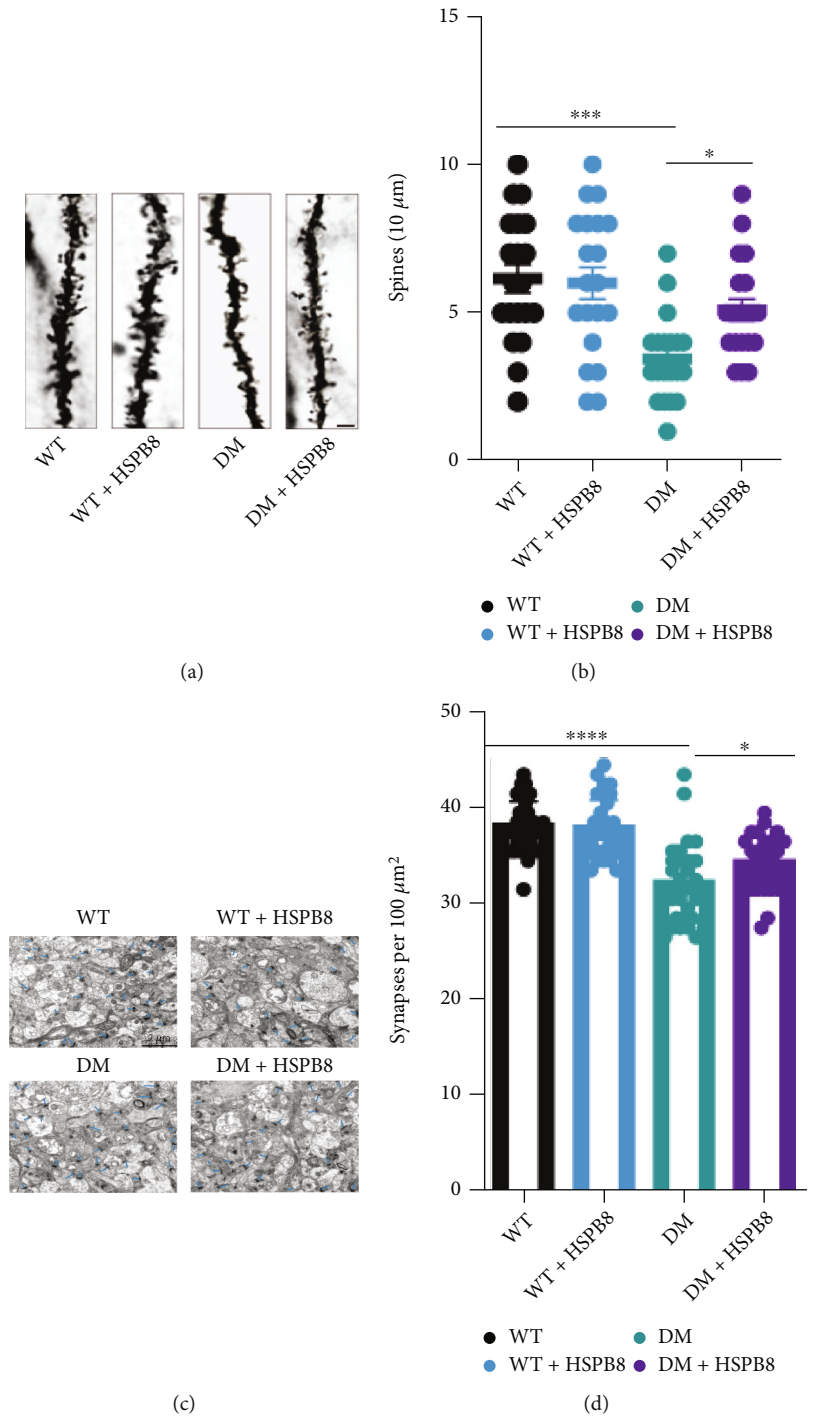

FIGURE 3: Overexpression of HSPB8 relieved synaptic damages in DM mice. (a, b) Dendritic spine density was detected by Golgi staining in the hippocampal regions and quantitative analysis. Scale Bar, 10 μm. ($n = 3$ mice per group). (c, d) The synaptic density in the hippocampus of mice was detected by electron microscopy and quantitative analysis ($n = 3$ mice for each group). Blue arrows indicate synapses. Scale bar = 2 μm. All data are shown as the mean ± SEM. One-way ANOVA test followed by Tukey's post hoc test, $^{*}p < 0.05$, ***, $p < 0.001$.

These results suggest that HSPB8 overexpression relieved cognitive dysfunction in DM mice.

3.3. HSPB8 Overexpression Relieves Synaptic Damages in DM Mice. Golgi staining was performed to reveal the change of density of the spine in the hippocampus.

We observed a reduction in spine density in the DM group when compared with the WT group.

Then, HSPB8 overexpression ameliorated the decrease of spine density in DM mice (Figures 3(a) and 3(b)). Furthermore, we performed transmission electron microscopy. The result showed a significant synapse loss in the

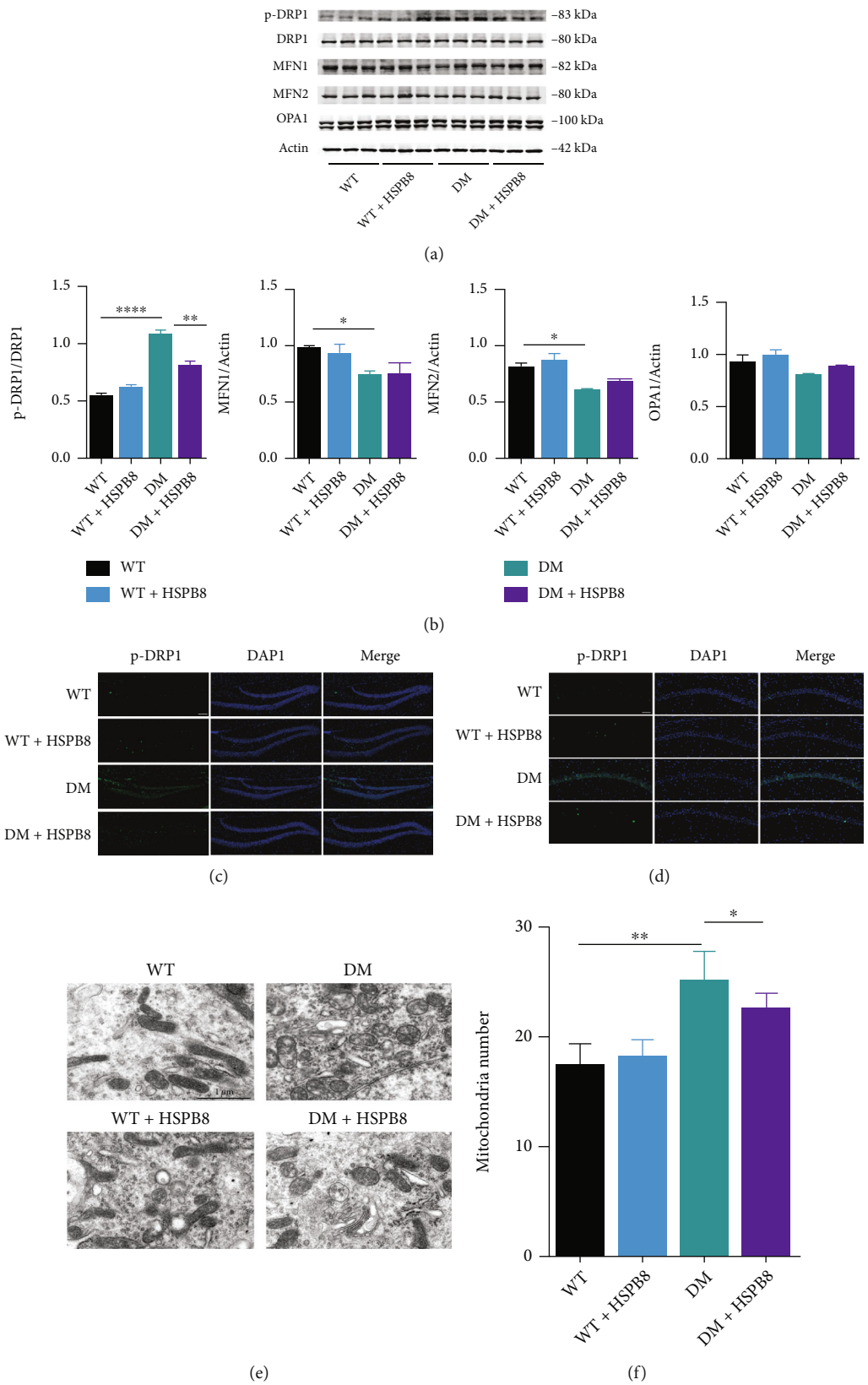

Figure 4: Continued.

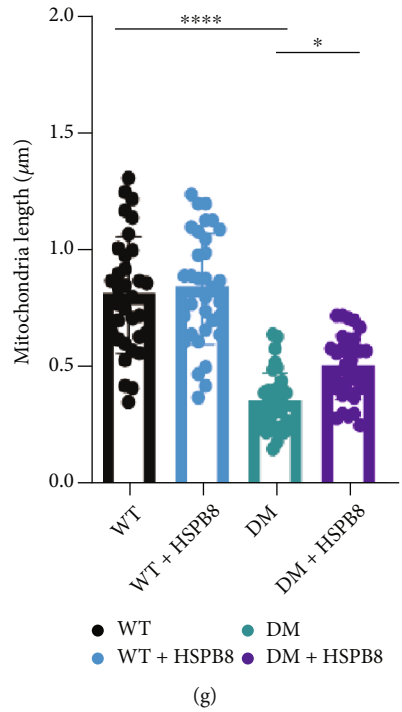

Figure 4: HSPB8 overexpression in the hippocampus alleviates mitochondrial fission. (a) Expressions of p-Drp1, Drp1, MFN1, MFN2, and OPA1 in the hippocampus were detected by Western blot. β-Actin was used as loading control. ($n = 5$ each group) and (b) quantitative analysis. *, $p < 0.05$, **, $p < 0.01$, ****, $p < 0.0001$. (c, d) Representative images of immunofluorescence staining against p-Drp1 (green) in the (dentate gyrus) DG and CA1. Nuclei were counterstained with DAPI (blue) ($n = 3$ mice per group). Scale bar = 100 μm. (e) Representative electron microscopy images showing mitochondrial morphology in hippocampal neurons ($n = 3$ mice per group). Scale bar = 1 μm. (f, g) Measurements of mitochondrial numbers and mitochondrial length. One-way ANOVA test followed by Tukey's post hoc test. Data are shown as the mean ± SEM. *$p < 0.05$, **, $p < 0.01$.

hippocampus of DM group when compared with the WT group. Notably, HSPB8 overexpression increased the number of synapses in the hippocampus of DM mice (Figures 3(c) and 3(d)). These data suggest that HSPB8 overexpression relieved synaptic damages in DM mice.

3.4. HSPB8 Overexpression in the Hippocampus Alleviates Mitochondrial Fission. Mitochondria are highly dynamic organelles, continuously going through fission and fusion. Dynein-related protein 1 (DRP1) is a critical regulator resulting in mitochondrial fission. We did not detect a significant increase in DRP1 expression in the hippocampus of DM group compared to WT group. However, the result of western blotting showed that p-Drp1/Drp1 was upregulated (Figures 4(a) and 4(b)). The levels of p-Drp1 were also upregulated in the hippocampus of DM group compared with WT group, as shown by immunostaining (Figure 4(c)). After HSPB8 overexpression, western blotting and immunostaining showed decreased expression levels of p-Drp1/Drp1 (Figures 4(a)–4(c)). In addition, we examined the levels of mitochondrial fusion proteins Mitofusin-1 (MFN1), Mitofusin-1 (MFN2), and optic atrophy1 (OPA1) by western blot. As shown in Figures 4(a) and 4(b), the levels of MFN1 and MFN2 were reduced in DM group compared to WT group. However, HSPB8 overexpression did not affect their expression. Electron microscopy revealed that the size of mitochondria in the hippocampus of the DM group was decreased compared to the WT group (Figure 4(d)). HSPB8 overexpression decreased the number but increased the length of the mitochondrial in DM + HSPB 8 group compared with DM group (Figures 4(f) and 4(g)).

3.5. HSPB8 Overexpression in the Hippocampus Alleviates Oxidative Stress. Next, due to the important role of oxidative stress (OS) in the T2DM-related cognitive decline, we explored the role of HSPB8 on OS. As shown in Figures 5(a) and 5(b), the activity of superoxide dismutase 1 (SOD) and catalase (CAT) was reduced in the hippocampus of DM group compared with WT group. Malondialdehyde (MDA), used to assess lipid peroxidation, was significantly elevated in DM mice (Figure 5(a)). HSPB8 overexpression reversed the pathological changes in DM mice. Western blotting revealed the same results that protein levels of critical antioxidant enzymes SOD1 and CAT were significantly declined in the DM mice compared with WT mice (Figures 5(d)–5(f)). Moreover, HSPB8 overexpression increased the expression of SOD1 and CAT in the hippocampus of DM mice.

Taken together, our findings revealed that HSPB8 could alleviate oxidative stress.

3.6. HSPB8 Overexpression in the Hippocampus Alleviates NLRP3 Inflammation in DM Mice. In this study, we also evaluated the effect of NLRP3 in DM mice. NLRP3 inflammasome signals, including NLRP3, ASC (apoptosis-

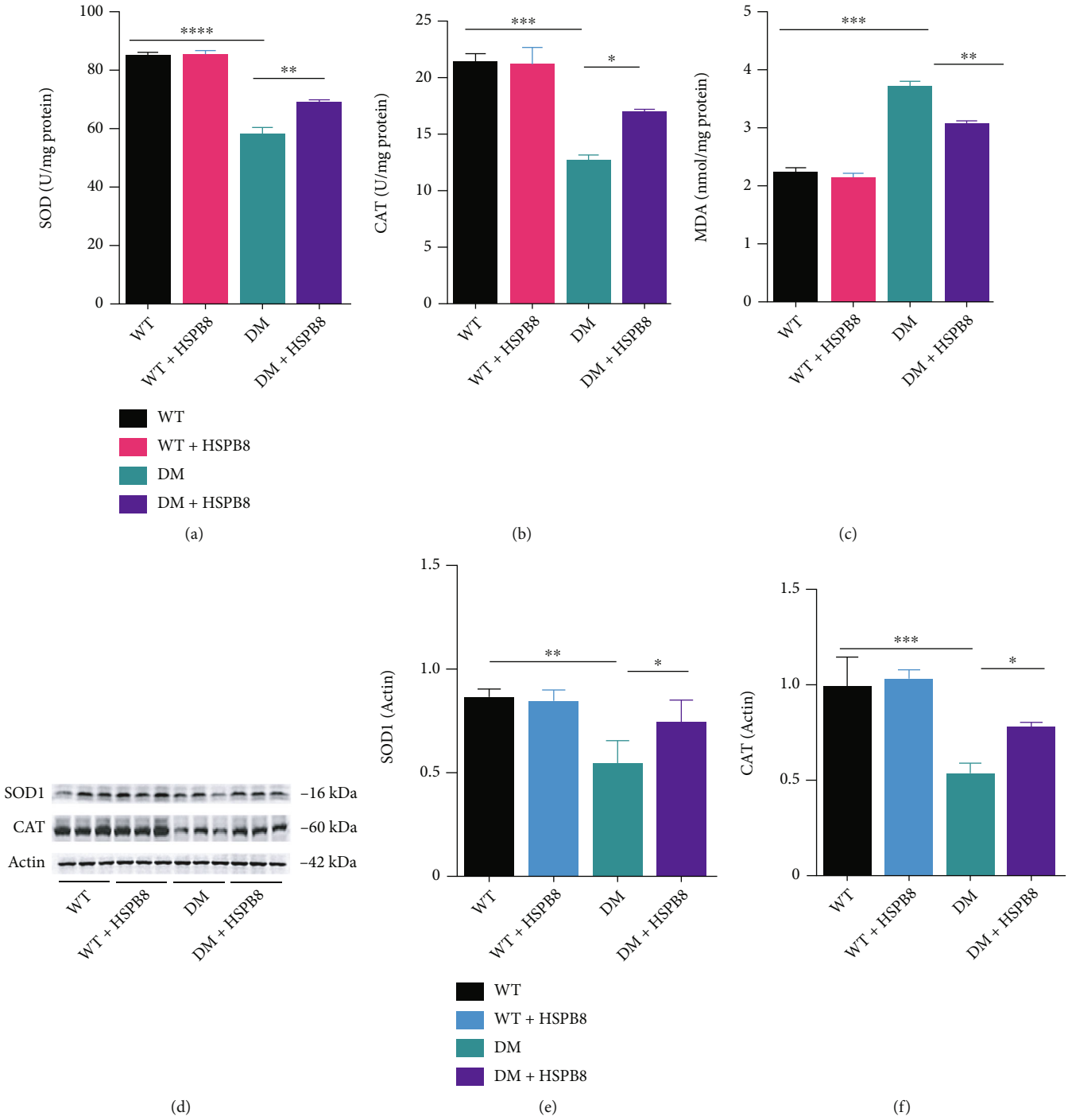

Figure 5: HSPB8 overexpression in the hippocampus alleviates oxidative stress. (a–c) The superoxide dismutase (SOD), catalase (CAT), and malondialdehyde (MDA) levels in the hippocampus of four groups ($n = 3$ mice per group). (d–f) Western blotting and quantification of SOD1 and CAT in the hippocampus ($n = 5$ mice per group). β-Actin was used as loading control. All data are shown as the mean ± SEM . One-way ANOVA test followed by Tukey's post hoc test, $^{*}p < 0.05$, **, $p < 0.01$, ***, $p < 0.001$, ****, $p < 0.0001$.

associated speck-like protein), cleaved caspase1 p20, and IL-1β (interleukin-1β), were measured by western blotting, as shown in Figures 6(a)–6(e).

NLRP3, ASC, cleaved caspase1 p20, and IL-1β were upregulated in the hippocampus of the DM mice compared with WT mice. However, HSPB8 overexpressing reversed these changes (Figures 6(a)–6(e)).

These results suggest that HSPB8 overexpression inhibits NLRP3 inflammasome activation in DM mice.

3.7. HSPB8 Overexpression Attenuates MMP and NLRP3 Inflammasome Activation in High Glucose-Treated N2a Cells. The protein level of HSPB8 was significantly upregulated in high glucose-treated cells when compared with

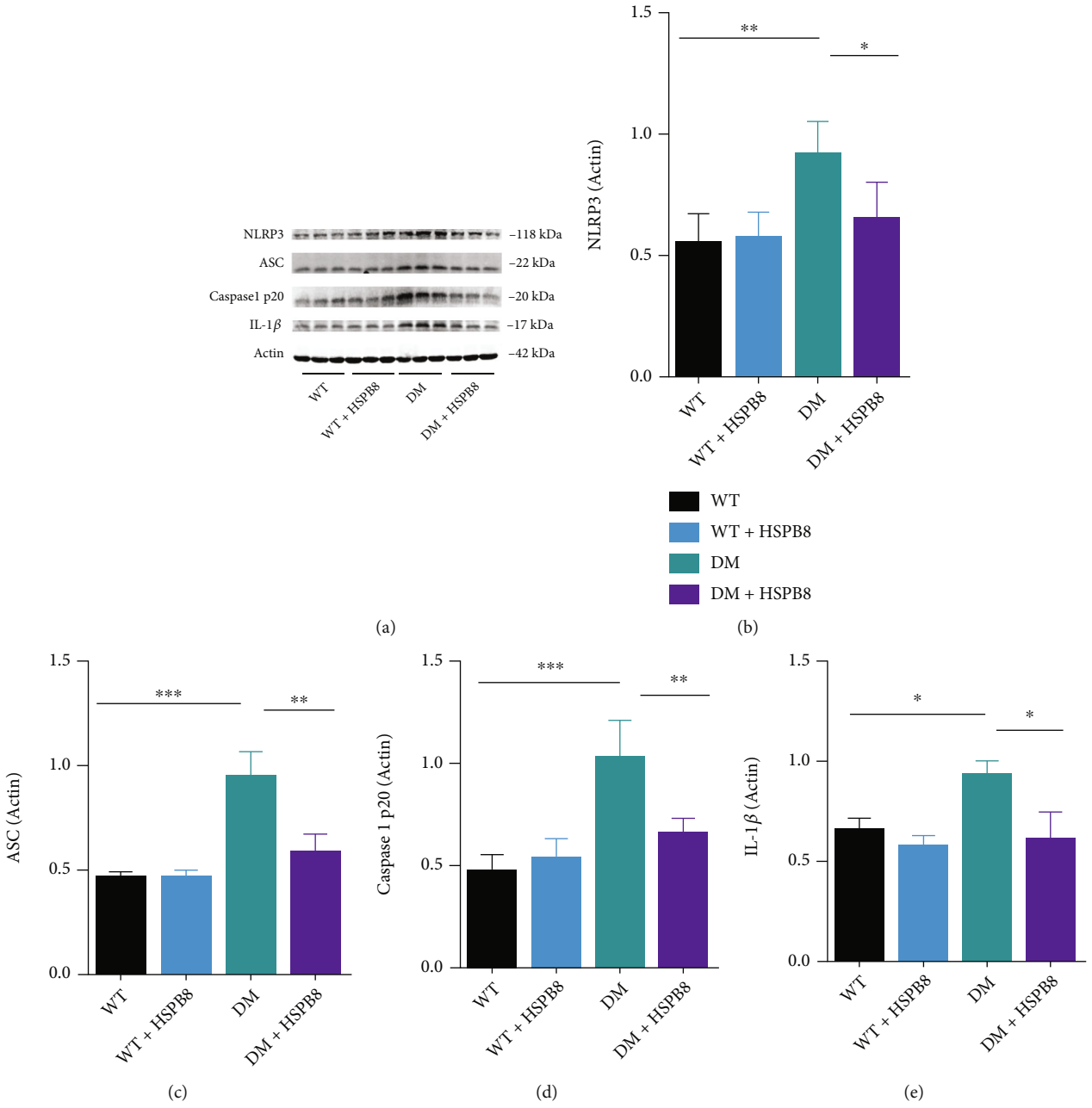

FIGURE 6: HSPB8 overexpression in the hippocampus alleviates NLRP3 inflammation in DM mice. (a–e) Western blotting and quantification of NLRP3, ASC, caspase-1 p20, and IL-1β levels in the hippocampus of four groups of mice ($n = 5$ each group). β-Actin was used as loading control. All data are shown as the mean ± SEM. One-way ANOVA test followed by Tukey's post hoc test, $^{*}p < 0.05$, **, $p < 0.01$, ***, $p < 0.001$.

exposed to normal glucose (NG) (Figure 7(a)). Mitochondrial membrane potential (MMP) was measured by JC-1 staining. High glucose treatment decreased the MMP in N2a cells compared with cells treated with NG, while overexpression of HSPB8 and mdivi-1 treatment reversed high glucose-mediated downregulation of MMP (Figures 7(b) and 7(c)). In addition, we evaluated the effect of HSPB8 on DRP1 at S616 phosphorylation in N2a cells (Figures 7(d) and 7(e)). HSPB8 overexpression and Mdivi-1 treatment decreased the ratio of p-Drp1/Drp1 (Figure 7(a)). In the meantime, the protein levels of NLRP3, cleaved caspase1 p20, ASC, and IL-1β were also decreased (Figures 7(f)–7(i)).

These results suggest that HSPB8 overexpression attenuates MMP and NLRP3 inflammasome activation in HG-treated N2a cells via inhibiting mitochondrial fission.

4. Discussion

In this study, we report elevated expression of HSPB8 in the hippocampus of diabetic mice and the N2a cells exposed to

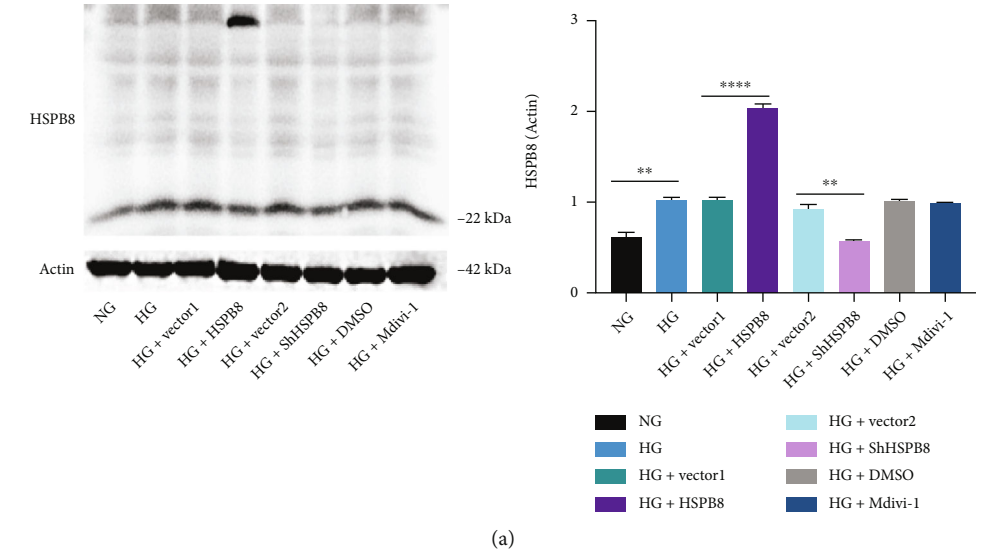

(a)

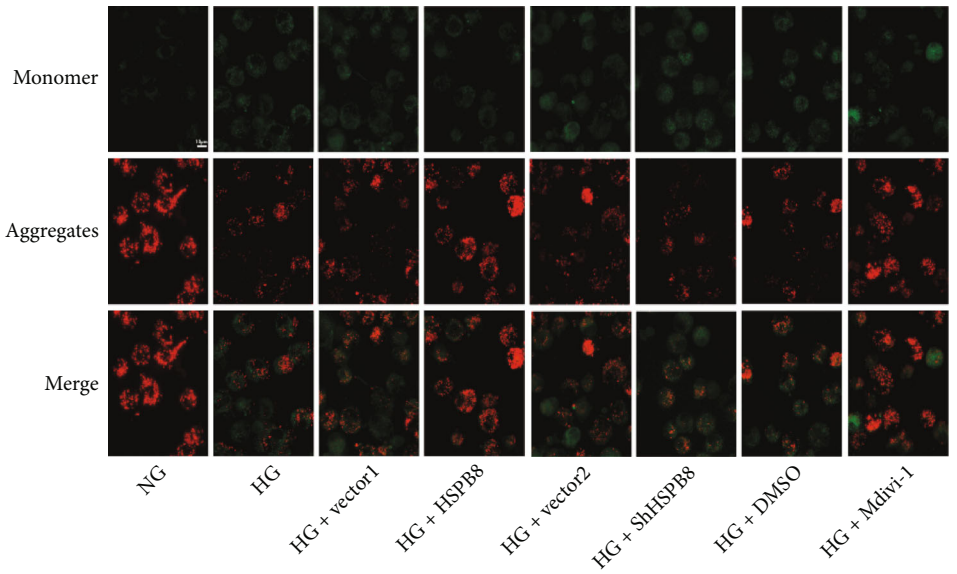

(b)

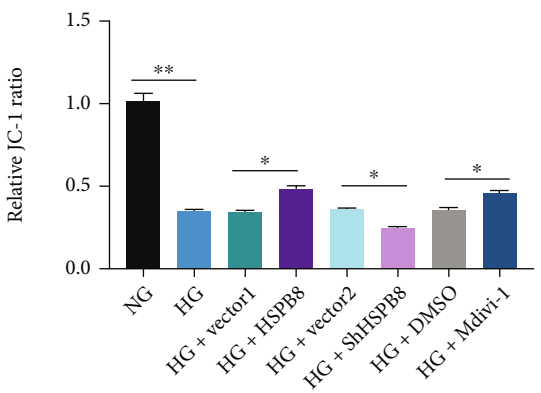

(c)

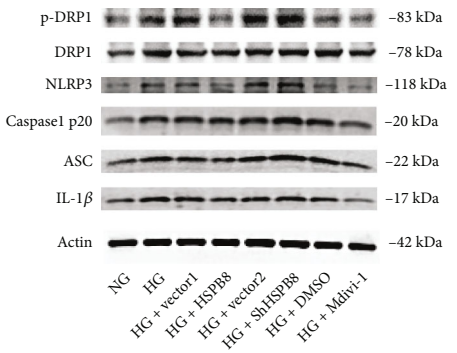

(d)

Figure 7: Continued.

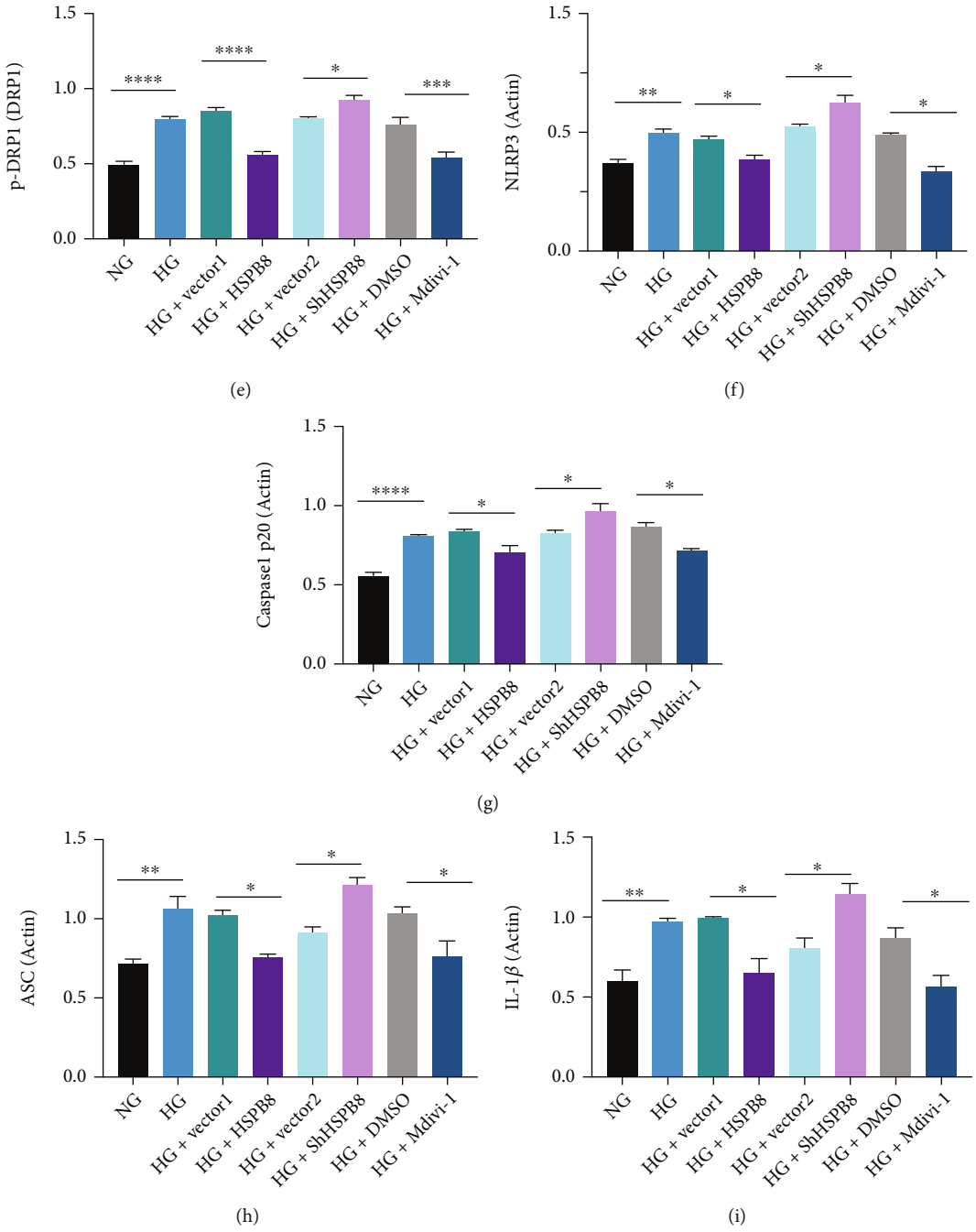

Figure 7: Overexpression of HSPB8 attenuates MMP and NLRP3 inflammasome activation in high glucose treated N2a cells. (a) Representative western blot images and quantitative analyses of HSPB8 in cells from all groups. β-Actin was used as loading control. (b) Representative images of JC-1 immunochemistry staining showing the mitochondrial membrane potential in each group of cells. (c) Relative quantitative comparison of red-to-green fluorescence intensity ratios between each group. (d–i) Expressions of p-Drp1, Drp1, NLRP3, cleaved caspase1 p20, and IL-1β in N2A cells of all groups were detected by western blot and quantitative analysis. β-Actin was used as loading control. All data are shown as the mean ± SEM. Two-tailed Student's t-test, $^{*}p < 0.05$, **, $p < 0.01$, ***, $p < 0.001$, ****, $p < 0.0001$.

high glucose. The heat shock family is composed of many proteins which are induced by various stress. HSPB8 is a kind of small heat shock protein [18]. Our result is consistent with previous experimental studies showing upregulated protein levels of HSPB8 under various stress. According to the previous reports, it exacted beneficial effect on alleviating mitochondrial biogenesis, oxidative stress, endothelial cell activation, and reduced apoptosis [4–7]. HSPB8 is mainly regulated by heat shock factor signaling; however, it was prevented from further increasing due to a negative feedback loop between the heat shock factor and HSPB8. Thus, HSPB8 cannot constantly increase and fully exert its effects under stress [7, 19]. The current study demonstrated that overexpression of HSPB8 exacted protective

effects, which in turn ameliorated the excessive mitochondrial fission, aggravated neuroinflammation, reduced oxidative stress, and ultimately relieved cognitive impairments.

Mitochondria are highly dynamic organelles that continuously change their size, shape, and numbers via fusion and fission to supply the energy required for the cells and maintain metabolic homeostasis [8, 20]. An increasing number of studies suggested that Dynein-related protein 1 (DRP1) is a critical regulator in mitochondrial fission. Protein phosphorylation is a posttranslational modification. It is widely used to regulate protein functions in cells. The phosphorylation residue of p-Drp1S616 was a vital residue for regulating DRP1. Increasing p-Drp1S616 showed extended phosphorylation of DRP1 and induced excessive mitochondrial fission [21–23]. In this study, evidence showed that the expression of p-Drp1S616 was upregulated in the hippocampus of DM mice. Our finding is consistent with the results that the expression of p-Drp1S616 in the hippocampus of leptin-deficient (ob/ob) was elevated [24]. In the hippocampus of DM mice, transmission electron microscopy demonstrated that mitochondrial number was increased, and length was decreased compared with WT mice. Conversely, overexpression of HspB8 could downregulate the number and increase the length of mitochondria. p-Drp1S616 was increased in N2a cells exposed to high glucose. These findings are consistent with the in vivo results. In addition, JC-1 was performed to investigate mitochondrial membrane potential (MMP). High glucose exposed N2a cells showed decreased MMP. HSPB8 overexpression inhibited high glucose-induced loss of membrane potential.

Hippocampus is rich in mitochondria and generates energy for synaptic activity. Mitochondrial dynamics are impaired in the hippocampus of diabetic mice [25], which results in reducing energy metabolism, disrupting cell signal cascade, and ultimately causing synaptic damage and cognitive dysfunction [26–28]. In the present study, the DM mice displayed excessive mitochondrial fission. Abnormal mitochondrial dynamics may contribute to neuronal damage leading to lack of ATP energy in the hippocampus. These findings indicated that HSPB8 might ameliorate synaptic damage and cognitive dysfunction in diabetic mice due to regulating mitochondrial fission. Furthermore, the expression levels of MFN1, MFN2, and OPA1 were decreased. However, HSPB8 overexpression did not change their levels in DM mice, indicating that HSPB8 may not be able to regulate mitochondrial fusion, or we need more samples to explore the effect.

Oxidative stress (OS) plays a crucial role in the pathogenesis of various neurodegenerative diseases [29, 30]. It could reduce the production of ATP, which is critical for neuron survival and metabolism. Therefore, OS is acknowledged as a key factor in the deterioration of learning and memory in the hippocampus [31–33]. In this study, we explored several certain biochemical parameters such as SOD, MDA, and catalase. Results showed decreased activity of SOD and catalase and elevated levels of MDA in the hippocampus of DM mice compared with WT mice. HSPB8 overexpression reversed described levels for cognitive decline. Additionally, the western blotting of SOD1 and catalase showed consistent results. As antioxidant enzyme, SOD1 and catalase were reduced in DM mice compared with WT mice, leading to a subsequent increase in oxidative stress. HSPB8 overexpression suggested an ameliorative antioxidative capacity in the hippocampus of DM mice. HSPB8 overexpression helped to mediate the oxidative stress system and improved cognitive impairment. These results concordant with previous findings that HSPB8 overexpression protects cells from oxidative stress [6, 7].

NLRP3 inflammasome activation is known to contribute to diabetes and dementia by triggering IL-1β maturation. NLRP3 inflammasome activation was also observed in diabetic cognitive impairment model mice/rats [34, 35]. Mitochondrial fission was reported to regulate NLRP3 inflammasome activation [36–38]. Further experiments in vitro revealed that when the ratio of p-Drp1S616/DRP1 was upregulation, the activation of NLRP3 inflammasomes, including NLRP3, cle-caspase-1, and IL-1β was increased. HSPB8 overexpression or treatment with Mdivi-1 (a specific inhibitor of Drp1) inhibited DRP1 phosphorylation at Ser-616 and thus reduced excessive mitochondrial fission in N2a cells exposed to high glucose. This result is consistent with previous studies that mdivi-1 exacted the protection by decreasing phosphorylation of DRP1 at serine 616 (p-Drp1S616) [39–41]. It is reported that exogenous HSPB8 significantly conveys neuroprotection via attenuation of mitochondrial damage partly by suppressed drp1-mediated mitochondrial fission through AMPK-PGC1α signaling pathway after subarachnoid hemorrhage (SAH). Whereas knockdown of HSPB8 reversed the above protective effects [5]. According to the above, HSBP8 should be the upstream cause of downregulation of p-Drp1S616. Importantly, we observed that the activation of NLRP3 inflammasomes was downregulated after treatment with HSPB8 or mdivi-1. Mdivi-1 attenuated activation of NLRP3 inflammasomes by downregulating mitochondrial fission in N2a cells exposed to high glucose. At the same time, mdivi-1 treatment did not affect the expression of HSPB8. On the contrary, knocking down the expression of HSPB8 elevated the levels of p-Drp1/Drp1, NLRP3, cleaved caspase-1 p20, and IL-1β. Collectively, the available evidence indicated that HSPB8 could downregulate mitochondrial fission, thus suppress the activation of NLRP3 inflammasome. Our findings confirm that regulation of mitochondrial dynamics could be a new therapeutic alternative for diabetic complications [25]. At the same time, we provide a new possibility for the activation of NLRP3.

5. Conclusions

In the present study, we revealed elevated expression of HSPB8 protein in the hippocampus of diabetic mice. Overexpressing HSPB8 in the hippocampi could inhibit NLRP3 inflammasome activation via regulation of Drp1 phosphorylation (p-Drp1S616), reduce oxidative stress, and relieve cognitive impairments in diabetic mice. These results suggest that HSPB8 could be a promising therapeutic target for Type 2 diabetes mellitus(T2DM)-related cognitive decline.

Abbreviations

STZ: Streptozotocin
HFD: High-fat diet
NOR: Novel object recognition
MWM: Morris water maze
WB: Western blot
MMP: Mitochondrial membrane potential
OS: Oxidative stress
HSP: Heat shock proteins
SOD: Superoxide dismutase
CAT: Catalase
MDA: Malondialdehyde.

Data Availability

The data sets used for the current study are available from the corresponding author upon reasonable request.

Conflicts of Interest

The authors declare that the research was conducted in the absence of any commercial or financial relationships that could be construed as a potential conflicts of interest.

Authors' Contributions

Li Gang and Ma Rong designed the study. Chang Yanmin performed research and wrote the manuscript. Li Gang, Ma Rong, Wu Yanqing, Jiang Xingjun, Zhu Jiahui, and Wang Cailin analyzed the data and revised the manuscript.

Acknowledgments

This work is supported by the grant from the National Natural Science Foundation of China (no. 81974161).

References

[1] P. S. Koekkoek, L. J. Kappelle, E. van den Berg, G. E. H. M. Rutten, and G. J. Biessels, "Cognitive function in patients with diabetes mellitus: guidance for daily care," *The Lancet Neurology*, vol. 14, no. 3, pp. 329–340, 2015.

[2] R. J. McCrimmon, C. M. Ryan, and B. M. Frier, "Diabetes and cognitive dysfunction," *The Lancet*, vol. 379, no. 9833, pp. 2291–2299, 2012.

[3] K. Little, M. Llorian-Salvador, S. Scullion et al., "Common pathways in dementia and diabetic retinopathy: understanding the mechanisms of diabetes-related cognitive decline," *Trends in Endocrinology and Metabolism*, vol. 33, no. 1, pp. 50–71, 2022.

[4] F. Li, B. Yang, T. Li, X. Gong, F. Zhou, and Z. Hu, "HSPB8 over-expression prevents disruption of blood–brain barrier by promoting autophagic flux after cerebral ischemia/reperfusion injury," *Journal of Neurochemistry*, vol. 148, no. 1, pp. 97–113, 2019.

[5] H. Fan, R. Ding, W. Liu et al., "Heat shock protein 22 modulates NRF1/TFAM-dependent mitochondrial biogenesis and DRP1-sparked mitochondrial apoptosis through AMPK-PGC1α signaling pathway to alleviate the early brain injury of subarachnoid hemorrhage in rats," *Redox Biology*, vol. 40, article 101856, 2021.

[6] W. Wu, L. Lai, M. Xie, and H. Qiu, "Insights of heat shock protein 22 in the cardiac protection against ischemic oxidative stress," *Redox Biology*, vol. 34, article 101555, 2020.

[7] L. Yu, Q. Liang, W. Zhang et al., "HSP22 suppresses diabetes-induced endothelial injury by inhibiting mitochondrial reactive oxygen species formation," *Redox Biology*, vol. 21, article 101095, 2019.

[8] T. Cali and G. Szabadkai, "Organelles: the emerging signalling chart of mitochondrial dynamics," *Current Biology*, vol. 28, no. 2, pp. R73–R75, 2018.

[9] S. L. Archer, "Mitochondrial dynamics–mitochondrial fission and fusion in human diseases," *The New England Journal of Medicine*, vol. 369, no. 23, pp. 2236–2251, 2013.

[10] H. Chen and D. C. Chan, "Mitochondrial dynamics in regulating the unique phenotypes of cancer and stem cells," *Cell Metabolism*, vol. 26, no. 1, pp. 39–48, 2017.

[11] W. Wang, F. Zhao, X. Ma, G. Perry, and X. Zhu, "Mitochondria dysfunction in the pathogenesis of Alzheimer's disease: recent advances," *Molecular Neurodegeneration*, vol. 15, no. 1, p. 30, 2020.

[12] A. Chakravorty, C. T. Jetto, and R. Manjithaya, "Dysfunctional mitochondria and mitophagy as drivers of Alzheimer's disease pathogenesis," *Neuroscience*, vol. 11, p. 11, 2019.

[13] D. C. Chan, "Fusion and fission: interlinked processes critical for mitochondrial health," *Annual Review of Genetics*, vol. 46, no. 1, pp. 265–287, 2012.

[14] Y. Wang, M. Lu, L. Xiong et al., "Drp1-mediated mitochondrial fission promotes renal fibroblast activation and fibrogenesis," *Cell Death & Disease*, vol. 11, no. 1, p. 29, 2020.

[15] J. Sun, X. Liu, C. Shen, W. Zhang, and Y. Niu, "Adiponectin receptor agonist AdipoRon blocks skin inflamm-ageing by regulating mitochondrial dynamics," *Cell Proliferation*, vol. 54, no. 12, article e13155, 2021.

[16] H. L. Wan, X. Y. Hong, Z. H. Zhao et al., "STAT3 ameliorates cognitive deficits via regulation of NMDAR expression in an Alzheimer's disease animal model," *Theranostics*, vol. 11, no. 11, pp. 5511–5524, 2021.

[17] X. Zhu, H. Liu, Y. Liu, Y. Chen, Y. Liu, and X. Yin, "The antidepressant-like effects of hesperidin in streptozotocin-induced diabetic rats by activating Nrf2/ARE/glyoxalase 1 pathway," *Frontiers in Pharmacology*, vol. 11, p. 1325, 2020.

[18] X. Wang, H. Gu, W. Huang et al., "Hsp20-mediated activation of exosome biogenesis in cardiomyocytes improves cardiac function and angiogenesis in diabetic mice," *Diabetes*, vol. 65, no. 10, pp. 3111–3128, 2016.

[19] J. Tower, "Hsps and aging," *Trends in Endocrinology and Metabolism*, vol. 20, no. 5, pp. 216–222, 2009.

[20] C. Garone, M. Minczuk, L. Tilokani, S. Nagashima, V. Paupe, and J. Prudent, "Mitochondrial dynamics: overview of molecular mechanisms," *Essays in Biochemistry*, vol. 62, no. 3, pp. 341–360, 2018.

[21] Q. Hu, H. Zhang, N. Gutiérrez Cortés et al., "Increased Drp1 acetylation by lipid overload induces cardiomyocyte death and heart dysfunction," *Circulation Research*, vol. 126, no. 4, pp. 456–470, 2020.

[22] W. Yu, X. Wang, J. Zhao et al., "Stat2-Drp1 mediated mitochondrial mass increase is necessary for pro- inflammatory differentiation of macrophages," *Redox Biology*, vol. 37, p. 101761, 2020.

[23] L. Xie, F. Shi, Y. Li et al., "Drp1-dependent remodeling of mitochondrial morphology triggered by EBV-LMP1 increases cisplatin resistance," *Signal Transduction and Targeted Therapy*, vol. 5, no. 1, p. 56, 2020.

[24] G. Park, J. Y. Lee, H. M. Han et al., "Ablation of dynamin-related protein 1 promotes diabetes-induced synaptic injury in the hippocampus," *Cell Death & Disease*, vol. 12, no. 5, p. 445, 2021.

[25] S. Huang, Y. Wang, X. Gan et al., "Drp1-mediated mitochondrial abnormalities link to synaptic injury in diabetes model," *Diabetes*, vol. 64, no. 5, pp. 1728–1742, 2015.

[26] M. Manczak and P. H. Reddy, "Abnormal interaction between the mitochondrial fission protein Drp1 and hyperphosphorylated tau in Alzheimer's disease neurons: implications for mitochondrial dysfunction and neuronal damage," *Human Molecular Genetics*, vol. 21, no. 11, pp. 2538–2547, 2012.

[27] C. Espino de la Fuente-Munoz, M. Rosas-Lemus, P. Moreno-Castilla, F. Bermudez-Rattoni, S. Uribe-Carvajal, and C. Arias, "Age-dependent decline in synaptic mitochondrial function is exacerbated in vulnerable brain regions of female 3xTg-AD mice," *International Journal of Molecular Sciences*, vol. 21, no. 22, p. 8727, 2020.

[28] H. Chen, J. M. McCaffery, and D. C. Chan, "Mitochondrial fusion protects against neurodegeneration in the cerebellum," *Cell*, vol. 130, no. 3, pp. 548–562, 2007.

[29] F. R. Buccellato, M. D'Anca, C. Fenoglio, E. Scarpini, and D. Galimberti, "Role of oxidative damage in Alzheimer's disease and neurodegeneration: from pathogenic mechanisms to biomarker discovery," *Antioxidants (Basel)*, vol. 10, no. 9, p. 1353, 2021.

[30] A. Jurcau, "Insights into the pathogenesis of neurodegenerative diseases: focus on mitochondrial dysfunction and oxidative stress," *International Journal of Molecular Sciences*, vol. 22, no. 21, p. 11847, 2021.

[31] X. Yang, R. Wang, H. Zhou et al., "β-Hydroxybutyrate alleviates learning and memory impairment through the SIRT1 pathway in D-galactose-injured mice," *Frontiers in Pharmacology*, vol. 12, article 751028, 2021.

[32] B. Zhao, B. Ren, R. Guo et al., "Supplementation of lycopene attenuates oxidative stress induced neuroinflammation and cognitive impairment via Nrf2/NF-κB transcriptional pathway," *Food and Chemical Toxicology*, vol. 109, Part 1, pp. 505–516, 2017.

[33] E. Trushina and C. T. McMurray, "Oxidative stress and mitochondrial dysfunction in neurodegenerative diseases," *Neuroscience*, vol. 145, no. 4, pp. 1233–1248, 2007.

[34] P. Liu, H. Li, Y. Wang et al., "Harmine ameliorates cognitive impairment by inhibiting NLRP3 inflammasome activation and enhancing the BDNF/TrkB signaling pathway in STZ-induced diabetic rats," *Frontiers in Pharmacology*, vol. 11, p. 535, 2020.

[35] C.-W. Li, M.-Z. Deng, Z.-J. Gao et al., "Effects of compound K, a metabolite of ginsenosides, on memory and cognitive dysfunction in db/db mice involve the inhibition of ER stress and the NLRP3 inflammasome pathway," *Food & Function*, vol. 11, no. 5, pp. 4416–4427, 2020.

[36] R. Rong, R. Yang, H. Li et al., "The roles of mitochondrial dynamics and NLRP3 inflammasomes in the pathogenesis of retinal light damage," *Annals of the New York Academy of Sciences*, vol. 1508, no. 1, pp. 78–91, 2022.

[37] O. Kepp, L. Galluzzi, and G. Kroemer, "Mitochondrial control of the NLRP3 inflammasome," *Nature Immunology*, vol. 12, no. 3, pp. 199-200, 2011.

[38] Y. Qin, Y. Yu, C. Yang et al., "Atractylenolide I inhibits NLRP3 Inflammasome activation in colitis-associated colorectal cancer via suppressing Drp1-mediated mitochondrial fission," *Frontiers in Pharmacology*, vol. 12, article 674340, 2021.

[39] Q. R. Wu, D. L. Zheng, P. M. Liu et al., "High glucose induces Drp1-mediated mitochondrial fission via the Orai1 calcium channel to participate in diabetic cardiomyocyte hypertrophy," *Cell Death & Disease*, vol. 12, no. 2, p. 216, 2021.

[40] C. Duan, L. Wang, J. Zhang et al., "Mdivi-1 attenuates oxidative stress and exerts vascular protection in ischemic/hypoxic injury by a mechanism independent of Drp1 GTPase activity," *Redox Biology*, vol. 37, article 101706, 2020.

[41] X. Zhuang, X. Sun, H. Zhou et al., "Klotho attenuated doxorubicin-induced cardiomyopathy by alleviating dynamin-related protein 1 - mediated mitochondrial dysfunction," *Mechanisms of Ageing and Development*, vol. 195, article 111442, 2021.

Hindawi
Oxidative Medicine and Cellular Longevity
Volume 2022, Article ID 7812407, 13 pages
https://doi.org/10.1155/2022/7812407

Research Article

Recurrent Hypoglycemia Impaired Vascular Function in Advanced T2DM Rats by Inducing Pyroptosis

Minghao Luo,[1] **Yu Hu**,[1] **Dingyi Lv**,[1] **Lingyun Xie**,[1] **Shenglan Yang**,[1] **Deyu Zuo**,[2] **Yuzhou Xue**,[1] **and An He**[1]

[1]*Division of Cardiology, The First Affiliated Hospital of Chongqing Medical University, Chongqing, China*
[2]*Department of Rehabilitation Medicine, Chongqing Traditional Chinese Medicine Hospital, Chongqing, China*

Correspondence should be addressed to An He; heanaichirou@163.com

Received 27 May 2022; Revised 14 June 2022; Accepted 23 June 2022; Published 23 July 2022

Academic Editor: Tao Zheng

Background. Hypoglycemia is a dangerous side effect of intensive glucose control in diabetes. Even though it leads to adverse cardiovascular events, the effects of hypoglycemia on vascular biology in diabetes have not been adequately studied. *Methods*. Aged Sprague-Dawley rats were fed a high-fat diet and given streptozotocin to induce type 2 diabetes mellitus (T2DM). Acute and recurrent hypoglycemia were then induced by glucose *via* insulin administration. Vascular function, oxidative stress, and pyroptosis levels in aortic tissue were assessed by physiological and biochemical methods. *Results*. Hypoglycemia was associated with a marked decrease in vascular function, elevated oxidative stress, and elevated pyroptosis levels in the thoracic aorta. The changes in oxidative stress and pyroptosis were greater in rats with recurrent hypoglycemia than in those with acute hypoglycemia. *Conclusions*. Hypoglycemia impaired vascular function in aged rats with T2DM by inducing pyroptosis. The extent of injury increased with the duration of blood glucose fluctuation.

1. Introduction

Type 2 diabetes mellitus (T2DM) is characterized by hyperinsulinemia and hyperglycemia and is the most common type of diabetes mellitus, and the vascular inflammation that accompanies T2DM usually leads to a variety of serious complications [1, 2]. The prevalence of T2DM increases with age, and current studies show that the elderly have a relatively high incidence and an increased risk of serious complications [1–6]. Glucose control therapy is the preferred clinical intervention for T2DM. Intensive glucose control can result in hypoglycemia, a dangerous side effect that can lead to adverse cardiovascular events, and elderly patients are at increased risk [4, 6]. The pathophysiology of hypoglycemia includes increased oxidative stress that can result in vascular injury, and recurrent hypoglycemia can interfere with vascular homeostasis, especially endothelial function [4]. Although an association between hypoglycemia and vascular dysfunction in diabetes has been shown, the underlying molecular mechanisms remain elusive and controversial. Endothelium-dependent vasodilatation is regulated by endothelial nitric oxide synthase (eNOS). As hypoglycemia in diabetes interferes with endothelial function, including endothelium-dependent vasodilation, eNOS activity may be affected [7–14].

Pyroptosis is a type of inflammatory programmed cell death. It is mediated by gasdermin (GSDM) and is characterized by inflammasome activation, caspase activation, and formation of cell membrane pores [15–17]. GSDMD-mediated pyroptosis has a role in the occurrence and development of diabetic cardiomyopathy and diabetic nephropathy [15, 18, 19]. Although the relationship between diabetic vascular injury and pyroptosis is not well established, current studies prompted us to clarify the significance of pyroptosis in diabetic vascular injury, the initial engine in pathological progress of diabetes.

Diabetic hypoglycemia promotes mitochondrial dysfunction in vascular cells that consequently increases the levels of reactive oxygen species (ROS) [20–23]. Increased expression of proinflammatory cytokines stimulates inducible nitric oxide

synthase (iNOS) expression, which results in the aggravation of oxidative stress and worsening of chronic inflammation and endothelial dysfunction in diabetes [24, 25]. Oxidative stress-mediated activation of nucleotide-binding domain and leucine-rich repeat-containing receptor 3 (NLRP3) inflammasomes occurs in pyroptosis [26–28]. Hence, we hypothesized that hypoglycemia may induce pyroptosis by increasing oxidative stress that results in vascular dysfunction.

2. Material and Methods

2.1. Animals. Male 12-month-old Sprague-Dawley rats weighing 380–420 g were purchased from the Experimental Animal Center of Chongqing Medical University. All animal procedures were carried out following the guidelines on the China Animal Protection Law and were approved by the Institutional Ethics Committee of Chongqing Medical University. Animals were kept in a 12 h light–dark cycle at 22–25°C with *ad libitum* access to food and water. The aged rats were randomly divided into four groups ($n = 6$): an aged control, T2DM model (DM), T2DM hypoglycemia (H-DM), and T2DM recurrent hypoglycemia (RH-DM). Rats were fed a high-fat diet (HFD) combined with streptozotocin (STZ) to induce T2DM. Rats in the diabetes groups were fed an HFD (Nantong, Jiangsu, China) for 12 weeks followed by intraperitoneal injection of 35 mg/kg STZ (Sigma, MO, USA) in pH 4.2–4.5 citric acid [29, 30]. The citrate buffer vehicle was injected into control rats. Twelve weeks after STZ injection, rats with three consecutive random blood glucose levels > 16.7 mmol/L and diabetes behavior changes (e.g. increased food intake, increased urination, and weight loss) were considered successful T2DM models.

2.2. Diabetic Rat Hypoglycemia Model. To induce severe hypoglycemia, diabetic rats were injected with insulin (Wanbang, China) 10.0 units/kg at 8:00–9:00 in the morning after an overnight fast. Control rats were given an equal volume of phosphate buffered saline (PBS) instead of insulin. The diabetic rat hypoglycemia model (Figure 1) included an acute hypoglycemia group (hypoglycemia for 4 h/1 day) and a recurrent hypoglycemia group (hypoglycemia for 1 h/5 days). After insulin injection, blood samples were obtained by tail prick for blood glucose monitoring every 30 min to ensure that the rats maintained the glucose levels in severe hypoglycemia (<2.3 mmol/L). Rats were given 50% glucose in PBS to terminate the hypoglycemia episode. None of rats experienced seizures or coma during hypoglycemia attack. All rats were sacrificed by sodium pentobarbital anesthesia, and blood samples and aortas were collected for subsequent experiments.

2.3. Western Blot Assays and Antibodies. Thoracic aortas were isolated, immersed in liquid nitrogen, and then immediately transferred to a −80°C refrigerator until used in western blot assays. Proteins were separated by 10% sodium dodecyl sulfate polyacrylamide gel electrophoresis and incubated with primary antibodies: eNOS (1 : 1000, ab300071, Abcam), iNOS (1 : 1000, ab283655, Abcam), NOX2 (1 : 2000, 19013-1-AP, ProteinTech), NOX4 (1 : 2000, 14347-1-AP, ProteinTech), p-p65 (1 : 1000, 3033, Cell Signaling Technology), p65 (1 : 1000, 8242, Cell Signaling Technology), NLRP3 (1 : 1000, NBP2-12446, NOVUS), ASC (1 : 1000, sc-514414, Santa Cruz), Caspase-1 (1 : 1000, bs-10743R, Bioss), cGAS (1 : 1000, NBP3-16666, NOVUS), STING (1 : 1000, CST50494, Cell Signaling Technology), GSDMD (1 : 1000, NBP2-33422, NOVUS), Bax (1 : 1000, 50599-2-Ig, ProteinTech), Bcl-2 (1 : 1000, 26593-1-AP, ProteinTech), and β-actin (1 : 5000, 20536-1-AP, ProteinTech). The membranes were then incubated with horseradish peroxidase-conjugated anti-rabbit or anti-mouse IgG (1 : 5000, ProteinTech) secondary antibodies for 2 h at 37°C and visualized a with chemiluminescent reagent kit (Beyotime, Shanghai, China). The lane densities were read with a Bio-Rad imaging system.

2.4. Oxidative Stress Determination. Blood samples were collected with vacuum hemostix, and the sera were stored at −80°C. Antioxidant and oxidative stress indicators in serum were assayed with reagent kits provided by the Nanjing Jiancheng Bioengineering Institute (Nanjing, China) [31]. Superoxide dismutase (SOD) activity was assayed by the hydroxylamine method. Glutathione peroxidase (GSH-Px) activity was assayed by a colorimetric method. Malondialdehyde (MDA) was assayed by the thiobarbituric acid method.

2.5. Vascular Reactivity Tests. Thoracic aortas were removed and placed in an oxygen-containing physiological salt solution (PSS) buffer [32]. Adherent fat and connective tissues were removed, and the vascular tissue was cut into 3 mm rings to measure vascular tone as previously described. Briefly, the aortic rings were mounted horizontally on an isometric force transducer (DMT620 Multi Wire Myograph; DMT) in chambers filled with 5 mL PSS buffer at 37°C and aerated with 95% O_2 and 5% CO_2. The aortic rings were allowed to equilibrate for 90 min at an initial tension of 1.5 g. Concentrations of 10^{-9} to 10^{-5} M acetylcholine (ACh) for endothelium-dependent relaxation, sodium nitroprusside (SNP) for endothelium-independent relaxation, and phenylephrine (PE) were added and concentration–response curves were plotted. Vascular function was reported as the EC_{50}, the concentration that produced 50% of the maximum response, E_{max}, the maximum response, and area under the curve (AUC), which are determined by nonlinear regression analysis using GraphPad version 9.0.

2.6. Vascular Morphology. A section of the aorta was dissected from each rat, fixed in 4% paraformaldehyde, embedded in paraffin, sectioned at 5 μm, and mounted on slides. The slides were transferred to an oven and baked for 30 min at 60°C to melt the wax, which was then removed by treatment with xylene for 20 min. Tissue sections were rehydrated in a descending ethanol series of 100% for 5 min and 95%, 90%, 80%, and 70% for 3 min each. After washing three times in PBS, the sections were stained with hematoxylin and eosin or incubated with a primary antibody. All images were captured with a Leica DM4B upright microscope (Leica Inc., Germany).

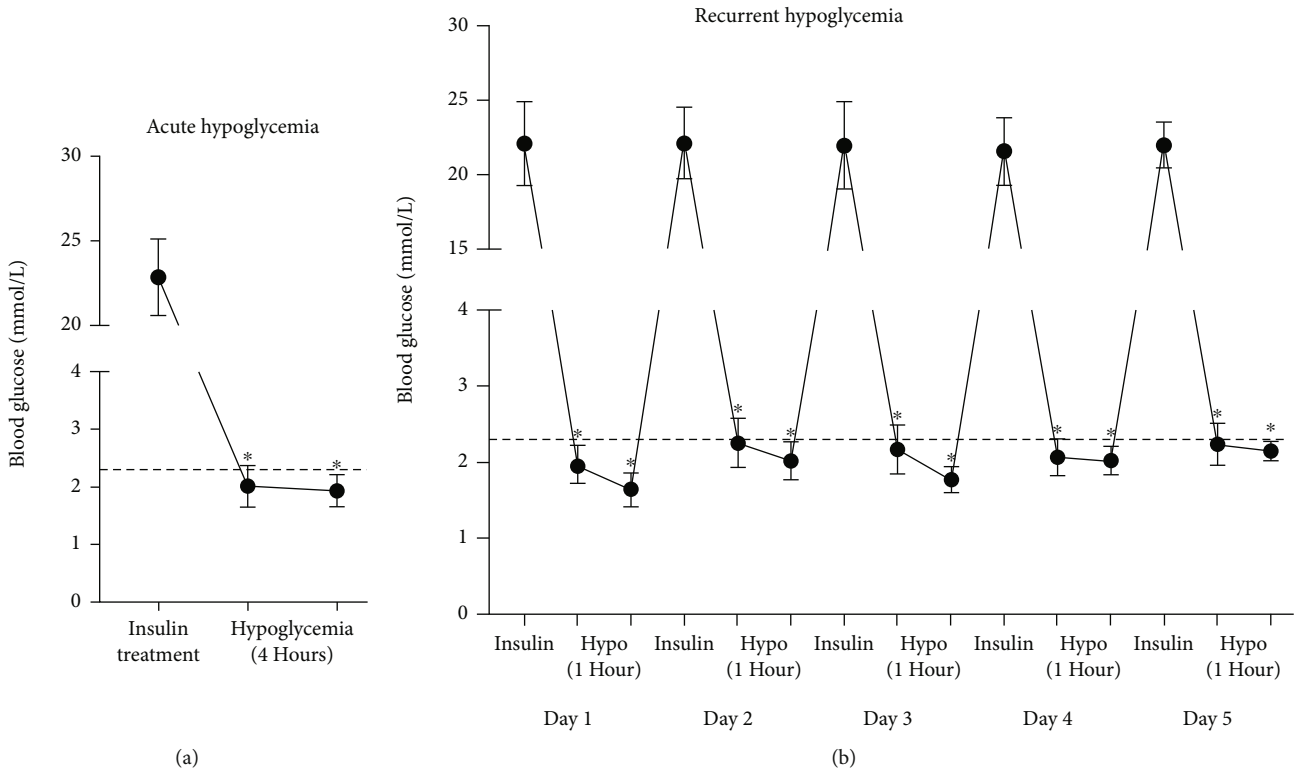

Figure 1: Glucose levels in T2DM model rats and insulin-induced acute or recurrent hypoglycemia; $^{*}p < 0.05$ pretreatment vs. posttreatment.

2.7. Immunohistochemical Staining. After dewaxing and rehydration, tissue sections were placed in citrate buffer and boiled for 5 min for antigen retrieval, washed twice with PBS, and blocked with 5% goat serum for 30 min. Tissue sections were incubated overnight with primary antibodies overnight at 4°C, washed three with PBS, incubated for 1 h at 37°C with secondary antibodies, and then washed three times with PBS. After diaminobenzidine color development for 5 min, the slides were washed with distilled water to remove float color, and the tissue was counterstained with hematoxylin for 10 s. The tissue was dehydrated in an ethanol gradient with 3 min at each concentration, cleared in xylene for 5 min, mounted with resin, and observed by light microscopy (Leica Inc., Germany). The primary antibodies used were eNOS (1 : 200, ab300071, Abcam), iNOS (1 : 200, ab283655, Abcam), NLRP3 (1 : 200, NBP2-12446, NOVUS), and GSDMD (1 : 200, NBP2-33422, NOVUS). Area quantitative assessment of immunohistochemical staining was performed by the ImageJ 1.8 software (USA).

2.8. Immunofluorescence Staining. Aorta sections were permeabilized with 0.1% Triton X-100 in PBS for 20 min, blocked with 5% goat serum for 1 h, and incubated with antibodies overnight at 4°C. The tissue sections were then incubated for 5 minutes with 4′,6-diamidino-2-phenylindole (DAPI) and then for 1 h with fluorescence-conjugated secondary antibodies (Beyotime, Shanghai, China) in the dark at 37°C. Tissues were observed by fluorescence microscopy (Leica Microsystems, Germany). The antibodies used were 8-OHdG (1 : 200, bs-1278R, Bioss), NLRP3 (1 : 200, NBP2-12446, NOVUS), and GSDMD (1 : 200, NBP2-33422, NOVUS). Fluorescence intensity was quantified using the ImageJ 1.8 software.

2.9. Data Analysis. Numeric values were reported as the means ± standard deviation. Normality of the distribution of data was assessed by the Shapiro-Wilk normality test. To calculate the comparisons between 2 groups, normally or nonnormally distributed data were compared using the unpaired 2-tailed Student t tests or the Mann–Whitney U test, respectively. To calculate the comparisons between multiple groups (≥3 groups), normally or nonnormally distributed data were compared using one-way analysis of variance (ANOVA) followed by the Bonferroni post hoc test or Kruskal-Wallis test followed by the Dunn post hoc test, respectively. The statistical analysis was performed with GraphPad Prism 9.0. p values < 0.05 were considered statistically significant.

3. Results

3.1. Establishment of Acute or Recurrent Hypoglycemia Models in Aged T2DM Rats. The primary purpose of the study was to establish a reliable rat model of T2DM hypoglycemia. As shown in Figure 1, diabetes was induced by STZ (10.0 units/kg), which destroyed pancreatic β-cells and induced insulin resistance when combined with an HFD. We observed a significant increase in blood glucose levels (22.8 ± 2.2 mM). As shown in Figure 1(a), insulin treatment resulted in severe hypoglycemia (2.0 ± 0.3 mM/L) in the H-

DM group that was maintained for 4 h. As shown in Figure 1(b), the blood glucose values in the RH-DM group reached the target levels for 5 consecutive days. Subsequent procedures were based on this model.

3.2. Vascular Function, eNOS, and iNOS Expression in Response to Acute and Recurrent Hypoglycemia in Aged T2DM Rats. We first evaluated vascular function in the study groups, which was reported as EC_{50} and E_{max}. The effect of hypoglycemia on vasodilation of the aorta was evaluated by ACh- and SNP-induced relaxation responsiveness. As shown in Figures 2(a) and 2(b), after the tension of PE-mediated vasoconstriction was balanced, ACh or SNP (10^{-9}–10^{-5} M) was added in half-log increments. Compared with control, ACh-induced dilation function was impaired in DM (–log EC_{50}: control 7.10, DM 6.44; AUC: control 199.0, DM 155.0; $p < 0.05$). Acute and recurrent hypoglycemia significantly exacerbated ACh-induced vasodilation of the aorta, compared with DM (–log EC_{50}: H-DM 6.10, RH-DM 5.88; AUC: H-DM 102.9, RH-DM 30.3; $p < 0.05$). ACh-induced relaxation in the group with recurrent hypoglycemia was worse than that in the group with acute hypoglycemia ($p < 0.05$). There were no significant differences in the SNP-induced vasodilation function among the groups (Figure 2(b); $p > 0.05$). The results indicate that hypoglycemia in the model rats impaired endothelium-dependent relaxation and that recurrent hypoglycemia had a potentially more harmful effect on the endothelium-dependent relaxation.

Studies have shown an enhanced response to catecholamines in DM [33–35]. We therefore explored the role of hypoglycemia on the contraction of the aortas of the model rats (Figure 2(c)). The E_{max} of PE-induced contraction was increased in DM rats compared with controls (E_{max}: control 16.96, DM 22.06; AUC: control 35.37, DM 52.12; $p < 0.05$), but the EC_{50} was not significantly affected ($p < 0.05$). The results showed that both acute and recurrent hypoglycemia significantly raised PE-induced contraction of aortas from model rats (E_{max}: H-DM 27.74, RH-DM 29.23; AUC: H-DM 66.19, RH-DM 70.82; $p < 0.05$).

We also determined the expression of two nitric oxide synthases, eNOS, and iNOS, in the aorta. As shown in Figure 2(d), eNOS protein expression decreased, and that of iNOS increased in DM compared with control ($p < 0.05$). Interestingly, insulin treatment significantly increased eNOS expression in the hypoglycemia groups compared with DM ($p < 0.05$), and expression was higher in the RH-DM than in the H-DM group (DM 0.54-, H-DM 1.13-, and RH-DM 1.76-fold compared with controls; $p < 0.05$). H-DM and RH-DM significantly increased iNOS expression in the aortas (DM 1.51-, H-DM 2.80-, and RH-DM 3.34-fold compared with controls; $p < 0.05$).

Vascular morphology analysis revealed that inflammatory cell infiltration of the intima and subintimal layers was significantly increased in diabetic compared with nondiabetic rats, with disruption of the morphology of the endothelium and smooth muscle layers (gray arrows). Importantly, inflammatory cell infiltration and disruption of endothelial structures were worse in the H-DM and RH-DM groups (Figure 2(e)). The results of eNOS and iNOS immunohistochemical staining are shown in Figure 2(e). Acute and recurrent hypoglycemia significantly increased the area of iNOS in DM, especially in the endothelium and perivascular tissue. Rupture of the endothelial layers was obvious in the hypoglycemic groups (gray arrows).

3.3. Oxidative Stress in Aged T2DM Rats with Acute and Recurrent Hypoglycemia. NADPH oxidase (NOX) 2 and 4 are key enzymes involved in electron transfer in the cell membrane and are sources of ROS in the cardiovascular system [36, 37]. To determine the level of oxidative stress, we assayed the expression of NOX2 and NOX4 in the aorta by western blotting. As shown in Figure 3(a), H-DM and RH-DM significantly increased NOX2 and NOX4 expressions in the aortas of model rats (NOX2: DM 1.59-, H-DM 1.89-, and RH-DM 2.20-fold compared with controls; NOX4: DM 1.55-, H-DM 2.22-, and RH-DM 2.50-fold compared with control). To further investigate the effects of hypoglycemia on oxidative stress, SOD and GSH-Px (antioxidant enzymes active against free radicals), and MDA (an indicator of lipid peroxidation) were assayed in serum (Figures 3(b)–3(d)). Antioxidant activity was significantly higher in the RH-DM group than in the other groups ($p < 0.05$). To better understand the effects of diabetic hypoglycemia on vascular damage and the underlying mechanisms, we assayed 7,8-dihydro-8-oxo-2-deoxyguanosine (8-OHdG) in aorta tissue by immunofluorescence. 8-OHdG is formed in aerobic organisms by the oxidation of DNA and reflects the level of cellular oxidative stress and the degree of mitochondrial damage [38, 39]. 8-OHdG levels were higher in the hypoglycemia groups than in the DM group, and all tissues of the aorta were involved (Figure 3(e)).

3.4. The Nuclear Factor Kappa B (NF-κB), NLRP3, and Cyclic Guanosine Monophosphate–Adenosine Monophosphate Synthase– (cGAS–) Stimulator of Interferon Genes (STING) Pathways in Acute and Recurrent Hypoglycemia in Aged T2DM Rats. The NF-κB inflammatory pathway promotes NLRP3 transcription, which in turn causes vascular dysfunction in diabetes [40, 41]. As shown in Figure 4(a), the percentage of phosphorylated NF-κB core protein p65 increased to 2.57-fold in the aortas from rats with acute hypoglycemia and to 3.48-fold in those with recurrent hypoglycemia compared with control rats at baseline. The role of pyroptosis induced by NLRP3 inflammasomes in diabetic vascular dysfunction has been confirmed. We used western blotting to assay the expression of NLRP3, apoptosis-associated speck-like protein (ASC), and cleaved caspase-1 in aorta tissue (Figure 4(b)). The related proteins detected in the H-DM and RH-DM groups were activated compared with the DM group ($p < 0.05$). NLRP3 pathway activity was higher in the RH-DM group than in the other groups (NLRP3: DM 1.74-, H-DM 2.09-, and RH-DM were 2.45-fold compared with control; $p < 0.05$). The expression and location of NLRP3 were determined by immunohistochemistry (Figure 4(c)) and immunofluorescence (Figure 4(d)). NLRP3 expression was stronger in rats with hypoglycemia

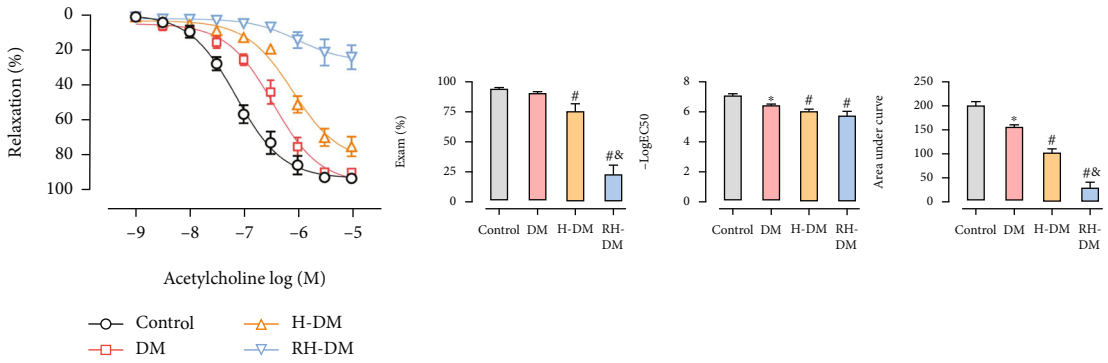

(a)

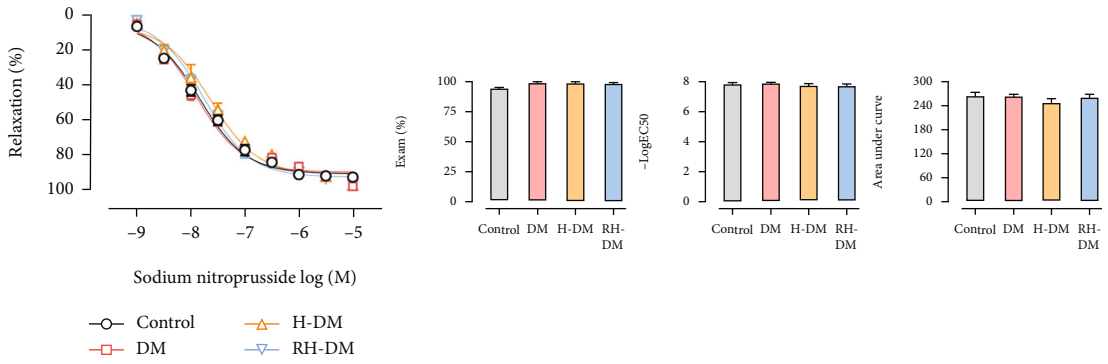

(b)

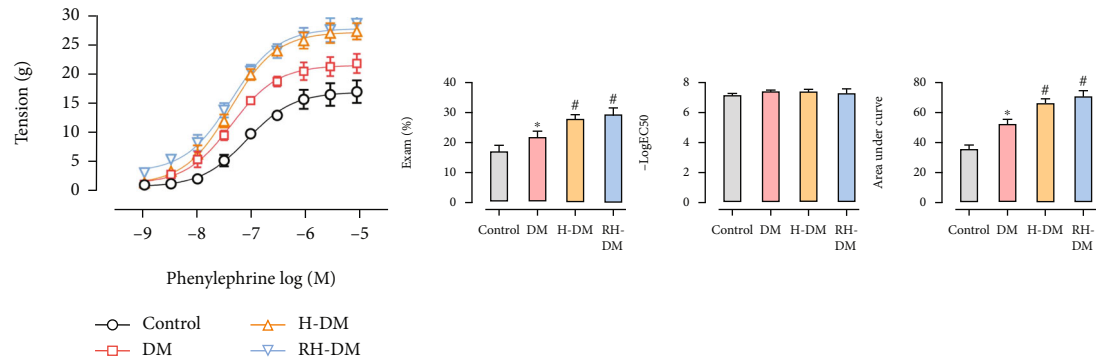

(c)

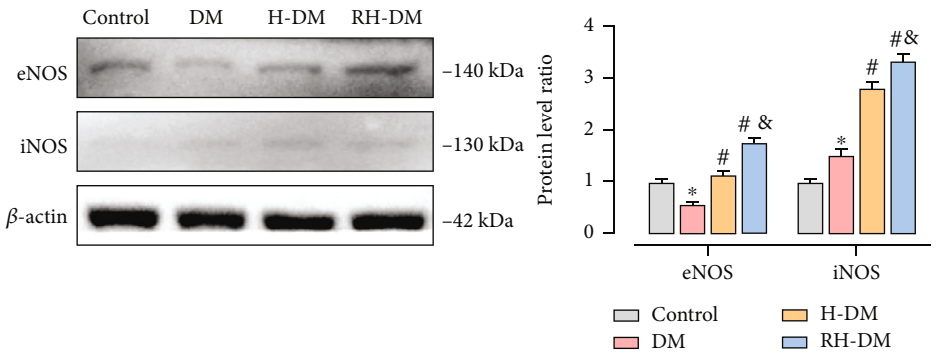

(d)

Figure 2: Continued.

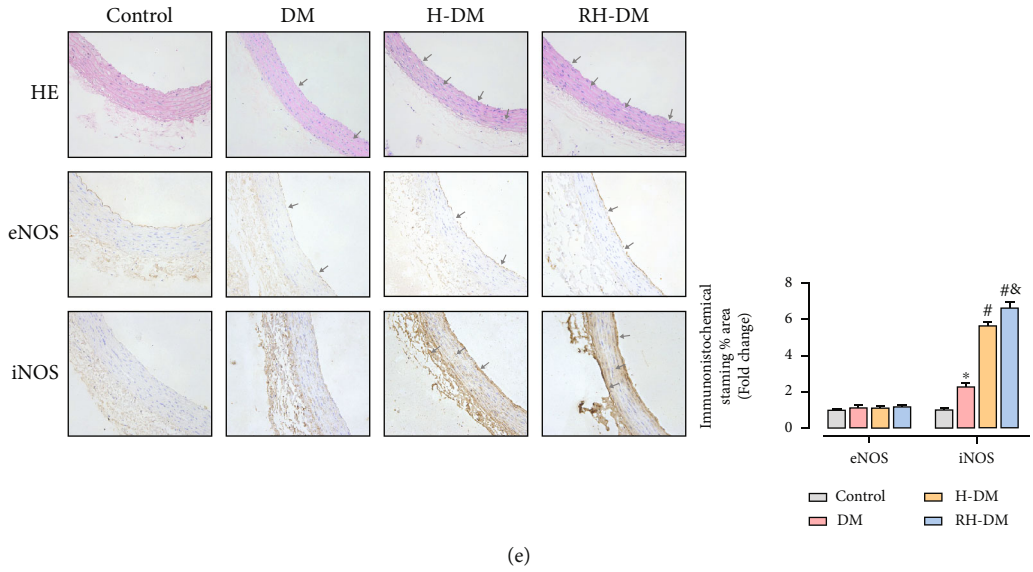

(e)

Figure 2: Vascular function, eNOS, and iNOS expression in aortas from aged T2DM rats in response to acute and recurrent hypoglycemia. (a) ACh- and (b) SNP-induced relaxation responsiveness and (c) PE-induced contraction responsiveness in controls, aged diabetes (DM), acute hypoglycemia (H-DM), and recurrent hypoglycemia (RH-DM) groups were determined by testing the reactivity of aorta rings. Vascular function was reported by EC_{50}, E_{max}, and the AUC. eNOS and iNOS protein expressions were assayed in (d) western blots and (e) by immunohistochemical staining. Aorta morphology was evaluated by hematoxylin and eosin staining; $^{*}p < 0.05$ DM vs. control; $^{\#}p < 0.05$ H-DM, RH-DM vs. DM; $^{\&}p < 0.05$ H-DM vs. RH-DM.

compared with the DM group, and all the vessel layers were involved (gray arrows).

cGAS–STING is a DNA sensor that triggers the innate immune response. cGAS produces the second messenger cGAMP and activates STING, which participates in autoimmune and inflammatory diseases [42]. The pathway was activated in the aortas of elderly diabetic rats ($p < 0.05$), and the difference between recurrent and acute hypoglycemia was not significant (cGAS: DM 1.36-, H-DM 1.78-, and RH-DM 1.62-fold compared with control).

3.5. Pyroptosis in Acute and Recurrent Hypoglycemia. To confirm whether acute and recurrent hypoglycemia affected pyroptosis activity in the aortas of diabetic rats, expression of the pyroptosis-associated protein GSDMD-N was assayed by western blotting, immunohistochemistry, and immunofluorescence. As shown in Figure 5(a), GSDMD-N expression increased in the DM group compared with control ($p < 0.05$). Insulin treatment significantly increased pyroptosis in the hypoglycemia groups compared with the DM group ($p < 0.05$), and pyroptosis activity was higher with RH-DM than with H-DM (DM 2.54-, H-DM 3.08-, and RH-DM 4.04-fold compared with control). As shown in Figures 5(b) and 5(c), GSDMD-N expression was stronger in rats with hypoglycemia compared with the DM group, and all the vessel layers were involved, especially the endovascular cortex (gray arrows). To assess the influence of acute and recurrent hypoglycemia on apoptosis, the expression of proapoptotic proteins (Bax) and antiapoptotic proteins (Bcl-2) was assayed. As shown in Figure 5(d), apoptosis was increased in in aorta tissue from the H-DM compared with the DM group ($p < 0.05$). Apoptosis rates in the RH-DM and DM groups were not significantly different, but apoptosis was significantly lower in the RH-DM than in the H-DM group (Bax: DM 1.55-, H-DM 1.83-, and RH-DM 1.62-fold compared with control; Bcl-2: DM 0.50-, H-DM 0.30-, and RH-DM 0.44-fold compared with control). Acute and recurrent hypoglycemia increased GSDMD-N expression and promoted pyroptosis. Apoptosis was not increased in rats with RH-DM.

4. Discussion

Our study found that hypoglycemia-induced vascular dysfunction in aged diabetes was associated with an increase of pyroptosis and is the first to report the effect of hypoglycemia on pyroptosis. Hypoglycemia is a common clinical event in diabetes patients, especially those with intensive glycemic control and using insulin or other hypoglycemic agents [4, 7, 43]. Most studies of diabetic hypoglycemia have focused on cognitive dysfunction [23, 43–45]. As glucose is the primary the energy source of the adult human brain, severe hypoglycemia, a blood glucose of <2.3 mM, can lead to coma, permanent brain damage, or death. Unfortunately, most instances of clinical hypoglycemia are not occasional but are recurrent and persistent. It is urgent to reveal the underlying mechanisms of cognitive deficits that result from RH and identify new intervention targets.

Most studies have shown that hypoglycemia promotes oxidative stress-induced brain damage in diabetes patients [21, 23, 43]. We believe that such events are mainly related to vascular damage. This study focused on vascular dysfunction in DM, which is a frequent complication that can result in generalized inflammation of small vessels and even

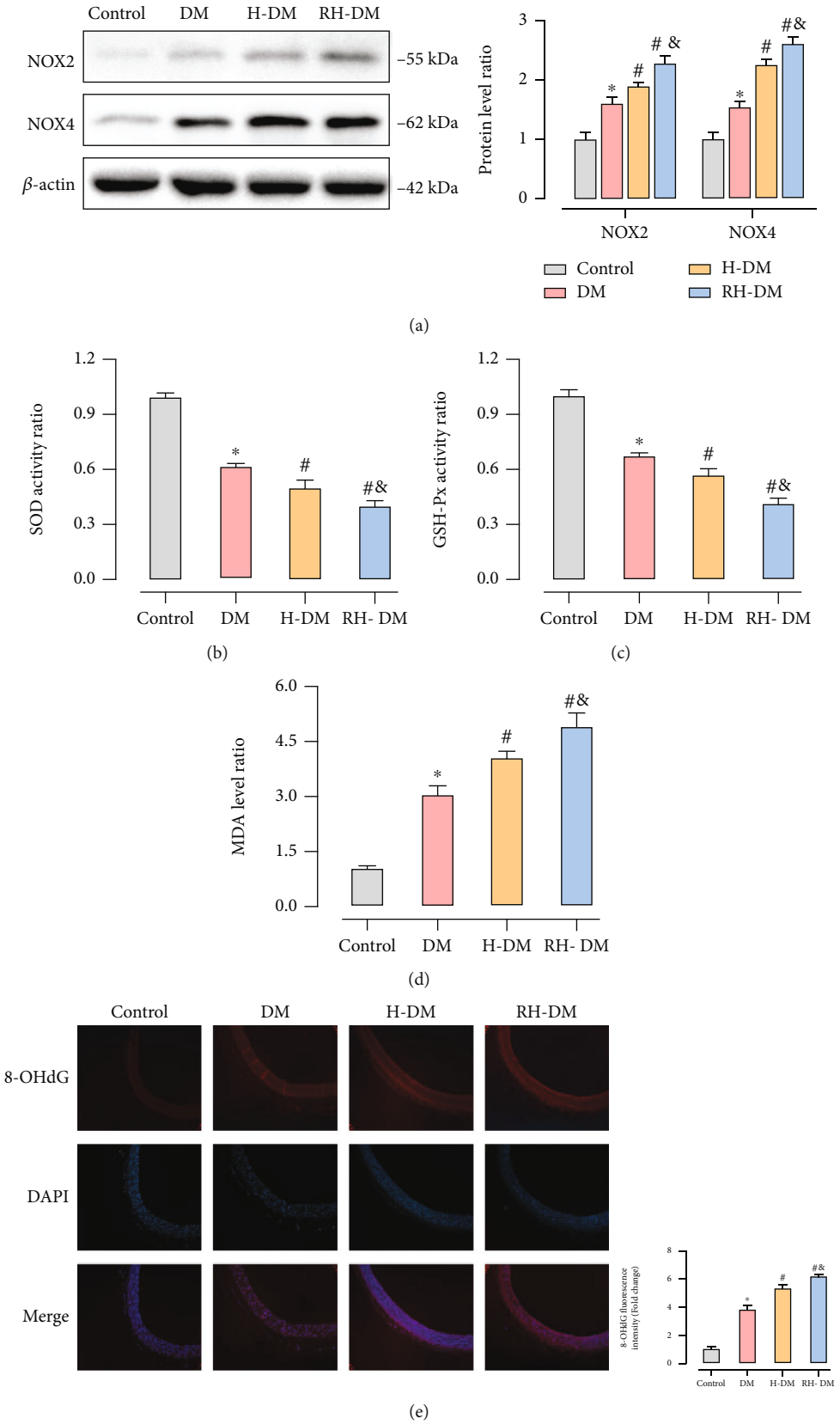

Figure 3: Oxidative stress in the aorta in response to acute and recurrent hypoglycemia in aged T2DM rats. NOX2/4 expression was assayed by (a) western blotting, (b) serum levels of SOD, (c) GSH-Px, and (d) MDA were tested. (e) 8-OHdG location and expression were determined by immunofluorescence; $^{*}p < 0.05$ DM vs. control; $^{\#}p < 0.05$ H-DM, RH-DM vs. DM; $^{\&}p < 0.05$ H-DM vs. RH-DM.

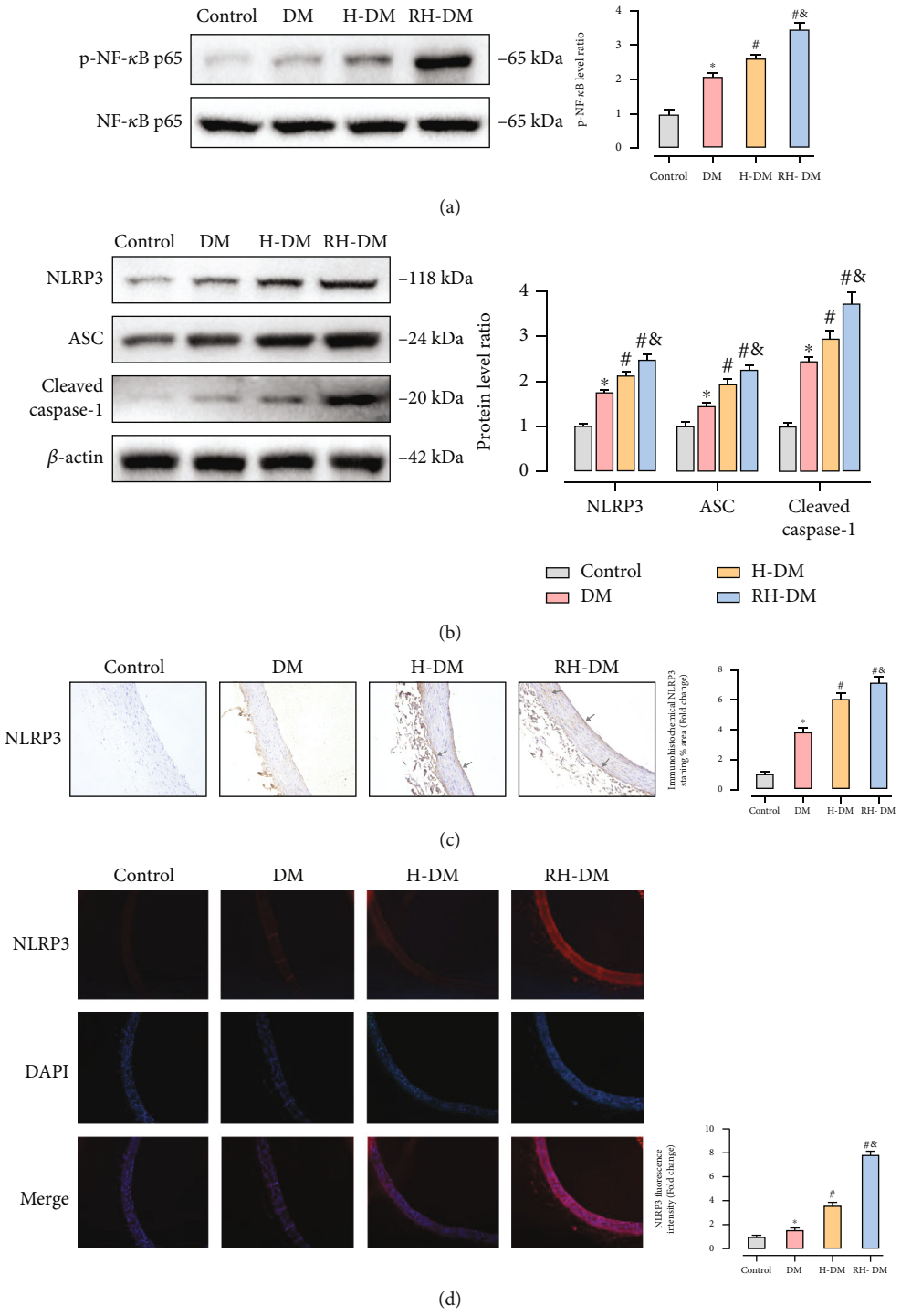

Figure 4: Continued.

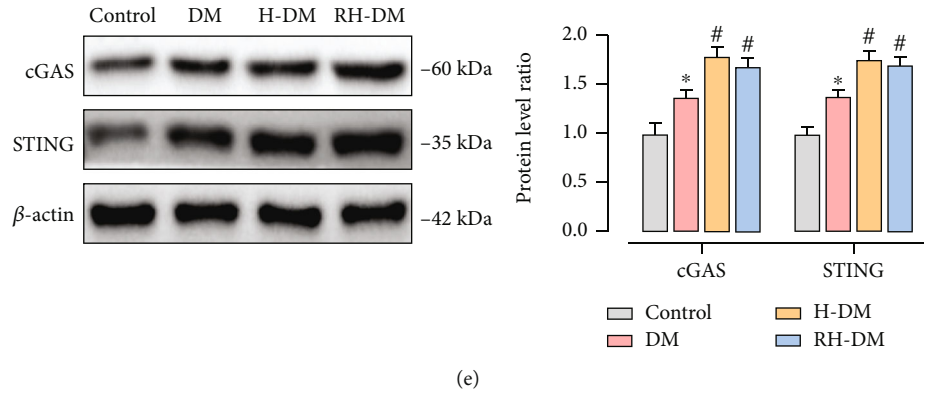

(e)

Figure 4: NF-κB, NLRP3, and cGAS–STING pathway activity of the aortas in response to acute and recurrent hypoglycemia in aged T2DM rats. (a) p-p65, NLRP3, ASC, (b) cleaved caspase-1, cGAS, and (e) STING expression were assayed by western blotting. The expression and location of NLRP3 were determined by (c) immunohistochemistry and (d) immunofluorescence; $^{*}p < 0.05$ DM vs. control; $^{\#}p < 0.05$ H-DM, RH-DM vs. DM; $^{\&}p < 0.05$ H-DM vs. RH-DM.

multiorgan failure. We used thoracic aortas as a representative vessel for the investigation of vascular function. The next step of our research team is to compare whether cerebrovascular and conduction vessels respond differently to hypoglycemic events.

Endothelial cells regulate vascular tension by the release of potent vasoactive substances such as nitric oxide. One causes of endothelial dysfunction is a decline in NO production [12, 32, 46]. In addition to the physiologic and biochemical findings, our study revealed impaired endothelial-dependent vasodilation responses to acute and recurrent hypoglycemia in aged diabetic rats. ACh promotes the release of factors such as NO and prostacyclin that cause relaxation. SNP directly affects vascular smooth muscle by increasing guanylate cyclase activity, resulting in an endothelium-independent relaxation [31]. We found that the response of the vascular smooth muscle to NO was not changed in the aortas of diabetes model rats and that hypoglycemia interfered with endothelium-dependent relaxation that was induced by Ach (Supplementary file 1).

It is noteworthy that eNOS and iNOS expressions were both the highest in the RH-DM group. The decoupling of eNOS induced by acute fluctuations of blood glucose in the endothelial cells of aged diabetic rats reduced the effectiveness of eNOS and resulted in an excess of peroxide anions [8–11]. Increased production of iNOS and decoupled eNOS led to accumulation of highly cytotoxic reactive nitrogen species, i.e., nitric oxide-derived compounds such as $ONOO^{-}$, which induces vascular hyporeactivity and cell death [47]. Most previous studies focused on how hyperglycemia induced vascular events by impairing eNOS activity or inducing eNOS uncoupling in diabetes [25, 46]. They did not adequately investigate the molecular mechanisms underlying the relationship between vessel damage and hypoglycemia. This is the first report that shows the recurrent hypoglycemia-induced eNOS decoupling, and we will investigate that relationship in future studies.

The endothelium of intact aortas from RH-DM and H-DM rats was more responsive to the contractile effects of norepinephrine than aortas from controls. The mechanisms are not completely understood, but some reasons for the increased vascular responsiveness to contractile agents are deficient endothelial activity, enhanced sensitivity of calcium channels, increased sensitivity to adrenergic agonists, enhanced oxidative stress, and decreased antioxidant defenses [34]. Two major conclusions from the study results are that the relaxation response to ACh was decreased by hypoglycemia and that the contractile response of the endothelium of intact aortas from diabetic rats to catecholamine was increased.

The prevalence of diabetes increases with age and is estimated as 20% in those 65–79 years of age [1]. Most previous studies have used young animals to model diabetes. In this study, an aged T2DM model was induced by STZ combined with 12 weeks of an HFD. Age is a key factor in determining both the risk of diabetes and subsequent outcomes [48]. Changes in molecular and cellular aging processes are currently believed to be the basis of cardiovascular disease, including autophagy, inflammation, oxidative stress, DNA damage, protease inactivation, and epigenetic disorders [49]. Aging is the greatest risk factor for most chronic diseases that have increased risks of morbidity and mortality. Aging is associated with progressive impairment of metabolic pathways that affect body composition, insulin resistance, mitochondrial dysfunction, and inflammation [5]. Aging research has focused on understanding the molecular mechanisms that regulate the aging process and identifying biomarkers that could help to predict age-related changes. The rats used in this study were 18 months old when they were sacrificed, which is an age equivalent to 50–60-year-old humans, in whom the incidence of diabetes is relatively high.

The activation pyroptosis involves the recognition of NLRP3 inflammasome agonists and inflammasome assembly and activation. NLRP3 has been reported to be activated by a variety of unrelated pathogen-associated molecular patterns (PAMPs) and damage-associated molecular patterns (DAMPs), but there is no evidence that NLRP3 binds directly to those effectors. Multiple molecular and cellular events, including ion flux, mitochondrial dysfunction,

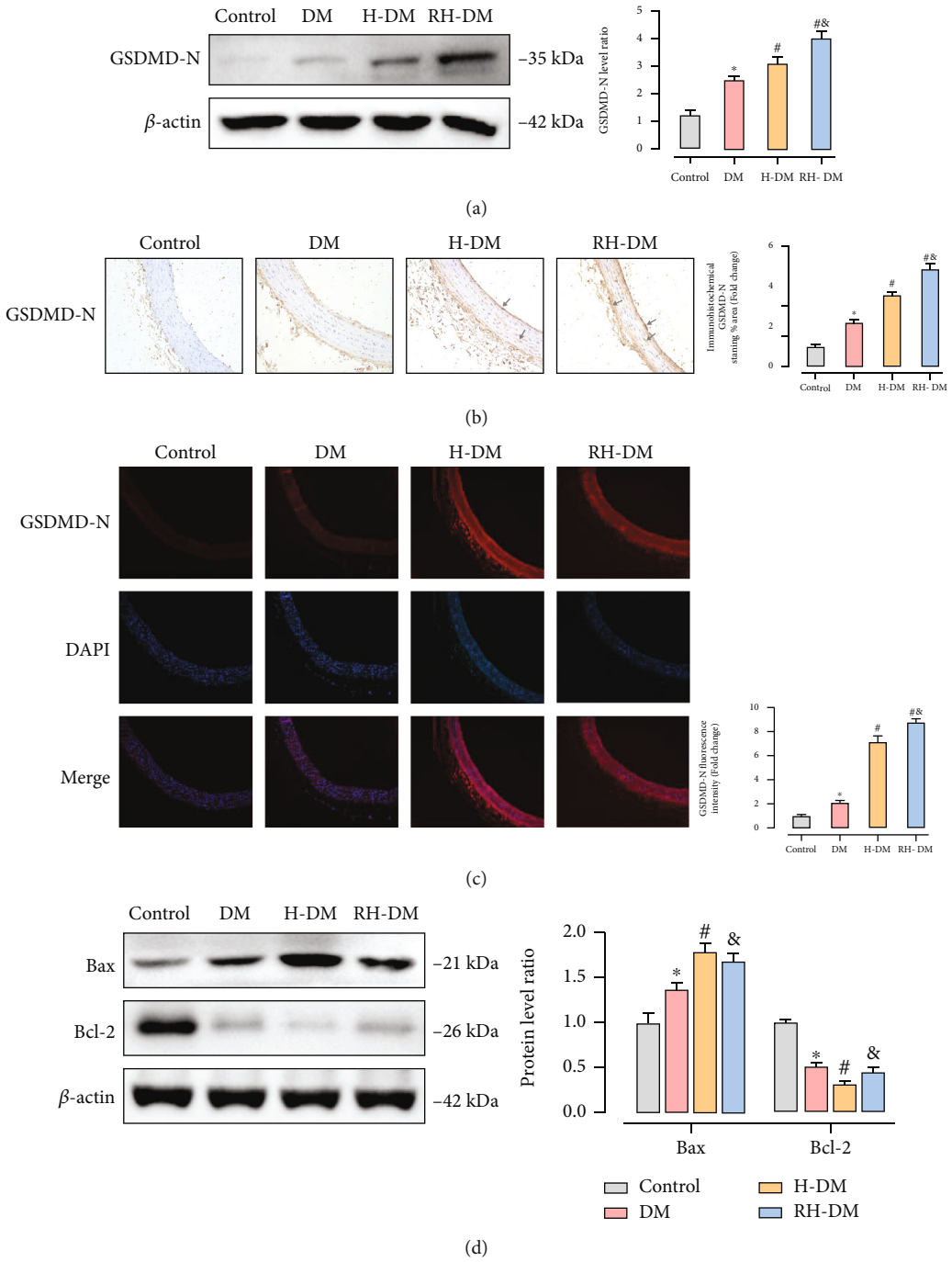

Figure 5: Pyroptosis in the aortas in response to acute and recurrent hypoglycemia in aged T2DM rats. (a) GSDMD-N, Bax, and (b) Bcl-2 expression were assayed by western blotting. Expression and location of GSDMD-N were identified by (b) immunohistochemistry and (c) immunofluorescence; $^{*}p < 0.05$ DM vs. control; $^{\#}p < 0.05$ H-DM, RH-DM vs. DM; $^{\&}p < 0.05$ H-DM vs. RH-DM.

release of ROS, and mitochondrial DNA (mtDNA) that induce NLRP3 stimuli, have been proposed as upstream signals for the assembly and activation of inflammasomes and caspase activation [28]. Activated caspases cleave gasdermin D at the interdomain loop to release the N-terminal pore-forming domain, which is then translocated to the plasma membrane to form pores induce pyroptosis. In contrast to other forms of cell death, pyroptosis has unique morphological and physical characteristics, including intact nuclei, cellular swelling, and plasma membrane rupture. In this study, changes in the levels of NOX2, NOX4, and 8-OHdG indicate that the release of ROS and mtDNA in model mice with hypoglycemia promoted pyroptosis (Supplementary file 3-5). Available evidence shows that activation of fatty acid oxidation followed by mtROS production may be a cause of endothelial dysfunction during hypoglycemia. cGAS is a cytoplasmic DNA biosensor that recognizes DNA from pathogens or damage. Mitochondrial metabolic stress has

been reported to contribute to diabetic cardiomyopathy by mtDNA-mediated activation of the cGAS–STING pathway. Interestingly, we observed that the cGAS–STING pathway was not significantly elevated in recurrent hypoglycemia compared with acute hypoglycemia, unlike NLRP3-mediated pyroptosis. That observation requires subsequent analysis and study.

Cell death is a fundamental physiological process in organ homeostasis, coordination of immune responses, and autoimmunity. Our understanding of the mechanisms orchestrating cellular death has increased substantially, and the modalities of programmed cell death that have been described highlight the complex mechanisms that tip the balance between different cell fates. The three most well understood modalities of cell death are apoptosis, necroptosis, and pyroptosis. Cell death is a very intricate game where distinct central players have the power to tip a fragile balance from life to death and include pro- and anti-inflammatory signals in the cell environment [50]. It has been suggested that pyroptosis is a form of apoptosis, and there is evidence that the two different modes of cell death act independently. New evidence suggests that members of the gasdermin superfamily promote apoptosis by permeabilizing mitochondria and participate in the final stages of the apoptotic program by inducing secondary pyroptosis [51]. The results shown in Figure 5 indicate that acute and recurrent hypoglycemia increased GSDMD-N expression and promoted pyroptosis and that apoptosis was lower in rats with RH-DM than it was in those with H-DM. In our study, apoptosis and pyroptosis levels were different, which further demonstrates the importance of pyroptosis in hypoglycemic responses.

Current studies of the complications of hypoglycemia in diabetes have primarily focused on brain injury induced by hypoglycemia [23, 43–45]. Studies of the effects of severe hypoglycemia in humans have yielded conflicting results. Severe hypoglycemia has been shown to alter brain structure and cause significant cognitive damage in many, but not all, studies. Reasons for the discrepancy are not known, but a major contributing factor may be the extent of glycemic control (including recurrent hypoglycemia) prior to episodes of severe hypoglycemia. There is evidence that recurrent episodes of moderate hypoglycemia protect the brain against damage caused by a subsequent episode of more severe hypoglycemia, a phenomenon known as hypoglycemia preconditioning [43]. These intriguing findings suggest that recurrent bouts of moderate hypoglycemia that occur with intensive glycemic control might, paradoxically, render an individual more prone but less vulnerable to an episode of severe hypoglycemia. It is more likely that the brain adapts to low glucose, but it is by no means certain that this tendency has individual benefits. The results of our study suggest that recurrent hypoglycemia did indeed damage vascular function (Supplementary file 1-5).

The association between severe hypoglycemia and increased risk of vascular events has been acknowledged in diabetes, but the exact mechanism has rarely been explored in recent years. In summary, our study found that pyroptosis had a key role in vascular dysfunction associated with hypoglycemia induced by glycemic control in a rat diabetes model induced by STZ and an HFD.

Data Availability

All data utilized in this study are included in this article, and all data supporting the findings of this study are available on reasonable request from the corresponding author.

Conflicts of Interest

The authors declare that there are no conflicts of interest.

Authors' Contributions

An He conceived the study and designed the experiments. Minghao Luo and Yu Hu performed the experiments. Minghao Luo and Dingyi Lv analyzed the data and drafted the manuscript. An He, Lingyun Xie, Deyu Zuo, Shenglan Yang, and Yuzhou Xue reviewed and revised the manuscript. All authors contributed to the article and approved the submitted version. Minghao Luo, Yu Hu, and Dingyi Lv contributed equally to this paper.

Acknowledgments

This work was supported by An He and the Innovation Program for Doctoral Student of the First Affiliated Hospital of Chongqing Medical University (CYYY-BSYJSCXXM-202202).

References

[1] J. E. Morley, "Diabetes and aging: epidemiologic overview," *Clinics in Geriatric Medicine*, vol. 24, no. 3, pp. 395–405, 2008.

[2] A. Sinclair, P. Saeedi, A. Kaundal, S. Karuranga, B. Malanda, and R. Williams, "Diabetes and global ageing among 65-99-year-old adults: Findings from the International Diabetes Federation Diabetes Atlas, 9th edition," *Diabetes Research and Clinical Practice*, vol. 162, p. 108078, 2020.

[3] A. Zeyfang, J. Wernecke, and A. Bahrmann, "Diabetes mellitus at an elderly age," *Experimental and Clinical Endocrinology & Diabetes*, vol. 129, no. S 01, pp. S20–S26, 2021.

[4] R. Bucala, "Diabetes, aging, and their tissue complications," *The Journal of Clinical Investigation*, vol. 124, no. 5, pp. 1887-1888, 2014.

[5] Z. Bloomgarden and G. Ning, "Diabetes and aging," *Journal of Diabetes*, vol. 5, no. 4, pp. 369–371, 2013.

[6] N. Laiteerapong, S. A. Ham, Y. Gao et al., "The legacy effect in type 2 diabetes: impact of early glycemic control on future complications (the diabetes & aging study)," *Diabetes Care*, vol. 42, no. 3, pp. 416–426, 2019.

[7] K. Tanaka, Y. Okada, K. Torimoto, K. Nishio, M. Narisawa, and Y. Tanaka, "Hypoglycemia induces vascular endothelial dysfunction in subjects with normal glucose tolerance," *Scientific Reports*, vol. 12, no. 1, p. 2598, 2022.

[8] C. R. Triggle and H. Ding, "A review of endothelial dysfunction in diabetes: a focus on the contribution of a dysfunctional eNOS," *Journal of the American Society of Hypertension*, vol. 4, no. 3, pp. 102–115, 2010.

[9] L. Gao, A. Yu, J. Liu, L. Ma, and J. Li, "eNOS uncoupling: a therapeutic target for ischemic foot of diabetic rat," *Experimental and Clinical Endocrinology & Diabetes*, vol. 127, no. 5, pp. 303–310, 2019.

[10] H. Ding and C. R. Triggle, "Endothelial dysfunction in diabetes: multiple targets for treatment," *Pflügers Archiv-European Journal of Physiology*, vol. 459, no. 6, pp. 977–994, 2010.

[11] A. K. Azemi, S. S. Mokhtar, L. J. Hou, S. Sharif, and A. Rasool, "Model for type 2 diabetes exhibits changes in vascular function and structure due to vascular oxidative stress and inflammation," *Biotechnic & Histochemistry*, vol. 96, no. 7, pp. 498–506, 2021.

[12] A. He, D. Zuo, X. Liang, Y. Guo, L. Suxin, and Y. Xia, "Hypoglycemia increases endothelial-dependent vasodilation through suppressing phosphorylation at threonine 495/497 site of endothelial nitric oxide synthase," *Microvascular Research*, vol. 133, p. 104075, 2021.

[13] C. Li, A. He, Y. Guo et al., "Hypertonic stress modulates eNOS function through O-GlcNAc modification at Thr-866," *Scientific Reports*, vol. 11, no. 1, p. 11272, 2021.

[14] A. He, S. Hu, Q. Pi et al., "Regulation of O-GlcNAcylation on endothelial nitric oxide synthase by glucose deprivation and identification of its O-GlcNAcylation sites," *Scientific Reports*, vol. 10, no. 1, p. 19364, 2020.

[15] Z. Cai, S. Yuan, X. Luan et al., "Pyroptosis-related inflammasome pathway: a new therapeutic target for diabetic cardiomyopathy," *Frontiers in Pharmacology*, vol. 13, p. 842313, 2022.

[16] J. Xu, S. Cai, J. Zhao et al., "Advances in the relationship between pyroptosis and diabetic neuropathy," *Frontiers in Cell and Development Biology*, vol. 9, p. 753660, 2021.

[17] C. Meng, C. Gu, S. He et al., "Pyroptosis in the retinal neurovascular unit: new insights into diabetic retinopathy," *Frontiers in Immunology*, vol. 12, p. 763092, 2021.

[18] B. E. Burdette, A. N. Esparza, H. Zhu, and S. Wang, "Gasdermin D in pyroptosis," *Acta Pharmaceutica Sinica B*, vol. 11, no. 9, pp. 2768–2782, 2021.

[19] Y. Zuo, L. Chen, H. Gu et al., "GSDMD-mediated pyroptosis: a critical mechanism of diabetic nephropathy," *Expert Reviews in Molecular Medicine*, vol. 23, p. e23, 2021.

[20] N. Kajihara, D. Kukidome, K. Sada et al., "Low glucose induces mitochondrial reactive oxygen species via fatty acid oxidation in bovine aortic endothelial cells," *Journal of Diabetes Investigation*, vol. 8, no. 6, pp. 750–761, 2017.

[21] M. Ashfaq, A. R. Moats, H. Northrup et al., "Hypoglycemia in mitochondrial disorders," *Mitochondrion*, vol. 58, pp. 179–183, 2021.

[22] A. Yoshinaga, N. Kajihara, D. Kukidome et al., "Hypoglycemia induces mitochondrial reactive oxygen species production through increased fatty acid oxidation and promotes retinal vascular permeability in diabetic mice," *Antioxidants & Redox Signaling*, vol. 34, no. 16, pp. 1245–1259, 2021.

[23] R. Gao, L. Ren, Y. Zhou et al., "Recurrent non-severe hypoglycemia aggravates cognitive decline in diabetes and induces mitochondrial dysfunction in cultured astrocytes," *Molecular and Cellular Endocrinology*, vol. 526, p. 111192, 2021.

[24] P. R. Nagareddy, Z. Xia, J. H. McNeill, and K. M. MacLeod, "Increased expression of iNOS is associated with endothelial dysfunction and impaired pressor responsiveness in streptozotocin-induced diabetes," *American Journal of Physiology. Heart and Circulatory Physiology*, vol. 289, no. 5, pp. H2144–H2152, 2005.

[25] T. V. Fiorentino, A. Prioletta, P. Zuo, and F. Folli, "Hyperglycemia-induced oxidative stress and its role in diabetes mellitus related cardiovascular diseases," *Current Pharmaceutical Design*, vol. 19, no. 32, pp. 5695–5703, 2013.

[26] M. R. Davanso, A. R. Crisma, T. T. Braga et al., "Macrophage inflammatory state in type 1 diabetes: triggered by NLRP3/iNOS pathway and attenuated by docosahexaenoic acid," *Clinical Science (London, England)*, vol. 135, no. 1, pp. 19–34, 2021.

[27] Z. Qiu, S. Lei, B. Zhao et al., "NLRP3 Inflammasome activation-mediated pyroptosis aggravates myocardial ischemia/reperfusion injury in diabetic rats," *Oxidative Medicine and Cellular Longevity*, vol. 2017, Article ID 9743280, 17 pages, 2017.

[28] I. M. Gora, A. Ciechanowska, and P. Ladyzynski, "NLRP3 inflammasome at the interface of inflammation, endothelial dysfunction, and type 2 diabetes," *Cells*, vol. 10, no. 2, p. 314, 2021.

[29] A. He, H. Yu, Y. Hu et al., "Honokiol improves endothelial function in type 2 diabetic rats via alleviating oxidative stress and insulin resistance," *Biochemical and Biophysical Research Communications*, vol. 600, pp. 109–116, 2022.

[30] A. He, J. Shen, Y. Xue et al., "Diacerein attenuates vascular dysfunction by reducing inflammatory response and insulin resistance in type 2 diabetic rats," *Biochemical and Biophysical Research Communications*, vol. 585, pp. 68–74, 2021.

[31] M. Luo, C. Cao, J. Niebauer et al., "Effects of different intensities of continuous training on vascular inflammation and oxidative stress in spontaneously hypertensive rats," *Journal of Cellular and Molecular Medicine*, vol. 25, no. 17, pp. 8522–8536, 2021.

[32] M. Luo, J. Meng, J. Yan et al., "Role of the nucleotide-binding domain-like receptor protein 3 inflammasome in the endothelial dysfunction of early sepsis," *Inflammation*, vol. 43, no. 4, pp. 1561–1571, 2020.

[33] C. Uluoglu, D. B. Durakoglugil, C. Karasu, G. Ozbey, A. Gunes, and H. Zengil, "The effect of experimental diabetes on the twenty-four-hour pattern of the vasodilator responses to acetylcholine and isoprenaline in the rat aorta," *Chronobiology International*, vol. 24, no. 6, pp. 1081–1094, 2007.

[34] M. Mulhern and J. R. Docherty, "Effects of experimental diabetes on the responsiveness of rat aorta," *British Journal of Pharmacology*, vol. 97, no. 4, pp. 1007–1012, 1989.

[35] N. L. Scarborough and G. O. Carrier, "Nifedipine and alpha adrenoceptors in rat aorta. II. Role of extracellular calcium in enhanced alpha-2 adrenoceptor-mediated contraction in diabetes," *The Journal of Pharmacology and Experimental Therapeutics*, vol. 231, no. 3, pp. 603–609, 1984.

[36] G. Salazar, "NADPH oxidases and mitochondria in vascular senescence," *International Journal of Molecular Sciences*, vol. 19, no. 5, p. 1327, 2018.

[37] A. B. García-Redondo, A. Aguado, A. M. Briones, and M. Salaices, "NADPH oxidases and vascular remodeling in cardiovascular diseases," *Pharmacological Research*, vol. 114, pp. 110–120, 2016.

[38] T. F. Huang, Z. P. Tang, S. Wang et al., "Decrease in serum levels of adiponectin and increase in 8-OHdG: a culprit for cognitive impairment in the elderly patients with type 2 diabetes," *Current Molecular Medicine*, vol. 20, no. 1, pp. 44–50, 2019.

[39] X. B. Wang, N. H. Cui, X. Liu, and X. Liu, "Mitochondrial 8-hydroxy-2'-deoxyguanosine and coronary artery disease in patients with type 2 diabetes mellitus," *Cardiovascular Diabetology*, vol. 19, no. 1, p. 22, 2020.

[40] J. Cheng, Q. Liu, N. Hu et al., "Downregulation of hsa_circ_0068087 ameliorates TLR4/NF-κB/NLRP3 inflammasome-mediated inflammation and endothelial cell dysfunction in

high glucose conditioned by sponging miR-197," *Gene*, vol. 709, pp. 1–7, 2019.

[41] M. H. Liu, "FGF-21 alleviates diabetes-associated vascular complications: inhibiting NF-κB/NLRP3 inflammasome-mediated inflammation," *International Journal of Cardiology*, vol. 185, pp. 320-321, 2015.

[42] T. Bao, J. Liu, J. Leng, and L. Cai, "The cGAS-STING pathway: more than fighting against viruses and cancer," *Cell & Bioscience*, vol. 11, no. 1, p. 209, 2021.

[43] E. C. Puente, J. Silverstein, A. J. Bree et al., "Recurrent moderate hypoglycemia ameliorates brain damage and cognitive dysfunction induced by severe hypoglycemia," *Diabetes*, vol. 59, no. 4, pp. 1055–1062, 2010.

[44] L. Lin, Y. Wu, Z. Chen, L. Huang, L. Wang, and L. Liu, "Severe hypoglycemia contributing to cognitive dysfunction in diabetic mice is associated with pericyte and blood-brain barrier dysfunction," *Frontiers in Aging Neuroscience*, vol. 13, p. 775244, 2021.

[45] C. He, P. Gao, Y. Cui et al., "Low-glucose-sensitive TRPC6 dysfunction drives hypoglycemia-induced cognitive impairment in diabetes," *Clinical and Translational Medicine*, vol. 10, no. 6, article e205, 2020.

[46] F. Paneni, J. A. Beckman, M. A. Creager, and F. Cosentino, "Diabetes and vascular disease: pathophysiology, clinical consequences, and medical therapy: part I," *European Heart Journal*, vol. 34, no. 31, pp. 2436–2443, 2013.

[47] K. Rehman and M. Akash, "Mechanism of generation of oxidative stress and pathophysiology of type 2 diabetes mellitus: how are they interlinked," *Journal of Cellular Biochemistry*, vol. 118, no. 11, pp. 3577–3585, 2017.

[48] A. I. Vinik, P. Camacho, S. Reddy et al., "Aging, diabetes, and falls," *Endocrine Practice*, vol. 23, no. 9, pp. 1117–1139, 2017.

[49] J. Sun, B. Cheng, Y. Su et al., "The potential role of m6A RNA methylation in the aging process and aging-associated diseases," *Frontiers in Genetics*, vol. 13, p. 869950, 2022.

[50] D. Bertheloot, E. Latz, and B. S. Franklin, "Necroptosis, pyroptosis and apoptosis: an intricate game of cell death," *Cellular & Molecular Immunology*, vol. 18, no. 5, pp. 1106–1121, 2021.

[51] K. Tsuchiya, "Inflammasome-associated cell death: pyroptosis, apoptosis, and physiological implications," *Microbiology and Immunology*, vol. 64, no. 4, pp. 252–269, 2020.

Hindawi
Oxidative Medicine and Cellular Longevity
Volume 2022, Article ID 1392896, 12 pages
https://doi.org/10.1155/2022/1392896

Research Article

Hydrogen Sulfide Ameliorated High Choline-Induced Cardiac Dysfunction by Inhibiting cGAS-STING-NLRP3 Inflammasome Pathway

Lu Bai,[1] **Jing Dai**,[2] **Yuxuan Xia**,[1] **Kaichuan He**,[1] **Hongmei Xue**,[1] **Qi Guo**,[1] **Danyang Tian**,[1] **Lin Xiao**,[1] **Xiangjian Zhang**,[3] **Xu Teng**,[1] **Yuming Wu**,[1,3] **and Sheng Jin**[1]

[1]*Department of Physiology, Hebei Medical University, Hebei 050017, China*
[2]*Department of Clinical Diagnostics, Hebei Medical University, Hebei 050017, China*
[3]*Hebei Collaborative Innovation Center for Cardio-Cerebrovascular Disease, 050017 Hebei, China*

Correspondence should be addressed to Sheng Jin; jinshengsheng@126.com

Received 2 June 2022; Accepted 12 July 2022; Published 22 July 2022

Academic Editor: Tao Zheng

Although it is an essential nutrient, high choline intake directly or indirectly via its metabolite is associated with increased risk of cardiovascular disease, the mechanism of which remains to be elucidated. The present study was performed to investigate whether hydrogen sulfide (H_2S) was involved in high choline-induced cardiac dysfunction and explore the potential mechanisms. We found that ejection fraction (EF) and fractional shortening (FS), the indicators of cardiac function measured by echocardiography, were significantly decreased in mice fed a diet containing 1.3% choline for 4 months as compared to the control, while applying 3,3-dimethyl-1-butanol (DMB) to suppress trimethylamine N-oxide (TMAO, a metabolite of choline) generation ameliorated the cardiac function. Subsequently, we found that feeding choline or TMAO significantly increased the protein levels of cyclic GMP-AMP (cGAMP) synthase (cGAS), stimulator of interferon genes (STING), NOD-like receptor protein 3 (NLRP3), caspase-1, and interleukin-1β (IL-1β) as compared to the control, which indicated the activation of cGAS-STING-NLRP3 inflammasome axis. Moreover, the protein expression of cystathionine γ-lyase (CSE), the main enzyme for H_2S production in the cardiovascular system, was significantly increased after dietary supplementation with choline, but the plasma H_2S levels were significantly decreased. To observe the effect of endogenous H_2S, CSE knockout (KO) mice were used, and we found that the EF, FS, and plasma H_2S levels in WT mice were significantly decreased after dietary supplementation with choline, while there was no difference between CSE KO + control and CSE KO + choline group. To observe the effect of exogenous H_2S, mice were intraperitoneally injected with sodium hydrosulfide (NaHS, a H_2S donor) for 4 months, and we found that NaHS improved the cardiac function and reduced the protein levels of cGAS, STING, NLRP3, caspase-1, and IL-1β in mice receiving dietary choline. In conclusion, our studies revealed that high choline diet decreased plasma H_2S levels and induced cardiac dysfunction via cGAS-STING-NLRP3 inflammasome axis while H_2S treatment could restore the cardiac function by inhibiting cGAS-STING-NLRP3 inflammasome axis.

1. Introduction

Choline is an essential bioactive micronutrient abundant in egg yolk, red meat, fish, dairy products, and soybean. Although it can be formed de novo by methylation of phosphatidylethanolamine, additional dietary intake of choline is also required or else will develop a deficiency state [1]. Because of its wide-ranging roles in biological processes including cholinergic neurotransmission, lipid transport, membrane phospholipids synthesis, and methyl group metabolism, inadequate intake or abnormal metabolism of choline can lead to neurological disorders, cancers, and

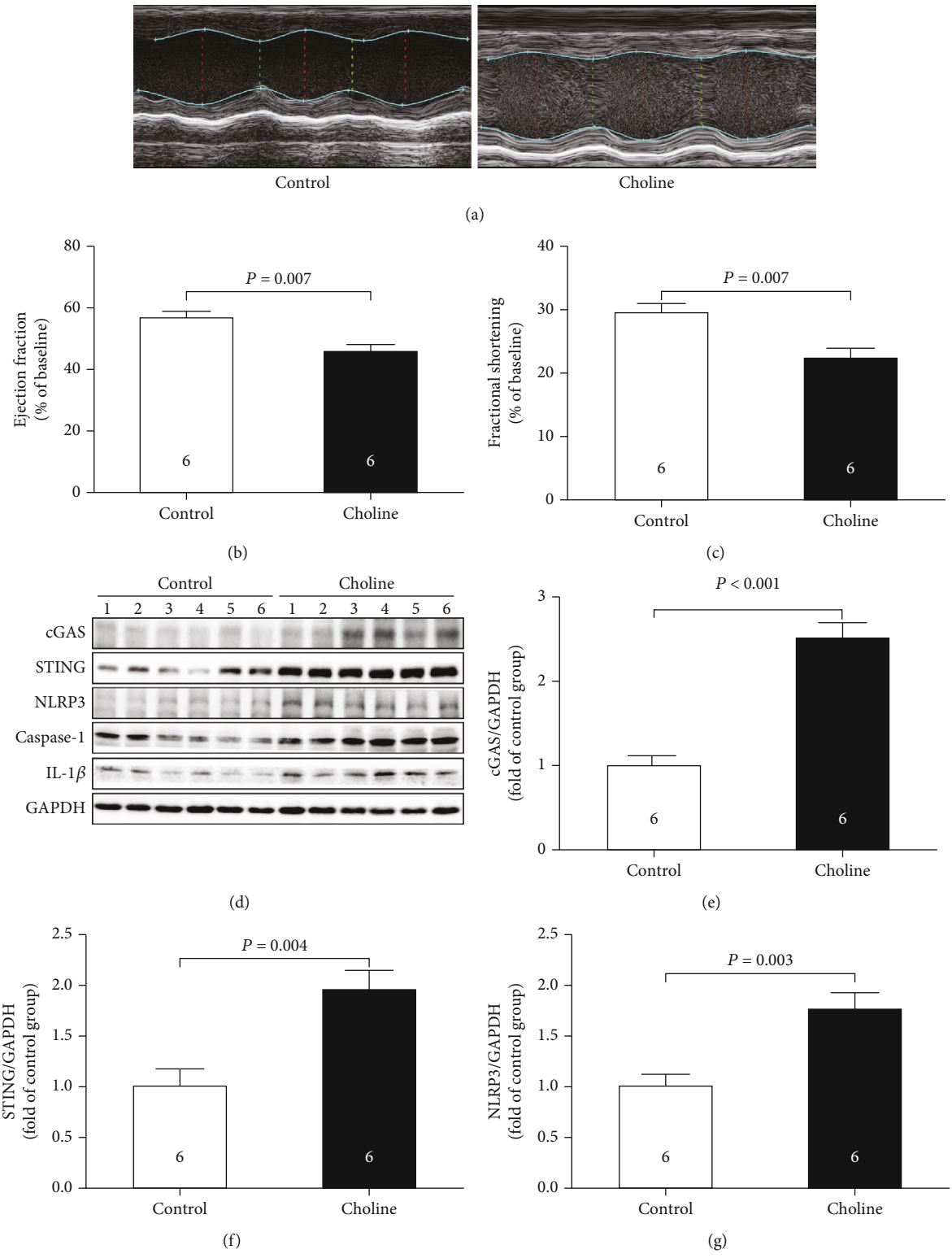

Figure 1: Continued.

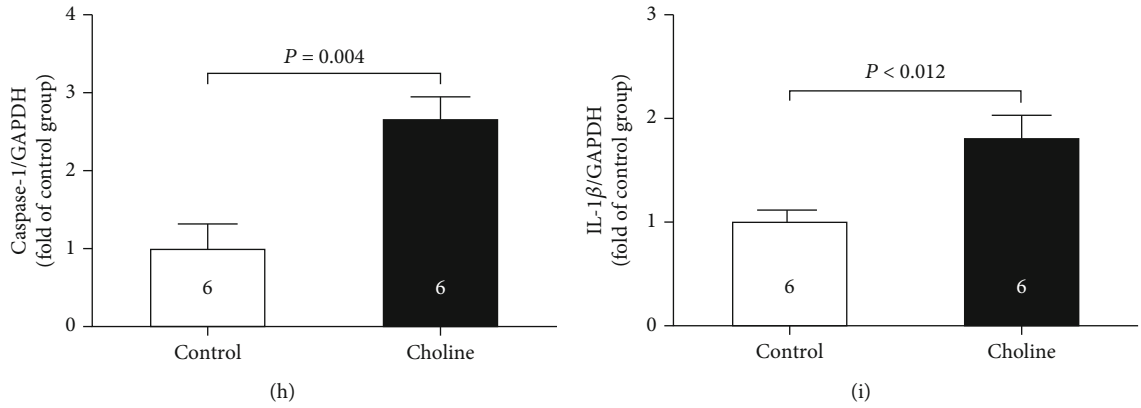

Figure 1: Dietary choline induced cardiac dysfunction in mice. (a) Representative M-mode images. (b) The changes of left ventricular ejection fraction (LVEF) after dietary supplementation with choline. (c) The changes of left ventricular fractional shortening (LVFS) after dietary supplementation with choline. (d)–(i) Representative western blots and quantitative analysis for cGAS, STING, NLRP3, caspase-1, and IL-1β protein expression in heart tissues after dietary supplementation with choline. Results are expressed as mean ± SEM. A P of <0.05 was considered significant.

cardiovascular disease, which can be cured clinically with choline [2–4]. However, an analysis of a large prospective cohort showed high choline intake was associated with increased risk of cardiometabolic mortality in racially diverse populations [5]. And a growing body of preclinical studies highlighted that high choline intake directly or indirectly via its metabolites such as trimethylamine N-oxide (TMAO) had been to a higher risk of heart disease. For example, Organ et al. reported that choline diet and its derived metabolite, TMAO, exacerbated pressure overload-induced heart failure [6]. Another study found that high-choline diet aggravated cardiac dysfunction, fibrosis, and inflammation in a mouse model of heart failure with preserved ejection fraction [7]. Nevertheless, the potential mechanism of high choline-induced cardiac dysfunction remains to be elucidated.

Hydrogen sulfide (H_2S) is a colorless, water-soluble, and corrosive gas with a characteristic odor of rotten eggs and was traditionally known as an environmental pollutant which is toxic to humans at high concentrations [8]. However, it was not until the pioneering work of Abe and Kimura in 1996 that H_2S was truly considered to be an endogenous gasotransmitter alongside carbon monoxide and nitric oxide [9]. In mammalian cells, H_2S is biosynthesized mainly from L-cysteine and/or L-homocysteine by three endogenous enzymes: cystathionine β-synthase (CBS), cystathionine γ-lyase (CSE), and 3-mercaptopyruvate sulfurtransferase (3-MST) coupled with cysteine aminotransferase. The tissue distribution of these H_2S-producing enzymes is different: CBS is predominantly expressed in the central nervous system, whereas CSE is mainly present in the cardiovascular system, and 3-MST is found primarily in the brain and erythrocytes [10, 11]. Numerous studies have shown that physiological concentration of H_2S plays a fundamental role in the cardiovascular system by regulating the biological functions and maintaining homeostasis [12, 13]. Conversely, lack of endogenous H_2S was detrimental and contributed to various cardiovascular diseases including atherosclerosis, hypertension, myocardial infarction, and heart failure [14–16]. However, whether high choline-induced cardiac dysfunction was associated with the changes in H_2S concentration has not previously been evaluated.

With this in mind, the aim of present study was to investigate whether H_2S was involved in high choline-induced cardiac dysfunction and explore the potential mechanisms.

2. Material and Methods

2.1. Animals and Treatments. All animal experimentals were performed according to the Guide for the Care and Use of Laboratory Animals published by the US National Institutes of Health (NIH Publication, 8th Edition, 2011) and approved by the Ethics Committee for Laboratory Animals Care and Use of Hebei Medical University. Male C57BL/6 J mice were provided from Vital River Laboratories (Beijing, China). CSE knockout (CSE KO) mice with C57BL/6 J genetic bases and its homozygote wild-type (WT) mice were bred from CSE heterozygous mice which were kindly provided as gifts by Professor Yichun Zhu (Fudan University, Shanghai, China). Mice were housed in plastic cages with 12 h light/12 h dark cycles at 22-24°C with 60% humidity and *ad libitum* access to standard rat chow and sterile tap water.

In order to observe the effect of choline, male C57BL/6 J mice were randomly divided into 2 groups: control group and choline group. The mice in the choline group were given a chow diet supplemented with 1.3% choline (Beijing Keao Xieli Feed Co., Ltd., Beijing, China) for 4 months, and the mice in the control group were given a regular chow diet for the same period.

In order to observe the effect of 3,3-dimethyl-1-butanol (DMB, the TMA lyase inhibitors), male C57BL/6 J mice were randomly divided into 3 groups: control group, choline group, and choline + DMB group. The mice in the choline group and choline + DMB group were given a chow diet supplemented with 1.3% choline for 4 months. The mice in the choline + DMB group were fed with 1.3% DMB

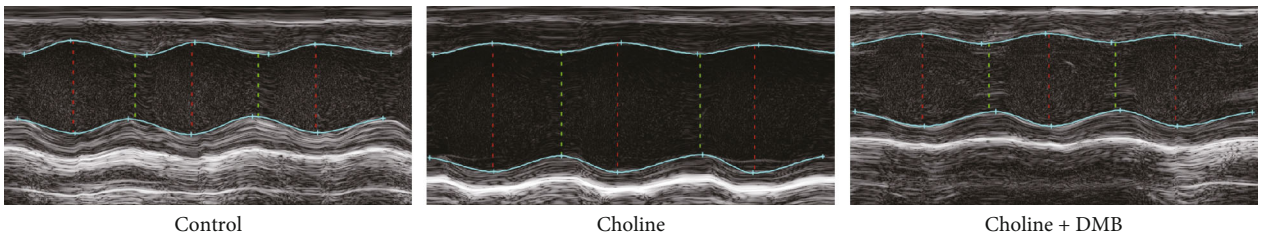

(a)

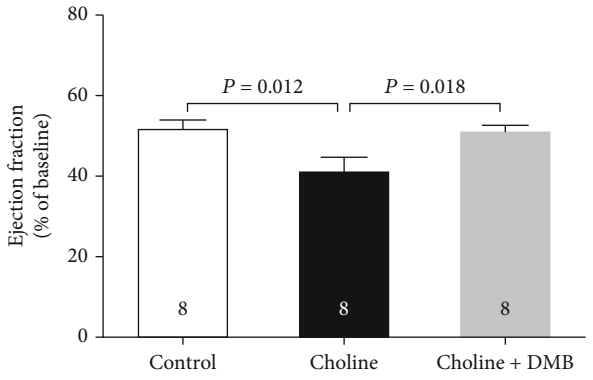

(b)

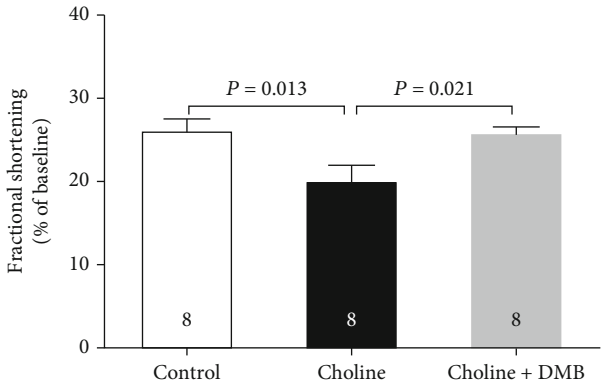

(c)

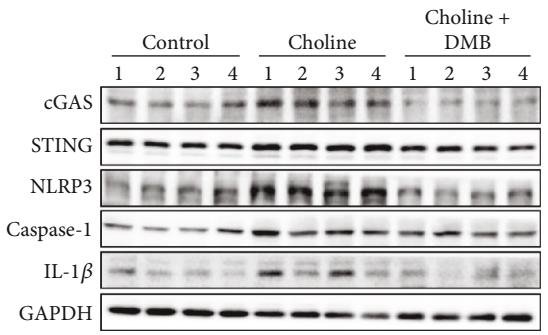

(d)

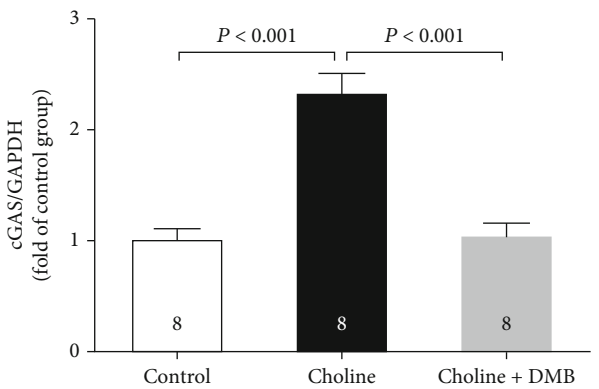

(e)

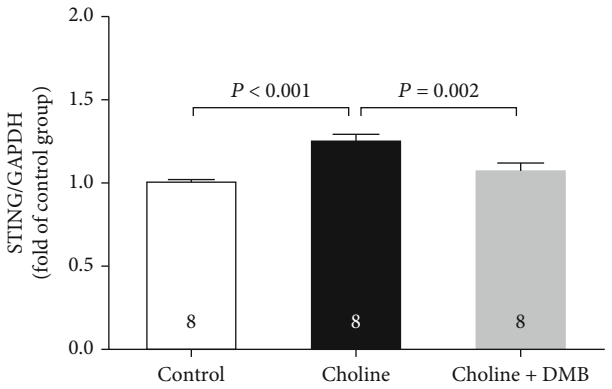

(f)

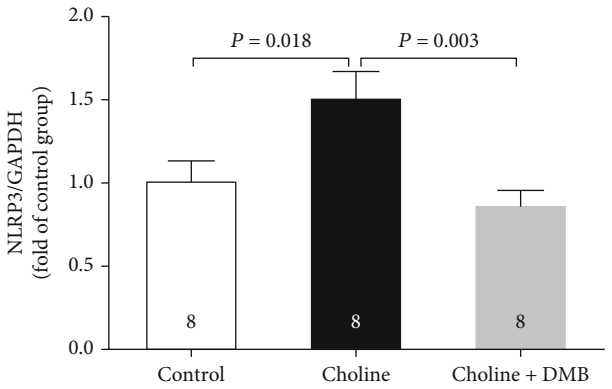

(g)

Figure 2: Continued.

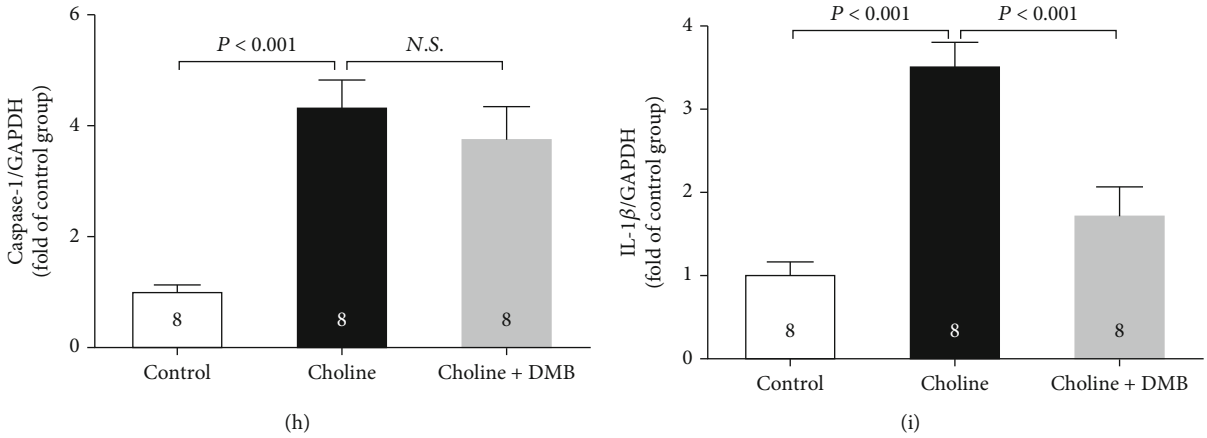

Figure 2: Dietary choline induced cardiac dysfunction by generating TMAO in mice. (a) Representative M-mode images. (b) The changes of left ventricular ejection fraction (LVEF) after DMB supplementation. (c) The changes of left ventricular fractional shortening (LVFS) after DMB supplementation. (d)–(i) Representative western blots and quantitative analysis for cGAS, STING, NLRP3, caspase-1, and IL-1β protein expression in heart tissues after DMB supplementation. Results are expressed as mean ± SEM. A P of <0.05 was considered significant.

(Aladdin Biochemical Technology Co., Ltd., Shanghai, China) in the drinking water for 4 months.

In order to observe the effect of TMAO, male C57BL/6 J mice were randomly divided into 2 groups: control group and TMAO group. The mice in the TMAO group were fed with 1.3% TMAO (Aladdin Biochemical Technology Co., Ltd., Shanghai, China) in the drinking water for 2 months.

In order to observe the effect of exogenous H_2S, male C57BL/6 J mice were randomly divided into 3 groups: control group, choline group, and choline + sodium hydrosulfide (NaHS, a H_2S donor) group. The mice in the choline group and choline + NaHS group were given a chow diet supplemented with 1.3% choline for 4 months. The mice in the choline + NaHS group were intraperitoneally injected with NaHS (100 μmol/kg/day, Sigma-Aldrich Ltd., St. Louis., USA) for 4 months.

In order to observe the effect of endogenous H_2S, male CSE KO and WT mice were randomly divided into 4 groups: WT + control group, WT + choline group, CSE KO + control group, and CSE KO + choline group. The mice in the WT + choline group and CSE KO + choline group were given a chow diet supplemented with 1.3% choline for 4 months.

2.2. Echocardiography. At the end of the experiment, mice were anesthetized with 1% isoflurane, and the cardiac function was evaluated by using a VisualSonics Vevo 2100 system (FUJIFILM VisualSonics Inc., Toronto, Canada) as described in our previous research [17]. M-mode images of the left ventricle were recorded, and three consecutive cardiac cycles were selected to measure left ventricular ejection fraction and fractional shortening (LVEF and LVFS). And then, the heart was harvested and stored at -80°C until assay. Plasma was separated from the blood after centrifugation at 3500 rpm for 10 min and stored at -80°C until assay.

2.3. Measurement of H_2S Concentration in Plasma. The H_2S levels in plasma were measured according to the previously study [18]. Briefly, 30 μL of plasma was mixed with 80 μL monobromobimane (MBB, Sigma-Aldrich Ltd., St. Louis., USA) and 10 μL 0.1% ammonia with shaking for 1 h at room temperature for derivatization of sulfide, which called sulfide-dibimane. The reaction was then terminated with 10 μL 20% formic acid and centrifuged at 15000 × g for 10 min. The supernatants were stored at -80°C before the measurement of H_2S levels using liquid chromatography coupled with tandem mass spectrometry.

2.4. Western Blot Analysis. The protein expressions in myocardial tissue were evaluated by western blotting according to the previously study [19]. Frozen heart tissues were homogenized with ice-cold radio immunoprecipitation assay (RIPA) lysis buffer. Proteins were extracted and quantified by the bicinchoninic acid (BCA) method. Equal amount of protein samples was separated on 10% sodium dodecyl sulfate-polyacrylamide gel electrophoresis (SDS-PAGE) gels and transferred to polyvinylidene fluoride membranes. The membranes were blocked with 5% nonfat milk for 1 h and incubated with primary antibodies that recognized CSE (1 : 1000, Santa Cruz Biotechnology, the United States), cyclic GMP-AMP (cGAMP) synthase (cGAS, 1 : 1000, Proteintech Biotechnology, the United States), stimulator of interferon genes (STING, 1 : 1000, Proteintech Biotechnology, the United States), NOD-like receptor protein 3 (NLRP3, 1 : 1000, Proteintech Biotechnology, the United States), caspase-1 (1 : 1000, Proteintech Biotechnology, the United States), interleukin-1β (IL-1β, 1 : 1000, Proteintech Biotechnology, the United States), and GAPDH (1 : 5000, Proteintech Biotechnology, the United States) at 4°C overnight. Then, the membranes were incubated with horseradish peroxidase-conjugated secondary antibodies for 1 h after washing with TBST. Specific bands were detected with SuperSignal West Pico Chemiluminescent Substrate (Thermo, Scientific-Pierce, Waltham, the United States). The band intensity was quantified by ImageJ software.

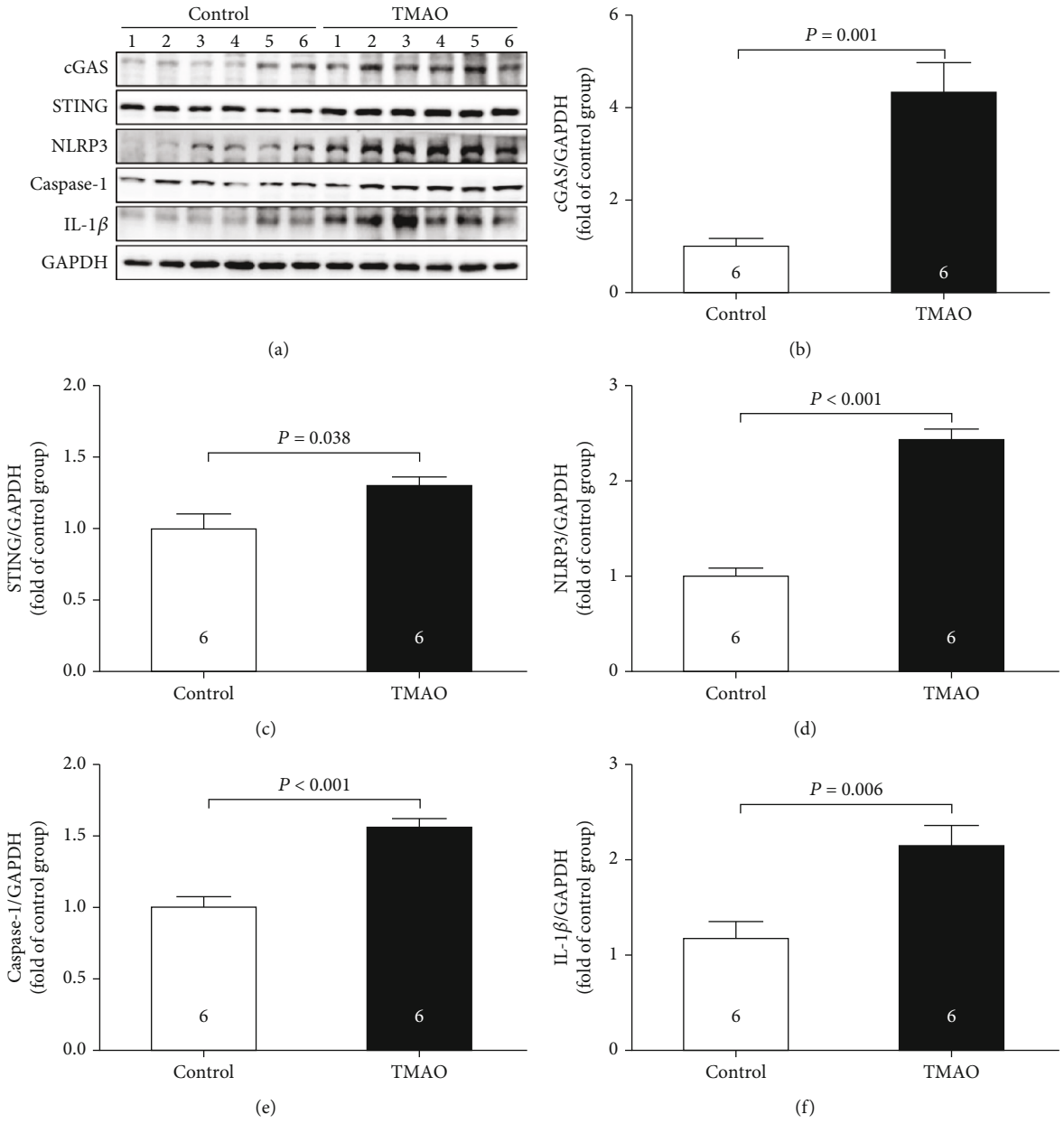

Figure 3: Dietary TMAO upregulated the protein expression of cGAS-STING-NLRP3 inflammasome axis. (a)–(f) Representative western blots and quantitative analysis for cGAS, STING, NLRP3, caspase-1, and IL-1β protein expression in heart tissues. Results are expressed as mean ± SEM. A P of <0.05 was considered significant.

2.5. Statistical Analysis. The experimental data were presented as mean ± SEM and statistical significance assessed in SPSS (SPSS 13.0, Inc., Chicago, the United States) using independent t-test to compare values between two groups and one-way ANOVA followed by least significant difference t-test to compare values between multiple groups. P < 0.05 was considered statistically significant.

3. Results

3.1. Dietary Choline Induced Cardiac Dysfunction in Mice. As was shown in Figures 1(a)–1(c), EF and FS, the indicators of cardiac function measured by echocardiography, were significantly decreased in mice fed a diet containing 1.3% choline as compared to the control. To better understand the mechanism of the action of dietary choline, we quantified the protein expression of cGAS-STING-NLRP3 inflammasome axis in the heart (Figures 1(d)–1(i)) and found that choline significantly increased the protein levels of cGAS, STING, NLRP3, caspase-1, and IL-1β as compared to the control.

3.2. Dietary Choline Induced Cardiac Dysfunction by Generating TMAO in Mice. To explore whether TMAO produced by choline degradation was involved in choline-induced cardiac dysfunction, DMB, a structural analog of

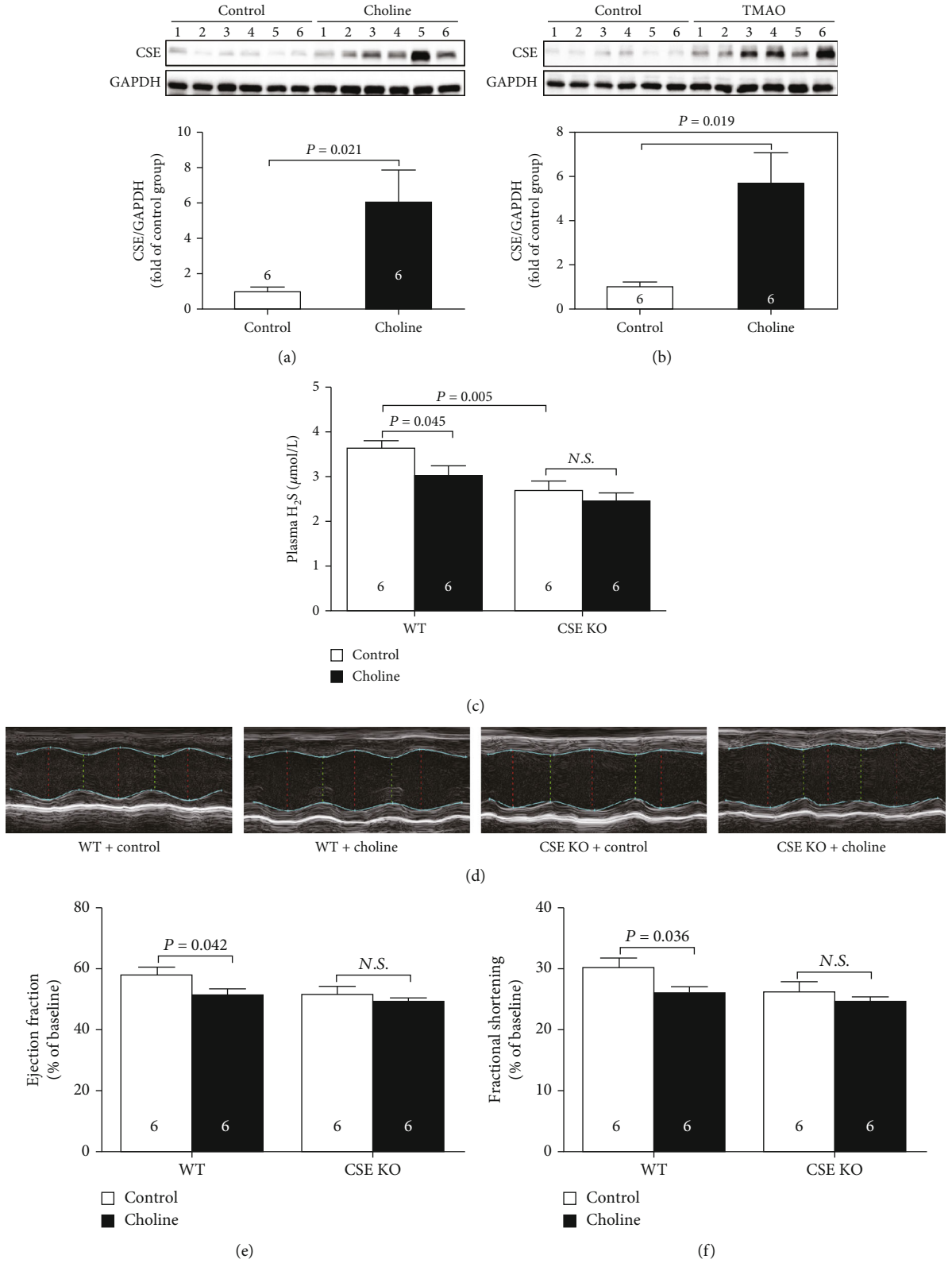

Figure 4: Dietary choline inhibited the endogenous production of H_2S. (a) Representative western blots and quantitative analysis for CSE protein expression in heart tissues after dietary supplementation with choline. (b) Representative western blots and quantitative analysis for CSE protein expression in heart tissues after dietary supplementation with TMAO. (c) Plasma H_2S levels in CSE KO mice. (d) Representative M-mode images in CSE KO mice. (e) The changes of left ventricular ejection fraction (LVEF) in CSE KO mice. (f) The changes of left ventricular fractional shortening (LVFS) in CSE KO mice. Results are expressed as mean ± SEM. A P of <0.05 was considered significant.

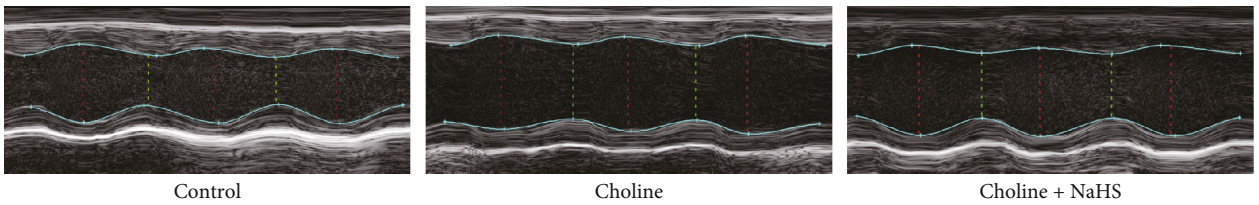

(a)

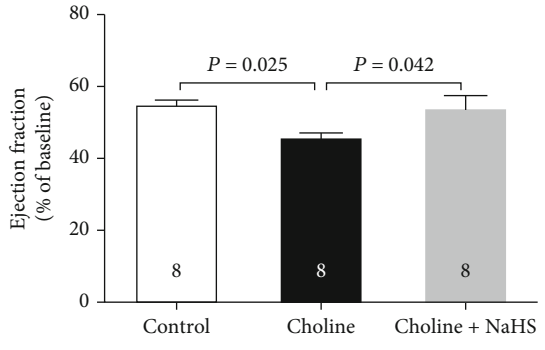

(b)

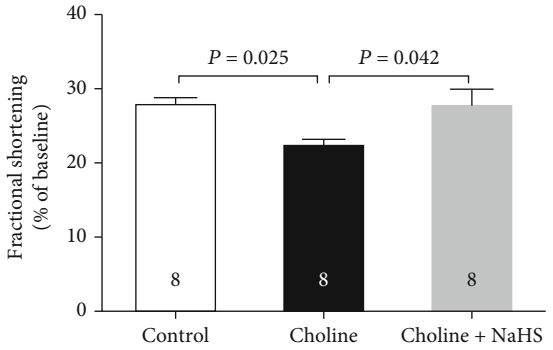

(c)

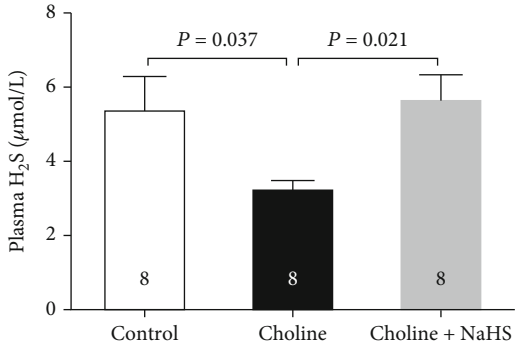

(d)

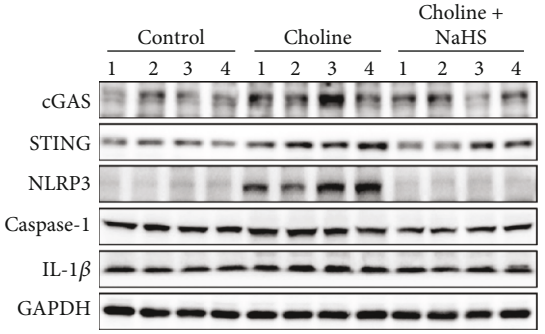

(e)

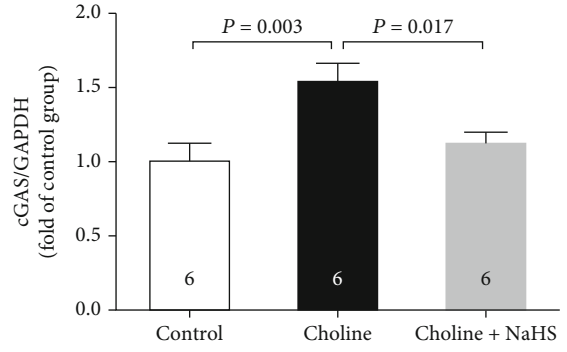

(f)

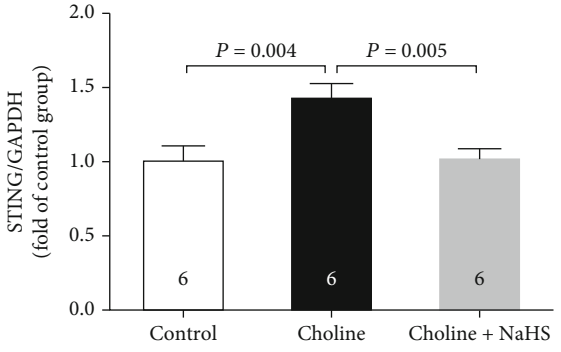

(g)

Figure 5: Continued.

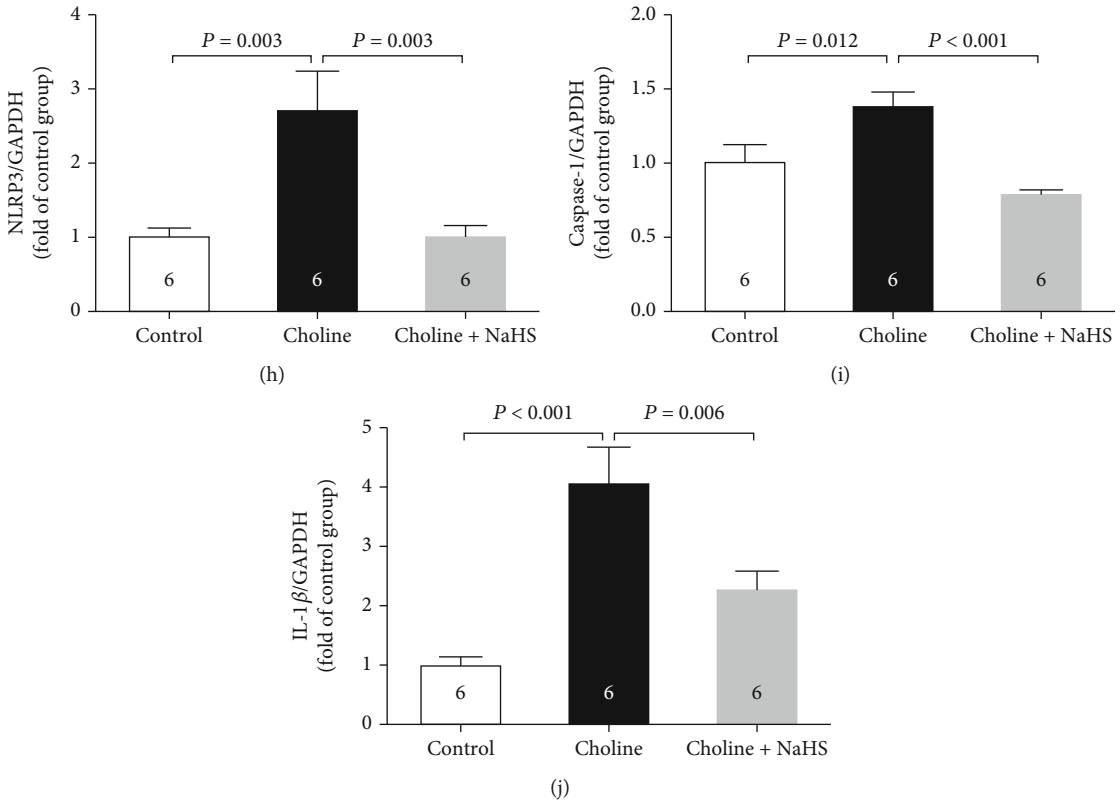

Figure 5: Exogenous H_2S improved choline induced-cardiac dysfunction. (a) Representative M-mode images. (b) The changes of left ventricular ejection fraction (LVEF) after NaHS treatment. (c) The changes of left ventricular fractional shortening (LVFS) after NaHS treatment. (d) Plasma H_2S levels after NaHS treatment. (e)–(j) Representative western blots and quantitative analysis for cGAS, STING, NLRP3, caspase-1, and IL-1β protein expression in heart tissues after NaHS treatment. Results are expressed as mean ± SEM. A P of <0.05 was considered significant.

choline, was used to inhibit TMAO formation. As was shown in Figure 2(a)–2(c), addition of DMB in the drinking water substantially ameliorated EF and FS as compared to the Choline group. DMB also markedly inhibited the choline diet-induced increase in the protein levels of cGAS, STING, NLRP3, caspase-1, and IL-1β (Figures 2(d)–2(i)). In addition, the protein levels of cGAS, STING, NLRP3, caspase-1, and IL-1β were significantly increased in mice receiving dietary TMAO as compared to the control (Figures 3(a)–3(f)).

3.3. Dietary Choline Inhibited the Endogenous Production of H_2S. As was shown in Figures 4(a) and 4(b), the protein expressions of CSE, the main enzyme for H_2S production in the cardiovascular system, were significantly increased after dietary supplementation with choline or TMAO, which indicated that endogenous H_2S was involved in choline-induced cardiac dysfunction. So, WT and CSE KO mice were fed with choline. As was shown in Figure 4(c), the plasma H_2S levels in WT mice were significantly decreased after dietary supplementation with choline, while there was no difference in the plasma H_2S levels between CSE KO + control and CSE KO + choline group. EF and FS were significantly decreased in the WT mice fed with choline, but there was also no significant difference in EF and FS between CSE KO + control and CSE KO + choline group (Figures 4(d)–4(f)).

3.4. Exogenous H_2S Improved Choline-Induced Cardiac Dysfunction. As was shown in Figures 5(a)–5(c), compared with the choline group, both EF and FS were significantly increased in the choline + NaHS group; meanwhile, the plasma H_2S levels were also markedly increased in the choline + NaHS group (Figure 5(d)). In addition, NaHS reduced the protein levels of cGAS, STING, NLRP3, caspase-1, and IL-1β in mice receiving dietary choline (Figure 5(e)–5(j)).

4. Discussion

In the present study, we found that high choline diet induced cardiac dysfunction via cGAS-STING-NLRP3 inflammasome axis while H_2S treatment could restore the cardiac function by inhibiting cGAS-STING-NLRP3 inflammasome axis.

Although it played vital physiological roles in the development and function of the cardiovascular system as an essential nutrient, emerging evidence implicated that higher dietary intakes of choline were also associated with increased risk of increased risk of acute myocardial infarction (MI) in patients with stable angina pectoris [20]. Moreover, a high-choline diet was shown to exacerbate the cardiac function and cardiac fibrosis of MI mice through accelerating the transformation of fibroblasts into myofibroblasts [21]. Choline in the diet can be metabolized to trimethylamine (TMA)

by the intestinal microorganisms. After being absorbed into the blood, TMA enters the liver and is oxidized to TMAO which is involved in the onset and development of cardiovascular disease. It was reported that two weeks of TMAO injection significantly induced cardiac hypertrophy and fibrosis in rats [22]. In the present study, the cardiac function represented by EF and FS was significantly decreased in mice after 4 months of 1.3% choline feeding, while applying DMB to suppress TMAO generation improved the cardiac function. Subsequently, we found that feeding choline or TMAO promoted NLRP3 inflammasome formation as well as caspase-1 and IL-1β activation. The NLRP3 inflammasome is an intracellular protein complex activated upon tissue injury. Once activated, it can trigger and amplify sterile inflammatory responses by activating and releasing IL-1β, which has been reported to involve in the pathophysiology cardiovascular disease [23, 24]. In line with our findings, one study reported that choline uptake in bone-marrow-derived macrophages regulated activation of the NLRP3 inflammasome, whereas impaired choline uptake and phosphorylation reduced NLRP3 inflammasome activation and inhibited IL-1β production [25]. Another study reported that TMAO aggravated doxorubicin-induced mouse cardiac fibrosis through activation of the NLRP3 inflammasome [26]. Moreover, Wu et al. reported that either a high-choline diet or TMAO enhanced the allogenic graft-versus-host (GVH) reaction which was mediated by NLRP3 inflammasome activation-induced macrophage polarization, whereas DMB reversed choline-induced GVH disease severity [27].

Given the chemical and structural diversity of NLRP3-activating stimuli, it is unlikely that those stimuli directly bind to and activated NLRP3. Instead, NLRP3 is likely to sense a common cellular signal induced in response to NLRP3 activators. Multiple molecular or cellular events including K^+ efflux, Ca^{2+} signaling, reactive oxygen species, mitochondrial dysfunction, and lysosomal damage, were involved in the activation of NLRP3 inflammasome assembly [28, 29]. Recently, it was found that mitochondrial DNA (mtDNA) which was released into the cytoplasm played an important role in the activation of the inflammasome [30]. The DNA sensor cGAS interacted with mtDNA and generated the second messenger cGAMP, which trigger the cGAS-STING-NLRP3 pathway to activate inflammasome response [31]. In the present study, we found that feeding choline or TMAO increased the protein expression of cGAS and STING, while DMB markedly inhibited the choline diet-induced increase in the protein levels of cGAS and STING, which indicated that feeding choline or TMAO activated the cGAS-STING pathway. Although there was no direct evidence that choline or TMAO promoted mtDNA release, it was confirmed that TMAO altered mitochondrial energy metabolism [32] and enhanced the mitochondrial impairments [33], which might induce mtDNA release to trigger the cGAS-STING -NLRP3 pathway [34].

As the third endogenous signaling gasotransmitter, H_2S participates in a wide spectrum of physiological processes in the body including regulating mitochondrial function. Although higher concentrations inhibit the electron transport chain [35], lower concentrations promote mitochondrial biogenesis and function [36, 37]. However, to the best of our knowledge, there are currently no studies exploring the link between H_2S and the cGAS-STING pathway. In the present study, we found that dietary choline significantly decreased the plasma H_2S levels, while application of H_2S donor, NaHS, significantly increased plasma H_2S levels and inhibited cGAS-STING pathway. However, how H_2S inhibited the cGAS-STING pathway still needed to be further elucidated. In addition, we also found that NLRP3 inflammasome activation was inhibited by NaHS, which was generally consistent with our previous studies and others' reports. Our previous studies clarified that H_2S improved hypertension-associated endothelial dysfunction [38] or attenuated lipopolysaccharide-induced acute kidney injury [39] by inhibiting NLRP3 inflammasome. H_2S was also reported to protect against dextran sulfate sodium-induced colitis [40] or paraquat-induced acute liver injury [41] by inhibiting NLRP3 inflammasome.

Moreover, we found that the protein expressions of CSE, the main enzyme for H_2S production in the cardiovascular system, were significantly increased after dietary supplementation with choline or TMAO, but the plasma H_2S levels were significantly decreased. Our results were consistent with previous studies in which a significant decrease in H_2S bioavailability was observed in the plasma, aorta, or myocardial tissue but a higher CSE expression in aorta or myocardial tissue [42, 43]. It was reported that the CSE could function as an inducible H_2S generating enzyme, whose expression was upregulated in cells by a range of stimuli including endoplasmic reticulum stress, oxidative stress, nutrient deprivation, and hyperhomocysteinemia [44]. The elevated CSE protein expression could be explained as a compensatory mechanism; although, this compensation did not increase plasma H_2S levels, which was due to the accelerated H_2S metabolism by choline or TMAO induced oxidative stress [45, 46]. On the other hand, CSE produced H_2S at the steady-state low intracellular Ca^{2+} concentrations in cells [47], whereas choline or TMAO could increase Ca^{2+} influx and/or Ca^{2+} release from intracellular stores to inhibit CSE activity and suppress H_2S generation [48, 49]. To further confirm the compensatory increased expression of CSE, CSE KO mice were used, and we found that the plasma H_2S levels in WT mice were significantly decreased after dietary supplementation with choline, while there was no difference in the plasma H_2S levels between CSE KO + control and CSE KO + choline group. Our finding meant that choline or TMAO relied on CSE protein to regulate H_2S levels, but the exact mechanisms remained unclear.

Several limitations of the present study should be noted. Firstly, direct evidence of how choline, TMAO, or H_2S regulated the cGAS-STING pathway needs to be found. Secondly, how choline or TMAO affected the expression of CSE or other H_2S generating enzyme need to be further explored in future studies.

In conclusion, our studies revealed that high choline diet decreased plasma H_2S levels and induced cardiac dysfunction via cGAS-STING-NLRP3 inflammasome axis while

H_2S treatment could restore the cardiac function by inhibiting cGAS-STING-NLRP3 inflammasome axis.

Data Availability

All data supported the findings of this study can be available from the corresponding author upon reasonable request.

Conflicts of Interest

The authors declare that there is no conflict of interests regarding the publication of this paper.

Acknowledgments

The authors would like to thank Professor Yichun Zhu (Fudan University, Shanghai, China) for kindly providing the CSE heterozygote mice. This study was supported by the National Natural Science Foundation of China (31871154, 91849120, and 31671185), the Natural Science Foundation of Hebei Province of China (H2020206417 and C2020206025), the Key R&D Project of Hebei Province (20277735D), and the Research Foundation for Higher Education of Hebei Province (ZD2019027).

References

[1] A. M. Wiedeman, S. I. Barr, T. J. Green, Z. Xu, S. M. Innis, and D. D. Kitts, "Dietary choline intake: current state of knowledge across the life cycle," *Nutrients*, vol. 10, no. 10, p. 1513, 2018.

[2] R. A. Bekdash, "Choline, the brain and neurodegeneration: insights from epigenetics," *Frontiers in Bioscience-Landmark*, vol. 23, no. 3, pp. 1113–1143, 2018.

[3] A. M. Mahmoud and M. M. Ali, "Methyl donor micronutrients that modify DNA methylation and cancer outcome," *Nutrients*, vol. 11, no. 3, p. 608, 2019.

[4] M. Xu, R. Q. Xue, Y. Lu et al., "Choline ameliorates cardiac hypertrophy by regulating metabolic remodelling and UPRmt through SIRT3-AMPK pathway," *Cardiovascular Research*, vol. 115, no. 3, pp. 530–545, 2019.

[5] J. J. Yang, L. P. Lipworth, X. O. Shu et al., "Associations of choline-related nutrients with cardiometabolic and all-cause mortality: results from 3 prospective cohort studies of blacks, whites, and Chinese," *The American Journal of Clinical Nutrition*, vol. 111, no. 3, pp. 644–656, 2020.

[6] C. L. Organ, H. Otsuka, S. Bhushan et al., "Choline diet and its gut microbe-derived metabolite, trimethylamine N-oxide, exacerbate pressure overload-induced heart failure," *Circulation. Heart Failure*, vol. 9, no. 1, article e002314, 2016.

[7] W. Shuai, J. Wen, X. Li, D. Wang, Y. Li, and J. Xiang, "High-choline diet exacerbates cardiac dysfunction, fibrosis, and inflammation in a mouse model of heart failure with preserved ejection fraction," *Journal of Cardiac Failure*, vol. 26, no. 8, pp. 694–702, 2020.

[8] P. Haouzi, T. Sonobe, and A. Judenherc-Haouzi, "Developing effective countermeasures against acute hydrogen sulfide intoxication: challenges and limitations," *Annals of the New York Academy of Sciences*, vol. 1374, no. 1, pp. 29–40, 2016.

[9] K. Abe and H. Kimura, "The possible role of hydrogen sulfide as an endogenous neuromodulator," *The Journal of Neuroscience*, vol. 16, no. 3, pp. 1066–1071, 1996.

[10] H. Kimura, "Hydrogen sulfide (H_2S) and polysulfide (H_2Sn) signaling: the first 25 years," *Biomolecules*, vol. 11, no. 6, p. 896, 2021.

[11] N. Nagahara, "Multiple role of 3-mercaptopyruvate sulfurtransferase: antioxidative function, H2S and polysulfide production and possible SOx production," *British Journal of Pharmacology*, vol. 175, no. 4, pp. 577–589, 2018.

[12] G. Meng, S. Zhao, L. Xie, Y. Han, and Y. Ji, "Protein S-sulfhydration by hydrogen sulfide in cardiovascular system," *British Journal of Pharmacology*, vol. 175, no. 8, pp. 1146–1156, 2018.

[13] S. Yuan, X. Shen, and C. G. Kevil, "Beyond a Gasotransmitter: hydrogen sulfide and polysulfide in cardiovascular health and immune response," *Antioxidants & Redox Signaling*, vol. 27, no. 10, pp. 634–653, 2017.

[14] S. Mani, H. Li, A. Untereiner et al., "Decreased endogenous production of hydrogen sulfide accelerates atherosclerosis," *Circulation*, vol. 127, no. 25, pp. 2523–2534, 2013.

[15] G. Yang, L. Wu, B. Jiang et al., "H_2S as a physiologic vasorelaxant: hypertension in mice with deletion of cystathionine gamma-lyase," *Science*, vol. 322, no. 5901, pp. 587–590, 2008.

[16] K. B. LaPenna, D. J. Polhemus, J. E. Doiron, H. A. Hidalgo, Z. Li, and D. J. Lefer, "Hydrogen sulfide as a potential therapy for heart failure-past, present, and future," *Antioxidants (Basel).*, vol. 10, no. 3, p. 485, 2021.

[17] H. Zhang, J. Dai, D. Tian et al., "Hydrogen sulfide restored the diurnal variation in cardiac function of aging mice," *Oxidative Medicine and Cellular Longevity*, vol. 2, no. 2021, Article ID 8841575, 2021.

[18] B. Tan, S. Jin, J. Sun et al., "New method for quantification of gasotransmitter hydrogen sulfide in biological matrices by LC-MS/MS," *Scientific Reports*, vol. 13, no. 7, p. 46278, 2017.

[19] S. Jin, B. Tan, X. Teng et al., "Diurnal fluctuations in plasma hydrogen sulfide of the mice," *Frontiers in Pharmacology*, vol. 6, no. 8, p. 682, 2017.

[20] A. Van Parys, V. Lysne, G. F. T. Svingen et al., "Dietary choline is related to increased risk of acute myocardial infarction in patients with stable angina pectoris," *Biochimie*, vol. 173, pp. 68–75, 2020.

[21] W. Yang, S. Zhang, J. Zhu et al., "Gut microbe-derived metabolite trimethylamine N-oxide accelerates fibroblast- myofibroblast differentiation and induces cardiac fibrosis," *Journal of Molecular and Cellular Cardiology*, vol. 134, pp. 119–130, 2019.

[22] Z. Li, Z. Wu, J. Yan et al., "Gut microbe-derived metabolite trimethylamine N-oxide induces cardiac hypertrophy and fibrosis," *Laboratory Investigation*, vol. 99, no. 3, pp. 346–357, 2019.

[23] Y. Wang, X. Liu, H. Shi et al., "NLRP3 inflammasome, an immune-inflammatory target in pathogenesis and treatment of cardiovascular diseases," *Clinical and Translational Medicine*, vol. 10, no. 1, pp. 91–106, 2020.

[24] M. Takahashi, "NLRP3 inflammasome as a key driver of vascular disease," *Cardiovascular Research*, vol. 118, no. 2, pp. 372–385, 2022.

[25] E. Sanchez-Lopez, Z. Zhong, A. Stubelius et al., "Choline uptake and metabolism modulate macrophage IL-1β and IL-18 production," *Cell Metabolism*, vol. 29, no. 6, pp. 1350–1362.e7, 2019.

[26] X. Li, J. Geng, J. Zhao et al., "Trimethylamine N-oxide exacerbates cardiac fibrosis via activating the NLRP3 Inflammasome," *Frontiers in Physiology*, vol. 10, no. 10, p. 866, 2019.

[27] K. Wu, Y. Yuan, H. Yu et al., "The gut microbial metabolite trimethylamine N-oxide aggravates GVHD by inducing M1 macrophage polarization in mice," *Blood*, vol. 136, no. 4, pp. 501–515, 2020.

[28] Y. Yang, H. Wang, M. Kouadir, H. Song, and F. Shi, "Recent advances in the mechanisms of NLRP3 inflammasome activation and its inhibitors," *Cell Death & Disease*, vol. 10, no. 2, p. 128, 2019.

[29] K. V. Swanson, M. Deng, and J. P. Ting, "The NLRP3 inflammasome: molecular activation and regulation to therapeutics," *Nature Reviews. Immunology*, vol. 19, no. 8, pp. 477–489, 2019.

[30] Z. Zhong, S. Liang, E. Sanchez-Lopez et al., "New mitochondrial DNA synthesis enables NLRP3 inflammasome activation," *Nature*, vol. 560, no. 7717, pp. 198–203, 2018.

[31] M. M. Gaidt, T. S. Ebert, D. Chauhan et al., "The DNA inflammasome in human myeloid cells is initiated by a STING-cell death program upstream of NLRP3," *Cell*, vol. 171, no. 5, pp. 1110–1124.e18, 2017.

[32] M. Makrecka-Kuka, K. Volska, U. Antone et al., "Trimethylamine N-oxide impairs pyruvate and fatty acid oxidation in cardiac mitochondria," *Toxicology Letters*, vol. 267, pp. 32–38, 2017.

[33] D. Li, Y. Ke, R. Zhan et al., "Trimethylamine-N-oxide promotes brain aging and cognitive impairment in mice," *Aging Cell*, vol. 17, no. 4, article e12768, 2018.

[34] C. H. Yu, S. Davidson, C. R. Harapas et al., "TDP-43 triggers mitochondrial DNA release via mPTP to activate cGAS/STING in ALS," *Cell*, vol. 183, no. 3, pp. 636–649.e18, 2020.

[35] E. Blackstone, M. Morrison, and M. B. Roth, "H_2S induces a suspended animation-like state in mice," *Science*, vol. 308, no. 5721, p. 518, 2005.

[36] B. D. Paul, S. H. Snyder, and K. Kashfi, "Effects of hydrogen sulfide on mitochondrial function and cellular bioenergetics," *Redox Biology*, vol. 38, article 101772, 2021.

[37] B. Murphy, R. Bhattacharya, and P. Mukherjee, "Hydrogen sulfide signaling in mitochondria and disease," *The FASEB Journal*, vol. 33, no. 12, pp. 13098–13125, 2019.

[38] J. Li, X. Teng, S. Jin et al., "Hydrogen sulfide improves endothelial dysfunction by inhibiting the vicious cycle of NLRP3 inflammasome and oxidative stress in spontaneously hypertensive rats," *Journal of Hypertension*, vol. 37, no. 8, pp. 1633–1643, 2019.

[39] Y. Chen, S. Jin, X. Teng et al., "Hydrogen sulfide attenuates LPS-induced acute kidney injury by inhibiting inflammation and oxidative stress," *Oxidative Medicine and Cellular Longevity*, vol. 2018, Article ID 6717212, 2018.

[40] M. Qin, F. Long, W. Wu et al., "Hydrogen sulfide protects against DSS-induced colitis by inhibiting NLRP3 inflammasome," *Free Radical Biology & Medicine*, vol. 137, pp. 99–109, 2019.

[41] Z. Liu, X. Wang, L. Li, G. Wei, and M. Zhao, "Hydrogen sulfide protects against Paraquat-induced acute liver injury in rats by regulating oxidative stress, mitochondrial function, and inflammation," *Oxidative Medicine and Cellular Longevity*, vol. 2020, Article ID 6325378, 2020.

[42] Y. Wang, X. Zhao, H. Jin et al., "Role of hydrogen sulfide in the development of atherosclerotic lesions in apolipoprotein E knockout mice," *Arteriosclerosis, Thrombosis, and Vascular Biology*, vol. 29, no. 2, pp. 173–179, 2009.

[43] L. Chang, B. Geng, F. Yu et al., "Hydrogen sulfide inhibits myocardial injury induced by homocysteine in rats," *Amino Acids*, vol. 34, no. 4, pp. 573–585, 2008.

[44] J. I. Sbodio, S. H. Snyder, and B. D. Paul, "Regulators of the transsulfuration pathway," *British Journal of Pharmacology*, vol. 176, no. 4, pp. 583–593, 2019.

[45] C. Y. Chen, H. B. Leu, S. C. Wang et al., "Inhibition of trimethylamine N-oxide attenuates neointimal formation through reduction of inflammasome and oxidative stress in a mouse model of carotid artery ligation," *Antioxidants & Redox Signaling*, vol. 2022, 2022.

[46] Y. Ke, D. Li, M. Zhao et al., "Gut flora-dependent metabolite trimethylamine-N-oxide accelerates endothelial cell senescence and vascular aging through oxidative stress," *Free Radical Biology & Medicine*, vol. 20, no. 116, pp. 88–100, 2018.

[47] Y. Mikami, N. Shibuya, Y. Ogasawara, and H. Kimura, "Hydrogen sulfide is produced by cystathionine γ-lyase at the steady-state low intracellular Ca^{2+} concentrations," *Biochemical and Biophysical Research Communications*, vol. 431, no. 2, pp. 131–135, 2013.

[48] R. Seddik, A. Bradaïa, and J. Trouslard, "Choline induces Ca^{2+} entry in cultured sympathetic neurones isolated from rat superior cervical ganglion," *European Journal of Pharmacology*, vol. 471, no. 3, pp. 165–176, 2003.

[49] W. Zhu, J. C. Gregory, E. Org et al., "Gut microbial metabolite TMAO enhances platelet hyperreactivity and thrombosis risk," *Cell*, vol. 165, no. 1, pp. 111–124, 2016.

Hindawi
Oxidative Medicine and Cellular Longevity
Volume 2022, Article ID 9687925, 15 pages
https://doi.org/10.1155/2022/9687925

Review Article

Relevance of NLRP3 Inflammasome-Related Pathways in the Pathology of Diabetic Wound Healing and Possible Therapeutic Targets

Youjun Ding,[1,2] **Xiaofeng Ding**,[3] **Hao Zhang**,[4] **Shiyan Li**,[4] **Ping Yang**,[4] **and Qian Tan**[1,4,5]

[1]*Department of Burns and Plastic Surgery, Nanjing Drum Tower Hospital Clinical College of Jiangsu University, No. 321, Zhongshan Road, Nanjing, Jiangsu, China*
[2]*Department of Emergency Surgery, The Fourth Affiliated Hospital of Jiangsu University (Zhenjiang Fourth People's Hospital), 20 Zhengdong Road, Zhenjiang, Jiangsu 212001, China*
[3]*Department of Burns and Plastic Surgery, Nanjing Drum Tower Hospital Clinical College of Traditional Chinese and Western Medicine, Nanjing University of Chinese Medicine, No. 321, Zhongshan Road, Nanjing, Jiangsu, China*
[4]*Department of Burns and Plastic Surgery, Nanjing Drum Tower Hospital, The Affiliated Hospital of Nanjing University Medical School, No. 321, Zhongshan Road, Nanjing, Jiangsu, China*
[5]*Department of Burns and Plastic Surgery, Anqing Shihua Hospital of Nanjing Drum Tower Hospital Group, Anqing, Anhui, China*

Correspondence should be addressed to Qian Tan; smmutanqian@sina.com

Received 2 April 2022; Revised 30 May 2022; Accepted 1 June 2022; Published 30 June 2022

Academic Editor: Tao Zheng

Wound healing is a major secondary complication in type 2 diabetes, which results in significant disability and mortality, imposing a significant clinical and social burden. Sustained activation of the Nod-like receptor protein (NLRP) inflammasome in wounds is responsible for excessive inflammatory responses and aggravates wound damage. The activation of the NLRP3 inflammasome is regulated by a two-step process: the priming/licensing (signal 1) step involved in transcription and posttranslation and the protein complex assembly (signal 2) step triggered by danger molecules. This review focuses on the advances made in understanding the pathophysiological mechanisms underlying wound healing in the diabetic microenvironment. Simultaneously, this review summarizes the molecular mechanisms of the main regulatory pathways associated with signal 1 and signal 2, which trigger the NLRP3 inflammasome complex assembly in the development of diabetic wounds (DW). Activation of the NLRP3 inflammasome-related pathway, involving the disturbance in Nrf2 and the NF-κB/NLRP3 inflammasome, TLR receptor-mediated activation of the NF-κB/NLRP3 inflammasome, and various stimuli inducing NLRP3 inflammasome assembly play a pivotal role in DW healing. Furthermore, therapeutics targeting the NLRP3 inflammasome-related pathways may promote angiogenesis, reprogram immune cells, and improve DW healing.

1. Introduction

Diabetes mellitus (DM), the most frequently diagnosed chronic metabolic disorder, affects more than 460 million individuals worldwide, and its prevalence is projected to increase to 642 million cases by 2040 [1]. Diabetic wounds (DW) are a major secondary complication of type 2 diabetes; the development of such wounds results in an increased risk of limb amputation and disability in patients [2]. Nonhealing wounds in patients with DM negatively affect the quality of life, mortality, and morbidity, and hence, pose a critical clinical challenge and impose an economic burden

worldwide [3]. In the past decade, many studies have concentrated on unresolved inflammation in the pathophysiology of DW healing, and relevant pathways have been disrupted in diabetes.

Inflammasomes, a class of cytosolic multiproteins, serve as a scaffold for caspase-dependent activation to promote cytokine maturation and the release of proinflammatory cytokines, which trigger potent inflammatory responses. In response to invading pathogens and endogenous danger signals, inflammasomes act as a part of the innate immune system against infections and mediate adaptive immune responses. Canonical inflammasomes are activated by pattern recognition receptors (PRRs), which recognize damage-associated molecular patterns (DAMPs) and pathogen-associated molecular patterns (PAMPs) [4]. The Nod-like receptor protein 3 (NLRP3) inflammasome, belonging to a class of PRRs, consists of the sensor receptor NLRP3, which refers to the nucleotide-binding oligomerization domain (NOD)-, leucine-rich repeat (LRR)-, and pyrin domain- (PYD-) containing protein 3; the adaptor protein of apoptosis-associated speck-like protein contains a caspase recruitment domain (ASC) and the effector protease caspase-1 [5]. The NLRP3-ASC-caspase-1-IL-Iβ-IL-18 axis plays a role in DW pathophysiology by regulating necroinflammation [6]. This review focuses on the molecular mechanisms underlying the NLRP3 inflammasome activity involved in the priming/licensing (signal 1) step and the protein complex assembly (signal 2) step in the pathogenesis of DW. It also summarizes the therapeutic approaches targeting the NLRP3 inflammasome and its related signals.

2. Introduction to NLRP3 Inflammasome

A two-step process is involved in the activation of NLRP3 inflammasomes [7] (Figure 1). Signal 1 corresponds to priming and licensing and is accompanied by priming during the transcription and posttranslation events of the NLRP3 inflammasome components. The licensing of the NLRP3 protein sensor plays a vital role in this process. Signal 2, which activates the NLRP3 inflammasome, involves exogenous pathogens and endogenous damage molecules and promotes the assembly of NLRP3, ASC, and procaspase-1 into a protein complex, which subsequently releases proinflammatory cytokines [8, 9].

2.1. Signal 1: Priming and Licensing. It is generally accepted that the process of priming and licensing involves the transcriptional and posttranslational activation of NLRP3, pro-IL-18, and pro-IL-1β along with the license for rapid activation towards the assembly of the NLRP3 inflammasome complex [10, 11]. Accumulating evidence suggests that nuclear factor kappa-B (NF-κB) signaling and the Fas-associated protein with death domain- (FADD-) caspase-8 pathway play essential roles in the priming response to proinflammatory cytokines and PRRs [12, 13]. NF-κB signaling can be activated by stimulation with molecules such as lipopolysaccharide (LPS), interleukin-1β (IL-1β), and tumor necrosis factor- (TNF-) α via upstream LPS/Toll-like receptor 4 (TLR4), IL-1β/IL-1R1, and TNF/TNF receptor pathways, triggering the upregulation of the transcriptional expression of NLRP3 inflammatory components [14, 15]. In addition, FADD-caspase-8 could influence the priming process by acting as an upstream regulator of the NF-κB signaling or triggering the activation of receptor-interacting serine/threo-nine-protein kinase (RIPK) 3/mixed lineage kinase domain-like pseudokinase (MLKL), which is required for mediating all processes [16].

2.2. Signal 2: Activation (Assembly) of the NLRP3 Inflammasome. The second step of NLRP3 inflammasome activation is mediated by PAMPs and DAMPs. In addition, numerous molecular or cellular events, including ROS generation, ion flux, mitochondrial dysfunction, and lysosomal destabilization, trigger the oligomerization of NLRP3, ASC, and procaspase-1 into the NLRP3 inflammasome complex, which leads to the cleavage of procaspase-1 into caspase-1. Activated caspase-1 cleaves pro-IL-1β and pro-IL-18 into active forms IL-1β and IL-18. The K+ efflux induced by various PAMPs/DAMPs can trigger the activation of NLRP3 inflammasome via pannexin-1. Intracellular hypokalemia caused by a decrease in cytosolic K+ is sufficient to activate the NLRP3 inflammasome [17]. In addition, since they act as K+ efflux channels, tandem pore domains in the weak inward rectifying K+ channel 2 (TWIK2) and P2X7 receptor (P2X7R) are necessary for this process [18, 19]. Similarly, an increase in intracellular Ca2+ concentration induced by endoplasmic reticulum (ER) Ca2+ release can also activate the assembly of the NLRP3 inflammasome through thioredoxin-interacting protein (TXNIP) [20, 21]. Furthermore, the exogenous and endogenous stimuli could induce the generation of mitochondrial reactive oxygen species (mtROS) by activating oxidative systems and thereby promote assembly and activation of NLRP3 inflammasome. Under oxidative stress conditions, nuclear factor erythroid-2-related factor (Nrf2) and TXNIP play vital roles [22, 23].

3. Main Factors Involved in the Pathogenesis of Diabetic Wound

Wound healing refers to the repair of damaged tissues and organs in the human body. In contrast to normal wound healing, which displays definite and orderly three phases, including inflammation, proliferation, and remodeling [24], the healing process of DW is impaired. It is associated with deficient angiogenesis, excessive formation of neutrophil extracellular traps (NETs), and phenotypic imbalance in macrophages (Mφ), which results in a persistent inflammation that aggravates the impaired DW healing.

3.1. Altered Angiogenesis in DW. Angiogenesis refers to the formation of new capillaries from an established vasculature [25]. One hallmark in the wound healing is robust angiogenesis [26]. The interplay between fibroblasts and endothelial cells (ECs) is centered on the role of numerous growth factors in both physiological and pathological angiogenesis [27, 28]. Vascular endothelial growth factor (VEGF) expressed by fibroblasts is essential mediators for angiogenesis and collagen synthesis that stimulate vessel formation in

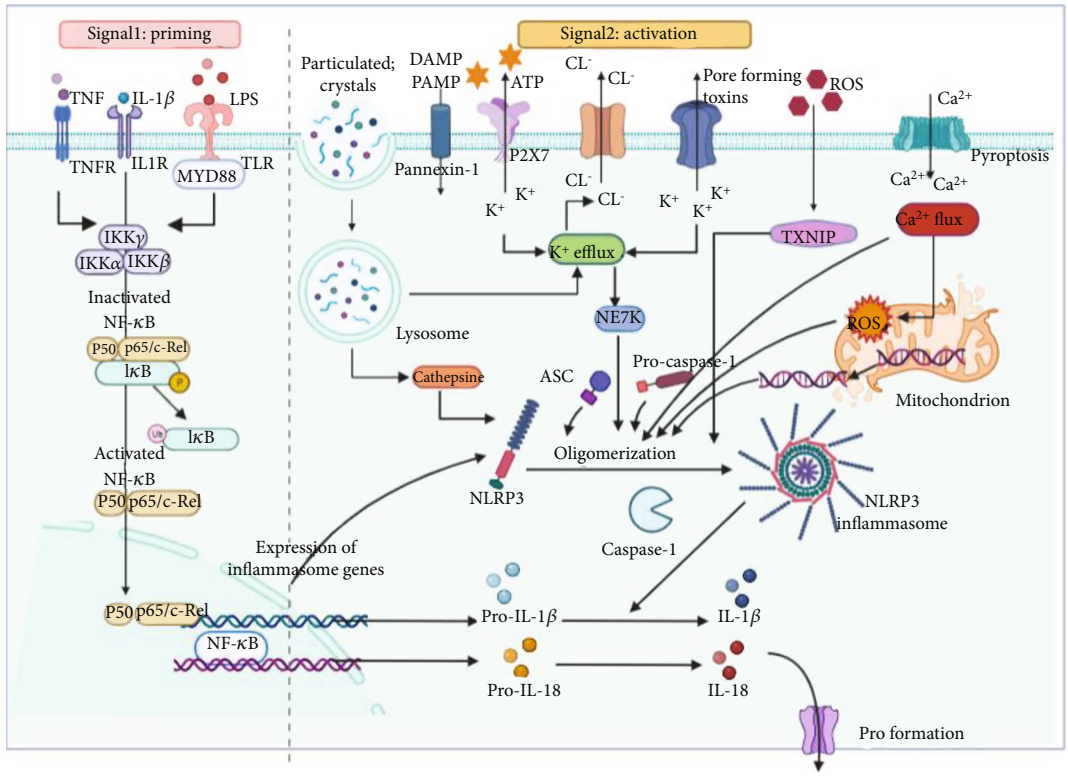

Figure 1: Overview of the molecular mechanisms of the priming and activation of the NLRP3 inflammasome. Activation of NLRP3 inflammasome involves a two-step process. The signal 1 (left) is referred to as priming that is primarily regulated by NF-κB-dependent transcriptional of NLRP3 components, which is activated by the stimuli of TLRs, TNFs, and cytokine receptors. The signal 2 (right) of NLRP3 inflammasome activation is induced by PAMPs and DAMPs. In addition, numerous molecular or cellular events include ROS generation, ion flux, mitochondrial dysfunction, and lysosomal destabilization that trigger the oligomerization of NLRP3, ASC, and procaspase-1 into NLRP3 inflammasome complex, which lead to the cleavage of procaspase-1 into caspase-1. The activated caspase-1 cleaves the pro-IL-1β and pro-IL-18 into active forms IL-1β and IL-18. Abbreviation: PAMPs: pathogen-associated molecular patterns; DAMPs: damage-associated molecular patterns; NLRP3: Nod-like receptor protein; ROS: reactive oxygen species; TLRs: Toll-like receptors; TNFs: tumor necrosis factor; NF-κB: nuclear factor kappa-B; TXNIP: thioredoxin-interacting protein; LPS: lipopolysaccharide.

ECs [27], whereas VEGF that functions as proangiogenic factor was remarkably reduced in patients with diabetic foot ulcer (DFU) and diabetic models [29]. The reduction in the expression of proangiogenic factors is responsible for the dysfunction of ECs, which results in poor EC growth, proliferation, and then impairing angiogenesis and wound healing [30]. NLRP3 inflammasome-related inflammation mediators are closely connected with the process of abnormal angiogenesis in wound healing. The effects of VEGF depend on its receptors that VEGF receptor-1 causes inflammation but VEGF receptor-2 leads to angiogenesis [31]. As discussed in further detail below, controlling NLRP3 inflammasome is considered as a useful treatment in DW, which could be evidenced by the increased expressions of angiogenesis-related factors, including VEGF and platelet-derived growth factor (PDGF) [32]. Hypoxia attributed to increased blood viscosity is also a key activator of the development and progression of abnormal vascular growth [33]. HIF-1α, as a critical regulator of oxygen homeostasis, plays a determinant role in healing outcomes [34]. In wounds, HIF-1 as a transcription activator regulates downstream target gene VEGF to responsible for angiogenic events that are altered in diabetes [35]. Exposure to hyperglycemia, the downregulation of HIF-1α causes low expression of VEGF and has a negative impact on ECs, which are susceptible to apoptosis and increased detachment and account for poor healing in DM patients [30, 36, 37]. Meanwhile, treatment with HIF-1α stabilizer could stimulate angiogenesis by activating HIF-1α/VEGF pathway to accelerate DW healing [32]. Pharmacological intervention that elevated expression of HIF-1α/VEGF pathway could further reduce the levels of inflammatory factors (IL-1β, TNF-α, and IL-6) [28, 38]. Furthermore, vascular endothelial injury induced by inflammation factors can lead to abnormal vascular proliferation, luminal narrowing, and poor local blood flow, which aggravates local hypoxia, thereby forms a vicious cycle, hindering DW healing [26, 39]. Overall, the multiple changes in proangiogenic and vascular maturation factors in diabetes are influenced by proinflammatory environment in DW, which perturb the proper wound healing with a large array of insufficient angiogenesis [40].

3.2. Role of NETs in DW. Neutrophils, regarded as a double-edged sword, are the first immune cells to migrate into the wound bed and participate in the elimination of pathogens and damaged cells. Inflammation is a key step required for

initiation of wound repair. While a suitable infiltration of neutrophils in the wound allows for prevention of infection, prolonged persistence of neutrophils drives tissue damage in which injured tissues and the inflammatory response self-sustain each other [41]. In response to pathogen invasion, neutrophils release modified chromatin structures, such as their nuclear and granular contents, to form a meshwork known as NETs. Abnormal activation of NET can also contribute to the inflammatory loop [42]. NETs persist in diabetes, and their continuous presence can predisposed patients to mortality in the form of NETosis, which has been confirmed in clinical trials in patients with DFU. Furthermore, the initiation of NETosis is closely related to peptidylarginine deiminase 4 (PAD4), whose expression is upregulated in DW [43]. Inhibition of NETosis by Cl-amidine (PAD4 inhibitor) and disruption of NETs by DNase 1 can ameliorate chronic inflammation in wounds and is conducive to wound healing [44]. In addition to its regulation of macrophages through the NLRP3 inflammasome to sustain a local persistent inflammatory response, NET can affect EC activity by increasing its death and motility [45, 46]. Notably, the Janus face of NET during wound healing should be considered. Recently, patients with DW who showed NETs with a low level of cathelicidin (LL-37) demonstrated poor antimicrobial action to increase the risk of wound healing-related disorders. Additionally, treatment with the macrolide clarithromycin can restore the antibacterial activities in patients via upregulation of the expression of LL-37 on NETs [47]. These studies suggest that the NET process is highly resolutive, and therapeutic tools restoring their balance with immune cells in DW are promising.

3.3. Focus on Macrophage Polarization in DW. Mφ derived from monocytes participates in each phase of the wound healing process because they kill pathogenic microbes, remove damaged tissue, and produce growth factors [48]. In response to complex microenvironments and molecular mediators, Mφ is polarized into the classical pr-inflammatory M1 or alternative anti-inflammatory M2 [49]. The orderly transition from M1 to M2 results in beneficial effects on wound healing, particularly in tissue remodeling and angiogenesis [50]. During the normal wound healing process, M1 predominates for the first three days. Subsequently, transition to the M2 phenotype is observed, which peaks on the seventh day [51]. In the DW state, chronic low-grade inflammation that persists indefinitely is a key cause of nonhealing of wounds [52], wherein M1 persists continuously and cannot transit to M2 phenotypes. In addition, Ganesh et al. [53] found that the levels of proinflammatory cytokines, including interleukin-1 beta (IL-1β), tumor necrosis factor-alpha (TNF-α), and interferon-gamma (IFN-γ), are elevated in DW, which induces local hyperglycemia, accumulation of advanced glycation end products (AGEs), and ROS, along with an increase in chronic inflammation [49]. The same outcome has been observed in animal experiments, in which macrophages from normal mice switched from a pro- to anti-inflammatory phenotype on the tenth day, while diabetic mice displayed a twofold higher expression of proinflammatory factors IL-1β and IFN-γ [54], which facilitated the maintenance of the proinflammatory M1 phenotype. The phenotypic imbalance of Mφ is closely related to the activity of the NLRP3 inflammasome, which is influenced by the abundance of proinflammatory factors [55]. Importantly, the activation of the NLRP3 inflammasome in M1 with increased IL-1β levels can form a positive feedback loop to amplify the proinflammatory effect of M1, which is attributed to the failure of the transition of Mφ to the M2 phenotype in DW [56]. Due to the influence of intricate etiologies in DW, the transformation from proinflammatory M1 to anti-inflammatory M2 can be deferred or even absent; this hampers the switch from the inflammatory to the proliferation phase during tissue repair, consequently impairing the wound healing process [57].

4. Correlation of the NLRP3 Inflammasome Pathway with DW

4.1. Crosstalk between Nrf2 and NF-κB/NLRP3 Inflammasome (Signal 1) in DW. Nrf2, a master regulator of antioxidant defenses, modulates the redox homeostasis of cells by binding to antioxidant response elements (AREs) of antioxidative genes encoding antioxidant enzymes after heterodimerization with musculoaponeurotic fibrosarcoma oncogene homolog (Maf) proteins under endogenous and exogenous stress conditions [58]. Under physiological conditions, Nrf2 binds to Keap1, which negatively regulates Nrf2 by targeting its proteasomal degradation. However, under stress conditions, Nrf2 dissociates from the Nrf2-Keap1 complex, translocates into the nucleus, and subsequently induces the expression of antioxidant genes [59]. Nrf2 can limit the inflammatory response induced by NF-κB, thereby suppressing NLRP3 inflammasome activity [60, 61]. In contrast, NF-κB can reduce the expression of Nrf2 signaling by competing with Nrf2 for the transcriptional coactivator CREB-binding protein (CBP) p300 complex [62]. Furthermore, P65 (the canonical NF-κB subunit) can prevent the formation of the Nrf2-Maf heterodimer by improving the recruitment of histone deacetylase 3 (HDAC3) to MafK, which decreases the expression of Nrf2-mediated ARE-related genes [63]. Therefore, the roles of Nrf2 and the NF-κB/NLRP3 inflammasome in wound healing are reciprocal.

The mechanism underlying impairments in DW healing involves the induction of premature senescence in endothelial progenitor cells (EPCs) due to excessively high ROS levels in a hyperglycemic environment; this results in the deficiency of repair and angiogenesis [64]. Given that Nrf2 plays an essential role in normal endothelial angiogenesis, disruption of Nrf2 signaling might be a mechanism underlying impaired angiogenesis observed in DW healing [65]. The circulatory levels of Nrf2 and its downstream targets are reduced in patients with type 2 diabetes and DFU compared to those in control subjects [66, 67]. Similar results were also observed in diabetic rat models [68]. High glucose (HG) levels increase the levels of the p65 canonical NF-κB subunit, leading to activation of the inflammatory process, which in turn, negatively regulates Nrf2 [69]. However, as an

antioxidant protective mechanism, perilesional skin tissues of patients with diabetes are under the influence of high oxidative stress, which induces compensatory activation of the Nrf2, downstream heme oxygenase 1 (HO-1), and NAD(P)H quinone dehydrogenase 1 (NQO1) genes, albeit not to normal levels [70]. The pharmacological activation of Nrf2 and inhibition of NF-κB promotes DW healing, which is a promising therapeutic target [71].

4.2. TLR Receptor-Mediated Activation of NF-κB/NLRP3 Inflammasome (Signal 1) in DW. TLR signals, particularly TLR4, are essential stimuli that activate the NF-κB pathway by binding to its downstream partner, MyD88 [72]. The role of TLR is primarily influenced by their activation with ligands and is closely associated with the microenvironment in DW. The expression of TLR 2, 4, and 6 was persistently upregulated from injury to the tenth day in DW, while in non-DW, the levels of TLRs recovered, reaching those observed at the baseline [73, 74]. The NF-κB pathway, mediated by continuous stimuli of TLRs, contributes to diabetes-associated delayed wound healing and eventually triggers a cascade of amplified inflammatory responses that hinder wound healing. Similar findings were revealed in patients with DW; the increased TLR4 expression was observed along with that of the downstream markers of activation, including MyD88, IRAK, NF-κB, and IL-1β [75]. Furthermore, genetic deletion of TLR4 in diabetic mice ameliorated wound healing [76]. Taken together, these studies suggest that TLR-MyD88-NF-κB signaling maintains DW in an inflammatory state to delay wound healing. Notably, the NF-κB pathway is the best-known signal for transcriptional activation of NLRP3 inflammasome components.

Neutrophils are the main leukocytes at wound sites and play a vital role in healing [77]. The pathogenesis of diabetes involves inflammatory or metabolic processes, such as neutrophilia and hyperglycemia, which result in the formation of NETosis mediated by neutrophils [44]. The effect of high concentrations of NETs on DW is responsible for infection and the subsequent worsening of wounds [78]. The major components of NET, including histones and DNA, are recognized by TLR receptors as endogenous DAMPs [79]. NET is a key scaffold in DW that acts as a priming signal for NLRP3 activation through the TLR4/9/NF-κB pathway in macrophages. NET-driven NLRP3 inflammasome activity in Mφ further induces the infiltration of innate immune cells into the diabetic wound, which severely impairs wound healing [80, 81].

NLRP3 inflammasome activity is required for keratinocytes to respond to a range of irritants. However, excess inflammasome/IL-1 activity in keratinocytes other than macrophages also aggravates DW healing [82, 83]. Upon exposure to HG, the NLRP3 inflammasome in keratinocytes is activated by excess ROS, which inhibits the proliferation and migration of keratinocytes. Recently, Lee et al. [84] used a model of wound healing with epidermal deletion of caspase-8 and observed an elevated level of caspase-1 mediated by NF-κB, which directly binds to the caspase-1 promoter. However, the deletion of NF-κB, loss of caspase-1, or inhibition of IL-1R in keratinocytes disrupted the inflammatory phase of cutaneous wound closure and impaired the proliferative phase of ECs, resulting in delayed cutaneous wound closure. Thus, basal immune response and inflammation resolution are essential homeostatic mechanisms for maintenance of wound healing.

4.3. Relationship between DW and NLRP3 Inflammasome Assembly (Signal 2). When induced by PAMPs or DAMPs, the conformation of NLRP3 is changed, and the NACHT domain is exposed, which triggers oligomerization of the NLRP3 inflammasome complex (signal 2). This complex is involved in a series of signaling pathways [85]. In DW, multiple stimuli that disturb intracellular homeostasis can result in persistent NLRP3 inflammasome activity, promote maturation and secretion of proinflammatory cytokines, and hinder wound healing [86].

4.3.1. Reactive Oxygen Species and Mitochondrial Reactive Oxygen Species. In addition to the stimulant role of the NLRP3 inflammasome in macrophages, the ROS-mediated pathway is required as a common step for the activation of the NLRP3 inflammasome (signal 2). The high accumulation of ROS results in an increase in membrane permeability, disrupts the balance of ions in cells, and further intensifies the stimulation of DAMPs [87]. As a key modulator of intracellular ROS, TXNIP is a pivotal mediator of ROS-induced NLRP3 inflammasome activity [88]. In the HG-induced state, the level of TXNIP protein increases, which further stimulates the downstream NLRP3 inflammasome [89]. The activity of xanthine oxidoreductase (XOR), a source of ROS in chronic wounds, is elevated, which drives ROS overproduction in the diabetic wound environment [90]. The secretion of IL-1β, which further amplifies inflammation, can be stimulated by XOR. Moreover, wound tissue isolated from diabetic patients shows increased expression of the NLRP3 inflammasome, which is activated by ROS in the DW environment [91]. Excess production of free radicals can cause progressive damage to DW via lipid peroxidation and protein modification, which increases their susceptibility to inflammatory responses [92]. Inhibition of ROS by N-acetylcysteine (NAC), a free radical scavenger, blocks the activation of the NLRP3 inflammasome, which accelerates impaired wound healing in a diabetic rat model [93]. Mitochondria are the main source of ROS, which act as DAMPs in damaged cells that trigger the NLRP3 inflammasome in macrophages, partially via ATP derived from mitochondria and P2X7 expression [94]. Mitochondrial DAMPs and mtROS drive DW, in which inflammation and mitochondrial dysfunction self-sustain each other. [95]. The application of mtROS scavengers on inflamed wounds attenuates IL-1β and IL-18 production [96]. In addition, experimental findings linking excessive ROS to the pathogenesis of diabetic wounds have been demonstrated in vitro. These findings implicate the NLRP3 inflammasome as a pathogenic mediator of downstream apoptosis. Fibroblasts derived from the wounds of patients with DFU showed an increased level of apoptosis induced by prolonged ROS-mediated activation of the NLRP3 inflammasome [97]. Apoptosis depends on the NLRP3 inflammasome as it is blocked by an inhibitor (BAY 11-7082) of the NLRP3 inflammasome.

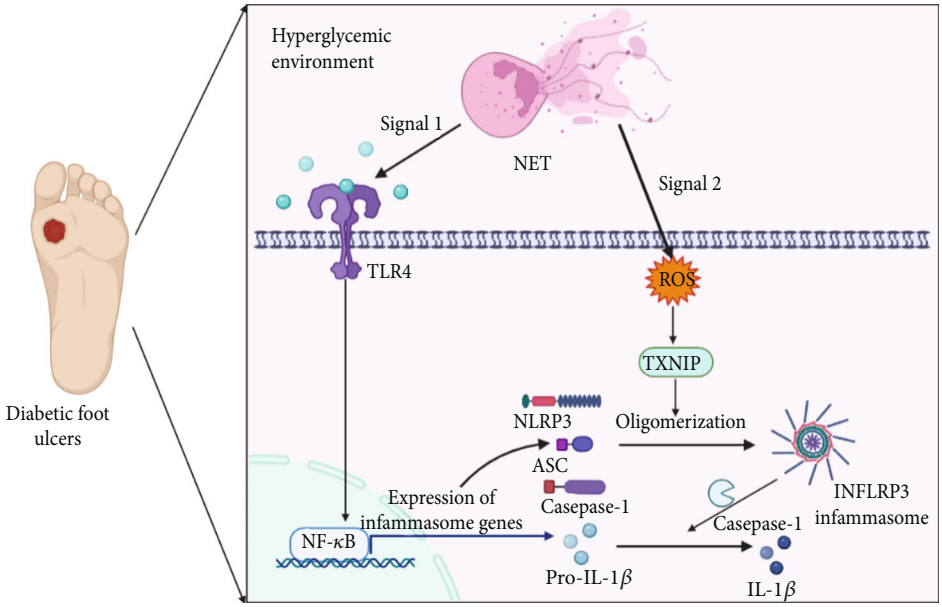

Figure 2: Overview of the activation of NLRP3 inflammasome in Mφ by NETs, leading to nonresolution of inflammation in diabetic foot ulcers. DW microenvironment stimulates the neutrophils to form NETs. Stimulation of the activation of the NLRP3 inflammasome by NETs in macrophages is regulated by two steps, which involves the priming process mediated by the TLR4/NF-κB pathway and the assembly process mediated by the ROS/TXNIP pathway. NET-driven NLRP3 inflammasome activity in Mφ further induces the infiltration of the innate immune cells into the diabetic wound, which severely impairs wound healing. Abbreviation: NETs: neutrophil extracellular traps; DW: diabetic wound; Mφ: macrophages; NLRP3: Nod-like receptor protein; ROS: reactive oxygen species; TXNIP: thioredoxin-interacting protein; TLR4: Toll-like receptor 4; NF-κB: nuclear factor kappa-B.

Based on these observations, the NLRP3 inflammasome is constantly activated by excessive ROS in diabetic wounds, which induces downstream inflammatory events of "glucotoxicity" [98], and thereby promotes caspase-8/3-dependent apoptosis, exacerbates skin remodeling, and impairs wound healing in diabetic patients.

In addition to the TLR4/9/NF-κB pathway, NETs also induce the overproduction of ROS, promoting the targeting of NLRP3 by TXNIP, which stimulates the assembly of the NLRP3 inflammasome in macrophages [45] (Figure 2). Collectively, the stimulation of NLRP3 inflammasome activation mediated by NETs in macrophages is regulated in two steps: priming by the NF-κB pathway and assembly by the mediated by ROS/TXNIP pathway. In addition to being driven by IL-1β, NETosis can also predispose to a self-perpetuating cycle of sustained IL-1β and IL-18 release, triggering the accumulation of proinflammatory cytokines and ROS in diabetic wound sites, which aggravates wound inflammation [99, 100]. Strategies aimed at inhibiting NETosis and eliminating NETs significantly improve the wound repair process in diabetes, uncovering a novel therapeutic approach for DWs.

4.3.2. Potassium (K+) Efflux. Exogenous ATP causing K+ outflow has emerged as a key upstream event in the assembly of the NLRP3 inflammasome and release of mature IL-1β. P2X7R, a distinct gated ion channel, is gated by ATP to participate in the maturation of IL-1β via K+ efflux [101]. Macrophages from diabetic mice displayed a high level of NLRP3 inflammasome components, and treatment with zoledronate, a nitrogen-containing bisphosphonate, which augments persistent NLRP3 activation by the K+/P2X7R/ROS pathway but not by lysosomal rupture contributes to impaired oral socket wound healing [56]. In addition, evidence of the critical role of inflammasome inhibitors in DWs is centered on observations of neovascularization; the expression of such inhibitors is reduced in a diabetic environment. Persistent inflammation leads to a decrease in collagen organization and neovascularization, which is associated with several angiogenic factors, including VEGF and chemokine CXCL12 [102, 103]. For instance, drugs that block P2X7R improve angiogenesis, which is associated with the expression of VEGF and CXCL12, and ameliorate wound healing [104]. Recently, NEK7, a potassium-specific protein, was shown to activate the NLRP3 inflammasome by acting downstream of K+ efflux to trigger the process of NLRP3 oligomerization and punctate ASC aggregation, which was confirmed by the observation showing that blocking the contact between NLRP3 and NEK7 could directly inhibit the activation of the NLRP3 inflammasome [105, 106]. To understand whether NEK7/NLRP3 is associated with diabetic foot, Cai et al. [107] compared the expression of NEK7/NLRP3 between patients with and without diabetic foot to show that the NEK7/NLRP3 pathway, which was significantly increased in patients with diabetic foot, drove the pathogenesis of diabetic foot.

4.3.3. Lysosomal Destabilization. Disruption of lysosomes and release of cathepsins are essential stimuli of the NLRP3 inflammasome. Phagocytosis of certain particulate matter,

including cholesterol crystals, uric acid, and silica, stimulates the activation of the NLRP3 inflammasome. The phagocytosis is induced by lysosomal destabilization and rupture, followed by the release of cathepsin B into the cytoplasm [108, 109]. Cathepsin B directly connects with the C-terminal LRR domain of NLRP3, which facilitates oligomerization of the NLRP3 inflammasome [110]. Under conditions involving excess nutrition, excessive uptake of LDL particles with impaired lysosomal hydrolysis can drive lysosomal membrane permeabilization, which allows the leakage of lysosomal contents, such as lipase, cathepsins, and Ca2+, the canonical stimulators of inflammatory pathways [111]. Lipotoxicity is responsible for inflammatory dysfunction of macrophages in impaired DW healing. The connection between lipid stress and lysosomal pathology is associated with glutamine metabolism, which could overwhelm the mitochondria and further exacerbate the accumulation of saturated fatty acid (SFAs) palmitate. SFAs play a role in lysosomal dysfunction in macrophages such that they alter the responses of macrophages to inflammatory stimuli [112].

5. Advances in Targeting NLRP3 for the Treatment of DW

5.1. Therapeutic Targeting of NLRP3 Inflammasome Priming (Signal 1) in DW. Various pharmacological approaches have focused on initiation events for NLRP3 inflammasome activation, which have been approved for the treatment of DW (Table 1, Figure 3). Deubiquitination of NLRP3 is required for the priming signal during NLRP3 inflammasome activation [10]. Treatment with MF-094, a selective USP30 inhibitor, can block the deubiquitination of NLRP3 and decrease the expression of its downstream target caspase-1 to promote wound healing in DFU [113]. Heparan sulfate can reduce the levels of IL-1β, IL-18, NLRP3, and ASC, accompanied by the increased expression of caspase-12 and proteinase inhibitor-9 that inhibit NLRP3 inflammasome assembly, thereby improving wound healing [114]. In addition, paeoniflorin could accelerate wound healing by downregulating the NF-κB-mediated inflammatory response by inhibiting CXCR2 in rats with DFU [115]. In addition, common DW treatments also target the link between energy sensing and the NLRP3 inflammasome in DW. The mammalian target of rapamycin (mTOR), a threonine/serine kinase, can act as an immune regulator of anti-inflammatory and proinflammatory cytokine expression [116]. Moreover, upstream AMP-activated protein (AMPK) and downstream NF-κB contribute to HG-induced inflammation. Metformin, an orally administered biguanide, improves DW healing by promoting M2 macrophage polarization via upregulation of the AMPK/mTOR signaling pathway and subsequent inhibition of the NLRP3 inflammasome [117]. The effect of rapamycin on wound healing whether delaying or promoting wound healing has been of concern [118]. Although rapamycin impairs wound healing in kidney transplantation that is associated with their antiproliferative properties [119], it is also regarded as a potential therapeutic drug for DW healing that suppresses the phosphorylation of mTOR and subsequent NF-κB-mediated NLRP3 inflammasome [120]. The effects of the Wnt signaling pathway on the wound healing process could be attributed to the promotion of angiogenesis and amelioration of the inflammatory response [121]. Wnt7a can improve wound healing and inhibit autophagy and inflammation induced by HG, such as LC3A/B, p62, and NLRP3 [122].

Activation of Nrf2-mediated antioxidant defenses and suppression of NF-κB/NLRP3 inflammasome-mediated anti-inflammatory effects are beneficial in diabetic wound healing. Gallocatechin-silver nanoparticle-impregnated cotton gauze patches could ameliorate DW healing by suppressing oxidative stress and inflammatory response through the Nrf2/HO-1 and TLR4/NF-κB pathways, accompanied by elevated levels of antioxidant enzymes, increased levels of growth factors and Nrf2, and decreased NF-κB-mediated inflammatory response [123]. It is likely that supplementation with genistein could also accelerate DW healing owing to its effects on the enhancement of Nrf2-mediated antioxidant defense, suppressing NF-κB-related inflammatory responses and restoring the NLRP3 inflammasome [124]. Recently, traditional herbal medicines with many active compounds recognized as Nrf2 cofactors have been reported to be beneficial for DW healing. The active compounds (4-vinyl catechol, 4-ethyl catechol, and alkyl catechols) of *Barleria lupulina* and *Morinda citrifolia*, natural herbs, have been identified as natural Nrf2 activators, which are used in clinical DW healing. Plumbagin from *Plumbago zeylanica*, neferine from *Nelumbo nucifera*, rutin from buckwheat, and luteolin could promote diabetic wound healing by improving the expression of Nrf2-mediated antioxidant enzymes and inhibiting the expression of NF-κB-associated inflammatory cytokines [125–128]. Furthermore, diet-associated compounds, such as sulforaphane and curcumin, act in a redox-sensitive manner in response to Nrf2 activation, which reduces the apoptosis of perilesional skin tissue and the expression of MMP9 to accelerate DW healing [129].

5.2. Therapeutic Targeting of NLRP3 Inflammasome Assembly (Signal 2) in Diabetic Wound. Recently, strategies that preferentially target NLRP3 inflammasome assembly, such as pharmacological inhibitors, have been described and are beneficial for DW repair. Reducing excessive ROS levels by the application of antioxidants that block NLRP3 inflammasome upstream signaling improves wound healing in experimental models. For example, mitochondria-targeted antioxidants, such as 10-(6-plastoquinonyl) decyltriphenylphosphonium (SkQ1), can improve the resolution of the inflammatory phase in inflamed wounds, which is accompanied by a decrease in the proportion of neutrophils and an increase in the proportion of macrophages. These effects were reliant on the reduction in IL-1β and IL-18 levels [130]. Similarly, the inhibition of XOR-derived ROS protects against DW healing, which is associated with NLRP3 inflammasome activity. Besides, given that TXNIP is a vital regulator of the ROS-mediated NLRP3 inflammasome, inhibiting TXNIP by fenofibrate, a PPARα agonist, can target NLRP3 inflammasome activation to exert a beneficial effect during DW treatment [131].

Table 1: Summary of treatment strategies by modulating NLRP3 inflammasome pathways in DW.

Signal 1	Agent	Mechanism	Indicators	Diabetic wound healing	Model
	GC-AgNPs-CGP	Activate Nrf2/HO-1 and inhibit TLR4/NF-κB pathways	MDA↓, SOD↑, Nrf2↑, Nqo-1↑, HO-1↑, Keap-1↓, MMP-2↓	Improve the wound healing	CGP dressed diabetic Sprague Dawley rats
	Genistein	Improve cutaneous Nrf2-related antioxidant and reduce NF-κB-associated inflammation	NLRP3↑, ASC↑, caspase-1↑, IL-1β↑, NF-κB↓, Nrf2↑, HO-1↓	Accelerate delayed wound healing	Alloxan monohydrate induced mice
	Plumbagin	Improve antioxidant status and reduce inflammation	Nrf2↑, MMP-2↓, NF-κB↓, TNF-α↓, IL-6↓, IL-1β↓	Improve wound healing activity	STZ-induced Wistar albino rats
	Neferine	Inhibit inflammatory cytokines and Nrf2 pathway	Nrf2↑, SOD↑, CAT↑, GPx↑, NF-κB↓, TNF-a↓, IL-6↓, IL-1β↓	Promote faster wound healing	STZ-induced Wistar rats
	Rutin	Reduce oxidative stress and inflammatory response	Nrf2↑, SOD1↑, GPx↑, HO-1↑, MMP-2↓, NFκB↓, TNF-α↓, IL-6↓, IL-1β↓	Promote wound healing	STZ-induced Wistar rats
	Luteolin	Inactivate NF-κB and upregulate Nrf2	Nrf2↑, SOD1↑, GPx↑, MMP-9↓, NF-κB↓, TNF-α↓, IL-6↓, IL-1β↓	Promote wound restoration	STZ-induced rats
	Metformin	Regulate AMPK/NLRP3 inflammasome pathway	NLRP3↓, IL-1β↓, caspase-1↓, p-AMPK/AMPK↑, p-mTOR/mTOR↓, IL-10↑	Accelerate the wound healing	Sprague-Dawley rats
	Rapamycin	Inhibit mTOR/NF-κB pathways	NLRP3↓, ASC↓, caspase-1↓, mTOR phosphorylation↓, NF-κB↓	Accelerate the wound healing	THP-1-derived macrophages
	Wnt7a	Regulate high autophagic and inflammatory response	NLRP3↓, LC3A/B↓, IL-1β↓, caspase-1↓, TLR4↓, p62↓, TNF-a↓	Accelerate diabetic wound healing process	STZ-induced Sprague-Dawley rats
	Paeoniflorin	Inhibit NF-κB and NLRP3 signaling pathways	CXCR2↓, NF-κB↓, NLRP3↓, cleaved caspase-1↓	Attenuate wound inflammation and better wound healing	STZ-induced Sprague-Dawley rats
	Topical calcitriol application	Suppress NLRP3-IL-1β signaling pathway	NLRP3↓, pro-IL-1β↓, IL-1β↓, cleaved caspase-1↓, ASC↓	Promotes corneal wound healing	STZ-induced C57BL/6 mice
	MF-094	Inhibit the NLRP3 inflammasome	NLRP3↓, caspase-1 p20↓	Accelerate diabetic wound healing	STZ-induced rats
	Sulforaphane	Alleviate oxidative stress, increase proliferation and migration, decrease apoptosis	Nrf2↑, HO-1↑, NQO1↑, TGF-β1↑, MMP9↓	Promote diabetic wound healing	STZ-induced diabetic mice
	Cinnamaldehyde	Alleviate oxidative stress, increase proliferation and migration, decrease apoptosis	Nrf2↑ ,HO-1↑, NQO1↑, TGF-β1↑, MMP10↓	Promote diabetic wound healing	STZ-induced diabetic mice

Table 1: Continued.

Signal 1	Agent	Mechanism	Indicators	Diabetic wound healing	Model
Signal 2					
	BAY 11–7, 082	Selectively inhibit NLRP3 inflammasome activity	Active caspase-1↓, IL-1β↓, IL-18↓, VEGF↑, and CXCL12↑	Improve the impaired healing pattern: a decrease time to complete skin healing	Db/db mice
	BBG	Purinergic P2X7 receptor inhibitor	Active caspase-1↓, IL-1β↓, IL-18↓, VEGF↑, and CXCL12↑	Improve the impaired healing pattern: a decreased time to complete skin healing	db/db mice
	Zol	Active K+/P2X7 receptor/ROS pathway	NLRP3↑, caspase-1↑, IL-1β↑	Impair oral socket wound healing	db/db mice
	BSP	Inhibit NLRP3 inflammasome activation	TNF-α↓, ROS↓, IL-1β↓, IL-18↓, caspase-1↓, NLRP3↓	Accelerate diabetic wound healing, suppress macrophage infiltration, and promote angiogenesis	High fat-diet feeding combined with streptozocin in C57BL/6 mice; macrophages
	YVAD	The caspase-1 inhibitor	IL-1β↓, IL-18↓, NLRP3↓	Improve wound healing	Keratinocytes and Mp
	Glyburide	Close ATP-sensitive potassium channels	IL-1β↓, IL-18↓, NLRP3↓	Improve wound healing	Keratinocytes and Mp
	Melatonin	Inhibition of NLRP3 inflammasome activation	TNF-α↓, IL-1β↓, IL-6↓, IL-8↓, NLRP3↓	Promote diabetic wound healing	Keratinocytes
	MFG-E8	Intergrin β3-limited P2X7 receptor pathways	Active caspase-1↓, IL-1β↓, IL-18↓, NLRP3↓	Improve angiogenesis and accelerates wound healing	Mfge8-/-diabetic mice, Mfge8-/-neutrophils
	Fenofibrate	Inhibition of ROS/TXNIP/NLRP3 pathway	TXNIP↓, active caspase-1↓, IL-1β↓ ,IL-18↓, NLRP3↓	Accelerate wound healing	STZ-induced diabetic mice, EPC
	NAC	A free radical scavenger	ROS↓, IL-1β↓ ,IL-18↓, caspase-1↓, NLRP3↓	Improve the wound healing	STZ-induced diabetic mice

Abbreviation: GC-AgNPs-CGP: gallocatechin-silver nanoparticle-impregnated cotton gauze patches; Nrf2: nuclear factor erythroid-2-related factor; HO-1: heme oxygenase 1; TLR4: Toll-like receptor 4; NF-κB: nuclear factor kappa-B; MDA: malonaldehyde; SOD: superoxide dismutase; Nqo-1:NADPH quinone oxidoreductase-1; Keap-1: Kelch-like ECH-associated protein 1; MMP-2: matrix metalloproteinase-2; NLRP3: Nod-like receptor protein 3; ASC: apoptosis-associated speck-like protein containing; IL-1β: interleukin-1; STZ: streptozocin; TNF-α: tumor necrosis factor-alpha; IL-6: interleukin-6; GPx: glutathione peroxidases; MMP-9: matrix metalloproteinase-9; AMPK: adenosine monophosphate-activated protein kinase; mTOR: mechanistic target of rapamycin; IL-10: interleukin-10; LC3A/B: microtubule-associated protein 1A/1B-light chain 3; TLR4: Toll-like receptor 4; CXCR2: C-X-C motif chemokine receptor 2; Mp: macrophage; VEGF: vascular endothelial growth factor; TGF-β1: transforming growth factor beta1; MMP10: matrix metalloproteinase-10; CXCL12: chemokine C-X-C motif ligand 12; ROS: reactive oxygen species; IL-18: interleukin-18; P2X7: BBG: brilliant blue G; Zol: zoledronate; BSP: Bletilla striata polysaccharide; YVAD: Tyr-Val-Ala-Asp; MFG-E8: milk fat globule epidermal growth factor VIII; NAC: N-acetylcysteine; TXNIP: thioredoxin-interacting protein.

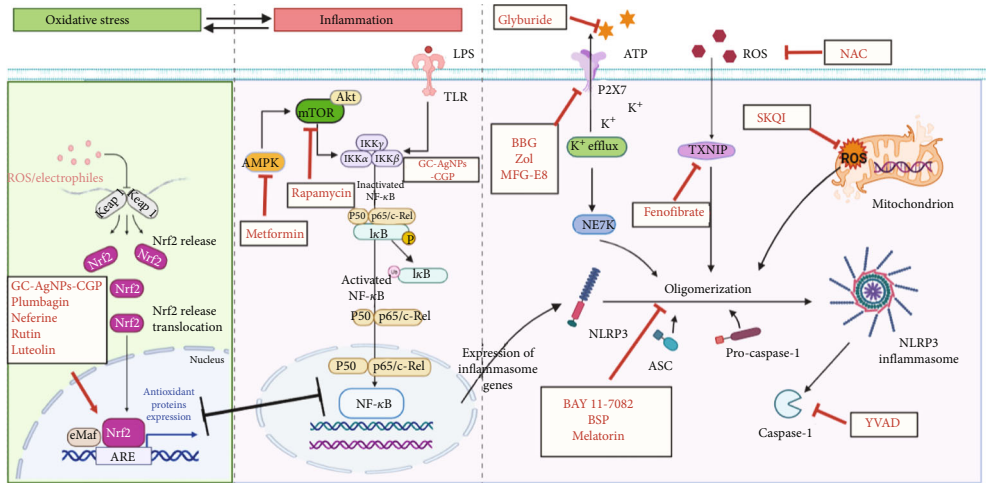

FIGURE 3: Therapeutic targeting of NLRP3 inflammasome in DW. Activation of Nrf2-mediated antioxidant defenses and suppression of NF-κB/NLRP3 inflammasome-mediated anti-inflammatory action are effective therapeutic strategies, which also include GC-AgNPs-CGP, plumbagin, neferine, rutin, and luteolin. Metformin and rapamycin target AMPK and mTOR to inhibit the NF-κB signaling pathway, consequently blocking the priming of the NLRP3 inflammasome. Glyburide suppresses NLRP3 oligomerization in an ATPase-dependent manner. P2X7 is a vital target of BBG, Zol, and MFG-E8. In addition, inhibition of TXNIP by fenofibrate can regulate the ROS-mediated NLRP3 inflammasome to exert a beneficial effect on DW. NAC and SKQ1 inhibit ROS and mROS, respectively, to block the assembly of the NLRP3 inflammasome. YVAD is a specific inhibitor of caspase-1. Additionally, BAY 11-7082, BSP, and melatonin directly black the oligomerization of NLRP3 to exert beneficial effect for DW healing. Abbreviation: DW: diabetic wound; NLRP3: Nod-like receptor protein; ROS: reactive oxygen species; TXNIP: thioredoxin-interacting protein; Nrf2: nuclear factor erythroid-2-related factor; GC-AgNPs-CGP: gallocatechin-silver nanoparticle-impregnated cotton gauze patches; AMPK: AMP-activated protein kinase; mTOR: mammalian target of rapamycin; BBG: brilliant blue G; Zol: zoledronate; MFG-E8: milk fat globule epidermal growth factor VIII; NAC: N-acetylcysteine; mROS: mitochondrial reactive oxygen species; BSP: Bletilla striata polysaccharide; SKQ1: 10-(6′-plastoquinonyl) decyltriphenylphosphonium; YVAD: Tyr-Val-Ala-Asp.

Persistent NLRP3 activation in macrophages disrupts the transformation of the inflammatory M1 phenotype to M2 phenotype, which results in delayed healing of DW [57]. Treatment with *Bletilla striata polysaccharide*, the main active ingredient of *Bletilla striata*, promotes wound healing by suppressing the NLRP3 inflammasome, and as a result, induces a switch from the proinflammatory M1 phenotype towards the prohealing M2 phenotype [132]. The external use of glibenclamide can show similar pharmacological effects by inhibiting NLRP3 inflammasome activity and reducing the expression of inflammatory factors to downregulate the MI phenotype and upregulate the M2 phenotype [48]. In addition, inflammatory responses at the site of the wound in diabetes are increasingly amplified through the inflammatory loop involving "NLRP3 inflammasome-NETs." Conditional deletion of milk fat globule epidermal growth factor VIII (MFG-E8) in diabetic mice aggravates wound damage and displays exaggerated activation of the NLRP3 inflammasome with largely fixed NETs. After treatment with recombinant MFG-E8, the production of NETosis is reduced, the activities of the NLRP3 inflammasome are significantly reduced, and the rate of DW healing is accelerated [100, 133]. The underlying protective mechanism of MFG-E8 is mediated via integrin $\beta 3$ and limiting P2X7R to regulate the activation of the NET-primed NLRP3 inflammasome.

Induced by the presence of bacteria or viruses, the NLRP3 inflammasome releases active caspase-1, which cleaves GSDMD into GSDMD-NT, triggering cell membrane pore formation, cell rupture, and release of inflammatory mediators [134]. This inflammatory cascade results in a rapid programmed cell death pattern accompanied with a robust inflammatory response, called "pyroptosis," which is also involved in the inhibition of the wound healing process in DFUs. Recently, Pastar et al. [135] showed that the process of pyroptosis was induced by intracellular *Staphylococcus aureus* in DFU tissue due to the striking suppression of perforin-2 (P-2), which dampens wound healing in patients with DFUs. Importantly, therapeutic approaches that restore P-2 levels could protect the skin against bacterial pathogens by suppressing the intracellular accumulation of *S. aureus* and targeting the pyroptotic pathway, which effectively promotes healing.

6. Limitations, Challenges, and Future Directions

DW displays a sustained inflammatory phase that has been identified as the most dysregulated process in wound healing, which impedes progression to the proliferative and remodeling phase [136]. Although the NLRP3 inflammasome exerts physiological roles in protecting the body against infection and producing cytokine, sustained activation triggers inflammatory cascade with "hurt both enemies and selves" [137]. Therefore, controlling it to maintain a balanced state will resolve inflammation and accelerate wound healing. With the application of multiomics approaches, transcriptomics, and proteomics of single cells, previously

unidentified targets are gradually revealed to decipher the mechanisms of pathogenicity in DW healing [138]. While the healing process of DW is complex and dynamic, these different inflammation pathways also have complex connections, as the NLRP3 inflammasome just scratching the surface. At present, there still lack studies about the crosstalk between multiple signal pathways in the DW or the changes of NLRP3 inflammasome in the different phases of DW healing. Thus, further in-depth research of the other factors in the processes of the wound healing phases will also provide us novel insights to clarify the pathogenic mechanisms of DW. Besides, new therapeutic approaches involving the multitarget, novel carrier, stem cells, and combination approaches have been evaluated and applied into clinic, while how to optimize personalized strategies with improvement of chronic inflammatory state in DW should be considered.

7. Conclusion

NLRP3 detects danger signals, leading to the activation of the NLRP3 inflammasome and release of proinflammatory cytokines, which play a vital role in DW. Significant advances have revealed the relationship between the molecular mechanisms of the priming/assembly step of NLRP3 inflammasome activation and the pathogenesis of DW. However, the crosstalk between other signaling pathways and NLRP3 inflammasome in DW healing and the differences in the expression of NLRP3 inflammasome from the temporal and spatial aspects, which influence the healing of DW, still need to be revealed. Undoubtedly, further in-depth study of the NLRP3 inflammasome may provide a novel interpretation of the healing process in DW, and the development of inflammasome agonists will provide a better option for patients with DW.

Data Availability

All data included in this study are available upon request by contact with the corresponding author.

Conflicts of Interest

The authors declare that they have no conflicts of interest.

Authors' Contributions

Youjun Ding and Xiaofeng Ding contributed equally to this work.

Acknowledgments

This work was supported by the National Natural Science Foundation of China (grant numbers 81671922, 81974288).

References

[1] P. Saeedi, I. Petersohn, P. Salpea et al., "Global and regional diabetes prevalence estimates for 2019 and projections for 2030 and 2045: Results from the International Diabetes Federation Diabetes Atlas," *Diabetes Research and Clinical Practice*, vol. 157, p. 107843, 2019.

[2] A. P. Veith, K. Henderson, A. Spencer, A. D. Sligar, and A. B. Baker, "Therapeutic strategies for enhancing angiogenesis in wound healing," *Advanced Drug Delivery Reviews*, vol. 146, pp. 97–125, 2019.

[3] S. Ellis, E. J. Lin, and D. Tartar, "Immunology of wound healing," *Current Dermatology Reports*, vol. 7, no. 4, pp. 350–358, 2018.

[4] Y. He, H. Hara, and G. Nunez, "Mechanism and regulation of NLRP3 inflammasome activation," *Trends in Biochemical Sciences*, vol. 41, no. 12, pp. 1012–1021, 2016.

[5] F. Martinon, K. Burns, and J. Tschopp, "The inflammasome: a molecular platform triggering activation of inflammatory caspases and processing of proIL-β," *Molecular Cell*, vol. 10, no. 2, pp. 417–426, 2002.

[6] S. R. Mulay, "Multifactorial functions of the inflammasome component NLRP3 in pathogenesis of chronic kidney diseases," *Kidney International*, vol. 96, no. 1, pp. 58–66, 2019.

[7] E. I. Elliott and F. S. Sutterwala, "Initiation and perpetuation of NLRP3 inflammasome activation and assembly," *Immunological Reviews*, vol. 265, no. 1, pp. 35–52, 2015.

[8] D. W. Shim and K. H. Lee, "Posttranslational regulation of the NLR family pyrin domain-containing 3 Inflammasome," *Frontiers in Immunology*, vol. 9, p. 1054, 2018.

[9] H. Sharif, L. Wang, W. L. Wang et al., "Structural mechanism for NEK7-licensed activation of NLRP3 inflammasome," *Nature*, vol. 570, no. 7761, pp. 338–343, 2019.

[10] C. M. McKee and R. C. Coll, "NLRP3 inflammasome priming: a riddle wrapped in a mystery inside an enigma," *Journal of Leukocyte Biology*, vol. 108, no. 3, pp. 937–952, 2020.

[11] K. V. Swanson, M. Deng, and J. P. Ting, "The NLRP3 inflammasome: molecular activation and regulation to therapeutics," *Nature Reviews. Immunology*, vol. 19, no. 8, pp. 477–489, 2019.

[12] I. S. Afonina, Z. Zhong, M. Karin, and R. Beyaert, "Limiting inflammation–the negative regulation of NF-κB and the NLRP3 inflammasome," *Nature Immunology*, vol. 18, no. 8, pp. 861–869, 2017.

[13] P. Gurung, P. K. Anand, R. K. S. Malireddi et al., "FADD and caspase-8 mediate priming and activation of the canonical and noncanonical Nlrp3 inflammasomes," *Journal of Immunology*, vol. 192, no. 4, pp. 1835–1846, 2014.

[14] T. Fernandes-Alnemri, S. Kang, C. Anderson, J. Sagara, K. A. Fitzgerald, and E. S. Alnemri, "Cutting edge: TLR signaling licenses IRAK1 for rapid activation of the NLRP3 inflammasome," *Journal of Immunology*, vol. 191, no. 8, pp. 3995–3999, 2013.

[15] D. Chauhan, L. Vande Walle, and M. Lamkanfi, "Therapeutic modulation of inflammasome pathways," *Immunological Reviews*, vol. 297, no. 1, pp. 123–138, 2020.

[16] S. Kang, T. Fernandes-Alnemri, C. Rogers et al., "Caspase-8 scaffolding function and MLKL regulate NLRP3 inflammasome activation downstream of TLR3," *Nature Communications*, vol. 6, no. 1, p. 7515, 2015.

[17] M. S. Mangan, E. J. Olhava, W. R. Roush, H. M. Seidel, G. D. Glick, and E. Latz, "Targeting the NLRP3 inflammasome in inflammatory diseases," *Nature Reviews. Drug Discovery*, vol. 17, no. 8, pp. 588–606, 2018.

[18] F. Cao, L. Q. Hu, S. R. Yao et al., "P2X7 receptor: a potential therapeutic target for autoimmune diseases," *Autoimmunity Reviews*, vol. 18, no. 8, pp. 767–777, 2019.

[19] A. Di, S. Xiong, Z. Ye et al., "The TWIK2 Potassium Efflux Channel in Macrophages Mediates NLRP3 Inflammasome-Induced Inflammation," *Immunity*, vol. 49, no. 1, pp. 56–65, 2018.

[20] F. Vanden Abeele, G. Bidaux, D. Gordienko et al., "Functional implications of calcium permeability of the channel formed by pannexin 1," *The Journal of Cell Biology*, vol. 174, no. 4, pp. 535–546, 2006.

[21] Y. Yang, J. Li, T. L. Han et al., "Endoplasmic reticulum stress may activate NLRP3 inflammasomes via TXNIP in pre-eclampsia," *Cell and Tissue Research*, vol. 379, no. 3, pp. 589–599, 2020.

[22] J. Dan Dunn, L. A. J. Alvarez, X. Zhang, and T. Soldati, "Reactive oxygen species and mitochondria: a nexus of cellular homeostasis," *Redox Biology*, vol. 6, pp. 472–485, 2015.

[23] J. M. Abais, M. Xia, Y. Zhang, K. M. Boini, and P. L. Li, "Redox regulation of NLRP3 inflammasomes: ROS as trigger or effector?," *Antioxidants & Redox Signaling*, vol. 22, no. 13, pp. 1111–1129, 2015.

[24] H. Cho, M. R. Blatchley, E. J. Duh, and S. Gerecht, "Acellular and cellular approaches to improve diabetic wound healing," *Advanced Drug Delivery Reviews*, vol. 146, pp. 267–288, 2019.

[25] T. N. Demidova-Rice, J. T. Durham, and I. M. Herman, "Wound healing angiogenesis: innovations and challenges in acute and chronic wound healing," *Advances in Wound Care*, vol. 1, no. 1, pp. 17–22, 2012.

[26] S. Patel, S. Srivastava, M. R. Singh, and D. Singh, "Mechanistic insight into diabetic wounds: pathogenesis, molecular targets and treatment strategies to pace wound healing," *Biomedicine & Pharmacotherapy*, vol. 112, p. 108615, 2019.

[27] X. Huang, P. Liang, B. Jiang et al., "Hyperbaric oxygen potentiates diabetic wound healing by promoting fibroblast cell proliferation and endothelial cell angiogenesis," *Life Sciences*, vol. 259, p. 118246, 2020.

[28] M. Zubair and J. Ahmad, "Role of growth factors and cytokines in diabetic foot ulcer healing: a detailed review," *Reviews in Endocrine & Metabolic Disorders*, vol. 20, no. 2, pp. 207–217, 2019.

[29] K. Zhou, Y. Ma, and M. S. Brogan, "Chronic and non-healing wounds: the story of vascular endothelial growth factor," *Medical Hypotheses*, vol. 85, no. 4, pp. 399–404, 2015.

[30] J. Q. Yu, X. F. Liu, L. K. Chin, A. Q. Liu, and K. Q. Luo, "Study of endothelial cell apoptosis using fluorescence resonance energy transfer (FRET) biosensor cell line with hemodynamic microfluidic chip system," *Lab on a Chip*, vol. 13, no. 14, pp. 2693–2700, 2013.

[31] L. S. Angelo and R. Kurzrock, "Vascular endothelial growth factor and its relationship to inflammatory mediators," *Clinical Cancer Research*, vol. 13, no. 10, pp. 2825–2830, 2007.

[32] C. J. Lin, Y. M. Lan, M. Q. Ou, L. Q. Ji, and S. D. Lin, "Expression of miR-217 and HIF-1α/VEGF pathway in patients with diabetic foot ulcer and its effect on angiogenesis of diabetic foot ulcer rats," *Journal of Endocrinological Investigation*, vol. 42, no. 11, pp. 1307–1317, 2019.

[33] A. A. Tandara and T. A. Mustoe, "Oxygen in Wound Healing?More than a Nutrient," *World Journal of Surgery*, vol. 28, no. 3, pp. 294–300, 2004.

[34] H. Thangarajah, D. Yao, E. I. Chang et al., "The molecular basis for impaired hypoxia-induced VEGF expression in diabetic tissues," *Proceedings of the National Academy of Sciences of the United States of America*, vol. 106, no. 32, pp. 13505–13510, 2009.

[35] L. Pang, P. Tian, X. Cui et al., "In situ photo-cross-linking hydrogel accelerates diabetic wound healing through restored hypoxia-inducible factor 1-alpha pathway and regulated inflammation," *ACS Applied Materials & Interfaces*, vol. 13, no. 25, pp. 29363–29379, 2021.

[36] L. Piconi, L. Quagliaro, R. Assaloni et al., "Constant and intermittent high glucose enhances endothelial cell apoptosis through mitochondrial superoxide overproduction," *Diabetes/Metabolism Research and Reviews*, vol. 22, no. 3, pp. 198–203, 2006.

[37] C. F. Bento and P. Pereira, "Regulation of hypoxia-inducible factor 1 and the loss of the cellular response to hypoxia in diabetes," *Diabetologia*, vol. 54, no. 8, pp. 1946–1956, 2011.

[38] T. J. Shaw and P. Martin, "Wound repair at a glance," *Journal of Cell Science*, vol. 122, no. 18, pp. 3209–3213, 2009.

[39] A. P. Sawaya, R. C. Stone, S. R. Brooks et al., "Deregulated immune cell recruitment orchestrated by FOXM1 impairs human diabetic wound healing," *Nature Communications*, vol. 11, no. 1, pp. 1–14, 2020.

[40] J. S. Chin, L. Madden, S. Y. Chew, and D. L. Becker, "Drug therapies and delivery mechanisms to treat perturbed skin wound healing," *Advanced Drug Delivery Reviews*, vol. 149, pp. 2–18, 2019.

[41] J. C. Brazil, M. Quiros, A. Nusrat, and C. A. Parkos, "Innate immune cell-epithelial crosstalk during wound repair," *The Journal of Clinical Investigation*, vol. 129, no. 8, pp. 2983–2993, 2019.

[42] G. Sollberger, D. O. Tilley, and A. Zychlinsky, "Neutrophil extracellular traps: the biology of chromatin externalization," *Developmental Cell*, vol. 44, no. 5, pp. 542–553, 2018.

[43] S. Swaidani and K. R. McCrae, "HITing back against NETs," *Blood*, vol. 135, no. 10, pp. 706-707, 2020.

[44] S. L. Wong, M. Demers, K. Martinod et al., "Diabetes primes neutrophils to undergo NETosis, which impairs wound healing," *Nature Medicine*, vol. 21, no. 7, pp. 815–819, 2015.

[45] D. Liu, P. Yang, M. Gao et al., "NLRP3 activation induced by neutrophil extracellular traps sustains inflammatory response in the diabetic wound," *Clinical Science (London, England)*, vol. 133, no. 4, pp. 565–582, 2019.

[46] L. Aldabbous, V. Abdul-Salam, T. McKinnon et al., "Neutrophil extracellular traps promote angiogenesis: evidence from vascular pathology in pulmonary hypertension," *Arteriosclerosis, Thrombosis, and Vascular Biology*, vol. 36, no. 10, pp. 2078–2087, 2016.

[47] A. Arampatzioglou, D. Papazoglou, T. Konstantinidis et al., "Clarithromycin enhances the antibacterial activity and wound healing capacity in type 2 diabetes mellitus by increasing LL-37 load on neutrophil extracellular traps," *Frontiers in Immunology*, vol. 9, p. 2064, 2018.

[48] R. E. Mirza, M. M. Fang, E. M. Weinheimer-Haus, W. J. Ennis, and T. J. Koh, "Sustained inflammasome activity in macrophages impairs wound healing in type 2 diabetic humans and mice," *Diabetes*, vol. 63, no. 3, pp. 1103–1114, 2014.

[49] K. Geng, X. Ma, Z. Jiang et al., "Innate immunity in diabetic wound healing: focus on the mastermind hidden in chronic

inflammatory," *Frontiers in Pharmacology*, vol. 12, p. 653940, 2021.

[50] P. Krzyszczyk, R. Schloss, A. Palmer, and F. Berthiaume, "The role of macrophages in acute and chronic wound healing and interventions to promote pro-wound healing phenotypes," *Frontiers in Physiology*, vol. 9, p. 419, 2018.

[51] A. E. Louiselle, S. M. Niemiec, C. Zgheib, and K. W. Liechty, "Macrophage polarization and diabetic wound healing," *Translational Research*, vol. 236, pp. 109–116, 2021.

[52] F. Prattichizzo, V. de Nigris, E. Mancuso et al., "Short-term sustained hyperglycaemia fosters an archetypal senescence-associated secretory phenotype in endothelial cells and macrophages," *Redox Biology*, vol. 15, pp. 170–181, 2018.

[53] G. V. Ganesh and K. M. Ramkumar, "Macrophage mediation in normal and diabetic wound healing responses," *Inflammation Research*, vol. 69, no. 4, pp. 347–363, 2020.

[54] R. Mirza and T. J. Koh, "Dysregulation of monocyte/macrophage phenotype in wounds of diabetic mice," *Cytokine*, vol. 56, no. 2, pp. 256–264, 2011.

[55] M. Hesketh, K. B. Sahin, Z. E. West, and R. Z. Murray, "Macrophage phenotypes regulate scar formation and chronic wound healing," *International Journal of Molecular Sciences*, vol. 18, no. 7, p. 1545, 2017.

[56] Q. Zhang, W. Yu, S. Lee, Q. Xu, A. Naji, and A. D. Le, "Bisphosphonate induces osteonecrosis of the jaw in diabetic mice via NLRP3/caspase-1-dependent IL-1β mechanism," *Journal of Bone and Mineral Research*, vol. 30, no. 12, pp. 2300–2312, 2015.

[57] A. E. Boniakowski, A. S. Kimball, B. N. Jacobs, S. L. Kunkel, and K. A. Gallagher, "Macrophage-mediated inflammation in normal and diabetic wound healing," *Journal of Immunology*, vol. 199, no. 1, pp. 17–24, 2017.

[58] I. Bellezza, I. Giambanco, A. Minelli, and R. Donato, "Nrf2-Keap1 signaling in oxidative and reductive stress," *Biochimica et Biophysica Acta (BBA)-Molecular Cell Research*, vol. 1865, no. 5, pp. 721–733, 2018.

[59] P. Canning, F. J. Sorrell, and A. N. Bullock, "Structural basis of Keap1 interactions with Nrf2," *Free Radical Biology & Medicine*, vol. 88, pp. 101–107, 2015.

[60] I. Bellezza, A. L. Mierla, and A. Minelli, "Nrf2 and NF-κB and their concerted modulation in cancer pathogenesis and progression," *Cancers (Basel)*, vol. 2, no. 2, pp. 483–497, 2010.

[61] F. G. Bauernfeind, G. Horvath, A. Stutz et al., "Cutting edge: NF-kappaB activating pattern recognition and cytokine receptors license NLRP3 inflammasome activation by regulating NLRP3 expression," *Journal of Immunology*, vol. 183, no. 2, pp. 787–791, 2009.

[62] M. E. Gerritsen, A. J. Williams, A. S. Neish, S. Moore, Y. Shi, and T. Collins, "CREB-binding protein/p300 are transcriptional coactivators of p65," *Proceedings of the National Academy of Sciences of the United States of America*, vol. 94, no. 7, pp. 2927–2932, 1997.

[63] G. H. Liu, J. Qu, and X. Shen, "NF-κB/p65 antagonizes Nrf2-ARE pathway by depriving CBP from Nrf2 and facilitating recruitment of HDAC3 to MafK," *Biochimica et Biophysica Acta*, vol. 1783, no. 5, pp. 713–727, 2008.

[64] X. Li, X. Xie, W. Lian et al., "Exosomes from adipose-derived stem cells overexpressing Nrf2 accelerate cutaneous wound healing by promoting vascularization in a diabetic foot ulcer rat model," *Experimental & Molecular Medicine*, vol. 50, no. 4, pp. 1–14, 2018.

[65] M. N. Valcarcel-Ares, T. Gautam, J. P. Warrington et al., "Disruption of Nrf2 signaling impairs angiogenic capacity of endothelial cells: implications for microvascular aging," *The Journals of Gerontology. Series A, Biological Sciences and Medical Sciences*, vol. 67, no. 8, pp. 821–829, 2012.

[66] D. Sireesh, U. Dhamodharan, K. Ezhilarasi, V. Vijay, and K. M. Ramkumar, "Association of NF-E2 related factor 2 (Nrf2) and inflammatory cytokines in recent onset type 2 diabetes mellitus," *Scientific Reports*, vol. 8, no. 1, pp. 1–10, 2018.

[67] U. Dhamodharan, A. Karan, D. Sireesh et al., "Tissue-specific role of Nrf2 in the treatment of diabetic foot ulcers during hyperbaric oxygen therapy," *Free Radical Biology & Medicine*, vol. 138, pp. 53–62, 2019.

[68] S. M. Seyydi, A. Tofighi, M. Rahmati, and J. T. Azar, "Exercise and _Urtica dioica extract_ ameliorate mitochondrial function and the expression of cardiac muscle nuclear respiratory factor 2 and peroxisome proliferator-activated receptor gamma coactivator 1-alpha in STZ-induced diabetic rats," *Gene*, vol. 822, p. 146351, 2022.

[69] J. S. Albert-Garay, J. R. Riesgo-Escovar, and R. Salceda, "High glucose concentrations induce oxidative stress by inhibiting Nrf2 expression in rat Muller retinal cells in vitro," *Scientific Reports*, vol. 12, no. 1, p. 1261, 2022.

[70] M. Long, M. Rojo de la Vega, Q. Wen et al., "An essential role of NRF2 in diabetic wound healing," *Diabetes*, vol. 65, no. 3, pp. 780–793, 2016.

[71] A. Jindam, V. G. Yerra, and A. Kumar, "Nrf2: a promising trove for diabetic wound healing," *Annals of Translational Medicine*, vol. 5, no. 23, p. 469, 2017.

[72] M. J. Portou, D. Baker, D. Abraham, and J. Tsui, "The innate immune system, toll-like receptors and dermal wound healing: a review," *Vascular Pharmacology*, vol. 71, pp. 31–36, 2015.

[73] M. R. Dasu, R. K. Thangappan, A. Bourgette, L. A. DiPietro, R. Isseroff, and I. Jialal, "TLR2 expression and signaling-dependent inflammation impair wound healing in diabetic mice," *Laboratory Investigation*, vol. 90, no. 11, pp. 1628–1636, 2010.

[74] K. Singh, N. K. Agrawal, S. K. Gupta, G. Mohan, S. Chaturvedi, and K. Singh, "Genetic and epigenetic alterations in toll like receptor 2 and wound healing impairment in type 2 diabetes patients," *Journal of Diabetes and its Complications*, vol. 29, no. 2, pp. 222–229, 2015.

[75] M. R. Dasu and S. J. Martin, "Toll-like receptor expression and signaling in human diabetic wounds," *World Journal of Diabetes*, vol. 5, no. 2, pp. 219–223, 2014.

[76] M. R. Dasu and I. Jialal, "Amelioration in wound healing in diabetic toll-like receptor-4 knockout mice," *Journal of Diabetes and its Complications*, vol. 27, no. 5, pp. 417–421, 2013.

[77] P. C. Grayson, C. Schauer, M. Herrmann, and M. J. Kaplan, "Review: neutrophils as invigorated targets in rheumatic diseases," *Arthritis & Rhematology*, vol. 68, no. 9, pp. 2071–2082, 2016.

[78] R. Njeim, W. S. Azar, A. H. Fares, S. T. Azar, H. Kfoury Kassouf, and A. A. Eid, "NETosis contributes to the pathogenesis of diabetes and its complications," *Journal of Molecular Endocrinology*, vol. 65, no. 4, pp. R65–R76, 2020.

[79] C. R. Lupfer, A. Rodriguez, and T. D. Kanneganti, "Inflammasome activation by nucleic acids and nucleosomes in

sterile inflammation... Or is it sterile?," *The FEBS Journal*, vol. 284, no. 15, pp. 2363–2374, 2017.

[80] M. K. S. Lee, G. Sreejit, P. R. Nagareddy, and A. J. Murphy, "Attack of the NETs! NETosis primes IL-1β-mediated inflammation in diabetic foot ulcers," *Clinical Science (London, England)*, vol. 134, no. 12, pp. 1399–1401, 2020.

[81] G. P. Fadini, L. Menegazzo, M. Rigato et al., "NETosis delays diabetic wound healing in mice and humans," *Diabetes*, vol. 65, no. 4, pp. 1061–1071, 2016.

[82] L. Feldmeyer, M. Keller, G. Niklaus, D. Hohl, S. Werner, and H. D. Beer, "The inflammasome mediates UVB-induced activation and secretion of interleukin-1β by keratinocytes," *Current Biology*, vol. 17, no. 13, pp. 1140–1145, 2007.

[83] H. Watanabe, O. Gaide, V. Pétrilli et al., "Activation of the IL-1 _β_ -processing inflammasome is involved in contact hypersensitivity," *The Journal of Investigative Dermatology*, vol. 127, no. 8, pp. 1956–1963, 2007.

[84] D. J. Lee, F. du, S. W. Chen et al., "Regulation and function of the caspase-1 in an inflammatory microenvironment," *The Journal of Investigative Dermatology*, vol. 135, no. 8, pp. 2012–2020, 2015.

[85] S. Paik, J. K. Kim, P. Silwal, C. Sasakawa, and E. K. Jo, "An update on the regulatory mechanisms of NLRP3 inflammasome activation," *Cellular & Molecular Immunology*, vol. 18, no. 5, pp. 1141–1160, 2021.

[86] A. K. Palmer, B. Gustafson, J. L. Kirkland, and U. Smith, "Cellular senescence: at the nexus between ageing and diabetes," *Diabetologia*, vol. 62, no. 10, pp. 1835–1841, 2019.

[87] D. Mayer, D. Armstrong, G. Schultz et al., "Cell salvage in acute and chronic wounds: a potential treatment strategy. Experimental data and early clinical results," *Journal of Wound Care*, vol. 27, no. 9, pp. 594–605, 2018.

[88] H. Jung, M. J. Kim, D. O. Kim et al., "TXNIP maintains the hematopoietic cell pool by switching the function of p53 under oxidative stress," *Cell Metabolism*, vol. 18, no. 1, pp. 75–85, 2013.

[89] S. Joshi, W. Wang, A. B. Peck, and S. R. Khan, "Activation of the NLRP3 inflammasome in association with calcium oxalate crystal induced reactive oxygen species in kidneys," *The Journal of Urology*, vol. 193, no. 5, pp. 1684–1691, 2015.

[90] A. L. Weinstein, F. D. Lalezarzadeh, M. A. Soares, P. B. Saadeh, and D. J. Ceradini, "Normalizing dysfunctional purine metabolism accelerates diabetic wound healing," *Wound Repair and Regeneration*, vol. 23, no. 1, pp. 14–21, 2015.

[91] X. Zhang, J. Dai, L. Li, H. Chen, and Y. Chai, "NLRP3 Inflammasome expression and signaling in human diabetic wounds and in high glucose induced macrophages," *Journal Diabetes Research*, vol. 2017, article 5281358, 7 pages, 2017.

[92] S. Yeoh-Ellerton and M. C. Stacey, "Iron and 8-isoprostane levels in acute and chronic wounds," *The Journal of Investigative Dermatology*, vol. 121, no. 4, pp. 918–925, 2003.

[93] J. Dai, X. Zhang, Y. Wang, H. Chen, and Y. Chai, "ROS-activated NLRP3 inflammasome initiates inflammation in delayed wound healing in diabetic rats," *International Journal of Clinical and Experimental Pathology*, vol. 10, no. 9, pp. 9902–9909, 2017.

[94] S. S. Iyer, W. P. Pulskens, J. J. Sadler et al., "Necrotic cells trigger a sterile inflammatory response through the Nlrp3 inflammasome," *Proceedings of the National Academy of Sciences of the United States of America*, vol. 106, no. 48, pp. 20388–20393, 2009.

[95] A. Meyer, G. Laverny, L. Bernardi et al., "Mitochondria: an organelle of bacterial origin controlling inflammation," *Frontiers in Immunology*, vol. 9, p. 536, 2018.

[96] J. Jabaut, J. L. Ather, A. Taracanova, M. E. Poynter, and K. Ckless, "Mitochondria-targeted drugs enhance Nlrp3 inflammasome-dependent IL-1β secretion in association with alterations in cellular redox and energy status," *Free Radical Biology & Medicine*, vol. 60, pp. 233–245, 2013.

[97] J. Dai, H. Chen, and Y. Chai, "Advanced glycation end products (AGEs) induce apoptosis of fibroblasts by activation of NLRP3 inflammasome via reactive oxygen species (ROS) signaling pathway," *Medical Science Monitor*, vol. 25, pp. 7499–7508, 2019.

[98] R. Zhou, A. Tardivel, B. Thorens, I. Choi, and J. Tschopp, "Thioredoxin-interacting protein links oxidative stress to inflammasome activation," *Nature Immunology*, vol. 11, no. 2, pp. 136–140, 2010.

[99] J. M. Kahlenberg, C. Carmona-Rivera, C. K. Smith, and M. J. Kaplan, "Neutrophil extracellular trap-associated protein activation of the NLRP3 inflammasome is enhanced in lupus macrophages," *Journal of Immunology*, vol. 190, no. 3, pp. 1217–1226, 2013.

[100] W. Huang, J. Jiao, J. Liu et al., "MFG-E8 accelerates wound healing in diabetes by regulating "NLRP3 inflammasome-neutrophil extracellular traps" axis," *Cell Death Discovery*, vol. 6, pp. 1–16, 2020.

[101] R. Zhou, A. S. Yazdi, P. Menu, and J. Tschopp, "A role for mitochondria in NLRP3 inflammasome activation," *Nature*, vol. 469, no. 7329, pp. 221–225, 2011.

[102] N. Ferrara, H. P. Gerber, and J. LeCouter, "The biology of VEGF and its receptors," *Nature Medicine*, vol. 9, no. 6, pp. 669–676, 2003.

[103] R. S. Apte, D. S. Chen, and N. Ferrara, "VEGF in signaling and disease: beyond discovery and development," *Cell*, vol. 176, no. 6, pp. 1248–1264, 2019.

[104] A. Bitto, D. Altavilla, G. Pizzino et al., "Inhibition of inflammasome activation improves the impaired pattern of healing in genetically diabetic mice," *British Journal of Pharmacology*, vol. 171, no. 9, pp. 2300–2307, 2014.

[105] Y. He, M. Y. Zeng, D. Yang, B. Motro, and G. Núñez, "NEK7 is an essential mediator of NLRP3 activation downstream of potassium efflux," *Nature*, vol. 530, no. 7590, pp. 354–357, 2016.

[106] H. He, H. Jiang, Y. Chen et al., "Oridonin is a covalent NLRP3 inhibitor with strong anti-inflammasome activity," *Nature Communications*, vol. 9, no. 1, p. 2550, 2018.

[107] H. Cai, P. Wang, B. Zhang, and X. Q. Dong, "Expression of the NEK7/NLRP3 inflammasome pathway in patients with diabetic lower extremity arterial disease," *BMJ Open Diabetes Research & Care*, vol. 8, no. 2, p. e001808, 2020.

[108] G. M. Orlowski, J. D. Colbert, S. Sharma, M. Bogyo, S. A. Robertson, and K. L. Rock, "Multiple cathepsins promote pro–IL-1β synthesis and NLRP3-mediated IL-1β activation," *Journal of Immunology*, vol. 195, no. 4, pp. 1685–1697, 2015.

[109] V. Hornung, F. Bauernfeind, A. Halle et al., "Silica crystals and aluminum salts activate the NALP3 inflammasome through phagosomal destabilization," *Nature Immunology*, vol. 9, no. 8, pp. 847–856, 2008.

[110] M. Bruchard, G. Mignot, V. Derangère et al., "Chemotherapy-triggered cathepsin B release in myeloid-derived suppressor cells activates the Nlrp3 inflammasome and promotes tumor growth," *Nature Medicine*, vol. 19, no. 1, pp. 57–64, 2013.

[111] E. Rampanelli, E. Orsó, P. Ochodnicky et al., "Metabolic injury-induced NLRP3 inflammasome activation dampens phospholipid degradation," *Scientific Reports*, vol. 7, no. 1, p. 2861, 2017.

[112] L. He, K. J. Weber, and J. D. Schilling, "Glutamine modulates macrophage lipotoxicity," *Nutrients*, vol. 8, no. 4, p. 215, 2016.

[113] X. Li, T. Wang, Y. Tao, X. Wang, L. Li, and J. Liu, "MF-094, a potent and selective USP30 inhibitor, accelerates diabetic wound healing by inhibiting the NLRP3 inflammasome," *Experimental Cell Research*, vol. 410, no. 2, p. 112967, 2022.

[114] T. Wang, J. Zhao, J. Zhang et al., "Heparan sulfate inhibits inflammation and improves wound healing by downregulating the NLR family pyrin domain containing 3 (NLRP3) inflammasome in diabetic rats," *Journal of Diabetes*, vol. 10, no. 7, pp. 556–563, 2018.

[115] X. Sun, X. Wang, Z. Zhao, J. Chen, C. Li, and G. Zhao, "Paeoniflorin inhibited nod-like receptor protein-3 inflammasome and NF-κB- mediated inflammatory reactions in diabetic foot ulcer by inhibiting the chemokine receptor CXCR2," *Drug Development Research*, vol. 82, no. 3, pp. 404–411, 2021.

[116] M. Temiz-Resitoglu, S. P. Kucukkavruk, D. S. Guden et al., "Activation of mTOR/IκB-α/NF-κB pathway contributes to LPS-induced hypotension and inflammation in rats," *European Journal of Pharmacology*, vol. 802, pp. 7–19, 2017.

[117] L. Qing, J. Fu, P. Wu, Z. Zhou, F. Yu, and J. Tang, "Metformin induces the M2 macrophage polarization to accelerate the wound healing via regulating AMPK/mTOR/NLRP3 inflammasome singling pathway," *American Journal of Translational Research*, vol. 11, no. 2, pp. 655–668, 2019.

[118] C. Ponticelli, "The pros and the cons of mTOR inhibitors in kidney transplantation," *Expert Review of Clinical Immunology*, vol. 10, no. 2, pp. 295–305, 2014.

[119] M. A. Mabood Khalil, S. M. Al-Ghamdi, U. S. Dawood et al., "Mammalian target of rapamycin inhibitors and wound healing complications in kidney transplantation: old myths and new realities," *Journal of Transplantation*, vol. 2022, Article ID 6255339, 28 pages, 2022.

[120] J. Dai, C. Jiang, H. Chen, and Y. Chai, "Rapamycin attenuates high glucose-induced inflammation through modulation of mTOR/NF-κB pathways in macrophages," *Frontiers in Pharmacology*, vol. 10, p. 1292, 2019.

[121] W. Wang, X. Yan, Y. Lin, H. Ge, and Q. Tan, "Wnt7a promotes wound healing by regulation of angiogenesis and inflammation: issues on diabetes and obesity," *Journal of Dermatological Science*, vol. 91, no. 2, pp. 124–133, 2018.

[122] W. Wang, F. Zhang, X. Yan, and Q. Tan, "Wnt7a regulates high autophagic and inflammatory response of epidermis in high-glucose environment," *Burns*, vol. 46, no. 1, pp. 121–127, 2020.

[123] N. R. Vendidandala, T. P. Yin, G. Nelli, V. R. Pasupuleti, S. Nyamathulla, and S. I. Mokhtar, "Gallocatechin-silver nanoparticle impregnated cotton gauze patches enhance wound healing in diabetic rats by suppressing oxidative stress and inflammation _via_ modulating the Nrf2/HO-1 and TLR4/NF- κB pathways," *Life Sciences*, vol. 286, p. 120019, 2021.

[124] H. Eo, H. J. Lee, and Y. Lim, "Ameliorative effect of dietary genistein on diabetes induced hyper- inflammation and oxidative stress during early stage of wound healing in alloxan induced diabetic mice," *Biochemical and Biophysical Research Communications*, vol. 478, no. 3, pp. 1021–1027, 2016.

[125] Y. Shao, M. Dang, Y. Lin, and F. Xue, "Evaluation of wound healing activity of plumbagin in diabetic rats," *Life Sciences*, vol. 231, p. 116422, 2019.

[126] J. Li, H. Chou, L. Li, H. Li, and Z. Cui, "Wound healing activity of neferine in experimental diabetic rats through the inhibition of inflammatory cytokines and nrf-2 pathway," *Artificial Cells, Nanomedicine, and Biotechnology*, vol. 48, no. 1, pp. 96–106, 2020.

[127] L. Y. Chen, C. N. Huang, C. K. Liao et al., "Effects of Rutin on wound healing in hyperglycemic rats," *Antioxidants (Basel)*, vol. 9, no. 11, p. 1122, 2020.

[128] L. Y. Chen, H. L. Cheng, Y. H. Kuan, T. J. Liang, Y. Y. Chao, and H. C. Lin, "Therapeutic potential of luteolin on impaired wound healing in streptozotocin-induced rats," *Biomedicine*, vol. 9, no. 7, p. 761, 2021.

[129] D. R. Senger and S. Cao, "Diabetic wound healing and activation of Nrf2 by herbal medicine," *Journal of Nature and Science*, vol. 2, no. 11, 2016.

[130] I. A. Demyanenko, V. V. Zakharova, O. P. Ilyinskaya et al., "Mitochondria-targeted antioxidant SkQ1 improves dermal wound healing in genetically diabetic mice," *Oxidative Medicine and Cellular Longevity*, vol. 2017, Article ID 6408278, 10 pages, 2017.

[131] Y. Deng, X. Han, Z. Yao et al., "PPARα agonist stimulated angiogenesis by improving endothelial precursor cell function via a NLRP3 Inflammasome pathway," *Cellular Physiology and Biochemistry*, vol. 42, no. 6, pp. 2255–2266, 2017.

[132] Y. Zhao, Q. Wang, S. Yan et al., "Bletilla striata polysaccharide promotes diabetic wound healing through inhibition of the NLRP3 inflammasome," *Frontiers in Pharmacology*, vol. 12, p. 659215, 2021.

[133] A. Das, S. Ghatak, M. Sinha et al., "Correction of MFG-E8 resolves inflammation and promotes cutaneous wound healing in diabetes," *Journal of Immunology*, vol. 196, no. 12, pp. 5089–5100, 2016.

[134] S. M. Man, R. Karki, and T. D. Kanneganti, "Molecular mechanisms and functions of pyroptosis, inflammatory caspases and inflammasomes in infectious diseases," *Immunological Reviews*, vol. 277, no. 1, pp. 61–75, 2017.

[135] I. Pastar, A. P. Sawaya, J. Marjanovic et al., "Intracellular Staphylococcus aureus triggers pyroptosis and contributes to inhibition of healing due to perforin-2 suppression," *The Journal of Clinical Investigation*, vol. 131, no. 24, 2021.

[136] S. A. Eming, P. Martin, and M. Tomic-Canic, "Wound repair and regeneration: mechanisms, signaling, and translation," *Science Translational Medicine*, vol. 6, no. 265, p. 265, 2014.

[137] H. M. Lee, J. J. Kim, H. J. Kim, M. Shong, B. J. Ku, and E. K. Jo, "Upregulated NLRP3 inflammasome activation in patients with type 2 diabetes," *Diabetes*, vol. 62, no. 1, pp. 194–204, 2013.

[138] G. Theocharidis, D. Baltzis, M. Roustit et al., "Integrated skin transcriptomics and serum multiplex assays reveal novel mechanisms of wound healing in diabetic foot ulcers," *Diabetes*, vol. 69, no. 10, pp. 2157–2169, 2020.

Hindawi
Oxidative Medicine and Cellular Longevity
Volume 2022, Article ID 3711371, 25 pages
https://doi.org/10.1155/2022/3711371

Research Article

Dietary Fatty Acid Regulation of the NLRP3 Inflammasome via the TLR4/NF-κB Signaling Pathway Affects Chondrocyte Pyroptosis

Xin Jin,[1] **Xin Dong**,[1] **Yingxu Sun**,[1] **Ziyu Liu**,[1] **Li Liu**,[1] **and Hailun Gu**[2]

[1]*Department of Nutrition and Food Hygiene, School of Public Health, China Medical University, 110122, China*
[2]*Department of Orthopedics, Shengjing Hospital, China Medical University, 110004, China*

Correspondence should be addressed to Hailun Gu; guhailun_@163.com

Received 6 February 2022; Accepted 12 April 2022; Published 4 May 2022

Academic Editor: Francesca Danesi

Dietary fatty acid (FA) content and type have different effects on obesity-associated osteoarthritis (OA), but the mechanisms underlying these differences are not fully understood. Inflammation activated by toll-like receptor 4 (TLR4)/nuclear factor-(NF-) κB signaling and pyroptosis induced by the NLRP3/caspase-1/gasdermin D (GSDMD) signaling pathway play important roles in OA development. Our aim in this study was to observe the effects of dietary FAs on the articular cartilage of obese post-traumatic OA model mice and on chondrocytes stimulated by lipopolysaccharide (LPS) and to determine whether the underlying mechanisms involve TLR4/NF-κB and NLRP3/caspase-1/GSDMD signaling pathways. Mice were fed high-fat diets rich in various FAs and underwent surgical destabilization of the medial meniscus to establish the obesity-related post-traumatic OA model. LPS-induced SW1353 chondrosarcoma cells were used to mimic OA status *in vitro*, and TLR4 inhibitors or TLR4 overexpressing lentivirus was administered. Analysis using weight-matched mice and multiple regression models revealed that OA was associated with dietary FA content and serum inflammatory factor levels, but not body weight. Diets rich in n-3 polyunsaturated fatty acids (PUFAs) attenuated OA and inhibited the TLR4/NF-κB and NLRP3/caspase-1/GSDMD signaling pathways, whereas diets rich in saturated fatty acids (SFAs), monounsaturated fatty acids (MUFAs), or n-6 PUFAs increased OA severity and activated these pathways. *In vitro* results for SFAs, n-6 PUFAs, and n-3 PUFAs were consistent with the animal experiments. However, those for MUFAs were not. FA effects on the NLRP3/caspase-1/GSDMD pathway were associated with the inhibition or activation of the TLR4 signaling pathway. In conclusion, diets rich in SFAs or n-6 PUFAs can exacerbate obesity-associated OA, whereas those rich in n-3 PUFAs have protective effects against this disease, due to their respective pro-/anti-inflammatory and pyroptotic effects. Further research on dietary FA supplements as a potential therapeutic approach for OA is needed.

1. Introduction

Osteoarthritis (OA) is a degenerative joint disease that affects 237 million people worldwide and is an important cause of disability in middle-aged and older adults [1]. The joint changes of OA, including articular cartilage degeneration, subchondral bone thickening, bone fragment formation, synovitis, and the degeneration of ligaments and menisci, result in decreased function and quality of life. Patients with OA face significant healthcare and social costs [2–4]. Joint trauma, aging, metabolic disorders, and obesity can trigger OA [5], but the pathogenesis of this disease is still not well known and needs to be investigated further.

In recent years, with the gradual increase in the prevalence of obesity, the incidence of obesity-related OA has increased [6]. In addition to obesity-related biomechanical risk factors, which increase intra-cartilage pressure and aggravate wear and tear in joints [7], obesity-related chronic inflammation and nutritional metabolism abnormalities play roles in the development of OA [8, 9]. Excessive nutritional intake leads to lipid influx beyond the storage capacity of adipose tissues, resulting in elevated circulatory fatty acid

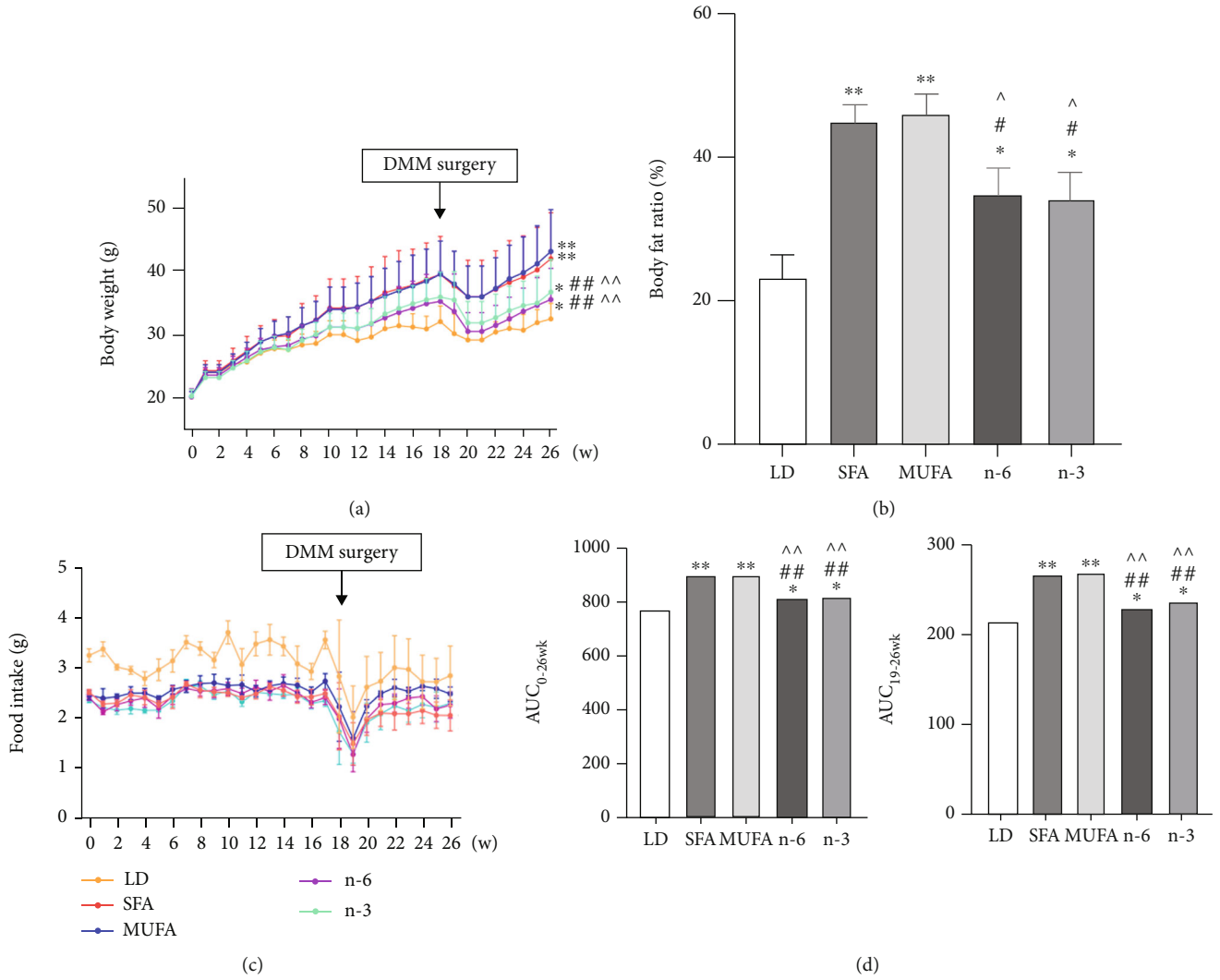

Figure 1: Effects of dietary FAs on body weight, body fat, and food intake in mice. (a) Body weight. (b) Body fat ratio at the end of 26 weeks of feeding. (c) Food intake. (d) The areas under weight curve of different FAs were calculated for the period from 0 to 26 weeks ($AUC_{0\text{-}26wk}$) and from 19 to 26 weeks ($AUC_{19\text{-}26wk}$), respectively. The data are presented as the means ± SD, $n = 15$. $^{*}p < 0.05$ and $^{**}p < 0.01$ versus the LD group; $^{\#}p < 0.05$ and $^{\#\#}p < 0.01$ versus the SFA group; $\wedge p < 0.05$ and $\wedge\wedge p < 0.01$ versus the MUFA group.

(FA) levels [10]. Increased FA accumulation in joints has been shown to be associated with cartilage damage severity in OA, with different FA types having distinct effects [11, 12]. Saturated fatty acids (SFAs) can increase the release of inflammatory factors such as interleukin- (IL-) 1β, causing degenerative changes in chondrocytes and having adverse effects on OA onset and progression [13]. Studies examining the effects of monounsaturated fatty acids (MUFAs) on OA have yielded variable results [14]. n-3 polyunsaturated fatty acids (PUFAs) have long been considered to be anti-inflammatory FAs with protective effects against OA [15]. However, inconsistent with previous results, the n-3 PUFA docosahexaenoic acid (DHA) was recently reported to induce pyroptosis in microglia and breast cancer cells [16, 17]. Conversely, n-6 PUFAs are considered to be pro-inflammatory FAs that increase cartilage degradation while promoting synovial inflammation, thereby accelerating OA progression [18]. Cohort studies have also shown that systemic levels of n-6 PUFAs correlate positively with the OA risk [19] and that increased ratios of n-6 to n-3 PUFAs have deleterious effects on cartilage [20]. However, the mechanisms mediating these different effects are not fully understood.

Toll-like receptor (TLR) 4, a member of the TLR family, mediates innate and adaptive immune responses [21, 22]. Through its downstream molecule myeloid differentiation factor (MyD)88, it signals to activate the nuclear factor-(NF-) κB pathway, leading to the production of various inflammatory cytokines [23]. TLR4 plays an important role in the development of OA [24].

Pyroptosis is a type of programmed cell death that is distinct from apoptosis and characterized by the disruption of the structural integrity of the cell membrane, leading to the release of cellular contents and thus the activation of a strong inflammatory response. Pyroptosis is mediated by inflammasomes, the most widely studied and well-characterized type of which is the NOD-like receptor protein (NLRP) 3 inflammasome [25]. NLRP3 inflammasome–

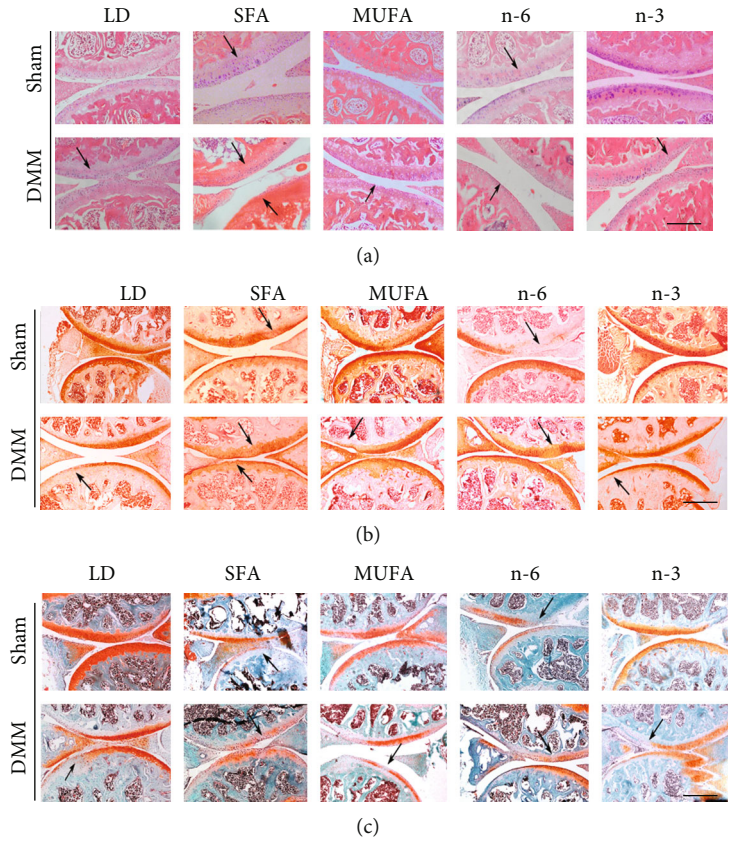

Figure 2: Continued.

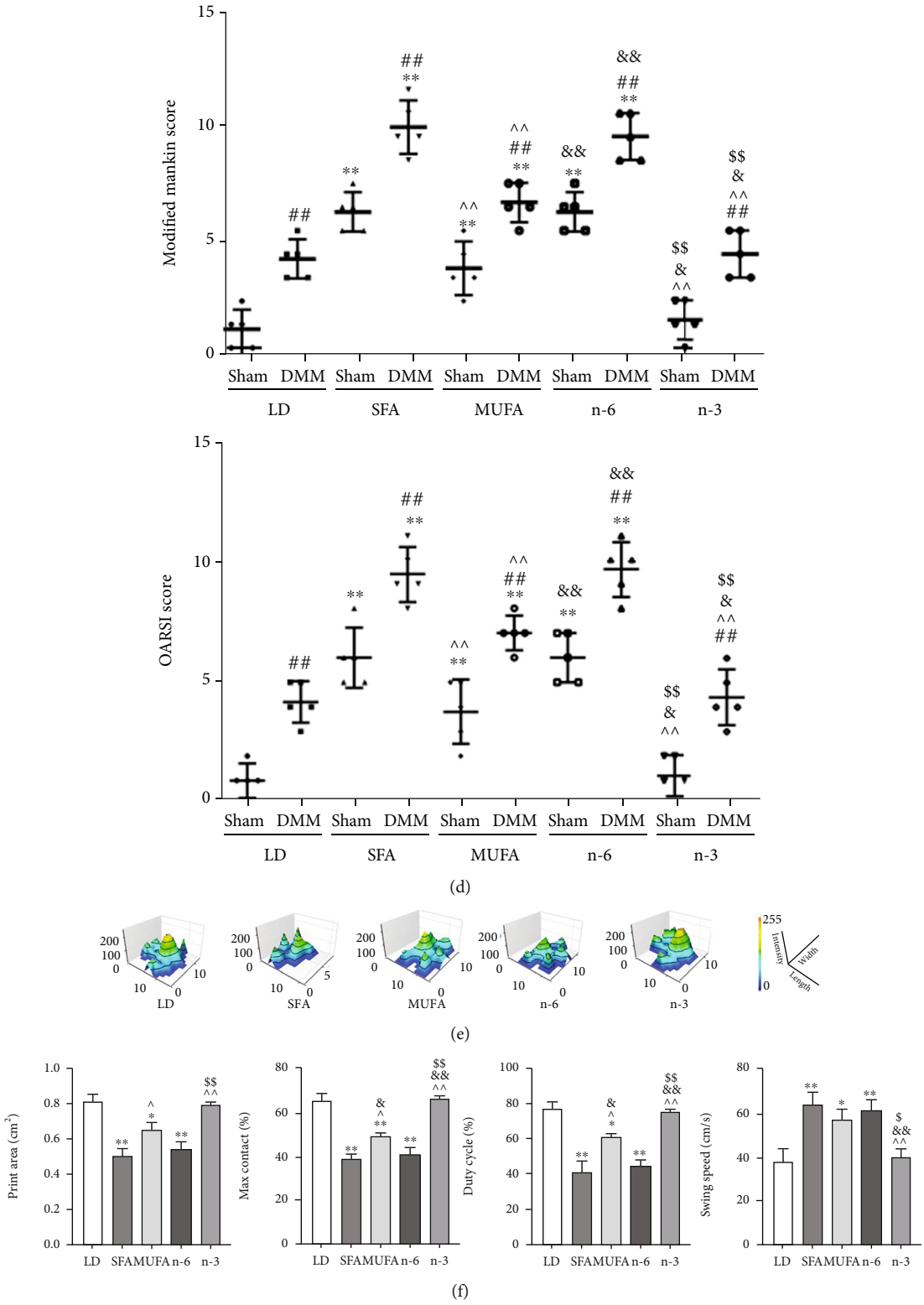

Figure 2: Effects of dietary FAs on articular cartilage in mice. (a) H&E staining (200x; scale bars = 100 μm). The arrows represented local aggregation or absence of cartilages. (b) Safranin O staining (100x; scale bars = 200 μm). The arrows indicated cartilage thinning or loss. (c) Safranin O/Fast Green staining (100x; scale bars = 200 μm). The arrows indicated the fuzzy fracture of the tide line. (d) Modified Mankin scores and OARSI scores. (e) Histogram of footprints of mice in each group from DMM hind limbs. (f) The bar graph data of print area (cm^2), max contact (%), duty cycle (%), and swing speed (cm/s). The data are presented as the means ± SD, $n = 5$. $^{*}p < 0.05$ and $^{**}p < 0.01$ versus the LD group; $^{\#}p < 0.05$ and $^{\#\#}p < 0.01$ versus the sham group; $\wedge p < 0.05$ and $\wedge\wedge p < 0.01$ versus the SFA group; $^{\&}p < 0.05$ and $^{\&\&}p < 0.01$ versus the MUFA group; $^{\$}p < 0.05$ and $^{\$\$}p < 0.01$ versus the n-6 group.

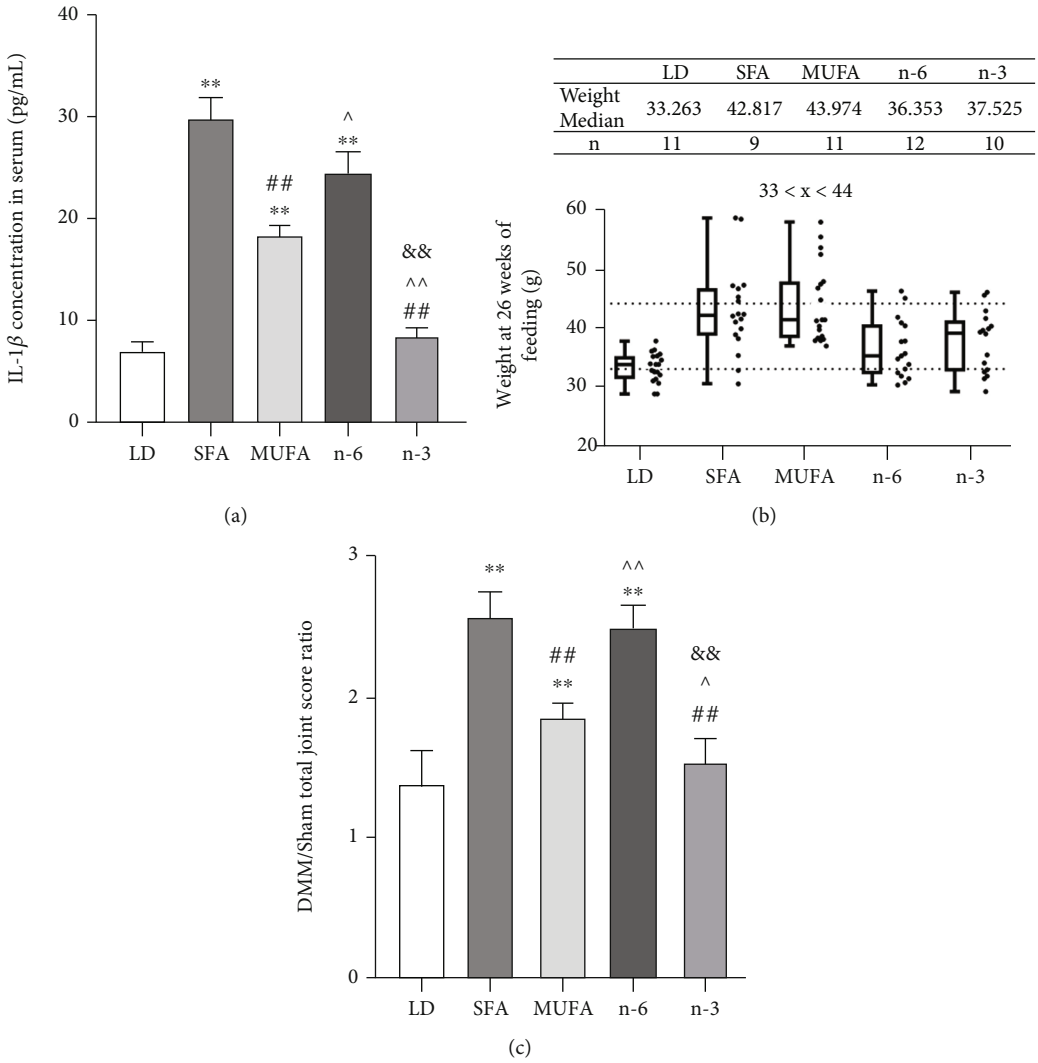

	LD	SFA	MUFA	n-6	n-3
Weight Median	33.263	42.817	43.974	36.353	37.525
n	11	9	11	12	10

Figure 3: The expression of IL-1β in serum and weight-matched strategy for analyzing the relationship between diet FAs and OA severity. (a) The concentration of IL-1β in serum was detected by ELISA, $n = 5$. (b) The mice whose weights were in the range of 33 to 44 grams were used for OA analysis at 26 weeks of feeding. The line of the box indicated median, and the length of the box represented interquartile range. (c) DMM-operated to sham-operated joint OA score ratio of the weight-matched mice. The data are presented as the means ± SD. $^{*}p < 0.05$ and $^{**}p < 0.01$ versus the LD group; $^{\#}p < 0.05$ and $^{\#\#}p < 0.01$ versus the SFA group; $\wedge p < 0.05$ and $\wedge\wedge p < 0.01$ versus the MUFA group; $^{\&}p < 0.05$ and $^{\&\&}p < 0.01$ versus the n-6 group.

Table 1: Relationships of biochemical and biomechanical factors to OA, determined by multiple regression.

Parameters	β	Sig.	95% C.I. for β
Biochemical			
FAs[a]	0.842	0.000	3.496-6.354
IL-1β	0.537	0.000	2.372-3.788
Biomechanical			
$AUC_{0\text{-}26wk}$	—	—	—
$AUC_{19\text{-}26wk}$	-0.229	0.065	-0.960-0.030

[a]Ordinal variable: LD and n-3 = 0, SFA, MUFA, and n-6 = 1. β: standardized coefficient.

mediated pyroptosis depends on the caspase-1–mediated classical inflammasome pathway and the caspase-4, -5, and -11–mediated non-classical inflammasome pathway. These pathways lead to the cleavage of the gasdermin D (GSDMD) protein, which releases the gasdermin-N structural domain, resulting in cell membrane pore formation, inflammatory factor release, and, ultimately, cell death [26–29]. Activated NLRP3 and caspase-1 effects depend on K^+ ion efflux, reactive oxygen species production, and phagocytosis to produce IL-1β, IL-18, and matrix-degrading enzymes, which exacerbates the pyroptosis inflammatory response, leading to cartilage degeneration and synovitis, and thereby accelerated OA progression [30, 31].

The differences in FA effects on OA may be due to differences in their mechanisms of regulating TLR4 and pyroptosis. SFAs can activate TLR4, producing an inflammatory response [32]. They can also increase the expression of the NLRP3 inflammasome, the activated form of which mediates the cleavage of pro–caspase-1 into active caspase-1, which cleaves pro–IL-1β and pro–IL-18 into their mature forms. The

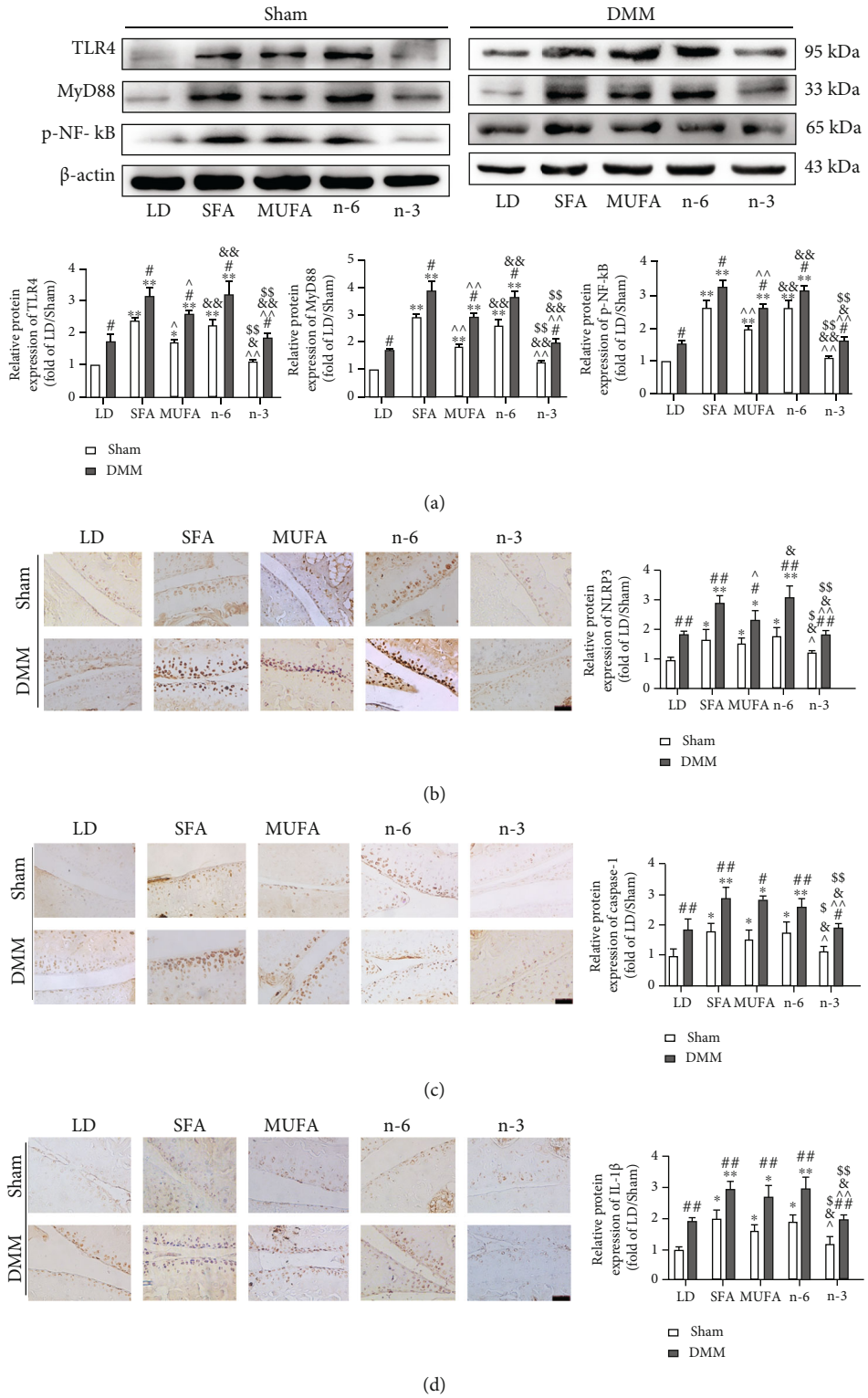

FIGURE 4: Effects of dietary FAs on TLR4/NF-κB signals and NLRP3 inflammasome as well as its downstream signals in articular cartilage of mice. (a) The relative expression of TLR4, MyD88, and p-NF-κB protein of knee articular cartilage was detected by Western blot. (b–d) Immunohistochemical staining was used to measure NLRP3, caspase-1, and IL-1β positive cells (200x, scale bars = 100 μm). The data are presented as the means ± SD, $n = 5$. $^{*}p < 0.05$ and $^{**}p < 0.01$ versus the LD group; $^{\#}p < 0.05$ and $^{\#\#}p < 0.01$ versus the sham group; $\wedge p < 0.05$ and $\wedge\wedge p < 0.01$ versus the SFA group; $^{\&}p < 0.05$ and $^{\&\&}p < 0.01$ versus the MUFA group; $^{\$}p < 0.05$ and $^{\$\$}p < 0.01$ versus the n-6 group.

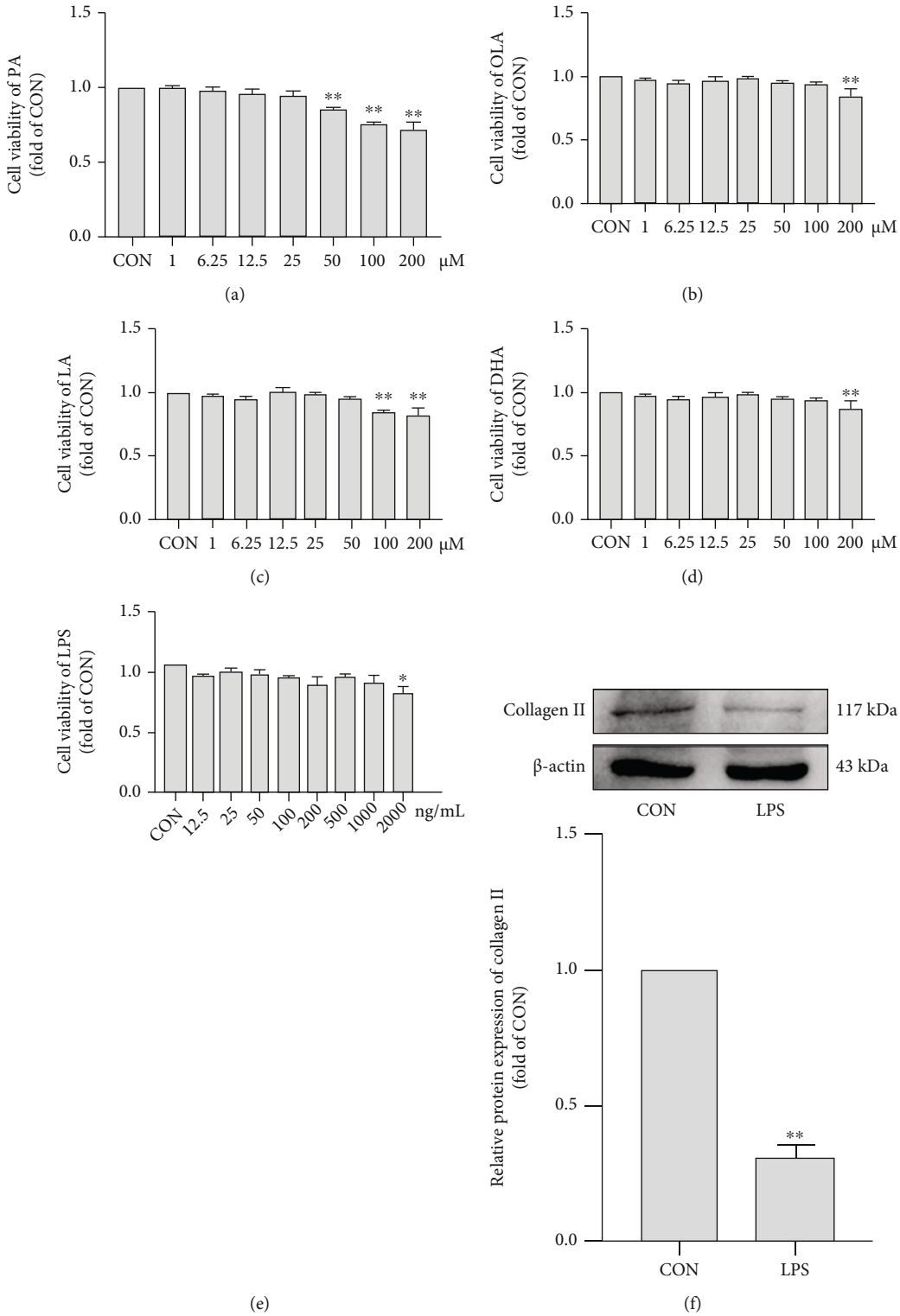

Figure 5: Effects of different FA types on chondrocyte viability and proliferation. Cell viability of PA (a), OLA (b), LA (c), and DHA (d) on SW1353 cells. (e) Cell viability of LPS on SW1353 cells. (f) The relative protein expression of Collagen II in SW1353 cells treated with LPS (1000 ng/mL) was detected by Western blot analysis. The data are presented as the means ± SD, $n = 3$. $^{*}p < 0.05$ and $^{**}p < 0.01$ versus the CON group.

mature IL-1β and IL-18 molecules are secreted through cell membrane pores constituted by GSDMD proteins and exacerbate the inflammatory response to pyroptosis [33–35]. In contrast, n-3 PUFAs can inhibit inflammatory signaling pathways by suppressing TLR-induced signaling [36, 37] and suppress NLRP3 inflammasome activity, resulting in anti-

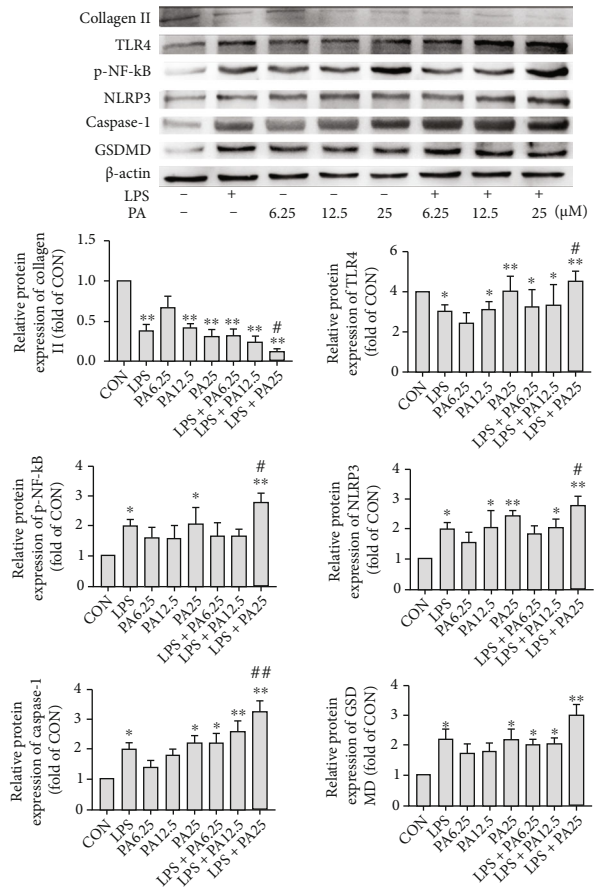

(a)

Figure 6: Continued.

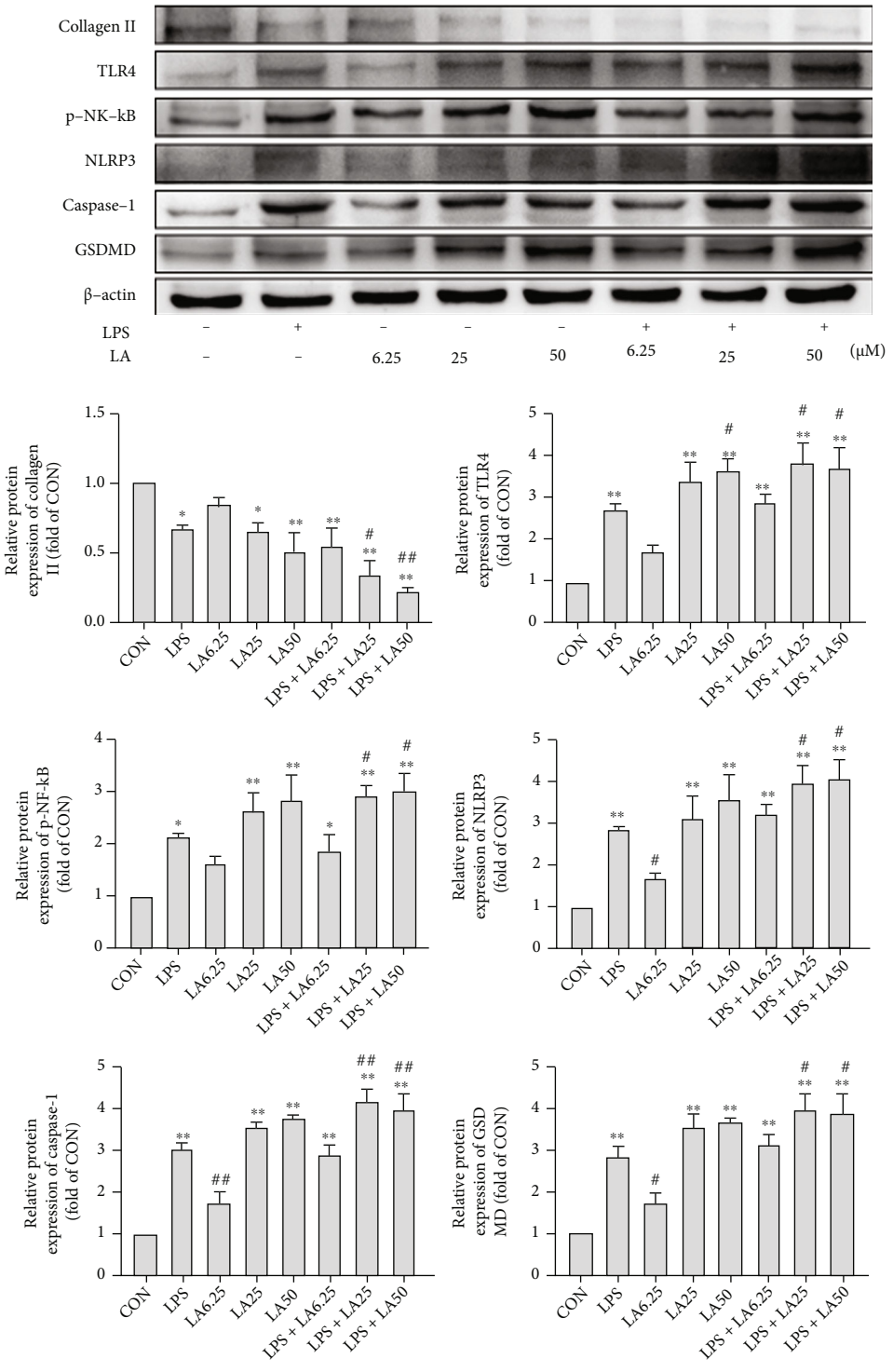

(b)

Figure 6: Continued.

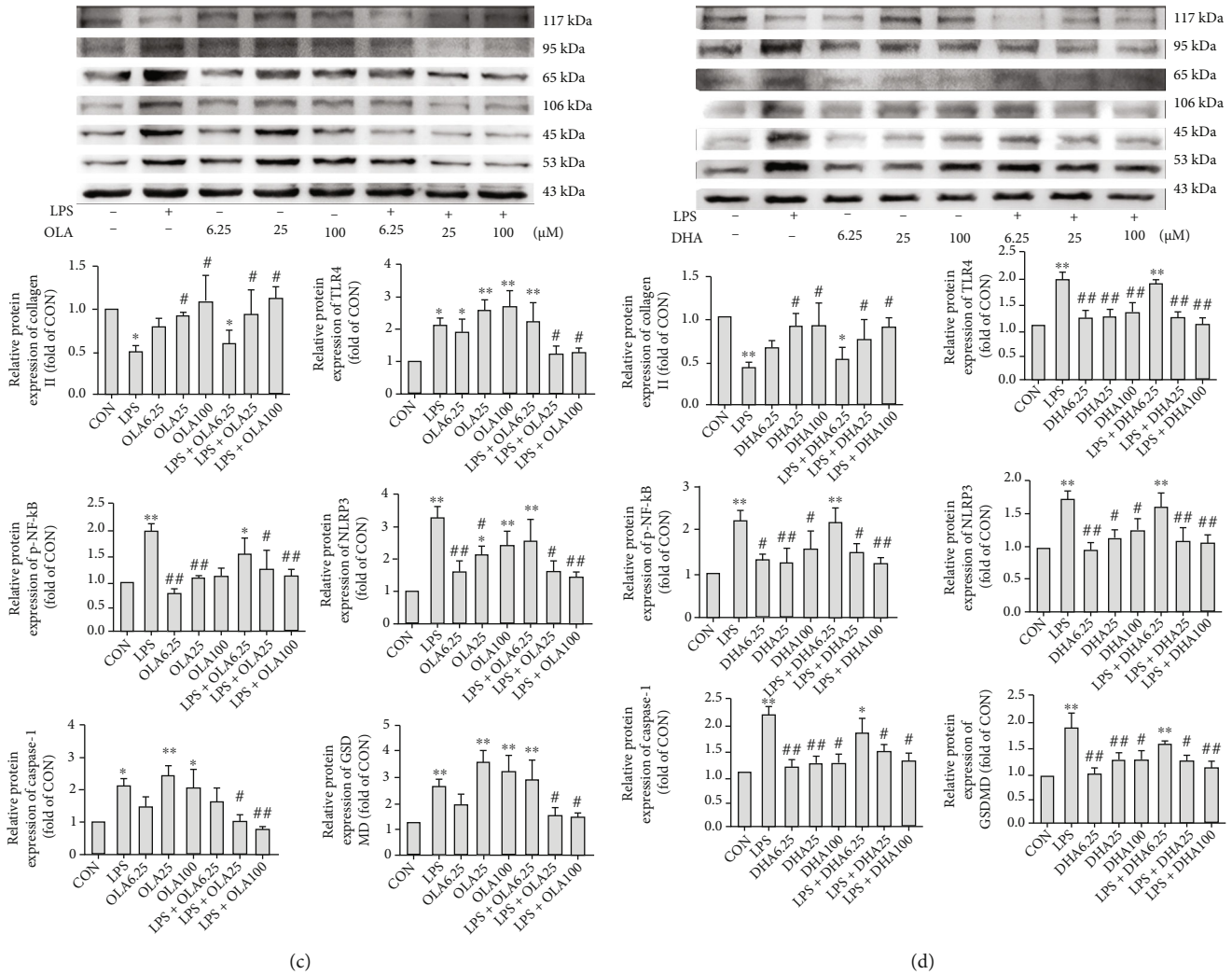

Figure 6: Effects of FAs on TLR4/NF-κB signaling and NLRP3/caspase-1/GSDMD signaling in chondrocytes. The relative protein expression of collagen II, TLR4, p-NF-κB, NLRP3, caspase-1, and GSDMD in SW1353 cells treated with various concentrations of PA (a), LA (b), OLA (c), and DHA (d) in the absence or presence of LPS for 24 h. The data are presented as the means ± SD, $n = 3$. $^{*}p < 0.05$ and $^{**}p < 0.01$ versus the CON group; $^{\#}p < 0.05$ and $^{\#\#}p < 0.01$ versus the LPS group.

inflammatory effects and the inhibition of pyroptosis development [38]. Few studies have examined the effects of MUFAs and n-6 PUFAs on TLR4 signaling and pyroptosis, and their results have been mixed.

The link between the TLR4/NF-κB signaling pathway and the NLRP3 inflammasome and its downstream signals may also be important for the understanding of FA effects on OA. In cardiomyocytes, SFAs can bind MD protein 2 directly, which induces MD2/TLR4 complex formation and the production of pro-inflammatory cytokines that activate TLR4 signaling, generating an inflammatory response [32] and activating NLRP3 inflammasomes. These inflammasomes, in turn, drive caspase-1 activation and GSDMD protein cleavage, ultimately leading to pyroptosis [39]. The effects of other FA types on inflammasomes remain unclear. Further exploration of FA effects on TLR4/NF-κB signaling and NLRP3 inflammasome–induced pyroptosis and the relationship between the two signaling pathways, may help to elucidate the roles of different FA mechanisms in OA, revealing possible intervention targets for obesity-related OA.

Thus, in the present study, we examined the hypothesis that different types of FA promote/reduce OA by up/down-regulating TLR4/NF-κB signaling, which in turn increases/decreases NLRP3 inflammasome expression to regulate inflammation and pyroptosis. To observe the effects of diets rich in different types of FA on obesity-associated OA, mice were fed high-fat diets rich in particular FAs (SFAs, MUFAs, n-6 PUFAs, or n-3 PUFAs) and subjected to surgical destabilization of the medial meniscus (DMM). To further examine the mechanisms of FA regulation of chondrocyte pyroptosis via TLR4 regulation, we tested the effects of different types of FA on the NLRP3 inflammasome and its downstream signals via activated or inhibited TLR4 expression in an *in-vitro* OA model produced by treating cells with lipopolysaccharide (LPS). Our study may provide

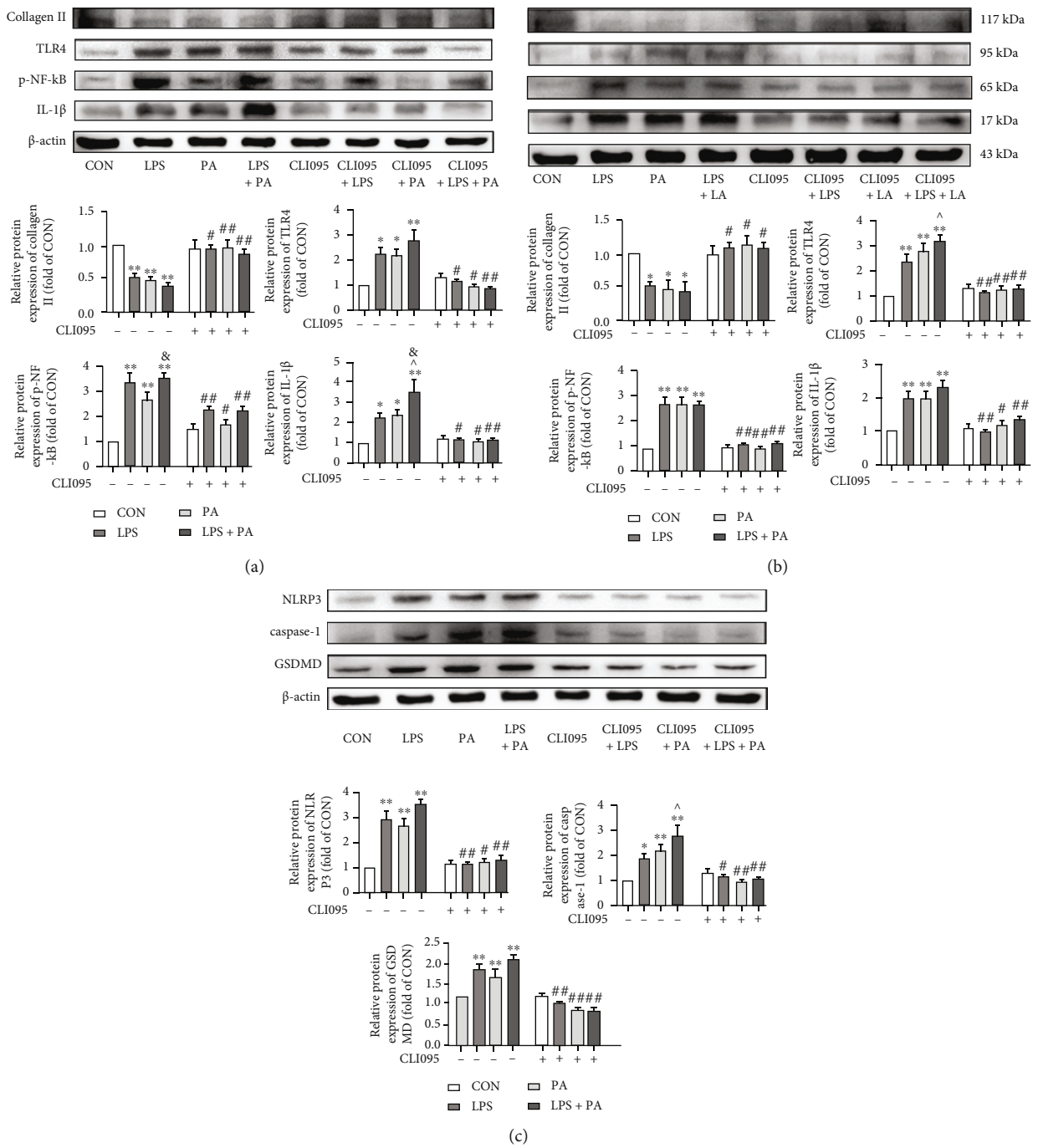

Figure 7: Continued.

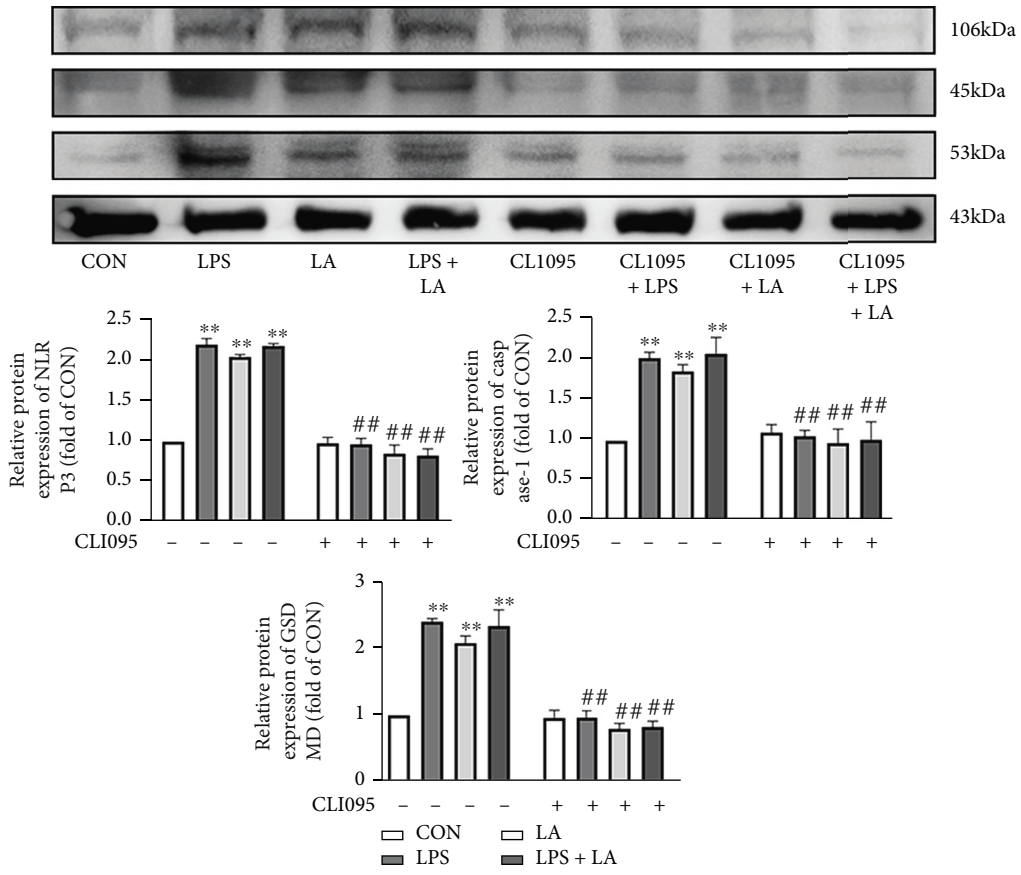

(d)

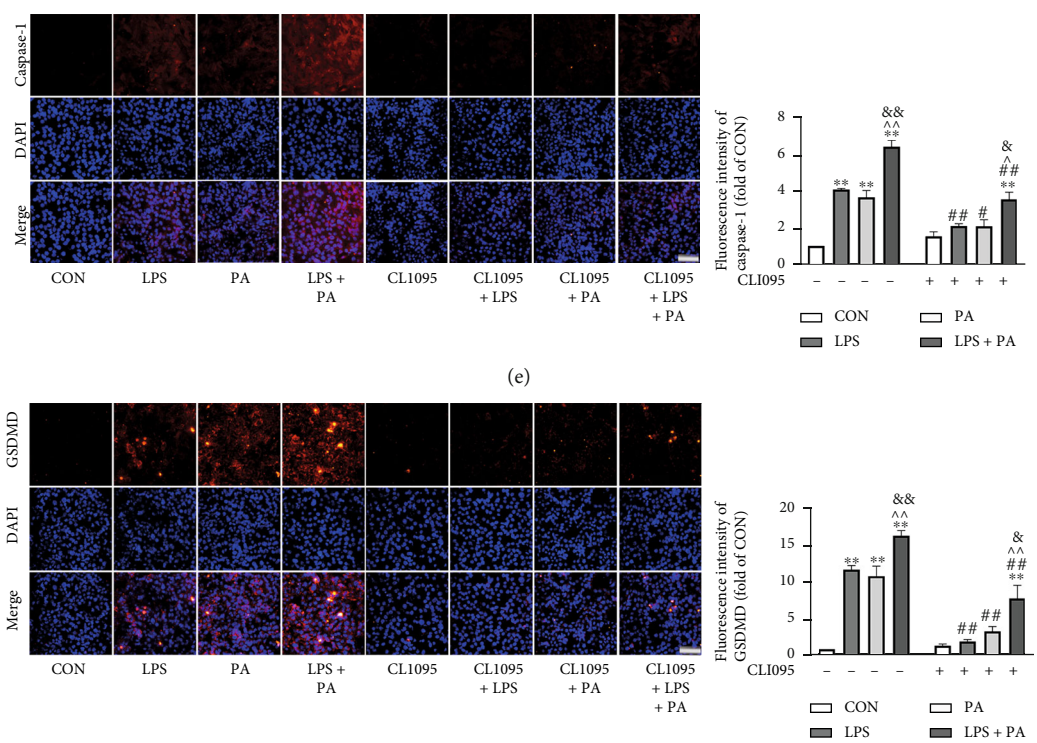

(e)

(f)

Figure 7: Continued.

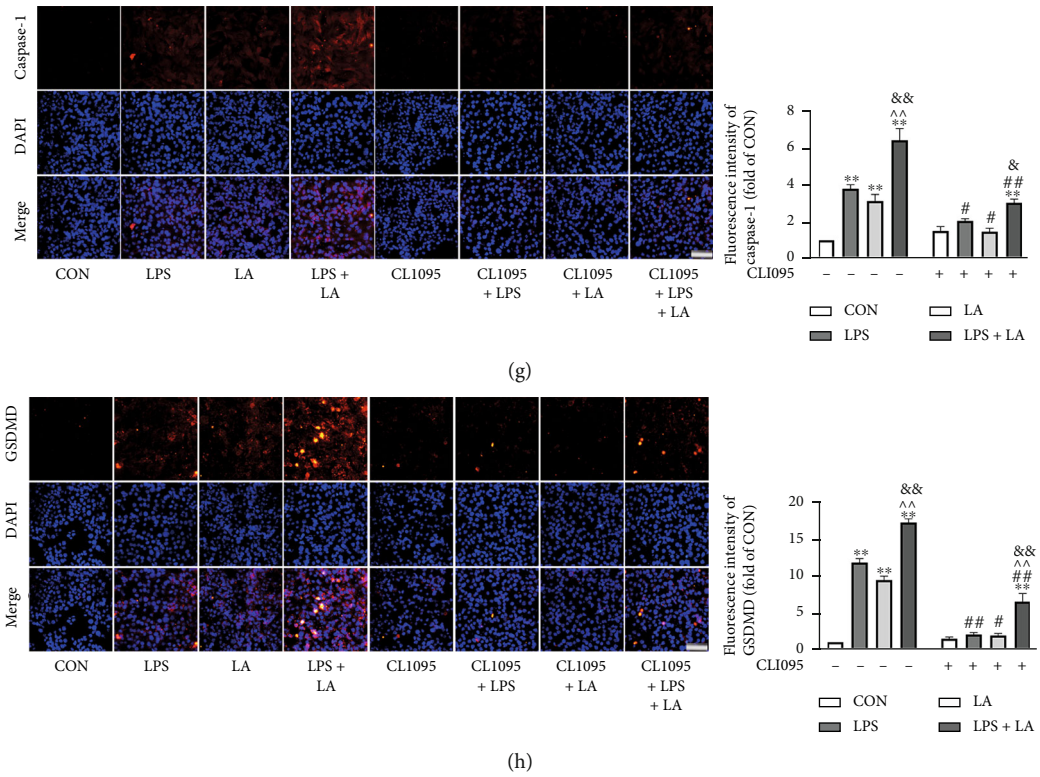

Figure 7: TLR4 inhibition attenuated SFA- and n-6 PUFA-mediated activation of NLRP3/caspase-1/GSDMD signaling. The relative protein expression of collagen II, TLR4, p-NF-κB, and IL-1β in SW1353 cells treated with PA (a) or LA (b). The relative protein expression of NLRP3, caspase-1, and GSDMD in SW1353 cells treated with PA (c) or LA (d). Immunofluorescent staining was used to detect the expression of caspase-1 (e, g) and GSDMD (f, h) in SW1353 cells treated with PA or LA (200x, scale bars = 100 μm). The data are presented as the means ± SD, $n = 3$. $^{*}p < 0.05$ and $^{**}p < 0.01$ versus the CON group; $^{\#}p < 0.05$ and $^{\#\#}p < 0.01$ versus the groups without CLI-095-pretreatment; $^{\wedge}p < 0.05$ and $^{\wedge\wedge}p < 0.01$ versus the LPS group; $^{\&}p < 0.05$ and $^{\&\&}p < 0.01$ versus the PA or LA group.

an experimental basis for the elucidation of the mechanisms underlying the effects of different types of FA on OA and the identification of potential therapeutic targets.

2. Materials and Methods

2.1. Animal Handling and Surgery. Six-week-old male C57BL/6 mice (weighing 18–22 g, $n = 75$) were purchased from the Department of Laboratory Animals of China Medical University. All animal experiments were approved by the Professional Committee on Animal Use and Ethics of China Medical University (SCXKLN2013-0009). The mice were randomized to five groups ($n = 15$ each) according to their body weights after 1 week of acclimatization feeding and then fed a low-fat diet (LD) or a SFA-rich, MUFA-rich, n-6 PUFA-rich (n-6), or n-3 PUFA-rich (n-3) diet (feed formulations are provided in Table S1). All groups of mice were fed and watered freely and maintained at room temperature (20–25°C) with 40–70% relative humidity. Their body weights and food intakes were recorded weekly.

At week 18, all mice underwent surgery consisting of sham surgery on the left hind limb and DMM on the right hind limb. After the operations, group-designated feeding was continued until week 26, at which time gait analysis and body fat measurements were performed, blood was drawn from the abdominal vein under ether anesthesia, the mice were killed by cervical dislocation, and both hind limbs were measured.

2.2. Histology. Whole knee joints ($n = 5$) were fixed in 4% paraformaldehyde, decalcified, paraffin-embedded, and sectioned at 6 μm thickness for histological and immunohistochemical evaluation. The sections were stained with saffron O (Solarbio, Beijing, China), hematoxylin-eosin (Solarbio), or saffron O/solid green (Solarbio) to reveal histological changes in the cartilage. Cartilage destruction severity was graded according to the modified Mankin [40] and Osteoarthritis Research Society International (OARSI) [41] scoring systems (scoring criteria are provided in Tables S2 and S3).

2.3. Gait Analysis. The automated Noldus (Wageningen, the Netherlands) system was used for gait analysis. Mice ($n = 5$) were placed individually in a CatWalk walkway and allowed to walk freely and traverse from one side to the other of the walkway's glass plate. Each mouse completed three successful walking tests in the test channel. Each footprint was imaged and analyzed using the CatWalk XT10.6 software (Noldus). The following parameters were calculated: print area (the complete surface area contacted by the paw during a stance phase), maximum contact (the total floor area contacted by the paw during the stance phase), duty cycle

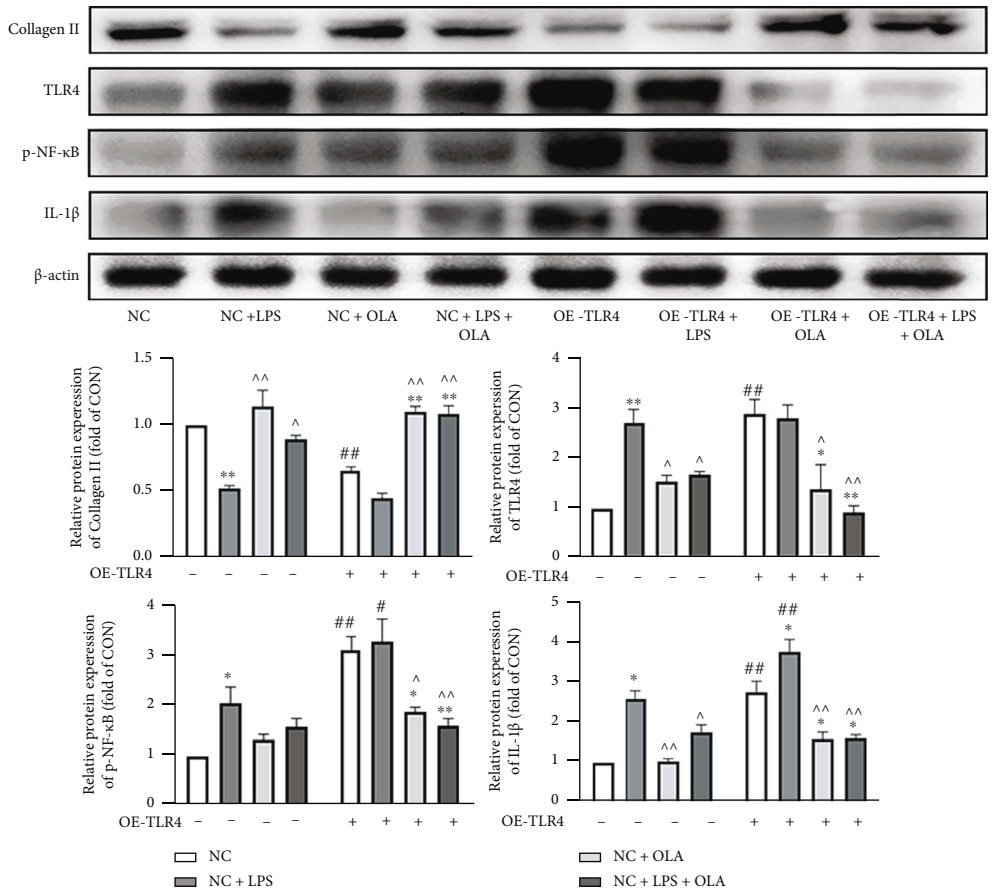

(a)

Figure 8: Continued.

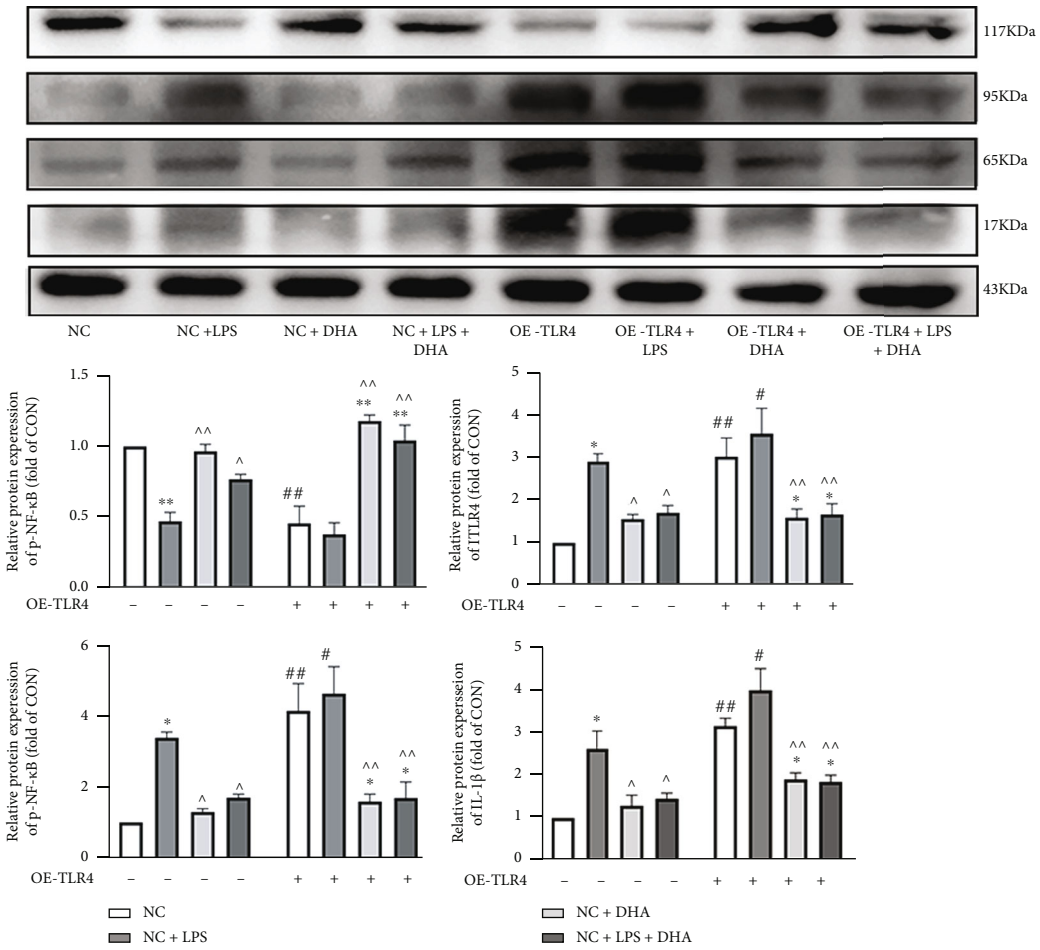

(b)

Figure 8: Continued.

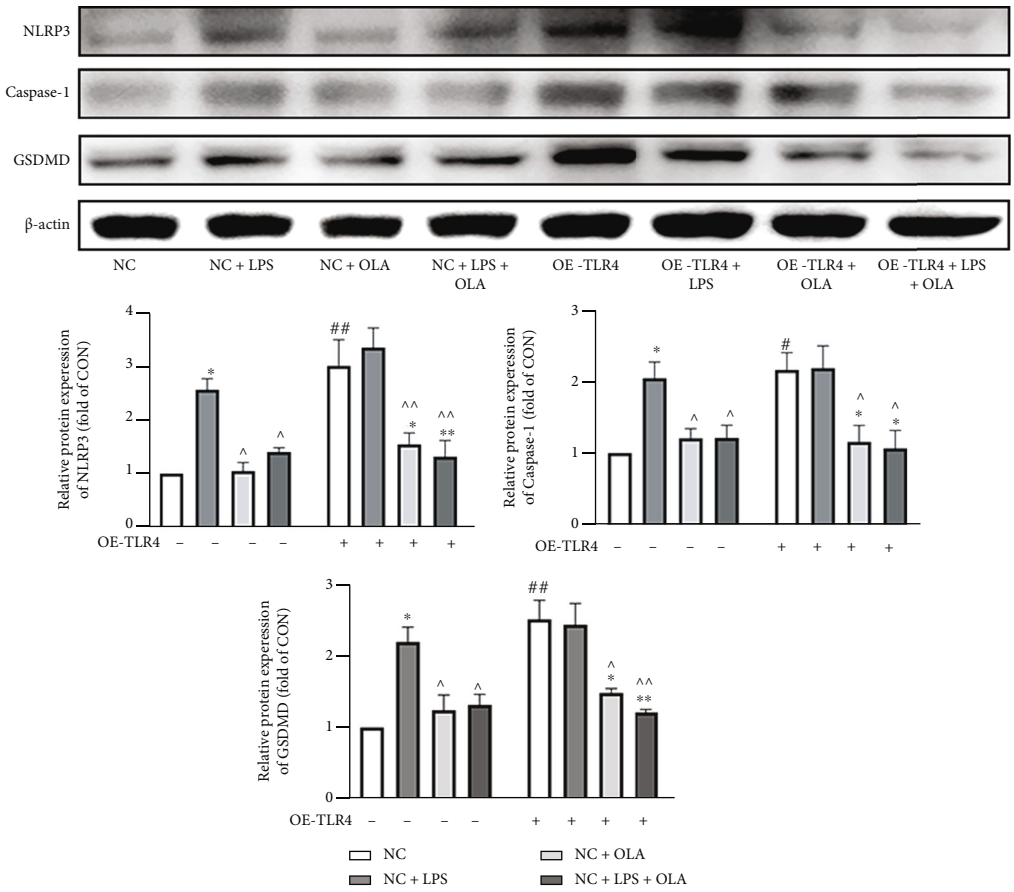

(c)

Figure 8: Continued.

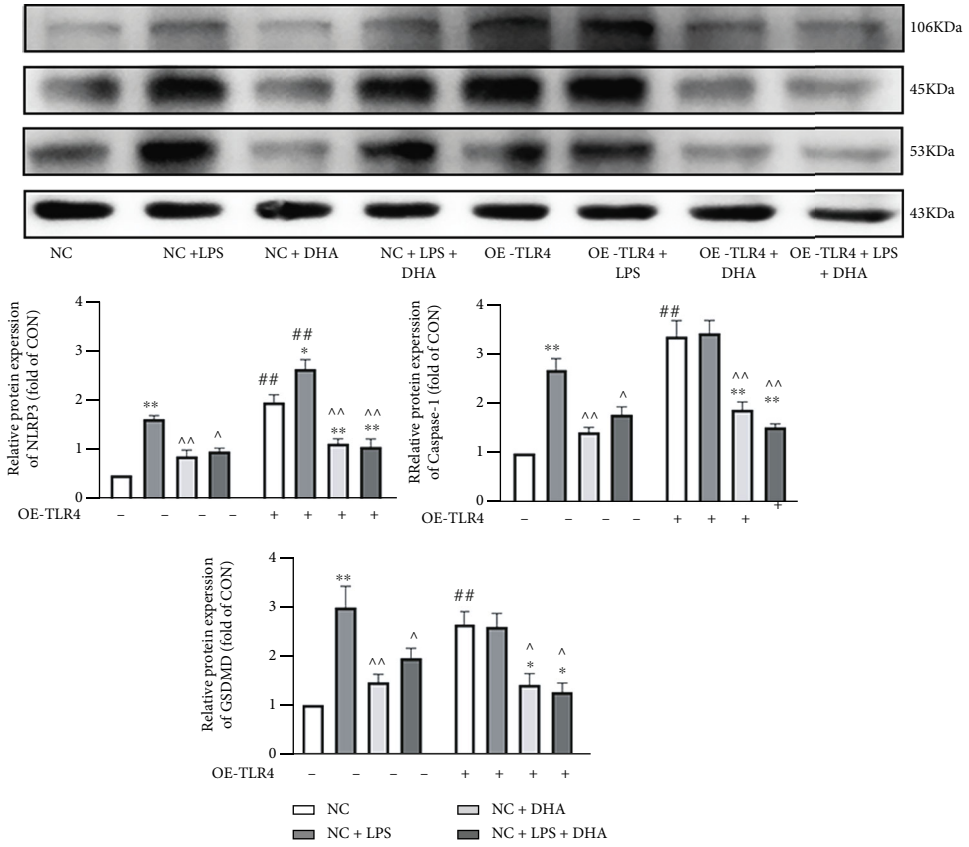

(d)

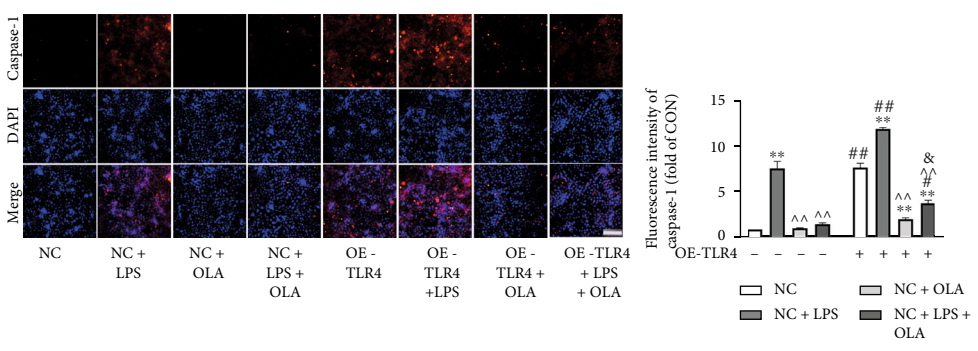

(e)

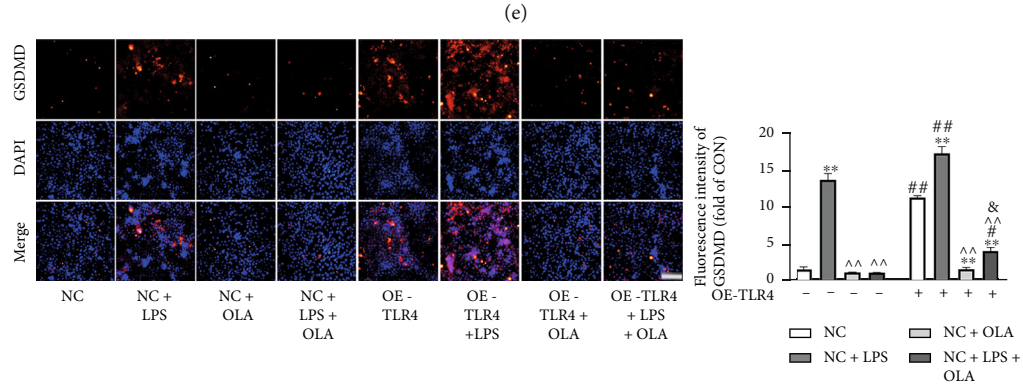

(f)

Figure 8: Continued.

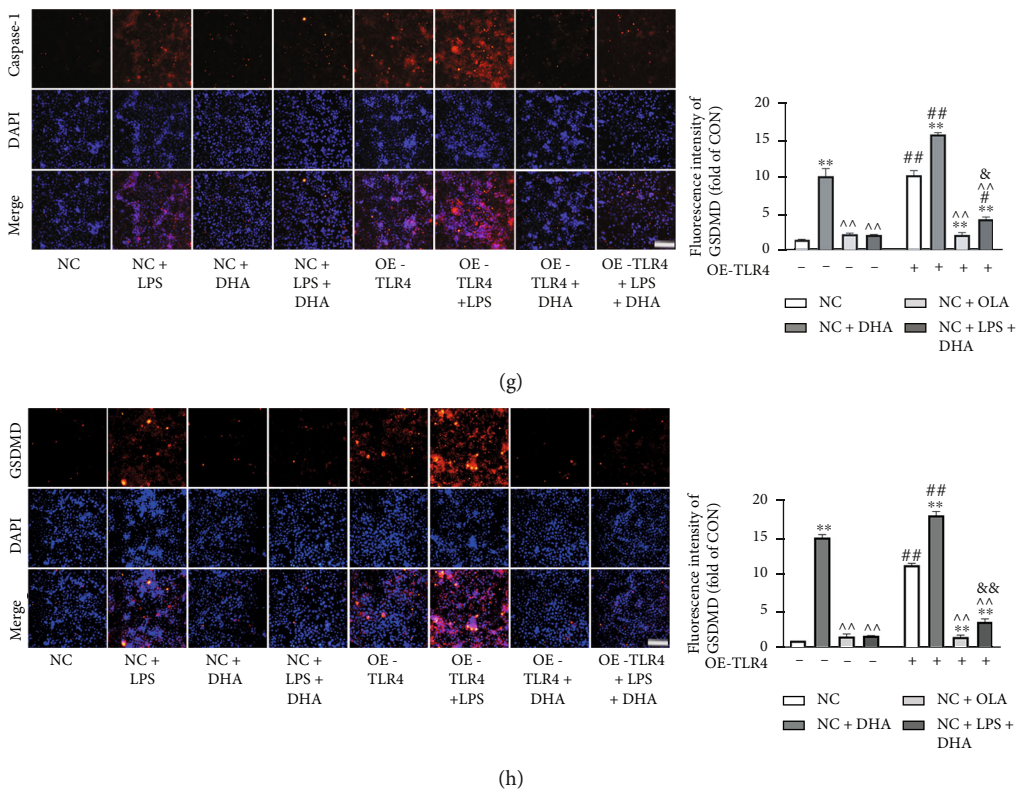

Figure 8: TLR4 overexpression reversed the inhibitory effect of n-3 PUFA and MUFA on NLRP3/caspase-1/GSDMD signaling in chondrocytes. The relative protein expression of collagen II, TLR4, p-NF-κB, and IL-1β in SW1353 cells treated with OLA (a) or DHA (b). The relative protein expression of NLRP3, caspase-1, and GSDMD in SW1353 cells treated with OLA (c) or DHA (d). Immunofluorescent staining was used to detect the expression of caspase-1 (e, g) and GSDMD (f, h) in SW1353 cells treated with OLA or DHA (200x, scale bars = 100 μm). The data are presented as the means ± SD, $n = 3$. $^{*}p < 0.05$ and $^{**}p < 0.01$ versus the NC group; $^{\#}p < 0.05$ and $^{\#\#}p < 0.01$ versus the groups without OE-TLR4-pretreatment; $\wedge p < 0.05$ and $\wedge\wedge p < 0.01$ versus the NC+LPS group; $^{\&}p < 0.05$ and $^{\&\&}p < 0.01$ versus the NC+OLA or NC+DHA group.

(stance duration as a percentage of the step cycle duration), and swing speed (speed of a paw's movement during the swing phase).

2.4. Immunohistochemistry. Antigen repair enzymes were added dropwise to slide-mounted sections, following the instructions of the immunohistochemistry kit used (MXB, Fujian, China). Then, the sections were incubated overnight with anti-NLRP3 (1 : 100; Abcam, Cambridge, UK), anti–caspase-1 (1 : 100; Abcam, Cambridge, UK), and anti–IL-1β (1 : 100; ImmunoWay, Plano, TX, USA) rabbit primary antibodies at 4°C. Thereafter, the sections were incubated with horseradish peroxidase- (HRP-) conjugated anti-rabbit immunoglobulin G (IgG; Abcam) for 1 h at room temperature and cover-slipped with neutral balsam. Six fields of view on each section were selected randomly for optical density (OD) analysis at 400x under a light microscope (Olympus, Tokyo, Japan) using ImageJ (NIH Image, Washington DC, USA).

2.5. Enzyme-Linked Immunosorbent Assays. Enzyme-linked immunosorbent assays (ELISAs) were conducted in 96-well plates with ELISA kits (Boster, Wuhan, China) in accordance with the manufacturer's instructions. Briefly, 100 μL mouse serum samples ($n = 5$), 100 μL biotin-labeled antibody, and 100 μL ABC working solution were added to each plate well. Then, TMB color development solution was added dropwise. The color was allowed to develop in the dark for 15–20 min, and then 100 μL TMB reaction termination solution was added. OD values were determined at 450 nm with a microplate reader.

2.6. Cell Culture. SW1353 cells were purchased from the Cell Resource Center of Shanghai Institutes for Biological Sciences, Chinese Academy of Sciences. They were cultured in Dulbecco's modified Eagle medium (DMEM; Gibco, Grand Island, NY, USA) containing 10% fetal bovine serum (FBS; BI, Beit-Haemek, Israel) and 1% penicillin-streptomycin (KeyGEN Bio, Jiangsu, China) in a humidified incubator at 37°C and 5% CO_2.

2.7. Cell Treatment

2.7.1. Cell Proliferation/Viability Assay. Logarithmic-growth-phase SW1353 cells were incubated in 96-well plates with complete medium combined with LPS (Sigma, St. Louis, MO, USA; 12.5, 25, 50, 100, 200, 500, 1000, or 2000 ng/mL). Palmitic acid (PA), oleic acid (OLA), linolenic acid (LA), or DHA (Sigma; 1, 6.25, 12.5, 25, 50, 100, or 200 μM) was added, and the cells were then incubated at

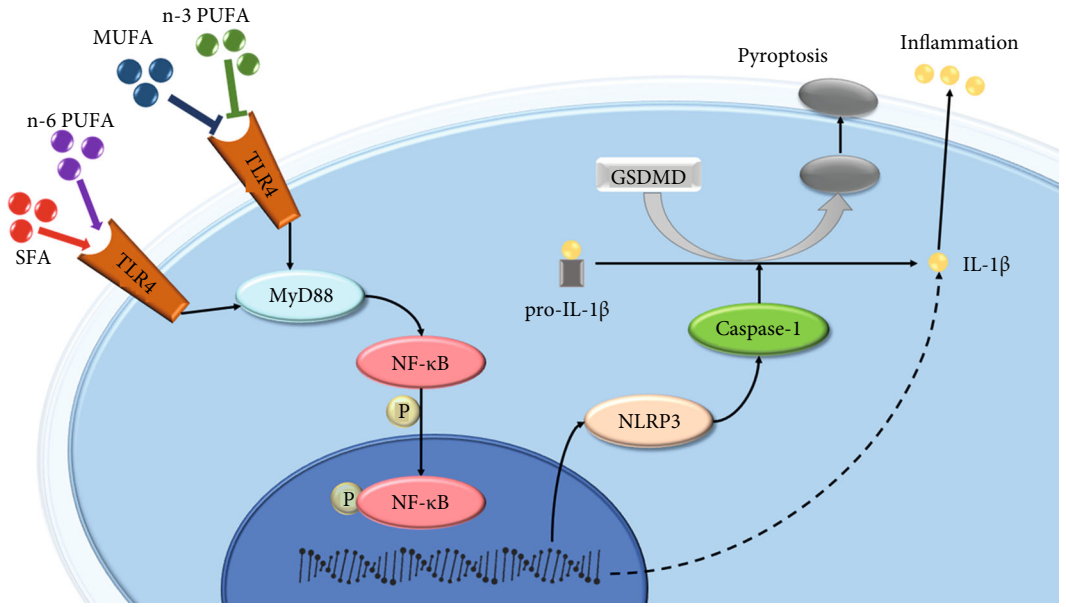

Figure 9: Schematic of the mechanism of FAs regulation of the NLRP3 inflammasome in chondrocytes.

37°C for 24 h. To assess cell concentrations, 10 μL cell counting kit-8 reagent (KeyGEN Bio) was added to each well, and the plates were incubated in the dark for 2 h. Subsequently, OD values were measured at 450 nm using a microplate reader. Each assay was performed in triplicate.

2.7.2. FA Treatment. Cells were treated with LPS (1000 ng/mL) only or LPS plus an FA (concentrations of three different gradients) for 24 h. They were then collected for analysis.

2.7.3. CLI-095 Treatment. Cell media were replaced with DMEM containing 0.5% FBS and the TLR4 inhibitor CLI-095 (1 μg/mL; InvivoGen, San Diego, CA, USA) for 6 h. LPS (1000 ng/mL) was added with or without PA or LA (25 μM) and allowed to incubate for 24 h.

2.7.4. Cell Transfection with TLR4 Overexpression Lentivirus. Cells were transfected with TLR4 overexpression or negative control (NC) lentivirus (GenePharma, Shanghai, China) in DMEM containing 0.5% FBS for 6 h and then cultured in DMEM containing 10% FBS for 72 h. Puromycin (2 μg/mL) was added to screen for stably transfected cells. Following screening, transfected cells were exposed to media supplemented with LPS (1000 ng/mL), with or without OLA or DHA (25 μM), for 24 h.

2.8. Western Blot. Articular cartilages ($n = 5$) were ground under liquid nitrogen. Chondrocytes ($n = 3$) were collected, and protein was extracted directly by adding RIPA lysis buffer (Sangon Biotech, Shanghai, China) on ice. Protein concentrations were determined with a bicinchoninic acid kit (Dingguo Bio, Beijing, China). Sodium dodecyl sulphate–polyacrylamide gel electrophoresis was conducted, and the resultant protein bands were transferred to polyvinylidene fluoride membranes for 3 h. The membranes were blocked over 30 min at room temperature and then incubated overnight at 4°C with primary antibody targeting collagen II (1 : 500; Bioss, Beijing, China), β-actin (1 : 500; Bioss, Beijing, China), NLRP3 (1 : 1000; Abcam, Cambridge, UK), GSDMD (1 : 1000; Abcam, Cambridge, UK), caspase-1 (1 : 1000; Abcam, Cambridge, UK), TLR4 (1 : 1000; Santa Cruz Biotechnology, Santa Cruz, CA, USA), MyD88 (1 : 1000; Santa Cruz Biotechnology, Santa Cruz, CA, USA), or IL-1β (1 : 500; ImmunoWay, Plano, TX, USA). Subsequently, the membranes were incubated with HRP-conjugated goat anti-rabbit secondary antibody IgG (1 : 5000; ImmunoWay, Plano, TX, USA) for 1 h at room temperature. Following exposure to electrochemiluminescence reagent, images were developed and grayscale values of the bands were determined with ImageJ (NIH Image, Washington DC, USA). Semi-quantitative analysis was performed with β-actin serving as an internal reference. All experiments were repeated three times.

2.9. Immunofluorescence. Cells were cultured in 24-well plates, fixed in 4% paraformaldehyde, and then treated with 0.5% Triton X-100. After blocking with bovine serum albumin (Dingguo Biotech), the cells were incubated overnight with anti-GSDMD and anti–caspase-1 primary antibodies (1 : 100; Abcam, Cambridge, UK) at 4°C. After rinsing with Tris-buffered saline with 0.1% Tween 20, the cells were incubated with dropwise-added fluorescence-labeled goat anti-rabbit IgG (1 : 200; Zhongshan Jinqiao, Beijing, China) at room temperature in the dark for 2 h. The slices were sealed with an anti-fluorescence quencher (Dingguo Bio) and incubated for 5 min in the dark before being imaged under an inverted fluorescence microscope. Six randomly selected fields of view in each examined section were subjected to OD analysis at 200x using ImageJ (NIH Image, Washington DC, USA).

2.10. Statistical Analyses. The results are expressed as means ± standard deviations. One-way analyses of variance

were used for comparisons. When the data met the homogeneity of variance test condition, the least significant difference t test was used for two-way comparisons; otherwise, Dunnett's T3 method was used. In all cases, $p < 0.05$ was considered to reflect significant differences. The data were analyzed using SPSS 23.0 software (IBM Corporation, Armonk, NY, USA).

3. Results

3.1. Effects of Dietary FAs on Mouse Body Weight, Body Fat, and Food Intake. After 26 weeks of dietary treatment, the body weights and body fat ratios of mice in all high-fat diet groups were significantly greater than those in the LD group (Figures 1(a) and 1(b)). These values were lower in the n-6 and n-3 PUFA groups than in the SFA and MUFA groups. Food intake did not differ among high-fat diet groups (Figure 1(c)). To accurately detect the effects of body weight change over time on joints, we calculated areas under the body weight curve (AUCs) for mice in the different diet groups from baseline to 26 weeks and 19 to 26 weeks, respectively. The 0–26- and 19–26-week AUCs were higher in the high-fat groups than in the LD group, and higher in the SFA and MUFA groups than in the n-6 and n-3 PUFA groups (Figure 1(d)).

3.2. Effects of Dietary FAs on Mouse Articular Cartilage. Sham-operated joints from the SFA and n-6 PUFA groups showed mild OA-like damage, whereas those from the MUFA and n-3 PUFA groups showed no significant abnormality. The degree of OA in joints subjected to DMM was significantly augmented in all groups, but lesions in the n-3 PUFA group were similar to those in the LD group and less severe than those in the other groups (Figures 2(a)–2(c)). The Mankin and OARSI scores for joints subjected to DMM were significantly worse in the SFA and n-6 PUFA groups than in the LD and n-3 PUFA groups. Scores for the MUFA group were higher than those for the LD and n-3 PUFA groups, but lower than those for the SFA and n-6 PUFA groups (Figure 2(d)). Compared with the LD group, the SFA, MUFA, and n-6 PUFA groups had more irregular gaits; significantly smaller footprint area, maximum contact, duty cycle, swing speed, maximum footprint contact, and support ratio values; and significantly increased swing speeds in the DMM-modified limbs. The most significant differences were between the SFA and n-6 PUFA groups, and no significant difference was observed between the LD and n-3 PUFA groups (Figures 2(e) and 2(f)).

3.3. Relationships among Dietary FAs, Body Weight, Serum Inflammatory Factors, and OA in Mice. Serum IL-1β levels were significantly higher in the SFA, MUFA, and n-6 PUFA groups than in the LD group and did not differ between the LD and n-3 PUFA groups. The MUFA group's mean serum IL-1β level was significantly higher than that in the n-3 PUFA group and lower than that in the SFA and n-6 PUFA groups (Figure 3(a)). The DMM/sham joint score ratios were significantly higher in the SFA, n-6 PUFA, and MUFA groups than in the LD group after controlling for body weight factors (Figures 3(b) and 3(c)). Multiple regression analysis showed that dietary FAs and IL-1β levels were associated significantly with OA, rather than body weight (Table 1).

3.4. Effects of Dietary FAs on TLR4/NF-κB Signals and the NLRP3 Inflammasome and Its Downstream Signals in Mouse Articular Cartilage. Western blot analysis of articular cartilage from joints subjected to DMM and sham operation showed that TLR4, MyD88, and phosphorylated- (p-) NF-κB protein levels were significantly higher in the SFA, MUFA, and n-6 PUFA groups than in the LD and n-3 PUFA groups and that those in the latter two groups were similar. These levels were significantly higher in the SFA and n-6 PUFA groups than in the MUFA group. For all groups, TLR4, MyD88, and p-NF-κB protein levels were higher in articular cartilage from joints subjected to DMM than in that from joints subjected to sham operation (Figure 4(a)).

Similarly, immunohistochemical analysis showed significantly increased NLRP3, caspase-1, and IL-1β expression in the SFA, MUFA, and n-6 PUFA groups compared with the LD and n-3 PUFA groups, with no significant difference between the latter. For all groups, the expression levels of these proteins were significantly higher in cartilage from joints subjected to DMM than in sham operation joints (Figures 4(b)–4(d)).

3.5. Effects of Different FA Types on Chondrocyte Viability and Proliferation. PA, OLA, LA, and DHA did not affect the viability or proliferation of SW1353 chondrocytes at concentrations $\leq 25\,\mu$M. PA at the concentration of $50\,\mu$M, LA at the concentration of $100\,\mu$M, and OLA and DHA at the concentration of $200\,\mu$M reduced cell viability and proliferation (Figures 5(a)–5(d)). At concentrations ≤ 1000 ng/mL, LPS had no significant effect on the viability or proliferation of cells (Figure 5(e)). However, 1000 ng/mL LPS significantly reduced type II collagen expression in the cells (Figure 5(f)). Thus, we used 1000 ng/mL LPS to treat cells to mimic OA status *in vitro*.

3.6. SFA and n-6 PUFA Treatments Enhanced TLR4/NF-κB Signaling and the NLRP3/caspase-1/GSDMD Signaling Pathway, whereas n-3 PUFA and MUFA Treatments Attenuated Them, in Chondrocytes. LPS treatment significantly increased the expression of TLR4, p–NF-κB, NLRP3, and the pyroptosis-related proteins caspase-1 and GSDMD. PA and LA at the concentration of $25\,\mu$M reduced type II collagen expression and increased TLR4, p-NF-κB, NLRP3, caspase-1, and GSDMD expression. These treatments also enhanced the LPS induction effects (Figures 6(a) and 6(b)). In contrast, cells exposed to $25\,\mu$M concentrations of OLA and DHA showed a significant increase in type II collagen and dramatic decreases in TLR4, p-NF-κB, NLRP3, caspase-1, and GSDMD levels and could reverse LPS-induced changes in these proteins (Figures 6(c) and 6(d)).

3.7. TLR4 Inhibition Attenuated the SFA- and n-6 PUFA–Mediated Activation of NLRP3/caspase-1/GSDMD Signaling. TLR4 inhibition with CLI-095 increased chondrocyte type II collagen expression significantly while

decreasing TLR4, p-NF-κB, NLRP3, caspase-1, GSDMD, and IL-1β protein expression (Figures 7(a)–7(d)). Additionally, TLR4 inhibitor treatment reversed the decrease in type II collagen and upregulation of p-NF-κB, NLRP3, caspase-1, GSDMD, and IL-1β protein expression induced by PA and LA (Figures 7(a)–7(d)). caspase-1 and GSDMD immunofluorescence analyses yielded similar results (Figures 7(e)–7(h)).

3.8. TLR4 Overexpression Reversed the Inhibitory Effects of n-3 PUFA and MUFA on NLRP3/caspase-1/GSDMD Signaling in Chondrocytes. We used 30 multiplicity-of-infection TLR4 overexpression lentivirus in combination with puromycin to treat and screen chondrocytes (Fig. S1). Chondrocytes transfected with TLR4 overexpression lentivirus had significantly reduced type II collagen expression and markedly increased TLR4, p-NF-κB, NLRP3, caspase-1, GSDMD, and IL-1β protein expression compared with the NC group (Figures 8(a)–8(d)). Additionally, TLR4 overexpression lentivirus treatment reversed the increase in type II collagen and down-regulation of p–NF-κB, NLRP3, caspase-1, GSDMD, and IL-1β protein expression induced by OLA and DHA (Figures 8(a)–8(d)). This pattern of caspase-1 and GSDMD results was replicated in the immunofluorescence experiments (Figures 8(e)–8(h)).

4. Discussion

Obesity is a major risk factor for the development of OA, which is associated with a chronic low-grade inflammatory state and elevated circulating levels of adipokines and free FAs. Diet composition, especially FA content and caloric intake, may impact OA severity in a joint-specific manner [42, 43]. Notably, n-6/n-3 PUFA dietary ratios have been associated with markers of metabolic disorders, including obesity, insulin resistance, and inflammation. SFA, MUFA, and n-3 and n-6 PUFA have been detected in the synovial fluid of knee joints of patients with and without OA, and the n-6/n-3 PUFA ratio is significantly higher in patients with OA [44].

In the present study, the n-6/n-3 PUFA ratio in the feed for the n-6 PUFA group was close to that of the traditional Western diet (i.e., 24.6 : 1). Conversely, the n-6/n-3 PUFA ratio in the feed given to the n-3 group was the generally recommended healthy ratio of 4.2 : 1, and the ratio for the SFA and MUFA groups matched that of the LD group (7.4 : 1). Compared with mice fed a low-fat diet, mice fed diets rich in SFAs or n-6 PUFAs showed mild OA-like changes in articular cartilage, and the lesions in joints subjected to DMM surgery were more severe. Consistent with our findings, Wu et al. [18] found that mice fed SFA- and n-6 PUFA–enriched diets tended to develop severe OA and synovitis with systemic inflammation. In the present study, the joints of mice fed diets rich in MUFAs or n-3 PUFAs that were not subjected to DMM had no significant lesions. Joints in the MUFA group changed significantly after DMM surgery, and mice in the n-3 PUFA group developed lesions to a similar extent as did those in the LD group (much less than in the SFA, MUFA, and n-6 PUFA groups). These results suggest that n-3 PUFAs have a protective effect on the development of obesity-related OA and contribute to posttraumatic joint repair.

Because the mean body weights of mice fed high-fat diets were significantly greater than those of the LD group and those of mice in the SFA and MUFA groups were greater than those of mice in the n-6 and n-3 PUFA groups, we controlled for the confounding factor of body weight [18]. After such control, we found that the above-mentioned differences among groups persisted, further indicating that the anti-OA effect of n-3 PUFA was independent of body weight and supporting the inference that the intergroup differences can be attributed to the effects of different types of FA. Diets rich in n-3 PUFAs appear to attenuate traumatic OA in obese mice and support the repair of OA-like damage, whereas the consumption of SFAs and n-6 PUFAs has been associated with greater osteophyte formation, synovitis, and macrophage infiltration of the synovium [9].

Little is known about the effects of MUFAs on joints. In this study, our histological and gait analyses revealed the effects of a high-fat diet rich in MUFAs on mouse articular cartilage were similar to those of a diet rich in n-3 PUFAs. However, MUFAs did not reduce cartilage damage caused by DMM. This negative finding, combined with the serum IL-1β level data, suggests that a diet rich in MUFAs also has a proinflammatory effect, but to a much less extent than do diets rich in SFAs or n-6 PUFAs. Our results suggest that dietary factors play a more important role in obesity-related posttraumatic OA than do mechanical factors. Different types of FA may have different effects on OA, and exploring their mechanisms of action is of great value for the prevention and treatment of obesity-related OA from a dietary perspective.

TLR4 is the most expressed TLR in chondrocytes, and its expression in joint tissues increases with OA severity [45]. Moreover, the inhibition of TLR4 expression in cartilage has been shown to reduce OA severity in rats [46]. The TLR4 signaling pathway is considered to be a main trigger of obesity-induced inflammation, and the TLR4/NF-κB signaling pathway is an important mechanism that regulates the chondrocyte OA inflammatory response [47]. In addition, obesity disrupts mitochondrial integrity, leading to the release of reactive oxygen species, which triggers the formation of NLRP3 inflammasome complexes [48]. Activation of the NLRP3 inflammasome activates caspase-1, mediates cellular pyroptosis through the NLRP3/caspase-1/GSDMD pathway, and produces inflammatory mediators such as IL-1β and IL-18, triggering a series of inflammatory responses [16] that play important roles in the development of OA. Thus, in the present study, we explored the effects of four FAs on the TLR4/NF-κB signaling pathway and the activation of the NLRP3 inflammasome and its downstream signals from the perspective of overall diet and single FAs. Our finding that diets rich in SFAs, MUFAs, or n-6 PUFAs increase the expression of the TLR4/NF-κB signaling pathway and NLRP3 proteins, whereas a diet rich in n-3 PUFA did not significantly change protein expression, suggests that the pro- or anti-inflammatory effects of dietary FAs are related to the regulation of the TLR4/MyD88/NF-κB signaling pathway and NLRP3 inflammasome.

We also observed that the expression levels of TLR4, NF-κB, NLRP3, and IL-1β were not significantly elevated in

joints from the n-3 PUFA group subjected to DMM compared with joints subjected to sham operation, consistent with the idea that the n-3 PUFA–rich diet had anti-inflammatory and antipyroptotic effects and contributed to postinjury repair. The cellular assays also showed that SFAs and n-6 PUFAs activated TLR4/NF-κB and NLRP3/caspase-1/GSDMD signaling, whereas n-3 PUFAs had an inhibitory effect. The *in vitro* effects of MUFAs on these proteins differed from those observed in the animal experiment; MUFAs had anti-inflammatory and antipyroptotic effects *in vitro* that were similar to those of n-3 PUFAs.

SFA, acting as a non-microbial TLR4 agonist, can initiate TLR4-mediated inflammatory responses [37]. It can be recognized by the CD14-TLR4-MD2 complex and trigger inflammatory pathways, and may lead to alterations in the gut microbiota that produce excess LPS after high-fat intake, inducing a TLR4 inflammatory response through MyD88-dependent and/or MyD88-independent pathways, which in turn promote NF-κB expression. PA has been shown to have pro-apoptotic and pro-inflammatory effects on articular cartilage through TLR4's upregulation of IL-6 and cyclooxygenase 2 expression in IL-1β–induced chondrocytes [49]. In addition, an SFA-enriched high-fat diet fed to mice activated NLRP3 inflammasomes in macrophages and dendritic cells and increased IL-1β secretion in adipose tissue [50], thereby promoting the progression of OA [51].

In contrast, n-3 PUFAs, such as DHA and eicosapentaenoic acid, exert anti-inflammatory effects by attenuating LPS or SFA activation of TLR4 signaling [52]. n-3 PUFAs can inhibit TLR4-induced signaling and target gene expression [53, 54], perhaps via anti-inflammatory effects mediated by G protein-coupled receptor 120. Oh et al. [55] found that the stimulation of G protein-coupled receptor 120 with n-3 PUFAs inhibited TLR4 signaling, possibly due to the binding of β-arrestin-2 to TAB1, leading to the inhibition of TAK1 phosphorylation and activation, which in turn blocks TLR4 signaling. In addition, n-3 PUFA treatment has been reported to disrupt TLR4 translocation to lipid rafts, thereby preventing TLR4 activation [53]. Additionally, Chen et al. [56] found that n-3 PUFA supplementation inhibited the expression of TLR4/NF-κB signaling pathway–related proteins and reduced subsequent inflammatory responses. Similarly, n-3 PUFAs have been shown to inhibit NLRP3 inflammasome activity in human adipose tissue by downregulating inflammatory gene expression in adipocytes and mononuclear macrophages [57]. Our study yielded similar results in mouse cartilage and SW1353 chondrocytes.

We found that the role of n-6 PUFA was similar to that of SFA and differed from that of n-3 PUFA. High n-6 PUFA intake has been reported to upregulate TLR4 expression [58], and a high dietary n-3/n-6 PUFA ratio has been shown to ameliorate obesity-associated inflammation and insulin resistance by inhibiting TLR4 activation in rats [58], which also reflects TLR4 upregulation by n-6 PUFA. An n-6 PUFA–enriched high-fat diet induced hepatic steatosis and fibrosis, along with the activation of the NLRP3 inflammasome, in mice [59], whereas the inhibition of n-6 PUFA metabolites reduced pro-inflammatory factor secretion and inhibited NLRP3 inflammasome activation [60]. Our results suggest that the effects of n-6 PUFA on TLR4 and the NLRP3 inflammasome are similar to those of SFA and that n-6 PUFA can promote OA progression.

The results of studies examining MUFA effects have been inconsistent. Some studies have shown that a MUFA-enriched high-fat diet stimulates the TLR4 inflammatory pathway by increasing JNK and STAT3 binding protein activation [61] and decreases NLRP3 inflammasome activation while reducing IL-1β secretion in adipose tissue and immune cells [50, 62]. OLA causes toxic damage to rat hepatocytes through the activation of MAPK/TLR4 signaling [63]. However, it has also been shown to inhibit TLR4-mediated inflammatory responses in monocytes and macrophages, reduce TLR4 and p–NF-κB expression, and have anti-inflammatory effects [64]. In our animal experiments, we found that a MUFA-enriched high-fat diet increased the expression of TLR4/NF-κB and NLRP3 inflammasome proteins, whereas chondrocytes treated with MUFA showed down-regulation of the TLR4/NF-κB and NLRP3/caspase-1/GSDMD signaling pathways. This difference may reflect the ability of MUFA to inhibit TLR4 and NLRP3 inflammasome expression, with anti-inflammatory and anti-pyroptosis effects, but to a weaker extent than can n-3 PUFA. MUFA-rich high-fat feeds contain not only MUFAs but also other pro-inflammatory FAs, such as SFA and n-6 PUFA, which can weaken or even reverse the effects of MUFA, causing contradiction in the results of *in vitro* and *in vivo* experiments. Such contradictory results have been obtained in other studies. For example, Pietraszek et al. [65] found that MUFA-rich macadamia oil intake induced a postprandial anti-inflammatory response, but also increased the expression of pro-inflammatory genes, in healthy human subjects. Rocha et al. [66] showed that MUFA, although pro-inflammatory, had an anti-inflammatory effect relative to SFA-rich high-fat diets. These findings suggest that the effects of dietary MUFAs are influenced by various factors, including those related to the proportions of various FAs added to diets, feeding times, and tissue types.

Activation of the TLR4-mediated signaling pathway leads to NF-κB p65 phosphorylation, which may be a key signal in NLRP3 inflammasome and pyroptosis activation [67, 68]. Yabuta and Shidoji [69] showed that the activation of the TLR4/NF-κB signaling pathway activated NLRP3 inflammasomes, and thus caspase-1, generating GSDMD N-terminal fragments of the plasma membrane that induced cellular pyroptosis. To further clarify whether crosstalk between the TLR4/NF-κB and NLRP3/caspase-1/GSDMD signaling pathways is part of the mechanisms underlying the actions of the four types of FA examined on chondrocytes in this study, we administered a TLR4 inhibitor to the SFA and n-6 PUFA groups and TLR4 overexpression lentivirus to the MUFA and n-3 PUFA groups, based on our preliminary data. When TLR4 was inhibited, the expression of the NLRP3 inflammasome and pyroptosis-related proteins caspase-1 and GSDMD was reduced after SFA or n-6 PUFA treatment, suggesting that the pro-inflammatory and pro-pyroptotic effects of SFA and n-6 PUFA are mediated through the TLR4/NF-κB signaling pathway. When TLR4 was overexpressed, MUFA and n-3 PUFA

supplementation reduced NLRP3, GSDMD, and caspase-1 expression, suggesting that the anti-inflammatory and anti-pyroptotic effects of MUFA and n-3 PUFA are also mediated through the TLR4 signaling pathway. Thus, TLR4/NF-κB may play a more important role in mediating the effects of these four FAs on chondrocytes by acting as an upstream signal for the NLRP3/caspase-1/GSDMD signaling pathway.

5. Conclusions

In the present study, we found that SFA-, MUFA-, and n-6 PUFA–enriched diets were pro-inflammatory and pro-pyroptotic, promoting obesity-related OA, although the MUFA-enriched diet had a much weaker effect than did the other two diets. An n-3 PUFA–enriched diet had anti-inflammatory and anti-pyroptotic effects, protecting against obesity-related OA development. These effects are associated with activation/inhibition of the TLR4/NF-κB signaling pathway in articular cartilage, which in turn upregulates/downregulates the NLRP3 inflammasome, thereby inducing cellular pyroptosis. Our results support the promotion of diets rich in n-3 PUFAs. MUFA may have anti-inflammatory and anti-pyroptotic effects, but the achievement of these effects may require adherence to appropriate FA ratios. Figure 9 illustrates the mechanism of FA regulation of the NLRP3 inflammasome in chondrocytes. This study reveals possible mechanisms underlying the effects of different types of FA on OA. Additionally, our findings provide a theoretical basis for the prevention and treatment of obesity-related OA from a dietary perspective.

Data Availability

The data used to support the findings of this study are available from the corresponding author upon request.

Conflicts of Interest

The authors declare that they have no known competing financial interests or personal relationships that could have appeared to influence the work reported in this paper.

Authors' Contributions

Xin Jin was responsible for investigation, validation, data curation, and writing original draft. Xin Dong was responsible for investigation, validation, and data curation. Yingxu Sun was responsible for investigation, validation, and data curation. Ziyu Liu was responsible for investigation, validation, and data curation. Li Liu was responsible for funding acquisition, methodology, investigation, and validation. Hailun Gu was responsible for conceptualization, funding acquisition, methodology, visualization, writing, review, and editing.

Acknowledgments

This study was supported by the National Natural Science Foundation of China (82073541), Educational Department of Liaoning Province (LJKZ0747), and the Key R & D Program of Liaoning Province (2020JH2/10300144).

Supplementary Materials

Supplementary Table S1: composition of experimental diets. Supplementary Table S2: the standard of Modified Mankin score. Supplementary Table S3: OA cartilage histopathology grade assessment—OARSI. Supplementary Figure S1: transfection effect of TLR4 overexpressing lentivirus in chondrocytes. *(Supplementary Materials)*

References

[1] G. B. D. Disease, I. Injury, and C. Prevalence, "Global, regional, and national incidence, prevalence, and years lived with disability for 310 diseases and injuries, 1990-2015: a systematic analysis for the Global Burden of Disease Study 2015," *Lancet*, vol. 388, pp. 1545–1602, 2016.

[2] D. Pereira, E. Ramos, and J. Branco, "Osteoarthritis," *Acta Médica Portuguesa*, vol. 28, no. 1, pp. 99–106, 2015.

[3] R. Barnett, "Osteoarthritis," *The Lancet*, vol. 391, article 10134, p. 1985, 2018.

[4] M. J. McAllister, M. Chemaly, A. J. Eakin, D. S. Gibson, and V. E. McGilligan, "NLRP3 as a potentially novel biomarker for the management of osteoarthritis," *Osteoarthritis and Cartilage*, vol. 26, no. 5, pp. 612–619, 2018.

[5] N. S. Harasymowicz, A. Dicks, C. L. Wu, and F. Guilak, "Physiologic and pathologic effects of dietary free fatty acids on cells of the joint," *Annals of the New York Academy of Sciences*, vol. 1440, no. 1, pp. 36–53, 2019.

[6] V. L. Johnson and D. J. Hunter, "The epidemiology of osteoarthritis," *Best Practice & Research. Clinical Rheumatology*, vol. 28, no. 1, pp. 5–15, 2014.

[7] J. Sanchez-Adams, H. A. Leddy, A. L. McNulty, C. J. O'Conor, and F. Guilak, "The mechanobiology of articular cartilage: bearing the burden of osteoarthritis," *Current Rheumatology Reports*, vol. 16, no. 10, p. 451, 2014.

[8] A. W. Visser, R. de Mutsert, S. le Cessie et al., "The relative contribution of mechanical stress and systemic processes in different types of osteoarthritis: the NEO study," *Annals of the Rheumatic Diseases*, vol. 74, no. 10, pp. 1842–1847, 2015.

[9] X. Wang, D. Hunter, J. Xu, and C. Ding, "Metabolic triggered inflammation in osteoarthritis," *Osteoarthritis and Cartilage*, vol. 23, no. 1, pp. 22–30, 2015.

[10] M. Loef, J. W. Schoones, M. Kloppenburg, and A. Ioan-Facsinay, "Fatty acids and osteoarthritis: different types, different effects," *Joint, Bone, Spine*, vol. 86, no. 4, pp. 451–458, 2019.

[11] F. N. Ghadially, G. Meachim, and D. H. Collins, "Extra-cellular lipid in the matrix of human articular cartilage," *Annals of the Rheumatic Diseases*, vol. 24, no. 2, pp. 136–146, 1965.

[12] D. H. Collins, F. N. Ghadially, and G. Meachim, "Intra-cellular lipids of cartilage," *Annals of the Rheumatic Diseases*, vol. 24, no. 2, pp. 123–135, 1965.

[13] M. C. Naranjo, I. Garcia, B. Bermudez et al., "Acute effects of dietary fatty acids on osteclastogenesis via RANKL/RANK/OPG system," *Molecular Nutrition & Food Research*, vol. 60, no. 11, pp. 2505–2513, 2016.

[14] B. Lu, J. B. Driban, C. Xu, K. L. Lapane, T. E. McAlindon, and C. B. Eaton, "Dietary fat intake and radiographic progression of knee osteoarthritis: data from the osteoarthritis initiative," *Arthritis Care & Research*, vol. 69, no. 3, pp. 368–375, 2017.

[15] L. Votava, A. G. Schwartz, N. S. Harasymowicz, C. L. Wu, and F. Guilak, "Effects of dietary fatty acid content on humeral cartilage and bone structure in a mouse model of diet-induced obesity," *Journal of Orthopaedic Research*, vol. 37, no. 3, pp. 779–788, 2019.

[16] M. Srikanth, K. Chandrasaharan, X. Zhao, K. Chayaburakul, W. Y. Ong, and D. R. Herr, "Metabolism of docosahexaenoic acid (DHA) induces pyroptosis in BV-2 microglial cells," *Neuromolecular Medicine*, vol. 20, no. 4, pp. 504–514, 2018.

[17] N. Pizato, B. C. Luzete, L. Kiffer et al., "Omega-3 docosahexaenoic acid induces pyroptosis cell death in triple- negative breast cancer cells," *Scientific Reports*, vol. 2018, p. 8, 2018.

[18] C. L. Wu, D. Jain, J. N. McNeill et al., "Dietary fatty acid content regulates wound repair and the pathogenesis of osteoarthritis following joint injury," *Annals of the Rheumatic Diseases*, vol. 74, no. 11, pp. 2076–2083, 2015.

[19] K. R. Baker, N. R. Matthan, A. H. Lichtenstein et al., "Association of plasma n-6 and n-3 polyunsaturated fatty acids with synovitis in the knee: the MOST study," *Osteoarthritis and Cartilage*, vol. 20, no. 5, pp. 382–387, 2012.

[20] A. P. Simopoulos, "Importance of the ratio of omega-6/omega-3 essential fatty acids: evolutionary aspects," *World Review of Nutrition and Dietetics*, vol. 92, pp. 1–22, 2003.

[21] H. An, C. Qian, and X. Cao, "Regulation of Toll-like receptor signaling in the innate immunity," *Science China. Life Sciences*, vol. 53, no. 1, pp. 34–43, 2010.

[22] H. J. Anders, B. Banas, and D. Schlondorff, "Signaling danger: toll-like receptors and their potential roles in kidney disease," *Journal of the American Society of Nephrology*, vol. 15, no. 4, pp. 854–867, 2004.

[23] F. G. Bauernfeind, G. Horvath, A. Stutz et al., "Cutting edge: NF-kappaB activating pattern recognition and cytokine receptors license NLRP3 inflammasome activation by regulating NLRP3 expression," *Journal of Immunology*, vol. 183, no. 2, pp. 787–791, 2009.

[24] R. Gomez, A. Villalvilla, R. Largo, O. Gualillo, and G. Herrero-Beaumont, "TLR4 signalling in osteoarthritis–finding targets for candidate DMOADs," *Nature Reviews Rheumatology*, vol. 11, no. 3, pp. 159–170, 2015.

[25] H. H. Shen, Y. X. Yang, X. Meng et al., "NLRP3: a promising therapeutic target for autoimmune diseases," *Autoimmunity Reviews*, vol. 17, no. 7, pp. 694–702, 2018.

[26] Y. Zu, Y. Mu, Q. Li, S. T. Zhang, and H. J. Yan, "Icariin alleviates osteoarthritis by inhibiting NLRP3-mediated pyroptosis," *Journal of Orthopaedic Surgery and Research*, vol. 14, no. 1, p. 307, 2019.

[27] L. R. Zhao, R. L. Xing, P. M. Wang et al., "NLRP1 and NLRP3 inflammasomes mediate LPS/ATP-induced pyroptosis in knee osteoarthritis," *Molecular Medicine Reports*, vol. 17, pp. 5463–5469, 2018.

[28] S. B. Kovacs and E. A. Miao, "Gasdermins: effectors of pyroptosis," *Trends in Cell Biology*, vol. 27, no. 9, pp. 673–684, 2017.

[29] J. Shi, W. Gao, and F. Shao, "Pyroptosis: gasdermin-mediated programmed necrotic cell death," *Trends in Biochemical Sciences*, vol. 42, no. 4, pp. 245–254, 2017.

[30] X. Wu, H. Zhang, W. Qi et al., "Nicotine promotes atherosclerosis via ROS-NLRP3-mediated endothelial cell pyroptosis," *Cell Death & Disease*, vol. 9, no. 2, p. 171, 2018.

[31] C. Jin, P. Frayssinet, R. Pelker et al., "NLRP3 inflammasome plays a critical role in the pathogenesis of hydroxyapatite-associated arthropathy," *Proceedings of the National Academy of Sciences of the United States of America*, vol. 108, no. 36, pp. 14867–14872, 2011.

[32] Y. Wang, Y. Qian, Q. Fang et al., "Saturated palmitic acid induces myocardial inflammatory injuries through direct binding to TLR4 accessory protein MD2," *Nature Communications*, vol. 8, no. 1, article 13997, 2017.

[33] Y. He, H. Hara, and G. Nunez, "Mechanism and regulation of NLRP3 inflammasome activation," *Trends in Biochemical Sciences*, vol. 41, no. 12, pp. 1012–1021, 2016.

[34] O. M. Finucane, C. L. Lyons, A. M. Murphy et al., "Monounsaturated fatty acid-enriched high-fat diets impede adipose NLRP3 inflammasome-mediated IL-1β secretion and insulin resistance despite obesity," *Diabetes*, vol. 64, no. 6, pp. 2116–2128, 2015.

[35] C. M. Reynolds, F. C. McGillicuddy, K. A. Harford, O. M. Finucane, K. H. G. Mills, and H. M. Roche, "Dietary saturated fatty acids prime the NLRP3 inflammasome via TLR4 in dendritic cells—implications for diet-induced insulin resistance," *Molecular Nutrition & Food Research*, vol. 56, no. 8, pp. 1212–1222, 2012.

[36] P. Kang, Y. Wang, X. Li et al., "Effect of flaxseed oil on muscle protein loss and carbohydrate oxidation impairment in a pig model after lipopolysaccharide challenge," *The British Journal of Nutrition*, vol. 123, no. 8, pp. 859–869, 2020.

[37] D. M. Rocha, A. P. Caldas, L. L. Oliveira, J. Bressan, and H. H. Hermsdorff, "Saturated fatty acids trigger TLR4-mediated inflammatory response," *Atherosclerosis*, vol. 244, pp. 211–215, 2016.

[38] K. A. Wierenga, J. Wee, K. N. Gilley et al., "Docosahexaenoic acid suppresses silica-induced inflammasome activation and IL-1 cytokine release by interfering with priming signal," *Frontiers in Immunology*, vol. 10, p. 2130, 2019.

[39] M. M. Hughes and L. A. J. O'Neill, "Metabolic regulation of NLRP3," *Immunological Reviews*, vol. 281, no. 1, pp. 88–98, 2018.

[40] H. Kim, G. Yang, J. Park, J. Choi, E. Kang, and B. K. Lee, "Therapeutic effect of mesenchymal stem cells derived from human umbilical cord in rabbit temporomandibular joint model of osteoarthritis," *Scientific Reports*, vol. 9, no. 1, p. 13854, 2019.

[41] K. P. Pritzker, S. Gay, S. A. Jimenez et al., "Osteoarthritis cartilage histopathology: grading and staging," *Osteoarthritis and Cartilage*, vol. 14, no. 1, pp. 13–29, 2006.

[42] S. Thomas, H. Browne, A. Mobasheri, and M. P. Rayman, "What is the evidence for a role for diet and nutrition in osteoarthritis?," *Rheumatology*, vol. 57, Supplement_4, pp. iv61–iv74, 2018.

[43] C. L. Wu, K. A. Kimmerling, D. Little, and F. Guilak, "Serum and synovial fluid lipidomic profiles predict obesity-associated osteoarthritis, synovitis, and wound repair," *Scientific Reports*, vol. 7, no. 1, p. 44315, 2017.

[44] A. Van de Vyver, S. Clockaerts, C. H. A. van de Lest et al., "Synovial fluid fatty acid profiles differ between osteoarthritis and healthy patients," *Cartilage*, vol. 11, no. 4, pp. 473–478, 2020.

[45] M. B. Goldring, "Chondrogenesis, chondrocyte differentiation, and articular cartilage metabolism in health and osteoarthritis," *Therapeutic Advances in Musculoskeletal Disease*, vol. 4, no. 4, pp. 269–285, 2012.

[46] J. Li, Z. G. Xie, Y. Xie, and Q. R. Dong, "Calcitonin treatment is associated with less severe osteoarthritis and reduced toll-like receptor levels in a rat model," *Journal of Orthopaedic Science*, vol. 19, no. 6, pp. 1019–1027, 2014.

[47] Y. Fu, J. Lei, Y. Zhuang, K. Zhang, and D. Lu, "Overexpression of HMGB1 A-box reduced IL-1β-induced MMP expression and the production of inflammatory mediators in human chondrocytes," *Experimental Cell Research*, vol. 349, no. 1, pp. 184–190, 2016.

[48] S. S. Iyer, Q. He, J. R. Janczy et al., "Mitochondrial cardiolipin is required for Nlrp3 inflammasome activation," *Immunity*, vol. 39, no. 2, pp. 311–323, 2013.

[49] O. Alvarez-Garcia, N. H. Rogers, R. G. Smith, and M. K. Lotz, "Palmitate has proapoptotic and proinflammatory effects on articular cartilage and synergizes with interleukin-1," *Arthritis & Rhematology*, vol. 66, no. 7, pp. 1779–1788, 2014.

[50] H. Wen, D. Gris, Y. Lei et al., "Fatty acid-induced NLRP3-ASC inflammasome activation interferes with insulin signaling," *Nature Immunology*, vol. 12, no. 5, pp. 408–415, 2011.

[51] Z. Aibibula, M. Ailixiding, M. Iwata et al., "Xanthine oxidoreductase activation is implicated in the onset of metabolic arthritis," *Biochemical and Biophysical Research Communications*, vol. 472, no. 1, pp. 26–32, 2016.

[52] M. M. Rogero and P. C. Calder, "Obesity, inflammation, toll-like receptor 4 and fatty acids," *Nutrients*, vol. 10, no. 4, p. 432, 2018.

[53] S. W. Wong, M. J. Kwon, A. M. Choi, H. P. Kim, K. Nakahira, and D. H. Hwang, "Fatty acids modulate Toll-like receptor 4 activation through regulation of receptor dimerization and recruitment into lipid rafts in a reactive oxygen species-dependent manner∗," *The Journal of Biological Chemistry*, vol. 284, no. 40, pp. 27384–27392, 2009.

[54] J. Y. Lee, J. Ye, Z. Gao et al., "Reciprocal modulation of Toll-like receptor-4 signaling pathways involving MyD88 and phosphatidylinositol 3-kinase/AKT by saturated and polyunsaturated fatty acids∗," *The Journal of Biological Chemistry*, vol. 278, no. 39, pp. 37041–37051, 2003.

[55] D. Y. Oh, S. Talukdar, E. J. Bae et al., "GPR120 is an omega-3 fatty acid receptor mediating potent anti-inflammatory and insulin-sensitizing effects," *Cell*, vol. 142, no. 5, pp. 687–698, 2010.

[56] X. Chen, S. Wu, C. Chen et al., "Omega-3 polyunsaturated fatty acid supplementation attenuates microglial-induced inflammation by inhibiting the HMGB1/TLR4/NF-κB pathway following experimental traumatic brain injury," *Journal of Neuroinflammation*, vol. 14, no. 1, p. 143, 2017.

[57] A. M. Murphy, C. L. Lyons, O. M. Finucane, and H. M. Roche, "Interactions between differential fatty acids and inflammatory stressors– impact on metabolic health," *Prostaglandins, Leukotrienes, and Essential Fatty Acids*, vol. 92, pp. 49–55, 2015.

[58] H. Q. Liu, Y. Qiu, Y. Mu et al., "A high ratio of dietary n-3/n-6 polyunsaturated fatty acids improves obesity- linked inflammation and insulin resistance through suppressing activation of TLR4 in SD rats," *Nutrition Research*, vol. 33, no. 10, pp. 849–858, 2013.

[59] C. C. Sun, C. Y. Zhang, J. X. Duan et al., "PTUPB ameliorates high-fat diet-induced non-alcoholic fatty liver disease via inhibiting NLRP3 inflammasome activation in mice," *Biochemical and Biophysical Research Communications*, vol. 523, no. 4, pp. 1020–1026, 2020.

[60] H. H. Yang, J. X. Duan, S. K. Liu et al., "A COX-2/sEH dual inhibitor PTUPB alleviates lipopolysaccharide-induced acute lung injury in mice by inhibiting NLRP3 inflammasome activation," *Theranostics*, vol. 10, no. 11, pp. 4749–4761, 2020.

[61] S. Lager, F. Gaccioli, V. I. Ramirez, H. N. Jones, T. Jansson, and T. L. Powell, "Oleic acid stimulates system A amino acid transport in primary human trophoblast cells mediated by toll-like receptor 4," *Journal of Lipid Research*, vol. 54, no. 3, pp. 725–733, 2013.

[62] G. Ravaut, A. Légiot, K. F. Bergeron, and C. Mounier, "Monounsaturated fatty acids in obesity-related inflammation," *International Journal of Molecular Sciences*, vol. 22, p. 330, 2021.

[63] H. Zhang, J. Wang, L. Yang et al., "Effect of oleic acid on induction of steatosis and cytotoxicity in BRL 3A cells," *Journal of Cellular Biochemistry*, vol. 120, no. 12, pp. 19541–19554, 2019.

[64] A. B. Santamarina, L. P. Pisani, E. J. Baker et al., "Anti-inflammatory effects of oleic acid and the anthocyanin keracyanin alone and in combination: effects on monocyte and macrophage responses and the NF-κB pathway," *Food & Function*, vol. 12, no. 17, pp. 7909–7922, 2021.

[65] A. Pietraszek, S. Gregersen, and K. Hermansen, "Acute effects of dietary fat on inflammatory markers and gene expression in first-degree relatives of type 2 diabetes patients," *The Review of Diabetic Studies*, vol. 8, no. 4, pp. 477–489, 2011.

[66] D. Rocha, L. L. Lopes, A. da Silva, L. L. Oliveira, J. Bressan, and H. H. M. Hermsdorff, "Orange juice modulates proinflammatory cytokines after high-fat saturated meal consumption," *Food & Function*, vol. 8, no. 12, pp. 4396–4403, 2017.

[67] S. Xu, J. Wang, J. Jiang et al., "TLR4 promotes microglial pyroptosis via lncRNA-F630028O10Rik by activating PI3K/AKT pathway after spinal cord injury," *Cell Death & Disease*, vol. 11, no. 8, p. 693, 2020.

[68] X. Chen, G. Liu, Y. Yuan, G. Wu, S. Wang, and L. Yuan, "NEK7 interacts with NLRP3 to modulate the pyroptosis in inflammatory bowel disease via NF-κB signaling," *Cell Death & Disease*, vol. 10, no. 12, p. 906, 2019.

[69] S. Yabuta and Y. Shidoji, "TLR4-mediated pyroptosis in human hepatoma-derived HuH-7 cells induced by a branched-chain polyunsaturated fatty acid, geranylgeranoic acid," *Bioscience Reports*, vol. 40, no. 4, 2020.

Hindawi
Oxidative Medicine and Cellular Longevity
Volume 2022, Article ID 4608914, 21 pages
https://doi.org/10.1155/2022/4608914

Research Article

Attenuation of ROS/Chloride Efflux-Mediated NLRP3 Inflammasome Activation Contributes to Alleviation of Diabetic Cardiomyopathy in Rats after Sleeve Gastrectomy

Songhan Li,[1] Shuohui Dong,[1] Bowen Shi,[1] Qian Xu,[1] Linchuan Li,[2] Shuo Wang,[3] Wenjie Zhang,[1] Mingwei Zhong,[2] Jiankang Zhu,[2] Yugang Cheng,[2] Guangyong Zhang,[2] and Sanyuan Hu[1]

[1]*Department of General Surgery, Shandong Qianfoshan Hospital, Cheeloo College of Medicine, Shandong University, Jinan, Shandong 250014, China*
[2]*Department of General Surgery, The First Affiliated Hospital of Shandong First Medical University, Jinan, Shandong 250014, China*
[3]*Department of Gastroenterological Surgery, Peking University People's Hospital, Beijing 100044, China*

Correspondence should be addressed to Sanyuan Hu; husanyuan1962@hotmail.com

Received 17 November 2021; Accepted 29 March 2022; Published 19 April 2022

Academic Editor: Juyi Li

Diabetic cardiomyopathy (DCM) can develop in diabetes mellitus and is a major cause of morbidity and mortality. Surgical bariatric surgery procedures, such as sleeve gastrectomy (SG), result in remission of type 2 diabetes and have benefits regarding systolic and diastolic myocardial function. The NLR family pyrin domain containing 3 (NLRP3) inflammasome appears to participate in the development of DCM. However, whether SG surgery affects myocardial NLRP3 inflammasome-related pyroptosis to improve cardiac function remains unclear. This study was aimed at investigating the effect of SG surgery on NLRP3-associated pyroptosis in rats with DCM. We also examined cellular phenotypes and molecular mechanisms in high glucose-stimulated myocytes. The rat model of DCM was established by high-fat diet feeding and low-dose streptozotocin injection. We observed a metabolic benefit of SG, including a reduced body weight, food intake, and blood glucose levels and restored glucose tolerance and insulin sensitivity postoperatively. We observed a marked decline in glucose uptake in rats with DCM, and this was restored after SG. Also, SG alleviated the dysfunction of myocardial contraction and diastole, delayed the progression of DCM, and reduced the NLRP3 inflammasome-mediated myocardial pyroptosis *in vivo*. H9c2 cardiomyocytes showed membrane disruption and DNA damage under a high glucose stimulus, which suggested myocardial pyroptosis. Using a ROS scavenger or chloride channel blocker *in vitro* restored myocardial NLRP3-mediated pyroptosis. Furthermore, we found that chloride efflux acted downstream of ROS generation. In conclusion, SG may ameliorate or even reverse the progression of DCM. Our study provides evidence that the SG operation alleviates NLRP3 inflammasome dysregulation in DCM. Clearance of ROS overburden and suppression of chloride efflux due to SG might act as the proximal event before inhibition of NLRP3 inflammasome in the myocardium, thus contributing to morphological and functional alleviation of DCM.

1. Introduction

Diabetic cardiomyopathy (DCM) is a distinct disease entity that develops in diabetes mellitus (DM) and does not come after any coronary artery disease, hypertension, or valvular heart disease [1, 2]. Currently, DCM is recognized as the predominant cause of morbidity and mortality among people suffering from DM [3]. At the onset of diabetes, owing to insulin resistance and metabolic shifts in cardiomyocytes, intracellular lipid and lipotoxicity were accumulated; afterwards, mitochondrial dysfunction and accumulation of reactive oxygen species (ROS) occurred in cardiomyocytes [2].

Ultimately, these pathological alternations bring about cardiomyocyte death, inflammatory response, and fibrotic remodeling [4].

Surgical bariatric surgery procedures such as sleeve gastrectomy (SG) are currently one of the most prevalent treatments for obesity and its related metabolic disorders [5]. Plenty of evidence have shown that SG results in effective remission of type 2 diabetes (T2DM) and associated complications [6, 7]. A couple of studies evaluated that the SG had benefits regarding systolic and diastolic myocardial function in patients with DCM or in rat models [8, 9], whereas, to date, the underlying mechanism of SG remains to be integrated.

Pyroptosis is a type of proinflammatory programmed cell death [10]. Activation of the canonical NLR family pyrin domain containing 3 (NLRP3) inflammasome can engage caspase-1 for cleaving gasdermin D (GSDMD) as well as turning proforms of interleukin- (IL-) 1β and IL-18 into active forms, finally leading to cell membrane pore formation and release of inflammatory cytokines [11]. A previous study showed that a deficit of NLRP3 improved insulin sensitivity in obese mice, which suggests that NLRP3 plays a significant role in metabolism [12]. Previous studies also showed that ablation of NLRP3 in rats with DCM could significantly reduce myocardial pyroptosis and induce inflammatory response [13, 14]. These previous findings suggest that the NLRP3 inflammasome participates in the development of DCM. Additionally, studies have shown that bariatric surgery inhibits NLRP3 activation in pancreatic islets, hepatocytes, and adipose tissues, causing anticell death and anti-inflammatory effects [15–18]. Notwithstanding, whether SG surgery affects myocardial NLRP3 inflammasome-related pyroptosis for the improvement of cardiac function remains unclear.

To address these issues, we established a rat model of DCM by high-fat diet (HFD) feeding and low-dose streptozotocin (STZ) injection compared with chow diet-fed rats as controls. SG or sham surgery was performed to investigate the effect of SG surgery on NLRP3-associated pyroptosis in rats with DCM. Furthermore, cellular phenotypes and molecular mechanisms were examined in high glucose-stimulated myocytes.

2. Materials and Methods

2.1. Animals. All animal protocols were approved by the Medical Ethical Committee of the Shandong Provincial Qianfoshan Hospital, Shandong University. Male Wistar rats at the age of approximately 6 weeks were purchased from Beijing Weitong Lihua Experimental Animal Technology and were placed in an environment with access to feed and water with alternate 12-hour light and dark cycles at $22 \pm 2^{\circ}$C. After one-week-long adaptive feeding, two groups of rats were kept in a high-fat diet (HFD, 60% of calories as fat, Xietong Biotech, Nanjing, China) for four weeks to induce obesity and insulin resistance, while the other group was fed with normal chow. After 12 h fasting, we intraperitoneally injected rats with streptozotocin (STZ; 35 mg/kg, Sigma-Aldrich, St. Louis, MO, USA) dissolved in sodium citrate buffer pH 4.5 (Solarbio, Beijing, China) to produce the type 2 diabetic models. One week after STZ administration, fasting blood glucose (FBG) was measured with a glucometer (Roche One Touch Ultra, LifeScan, CA, USA). Only rats with FBG exceeding 11.1 mmol/L were regarded as promising diabetic models [19]. Diabetic rats were fed with HFD for 8 weeks after STZ injection for a stable DCM model establishment, as described by previous studies; after eight-week STZ injection when the stable T2DM model is established, the onset of cardiac dysfunction is observed as well [20, 21].

2.2. Surgical Procedures. Prior to surgery, rats were fed with 10% Ensure (Abbott Laboratories, Abbott Park, IL, USA) for 2 days and then fasted overnight and underwent SG or sham surgery under anesthesia with 2% isoflurane. SG and sham surgery were performed in accordance with a previous report [22]. Afterwards, the rats were caged individually, and the diet was transited gradually from liquid diet to high-fat diet consistent with the preoperative feeding strategy. Food intake and body weight were recorded per week. The rats were euthanized 8 weeks after surgery.

2.3. Oral Glucose Tolerance Test and Insulin Tolerance Test. An oral glucose tolerance test (OGTT) and insulin tolerance test (ITT) were performed before surgery and at 8 weeks after surgery. Blood glucose was monitored from the tail vein of fasting rats at baseline and 10, 30, 60, and 120 min after the administration of intragastric gavage of 20% glucose (1 g/kg) for the OGTT or intraperitoneal injection of human insulin (0.5 IU/kg) for the ITT. The homeostasis model assessment of basal insulin resistance (HOMA-IR) was evaluated as FBG (mmol/L) $\times$ fasting insulin (mIU/L)/22.5.

2.4. Cardiac Function. Echocardiography examination was performed before the surgery to prove the successful establishment of DCM models and at 8 weeks after surgery to observe the clinical effects of SG. Rats were anesthetized with 2% isoflurane for transthoracic echocardiography with an RMB710 transducer using the Vevo 3100 system (VisualSonics, Toronto, Canada). The left ventricular end-diastolic diameter (LVEDd), left ventricular ejection fractions (LVEF), fractional shortening (FS), and early-to-late mitral diastolic flow ratio (E/A) along with isovolumic relaxation time (IVRT) were measured.

2.5. ^{18}F-FDG PET of Rat Heart Imaging. PET scans were performed at 8 weeks after surgery. Fasting rats were made to inhale isoflurane and fixed with cannulas. After intravenous injection with 29.6 MBq (800 μCi) of ^{18}F-FDG, rats were maintained for one hour and the hearts were scanned with a Positron Emission Computed Tomography (PET) scanner (Metis 1800, Madic Technology, China).

2.6. Histology and Immunohistochemistry. Each rat myocardial sample, formalin-fixed and paraffin-embedded, was cut into 5 μm sections. Slides were stained with haematoxylin and eosin (H&E) for standard histology. The distribution of collagen was carried out by Masson's trichrome staining and picrosirius red staining. The quantitative analysis of

the cardiomyocyte size and collagen volume was measured with the Image-Pro Plus 6.0 (Media Cybernetics, Bethesda, MD, USA). Frozen sections were stained with Oil Red O to detect liquid content. Terminal deoxynucleotidyl transferase-mediated dUTP nick end-labeling (TUNEL) staining was utilized to assess cell death (Servicebio, Wuhan, China). After antigen retrieval in a citrate buffer (0.01 M, pH 6.0) and endogenous peroxidase blocking, slides were incubated with primary antibodies against collagen I (Affinity, AF0134, 1 : 100), collagen III (Affinity, AF0136, 1 : 100), NLRP3 (Abcam, ab210491, 1 : 200), ASC (Affinity, DF6304, 1 : 100), GSDMD (Affinity, AF4012, 1 : 100), IL-1β (Abcam, ab9722, 1 : 200), IL-18 (ProteinTech, 10663-1-AP, 1 : 300), and NEK7 (Affinity, DF4467, 1 : 100) at 4°C overnight. Thereafter, the tissues were incubated with HRP-conjugated secondary antibodies at 37°C for 30 minutes and observed with microscope (ZEISS, Axio Vert.A1, Jena, Germany).

2.7. Transmission Electron Microscopy. One-millimeter LV cubes were prefixed in 2.5% glutaraldehyde overnight at 4°C and postfixed in 1% osmium tetroxide for 2 h at 4°C. Samples were then dehydrated through an ethanol series and embedded in Epon. After complete polymerization and cutting into ultrathin sections, the sections were stained with uranyl acetate and lead citrate which were then examined using a transmission electron microscope (Hitachi, HT-7800, Japan).

2.8. Cell Culture and Treatment. H9c2 rat cardiomyocytes were cultured in low glucose DMEM (5.5 mM) supplemented with 10% FBS in a 5% CO_2 thermostatic (37°C) incubator. After serum starvation overnight, cells were exposed to high glucose (HG, 33.3 mM) for 48 h. For the ROS scavenger, H9c2 cells were pretreated with 1 mM N-acetyl-L-cysteine (NAC, MCE, Shanghai, China) before the stimulation of HG for 12 h. For chloride efflux inhibition, additionally, 100 μM indanyloxyacetic acid-94 (IAA-94, MCE, Shanghai, China) was administered for 24 h.

2.9. Flow Cytometry. The levels of glucose uptake, intracellular ROS load, and chloride concentration were determined through flow cytometry. When indicated H9c2 cells in 6-well plates had reached 80% confluence, they were treated under respective stimulation as described in Section 2.8. After being washed with cold PBS three times, 2-deoxyglucose analog (2-NBDG, MCE, Shanghai, China) was added at a final concentration of 50 μM in glucose-free DMEM for 30 min. And H9c2 cells ware incubated with 2 μM DCFH-DA (Beyotime, Shanghai, China) in low glucose DMEM for 20 min. Also, 10 μM N-(ethoxycarbonylmethyl)-6-methoxyquinolinium bromide (MQAE, MCE, New Jersey, USA) was added into the complete low glucose DMEM, and cells were incubated for 60 min. Cells were all cultured with probes in a 37°C 10% CO_2 humidified incubator. Then, the cells were washed with ice-cold PBS and digested with trypsin-EDTA and kept on ice protected from light. The fluorescence intensity of 2-NBDG, DCFH-DA, and MQAE (FITC channel) in labelled cells was detected through a BD FACSAria II instrument (BD, USA). 20,000 events from each specimen were measured to pledge sufficient data. The data were analyzed by FlowJo v10 (FlowJo, Ashland, OR, USA), and the polygonal gating strategy was used to exclude debris.

2.10. Caspase-1 Activity Detection. The caspase-1 activity was detected with a Caspase-1 Activity Assay Kit (BestBio, Shanghai, China). Firstly, cells were lysed in 100 μL lysis buffer on ice for 15 min. 10 μL supernatant was retained and remixed with 90 μL detection buffer and 10 μL caspase-1 substrate (Ac-YVAD-MCA) at 37°C for 2 h. Then, the optical density of samples was read on a microplate reader (Bio-Rad, CA, USA) at 405 nm.

2.11. LDH Release Detection. Lactate dehydrogenase (LDH) in the supernatant was measured using the LDH Release Assay Kit (Beyotime, Beijing, China) according to the manufacturer's protocol. The percentage of LDH release was computed as (experimental LDH − spontaneous LDH)/(maximum LDH release − spontaneous LDH).

2.12. Glucose Determination in Supernatants. The content of glucose in the supernatants was quantified using a Glucose Colorimetric Assay Kit (GOD-POD Method, Elabscience, Wuhan, China). H9c2 cells were seeded into 6-well plates and grown to 80% confluency under respective stimulation. The culture medium was changed to low glucose DMEM after 48 h and incubated for 24 h. The enzyme solution was configured according to the instruction manual. 3 μL of supernatant of all samples and 300 μL enzyme solution was transferred to a 96-well plate. After incubation at 37°C for 15 min, the final OD values were determined at 505 nm in a spectrophotometer. The concentrations of glucose were recorded according to the standard curve.

2.13. Chloride Detection in Supernatants. The chloride concentration in the supernatants was examined using a Chloride Colorimetric Assay Kit (Elabscience, Wuhan, China). H9c2 cells were also seeded into 6-well plates with a distinctive stimulus. The culture medium was removed, and cells were incubated with low glucose DMEM for 24 h. The chromogenic agent was configured according to the standard protocol. 10 μL of supernatants and 250 μL of a chromogenic agent were added to a 96-well plate. The OD values were calculated at 460 nm after incubation at room temperature for 5 min. And concentrations of the samples were determined from the standard curve.

2.14. Cell Death Assay. The TUNEL assay was used to detect DNA fragmentation, and the probe E42 staining was used to evaluate the membranal disruption. Cells were cultured on cell climbing slices. The TUNEL assay was performed with a TUNEL Cell Apoptosis Detection Kit (Servicebio, Wuhan, China) according to the given protocol. The cellular membrane-disrupted cells were labeled probe E42 under the instruction of the Cell Membrane Integrity Assay Kit (BestBio, Shanghai, China). Nuclei were stained with DAPI. Images were acquired on a confocal microscope (Leica, TSP2, Wetzlar, Germany).

2.15. Western Blot. Heart tissue proteins were extracted with the Total Protein Extraction Kit for Muscles (Invent Biotechnologies, Beijing, China). Cell proteins were lysed in a RIPA lysis buffer (Solarbio, Beijing, China). Membrane protein of H9c2 cells were prepared using the Minute Plasma Membrane Protein Isolation Kit (Invent Biotechnologies, Beijing, China). The protein extracts were separated using the 10% SDS-PAGE and followed by transferring to the PVDF membrane (Millipore, Cork, Ireland). After one-hour blocking in 5% fat-free milk, the membrane was incubated with primary antibodies at 4°C overnight. At the following day, secondary antibody (ProteinTech, Wuhan, China, SA00001-1/2, 1 : 5000) incubation was performed before the enhanced chemiluminescence (Millipore, Billerica, USA) with imagination via an Amersham Imager 680 (GE, Boston, USA). We used antibodies against NLRP3 (Abcam, Cambridge, UK, ab210491, 1 : 1000), IL-1β (ab9722, 1 : 2000), procaspase-1 +p10+p12 (ab179515, 1 : 1000), SOD2 (ab68155, 1 : 1000), IL-18 (ProteinTech, Wuhan, China, 10663-1-AP, 1 : 2000), TXNIP (18243-1-AP, 1 : 1000), CLIC1 (14545-1-AP, 1 : 1000), CLIC4 (66343-1-Ig, 1 : 2000), beta-tubulin (10068-1-AP, 1 : 5000), ATP1A1 (14418-1-AP, 1 : 10000), GSDMD (Affinity, Cincinnati, OH, USA, AF4012, 1 : 1000), ASC (DF6304, 1 : 1000), NEK7 (DF4467, 1 : 1000), NF-κB p65 (CST, MA, USA, #8242, 1 : 1000), and phospho-NF-κB p65 (Ser536, #3033, 1 : 1000).

2.16. RNA Extraction and Real-Time PCR. Total RNA of heart tissues and cell samples were extracted using a TRIzol reagent (Invitrogen, Carlsbad, CA, USA). cDNA synthesis was performed with a ReverTra Ace qPCR RT Kit (Toyobo, Osaka, Japan), and real-time PCR was performed using a SYBR Green Kit (Toyobo, Osaka, Japan) on the Roche LightCycler 480 System (Roche, Basel, Switzerland). The primer sequences are shown as in Table 1.

2.17. Immunofluorescence. The double-labeling localization of NLRP3 and CD68 were observed using immunofluorescence methods. 8 μm thick frozen sections were blocked with 2% BSA and incubated with primary antibodies against NLRP3 (Abcam, ab210491) and CD68 (Abcam, ab955) overnight at 4°C. After incubation with two different fluorescent secondary antibodies for 30 minutes at 37°C, slides were stained with DAPI.

The expression and localization of protein CLIC1 and CLIC4 were observed via immunofluorescence. H9c2 cells were cultured in 24-well plates and fixed with 4% paraformaldehyde, after which 0.1% of Triton X-100 was used for membrane permeabilization and 2% BSA for blocking. Thereafter, cells were incubated with primary antibodies CLIC1 (ProteinTech, 14545-1-AP, 1 : 100) and CLIC4 (66343-1-Ig, 1 : 200) at 4°C overnight. After staining with fluorescent secondary antibody and DAPI, images were observed by an immunofluorescence microscopy (Olympus, IX73, Tokyo, Japan).

2.18. Statistical Analysis. The data were presented as mean ± standard deviation (SD) and were analyzed using SPSS 22.0 (SPSS, Chicago, USA). Body weight, food intake, and FBG over time were analyzed using the two-way ANOVA and Tukey-Kramer tests. Other data were analyzed among groups using one-way ANOVA with subsequent Bonferroni or Dunnett's T3 correction. $P < 0.05$ was considered statistically significant.

Table 1: Primers used for qRT-PCR.

Gene	Sequence
Nlrp3	Forward: 5′-GCAGCGATCAACAGGCGAGAC-3′ Reverse: 5′-TCCCAGCAAACCTATCCACTCCTC-3′
Pycard	Forward: 5′-GATTATGGAAGAGTCTGGAGCTGTGG-3′ Reverse: 5′-ATGAGTGCTTGCCTGTGTTGGTC-3′
Casp1	Forward: 5′-AAACACCCACTCGTACACGTCTTG-3′ Reverse: 5′-AGGTCAACATCAGCTCCGACTCTC-3′
Gsdmd	Forward: 5′-AAGACTTCCAAGGCCTGCGT-3′ Reverse: 5′-CATGCTGGGCTGGTCCTGTA-3′
Il-1b	Forward: 5′-GACCTGTTCTTTGAGGCTGACA-3′ Reverse: 5′-CTCATCTGGACAGCCCAAGTC-3′
Il-18	Forward: 5′-CGACCGAACAGCCAACGAATCC-3′ Reverse: 5′-TCACAGATAGGGTCACAGCCAGTC-3′
Nek7	Forward: 5′-GGCTGTCTGCTGTATGAGATGGC-3′ Reverse: 5′-GATCTGATGGGAGAGGTGGGTAGTC-3′
Txnip	Forward: 5′-GCCAGACCAAAGTGCTCACTCAG-3′ Reverse: 5′-GAGACTCTTGCCACGCCATGATG-3′
Sod2	Forward: 5′-TCCCTGACCTGCCTTACGACTATG-3′ Reverse: 5′-TCGTGGTACTTCTCCTCGGTGAC-3′
Clic1	Forward: 5′-TCCCAGCCATAAACCATCCATTGTG-3′ Reverse: 5′-ATTCTGCCAGGGTGCTTTCTCTTG-3′
Clic4	Forward: 5′-TGAACGGACTGAAGGAGGAGGAC-3′ Reverse: 5′-GGTGGTGACACTGAACACGACTC-3′
Tubb3	Forward: 5′-CGTCCACCTTCATCGGCAACAG-3′ Reverse: 5′-TCGGCCTCGGTGAACTCCATC-3′

3. Results

3.1. Sleeve Gastrectomy Remarkably Alleviates General Characteristics and Glucose Homeostasis in Rats with Obesity and T2DM. Body weight curves of the three groups including the control group, sham group, and SG group are illustrated in Figure 1(a). Body weight in the sham surgery group and the SG group plateaued at 1 week postoperatively and gradually increased in weight thereafter. Body weight persistently showed a difference between the sham and SG groups. To determine the alternation in feeding behavior, we measured the food intake after surgery (Figure 1(b)). The sham and SG groups consumed fewer calories during the first week following surgery, which may have resulted from transient surgical stress. However, this appetite deficit of rats in the sham group was restored at a later time, while rats in the SG group remained hypophagic continuously, and this enabled maintenance of a reduced body weight. To evaluate the effects of SG on glucose

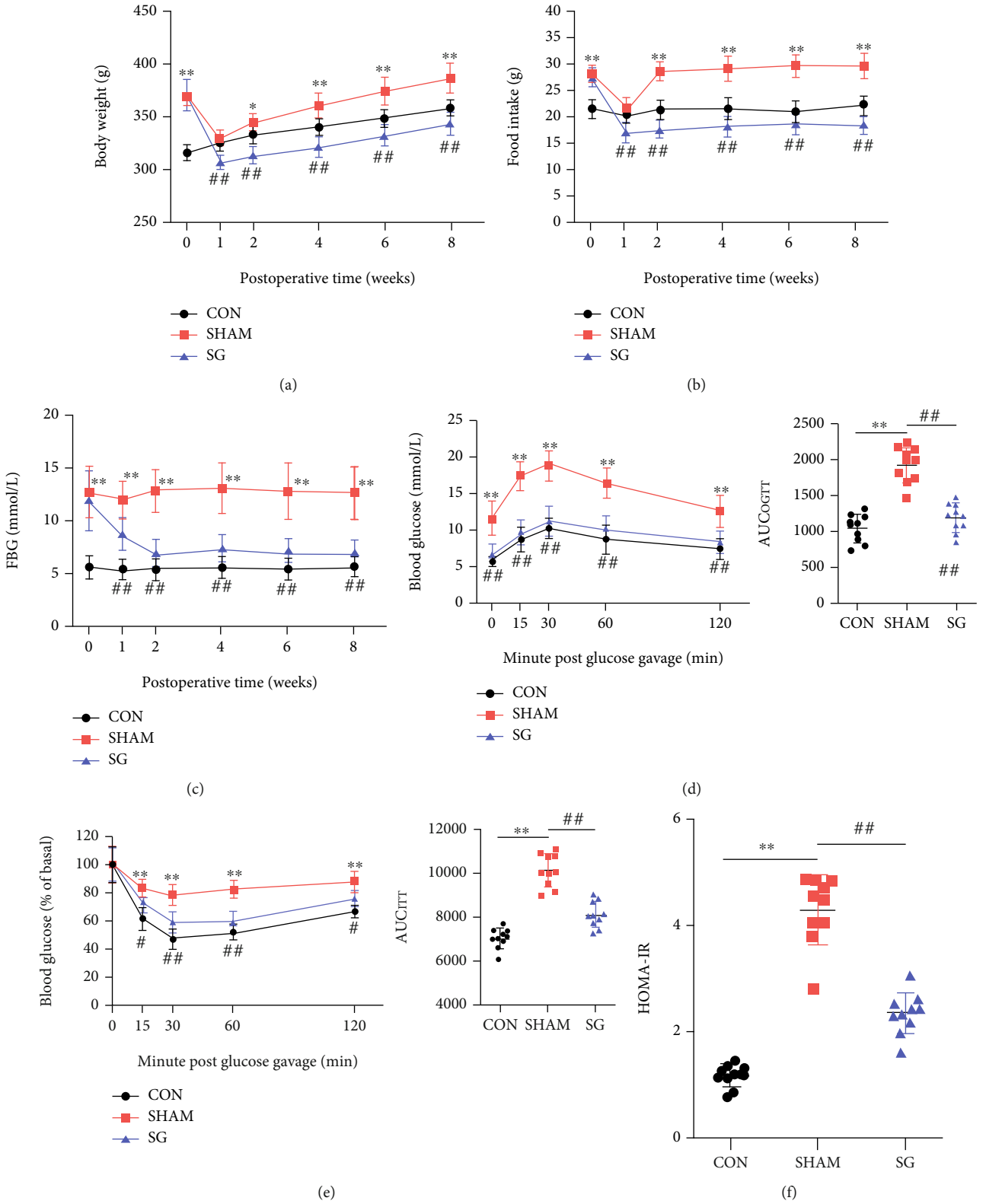

Figure 1: Effects of SG on body weight, food intake, and glucose homeostasis in diabetic rats. (a) Body weight, (b) food intake, and (c) fasting blood glucose before and after SG surgery. (d) OGTT curve and (e) ITT curve were carried out 4 weeks postoperatively. AUC_{OGTT} and AUC_{ITT} were calculated, respectively. (f) Values of HOMA-IR at 4 weeks after SG surgery. Data are presented as mean ± SD. $^{*}P < 0.05$ and $^{**}P < 0.01$ CON vs. SHAM; $^{\#}P < 0.05$ and $^{\#\#}P < 0.01$ SG vs. SHAM. $n = 10$ in each group.

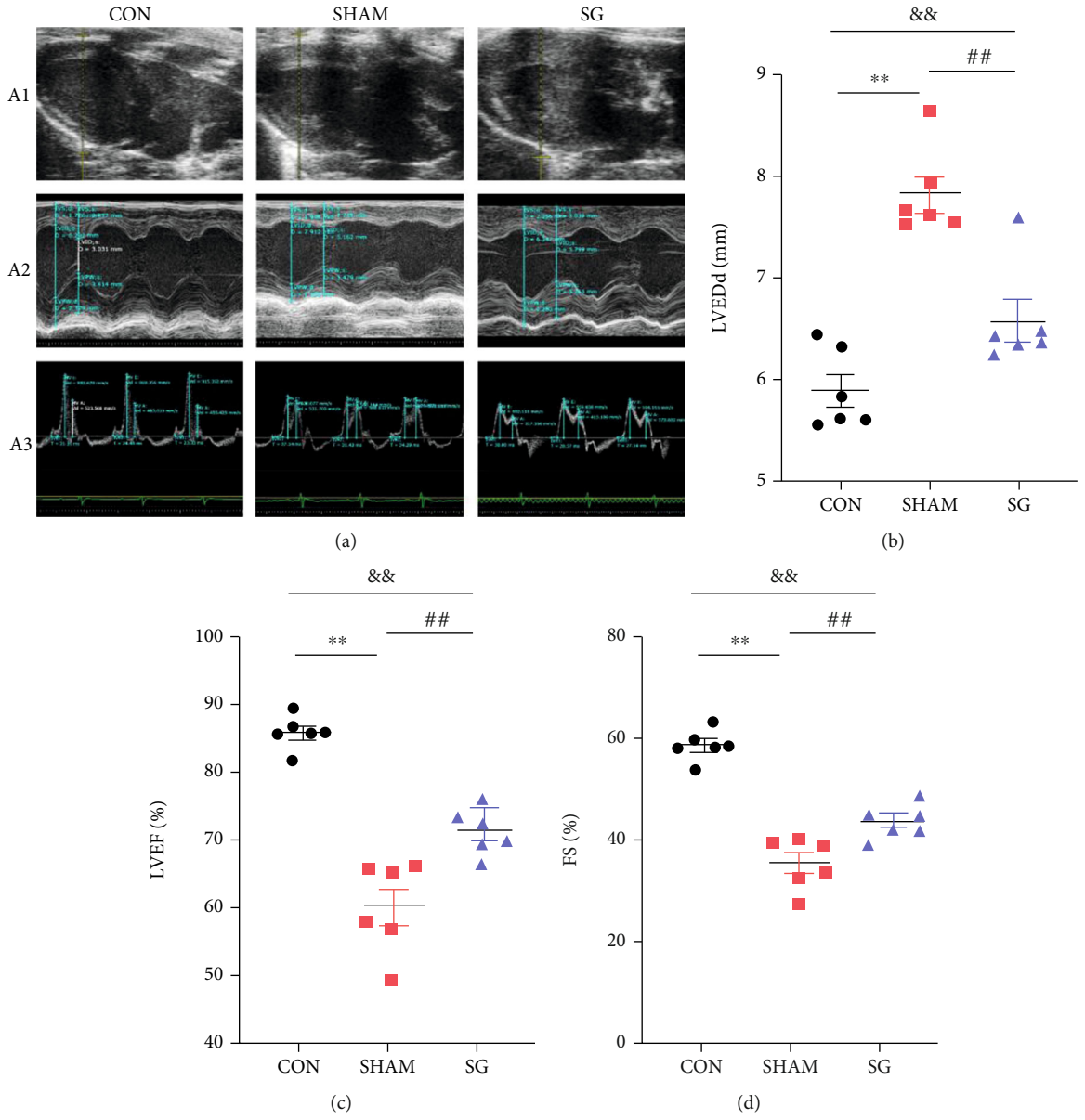

Figure 2: Continued.

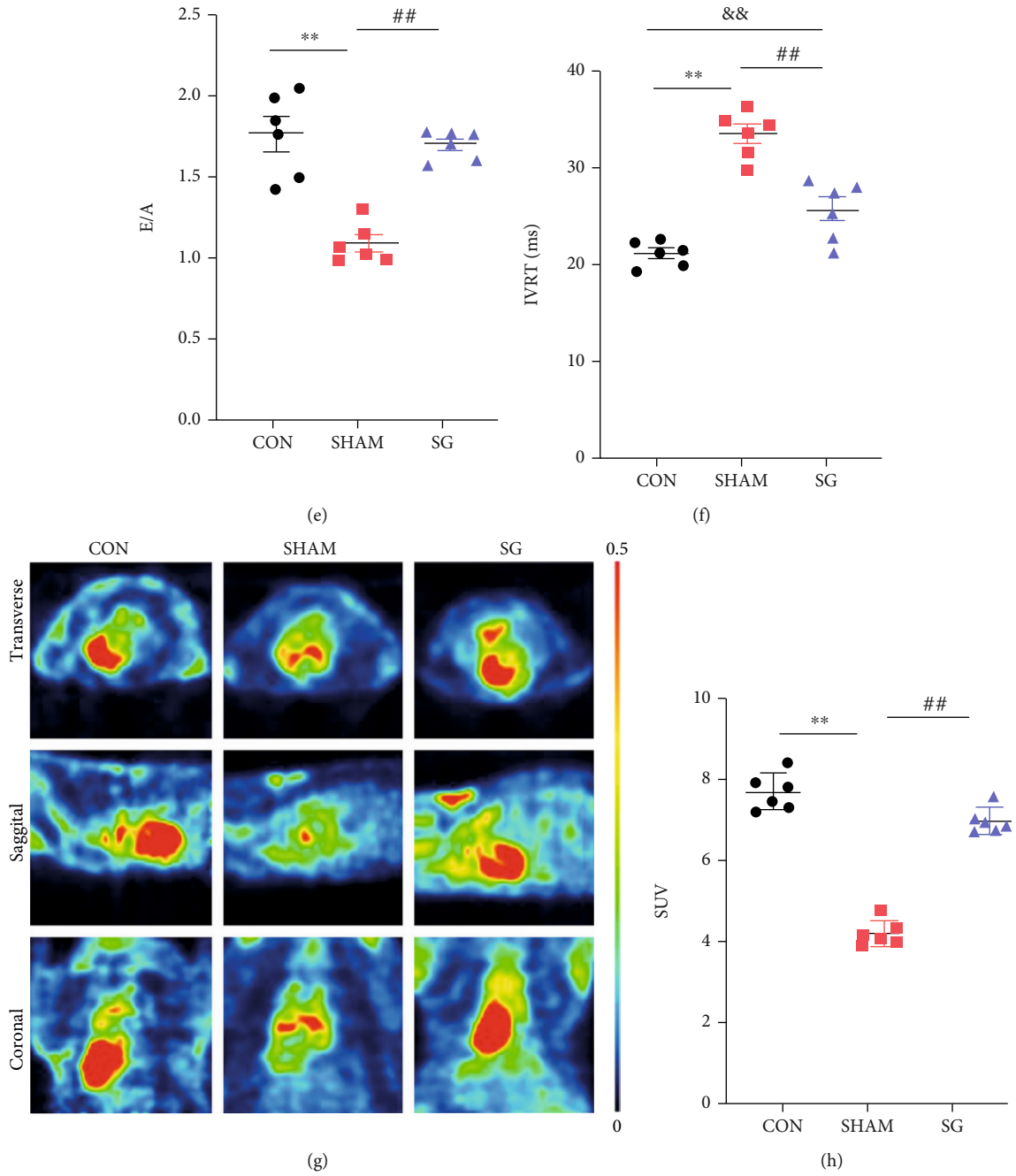

Figure 2: SG abrogates cardiac dysfunction and improves myocardial metabolism in rats with DCM. (a) Echocardiography: (a1) representative images of 2D echocardiograms; (a2) M-mode echocardiograms; (a3) mitral inflow shown by pulse-wave Doppler echocardiograms. Echocardiographic measurements including (b) LVEDd, (c) LVEF, (d) FS, (e) ratio of E/A, and (f) IVRT. (g) Representative transverse, sagittal, and coronal axis images of the heart showing ^{18}F-FDG distribution via PET-scans. (h) Standard uptake value (SUV). Data are presented as mean ± SD. $^{**}P < 0.01$ CON vs. SHAM; $^{\#\#}P < 0.01$ SG vs. SHAM; $^{\&\&}P < 0.01$ CON vs. SG. $n = 6$ in each group.

homeostasis, FBG concentrations were regularly recorded (Figure 1(c)). FBG sharply decreased in the first 2 weeks and were stable afterwards. Rats in the SG group exhibited a substantial improvement in the ability to clear oral gavage of glucose, as reflected by a 38% drop in the area under the curve (AUC) relative to the sham group (Figure 1(d)). ITT was performed, and it showed a lower AUC in the SG group compared with the sham group, indicating that SG improved insulin sensitivity (Figure 1(e)). The HOMA-IR value significantly alleviated after SG, which was in agreement with the above-mentioned results (Figure 1(f)).

3.2. SG Attenuates Diabetic-Induced Cardiac Dysfunction and Myocardial Metabolism. An echocardiographic examination was carried out 8 weeks postsurgery for assessing cardiac function (Figure 2(a)). Rats that underwent sham

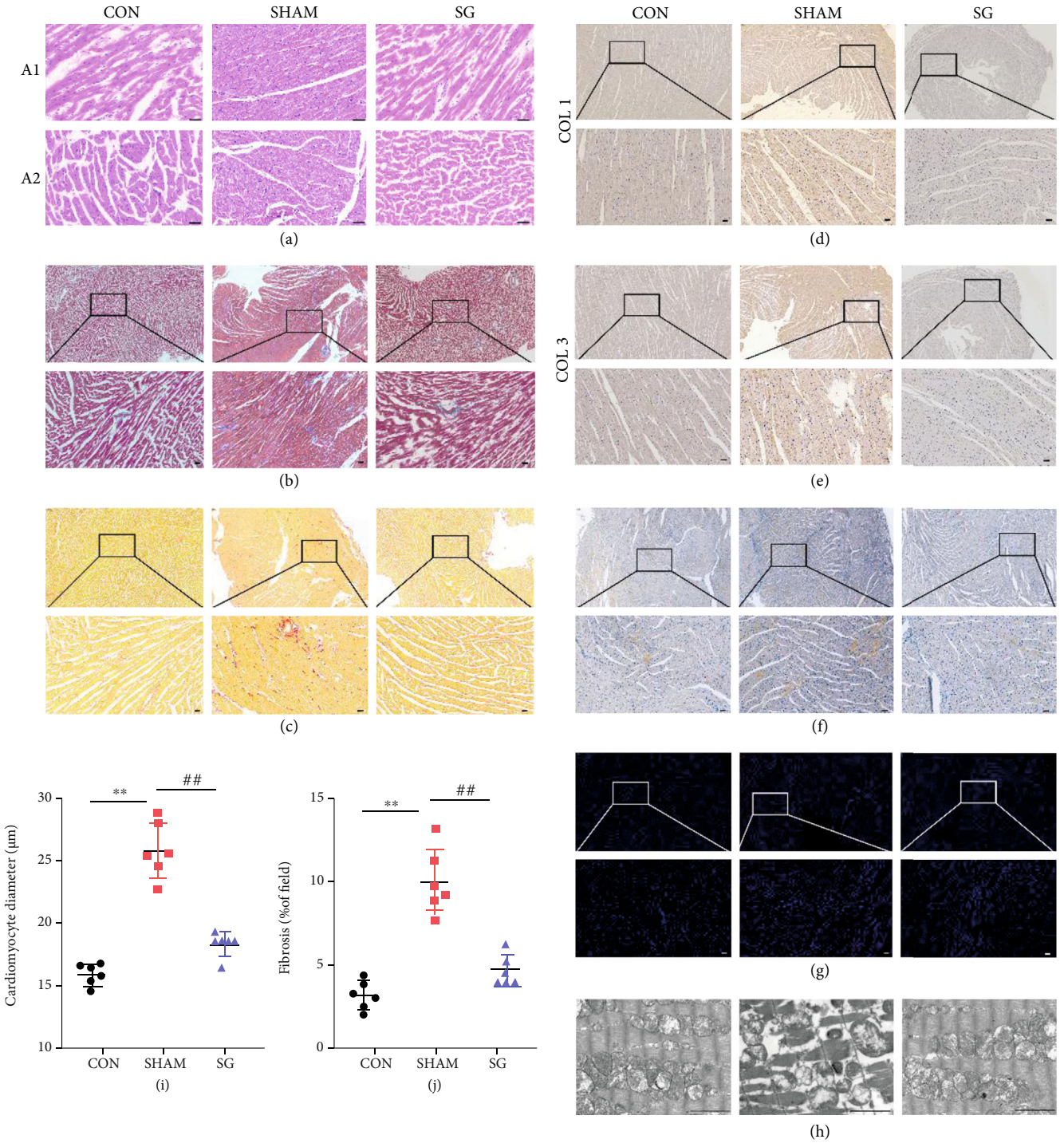

Figure 3: Effects of SG on diabetic-induced cardiac remodeling. (a) Representative (a1) longitudinal and (a2) transverse H&E staining of left ventricle. Scale bar, 50 μm. (b) Staining of Masson trichrome; dark blue indicates collagen fibers. Scale bar, 50 μm. (c) Sirus red staining; note the dense collagen staining. Scale bar, 50 μm. Immunohistochemical staining of (d) collagen I and (e) collagen III. Scale bar, 50 μm. (f) Oil Red O staining quantifies lipid accumulation. Scale bar, 50 μm. (g) The TUNEL assay was performed to identify DNA nicks; red plots indicate TUNEL-positive cells. Scale bar, 50 μm. (h) Representative transmission electron micrographs. Scale bar, 2 μm (h) Quantitative analysis of the cardiomyocyte size. (i) Semiquantification of collagen volume in total left ventricle. Data are presented as mean ± SD. $^{**}P < 0.01$ CON vs. SHAM; $^{\#\#}P < 0.01$ SG vs. SHAM. $n = 6$ in each group.

surgery had a higher LVEDd and IVRT along with greater impaired LVEF and FS and a higher E/A ratio compared with those in the control group. Echocardiographic analysis demonstrated systolic and diastolic dysfunction in the sham group. However, in comparison to the sham group, SG surgery mitigated these unfavorable changes, as evidenced by significantly reduced LVEF and IVRT with a restored LVEF, FS, and E/A ratio (Figures 2(b)–2(f)).

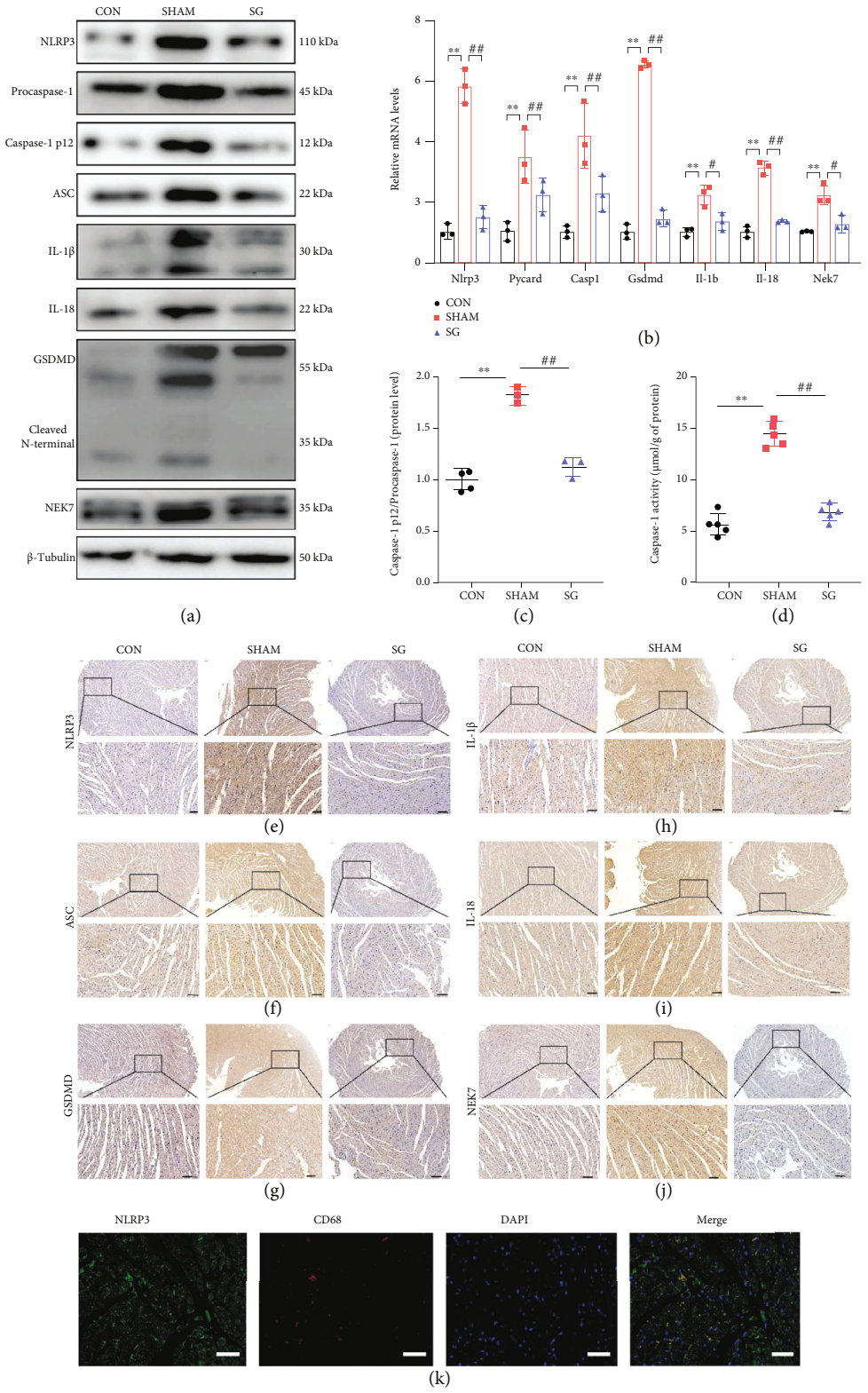

Figure 4: SG attenuates the activation of NLRP3 in diabetic myocardium. (a) Protein levels of NLRP3-related molecules shown by western blot. β-Tubulin was an internal reference control. $n = 3$ in each group. (b) Relative mRNA levels of *Nlrp3*-relaterd genes shown by real-time RT-PCR. *Tubb3* served as a reference gene. $n = 3$ in each group. (c) Ratio of caspase-1 p12/procaspase-1. $n = 3$ in each group. (d) Caspase-1 activity in heart tissues. $n = 6$ in each group. Immunohistochemical staining of (e) NLRP3, (f) ASC, (g) GSDMD, (h) IL-1β, (i) IL-18, and (j) NEK7. Scale bar, 50 μm. (k) Double-labeling immunofluorescence of NLRP3 and CD68. Scale bar, 50 μm. Data are presented as mean ± SD. $^{**}P < 0.01$ CON vs. SHAM; $^{\#\#}P < 0.01$ SG vs. SHAM. $n = 3$ in each group.

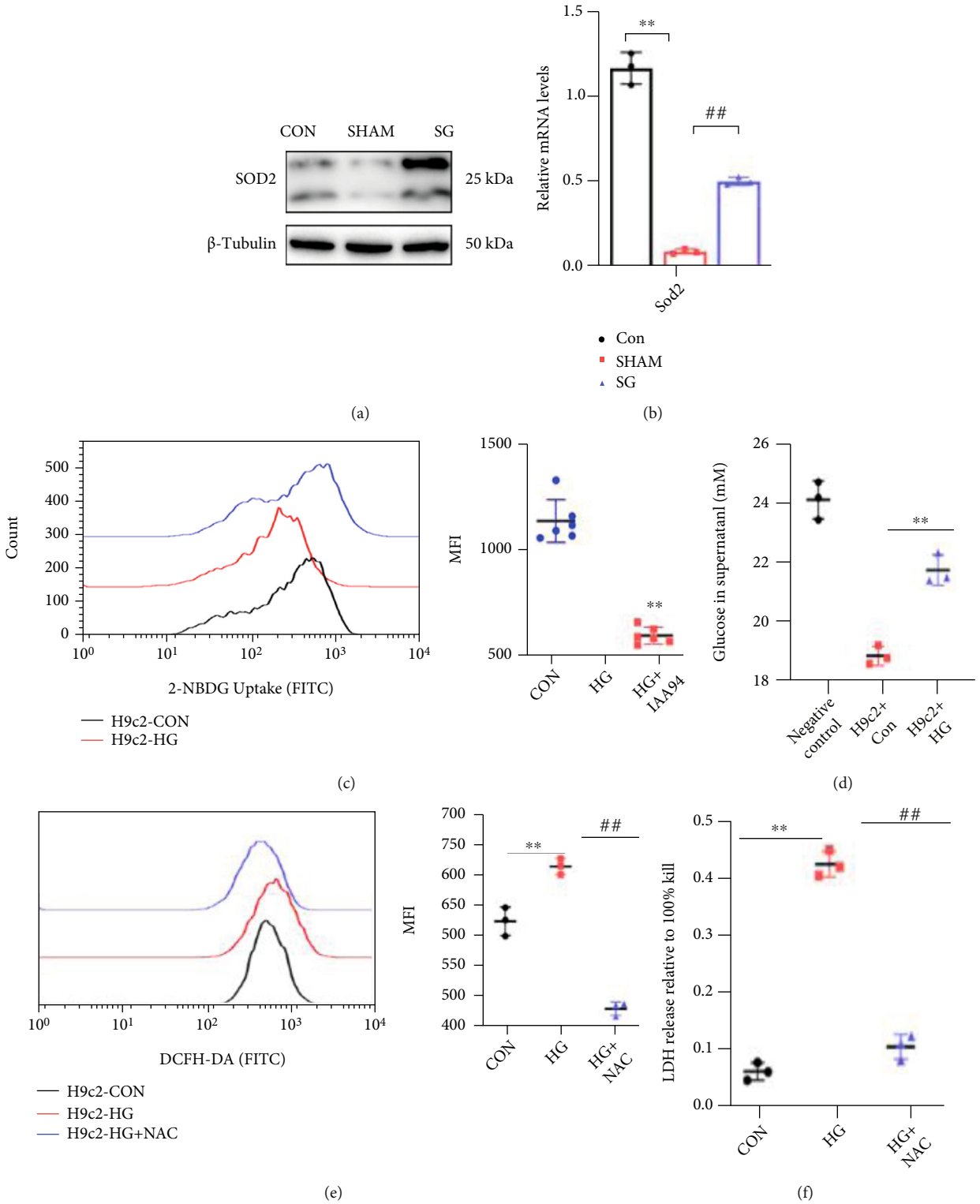

Figure 5: Continued.

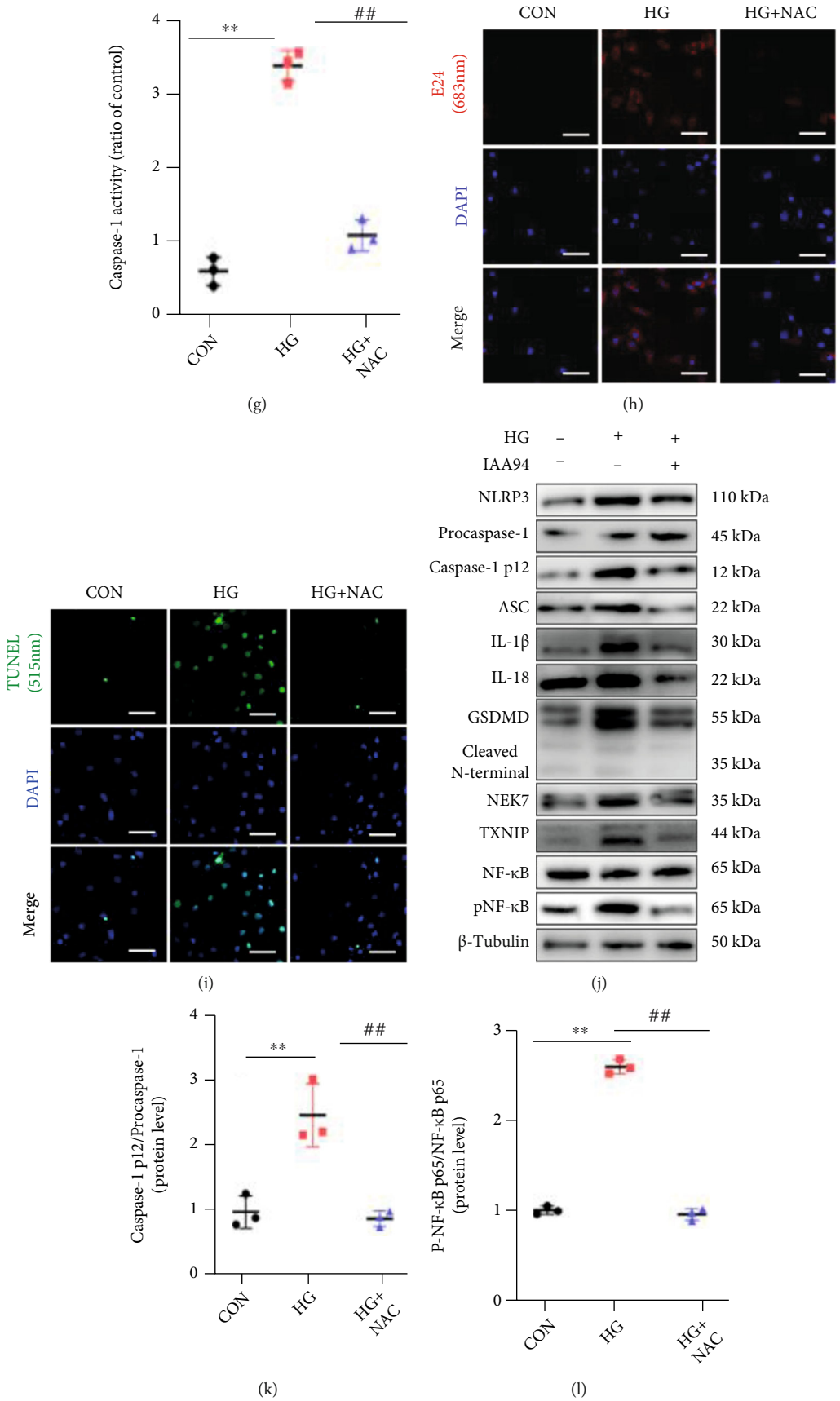

Figure 5: Continued.

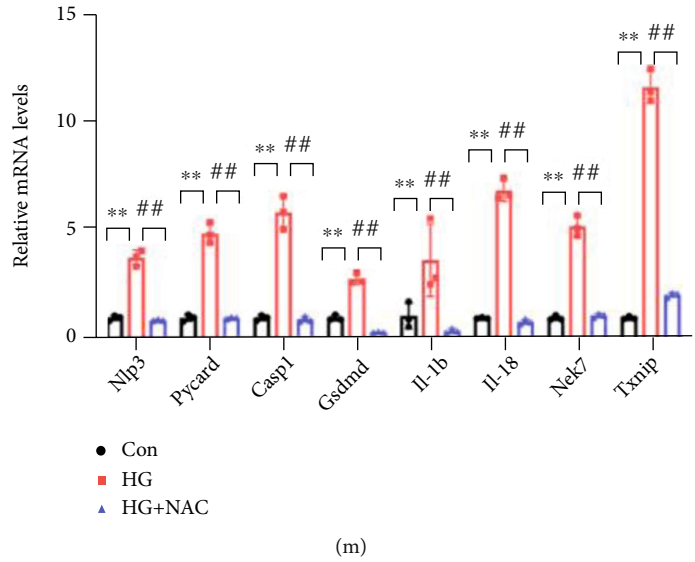

Figure 5: High glucose-induced ROS overload served as a trigger of NLRP3-mediated pyroptosis in H9c2 cells. (a) Protein expression of SOD2 in heart tissues. (b) mRNA expression of *Sod2* relative to *Tubb3* in hearts. (c) Flow cytometry quantified the 2-NBDG signals in HG-stimulated H9c2 cells. (d) Glucose concentrations in supernatants. (e) Intracellular ROS levels were assessed using DCFH-DA and flow cytometry. (f) The release of LDH percentage from H9c2 cells was reported to the total LDH release. (g) Caspase-1 activity of H9c2 cells. (h) H9c2 cells with membrane disintegrity were stained with red fluorescence by cell probe E42. (i) TUNEL staining of H9c2 cells. (j) Protein levels of NLRP3-related molecules shown by western blot in H9c2 cells treated with HG or HG+NAC. (k) The ratio of caspase-1 p12/procaspase-1 and (l) phospho-NF-κB/total NF-κB is shown. (m) Relative mRNA expression of *Nlrp3*-related molecules in H9c2 cells, *Tubb3* as the internal reference. Data are presented as mean ± SD. $^{**}P < 0.01$ CON vs. HG; $^{\#\#}P < 0.01$ HG+NAC vs. HG. $n = 6$ in 2-NBDG uptake experiment and $n = 3$ in each group in other experiments.

Insulin resistance is one of the main triggers of DCM, of which impaired myocardial glucose uptake is a pathophysiological hallmark. PET scans were carried out after ^{18}F-FDG injection to scale the levels of myocardial glucose uptake, and the standard uptake value (SUV) of the sham group was definitely decreased compared with the control group, yet SUV of the SG group was restored, indicating that SG surgery alleviated diabetic-induced myocardial insulin resistance (Figures 2(g) and 2(h)).

3.3. SG Reverses Myocardial Remodeling in Rats with DCM. Structural and functional derangement of cardiac tissue is a key characteristic of DCM, consisting of hypertrophy, myocardial fibrosis, and contractile dysfunction in both diastolic and systolic phases. H&E staining showed hypertrophy of cardiomyocytes in the sham group, which was reversed after SG operation (Figures 3(a) and 3(i)). Sirius red and Masson trichrome staining detected a rising level of cardiac fibrosis in the sham group, whereas SG surgery brought about alleviation of fibrosis (Figures 3(b), 3(c), and 3(j)). Consistently, IHC staining of collagen I and collagen III showed elevated collagen deposition in the sham group, which was abrogated after SG operation (Figures 3(d) and 3(e)). Also, Oil Red O staining manifested those diabetic myocardial sections obviously stained with red droplets which were mitigated postoperatively, suggesting the alleviation of lipid deposition (Figure 3(f)). Furthermore, the TUNEL assay showed that SG reduced the ratio of TUNEL-positive cardiomyocytes indicative of decreased nicked DNA ends (Figure 3(g)). Transmission electron microscopy revealed disordered sarcomeres, swollen mitochondria with disorganized cristae, loss of intracellular contents, and the presence of pyroptosome in the heart of the sham group, whereas in the SG group, layers of uniformly shaped mitochondria with abundant and organized cristae intervened between regularly aligned myofibrils (Figure 3(h)). All of these results suggested that SG remarkably reversed the DCM-induced cardiac remodeling.

3.4. Effects of SG on NLRP3-Activated Pyroptosis in Cardiomyocytes. Pyroptosis serves as an inflammatory form of programmed cell death [10]. Previous studies have elucidated that the NLRP3 inflammasome is activated in the myocardium when exposed to hyperglycemia and pyroptosis which contributed to the development of DCM [13]. In this study, western blotting showed that NLRP3 inflammasomes were activated in the DCM model, as shown by the overexpression of NLRP3, apoptosis-associated speck-like protein (ASC), caspase-1, cleaved caspase-1, IL-1β, IL-18, NEK7, and GSDMD as well as its N-terminal fragment. Postoperatively, protein levels of the above related to the NLRP3-caspase 1 pathway were favorably reduced (Figure 4(a)). Similarly, real-time RT-PCR showed that relative transcriptional levels of NLRP3 inflammasome-related key genes were restrained in the SG group compared to the sham group (Figure 4(b)). Notably, a reluctantly high level of caspase-1 activity in the sham group was averted after SG performance (Figures 4(c) and 4(d)). Additionally, IHC staining of the three groups was performed to further confirm protein expression of NLRP3, ASC, GSDMD, and

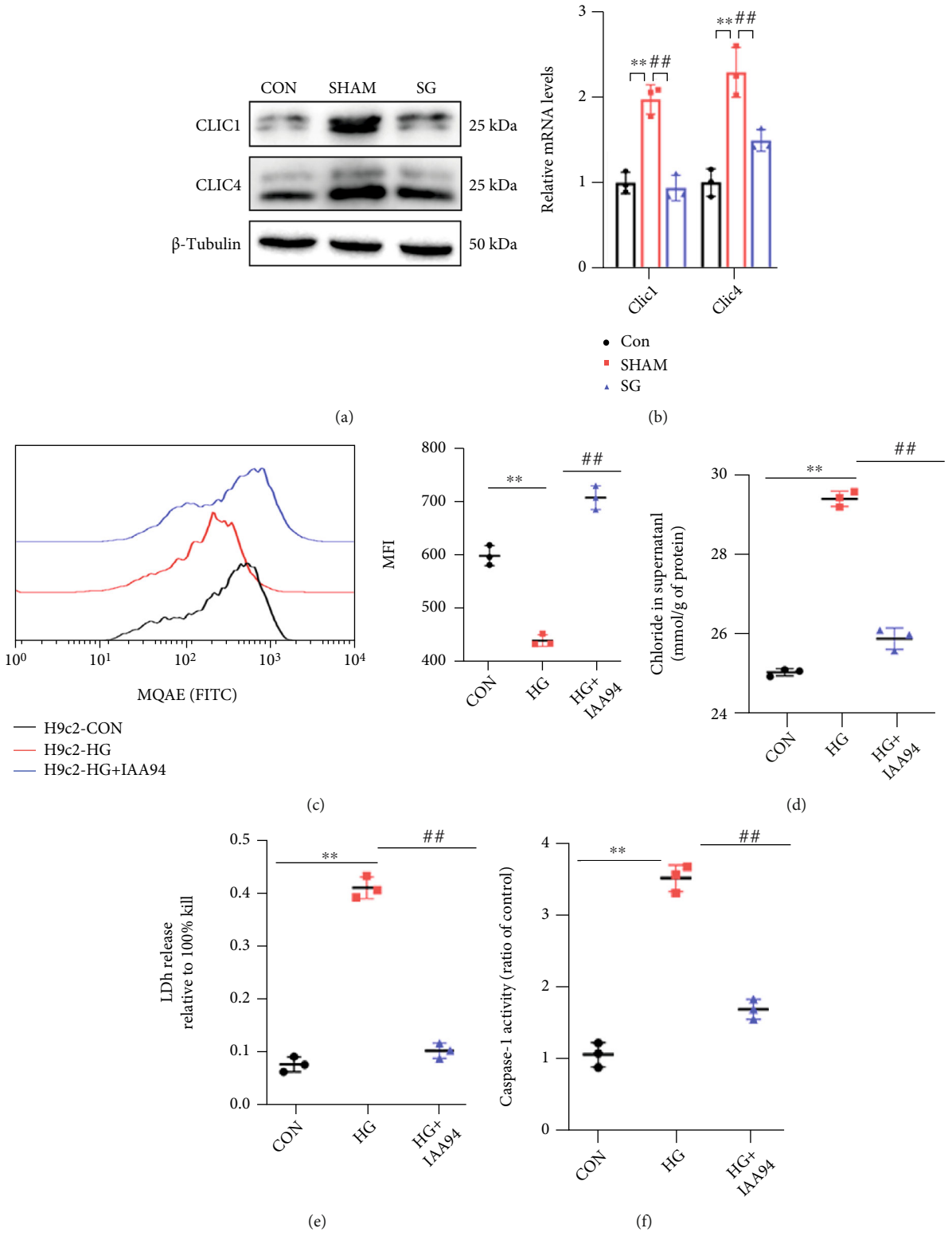

Figure 6: Continued.

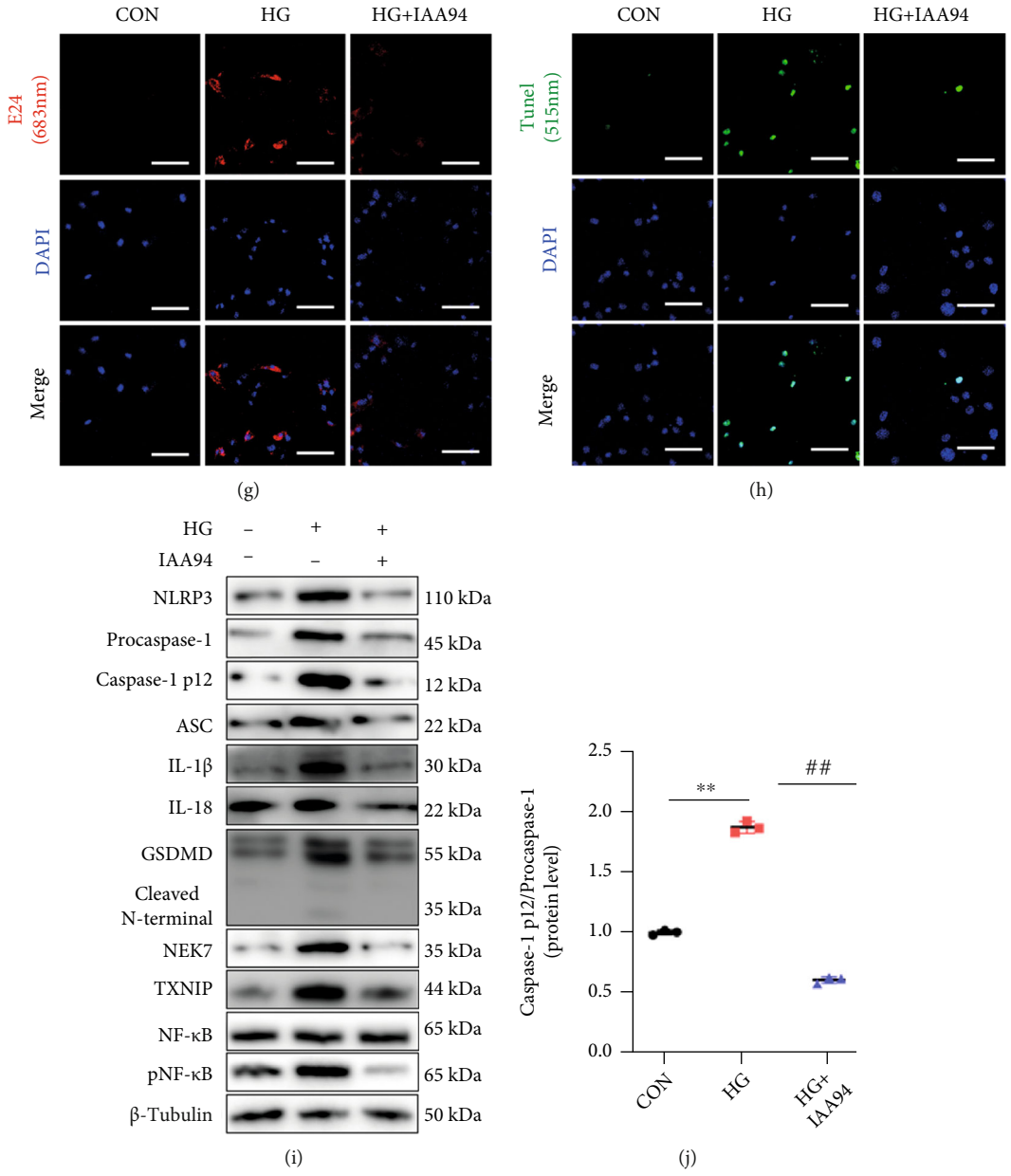

Figure 6: Continued.

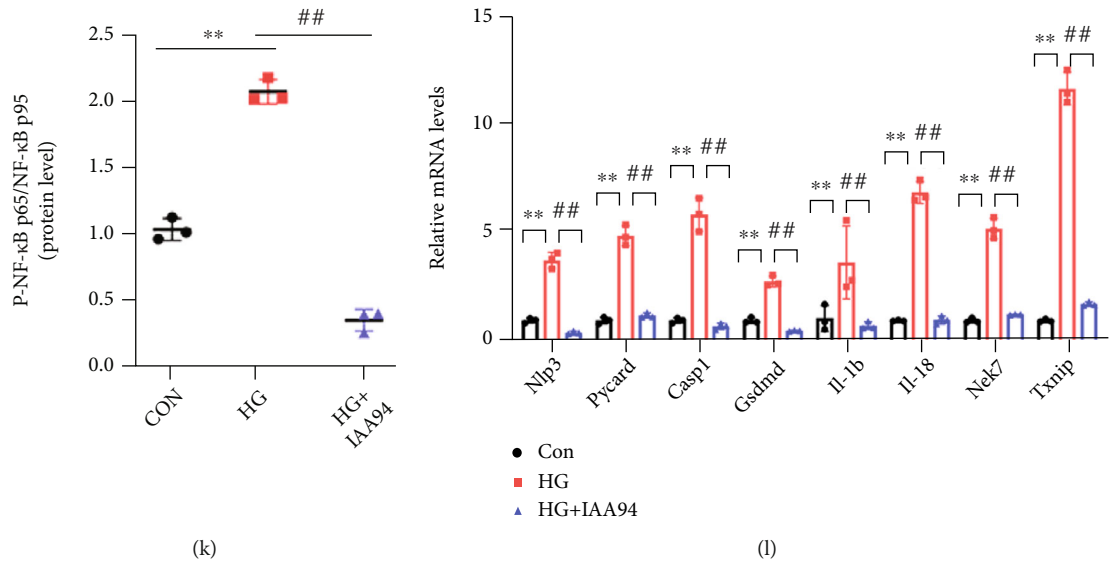

Figure 6: Chloride intracellular channel-dependent chloride efflux induced pyroptosis mediated by NLRP3 inflammasomes in H9c2 cells. (a) Protein expression of CLIC1 and CLIC4 in heart tissues. (b) Relative mRNA expression of *Clic1* and *Clic4* in hearts. (c) IAA-94 was used to block chloride efflux, and the intracellular chloride was measured with MQAE, a chloride-sensitive dye. (d) Chloride concentrations in supernatants. (e) The LDH release measured by a colorimetric assay. (f) Caspase-1 activity. (g) E42 staining indicated the membrane integrity. (h) TUNEL staining of H9c2 cells. (i) Protein levels of NLRP3-related molecules. (j) The ratio of caspase-1 p12/procaspase-1 and (k) the ratio of phospho-NF-κB/total NF-κB. (l) Relative mRNA expression of *Nlrp3*-related molecules in H9c2 cells, *Tubb3* as the internal reference. Data are presented as mean ± SD. $^{**}P < 0.01$ CON vs. HG; $^{\#\#}P < 0.01$ HG+IAA-94 vs. HG. $n = 3$ in each group.

NEK7 (Figures 4(e)–4(g) and 4(j)). And the infiltration of inflammatory factors IL-1β and IL-18 was decreased post-SG surgery (Figures 4(h) and 4(i)). Using a macrophage marker CD68, we double labeled the NLRP3 and CD68 in heart sections and found that the NLRP3 was expressed not only in the macrophages but also in myocardial cells (Figure 4(k)). The above-mentioned results suggested that SG ameliorated the activation of NLRP3-related pathway molecules transcriptionally and posttranscriptionally in the diabetic myocardium.

3.5. High Glucose-Induced ROS Accumulation Acts as a Key Trigger of NLRP3-Mediated Pyroptosis in Cardiomyocytes. Hyperglycemia, associated with T2DM, increases the burden of oxidative stress [23]. Rising reactive oxygen species (ROS) production and impaired ROS clearance seem to contribute to the pathological progression of DCM [24]. It is well recognized that mitochondrial manganese superoxide dismutase (SOD2) played a role in ROS scavenging [25]. We found that the expression of SOD2 in the heart was lower in the sham group than in the SG group (Figures 5(a) and 5(b)). This finding suggested that the decline in ROS levels might have contributed to the restoration of cardiac dysfunction after SG surgery.

In order to mimic the in vivo environment of T2DM, H9c2 cells were starved in low-glucose DMEM with 2% FBS overnight, followed by stimulation with HG for 48 h. The ability of H9c2 cells to uptake the 2-NBDG was measured by flow cytometry. There was a decline in the mean fluorescence intensity (MFI) of 2-NBDG in HG-stimulated cells compared with control cells (Figure 5(c)). Additionally, glucose concentrations in the supernatant were determined by the GOD-POD method to indirectly reflect the ability of glucose uptake (Figure 5(d)). A marked reduction in the capacity for glucose uptake showed partial insulin resistance in HG-H9c2 cells. We pretreated cells for 12 h with NAC (1 mM), a specific ROS scavenger, to deplete intracellular ROS levels. After treatment, H9c2 cells were treated with the redox-sensitive fluorescent dye DCFH-DA for 0.5 h, and ROS levels were determined using flow cytometry. HG remarkably upregulated the fluorescent staining of ROS, whereas ROS levels were partially cleared by NAC (Figure 5(e)). Furthermore, we examined LDH release in culture supernatants and dyed membrane-disrupted cells with the probe E42 (Figures 5(f) and 5(h)). The outcomes of these two experiments suggested that high ROS accretion in the train of HG stimulation could arouse the plasma membranal disintegrity, which was a main feature in the pyroptosis of cells.

Caspase-1 activity, which is inevitable in NLRP3-dependent pyroptosis, zoomed in the HG condition and decreased with NAC treatment (Figure 5(g)). As the ROS burden rose with HG stimuli, there was a high proportion of TUNEL-positive cells of which DNA fragmentation might have been mediated by ROS and NLRP3 inflammasome-induced pyroptosis. However, the presence of NAC lowered the ratio of TUNEL staining (Figure 5(i)). Previous studies have demonstrated that the NLRP3 inflammasome is activated in a ROS/TXNIP/nuclear factor-κB/p65 manner. Western blotting showed that HG upregulated the expression of NLRP3-related molecules, and this was alleviated by the ROS scavenger NAC (Figures 5(j)–5(l)). Real-time RT-PCR results were in agreement with the protein results (Figure 5(m)).

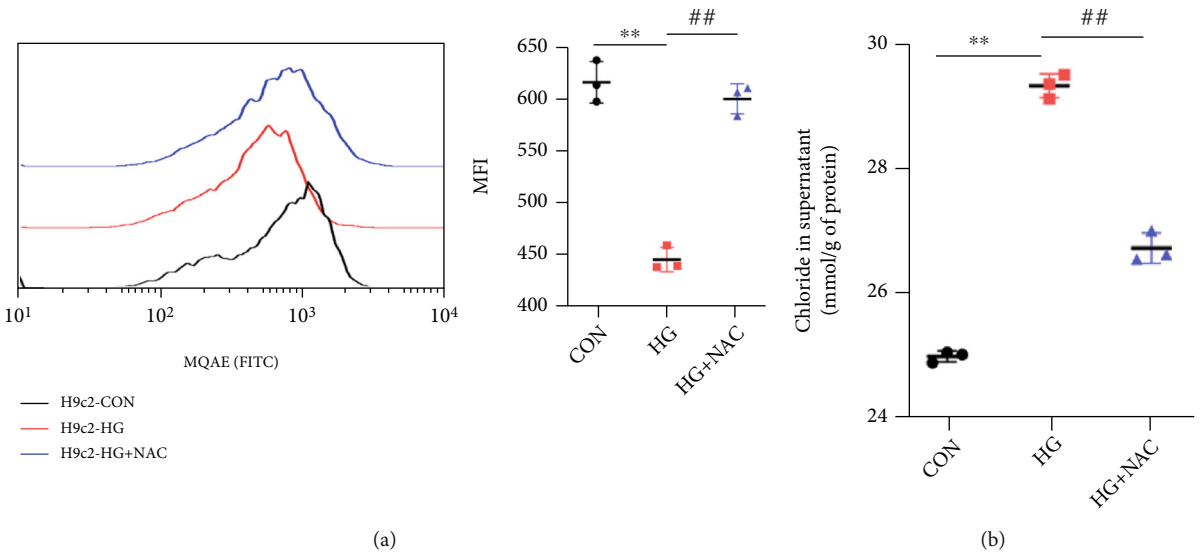

(a) (b)

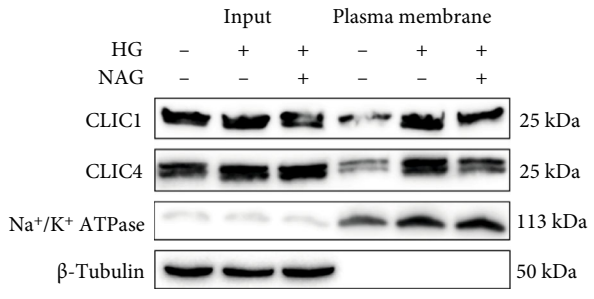

(c)

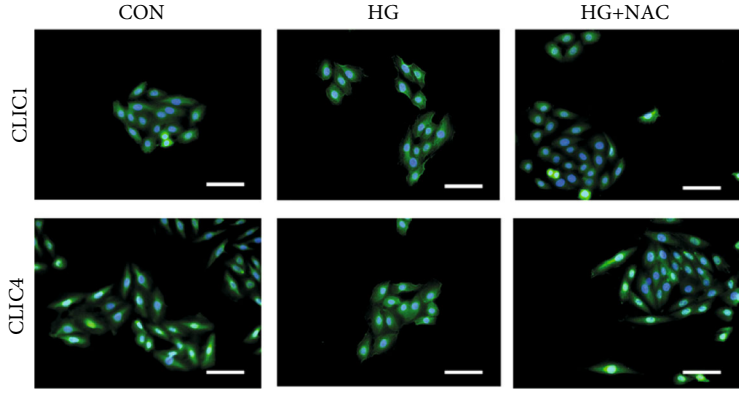

(d)

Figure 7: Continued.

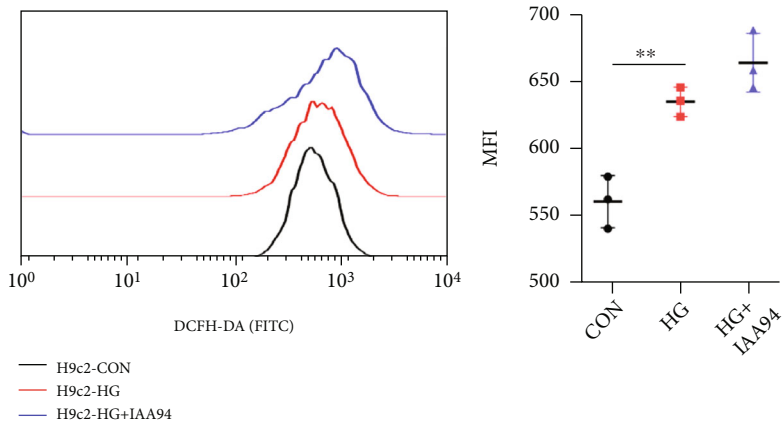

(e)

Figure 7: ROS promoted chloride efflux and plasma membrane translocation of CLICs in H9c2 cells. (a) The effect of ROS levels on chloride efflux was determined by MQAE in H9c2 cells with HG or HG+NAC treatments. (b) Chloride concentrations in supernatants after NAC treatment. (c) Immunoblot analysis of the indicated proteins in total lysates (input) or isolated plasma membrane in H9c2 cells treated with HG or HG+NAC. (d) Immunofluorescence of CLIC1 and CLIC4 in H9c2 cells. (e) ROS levels were assessed with DCFH-DA in H9c2 cells with HG or HG+IAA94 treatments. Data are presented as mean ± SD. $^{**}P < 0.01$ CON vs. HG; $^{\#\#}P < 0.01$ HG+IAA-94 vs. HG. $n = 3$ in each group.

In summary, ROS might induce NLRP3 pathway-mediated pyroptosis in cardiomyocytes under the HG condition, which could be rescued by the ROS scavenger.

3.6. CLIC-Dependent Chloride Efflux Serves as an Upstream Event for Myocardial Pyroptosis Mediated by NLRP3 Inflammasome. The chloride efflux associated with the chloride intracellular channel (CLIC) proteins CLIC1 and CLIC4, were found to drive NEK7-NLRP3 activation [26]. Moreover, inhibition of volume-sensitive chloride currents had been reported to blunt apoptotic cell death and contractile dysfunction in cardiomyocytes [27]. Wondering whether chloride flow is involved in cardiac pyroptosis, we initially detected mRNA and protein levels of CLIC1 and CLIC4 in three rat models (Figures 6(a) and 6(b)). Both CLIC1 and CLIC4 declared a higher expression in DCM rats and decreased with the operation of SG. Identical HG stimulation was utilized for H9c2 cells, yet IAA-94 (100 μM), which was a blocker of epithelial chloride channels, was used to inhibit the chloride efflux. The cells were loaded with the chloride-sensitive fluorescence probe MQAE to mark the intracellular chloride concentration via flow cytometry. The chloride efflux process was enhanced by an HG stimulus and could be abstained from by IAA-94 addition (Figure 6(c)). Measurement of chloride concentrations in supernatants by a colorimetric assay further confirmed this chloride concentration transition (Figure 6(d)). After chloride efflux inhibition, a reduction in LDH release and less dye with the probe E42 indicated repair of membrane disruption (Figures 6(e) and 6(g)). TUNEL staining and caspase-1 activity were also suppressed by IAA-94 (Figures 6(f) and 6(h)). Intriguingly, NLRP3-related molecules were also inhibited with the chloride efflux block, as shown by western blotting and real-time RT-PCR (Figures 6(i)–6(l)).

These findings suggest that intracellular chloride homeostasis functions as a signaling messenger to regulate NLRP3 inflammasome assembly and activation in cardiomyocytes.

3.7. ROS Might Function Upstream of Chloride Efflux and Promote Plasma Membrane Translocation of CLICs. Wondering if ROS promoted the CLIC-dependent chloride efflux in NLRP3 inflammasome activation in cardiac cells, we adopted the flow cytometry to examine chloride fluorescence intensity. We found that clearance of ROS production reversed the efflux of the chloride (Figure 7(a)). Chloride detection with a colorimetric assay also showed a decline in chloride concentrations in the supernatant (Figure 7(b)). Taken together, these findings suggested that chloride efflux was induced downstream of ROS production. Western analysis was conducted to detect membrane protein expression. Rearrangement of the CLIC structure with translocation to the cell membrane was observed in HG-induced high ROS conditions, while this was restored by NAC treatment (Figure 7(c)). Furthermore, plasma membrane translocation of CLIC1 and CLIC4 was shown with immunofluorescence (Figure 7(d)). Notwithstanding, provided that the chloride efflux was being inhibited by IAA-94, ROS levels were not altered afterwards (Figure 7(e)).

These results suggest that ROS can induce plasma membrane translocation of the CLIC-induced chloride efflux in cardiomyocytes, ultimately leading to NLRP3 activation.

4. Discussion

Bariatric surgery has remarkable metabolic benefits in obesity, T2DM, and following complications [6, 28, 29]. In the present study, we found that SG surgery alleviated the capability of myocardial contraction and diastole and delayed the progression of DCM. The deactivation of

NLRP3 inflammasome-mediated myocardial pyroptosis was observed after SG *in vivo*. As found *in vitro*, we speculate that the ROS–chloride efflux axis might perform as an upstream trigger for NLRP3 inflammasome activation in myocytes.

In the present study, we adopted the method of HFD feeding combined with low-dose STZ injection intraperitoneally to establish the DCM model. This procedure is widely acknowledged by researchers worldwide because it simulates the natural history and metabolic features of T2DM [30, 31]. Additionally, this method has been confirmed by previous studies on the induction of DCM models [31, 32]. In line with previous researches [33, 34], metabolic benefits of bariatric surgery were observed in our study, characterized by a reduced body weight, food intake, and blood glucose levels and restored glucose tolerance as well as insulin sensitivity postoperatively. These improvements guaranteed the effect of SG surgery (Figure 1).

DCM is initially characterized by impaired cardiac insulin metabolic signaling with altered diastolic relaxation [35, 36]. Therefore, echocardiography was used to identify cardiac function in this study, and impairment of diastolic and systolic function in rats with DCM was improved after SG surgery. But the cardiac function cannot be restored as good as normal control rats. Notably, a well-recognized indicator of insulin sensitivity is glucose uptake [37]. ^{18}F-FDG-labelled PET-CT scans were carried out to visualize the ability of glucose uptake. We observed a marked decline in the glucose uptake in rats with DCM, and this was restored after SG surgery. These results consistently showed the potential therapeutic value of bariatric surgery in DCM [9, 38] (Figure 2).

Diabetic cardiac dysfunction exists due to pathological changes in the heart, such as cardiac hypertrophy, fibrotic myocardium remodeling, cell death, and ectopic lipid deposition [39–42]. In this study, cardiac hypertrophy was alleviated after SG surgery. Collagen deposition and fibrosis contribute to impaired contractility [42]. The excessive collagen distribution in both the interstitial and perivascular areas was remarkably diminished after the SG operation. Lipid deposition was also reduced with SG, which could lead to relief of lipotoxic cardiomyopathy [43]. These findings suggest that functional improvement was obtained by SG, ascribing these benefits to morphological transformation.

Pyroptosis is a type of programmed inflammatory cell death, which is provoked by sensing of danger or pathogenic signals and characterized by DNA damage, cell swelling, lysis, and inflammatory responses [44, 45]. Pyroptotic cells can also lead to DNA damage and become positive with TUNEL staining [46]. The NLRP3 inflammasome is a typical macromolecular trigger of pyroptosis. This inflammasome is a multimeric complex assembly of adapter and effector proteins, consisting of NLRP3, adapter protein apoptosis-associated speck-like protein, and caspase-1 [47]. The NLRP3 inflammasome serves as a platform to engage procaspase-1, which come into active ones through oligomerization. Activated caspase-1 then processes pro-IL-1β and pro-IL-18 to generate their active forms [48]. Additionally, the NLRP3 assembly primes the cleavage of pore-forming gasdermin D protein to initiate pyroptosis [49]. Recent evidence has shown a new component of the inflammasome, NEK7, which is a serine-threonine kinase associated with mitosis. NEK7 binds to NLRP3 to trigger its assembly [50]. In this study, we found more TUNEL-positive cells in the sham group than in the SG group. Additionally, SG treatment normalized alterations in myofilaments, swollen mitochondria, and the decreased number of cristae in diabetic rats (Figure 3). In this study, NLRP3-related molecules were activated in the diabetic myocardium, while they were inhibited with SG surgery. Taken together, we confirmed that SG surgery indeed alleviated the NLRP3 inflammasome activation and reversed myocardial pyroptosis (Figure 4). We hypothesize that the NLRP3 inflammasome is a pivotal reason why SG defers or even reverses the progression of DCM.

Abundant evidence has verified that ROS is important in the pathogenesis of T2DM [51]. ROS overload has been proposed as a mechanism involved in activating the NLRP3 inflammasome [52]. ROS-induced NF-κB activation during metabolic reprogramming incurs rapid NLRP3 transcription, thereby facilitating the NLRP3 inflammasome overexpression and the maturation of caspase-1 and IL-1b [53]. In regard to TXNIP, it is a ROS-sensitive molecule implicated in T2DM and a key regulator of NLRP3 inflammasome activation [54, 55]. In the current study, ROS levels were abrogated by SG. Additionally, we found that HG-stimulated H9c2 cardiomyocytes were under the condition of membrane disintegrity and DNA fraction, which implied myocardial pyroptosis. The NLRP3 pathway was also activated in the HG condition, in line with previous studies [13]. Use of a ROS scavenger led to a remarkable reduction in high NLRP3 expression. These results suggested that ROS acted as a crucial regulator of NLRP3 inflammasomes in myocytes (Figure 5).

Recent research has shown that the chloride efflux acts downstream of mitochondrial ROS production to activate the NLRP3 inflammasome in macrophages [26]. Additionally, inhibition of volume-sensitive chloride currents reduces cell death and reverses contractile dysfunction in cardiomyopathies [27]. To determine the mechanism participating in NLRP3 inflammasome activation in myocytes, we initially confirmed the transcriptional and posttranscriptional downregulation of CLICs after SG surgery. Using a chloride channel blocker, we observed restored myocardial NLRP3-mediated pyroptosis under a HG stimulus. This finding indicated that the chloride efflux might act as a signaling messenger to regulate NLRP3 assembly and activation directly or indirectly (Figure 6). Furthermore, we implied in our study that the chloride efflux acted downstream of ROS generation and that oxidative stress promoted CLICs to translocate to the cell membrane for biological function (Figure 7).

This study has several limitations. Firstly, the two general effects of SG are the weight loss and decrease in blood glucose, which both contribute to the amelioration of DCM development. So, it is tough to define whether the SG could directly alleviate DCM or the SG's outcome played the pivotal role. What is more, experiments will be further required to directly associate SG and the alleviation of

DCM with the role of ROS-chloride efflux-mediated NLRP3 inflammasome as an underlying mechanism.

Taken together, our study provides evidence that the NLRP3 inflammasome is downregulated in DCM after the SG operation. Additionally, the ROS overburden–chloride efflux axis might act as the proximal event before NLRP3 activation in the myocardium, thus contributing to morphological and functional alleviation of DCM. Notwithstanding, whether alleviation of NLRP3 inflammasome and its upstream mechanisms in the SG operation could be used as a new therapeutic target for T2DM and its related comorbidities remains to be further explored and elucidated.

5. Conclusions

Collectively, we identified for the first time that alleviation of NLRP3 inflammasome dysregulation and its upstream mechanisms by SG surgery, including ROS overload and chloride efflux, might embrace a rosy future as a promising therapeutic strategy for diabetes mellitus and its related comorbidities.

Data Availability

The detailed data used to support the findings of this study are available from the corresponding author upon request.

Conflicts of Interest

The authors declare to have no competing interests.

Acknowledgments

This work was supported by the National Science Foundation of China (82070869).

References

[1] G. Jia, M. A. Hill, and J. R. Sowers, "Diabetic cardiomyopathy: an update of mechanisms contributing to this clinical entity," *Circulation Research*, vol. 122, no. 4, pp. 624–638, 2018.

[2] Y. Tan, Z. Zhang, C. Zheng, K. A. Wintergerst, B. B. Keller, and L. Cai, "Mechanisms of diabetic cardiomyopathy and potential therapeutic strategies: preclinical and clinical evidence," *Nature Reviews Cardiology*, vol. 17, no. 9, pp. 585–607, 2020.

[3] N. D. Wong, Y. Zhao, R. Patel et al., "Cardiovascular risk factor targets and cardiovascular disease event risk in diabetes: a pooling project of the atherosclerosis risk in communities study, multi-ethnic study of atherosclerosis, and Jackson Heart Study," *Diabetes Care*, vol. 39, no. 5, pp. 668–676, 2016.

[4] G. Jia, V. G. DeMarco, and J. R. Sowers, "Insulin resistance and hyperinsulinaemia in diabetic cardiomyopathy," *Nature Reviews Endocrinology*, vol. 12, no. 3, pp. 144–153, 2016.

[5] Y. M. Ulrich-Lai and K. K. Ryan, "Neuroendocrine circuits governing energy balance and stress regulation: functional overlap and therapeutic implications," *Cell Metabolism*, vol. 19, no. 6, pp. 910–925, 2014.

[6] G. Mingrone, S. Panunzi, A. De Gaetano et al., "Bariatric-metabolic surgery versus conventional medical treatment in obese patients with type 2 diabetes: 5 year follow-up of an open-label, single-centre, randomised controlled trial," *Lancet*, vol. 386, no. 9997, pp. 964–973, 2015.

[7] J. P. Brito, V. M. Montori, and A. M. Davis, "Metabolic surgery in the treatment algorithm for type 2 diabetes: a joint statement by International Diabetes Organizations," *JAMA*, vol. 317, no. 6, pp. 635-636, 2017.

[8] M. Leung, M. Xie, E. Durmush, D. Y. Leung, and V. W. Wong, "Weight loss with sleeve gastrectomy in obese type 2 diabetes mellitus: impact on cardiac function," *Obesity Surgery*, vol. 26, no. 2, pp. 321–326, 2016.

[9] X. Huang, S. Liu, D. Wu et al., "Facilitated Ca (2+) homeostasis and attenuated myocardial autophagy contribute to alleviation of diabetic cardiomyopathy after bariatric surgery," *American Journal of Physiology. Heart and Circulatory Physiology*, vol. 315, no. 5, pp. H1258–h1268, 2018.

[10] N. S. Coll, P. Epple, and J. L. Dangl, "Programmed cell death in the plant immune system," *Cell Death and Differentiation*, vol. 18, no. 8, pp. 1247–1256, 2011.

[11] L. Agostini, F. Martinon, K. Burns, M. F. McDermott, P. N. Hawkins, and J. Tschopp, "NALP3 forms an IL-1β-processing inflammasome with increased activity in Muckle-Wells autoinflammatory disorder," *Immunity*, vol. 20, no. 3, pp. 319–325, 2004.

[12] R. Zhou, A. Tardivel, B. Thorens, I. Choi, and J. Tschopp, "Thioredoxin-interacting protein links oxidative stress to inflammasome activation," *Nature Immunology*, vol. 11, no. 2, pp. 136–140, 2010.

[13] B. Luo, F. Huang, Y. Liu et al., "NLRP3 inflammasome as a molecular marker in diabetic cardiomyopathy," *Frontiers in Physiology*, vol. 8, p. 519, 2017.

[14] B. Luo, B. Li, W. Wang et al., "NLRP3 gene silencing ameliorates diabetic cardiomyopathy in a type 2 diabetes rat model," *PLoS One*, vol. 9, no. 8, article e104771, 2014.

[15] A. O. Mocanu, A. Mulya, H. Huang et al., "Effect of Roux-en-Y gastric bypass on the NLRP3 inflammasome in pancreatic islets from Zucker diabetic fatty rats," *Obesity Surgery*, vol. 26, no. 12, pp. 3076–3081, 2016.

[16] A. O. Mocanu, A. Mulya, H. Huang et al., "Effect of Roux-en-Y gastric bypass on the NLRP3 inflammasome in adipose tissue from obese rats," *PLoS One*, vol. 10, no. 10, article e0139764, 2015.

[17] K. Sun, J. Wang, Z. Lan et al., "Sleeve gastroplasty combined with the NLRP3 inflammasome inhibitor CY-09 reduces body weight, improves insulin resistance and alleviates hepatic steatosis in mouse model," *Obesity Surgery*, vol. 30, no. 9, pp. 3435–3443, 2020.

[18] D. Wu, Z. B. Yan, Y. G. Cheng et al., "Deactivation of the NLRP3 inflammasome in infiltrating macrophages by duodenal-jejunal bypass surgery mediates improvement of beta cell function in type 2 diabetes," *Metabolism, Clinical and Experimental*, vol. 81, pp. 1–12, 2018.

[19] C. Bian, B. Bai, Q. Gao, S. Li, and Y. Zhao, "17β-estradiol regulates glucose metabolism and insulin secretion in rat islet β cells through GPER and Akt/mTOR/GLUT2 pathway," *Frontiers in Endocrinology*, vol. 10, pp. 531–531, 2019.

[20] V. A. Lacombe, S. Viatchenko-Karpinski, D. Terentyev et al., "Mechanisms of impaired calcium handling underlying subclinical diastolic dysfunction in diabetes," *American Journal of Physiology. Regulatory, Integrative and Comparative Physiology*, vol. 293, no. 5, pp. R1787–R1797, 2007.

[21] Y. Ti, G. L. Xie, Z. H. Wang et al., "TRB3 gene silencing alleviates diabetic cardiomyopathy in a type 2 diabetic rat model," *Diabetes*, vol. 60, no. 11, pp. 2963–2974, 2011.

[22] Y. Cheng, X. Huang, D. Wu et al., "Sleeve gastrectomy with bypass of proximal small intestine provides better diabetes control than sleeve gastrectomy alone under postoperative high-fat diet," *Obesity Surgery*, vol. 29, no. 1, pp. 84–92, 2019.

[23] A. E. Civitarese, P. S. MacLean, S. Carling et al., "Regulation of skeletal muscle oxidative capacity and insulin signaling by the mitochondrial rhomboid protease PARL," *Cell Metabolism*, vol. 11, no. 5, pp. 412–426, 2010.

[24] K. Huynh, B. C. Bernardo, J. R. McMullen, and R. H. Ritchie, "Diabetic cardiomyopathy: mechanisms and new treatment strategies targeting antioxidant signaling pathways," *Pharmacology & Therapeutics*, vol. 142, no. 3, pp. 375–415, 2014.

[25] G. Salazar, A. Cullen, J. Huang et al., "SQSTM1/p 62 and PPARGC1A/PGC-1alpha at the interface of autophagy and vascular senescence," *Autophagy*, vol. 16, no. 6, pp. 1092–1110, 2020.

[26] T. Tang, X. Lang, C. Xu et al., "CLICs-dependent chloride efflux is an essential and proximal upstream event for NLRP3 inflammasome activation," *Nature Communications*, vol. 8, no. 1, p. 202, 2017.

[27] A. d'Anglemont de Tassigny, A. Berdeaux, R. Souktani, P. Henry, and B. Ghaleb, "The volume-sensitive chloride channel inhibitors prevent both contractile dysfunction and apoptosis induced by doxorubicin through PI3kinase, Akt and Erk 1/2," *European Journal of Heart Failure*, vol. 10, no. 1, pp. 39–46, 2008.

[28] S. Ikramuddin, J. Korner, W. J. Lee et al., "Lifestyle intervention and medical management with vs without Roux-en-Y gastric bypass and control of hemoglobin A1c, LDL cholesterol, and systolic blood pressure at 5 years in the Diabetes Surgery Study," *JAMA*, vol. 319, no. 3, pp. 266–278, 2018.

[29] E. R. McGlone, I. Carey, V. Veličković et al., "Bariatric surgery for patients with type 2 diabetes mellitus requiring insulin: clinical outcome and cost-effectiveness analyses," *PLoS Medicine*, vol. 17, no. 12, article e1003228, 2020.

[30] M. J. Reed, K. Meszaros, L. J. Entes et al., "A new rat model of type 2 diabetes: the fat-fed, streptozotocin-treated rat," *Metabolism, Clinical and Experimental*, vol. 49, no. 11, pp. 1390–1394, 2000.

[31] S. Skovso, "Modeling type 2 diabetes in rats using high fat diet and streptozotocin," *Journal of Diabetes Investigation*, vol. 5, no. 4, pp. 349–358, 2014.

[32] S. L. Ménard, E. Croteau, O. Sarrhini et al., "Abnormal in vivo myocardial energy substrate uptake in diet-induced type 2 diabetic cardiomyopathy in rats," *American Journal of Physiology. Endocrinology and Metabolism*, vol. 298, no. 5, pp. E1049–E1057, 2010.

[33] A. P. Chambers, L. Jessen, K. K. Ryan et al., "Weight-independent changes in blood glucose homeostasis after gastric bypass or vertical sleeve gastrectomy in rats," *Gastroenterology*, vol. 141, no. 3, pp. 950–958, 2011.

[34] H. E. Wilson-Perez, A. P. Chambers, K. K. Ryan et al., "Vertical sleeve gastrectomy is effective in two genetic mouse models of glucagon-like peptide 1 receptor deficiency," *Diabetes*, vol. 62, no. 7, pp. 2380–2385, 2013.

[35] C. H. Mandavia, A. R. Aroor, V. G. Demarco, and J. R. Sowers, "Molecular and metabolic mechanisms of cardiac dysfunction in diabetes," *Life Sciences*, vol. 92, no. 11, pp. 601–608, 2013.

[36] S. Dong, L. Qian, Z. Cheng et al., "Lactate and myocadiac energy metabolism," *Frontiers in Physiology*, vol. 12, article 715081, 2021.

[37] C. Moran, T. G. Phan, J. Chen et al., "Brain atrophy in type 2 diabetes: regional distribution and influence on cognition," *Diabetes Care*, vol. 36, no. 12, pp. 4036–4042, 2013.

[38] X. Huang, D. Wu, Y. Cheng et al., "Restoration of myocardial glucose uptake with facilitated myocardial glucose transporter 4 translocation contributes to alleviation of diabetic cardiomyopathy in rats after duodenal-jejunal bypass," *Journal of Diabetes Investigation*, vol. 10, no. 3, pp. 626–638, 2019.

[39] E. Levelt, C. T. Rodgers, W. T. Clarke et al., "Cardiac energetics, oxygenation, and perfusion during increased workload in patients with type 2 diabetes mellitus," *European Heart Journal*, vol. 37, no. 46, pp. 3461–3469, 2016.

[40] L. Cai, Y. Wang, G. Zhou et al., "Attenuation by metallothionein of early cardiac cell death via suppression of mitochondrial oxidative stress results in a prevention of diabetic cardiomyopathy," *Journal of the American College of Cardiology*, vol. 48, no. 8, pp. 1688–1697, 2006.

[41] H. M. Zhou, Y. Ti, H. Wang et al., "Cell death-inducing DFFA-like effector C/CIDEC gene silencing alleviates diabetic cardiomyopathy via upregulating AMPKa phosphorylation," *The FASEB Journal*, vol. 35, no. 5, article e21504, 2021.

[42] S. Walls, S. Diop, R. Birse et al., "Prolonged exposure to microgravity reduces cardiac contractility and initiates remodeling in Drosophila," *Cell Reports*, vol. 33, no. 10, article 108445, 2020.

[43] M. Nakamura, T. Liu, S. Husain et al., "Glycogen synthase kinase-3α promotes fatty acid uptake and lipotoxic cardiomyopathy," *Cell Metabolism*, vol. 29, no. 5, pp. 1119–1134.e12, 2019.

[44] P. Broz, P. Pelegrín, and F. Shao, "The gasdermins, a protein family executing cell death and inflammation," *Nature Reviews Immunology*, vol. 20, no. 3, pp. 143–157, 2020.

[45] K. A. Deets and R. E. Vance, "Inflammasomes and adaptive immune responses," *Nature Immunology*, vol. 22, no. 4, pp. 412–422, 2021.

[46] E. A. Miao, J. V. Rajan, and A. Aderem, "Caspase-1-induced pyroptotic cell death," *Immunological Reviews*, vol. 243, no. 1, pp. 206–214, 2011.

[47] M. M. Hughes and L. A. J. O'Neill, "Metabolic regulation of NLRP3," *Immunological Reviews*, vol. 281, no. 1, pp. 88–98, 2018.

[48] A. Lu, V. G. Magupalli, J. Ruan et al., "Unified polymerization mechanism for the assembly of ASC-dependent inflammasomes," *Cell*, vol. 156, no. 6, pp. 1193–1206, 2014.

[49] N. Kayagaki, I. B. Stowe, B. L. Lee et al., "Caspase-11 cleaves gasdermin D for non-canonical inflammasome signalling," *Nature*, vol. 526, no. 7575, pp. 666–671, 2015.

[50] H. Shi, Y. Wang, X. Li et al., "NLRP3 activation and mitosis are mutually exclusive events coordinated by NEK7, a new inflammasome component," *Nature Immunology*, vol. 17, no. 3, pp. 250–258, 2016.

[51] Z. Zhou, A. Mahdi, Y. Tratsiakovich et al., "Erythrocytes from patients with type 2 diabetes induce endothelial dysfunction via arginase I," *Journal of the American College of Cardiology*, vol. 72, no. 7, pp. 769–780, 2018.

[52] C. Dostert, V. Pétrilli, R. Van Bruggen, C. Steele, B. T. Mossman, and J. Tschopp, "Innate immune activation through Nalp3 inflammasome sensing of asbestos and silica," *Science*, vol. 320, no. 5876, pp. 674–677, 2008.

[53] F. Martinon, "Signaling by ROS drives inflammasome activation," *European Journal of Immunology*, vol. 40, no. 3, pp. 616–619, 2010.

[54] S. L. Masters, A. Dunne, S. L. Subramanian et al., "Activation of the NLRP3 inflammasome by islet amyloid polypeptide provides a mechanism for enhanced IL-1β in type 2 diabetes," *Nature Immunology*, vol. 11, no. 10, pp. 897–904, 2010.

[55] C. N. Brocker, D. Kim, T. Melia et al., "Long non-coding RNA Gm15441 attenuates hepatic inflammasome activation in response to PPARA agonism and fasting," *Nature Communications*, vol. 11, no. 1, p. 5847, 2020.

Hindawi
Oxidative Medicine and Cellular Longevity
Volume 2022, Article ID 5631099, 11 pages
https://doi.org/10.1155/2022/5631099

Research Article

Renal and Inflammatory Proteins as Biomarkers of Diabetic Kidney Disease and Lupus Nephritis

Nathan H. Johnson,[1] **Robert W. Keane**,[1,2] **and Juan Pablo de Rivero Vaccari**[2]

[1]*Department of Physiology and Biophysics, University of Miami Miller School of Medicine, Miami, FL, USA*
[2]*Department of Neurological Surgery and The Miami Project to Cure Paralysis, University of Miami Miller School of Medicine, Miami, FL, USA*

Correspondence should be addressed to Juan Pablo de Rivero Vaccari; jderivero@med.miami.edu

Received 29 December 2021; Revised 13 February 2022; Accepted 19 February 2022; Published 19 March 2022

Academic Editor: Tao Zheng

Current methods for differentiation of kidney disease types are unspecific and may be invasive. Thus, there is a need for development of new biomarkers of kidney disorders that are specific and less invasive. In this study, we analyzed serum samples of diabetic kidney disease (DKD) and lupus nephritis (LN) patients to identify biomarkers of these two disorders. Serum samples were analyzed by Simple Plex assays. We calculated the area under the curve (AUC) as well as receiver operating characteristics (ROC) to obtain the sensitivity and specificity and other biomarker-related variables of apoptosis-associated speck-like protein containing a caspase recruitment domain (ASC), interleukin- (IL-) 18, Lipocalin-2/NGAL, epidermal growth factor (EGF), u-Plasminogen Activator (uPA), and C-reactive protein (CRP) as potential biomarkers. Protein levels of ASC, IL-18, EGF, and Lipocalin-2/NGAL were higher in DKD and LN patients when compared to controls, whereas only uPA was elevated in DKD patients and CRP in LN patients. As determined by the AUC, of the six analytes studied, EGF (AUC = 0.9935), Lipocalin-2/NGAL (0.9554), ASC (0.7666), and uPA (0.7522) are reliable biomarkers of DKD, whereas EGF (1.000), Lipocalin-2/NGAL (0.9412), uPA (0.7443), and IL-18 (0.7384) are more reliable for LN. The biomarkers analyzed can differentiate between healthy and affected individuals. However, there was no difference between the levels of these biomarkers in DKD vs LN. Thus, although these biomarkers cannot be used to categorize patients between DKD and LN, they are useful as biomarkers of renal pathology.

1. Introduction

Kidney disease is a major health concern impacting more than 750 million people throughout the world and represents a significant burden to patients and health care systems [1]. Kidney disease is a generalized term representing an assortment of disorders impacting the renal system, each with complex and often uniquely distinctive pathologies [2]. Currently, the most widely used method for the diagnosis of kidney disease is through the measurement of the glomerular filtration rate (GFR) [2, 3]. Although long considered a "golden standard" for the detection of kidney disorders, a patient's GFR is typically determined by measuring the concentrations of kidney filtrates in blood plasma or in urine [3]. Since the GFR is the collective product of millions of glomeruli working concurrently, a patient's true GFR is often very difficult to establish [3]. Clinicians traditionally calculate an estimated glomerular filtration rate (eGFR) through measurement of serum creatinine and blood urea nitrogen (BUN) concentrations [2, 3]. Urinalysis may also be used to calculate a measured glomerular filtration rate (mGFR) by quantifying clearance of a readily filtered, exogenous substance such as inulin. Urinalysis is also used to detect proteinuria and to determine the albumin levels [2, 3]. Unfortunately, these methods traditionally used to determine GFR are nonspecific to the underlying cause of pathology and are often not significantly altered until much later in disease progression [2–4].

Of the kidney diseases, diabetic kidney disease (DKD) and lupus nephritis (LN) are two chronic disorders that

are typically not detected by altered GFR or proteinuria until much later in their development [4, 5]. In diabetic patients, DKD diagnosis is traditionally made when one or more of the following signs is present over a span of three months: a decreased eGFR (<60 ml/min/1.73 m^2), an increase in daily albumin excretion in urine (≥30 mg), or an increase in the urinary albumin/creatinine ratio (≥30 mg g^{-1}) [5]. In patients suffering from systemic lupus erythematosus (SLE), the development of LN is determined by increased protein in urine (>0.5 g daily), from the presence of cellular casts in urine, or from an increased urinary creatinine/protein level (>0.5) [6]. Additionally, LN may be diagnosed through renal biopsy. However, this method is invasive and potentially hazardous [4, 6]. Although DKD and LN are two different disorders, they have shared pathological attributes that are seen in almost every kidney disorder. Specifically, both disorders are known to cause increased expression of inflammatory proteins within the kidneys through activation of the inflammasome [7, 8].

The inflammasome is a multiprotein structure that allows for the assembly of inflammatory caspases and subsequent activation of cytokines to signal inflammation and cell death in native and neighboring cells [7, 9]. In cases of acute kidney injury and chronic kidney disease, the inflammasome has demonstrated a significant role in pathological development, as studies interfering with inflammasome activity have shown reduction in or regulation of pathological progression [8]. In DKD, studies have shown increased nucleotide binding domain- (NOD-) like receptor protein 3 (NLRP3) and absent in melanoma 2 protein (AIM2) expression within the kidneys and increased expression of the inflammatory cytokine interleukin- (IL-) 1β in serum [7]. In LN, studies have shown increased expression of NLRP3, caspase 1, and IL-1β in tissue collected by kidney biopsies and in podocytes [7, 10]. Thus, these studies show that the inflammasome is a promising target for the development of future therapeutics for renal diseases. Moreover, inflammasome proteins have been shown to be biomarkers of the inflammatory response associated with diagnosis of traumatic brain injury [11–14], stroke [15], depression [16], multiple sclerosis [17], mild cognitive impairment [18], Alzheimer's disease [18], nonalcoholic steatohepatitis [19], psoriasis [20], and age-related macular degeneration [21].

Identification of biomarkers involved in renal pathology has the potential to be used to monitor disease progression in patients newly diagnosed with diabetes or lupus so that more personalized treatment strategies may be utilized. Moreover, inflammasome proteins can also be used as theragnostic biomarkers to identify whether patients are responding positively or negatively to different treatment strategies. The purpose of this study was to investigate biomarkers of renal disease independently of whether the disease has an autoimmune origin or a chronic disease known to affect the kidneys. Moreover, considering the multifactorial aspects that contribute to renal diseases, in this study, we analyzed a combination of kidney disease-associated proteins (Lipocalin/NGAL, EGF and uPA), as well as proteins associated with inflammasome activity (ASC and IL-18) and general inflammation (CRP) with the aim of determining their reliability as potential biomarkers of kidney disease, specifically, DKD and LN.

2. Materials and Methods

2.1. Participants. Serum from patients with DKD and LN (Table 1) and age-matched controls were obtained from BiolVT (Hicksville, NY). Donor informed consent was provided by those participating in the study Prospective Collection of Samples for Research funded by SeraTrials, LLC. with IRB number 20170439. Age-matched control samples were obtained from patients with no medical diagnosis of any disease with a median of 50 years old, a mean of 49.02, and a range between 21 and 101. Patients in the DKD group had a median age of 62 years old and a range between 21 and 90, and those with LN had a median age of 43.5 and a range between 19 and 75. Patients in the DKD cohort consisted of 17 Caucasians, 10 of African descent, and 4 of other race, whereas in the LN group there were 17 Caucasians, 11 of African descent, and 4 of other races. Patients with DKD presented the following comorbidities: hypertension (23 patients), hypercholesterolemia, (6 patients) hypothyroidism (8 patients), gastroesophageal reflux disease (7 patients), and coronary artery disease (7 patients), whereas patients in the LN group presented with Hypertension (6 patients), gastroesophageal reflux disease (2 patients), and coronary artery disease (3 patients).

DKD patients were characterized by a cohort representing 4 of the 5 stages of the disease as determined by the eGFR in ml/min/1.73 m^2: 2 (guarded: 60-89), 3 (elevated: 30-59), 4 (high: 15-29), and 5 (severe: <15 or dialysis) [22]. Moreover, LN patients were in part diagnosed by kidney biopsy representing the following classifications: 2 (mesangial proliferative LN), 3 (focal LN affecting less than 50% of glumeruli), 4 (diffuse LN affecting more than 50% of glumeruli), and 5 (advanced sclerosing LN) [23].

In summary, in this proof-of-concept study, the inclusion/exclusion criteria were characterized by including patients with a positive diagnosis of either DKD or LN without an exclusion for age, race, or disease stage. Patients were included in the DKD cohort regardless of whether patients presented with either type I or type II diabetes. Due to the effects of DKD and LN on the renal system, patients with hypertension with a positive diagnosis for either DKD or LN were also included in the study. However, not having a diagnosis of HTN was not considered an excluding factor.

2.2. Simple Plex Assay. Concentration of inflammasome proteins (ASC and IL-18) and indicators of renal function (uPA, EGF, and Lipocalin/NGAL) and generalized inflammation (CRP) were measured in patients with DKD, LN, and in age-matched controls *via* Ella (Protein Simple) according to manufacturer instructions. Briefly, samples were diluted in diluent buffer and 50 μl of the sample was loaded on each well of a CART, and 1 ml of washing buffer was added to the respective well. Samples were then run in triplicates using a microfluidics system proprietary of the Ella Instrument (Protein Simple). Sample analysis was automatically

Table 1: Patients with DKD and lupus nephritis used in the study.

DKD patients	31
LN patients	32
Sex (DKD)	Males (55%)–female (45%) 17 - 14
Sex (LN)	Males (25%)–female (72%)–unspecified (3%) 8–23–1
Race (DKD)	
Caucasian	17 (55%)
African	10 (32%)
Other	4 (13%)
Race (LN)	
Caucasian	17 (53%)
African	11 (34%)
Other	4 (13%)
Age range (DKD)	
Range	21 - 90
Median	62
Mean	63.32
Age range (LN)	
Range	19 - 75
Median	43.5
Mean	44.91
Comorbidities (DKD)	
HTN	23 (74%)
Hypercholesterolemia	6 (19%)
Hypothyroidism	8 (26%)
GERD	7 (23%)
CAD	7 (23%)
Diabetes type I	2 (6%)
Diabetes type II	21 (68%)
Diabetes (type unspecified)	8 (26%)
Comorbidities (LN)	
HTN	6 (19%)
GERD	2 (6%)
CAD	3 (9%)
Disease stage (DKD)	
2	1 (3%)
3	7 (22%)
4	2 (7%)
5	2 (7%)
Unspecified	19 (61%)
Disease stage (LN)	
1	4 (12%)
3	6 (19%)
4	5 (16%)
5	2 (6%)
Unspecified	15 (47%)

HTN: hypertension; GERD: gastroesophageal reflux disease; CAD: coronary artery disease.

generated utilizing the Simple Plex Runner Software as described in [9].

2.3. Statistical and Biomarker Analyses. All samples were run for the expression of all analytes. Samples included in the analysis were only those that were within the lower and upper limit of detection for each analyte. Samples that presented protein levels outside the limit of detection of the assay for each analyte were dropped for such analyte. In addition, outliers were removed prior to further statistical analyses using the Robust regression and outlier removal (ROUT) method with a Q set to 1%. Differences between patien groups were tested by one-way ANOVA followed by Tukey's multiple comparison test. Significance was set at $p < 0.05$. Simple Plex data from DKD, LN, and control samples were analyzed utilizing Prism 9 software (GraphPad). Specificity, sensitivity, confidence interval (95%), standard deviation, p value, and likelihood ratio was identified through calculation of receiver operating characteristics (ROC) and the total area under the curve (AUC). Additionally, cut-off points and positive and negative predictive values were calculated along with overall assay accuracy. The cut-off point for each analyte was chosen based on the highest likelihood ratio in the sensitivity vs. 1-specificity plot, considering a higher sensitivity than higher specificity values, in order to obtain assays that provide a higher likelihood of reliability for the respective sensitivity for each analyte [24]. In addition, a two-tailed Pearson r correlation matrix was carried using Prism 9 software (GraphPad). Sample size in this study was calculated by power analysis with the power set to 0.8 and considering the standard deviation and the difference between the means to obtain a significance of 0.05 for each analyte.

Combination of biomarkers was achieved by fitting a logistic regression model to explain the diagnosis of either DKD or LN followed by calculation of the AUC using RStudio (version 1.2.5033).

ROC curve comparison between analytes was done as described in [25] using the following formula to obtain a critical ratio Z:

$$z = \frac{(A_1 - A_2)}{\sqrt{\mathrm{SE_1}^2 + \mathrm{SE_2}^2 - 2\mathrm{rSE_1SE_2}}}. \quad (1)$$

And the p value was determined using the following formula using Microsoft Excel (version 16.57):

$$= 2 * (1 - \mathrm{NORMSDIST(z)}) \quad (2)$$

3. Results

3.1. ASC and IL-18 Is Elevated in the Serum of Patients with DKD and LN. The inflammasome has been previously shown to be involved in the pathology of renal diseases [26]. To determine the levels of the inflammasome signaling proteins, ASC and IL-18, serum from DKD and LN patients, were analyzed and compared to age-matched healthy controls for the expression of ASC (Figure 1(a)) and IL-18 (Figure 1(b)) proteins. ASC and IL-18 proteins were shown

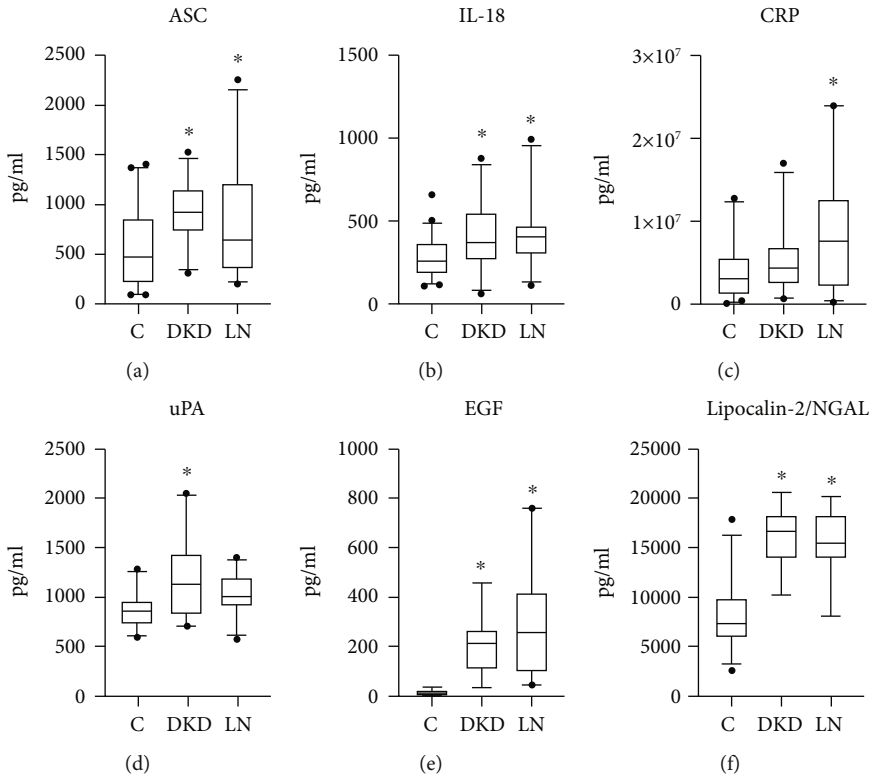

Figure 1: Biomarker protein levels in the serum of patients with DKD and LN. Box and whisker plots showing the protein levels in pg/ml of (a) ASC, (b) IL-18, (c) CRP, (d) uPA, (e) EGF, and (f) Lipocalin-2/NGAL in the blood serum of controls (C), diabetic kidney disease (DKD), and lupus nephritis (LN). Differences between groups were tested *via* one-way ANOVA followed by Tukey's multiple comparison test. Significance was set at $p < 0.05$. ASC: $N = 43$ C, 28 DKD, 32 LN; IL-18: $N = 43$ C, 31 DKD, 32 LN; CRP: $N = 39$ C, 23 DKD, 29 LN; uPA: $N = 23$ C, 20 DKD, 25 LN; EGF: $N = 17$ C, 18 DKD, 24 LN; and NGAL: $N = 24$ C, 14 DKD, 17 LN. Box and whiskers are shown for the 5th and 95th percentile. Dots correspond to data points outside the 5th and 95th percent confidence intervals. $^{*}p < 0.05$ compared to the control.

to be significantly elevated in both DKD and LN patients compared to healthy controls. These results suggest that innate immune inflammatory activity is present in the pathology of both DKD and LN.

3.2. Biomarkers of Renal Disease Are Elevated in the Serum of DKD and LN Patients. CRP is a well-known biomarker of general inflammation. Similarly, uPA, EGF, and Lipocalin-2 have demonstrated involvement in the pathology of renal disease [27]. We analyzed serum of patients with DKD and LN for the expression of CRP (Figure 1(c)), uPA (Figure 1(d)), EGF (Figure 1(e)), and Lipocalin-2/NGAL (Figure 1(f)). Levels of CRP were higher in the LN group and not in the DKD group, whereas levels of uPA were higher in the DKD group but not in the LN group. Protein levels of EGF and Lipocalin-2/NGAL were higher in both groups when compared to the control group. Thus indicating that in this cohort of patients, there is a renal dysfunction consistent with the diagnosis of chronic renal diseases.

3.3. Biomarkers of DKD. To assess if the tested proteins could be reliable biomarkers of DKD, the area under the curve (AUC) was calculated for each protein of interest (Table 2). Of the proteins of interest, EGF (Figure 2(e)) and Lipocalin/NGAL (Figure 2(f)) were shown to have the highest AUC, 0.9935 and 0.9554, respectively, followed by ASC, 0.7666 (Figure 2(a)); uPA, 0.7522 (Figure 2(d)); and IL-18, 0.6849 (Figure 2(b)). The AUC for CRP, 0.6254 (Figure 2(c)) was not significant. Sensitivity of Lipocalin-2 was 100%, with an 83% specificity and a cut-off point of 10,187 pg/ml. Similarly, for EGF, sensitivity was 100% with a 94% specificity and a cut-off point of 27.99 pg/ml. With a cut-off point of 632 pg/ml, the sensitivity for ASC was 89% with a 63% specificity (Table 3). These findings indicate that EGF, Lipocalin-2/NGAL, ASC, uPA, and IL-18 can be used as part of a biomarker panel to diagnose DKD.

3.4. Biomarkers of LN. To assess if the tested proteins could be reliable biomarkers of LN the area under the curve (AUC) was calculated for each protein of interest (Table 2). Of the proteins of interest, EGF (Figure 3(e)) and Lipocalin/NGAL (Figure 3(f)) were shown to have the highest AUC of 1.00 and 0.9412, respectively. The AUC for ASC was 0.6526 (Figure 3(a)); for uPA, 0.7443 (Figure 3(d)); for IL-18, 0.7384 (Figure 3(b)); and for, CRP 0.6844 (Figure 3(c)). Sensitivity of Lipocalin-2 was 88%, with an 83% specificity and a cut-off point of 10,516 pg/ml. Similarly, for EGF, the sensitivity was 100% with a 100% specificity and a cut-off point of 38.53 pg/ml. For uPA, the cut-off point was 890.3 pg/ml with an 84% sensitivity and a 65% specificity, whereas with

Table 2: Area under the curve.

(a)

Control vs. DKD				
Biomarker	AUC	STD. error	95% C.I.	p value
ASC	0.7666	0.05595	0.6570 to 0.8763	0.0002
IL-18	0.6849	0.06612	0.5553 to 0.8145	0.0069
CRP	0.6254	0.07273	0.4829 to 0.7680	0.1011
uPA	0.7522	0.07668	0.6019 to 0.9025	0.0047
EGF	0.9935	0.00877	0.9763 to 1.000	<0.0001
Lipocalin-2/ NGAL	0.9554	0.03177	0.8931 to 1.000	<0.0001

(b)

Control vs. LN				
Biomarker	AUC	STD. error	95% C.I.	p value
ASC	0.6526	0.06274	0.5296 to 0.7756	0.0245
IL-18	0.7384	0.05906	0.6226 to 0.8541	0.0004
CRP	0.6844	0.07027	0.5466 to 0.8221	0.0097
uPA	0.7443	0.07279	0.6017 to 0.8870	0.0037
EGF	1.000	0.000	1.000 to 1.000	<0.0001
Lipocalin-2/ NGAL	0.9412	0.3714	0.8684 to 1.000	<0.0001

(c)

DKD vs. LN				
Biomarker	AUC	STD. error	95% C.I.	p value
ASC	0.6373	0.07508	0.4901 to 0.7844	0.0684
IL-18	0.5222	0.07501	0.3752 to 0.6692	0.7623
CRP	0.5997	0.07994	0.4430 to 0.7564	0.2205
uPA	0.5980	0.09194	0.4178 to 0.7782	0.2630
EGF	0.5856	0.08860	0.4120 to 0.7593	0.3470
Lipocalin-2/ NGAL	0.5546	0.1057	0.3474 to 0.7618	0.6058

a cut-off point of 521.6 pg/ml, the sensitivity for ASC was 63% with a 53% specificity (Table 3). These findings indicate that EGF, NGAL, uPA, IL-18, ASC, and CRP can be used as part of a biomarker panel to diagnose LN.

Furthermore, we compared the ROC curves between all biomarkers analyzed for the cohorts of DKD (Supplementary Table 1) and LN (Supplementary Table 2) patients, and we found that in DKD patients the AUC was significantly different when comparing ASC with EGF ($p = 2.12E-05$), ASC with NGAL ($p = 0.0009$), CRP with EGF ($p = 0.03$), CRP with NGAL ($p = 2.29E-06$), uPA with EGF ($p = 0.001$), and uPA with NGAL ($p = 0.003$) (Supplementary Table 1), indicating that based on the AUC, in DKD, NGAL as a biomarker is consistently different to several of the other biomarkers analyzed. Similarly, when comparing the AUC for biomarkers in LN patients, the significant difference between curves was detected when comparing ASC with EGF ($p = 3.07E-08$), IL-18 with EGF ($p = 9.45E-06$), CRP with EGF ($p = 7.08E-06$) and uPA with EGF (0.0004) (Supplementary Table 2), indicating that in LN based on the AUC, EGF as a biomarker is consistently different to several of the other biomarkers analyzed.

In addition, we combined biomarkers that presented lower AUC values with those present in EGF and NGAL to determine if a combination of biomarkers would increase the AUC value. Accordingly, when combining ASC, IL-18, and uPA, we found that the AUC for the diagnosis of DKD, increased to 0.82, and this value was higher than the AUC obtained for each biomarker alone (0.77, 0.68, and 0.75, respectively). Similarly, for the diagnosis of LN, we combined IL-18 and uPA to obtain an AUC of 0.81 that was also higher than the AUC obtained for each of those two biomarkers alone (0.74).

3.5. Correlation between DKD Biomarkers. To determine the correlation across serum levels of ASC, IL-18, CRP, uPA, EGF, and NGAL, in DKD patients, a Pearson r correlation matrix was carried out (Figure 4). The greatest positive correlation was found between NGAL and EGF with an $r = 0.74$ ($p = 1.44E-05$) followed by EGF and IL-18 with an $r = 0.50$ ($p = 0.002$) and NGAL and uPA ($r = 0.43$, $p = 0.011$). The correlation between ASC and IL-18 was 0.39 ($p = 0.00073$) and between ASC and EGF was 0.37 ($p = 0.036$), indicating common trends in the expression between the proteins analyzed in this study in the serum of DKD patients.

3.6. Correlation between LN Biomarkers. To determine the correlation across serum levels of ASC, IL-18, CRP, uPA, EGF, and NGAL in LN patients, a Pearson r correlation matrix was carried out (Figure 5). The greatest positive correlation was found between NGAL and uPA with an $r = 0.48$ ($p = 0.003$) followed by EGF and NGAL ($r = 0.45$, $p = 0.014$). The correlation between ASC and CRP was $r = 0.39$ ($p = 0.001$), and between NGAL and CRP the correlation was $r = 0.37$ ($p = 0.03$), indicating common trends in the expression between the analyzed proteins in the serum of LN patients.

4. Discussion

DKD and LN are chronic renal disorders associated with kidney damage resulting from inflammation. In this study, we show an array of renal and inflammasome proteins that are not only elevated but are also reliable biomarkers of both disorders. In the serum of DKD and LN patients, we determined an increased expression of the inflammasome

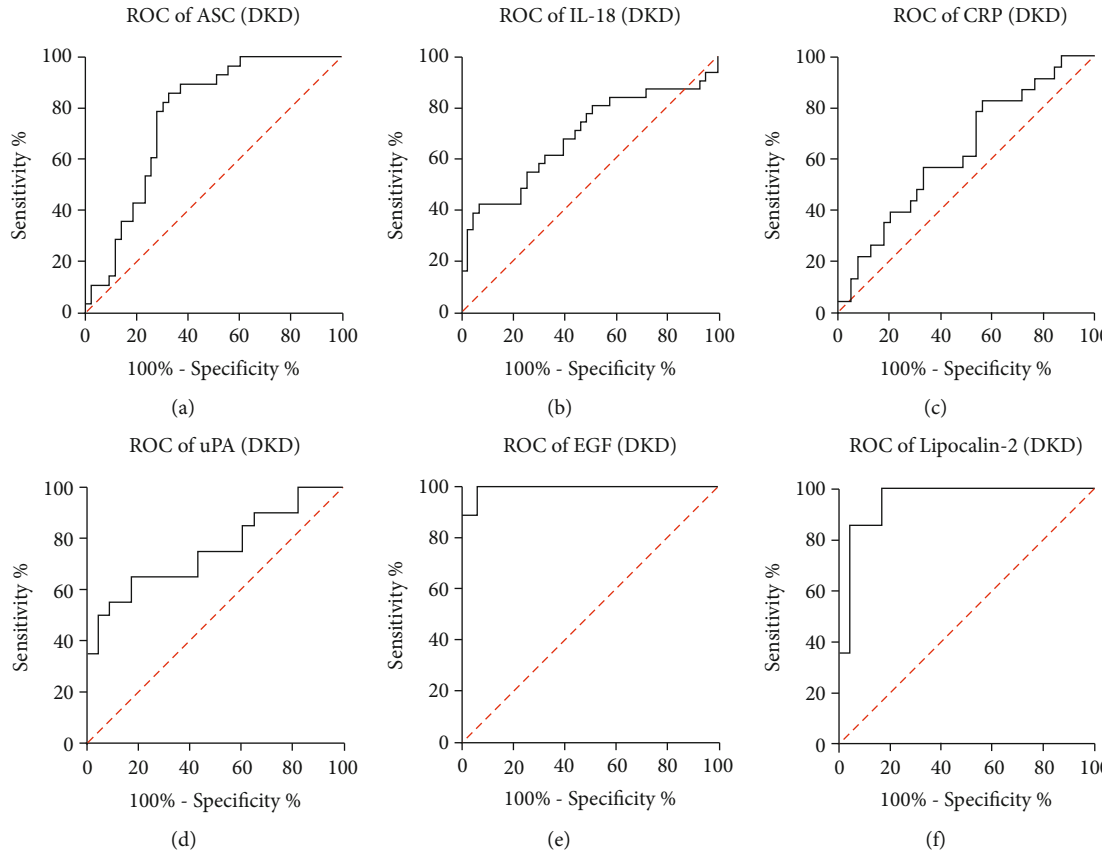

Figure 2: ROC curve of biomarker proteins in patients with DKD. ROC curves indicate the AUC (sensitivity vs 1-specificity) for (a) ASC, (b) IL-18, (c) CRP, (d) uPA, (e) EGF, and (f) Lipocalin-2/NGAL in the serum of patients with DKD. ASC: $N = 43$ C, 28 DKD, 32 LN; IL-18: $N = 43$ C, 31 DKD, 32 LN; CRP: $N = 39$ C, 23 DKD, 29 LN; uPA: $N = 23$ C, 20 DKD, 25 LN; EGF: $N = 17$ C, 18 DKD, 24 LN; and NGAL: $N = 24$ C, 14 DKD, 17 LN.

scaffolding protein ASC and increased levels of the proinflammatory cytokine IL-18. These findings suggest that inflammation plays a key role in the pathologies of both disorders. Studies have suggested that inflammasome activation is associated with the different pathological manifestations of chronic kidney diseases. For instance, proteinuria has been suggested to act as a NLRP3 activator, while calcium carbonate crystal accumulation, a contributor to fibrosis, was also implicated in NLRP3 activation and tubule inflammation [8].

In DKD, studies have suggested that resulting damage to nephrons and increased albumin excretion are the result of elevated levels in the downstream inflammasome-activated cytokines IL-1β and IL-18 [10]. The NLRP3 inflammasome has also been suggested to play a role in the pathology of LN. Accordingly, kidney damage was limited in experiments blocking NLRP3, caspase 1, and IL-18 activation in mouse models of LN [28–31]. Our study supports these findings in humans in that levels of ASC and IL-18 expressions were shown to be significantly elevated in both DKD and LN patients.

In addition to inflammasome activity, our study investigated the levels of other proteins associated with kidney disease and renal function. CRP is a well-established indicator of generalized inflammatory activity and tissue damage [32]. Elevated CRP has been demonstrated in patients with chronic kidney disease, and it has also been implicated in kidney ischemia/reperfusion injury [27, 32]. Here, CRP was elevated in patients with LN but not in DKD. This result is not surprising when considering the different etiologies of the two disorders. Elevated CRP is expected in LN given its role in the complement cascade, and the very close relationship between SLE and the complement system [4, 32].

uPA is produced by tubular epithelial cells, macrophages, and fibroblasts. It has been linked to podocyte function, with increased uAP expression associated with podocyte loss, degradation of renal filtration, and increased proteinuria [33]. It is also thought to play a role in preventing kidney stone formation [34]. In our study, uPA was increased in DKD but not in LN patients, which is consistent with findings in other studies [35].

Serum EGF and Lipocalin-2/NGAL were elevated in DKD and LN. EGF is expressed by cells within the ascending limb of the loop of Henle and the distal tubules and has been shown to have differing effects on renal disease pathology [36]. Lipocalin-2/NGAL is an iron-carrying protein that is expressed by tubular epithelial cells following acute kidney injury and chronic kidney disease [3]. In agreement with our results, other studies have seen increased NGAL expression in patients with LN and DKD [4, 27].

Table 3: Sensitivity and specificity.

(a)

Control vs. DKD Biomarker	Cut-off point (pg/ml)	Sensitivity (%)	Specificity (%)	PPV (%)	NPV (%)	Likelihood ratio	Accuracy (%)
ASC	>632	89	63	61	90	2.400	73
IL-18	>268.7	74	53	53	74	1.595	62
CRP	> 2,984,567	61	51	42	69	1.249	55
uPA	> 875	70	57	58	68	1.610	63
EGF	> 27.99	100	94	95	100	17.00	97
Lipocalin-2	> 10,187	100	83	78	100	6.00	89

(b)

Control vs. LN Biomarker	Cut-off point (pg/ml)	Sensitivity (%)	Specificity (%)	PPV (%)	NPV (%)	Likelihood ratio	Accuracy (%)
ASC	> 521.6	63	53	50	66	1.344	57
IL-18	> 278.9	78	58	58	78	1.866	67
CRP	> 3,768,714	66	62	56	71	1.703	63
uPA	> 890.3	84	65	72	79	2.415	75
EGF	> 38.53	100	100	100	100	—	100
Lipocalin-2	> 10,516	88	83	79	91	5.294	85

The usefulness of a biomarker is calculated from the ROC to obtain the AUC. The closer to 1.0 or 100%, the better the biomarker. In addition, the ROC provides the sensitivity and a specificity for different cut-off points and associated likelihood ratios to provide the reliability of assaying for a particular biomarker. Accordingly, a likelihood ratio above 1 is consistent with a reliable assay, and the higher this value, the more reliability there is. Moreover, a biomarker is also characterized by a PPV and a NPV which are affected by the prevalence of the disease within the cohort studied, and ultimately, one calculates the accuracy of each biomarker to diagnose the disease. Therefore, in this study, to assess the reliability of the above proteins as potential biomarkers for DKD and/or LN, we determined the ROC to obtain the AUC as well as the sensitivity, specificity, PPV, and NPV of all 6 analytes in this study. Of the analytes for DKD, EGF and Lipocalin-2/NGAL showed the best potential for use as biomarkers based on AUC of 0.99 for EGF and 0.96 for NGAL, followed by 0.76 for ASC and 0.75 for uPA. For EGF and Lipocalin-2/NGAL with cut-off points of 27.99 pg/ml and 10,187 pg/ml, respectively, the sensitivity was 100%. For EGF, the specificity was 94%, and for NGAL, it was 83%. Moreover, correlation matrices of the potential biomarkers showed the greatest correlation between EGF and Lipocalin-2/NGAL. The cut-off point for ASC was 632 pg/ml with a sensitivity of 89% and a specificity of 63%. Similarly, for LN, EGF presented an AUC of 1.0, followed by 0.94 for NGAL and 0.74 for uPA. The cut-off point for EGF was 38.53 pg/ml with a 100% sensitivity and specificity; for NGAL, the cut-off point was 10.516 pg/ml with a 88% sensitivity and 83% specificity, and for uPA, the cut-off point was 890.3 pg/ml with 84% sensitivity and 65% specificity.

In the serum of DKD patients, in addition to NGAL, EGF, and uPA, the inflammasome protein ASC is a reliable biomarker in DKD. Similarly, in the serum of LN, in addition to NGAL, EGF, and uPA, the proinflammatory cytokine IL-18 also presented an AUC consistent with a reliable biomarker of LN in serum. In LN, correlation matrices showed the greatest correlation between NGAL and uPA followed by NGAL and EGF. In fact, NGAL showed significant positive correlations with IL-18, EGF, uPA, and CRP. Thus, these findings point to Lipocalin-2/NGAL as a key biomarker in LN, whereas EGF showed significant positive correlations with ASC, IL-18, uPA, and NGAL, suggesting that EGF is a key biomarker in DKD.

Moreover, it is important to identify theragnostic biomarkers that can provide information regarding response to treatment. The involvement of the inflammasome in renal disease offers a viable therapeutic option to treat such diseases. Thus, we propose that ASC and IL-18 can be used as theragnostic biomarkers of therapies targeting the inflammasome in kidney diseases [37].

Moreover, in the DKD cohort, we performed a linear regression analysis to identify the effects of the biomarkers tested on this study on the eGFR. However, we did not detect a statistically significant contribution of any of these biomarkers to eGFR (data not shown), suggesting that the levels of these protein do not affect disease severity, but instead provide information about the inflammatory response associated with the disease. Similarly, a linear regression was carried out to determine the association between the different classifications of LN and these biomarkers (data not shown). However, no statistical significance was found either. Taken together, these data suggest that the proteins ASC, IL-18, uPA, EGF, NGAL, and CRP

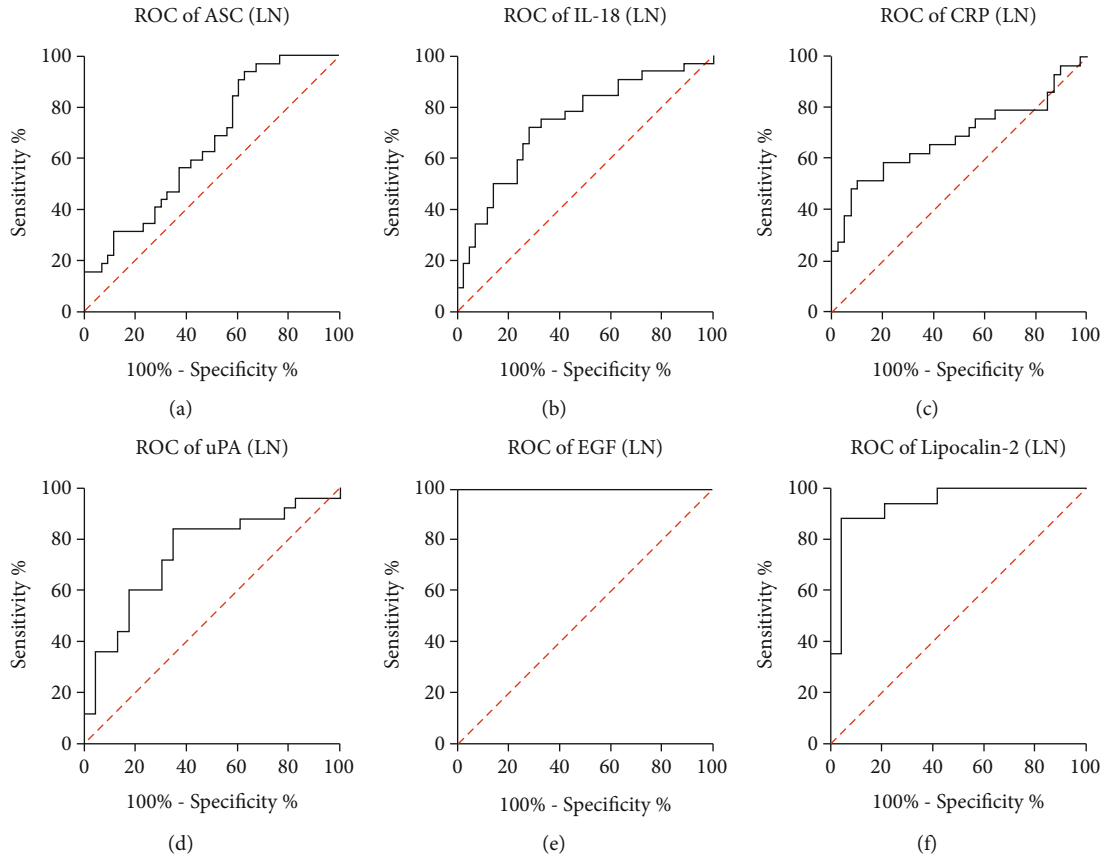

Figure 3: ROC curve of biomarker proteins in patients with LN. ROC curves indicate the AUC (sensitivity vs 1-specificity) for (a) ASC, (b) IL-18, (c) CRP, (d) uPA, (e) EGF, and (f) Lipocalin-2/NGAL in the serum of patients with LN. ASC: $N = 43$ C, 28 DKD, 32 LN; IL-18: $N = 43$ C, 31 DKD, 32 LN; CRP: $N = 39$ C, 23 DKD, 29 LN; uPA: $N = 23$ C, 20 DKD, 25 LN; EGF: $N = 17$ C, 18 DKD, 24 LN; and NGAL: $N = 24$ C, 14 DKD, 17 LN.

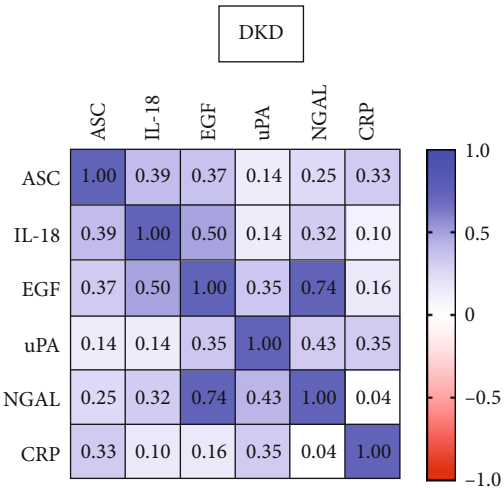

	ASC	IL-18	EGF	uPA	NGAL	CRP
ASC		0.00073	0.036376	0.366804	0.13214	0.012901
IL-18	0.00073		0.002473	0.369311	0.053916	0.438516
EGF	0.036376	0.002473		0.043547	1.44E-05	0.418545
uPA	0.366804	0.369311	0.043547		0.01113	0.04129
NGAL	0.13214	0.053916	1.44E-05	0.01113		0.817088
CRP	0.012901	0.438516	0.438516	0.04129	0.817088	

(b)

Figure 4: Correlation matrix of biomarker proteins in patients with DKD. (a) Plot shows the correlation between ASC, IL-18, CRP, uPA, EGF, and Lipocalin-2/NGAL in the serum of patients with DKD. (b) p values of significance of the Pearson correlation.

contribute significantly to the inflammatory response in renal diseases. However, these proteins do not provide specific clinical information pertaining to the individual pathologies of DKD and LN. Furthermore, future studies should aim at correlating disease severity using individual clinical parameters beyond disease severity to determine whether the potential biomarkers identified in this study can also be used as prognostic biomarkers. In addition, future studies

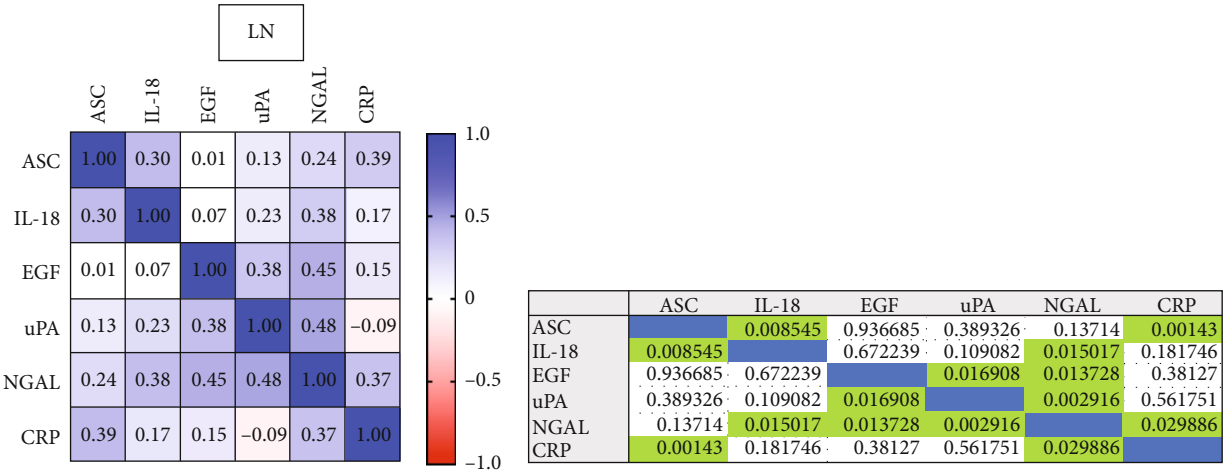

Figure 5: Correlation plot of biomarker proteins in patients with LN. (a) Plot shows the correlation between ASC, IL-18, CRP, uPA, EGF, and Lipocalin-2/NGAL in the serum of patients with LN. (b) p values of significance of the Pearson correlation.

should evaluate the effects of anti-inflammatory therapies in the population of DKD and LN patients to identify whether these proteins can be used as theranostic biomarkers.

In this study, the DKD cohort of patients consisted primarily of type II diabetes patients. Importantly, regardless of the type of diabetes, patients used in the DKD cohort presented kidney disease, suggesting that the findings in this project are more likely related to kidney disease due to diabetes than to the type of diabetes. Future studies are needed to compare the levels of these proteins between patients with type I *vs.* type II diabetes to differentiate whether type I and type II diabetes have different effects on the expression of ASC, IL-18, CRP, uPA, EGF, and NGAL.

Taken together, our results show that some of the most common proteins associated with kidney disease are reliable biomarkers for DKD and LN. Of these proteins, NGAL was the most reliable indicator in both DKD and LN. In addition, ASC is also a good biomarker in DKD. Further studies will focus on identifying how these biomarkers may change as DKD and LN pathology progresses, and whether they prove to be targets for developing therapies to limit DKD or LN progression. In conclusion, EGF and Lipocalin-2/NGAL proteins specifically associated with renal inflammation are reliable biomarkers for assessing chronic kidney disorders, and should be considered in studies looking at DKD and LN disease progression.

Data Availability

The data presented in this study are available on request from the corresponding author.

Ethical Approval

The studies involving human participants were reviewed and approved by Schulman Associates IRB.

Consent

The patients/participants provided their written informed consent to participate in this study. Donor's informed consent was provided by those participating in the study Prospective Collection of Samples for Research funded by SeraTrials, LLC., with IRB number 20170439.

Disclosure

ZyVersa Therapeutics was not involved in the study design, data collection, analysis and interpretation of data, as well as in the writing of this article or the decision to publish the results.

Conflicts of Interest

JPdRV and RWK are cofounders and managing members of InflamaCORE, LLC and have licensed patents on inflammasome proteins as biomarkers of injury and disease as well as on targeting inflammasome proteins for therapeutic purposes. JPdRV and RWK are Scientific Advisory Board Members of ZyVersa Therapeutics. NHJ declares no conflicts of interest. ZyVersa Therapeutics, Inc. has been granted a worldwide exclusive license for development and commercialization of inflammasome inhibitor, IC100, and related products for the treatment of inflammatory diseases, and for companion diagnostics.

Authors' Contributions

Conceptualization was done by JPdRV and RWK. Methodology was done by JPdRV. Formal analysis was done by JPdRV and NHJ. Investigation was done by JPdRV and NHJ. Resources were acquired by JPdRV and RWK. Data curation was done by JPdRV. Writing—original draft preparation, review, and editing were done by NHJ, JPdRV, and RWK. Project administration was done by JPdRV.

Funding acquisition was done by JPdRV and RWK. All authors have read and agreed to the published version of the manuscript.

Acknowledgments

This work was supported by a Sponsored Research agreement from ZyVersa Therapeutics to JPdRV and RWK. We thank Karen Cashmere and Nick LaBella for critically reading the manuscript.

Supplementary Materials

Supplementary Table 1: DKD: ROC curve comparison. Supplementary Table 2: LN: ROC curve comparison. *(Supplementary Materials)*

References

[1] D. C. Crews, A. K. Bello, G. Saadi, and for the World Kidney - Day Steering Committee, "Burden, access, and disparities in kidney disease," *Blood Purification*, vol. 48, no. 1, pp. 32–39, 2019.

[2] W. R. Zhang and C. R. Parikh, "Biomarkers of acute and chronic kidney disease," *Annual Review of Physiology*, vol. 81, no. 1, pp. 309–333, 2019.

[3] S. Lopez-Giacoman and M. Madero, "Biomarkers in chronic kidney disease, from kidney function to kidney damage," *World Journal Nephrology*, vol. 4, no. 1, pp. 57–73, 2015.

[4] S. Soliman and C. Mohan, "Lupus nephritis biomarkers," *Clinical Immunology*, vol. 185, pp. 10–20, 2017.

[5] M. C. Thomas, M. Brownlee, K. Susztak et al., "Diabetic kidney disease," *Nature Reviews. Disease Primers*, vol. 1, no. 1, p. 15018, 2015.

[6] B. H. Hahn, M. McMahon, A. Wilkinson et al., "American College of Rheumatology guidelines for screening, treatment, and management of lupus nephritis," *Arthritis Care Res (Hoboken)*, vol. 64, no. 6, pp. 797–808, 2012.

[7] T. Komada and D. A. Muruve, "The role of inflammasomes in kidney disease," *Nature Reviews. Nephrology*, vol. 15, no. 8, pp. 501–520, 2019.

[8] H. Xiang, F. Zhu, Z. Xu, and J. Xiong, "Role of inflammasomes in kidney diseases via both canonical and non-canonical pathways," *Frontiers in Cell and Development Biology*, vol. 8, p. 106, 2020.

[9] F. J. Brand 3rd, M. Forouzandeh, H. Kaur, F. Travascio, and J. P. de Rivero Vaccari, "Acidification changes affect the inflammasome in human nucleus pulposus cells," *J Inflamm (Lond)*, vol. 13, no. 1, p. 29, 2016.

[10] H. L. Hutton, J. D. Ooi, S. R. Holdsworth, and A. R. Kitching, "The NLRP3 inflammasome in kidney disease and autoimmunity," *Nephrology (Carlton)*, vol. 21, no. 9, pp. 736–744, 2016.

[11] S. Adamczak, G. Dale, J. P. de Rivero Vaccari, M. R. Bullock, W. D. Dietrich, and R. W. Keane, "Inflammasome proteins in cerebrospinal fluid of brain-injured patients as biomarkers of functional outcome: clinical article," *Journal of Neurosurgery*, vol. 117, no. 6, pp. 1119–1125, 2012.

[12] N. Kerr, S. W. Lee, J. Perez-Barcena et al., "Inflammasome proteins as biomarkers of traumatic brain injury," *PLoS One*, vol. 13, no. 12, article e0210128, 2018.

[13] J. Pérez-Bárcena, J. Rodríguez Pilar, O. Salazar et al., "Serum Caspase-1 as an independent prognostic factor in traumatic brain injured patients," *Neurocritical Care*, 2021.

[14] J. Pérez-Bárcena, C. Crespí, G. Frontera et al., "Levels of caspase-1 in cerebrospinal fluid of patients with traumatic brain injury: correlation with intracranial pressure and outcome," *Journal of Neurosurgery*, pp. 1–6, 2021.

[15] N. Kerr, M. García-Contreras, S. Abbassi et al., "Inflammasome proteins in serum and serum-derived extracellular vesicles as biomarkers of stroke," *Frontiers in Molecular Neuroscience*, vol. 11, p. 309, 2018.

[16] S. A. Syed, E. Beurel, D. A. Loewenstein et al., "Defective inflammatory pathways in never-treated depressed patients are associated with poor treatment response," *Neuron*, vol. 99, no. 5, pp. 914–924.e3, 2018, e3.

[17] R. W. Keane, W. D. Dietrich, and J. P. de Rivero Vaccari, "Inflammasome proteins as biomarkers of multiple sclerosis," *Frontiers in Neurology*, vol. 9, p. 135, 2018.

[18] X. O. Scott, M. E. Stephens, M. C. Desir, W. D. Dietrich, R. W. Keane, and J. P. de Rivero Vaccari, "The inflammasome adaptor protein ASC in mild cognitive impairment and Alzheimer's disease," *International Journal of Molecular Sciences*, vol. 21, no. 13, p. 4674, 2020.

[19] B. Cyr, R. W. Keane, and J. P. de Rivero Vaccari, "ASC, IL-18 and galectin-3 as biomarkers of non-alcoholic steatohepatitis: a proof of concept study," *International Journal of Molecular Sciences*, vol. 21, no. 22, p. 8580, 2020.

[20] M. Forouzandeh, J. Besen, R. W. Keane, and J. P. de Rivero Vaccari, "The inflammasome signaling proteins ASC and IL-18 as biomarkers of psoriasis," *Frontiers in Pharmacology*, vol. 11, p. 1238, 2020.

[21] C. Weaver, B. Cyr, J. C. de Rivero Vaccari, and J. P. de Rivero Vaccari, "Inflammasome proteins as inflammatory biomarkers of age-related macular degeneration," *Translational Vision Science & Technology*, vol. 9, no. 13, p. 27, 2020.

[22] F. National Kidney, "K/DOQI clinical practice guidelines for chronic kidney disease: evaluation, classification, and stratification," *American Journal of Kidney Diseases*, vol. 39, no. 2, pp. S1–S266, 2002.

[23] J. J. Weening, V. D. D'Agati, M. M. Schwartz et al., "The classification of glomerulonephritis in systemic lupus erythematosus revisited," *Kidney International*, vol. 65, no. 2, pp. 521–530, 2004.

[24] W. Fierz and X. Bossuyt, "Likelihood ratio approach and clinical interpretation of laboratory tests," *Frontiers in Immunology*, vol. 12, p. 655262, 2021.

[25] J. A. Hanley and B. J. McNeil, "A method of comparing the areas under receiver operating characteristic curves derived from the same cases," *Radiology*, vol. 148, no. 3, pp. 839–843, 1983.

[26] L. Li, W. Tang, and F. Yi, "Role of inflammasome in chronic kidney disease," *Advances in Experimental Medicine and Biology*, vol. 1165, pp. 407–421, 2019.

[27] A. Hashikata, A. Yamashita, S. Suzuki et al., "The inflammation-lipocalin 2 axis may contribute to the development of chronic kidney disease," *Nephrology, Dialysis, Transplantation*, vol. 29, no. 3, pp. 611–618, 2014.

[28] P. Y. Tsai, S. M. Ka, J. M. Chang et al., "Epigallocatechin-3-gallate prevents lupus nephritis development in mice via enhancing the Nrf2 antioxidant pathway and inhibiting NLRP3 inflammasome activation," *Free Radical Biology & Medicine*, vol. 51, no. 3, pp. 744–754, 2011.

[29] S. M. Ka, J. C. Lin, T. J. Lin et al., "Citral alleviates an accelerated and severe lupus nephritis model by inhibiting the activation signal of NLRP3 inflammasome and enhancing Nrf2 activation," *Arthritis Research & Therapy*, vol. 17, no. 1, p. 331, 2015.

[30] D. Ummarino, "NLRP3 inflammasome ignites podocyte dysfunction," *Nature Reviews Rheumatology*, vol. 13, no. 8, p. 451, 2017.

[31] F. Bonomini, M. Dos Santos, F. V. Veronese, and R. Rezzani, "NLRP3 inflammasome modulation by melatonin supplementation in chronic pristane-induced lupus nephritis," *International Journal of Molecular Sciences*, vol. 20, no. 14, p. 3466, 2019.

[32] J. R. Thiele, J. Zeller, J. Kiefer et al., "A conformational change in C-reactive protein enhances leukocyte recruitment and reactive oxygen species generation in ischemia/reperfusion injury," *Frontiers in Immunology*, vol. 9, p. 675, 2018.

[33] L. Raij, R. Tian, J. S. Wong, J. C. He, and K. N. Campbell, "Podocyte injury: the role of proteinuria, urinary plasminogen, and oxidative stress," *American Journal of Physiology. Renal Physiology*, vol. 311, no. 6, pp. F1308–F1317, 2016.

[34] G. Zhang and A. A. Eddy, "Urokinase and its receptors in chronic kidney disease," *Frontiers in Bioscience*, vol. 13, no. 13, pp. 5462–5478, 2008.

[35] D. D. Qin, D. Song, J. Huang, F. Yu, and M. H. Zhao, "Plasma-soluble urokinase-type plasminogen activator receptor levels are associated with clinical and pathological activities in lupus nephritis: a large cohort study fom China," *Lupus*, vol. 24, no. 6, pp. 546–557, 2015.

[36] Y. Isaka, "Epidermal growth factor as a prognostic biomarker in chronic kidney diseases," *Annals of Translational Medicine*, vol. 4, no. 1, p. S62, 2016.

[37] C. Zhang, X. W. Zhu, L. L. Li et al., "A small molecule inhibitor MCC950 ameliorates kidney injury in diabetic nephropathy by inhibiting NLRP3 inflammasome activation," *Diabetes, metabolic syndrome and obesity: targets and therapy*, vol. 12, pp. 1297–1309, 2019.

Hindawi
Oxidative Medicine and Cellular Longevity
Volume 2021, Article ID 1806344, 22 pages
https://doi.org/10.1155/2021/1806344

Research Article

Metformin Corrects Glucose Metabolism Reprogramming and NLRP3 Inflammasome-Induced Pyroptosis via Inhibiting the TLR4/NF-κB/PFKFB3 Signaling in Trophoblasts: Implication for a Potential Therapy of Preeclampsia

Yang Zhang, Weifang Liu, Yanqi Zhong, Qi Li, Mengying Wu, Liu Yang, Xiaoxia Liu, and Li Zou

Department of Obstetrics and Gynecology, Union Hospital, Tongji Medical College, Huazhong University of Science and Technology, Wuhan, China

Correspondence should be addressed to Xiaoxia Liu; xiehesummer@hust.edu.cn and Li Zou; xiehezouli@hust.edu.cn

Received 28 June 2021; Revised 15 September 2021; Accepted 28 September 2021; Published 11 November 2021

Academic Editor: Francesca Danesi

NOD-like receptor family, pyrin domain-containing protein 3 (NLRP3) inflammasome-mediated pyroptosis is a crucial event in the preeclamptic pathogenesis, tightly linked with the uteroplacental TLR4/NF-κB signaling. Trophoblastic glycometabolism reprogramming has now been noticed in the preeclampsia pathogenesis, plausibly modulated by the TLR4/NF-κB signaling as well. Intriguingly, cellular pyroptosis and metabolic phenotypes may be inextricably linked and interacted. Metformin (MET), a widely accepted NF-κB signaling inhibitor, may have therapeutic potential in preeclampsia while the underlying mechanisms remain unclear. Herein, we investigated the role of MET on trophoblastic pyroptosis and its relevant metabolism reprogramming. The safety of pharmacologic MET concentration to trophoblasts was verified at first, which had no adverse effects on trophoblastic viability. Pharmacological MET concentration suppressed NLRP3 inflammasome-induced pyroptosis partly through inhibiting the TLR4/NF-κB signaling in preeclamptic trophoblast models induced via low-dose lipopolysaccharide. Besides, MET corrected the glycometabolic reprogramming and oxidative stress partly via suppressing the TLR4/NF-κB signaling and blocking transcription factor NF-κB1 binding on the promoter PFKFB3, a potent glycolytic accelerator. Furthermore, PFKFB3 can also enhance the NF-κB signaling, reduce NLRP3 ubiquitination, and aggravate pyroptosis. However, MET suppressed pyroptosis partly via inhibiting PFKFB3 as well. These results provided that the TLR4/NF-κB/PFKFB3 pathway may be a novel link between metabolism reprogramming and NLRP3 inflammasome-induced pyroptosis in trophoblasts. Further, MET alleviates the NLRP3 inflammasome-induced pyroptosis, which partly relies on the regulation of TLR4/NF-κB/PFKFB3-dependent glycometabolism reprogramming and redox disorders. Hence, our results provide novel insights into the pathogenesis of preeclampsia and propose MET as a potential therapy.

1. Introduction

Preeclampsia (PE), characterized by new-onset hypertension typically after 20 weeks of gestation together with multisystem involvement, complicates 2%–8% of pregnancies globally with huge associated healthcare burdens to the whole of society [1]. Although the precise pathogenesis of PE remains elusive, pyroptosis, a newly discovered programmed cell death process accompanied by sterile inflammatory cascades, has now been proved existent in the preeclamptic placentas while its regulatory mechanism remains vague [2, 3].

Pyroptosis is efficiently controlled by the NOD-like receptor family, pyrin domain-containing protein 3 (NLRP3) inflammasome [4] composed of NLRP3, caspase 1, and apoptosis-associated speck-like protein containing a caspase recruitment domain (ASC). NLRP3 inflammasome generates interleukin- (IL-) 1β and IL-18 and maturates gasdermin D (GSDMD) to induce a lytic form of cell death, pyroptosis

[5]. Toll-like receptor 4 (TLR4), a crucial receptor of exogenous pathogen-associated molecular patterns (PAMPs) and endogenous damage-associated molecular patterns (DAMPs) [6], has been widely known to participate in cellular pyroptosis through activating its canonical downstream nuclear factor-κB (NF-κB) signaling [7, 8]. The NF-κB family of transcription factors, consisting of five Rel-homology-containing proteins (cRel, RelA, RelB, NF-κB1, and NF-κB2), forms numerous NF-κB dimers normally binding to inhibitors of NF-κB (IκB) in the cytoplasm. The phosphorylation of IκB kinase (IKK) contributes to the phosphorylation and degradation of IκB, resulting in the release and nuclear translocation of the NF-κB family of transcription factors, finally modulating the transcription of downstream genes, such as NLRP3 [9, 10]. Extensive research has reported the vital role of highly expressed and overactivated TLR4/NF-κB signaling in the preeclamptic placentas via causing trophoblastic inflammation, oxidative stress, and dysfunction [11, 12]. With the increased expression of NLRP3 and related mediators (caspase 1 and IL-1β) found in the placentas [13, 14], trophoblastic pyroptosis has now been suggested to be one of the PE pathogenesis [2, 3]. However, it remains to be verified whether the overactive TLR4/NF-κB signaling in preeclamptic trophoblasts triggers the NLRP3 inflammasome-induced pyroptosis.

Intriguingly, the TLR4/NF-κB signaling is closely related to cellular metabolic reprogramming. The activation of the TLR4/NF-κB signaling leads to the preferential use of glycolysis, instead of mitochondrial oxidative phosphorylation (OXPHOS) in macrophages and dendritic cells [15–17]. Regrettably, the metabolic characters of the preeclamptic placentas remain indefinite. Reportedly, the energy required to support the physiological activities of trophoblasts relies principally on glycometabolism [18]. There have been plenty of reports about mitochondrial destruction and dysfunction in the preeclamptic placentas [19]. The latest research has further claimed that preeclamptic trophoblasts are very likely to undergo the glycometabolic reprogramming to glycolysis [20]. Nonetheless, whether the overactive uteroplacental TLR4/NF-κB signaling reprograms glycometabolism in the preeclamptic placentas remains to be settled.

Recently published studies have suggested that NLRP3 inflammasome-induced pyroptosis can be modulated by some key glycolytic enzymes [21], such as hexokinase 1 (HK1) and M2 isoform of pyruvate kinase (PKM2). The inhibition of HK1 and PKM2 not only suppressed glycolysis flux but also mitigated NLRP3 inflammasome-activated pyroptosis [22, 23]. 6-Phosphofructo-2-kinase/fructose-2,6-bisphosphatase 3 (PFKFB3), a potent glycolytic regulator, accelerates glycolytic flux by promoting fructose-2,6-bisphosphate (F2,6P2) synthesis and facilitating the allosteric activation of 6-phosphofructo-1-kinase 1 (PFK1) [24]. PFKFB3 is expressed at a certain level in the normal placentas. However, we have previously reported that the PFKFB3 expression in the preeclamptic placentas was significantly increased, modulating the trophoblastic inflammation and oxidative stress via the NF-κB signaling [25]. Thus, it needs to be further clarified whether the trophoblastic glycolysis represented by PFKFB3 regulated the NLRP3 inflammasome-induced pyroptosis at the uteroplacental interface.

Up to now, there has been a clinical dilemma that current clinical therapies for PE are mainly symptomatic treatments, while, thus far, the only curative intervention for PE is the delivery of the fetus and placenta, albeit with raised consequent risks [26]. Hence, more possible therapeutic strategies remain to be further explored. Metformin (MET), the first-line therapy for type II diabetes, has long been clinically used for adjusting glycometabolism [27]. Surprisingly, randomized clinical trials, as well as meta-analyses, have reported the preventive and therapeutic effects of MET on PE while the underlying mechanism remains unclear [28, 29]. Previous studies have pointed out that MET effectively inhibits the TLR4/NF-κB signaling [30–32]. Recent studies have reported that MET prevents trophoblastic apoptosis caused by insulin toxicity [33] as well as alleviates pyroptosis in ischemia-reperfusion injuries [34, 35]. Moreover, the safety of taking MET during human pregnancies has been preliminarily ensured [36]. Thus, the therapeutic potential of MET in PE is worth in-depth study [26].

In the present study, we hypothesized that the TLR4/NF-κB/PFKFB3 pathway may be a novel link between metabolism reprogramming and NLRP3 inflammasome-induced pyroptosis in trophoblasts. Further, MET alleviates the NLRP3 inflammasome-induced pyroptosis, which partly relies on the regulation of TLR4/NF-κB/PFKFB3-dependent glycometabolism reprogramming and redox disorders. This research may provide novel insights into the pathogenesis of preeclampsia and propose MET as a potential therapy.

2. Materials and Methods

2.1. Cell Culture. The immortalized human extravillous trophoblast cell line HTR-8/SVneo was a kind gift from Dr. Charles Graham (Queen's University, Canada) [25]. Cells were cultured in RPMI 1640 medium (Hyclone) containing 10% fetal bovine serum (Gibco) and 100 U/ml penicillin-streptomycin solutions (PYG0016, Boster), under a 5% CO_2 atmosphere at 37°C.

2.2. Reagents and Treatment. HTR-8/SVneo cells were cultured with lipopolysaccharide (LPS, 200 ng/ml, Sigma) for 24 h to construct the preeclamptic trophoblast model as previously reported [10, 37–40]. 10~40 μM MET (S1950, Selleck Chemicals) were used for intervention. HTR-8/SVneo cells were pretreated with 3-(3-pyridinyl)-1-(4-pyridinyl)-2-propen-1-one (3PO, 10 μM, Merck Millipore) for 6 h to inhibit PFKFB3.

2.3. Cell Viability Assay. The trophoblastic viability was detected via the CCK8 assay (C0038, Beyotime). HTR8/SVneo cells were seeded at a density of 5×10^3 cells/well on 96-well plates. The cellular viability was determined at 24 h after being induced by MET. The CCK8 solution (10 μl) was added to each well, followed by 1 h of incubation at 37°C in the dark. The absorbance at 450 nm was measured using a Multimode Reader (Infinite F50, Tecan).

2.4. Apoptosis Analysis. The trophoblastic apoptosis was assessed using an Annexin V-FITC Apoptosis Detection Kit (BD Biosciences Pharmingen). Briefly, after the indicated treatments, the cells were resuspended in binding buffer and stained with 5 μl of propidium iodide (PI) and 5 μl of Annexin V-FITC. Subsequently, the stained cells were evaluated using a flow cytometer (BD Biosciences Pharmingen), and the percentage of apoptotic HTR-8/SVneo cells was Q2 plus Q3.

2.5. Cell Transfection. The pEX-1 vector (GenePharma, Shanghai, China) was used for PFKFB3 overexpression. The pEX-1 vector (Genechem, Shanghai, China) was used for TLR4 and NF-κB1 overexpression. The empty plasmid vector was used as the control. These plasmids were transfected into cells using Lipofectamine 3000 Reagent (Thermo Fisher Scientific) as required. The cells were transfected for 48 h and then collected for subsequent analyses. The transfection efficiency was evaluated using western blotting.

2.6. Western Blot Analysis. Proteins were extracted using radioimmunoprecipitation buffer and 100× phenylmethylsulfonyl. The protein concentration was measured by a BCA protein assay kit (P0010S, Beyotime). Sixty micrograms of protein per sample were subjected to 10% sodium dodecyl sulfate-polyacrylamide gel electrophoresis and transferred onto polyvinylidene fluoride membranes (0.45 μm pore size, Millipore). Then, the membranes were blocked with 5% nonfat milk in Tris-buffered saline containing 0.05% Tween 20 (TBST) for 1 h at room temperature. Next, the membranes were incubated, respectively, with TLR4 antibody (sc-293072, Santa Cruz), PFKFB3 antibody (13763-1-AP, Proteintech), NF-κB1 antibody (14220-1-AP, Proteintech), NF-κB p65 antibody (#8242, Cell Signaling Technology), phosphoNF-κB p65 antibody (#3033, Cell Signaling Technology), IκB antibody (A11397, ABclonal), phosphoIκB antibody (AP0614, ABclonal), phosphoIKK antibody (AP0891, ABclonal), NLRP3 antibody (19771-1-AP, Proteintech), caspase-1 antibody (22915-1-AP, Proteintech), ASC antibody (10500-1-AP, Proteintech), GSDMD antibody (20770-1-AP, Proteintech), and superoxide dismutase 2 (SOD2) antibody (A1340, ABclonal) overnight at 4°C. β-Actin antibody (20536-1-AP, Proteintech) was used as an internal control. The next day, they were brought to room temperature and washed with TBST three times. Then, the bands were incubated with appropriate secondary antibodies (1: 4,000, Affinity Biosciences) at room temperature for 1 h and visualized using an ECL kit (Millipore) according to the manufacturer's recommendations.

2.7. Enzyme-Linked Immunosorbent Assay (ELISA). Culture supernatant contents of IL-1β (HM10206, Bioswamp) and IL-18 (HM10337, Bioswamp) were assessed via the ELISA kits following the manufacturer's instructions.

2.8. Hoechst 33342/PI Double-Fluorescent Staining. Cellular pyroptosis was assessed using Hoechst 33342/PI double-fluorescent staining [41]. HTR-8/SVneo cells were cultured in six-well plates at a density of 5×10^5 cells per well, and the cells were transfected with varying constructs or treated with drugs. Next, the cells were stained with 10 μl Hoechst 33342 (C1027, Beyotime) solution at 37°C in the dark for 10 minutes, followed by staining with 5 μl PI at 25°C in the dark for 15 minutes. The stained cells were observed under a confocal microscope.

2.9. Electron Microscopy. For transmission electron microscope (TEM) observations, the samples were fixed in 4% paraformaldehyde (Sigma) and 2.5% glutaraldehyde (Sigma) in 0.1 M phosphate (Sigma) buffer overnight. After washing in 0.1 M phosphate buffer, the samples were postfixed for 1 h in 1% osmium tetroxide (Sigma) prepared in the same buffer. The samples were dehydrated with a graded series of ethyl alcohol concentrations, embedded in Epon 812, and polymerized at 60°C for 3 days. Ultrathin sections (60–70 nm) were obtained using an ultramicrotome (Leica Ultracut UCT, Germany). Ultrathin sections collected on grids (200 mesh) were examined in TEM (JEM 1010) operating at 60 kV, and images were recorded by a charge-coupled device camera (SC1000, Gatan). The images from electron microscopy were analyzed and measured by the ImageJ software for calculating the longest axis of mitochondrial length. At least over fifty mitochondria were measured and analyzed per sample to obtain data [42].

2.10. Mitochondrial Membrane Potential (MMP). MMP was evaluated via fluorescent probe JC-1 (C2006, Beyotime) using a confocal microscope. Normal mitochondria were presented as red while mitochondria with decreased MMP were presented as green. The ratio of green/red fluorescence intensity was calculated by ImageJ software to assess the MMP changes. At least 6 images per condition were analyzed. MMP was also evaluated by a flow cytometer. HTR-8/SVneo cells with healthy mitochondria were distributed in Q2, while cells with MMP decline were distributed in Q3.

2.11. Extracellular Acidification Rate (ECAR) and Oxygen Consumption Rate (OCR). For OCR and ECAR measurement, HTR-8/SVneo cells were seeded into Seahorse 24-well plates and were then treated according to the manufacturer's protocol after the indicated treatment. Seahorse Xfe24 analyzer (Seahorse Bioscience, Boston, MA, United States) was used for evaluation. All results were normalized to the cell number. For OCR measurement, oligomycin, carbonyl cyanide 4-(trifluoromethoxy) phenylhydrazone (FCCP), and rotenone were added. Basal respiration = (last rate measurement before oligomycin injection) – (minimum rate measurement after rotenone injection). Maximal respiration = (maximum rate measurement after FCCP injection) – (minimum rate measurement after rotenone injection). For ECAR evaluation, glucose, oligomycin, and 2-deoxyglucose (2-DG) were added according to the manufacturer's instructions. Glycolysis = (last rate measurement before oligomycin injection) – (minimum rate measurement before glucose injection). Glycolytic capacity = (maximum rate measurement after oligomycin injection) – (minimum rate measurement after 2 – DG injection).

2.12. Immunofluorescent Staining. Immunofluorescence in regards to the frozen placental tissues of the third trimester,

detection of PFKFB3 activity in the normotensive and preeclamptic placenta was performed as described previously [25]. Briefly, the primary antibodies were diluted in the appropriate blocking solution at the following concentrations: PFKFB3 antibody (1: 100; 13763-1-AP, Proteintech) and mouse anti-CK7 (1: 100; ab68459, Abcam). The secondary antibody was a FITC-labeled goat anti-rabbit IgG (Beyotime) and a Cy3-labeled goat anti-mouse IgG (Beyotime). The nuclei were stained with DAPI (Beyotime) for 3 min. HTR-8/SVneo cells in different groups cultured on coverslips were fixed by 4% paraformaldehyde for 20 min and then extracted with 0.5% Triton X-100 solution for 5 minutes. After blocking with TBST containing 1% bovine serum albumin, cells were incubated with indicated primary antibody NF-κB1 (1: 100; 14220-1-AP, Proteintech) for 1 h. After that, cells were washed and incubated with FITC-labeled goat anti-rabbit IgG (Beyotime) for 1 h, following with DAPI for 3 min. Images were captured with an inverted microscope and were analyzed by ImageJ.

2.13. Measurements of the Lactate Concentration, ATP Concentration, and NADPH/NADP+ Ratio. Extracellular lactate, intracellular ATP, and intracellular NADPH levels were measured using the following assay kits, according to the manufacturers' instructions: lactate assay kit (A019-2-1, Nanjing Jiancheng), ATP assay kit (S0027, Beyotime), and NADPH/NADP+ ratio (ab65349, Abcam).

2.14. Intracellular ROS Detection. Intracellular ROS generation was determined by fluorescent probe DCFH-DA (S0033, Beyotime). After washing twice with cold PBS, the HTR-8/SVneo cells were incubated with 10 μM DCFH-DA in the dark for 20 min. Green fluorescent images were captured using a confocal microscope. The level of intracellular ROS was also detected by flow cytometry. ImageJ and FlowJo software were used to analyze the results.

2.15. Chromatin Immunoprecipitation (ChIP) Assay. ChIP assays were conducted using the EZ-ChIP™ kit (Millipore). Briefly, protein-DNA complexes were cross-linked by 1% formaldehyde then quenched using 125 mM glycine. Cells were collected in shearing buffer (Diagenode, Denville, NJ, USA), and chromatin was sheared to an average DNA fragment size of 0.5-1 kb using a Bioruptor sonicator (Diagenode). After centrifugation, the supernatant was incubated with IgG or specific antibodies for NF-κB1, and chromatin DNA was purified and subjected to PCR detection. Primers for the PFKFB3 promoter are sense primer 5′-ATTGGCT GCTTTCATAGACCC-3′ and anti-sense primer 5′-CCAG GCTCAACCCATACTCC-3′.

2.16. Luciferase Reporter Gene Assays. Briefly, NF-κB1 response peak (p65 RE) and either wildtype or mutated PFKFB3 luciferase reporter vectors (containing a mutation in any of the predicted p65 binding sites) were transfected into the HTR-8/SVneo cells. After a 48 h incubation, the relative luciferase activity was measured with a dual-luciferase reporter system (RG027, Beyotime) using a Multimode Reader (Infinite M1000, Tecan).

2.17. RNA Extraction and qRT-PCR. Total RNA was isolated from the cells using RNAiso Plus (Takara, Japan) and then reversely transcribed using PrimeScript 1st RT Master Mix (Takara) according to the instructions of the manufacturer. The primer sequences were as follows: β-actin (internal group) forward primer: 5′-CACGATGGAGGGGCCGGAC TCATC-3′; reverse primer: 5′-TAAAGACCTCTATGCC AACACAGT-3′ and PFKFB3 forward primer: 5′-ATTGCG GTTTTCGATGCCAC-3′; reverse primer: 5′-GCCACAACT GTAGGGTCGT-3′. Quantitative real-time polymerase chain reaction (qRT-PCR) was performed on StepOne Real-Time PCR System with SYBR Premix Ex Taq (Takara) as described by the manufacturer's instructions. The qRT-PCR reaction consisted of a 95°C denaturation step for 30 s, 40 cycles (95°C for 5 s, 65°C for 30 s, and 60°C for 45 s) and an extension at 72°C for 60 s. The expression of target genes was established using the comparative cycle threshold (Ct; $2^{-\Delta\Delta CT}$) method.

2.18. Ubiquitination Assays. Ubiquitination assays were performed as described previously [43]. To assess the ubiquitination status of NLRP3, cells were collected in NETN buffer [20 mM Tris-HCl (pH 8), 100 mM NaCl, 1 mM EDTA, 0.5% Nonidet P-40, protease inhibitor mixture, and 1 mM phenylmethylsulfonyl fluoride], treated with 1% SDS, heated to 95°C for 15 min, and then diluted 10-fold in lysis buffer. The precleared lysates were incubated with the NLRP3 antibody (2 μg) in the presence of 40 μl of protein A/G agarose overnight at 4°C. Immunoprecipitates were collected by centrifugation for 1 min at 1000 × g at 4°C. The beads were then washed four times with lysis buffer. An aliquot (40 μl) of SDS-PAGE sample buffer (62.5 mM Tris-HCl, pH 6.8, 10% glycerol, 2% SDS, 0.001% bromophenol blue, and 10% β-mercaptoethanol) was added to the beads. Samples were resolved by SDS-PAGE, transferred to nitrocellulose membranes, and analyzed by immunoblotting with anti-ubiquitin antibody (1: 100, #3936, CST).

2.19. Statistical Analyses. For all analyses, data are shown as the mean ± standard deviation. The Student t-test was used for comparing two samples, and multigroup comparison was carried out using one-way ANOVA followed by Tukey's post hoc test. Statistical analysis was performed using GraphPad Prism 8.0 (USA). The P value of less than 0.05 was considered statistically significant. All data were obtained from ≥3 independent experiments.

3. Results

3.1. Pharmacological MET Concentrations Alleviated LPS-Induced NLRP3 Inflammasome Formation and Trophoblastic Pyroptosis. According to the MET pharmacokinetics in pregnancy [26, 44], we carefully designed a pharmacological MET concentration gradient (10~40 μM) in our study, which had no effects on trophoblastic viability or apoptosis through CCK-8 assays (Figure 1(a)) and flow cytometry analysis (Figures 1(b) and 1(c)). Low-dose LPS has long been utilized to induce preeclamptic trophoblast models [39, 40]. In line with the previous report [37], LPS (200 ng/ml, 24 h) in our study significantly upregulated the expressions of NLRP3,

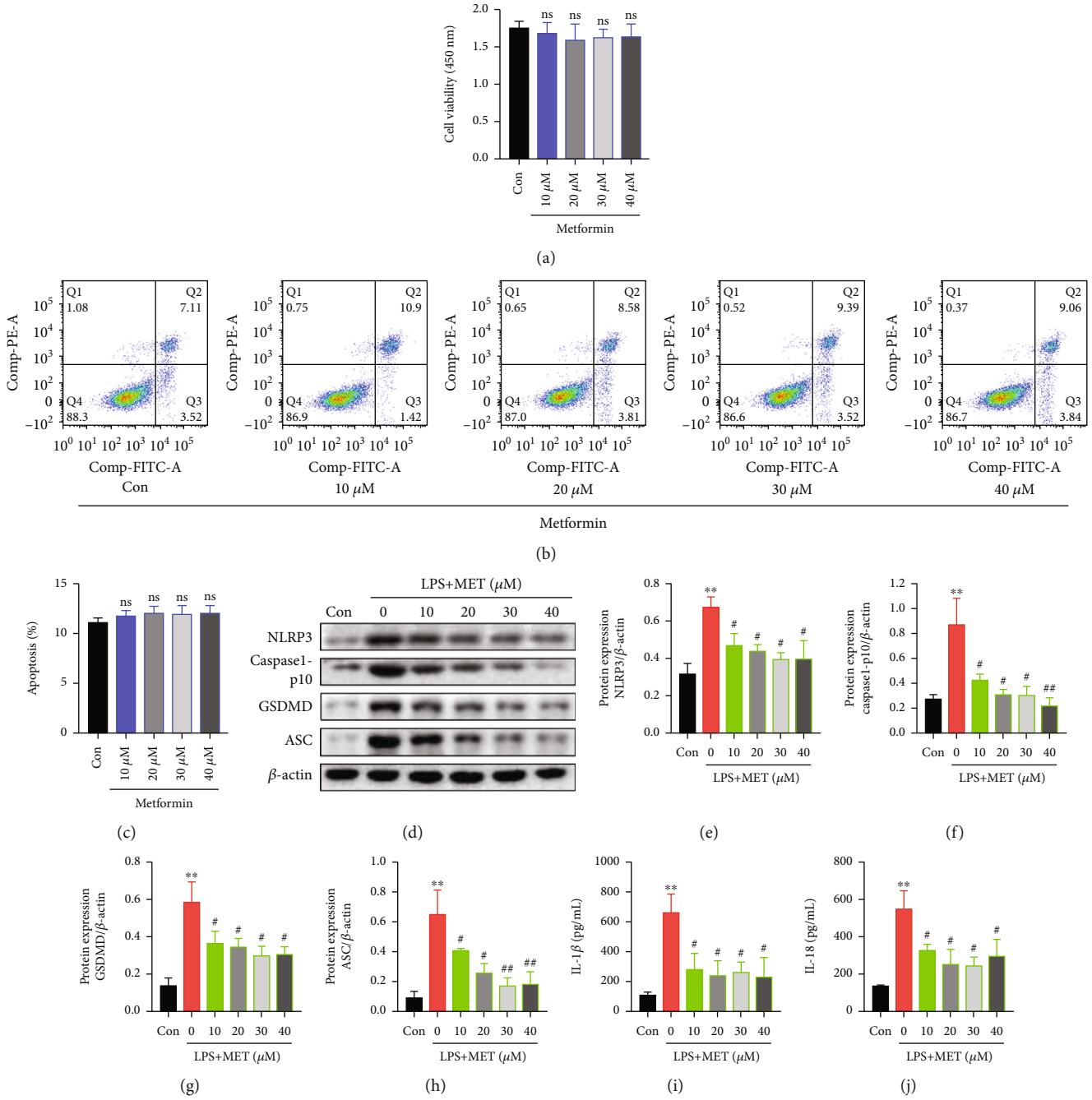

Figure 1: Pharmacological MET concentrations alleviated LPS-induced NLRP3 inflammasome formation and trophoblastic pyroptosis. (a) CCK-8 assays of HTR-8/SVneo cells treated with the indicated concentration of MET for 24 h. (b, c) Flow cytometry assays and quantitative analysis were performed to determine the apoptotic rates in HTR-8/SVneo cells treated with the indicated MET concentration for 24 h. (d–h) Western blot analysis of NLRP3, caspase1-p10, GSDMD, and ASC protein expression and densitometry quantification of NLRP3 (e), caspase1-p10 (f), GSDMD (g), and ASC (h) levels in HTR-8/SVneo cells were cultured with 200 ng/ml LPS and MET at different concentrations, respectively (10, 20, 30, and 40 μM). (i, j) ELISA analysis of IL-1β (i) and IL-18 (j) concentrations in cell culture medium. Data are shown as the mean ± SD from three independent experiments. ns: not significant compared with the Con group. $^{**}P < 0.01$ compared with the Con group. $^{\#}P < 0.05$ compared with the LPS group. $^{\#\#}P < 0.01$ compared with the LPS group by Student's t-test. SD: standard deviation.

caspase1-p10, ASC, and GSDMD proteins (Figures 1(d)–1(h)), as well as the secretion of IL-1β and IL-18 (Figures 1(i) and 1(j)) compared with the normal control. However, in our study, pharmacological MET concentrations downregulated NLRP3 expression and those downstream molecules in a dose-dependent manner (Figures 1(d)–1(j)). Given the previous studies and our data [33], 10 μM MET was chosen for subsequent experiments.

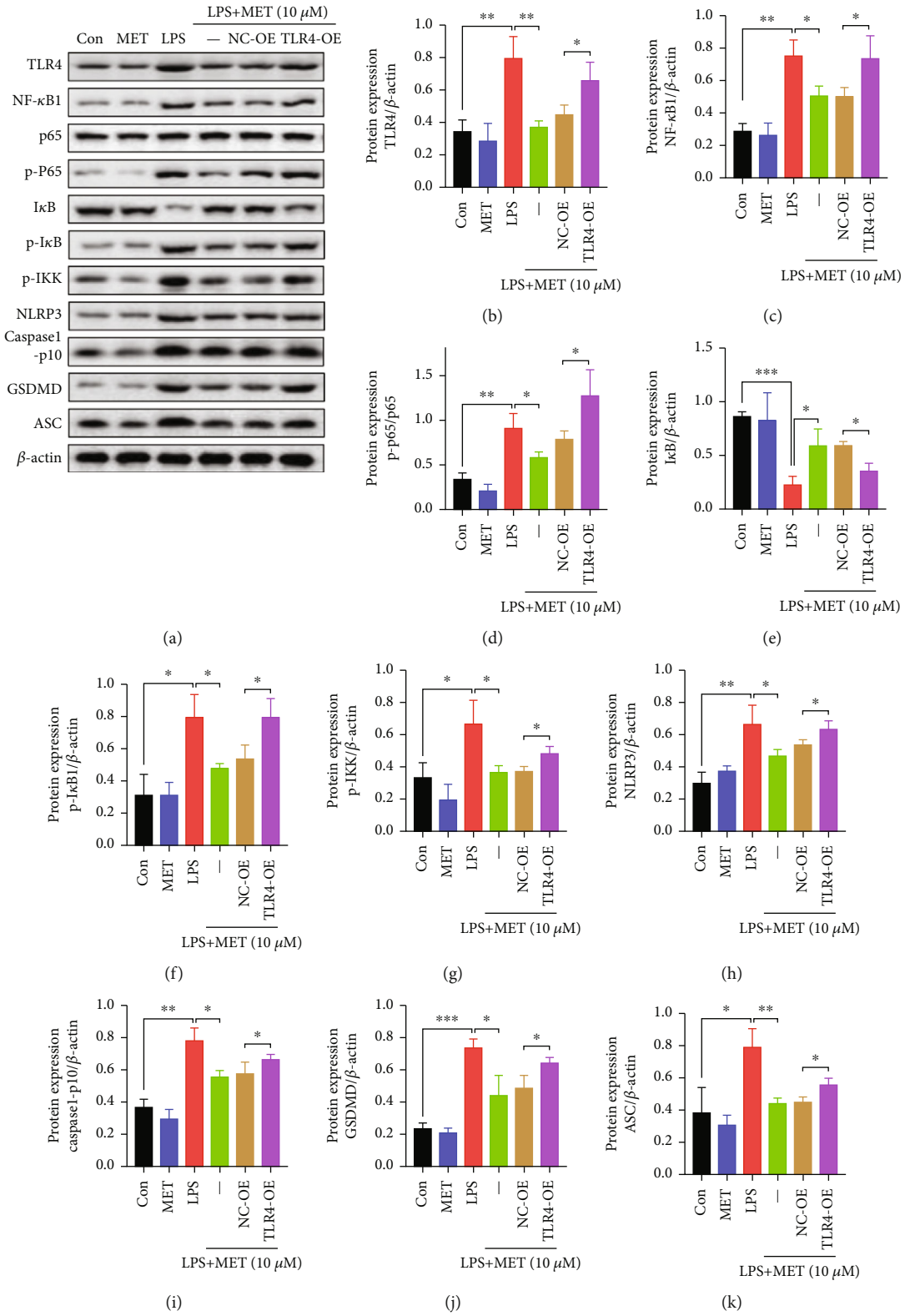

Figure 2: Continued.

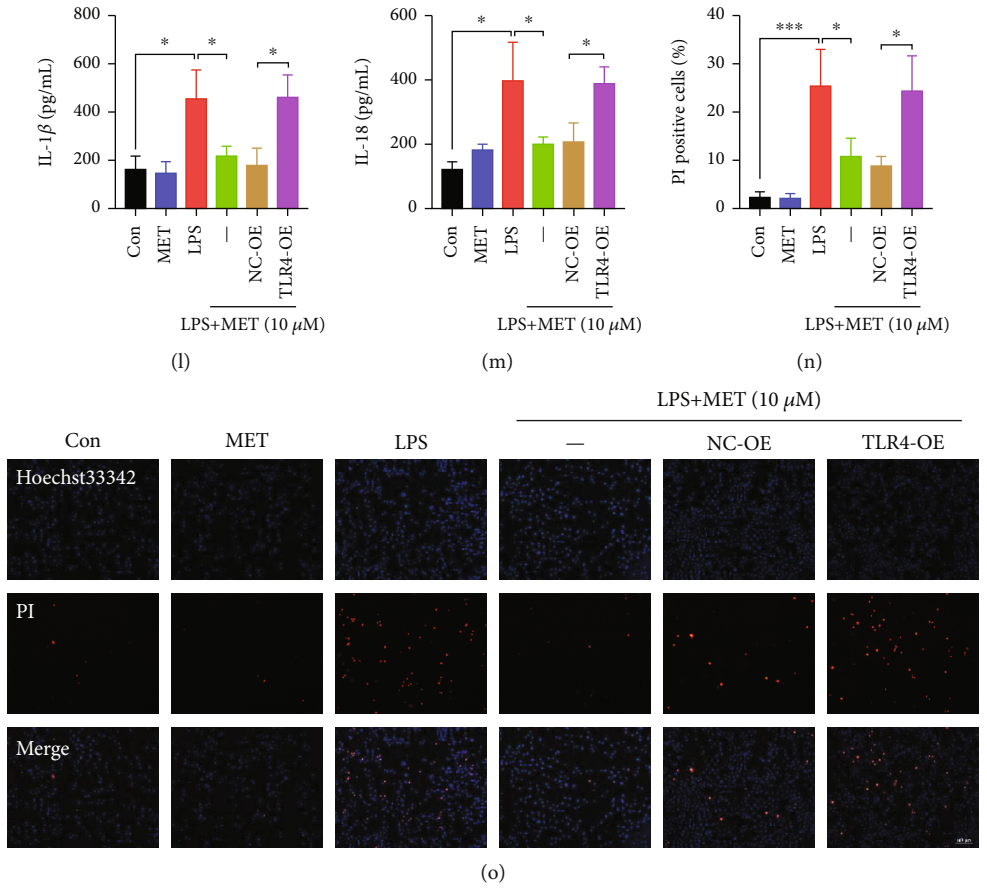

Figure 2: Pharmacological MET concentration suppressed NLRP3 inflammasome-induced pyroptosis partly through inhibiting the TLR4/NF-κB signaling. HTR-8/SVneo cells were transfected with TLR4 plasmid for overexpression or negative vector; 200 ng/ml LPS and 10 μM MET were subsequently incubated. (a–k) Western blot analysis of TLR4, NF-κB1, p65, p-p65, IκB, p-IκB, p-IKK, NLRP3, caspase1-p10, GSDMD, and ASC protein expression and densitometry quantification of TLR4 (b), NF-κB1 (c), p-p65/p65 (d), IκB (e), p-IκB (f), p-IKK (g), NLRP3 (h), caspase1-p10 (i), GSDMD (j), and ASC (k) levels. (l, m) ELISA analysis of IL-1β (l) and IL-18 (m) concentrations in cell culture medium from different groups. (n, o) Representative immunofluorescence images and quantification of double-fluorescent staining with PI (red) and Hoechst33342 (blue). Scale bar: 100 μm. Data are shown as the mean ± SD from three independent experiments. $^{*}P < 0.05$, $^{**}P < 0.01$, and $^{***}P < 0.001$ by Student's t-test. SD: standard deviation; NC-OE: negative vector; TLR4-OE: TLR4 overexpression plasmid.

3.2. Pharmacological MET Concentration Suppressed NLRP3 Inflammasome-Induced Pyroptosis Partly through Inhibiting the TLR4/NF-κB Signaling. Firstly, we validated the efficiency of TLR4 overexpression plasmid after 48 h transfection by western blot analysis (Figure S1A). Compared with the normal control, LPS markedly exacerbated its recognized downstream NF-κB signaling, characterized by the increased protein expression of TLR4 and NF-κB1, phosphorylation states of NF-κB and p65 (p-p65), phosphorylation states of IκB (p-IκB), phosphorylation states of IKK (p-IKK), and the reduced expression of IκB (Figures 2(a)–2(g)). Nevertheless, MET treatment partly diminished all those effects, indicating that MET is an effective inhibitor of the TLR4/NF-κB signaling [45] (Figures 2(a)–2(g)). We further induced TLR4 overexpression to reactivate its canonical downstream NF-κB signaling (Figures 2(a)–2(g)), which upregulated the protein levels of NLRP3, caspase1-p10, ASC, and GSDMD (Figures 2(h)–2(k)) and enhanced IL-1β and IL-18 release (Figures 2(l) and 2(m)) again. Hoechst33342/PI staining experiment showed increased PI uptake in LPS-stimulated trophoblasts (Figures 2(n) and 2(o)). The amounts of the PI-stained cells were markedly reduced after MET treatment, which was partly reversed by TLR4 overexpression (Figures 2(n) and 2(o)). Hence, we verified that the TLR4/NF-κB signaling contributed to NLRP3 inflammasome-induced pyroptosis in trophoblasts while MET suppressed trophoblastic pyroptosis partly through inhibiting the TLR4/NF-κB signaling.

3.3. Pharmacological Concentration of MET Corrected Metabolic Reprogramming in Trophoblasts Partly via the Suppression of the TLR4/NF-κB Signaling. The mitochondrial was long cable-like, thin strips in normal trophoblasts. On TLR4/NF-κB activation, the trophoblastic mitochondria were divided into several fragments with mitochondrial swell and cristae damage, suggesting the mitochondrial structure disruption. Despite under LPS stimulation, mitochondria in the MET-treated cells showed a predominantly

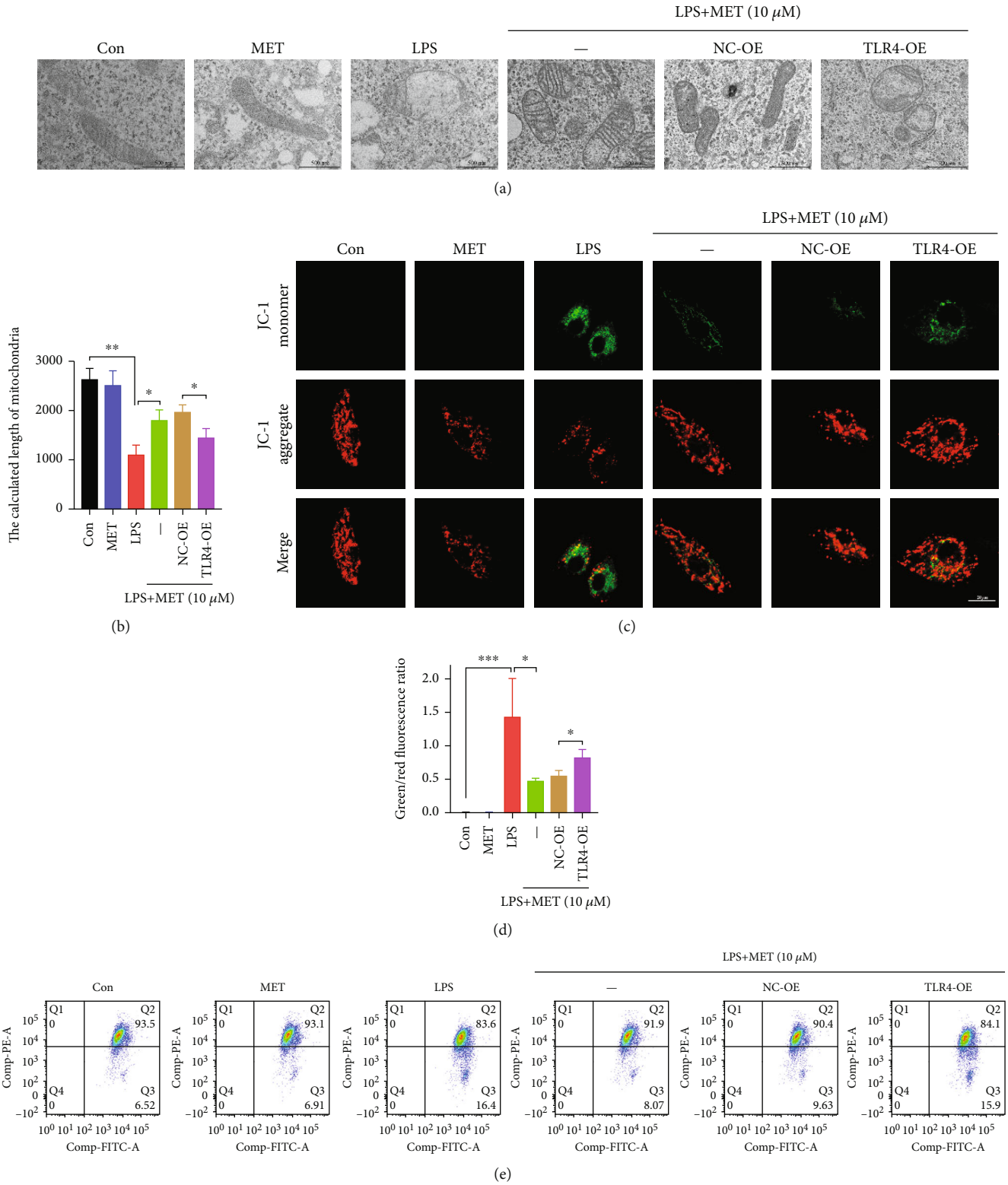

Figure 3: Continued.

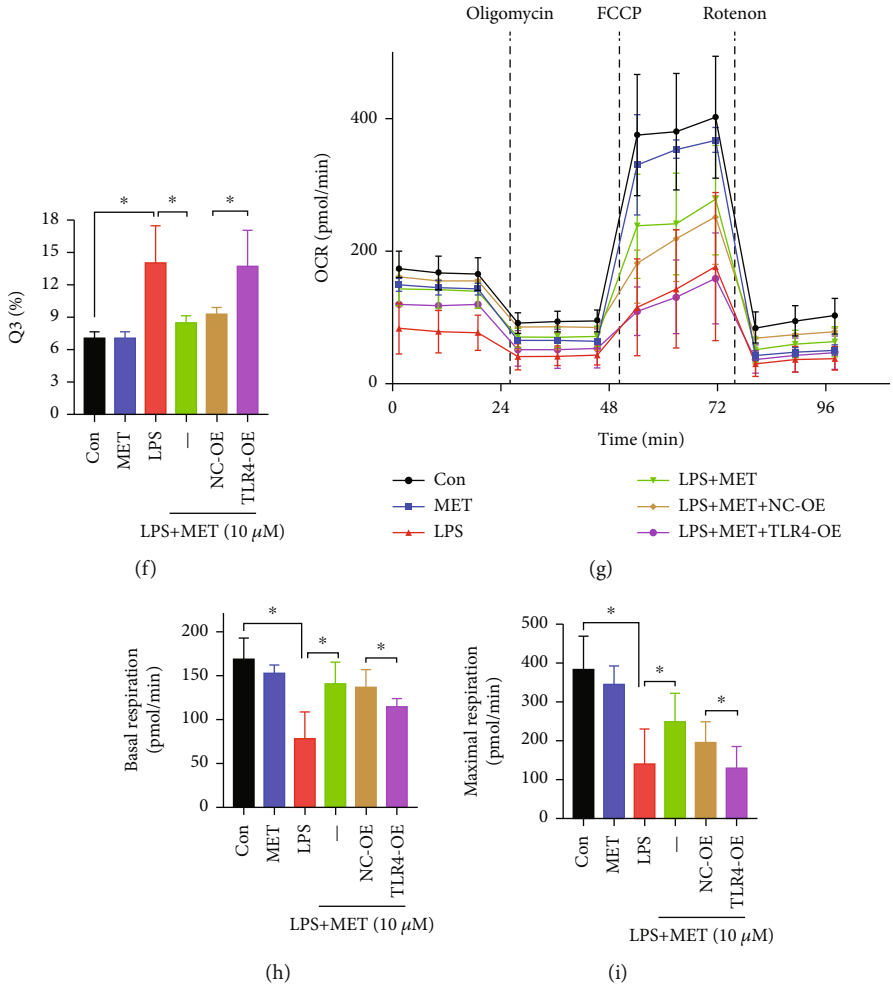

Figure 3: Pharmacological concentration of MET preserved mitochondrial homeostasis in trophoblasts partly via the suppression of the TLR4/NF-κB signaling. HTR-8/SVneo cells were transfected with TLR4 plasmid for overexpression or negative vector; 200 ng/ml LPS and 10 μM MET were subsequently incubated. (a, b) HTR-8/SVneo cells in different groups were observed by a transmission electron microscope to evaluate the mitochondrial structure, and the mitochondrial length was analyzed quantitatively. Scale bar: 500 nm. (c, d) MMP was evaluated by a confocal microscope. The ratio of green/red puncta was calculated to assess the MMP changes. At least 6 images per condition were analyzed. Scale bar: 20 μm. (e, f) Flow cytometry assays and quantitative analysis were also performed to determine the MMP of HTR-8/SVneo cells in different groups. (g–i) The OCR assay was used to observe the mitochondrial respiratory function. Data are shown as the mean ± SD from three independent experiments. $^{*}P < 0.05$, $^{**}P < 0.01$, and $^{***}P < 0.001$ by Student's t -test. SD: standard deviation; NC-OE: negative vector; TLR4-OE: TLR4 overexpression plasmid.

elongated form, which was partially destroyed by TLR4 overexpression, together with the swollen and broken cristae (Figures 3(a) and 3(b)). Mitochondrial membrane potential (MMP) assays via JC-1 fluorescence staining showed that LPS decreased the trophoblastic MMP while MET partly recovered it, although this effect was blocked by TLR4 overexpression (Figures 3(c) and 3(d)). Consistent results were also obtained from the JC-1 flow cytometry analysis (Figures 3(e) and 3(f)). OCR assays of OXPHOS were then conducted, further confirming that the OXPHOS was damaged on TLR4/NF-κB activation. The basal and maximum respiration rates were both improved after MET exposure, and this effect was blocked by TLR4-overexpression again (Figures 3(g)–3(i)).

Previously, we have reported that PFKFB3 is highly expressed in the preeclamptic placentas [25]. In this study, double labeling of immunofluorescence further demonstrated that PFKFB3 protein expressed in trophoblast cells was significantly increased in the preeclamptic trophoblasts (Figure 4(a)). In line with the latest report, LPS elevated PFKFB3 protein levels in this study, which was alleviated by pharmacological MET concentration [46]; however, TLR4 overexpression increased PFKFB3 expression again (Figures 4(b) and 4(c)). In lactate assays of culture medium, LPS significantly enhanced lactate release while we observed weaker lactate secretion in the LPS+MET group; however, TLR4 overexpression increased lactate secretion again (Figure 4(d)). Furthermore, measurement of ECAR revealed an abnormal increase in glycolysis and glycolysis capacity in the LPS group compared with the normal control group. This effect was partially abolished by MET treatment, though the TLR4 overexpression upregulated the glycolytic levels again

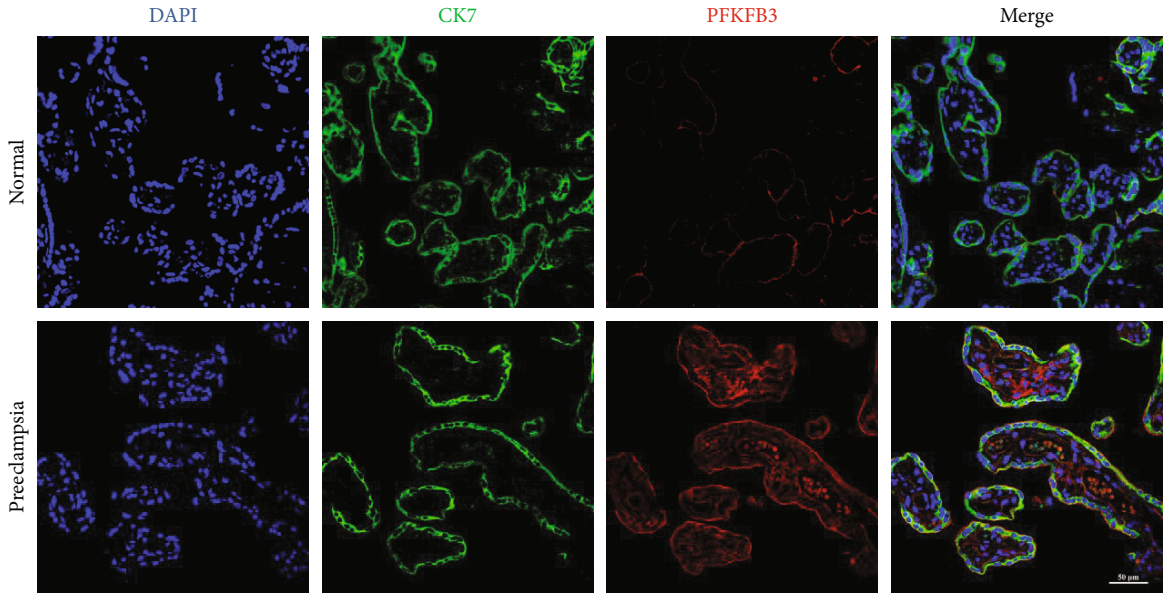

(a)

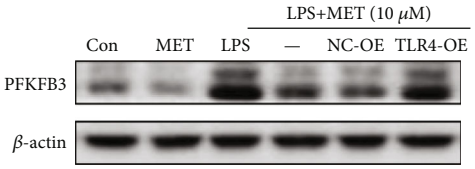

(b)

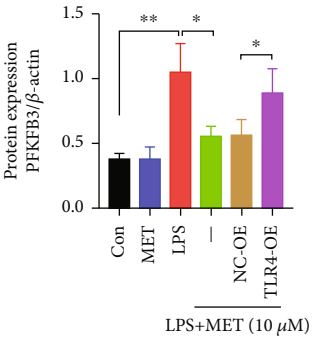

(c)

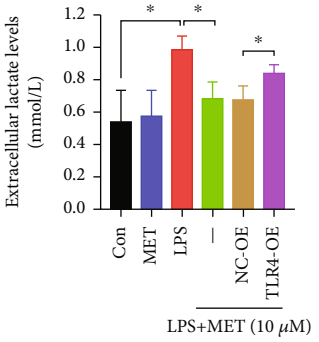

(d)

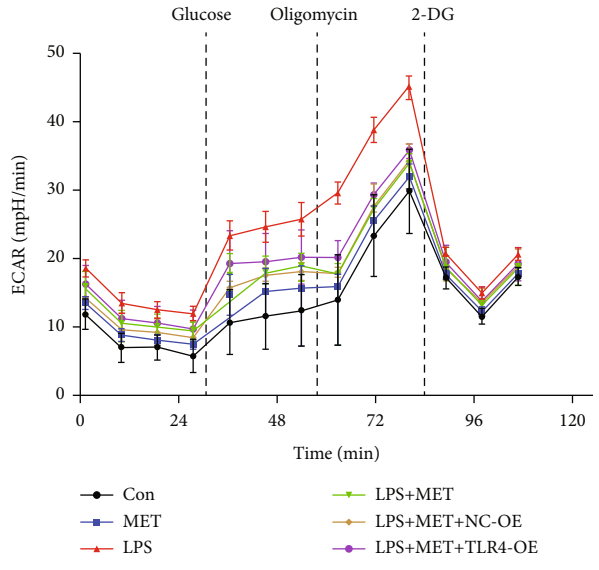

(e)

Figure 4: Continued.

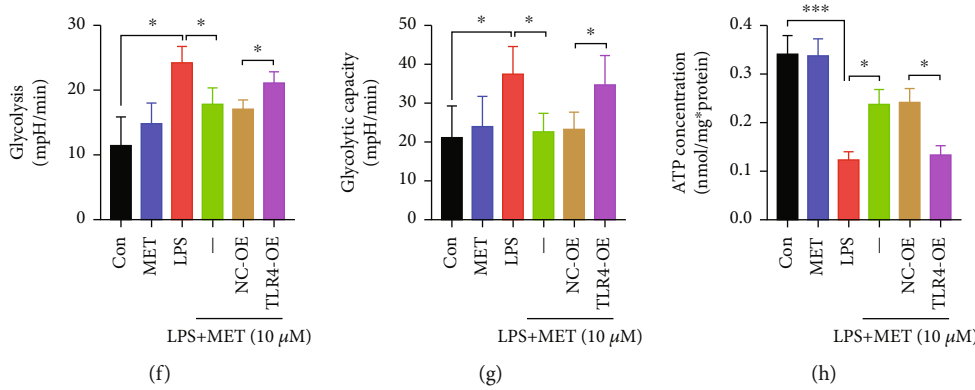

Figure 4: Pharmacological concentration of MET suppressed overactive glycolysis in trophoblasts partly via inhibiting the TLR4/NF-κB signaling. (a) Double labeling the immunofluorescence analysis of PFKFB3 (red) protein expression and localization in the placentae from full-term normal pregnancies and preeclampsia patients. DAPI (blue) and CK7 (green) for trophoblast localization. Scale bar: 50 μm. (b, c) Western blot analysis of PFKFB3 protein expression and the densitometry quantification. (d) Extracellular lactate release determination. (e–g) Glycolysis and glycolysis capacity were both detected by ECAR assay. (h) Cellular ATP concentration determination. Data are shown as the mean ± SD from three independent experiments. $^{*}P < 0.05$, $^{**}P < 0.01$, and $^{***}P < 0.001$ by Student's t-test. SD: standard deviation; NC-OE: negative vector; TLR4-OE: TLR4 overexpression plasmid.

(Figures 4(e)–4(g)). Eventually, trophoblast cells cultured with LPS exhibited ATP shortages despite the increased capacity for glycolysis, which was partially restored by MET treatment, although TLR4 overexpression abolished the protective effects of MET (Figure 4(h)). Hence, our data concluded that the overactive TLR4/NF-κB signaling disturbed the mitochondria and reprogrammed the glycometabolism to glycolysis represented by PFKFB3. Nevertheless, MET partly corrected the metabolic reprogramming through its inhibitory effects on TLR4/NF-κB.

3.4. Pharmacological Concentration of MET Restored the Trophoblastic Redox Homeostasis Partly through the Inhibition of the TLR4/NF-κB Signaling. NADPH, the reducing equivalents produced from pentose phosphate pathway, participates in the redox reaction. Therefore, we measured the NADPH/NADP+ ratio, which was diminished by LPS and induced again after MET exposure, though this effect was diminished by TLR4 overexpression again (Figure 5(a)). The immunofluorescence and flow cytometry data showed that LPS significantly increased the ROS levels while MET suppressed ROS generation in LPS-induced trophoblasts, though those were partly reversed via TLR4 overexpression (Figures 5(b)–5(e)). Furthermore, we tested the expression level of SOD2, a vital antioxidant. LPS significantly reduced the SOD2 expression while MET partly elevated the SOD2 expression, though it was decreased by TLR4 overexpression again (Figures 5(f) and 5(g)). Therefore, all these data indicated that pharmacological MET concentration restored the redox homeostasis in LPS-induced trophoblasts partly via the suppression of the TLR4/NF-κB signaling.

3.5. Pharmacological Concentration of MET Reduced the Transcription of PFKFB3 via Blocking Transcription Factor NF-κB1 Directly Binding on PFKFB3 Promoter. To explore the underlying mechanism by which inflammatory stimuli induce metabolic reprogramming, we wondered whether the glycolytic enzyme PFKFB3 could be modulated via the NF-κB signaling, a classic inflammatory pathway, at the transcriptional level. Transcription factor NF-κB1 was screened out from factors predicted by the PROMO database in the promoter sequence of PFKFB3 within a dissimilarity margin less or equal than 5% [47, 48]. We validated the efficiency of the NF-κB1 overexpression plasmid after 48 h transfection by western blot analysis (Figure S1B). LPS and NF-κB1 overexpression both enhanced the nuclear translocation of NF-κB1, though they were partly reversed by MET (Figure 6(a)). Then, according to the USCS database [49], we found the peak (from -248 bp to 155 bp relative to TSS) of the transcription factor NF-κB1 in the promotor sequence of PFKFB3. Moreover, according to the JASPAR database [50], we found the binding sites of NF-κB1 in the peak sequence (Figure 6(b)). Therefore, we hypothesized that PFKFB3 might be regulated via the transcription factor NF-κB1. Besides, consistent with the previous reports [30], our abovementioned data also mechanically proved MET an inhibitor of the NF-κB signaling. Thus, MET might decrease NF-κB1 binding on the PFKFB3 promoter. We performed a ChIP assay, showing that the level of NF-κB1 targeting PFKFB3 promoter could be significantly increased on LPS and NF-κB1, which could all be partly reversed by MET (Figure 6(c)). As further confirmation, we cloned the PFKFB3 promoter containing the peak of NF-κB1 to the PGL3.0-Basic reporter plasmid and dual-luciferase reporter assays showed that LPS and NF-κB1 overexpression remarkably upregulated the transcriptional activity of PFKFB3 vectors; however, MET treatment could eliminate these effects (Figure 6(d)). RT-PCR showed that LPS and NF-κB1 overexpression both elevated the mRNA expression of PFKFB3 in trophoblasts, which were partially reversed by MET (Figure 6(e)). All these above data indicated PFKFB3 as a newly identified transcriptional target of the NF-κB signaling, whereas MET

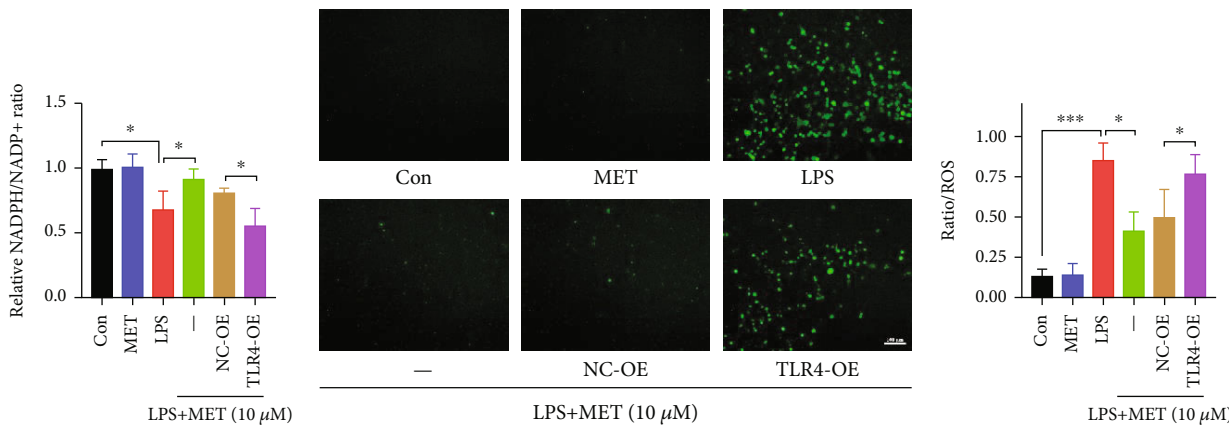

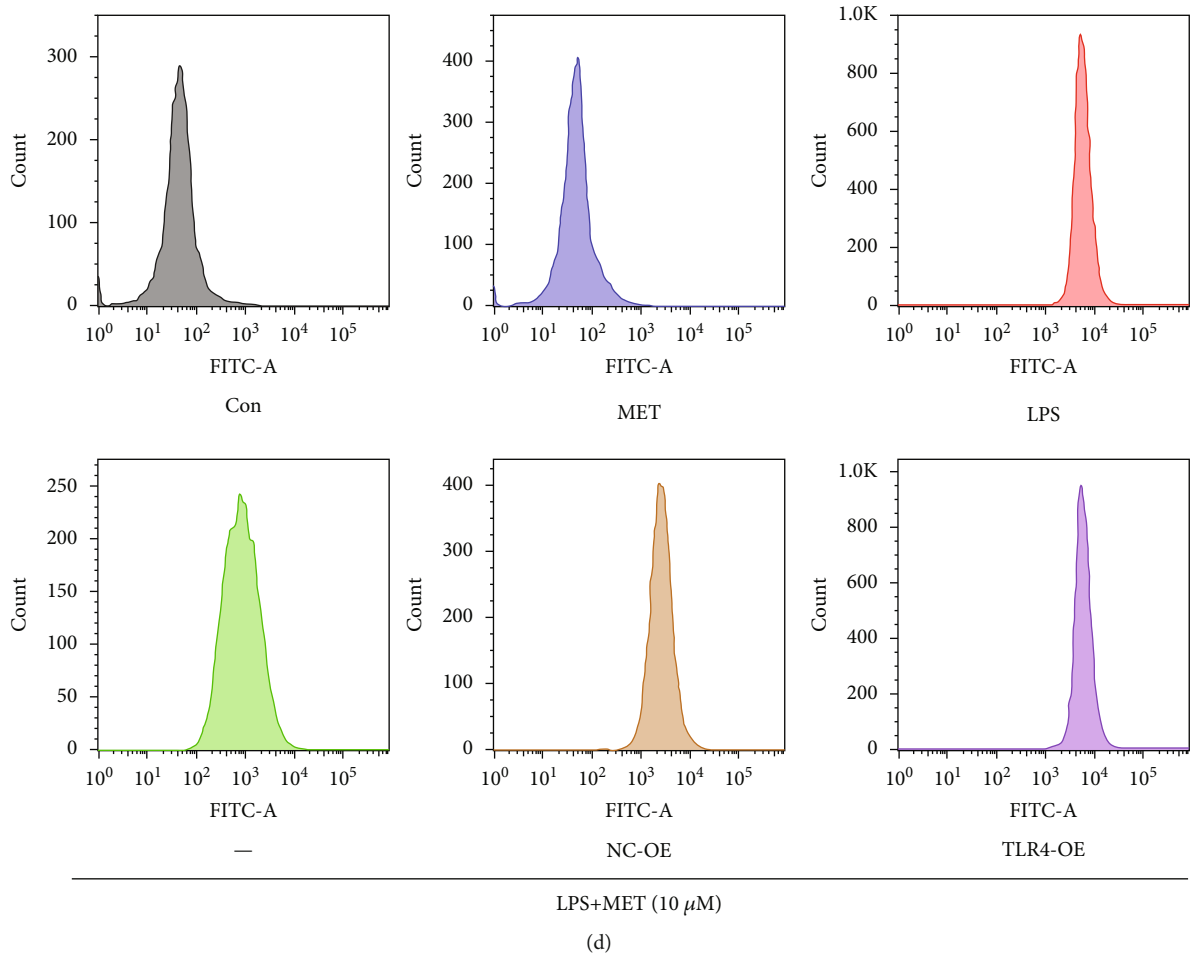

Figure 5: Continued.

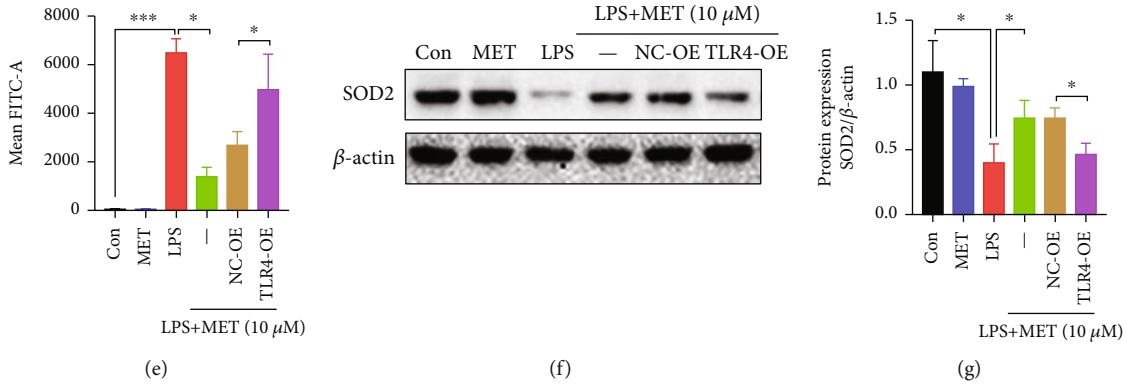

FIGURE 5: Pharmacological concentration of MET restored the trophoblastic redox homeostasis partly through the inhibition of the TLR4/NF-κB signaling. HTR-8/SVneo cells were transfected with TLR4 plasmid for overexpression or negative vector; 200 ng/ml LPS and 10 μM MET were subsequently incubated. (a) The cellular levels of NADPH were measured in HTR-8/SVneo cells in different groups. (b, c) Representative images showing DCFH-DA fluorescence signals (green) indicative of ROS and the comparison of mean fluorescence intensities across different groups. Scale bar: 100 μm. (d, e) Flow cytometry analysis and quantitative analysis of cellular ROS content in different groups. (f, g) Western blot analysis of SOD2 protein expression and the densitometry quantification. Data are shown as the mean ± SD from three independent experiments. $^{*}P < 0.05$, $^{**}P < 0.01$, and $^{***}P < 0.001$ by Student's t-test. SD: standard deviation; NC-OE: negative vector; TLR4-OE: TLR4 overexpression plasmid.

reduced the PFKFB3 transcription via blocking transcription factor NF-κB1 binding on the PFKFB3 promoter.

3.6. PFKFB3 Regulated the NF-κB Signaling as well as the NLRP3 Inflammasome-Induced Pyroptosis while the Pharmacological Concentration of MET Suppressed Pyroptosis Partly via Inhibiting PFKFB3. To order to verify whether glycolytic enzyme PFKFB3 participates in the TLR4/NF-κB/NLRP3 inflammasome-induced pyroptosis, we utilized a PFKFB3 inhibitor 3PO [51] at a concentration of 10 μM through CCK8 assays (Figure S1C). Compared with the LPS groups, 3PO inhibited the NF-κB signaling, further decreasing NLRP3, caspase1-p10, ASC, and GSDMD protein levels (Figures 7(a)–7(k)), upregulating the NLRP3 ubiquitination levels (Figure 7(l)), mitigating the IL-1β and IL-18 secretion (Figures 7(m) and 7(n)), and reducing the proportion of the PI-stained cells (Figures 7(o) and 7(p)).

We also validated the efficiency of the PFKFB3 overexpression plasmid after 48 h transfection by western blot analysis (Figure S1D). Compared with the NC-OE groups, PFKFB3 overexpression activated the NF-κB signaling again and downregulated the levels of NLRP3 ubiquitination, further increasing the protein expression of NLRP3 as well as those pyroptosis-relevant molecules (Figures 7(a)–7(n)). The analysis of the PI-stained cell also showed a similar trend (Figures 7(o) and 7(p)). Thus, we concluded that glycolytic enzyme PFKFB3 promoted trophoblastic inflammation and NLRP3 inflammasome-induced pyroptosis while MET suppressed those effects partly via inhibiting PFKFB3.

4. Discussion

In this study, we found that (1) pharmacological concentration of MET alleviated NLRP3 inflammasome-induced pyroptosis partly through inhibiting the TLR4/NF-κB signaling; (2) pharmacological MET concentration restored the metabolic and redox homeostasis in trophoblasts partly via the suppression of the TLR4/NF-κB signaling; (3) MET decreased the transcription of PFKFB3 via blocking transcription factor NF-κB1 binding on PFKFB3 promoter; (4) PFKFB3 augmented the NF-κB signaling as well as the NLRP3 inflammasome-induced pyroptosis while MET suppressed pyroptosis partly via inhibiting PFKFB3. This study clarifies that the TLR4/NF-κB/PFKFB3 pathway may be a novel link between glucose metabolism reprogramming and NLRP3 inflammasome-induced pyroptosis in trophoblasts. Further, MET inhibits the TLR4/NF-κB/PFKFB3 pathway to ameliorate trophoblastic metabolism disorders and pyroptosis, likely to be a plausible therapy to prevent and cure PE (Figure 8).

LPS, a classic TLR4 agonist, has long been used to make preeclamptic models for years as LPS amplifies the TLR4/NF-κB signaling to trigger trophoblastic inflammation [39, 40]. Consistent with the latest research [37, 52], our results showed that LPS significantly activated the TLR4/NF-κB signaling, further contributing to the NLRP3 inflammasome-induced pyroptosis. Because of the release of the proinflammatory factors IL-1β and IL-18, the NLRP3 inflammasome-induced pyroptosis is not only a crucial way to induce trophoblastic death in the preeclamptic placentas but also a possible amplifier of maternal systematic injury via triggering sterile inflammatory cascades. MET has long been found to exert inhibitory effects on the TLR4/NF-κB signaling [30–32]. Therefore, we wonder whether MET can ameliorate trophoblastic pyroptosis. Perhaps because almost all previous studies were conducted with supraphar-macological concentrations (doses) of MET that is much higher than maximally achievable therapeutic concentrations (10~40 μM) with the oral administration of 0.5–2.5 g/d [44], the results of those experiments may be too controversial to truly reflect the effects of MET on trophoblasts [53, 54]. Hence, we carefully chose the pharmacological concentration of MET (10 μM) according to the MET pharmacokinetics during pregnancy [33] and the CCK8 assays in this study.

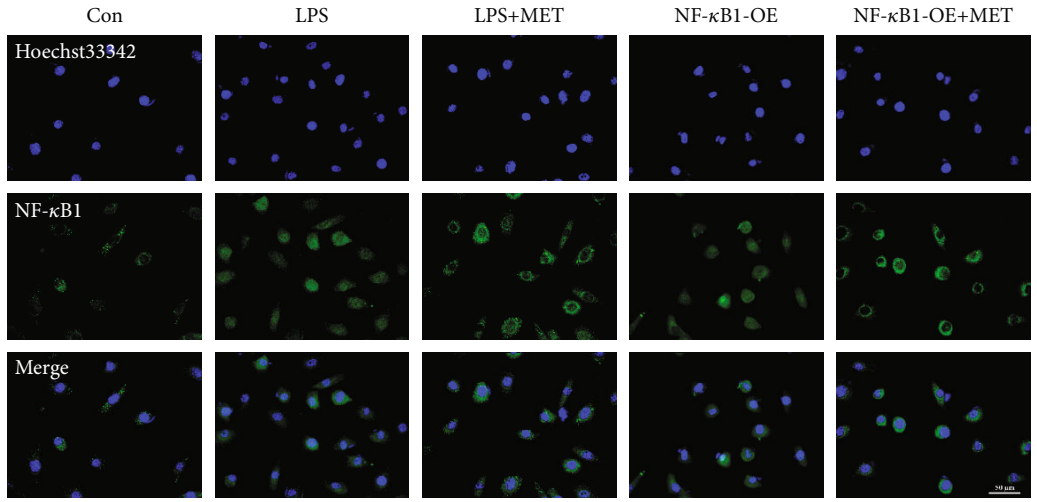

(a)

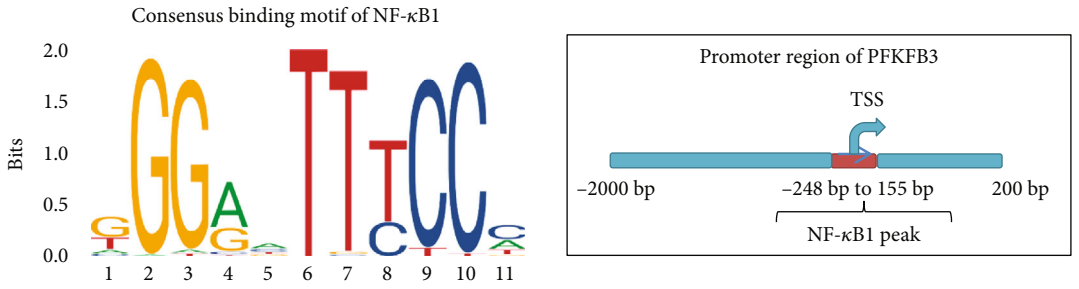

(b)

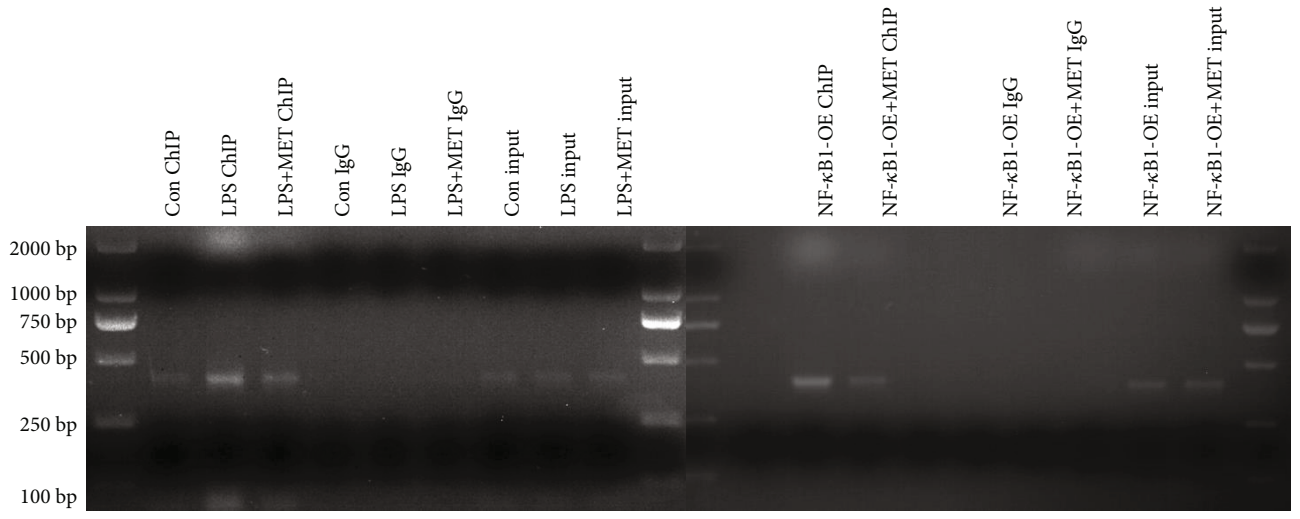

(c)

Figure 6: Continued.

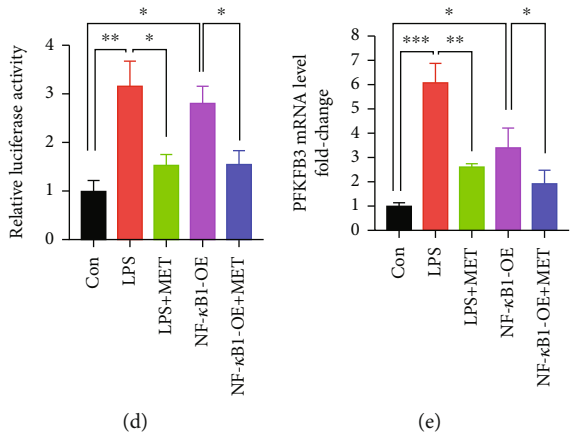

Figure 6: Pharmacological concentration of MET reduced the transcription of PFKFB3 via blocking transcription factor NF-κB1 directly binding on PFKFB3 promoter. HTR-8/SVneo cells were transfected with NF-κB1 plasmid for overexpression; 200 ng/ml LPS and 10 μM MET were subsequently incubated. (a) Representative images of NF-κB1 immunostaining in HTR-8/SVneo cells in different groups. At least 6 images per condition were analyzed. Scale bar: 50 μm. (b) Consensus binding motif of NF-κB1 from the JASPAR database and the NF-κB1 peak in the PFKFB3 promoter were found using the USCS database. (c) In the ChIP assay, PCR products of PFKFB3 in different groups are shown. DNA ChIP-ed with nonspecific IgG was used as a negative control. (d) Dual-luciferase reporter assays were performed to determine the PFKFB3 promoter activity in HTR8/SVneo cells in different groups. (e) qRT-PCR analysis of PFKFB3 mRNA levels in HTR-8/SVneo cells in different groups. Data are shown as the mean ± SD from three independent experiments. $^{*}P < 0.05$, $^{**}P < 0.01$, and $^{***}P < 0.001$ by Student's t-test. SD: standard deviation; NF-κB1-OE: NF-κB1 overexpression plasmid.

Our data showed that the pharmacological concentration of MET alleviated NLRP3 inflammasome-induced pyroptosis, which partly depended on inhibiting the TLR4/NF-κB signaling. Recently, *in vivo* study has reported that MET exerts protective effects on LPS-induced PE rat models partly through diminishing the NF-κB signaling to ameliorate placental injury, oxidative/nitrative stress, and systemic inflammatory responses [55]. Herein, our study further suggested that MET is beneficial to trophoblasts, which partly lies in the suppression of TLR4/NF-κB-primed pyroptosis.

Up till now, the characteristics of metabolism in the preeclamptic placentas remain ambiguous. A majority of studies have previously reported the mitochondrial swelling and broken cristae together with the mitochondrial dysfunction [56] in the preeclamptic placentas [57], thereby causing the reduced ATP synthesis [58]. But until now, very little research has focused on the glycolytic capacities in the preeclamptic placentas. Metabolomic analysis has found the upregulated concentration of the glycolytic product (lactate and pyruvate) [59, 60] in the serum from PE women, which impaired OXPHOS capacity while enhanced glycolysis in trophoblasts, resulting in a weak ATP synthesis [61] owing to the lower efficiency of glycolysis [20]. PE mice induced by soluble fms-like tyrosine kinase 1 (sFlt-1) showed accelerated glycolytic flux in the placenta labyrinth, together with the ATP shortage [62]. The expressions of glycolytic enzymes PKM2 and PFKFB3 are also abnormally increased in the preeclamptic human placentas [25, 63]. The research mentioned above collectively indicates the plausible metabolic switch to glycolysis in preeclamptic trophoblasts; however, whether it is associated with the TLR4/NF-κB signaling has yet to be confirmed. In our studies, LPS-induced TLR4/NF-κB activation destroyed mitochondrial structure and disrupted mitochondrial function in trophoblasts, which agrees with the latest research [64]. Meanwhile, TLR4/NF-κB activation caused the metabolic reprogramming to the augmented glycolysis, characterized by the elevated secretion of lactate and the increased expression of PFKFB3, the pacemaker of glycolysis. The metabolic reprogramming eventually leads to an ATP shortage in trophoblasts. Currently, it has been reported that MET probably has dual effects on mitochondria, characterized by diminishing impaired mitochondria via mitophagy concomitant with mitochondrial biogenesis to restore mitochondrial function [20]. Furthermore, suprapharmacological MET concentrations (1 mM) disturb mitochondrial respiration while pharmacological MET concentrations (50 μM) improve OXPHOS and mitochondrial function [65, 66]. Analogously, in our study, pharmacological MET concentration (10 μM) ameliorated the mitochondrial dysfunction and damages while suppressed the overactivated glycolysis, thus getting the trophoblastic metabolism back to track with the increased cellular ATP production, which may owe to the inhibitory effect of MET on the TLR4/NF-κB signaling. Consistent with the latest research [46, 67, 68], we also found that pharmacological concentration of MET downregulated the PFKFB3 expression, which is probably the mechanism for MET inhibiting the overactive glycolysis in trophoblasts. Therefore, MET could reverse the TLR4/NF-κB-induced metabolic reprogramming.

The reducing equivalent NADPH is tightly involved in the redox metabolism. In preeclamptic trophoblastic models, the decreased NADPH production symbolized the less diversion of glucose through the pentose phosphate pathway [69], also indicating the increased glycolysis flux as well as the oxidative stress. With the high levels of ROS and lower levels of SOD2 detected in TLR4/NF-κB-activated trophoblasts, our data further elucidated that the TLR4/NF-κB-

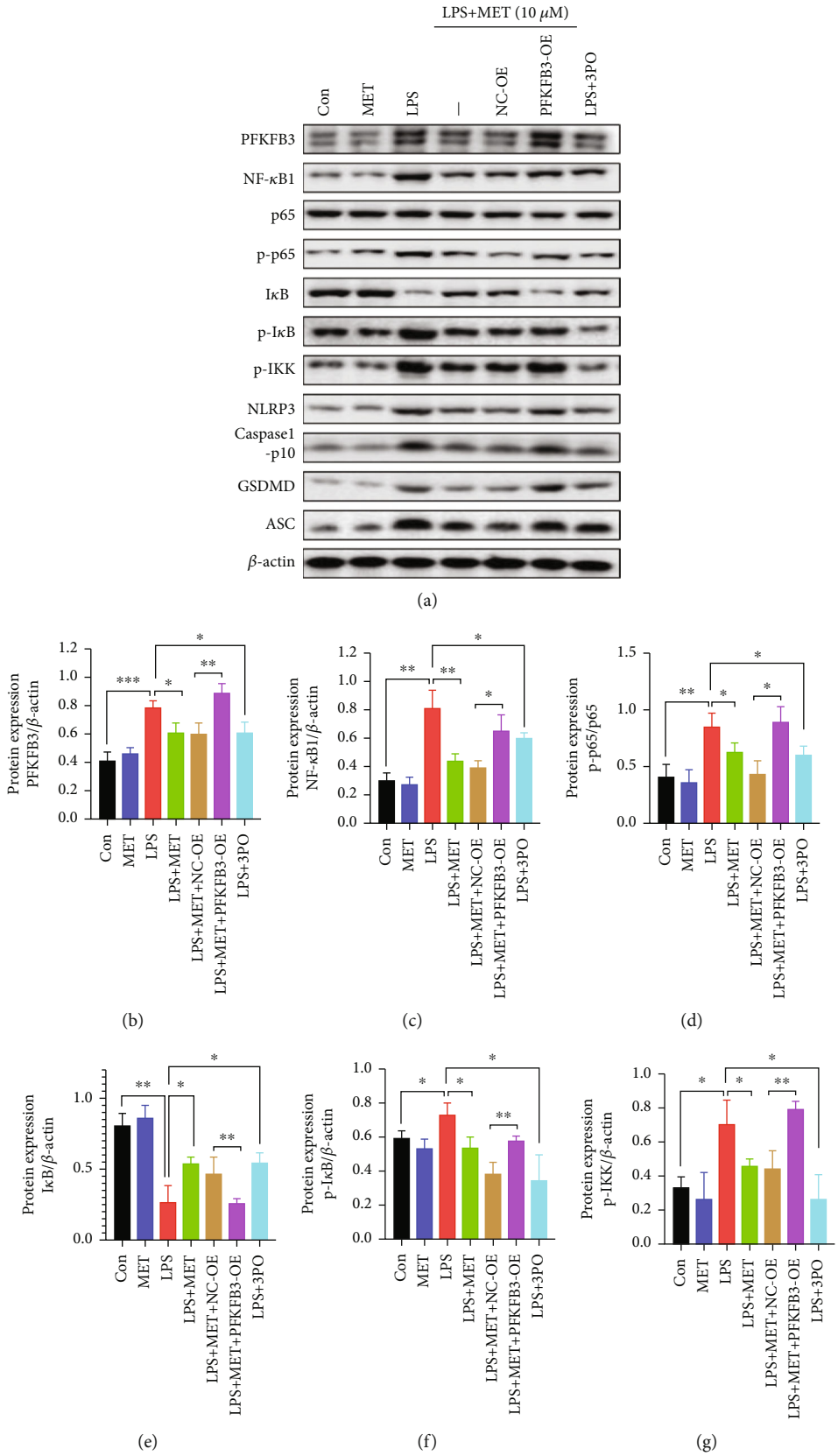

Figure 7: Continued.

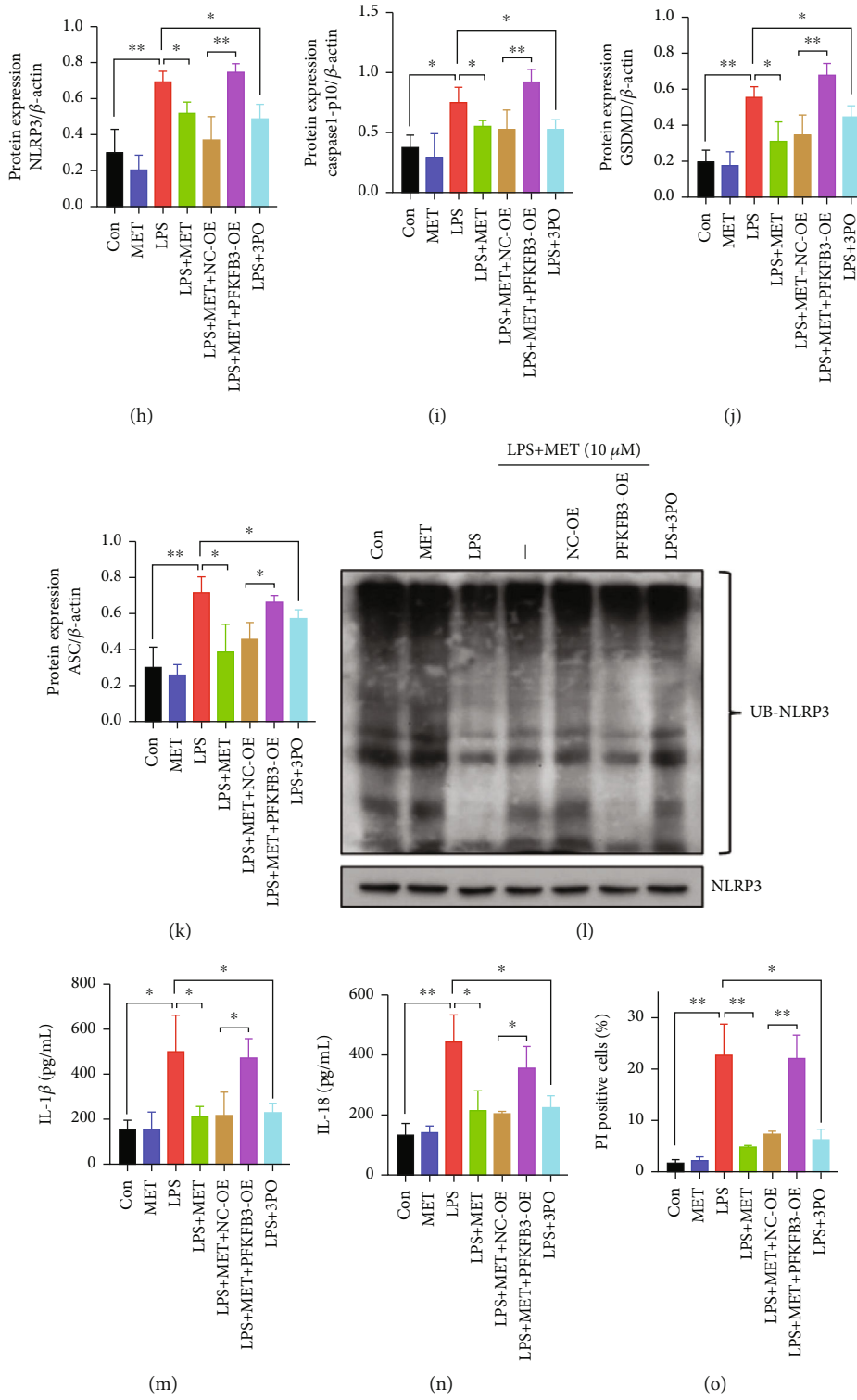

Figure 7: Continued.

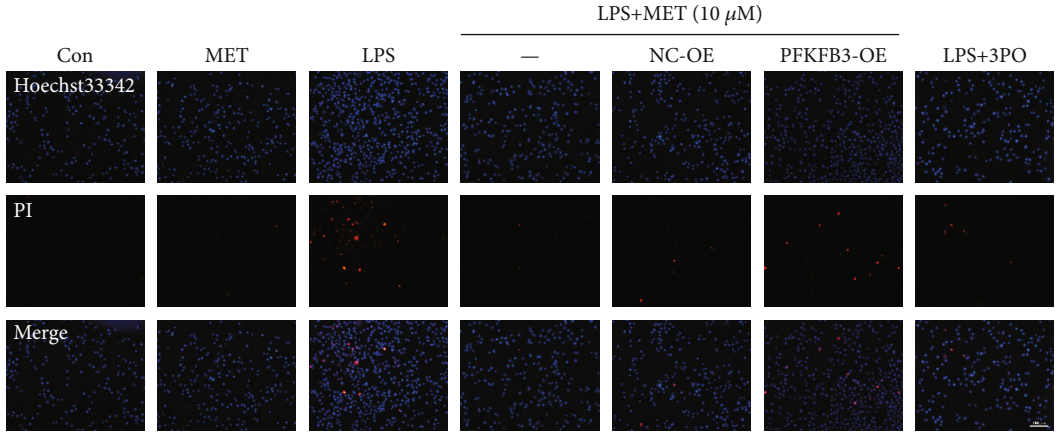

Figure 7: PFKFB3 modulated the NF-κB signaling as well as the NLRP3 inflammasome-induced pyroptosis while the pharmacological concentration of MET suppressed pyroptosis partly via inhibiting PFKFB3. HTR-8/SVneo cells were transfected with PFKFB3 plasmid for overexpression or negative vector; 200 ng/ml LPS, 10 μM MET, and 10 μM 3PO were subsequently incubated. (a–k) Western blot analysis of PFKFB3, NF-κB1, p65, p-p65, IκB, p-IκB, p-IKK, NLRP3, caspase1-p10, GSDMD, and ASC protein expression and densitometry quantification of PFKFB3 (b), NF-κB1 (c), p-p65/p65 (d), IκB (e), p-IκB (f), p-IKK (g), NLRP3 (h), caspase1-p10 (i), GSDMD (j), ASC (k) levels. (l) Analysis of NLRP3 ubiquitination levels in HTR-8/SVneo cells of different groups. (m, n) ELISA analysis of IL-1β (m) and IL-18 (n) concentrations in cell culture medium. (o, p) Representative immunofluorescence images and quantification of double-fluorescent staining with PI (red) and Hoechst33342 (blue). Scale bar: 100 μm. Data are shown as the mean ± SD from three independent experiments. $^{*}P < 0.05$, $^{**}P < 0.01$, and $^{***}P < 0.001$ by Student's t-test. SD: standard deviation; NC-OE: negative vector; PFKFB3-OE: PFKFB3 overexpression plasmid.

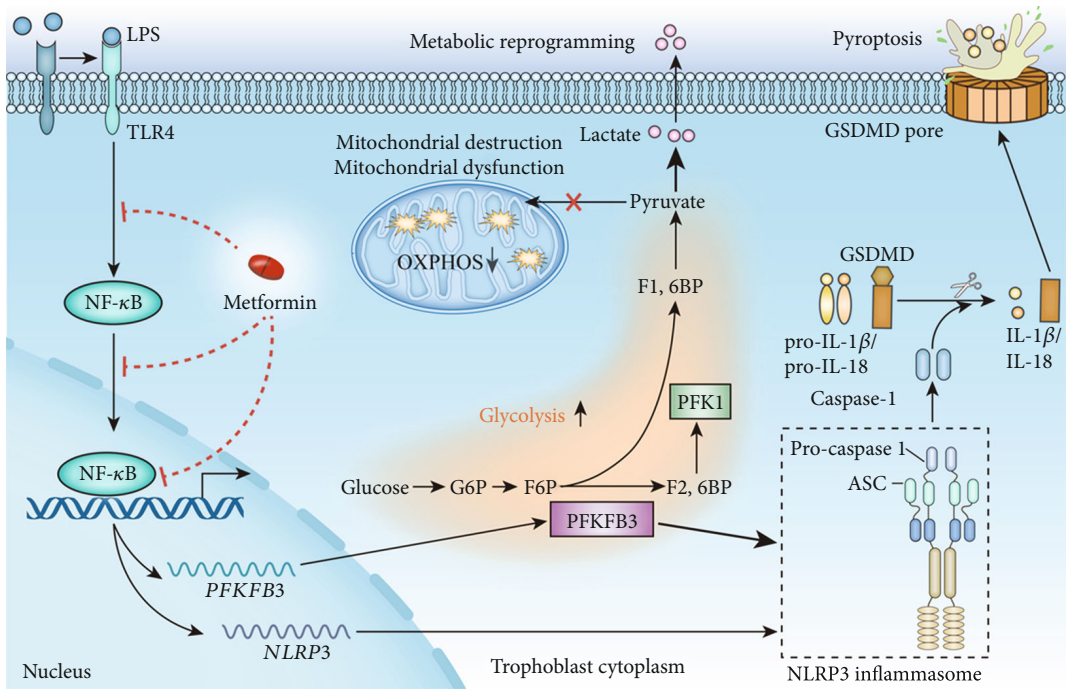

Figure 8: A mechanism diagram. LPS-induced TLR4/NF-κB activation caused NLRP3 inflammasome-induced pyroptosis in trophoblasts. Besides, the TLR4/NF-κB signaling caused mitochondrial destruction and dysfunction; meanwhile, it reprogrammed the glycometabolism to glycolysis with increased PFKFB3 expression. The TLR4/NF-κB signaling induced PFKFB3 expression by transcriptional factor NF-κB1 binding PFKFB3 promoter region. Glycolytic enzyme PFKFB3 further exacerbated NLRP3 inflammasome-induced pyroptosis, leading to positive feedback. Metformin inhibited the TLR4/NF-κB/PFKFB3 signaling to break the vicious circle, expected to be a novel candidate for preeclamptic therapies.

induced metabolic disorders might inextricably link with the redox disturbances in the PE placentas. Amounts of research have demonstrated that MET can suppress oxidative stress [70]. In vivo study has further demonstrated that MET restored the SOD activity in LPS-induced PE rat models [55]. Also, we have previously reported that PFKFB3 could enhance oxidative stress in LPS-induced trophoblasts [25]. In this study, MET also decreased the TLR4/NF-κB-induced ROS level, which may partly rely on the PFKFB3 inhibition as well as the recuperative NADP+/NADPH ratio and SOD2 level. Therefore, MET may reverse the TLR4/NF-κB-induced metabolic reprogramming and preserved redox homeostasis in trophoblasts.

Previously, we reported that the trophoblastic PFKFB3 expression was significantly upregulated in response to the TLR4 activation [25] while the concrete molecular mechanisms remain unclear. Based on the PFKFB3 promoter sequence, we speculated that transcription factor NF-κB1 is crucial for PFKFB3 expression. Moreover, the nuclear translocation of NF-κB1 in our study was increased once LPS activated or NF-κB1 overexpression; however, those were all reversed by MET. Afterward, dual-luciferase reporter assays and ChIP assays further indicated that LPS stimulation and NF-κB1 overexpression both cause the increased PFKFB3 expression by NF-κB1 directly binding PFKFB3 promoter region while MET decreased the transcription of PFKFB3 via blocking transcription factor NF-κB1 binding on PFKFB3 promoter.

There is accumulating evidence suggesting that cellular metabolic reprogramming to glycolysis closely interacted with the phenotype switch to the proinflammatory states [71]. The abovementioned data showed that the TLR4/NF-κB signaling was an upstream regulator of PFKFB3. However, our previous study has reported that LPS increased the protein expression of PFKFB3 and activated the NF-κB signaling while PFKFB3 knockdown via PFKFB3 siRNA in LPS-induced trophoblasts significantly inhibited the NF-κB signaling [25]. The pharmacological inhibition of PFKFB3 by 3PO in this study also suppressed the NF-κB signaling. Thus, there might be a positive feedback loop between the PFKFB3-activated glycolysis and the NF-κB signaling. Recently, NLRP3 inflammasome was reported to modulate glycolysis by increasing PFKFB3 in macrophages [72]. However, PFKFB3 not only positively modulated the NF-κB signaling but also further activated inflammasome-induced pyroptosis in our study, which attracts us to continue in-depth study in the future as there may exist intricate and feedback relationships between metabolism and inflammatory immune responses. Most of the previous research [73–75] has pointed out that MET can inhibit NLRP3 inflammasome-induced pyroptosis, which owes much to the adenosine monophosphate-activated protein kinase (AMPK), a well-known metabolic sensor monitoring the cellular energy states. Consequently, MET is very likely to regulate cellular pyroptosis via its metabolic modulation effects. In our study, MET alleviated TLR4/NF-κB-stimulated pyroptosis in trophoblasts, which also partly depended on the PFKFB3 inhibition. Ubiquitination is a crucial posttranslational modification of NLRP3 as deubiquitination of NLRP3 is essential for its activation [76]. NLRP3 in resting cells is targeted for ubiquitylation and subsequent proteasomal degradation while LPS primes the NLRP3 inflammasome by inhibiting its ubiquitination and degradation [77]. In this study, LPS significantly reduced the ubiquitination level of NLRP3 while MET partly restore it. However, PFKFB3 overexpression decreased the NLRP3 ubiquitination again. Meanwhile, PFKFB3 inhibitor 3PO significantly upregulated the NLRP3 ubiquitination level in LPS-induced trophoblasts. Thus, all those indicated that PFKFB3 may modulate the NLRP3 inflammasome assembly partly via regulating NLRP3 ubiquitination. However, the underlying mechanism between PFKFB3 and NLRP3 ubiquitination is still not well understood and follow-up experiments are necessary. We clarified that MET suppressed the trophoblastic pyroptosis, which may be partly related to the protection of mitochondrial homeostasis as well as the inhibition of the glycolytic enzyme PFKFB3, thus breaking the vicious circle.

Originally introduced as the first-line therapy for type 2 diabetes mellitus, MET has now been found in clinical trials to significantly reduce the incidence of gestational hypertension and PE in pregnant women with multiple PE-related risks. Additionally, the safety of taking MET during human pregnancies has been preliminarily ensured. Relevant lab studies have demonstrated that the underlying mechanism includes proangiogenic benefits, endothelial protection, anti-inflammatory activities, metabolic modulation, and protective effects on trophoblasts to improve placental development. Together with its easy administration, global availability, and low cost, MET is expected to be a promising option for the prevention and treatment of PE. Nonetheless, there are still some limitations in current studies, and the design of the relevant research scheme is supposed to be further improved in the future. Concretely, experimental MET concentration and PE models should be cautiously chosen. Also, further studies on both short-term and long-term risks and benefits for the fetus are necessary. Furthermore, the clinical trial protocol should be further optimized to evaluate the reduction in the prevalence of PE as a primary endpoint. Therefore, we look forward to more high-quality randomized controlled trials and well-designed lab studies in the future to clarify the place of MET in the prevention and treatment of PE [26].

5. Conclusion

Our study verified that the TLR4/NF-κB/PFKFB3 signaling might be a novel link between the reprogrammed glycometabolism and trophoblastic pyroptosis, providing novel insights into the pathogenesis of preeclampsia. However, the pharmacological concentration of MET corrects glycometabolism reprogramming, oxidative stress, and NLRP3 inflammasome-induced pyroptosis partly via inhibiting the TLR4/NF-κB/PFKFB3 signaling in trophoblasts, which further supports that MET is expected to be a promising option for the prevention and treatment of PE.

Data Availability

The data are included in the article to support the findings of this study.

Conflicts of Interest

The authors have declared that no competing interest exists.

Authors' Contributions

Li Zou, Xiaoxia Liu, and Yang Zhang conceived and designed the study. Yang Zhang, Weifang Liu, and Yanqi Zhong acquired, analyzed, and interpreted the data. Yang Zhang, Qi Li, Mengying Wu, and Liu Yang drafted and edited the manuscript. Yang Zhang, Weifang Liu, Yanqi Zhong, Qi Li, Xiaoxia Liu, and Li Zou critically revised the manuscript for intellectual content. All authors approved the final version of the manuscript.

Acknowledgments

This work was supported by the National Nature Science Foundation of China (No. 82001584 to Xiaoxia Liu and No. 82101788 to Weifang Liu) and the Nature Science Foundation of Hubei Province, China (2020CFB411 to Xiaoxia Liu).

Supplementary Materials

Supplementary Figure S1: overexpression efficacy identification and CCK8 assay. *(Supplementary Materials)*

References

[1] C. W. Ives, R. Sinkey, I. Rajapreyar, A. T. N. Tita, and S. Oparil, "Preeclampsia–Pathophysiology and Clinical Presentations:," *Journal of the American College of Cardiology*, vol. 76, no. 14, pp. 1690–1702, 2020.

[2] K. Shirasuna, T. Karasawa, and M. Takahashi, "Role of the NLRP3 inflammasome in preeclampsia," *Frontiers in Endocrinology*, vol. 11, p. 80, 2020.

[3] M. W. Socha, B. Malinowski, O. Puk, M. Dubiel, and M. Wiciński, "The NLRP3 inflammasome role in the pathogenesis of pregnancy induced hypertension and preeclampsia," *Cell*, vol. 9, no. 7, p. 1642, 2020.

[4] D. Liu, X. Zeng, X. Li, J. L. Mehta, and X. Wang, "Role of NLRP3 inflammasome in the pathogenesis of cardiovascular diseases," *Basic Research in Cardiology*, vol. 113, no. 1, 2018.

[5] C. Lebeaupin, E. Proics, C. H. D. de Bieville et al., "ER stress induces NLRP3 inflammasome activation and hepatocyte death," *Cell Death & Disease*, vol. 6, no. 9, article e1879, 2015.

[6] T. Kawai and S. Akira, "The role of pattern-recognition receptors in innate immunity: update on Toll-like receptors," *Nature Immunology*, vol. 11, no. 5, pp. 373–384, 2010.

[7] T. Fernandes-Alnemri, S. Kang, C. Anderson, J. Sagara, K. A. Fitzgerald, and E. S. Alnemri, "Cutting edge: TLR signaling licenses IRAK1 for rapid activation of the NLRP3 inflammasome," *Journal of Immunology (Baltimore, Md : 1950)*, vol. 191, no. 8, pp. 3995–3999, 2013.

[8] Z. Liu, L. Gan, Y. Xu et al., "Melatonin alleviates inflammasome-induced pyroptosis through inhibiting NF-κB/GSDMD signal in mice adipose tissue," *Journal of Pineal Research*, vol. 63, no. 1, 2017.

[9] Y. He, H. Hara, and G. Núñez, "Mechanism and regulation of NLRP3 inflammasome activation," *Trends in Biochemical Sciences*, vol. 41, no. 12, pp. 1012–1021, 2016.

[10] K. Tamura, G. Ishikawa, M. Yoshie et al., "Glibenclamide inhibits NLRP3 inflammasome-mediated IL-1β secretion in human trophoblasts," *Journal of Pharmacological Sciences*, vol. 135, no. 2, pp. 89–95, 2017.

[11] Z. Mei, B. Huang, X. Qian, Y. Zhang, and B. Teng, "Gastrodin improves preeclampsia-induced cell apoptosis by regulation of TLR4/NF-κB in rats," *Food Science & Nutrition*, vol. 8, no. 2, pp. 820–829, 2020.

[12] H. Sha, Y. Ma, Y. Tong, J. Zhao, and F. Qin, "Apocynin inhibits placental TLR4/NF-κB signaling pathway and ameliorates preeclampsia-like symptoms in rats," *Pregnancy Hypertens*, vol. 22, pp. 210–215, 2020.

[13] I. CW, M. Romão-Veiga, M. L. Matias et al., "Increased expression of NLRP3 inflammasome in placentas from pregnant women with severe preeclampsia," *Journal of Reproductive Immunology*, vol. 123, pp. 40–47, 2017.

[14] G. S. Støndle, G. B. Silva, L. H. Tangerås et al., "Placental inflammation in pre-eclampsia by Nod-like receptor protein (NLRP)3 inflammasome activation in trophoblasts," *Clinical and Experimental Immunology*, vol. 193, no. 1, pp. 84–94, 2018.

[15] B. Everts, E. Amiel, S. C.-C. Huang et al., "TLR-driven early glycolytic reprogramming via the kinases TBK1-IKKε supports the anabolic demands of dendritic cell activation," *Nature Immunology*, vol. 15, no. 4, pp. 323–332, 2014.

[16] C. M. Krawczyk, T. Holowka, J. Sun et al., "Toll-like receptor-induced changes in glycolytic metabolism regulate dendritic cell activation," *Blood*, vol. 115, no. 23, pp. 4742–4749, 2010.

[17] G. Feng, X. Yang, Y. Li, X. Wang, S. Tan, and F. Chen, "LPS enhances platelets aggregation via TLR4, which is related to mitochondria damage caused by intracellular ROS, but not extracellular ROS," *Cellular Immunology*, vol. 328, pp. 86–92, 2018.

[18] G. J. Burton, E. Jauniaux, and A. J. Murray, "Oxygen and placental development; parallels and differences with tumour biology," *Placenta*, vol. 56, pp. 14–18, 2017.

[19] P. Vangrieken, S. Al-Nasiry, A. Bast et al., "Placental mitochondrial abnormalities in preeclampsia," *Reproductive Sciences (Thousand Oaks, Calif)*, vol. 28, no. 8, pp. 2186–2199, 2021.

[20] I. Aye, C. E. Aiken, D. S. Charnock-Jones, and S. GCS, "Placental energy metabolism in health and disease–significance of development and implications for preeclampsia," *American Journal of Obstetrics and Gynecology*, 2020.

[21] M. M. Hughes and L. A. J. O'Neill, "Metabolic regulation of NLRP3," *Immunological Reviews*, vol. 281, no. 1, pp. 88–98, 2018.

[22] J. S. Moon, S. Hisata, M. A. Park et al., "mTORC1-induced HK1-dependent glycolysis regulates NLRP3 inflammasome activation," *Cell Reports*, vol. 12, no. 1, pp. 102–115, 2015.

[23] M. Xie, Y. Yu, R. Kang et al., "PKM2-dependent glycolysis promotes NLRP3 and AIM2 inflammasome activation," *Nature Communications*, vol. 7, no. 1, 2016.

[24] A. Yalcin, S. Telang, B. Clem, and J. Chesney, "Regulation of glucose metabolism by 6-phosphofructo-2-kinase/fructose-2,6-bisphosphatases in cancer," *Experimental and Molecular Pathology*, vol. 86, no. 3, pp. 174–179, 2009.

[25] Y. Zhang, W. Liu, M. Wu et al., "PFKFB3 regulates lipopolysaccharide-induced excessive inflammation and cellular dysfunction in HTR-8/Svneo cells: implications for the role of PFKFB3 in preeclampsia," *Placenta*, vol. 106, pp. 67–78, 2021.

[26] Y. Zhang, X. Liu, L. Yang, and L. Zou, "Current researches, rationale, plausibility, and evidence gaps on metformin for the management of hypertensive disorders of pregnancy," *Frontiers in Pharmacology*, vol. 11, 2020.

[27] Z. Lv and Y. Guo, "Metformin and its benefits for various diseases," *Frontiers in Endocrinology*, vol. 11, 2020.

[28] J. L. Tarry-Adkins, S. E. Ozanne, and C. E. Aiken, "Impact of metformin treatment during pregnancy on maternal outcomes: a systematic review/meta-analysis," *Scientific Reports*, vol. 11, no. 1, p. 9240, 2021.

[29] A. Syngelaki, K. H. Nicolaides, J. Balani et al., "Metformin versus placebo in obese pregnant women without diabetes mellitus," *The New England Journal of Medicine*, vol. 374, no. 5, pp. 434–443, 2016.

[30] G. Kanigur Sultuybek, T. Soydas, and G. Yenmis, "NF-κB as the mediator of metformin's effect on ageing and ageing-related diseases," *Clinical and Experimental Pharmacology & Physiology*, vol. 46, no. 5, pp. 413–422, 2019.

[31] X. Li, L. Wang, X. Yang, and C. Huang, "Metformin attenuates ischemia-reperfusion injury of fatty liver in rats through inhibition of the TLR4/NF-κB axis," *Balkan Medical Journal*, vol. 37, no. 4, pp. 196–202, 2020.

[32] Y. Zhou, X. Y. Ma, J. Y. Han et al., "Metformin regulates inflammation and fibrosis in diabetic kidney disease through TNC/TLR4/NF-κB/miR-155-5p inflammatory loop," *World Journal of Diabetes*, vol. 12, no. 1, pp. 19–46, 2021.

[33] M. Vega, M. Mauro, and Z. Williams, "Direct toxicity of insulin on the human placenta and protection by metformin," *Fertility and Sterility*, vol. 111, no. 3, pp. 489–496.e5, 2019.

[34] Y. Jia, R. Cui, C. Wang et al., "Metformin protects against intestinal ischemia-reperfusion injury and cell pyroptosis via TXNIP-NLRP3-GSDMD pathway," *Redox Biology*, vol. 32, p. 101534, 2020.

[35] J. Zhang, L. Huang, X. Shi et al., "Metformin protects against myocardial ischemia-reperfusion injury and cell pyroptosis via AMPK/NLRP3 inflammasome pathway," *Aging*, vol. 12, no. 23, pp. 24270–24287, 2020.

[36] R. D. Vanlalhruaii, R. Ramachandran, J. E. Mathews et al., "How safe is metformin when initiated in early pregnancy? A retrospective 5-year study of pregnant women with gestational diabetes mellitus from India," *Diabetes Research and Clinical Practice*, vol. 137, pp. 47–55, 2018.

[37] S. Park, J. Shin, J. Bae, D. Han, and H. W. J. C. Park, "SIRT1 alleviates LPS-induced IL-1β production by suppressing NLRP3 inflammasome activation and ROS production in trophoblasts," *Cells*, vol. 9, no. 3, p. 728, 2020.

[38] E. Laresgoiti-Servitje, "A leading role for the immune system in the pathophysiology of preeclampsia," *Journal of Leukocyte Biology*, vol. 94, no. 2, pp. 247–257, 2013.

[39] M. M. Faas, G. A. Schuiling, J. F. Baller, C. A. Visscher, and W. W. Bakker, "A new animal model for human preeclampsia: Ultra-lowdose endotoxin infusion in pregnant rats," *American Journal of Obstetrics and Gynecology*, vol. 171, no. 1, pp. 158–164, 1994.

[40] P. Xue, M. Zheng, P. Gong et al., "Single administration of ultra-low-dose lipopolysaccharide in rat early pregnancy induces TLR4 activation in the placenta contributing to preeclampsia," *PLoS One*, vol. 10, no. 4, article e0124001, 2015.

[41] Y. Zhang, X. Liu, X. Bai et al., "Melatonin prevents endothelial cell pyroptosis via regulation of long noncoding RNA MEG3/miR-223/NLRP3 axis," *Journal of Pineal Research*, vol. 64, no. 2, 2018.

[42] J. Choi, B. J. Seo, H. La et al., "Comparative analysis of the mitochondrial morphology, energy metabolism, and gene expression signatures in three types of blastocyst-derived stem cells," *Redox Biology*, vol. 30, p. 101437, 2020.

[43] J. Fu, "Catalytic-independent inhibition of cIAP1-mediated RIP1 ubiquitination by EGLN3," *Cellular Signalling*, vol. 28, no. 2, pp. 72–80, 2016.

[44] L. He and F. E. Wondisford, "Metformin action: concentrations matter," *Cell Metabolism*, vol. 21, no. 2, pp. 159–162, 2015.

[45] M. Hu, Y. Zhang, X. Li et al., "TLR4-associated IRF-7 and NFκB signaling act as a molecular link between androgen and metformin activities and cytokine synthesis in the PCOS endometrium," *The Journal of Clinical Endocrinology and Metabolism*, vol. 106, no. 4, pp. 1022–1040, 2021.

[46] C. J. Tang, J. Xu, H. Y. Ye, and X. B. Wang, "Metformin prevents PFKFB3-related aerobic glycolysis from enhancing collagen synthesis in lung fibroblasts by regulating AMPK/mTOR pathway," *Experimental and Therapeutic Medicine*, vol. 21, no. 6, p. 581, 2021.

[47] X. Messeguer, R. Escudero, D. Farré, O. Núñez, J. Martínez, and M. M. Albà, "PROMO: detection of known transcription regulatory elements using species-tailored searches," *Bioinformatics (Oxford, England)*, vol. 18, no. 2, pp. 333-334, 2002.

[48] D. Farré, R. Roset, M. Huerta et al., "Identification of patterns in biological sequences at the ALGGEN server: PROMO and MALGEN," *Nucleic Acids Research*, vol. 31, no. 13, pp. 3651–3653, 2003.

[49] W. J. Kent, C. W. Sugnet, T. S. Furey et al., "The human genome browser at UCSC," *Genome Research*, vol. 12, no. 6, pp. 996–1006, 2002.

[50] O. Fornes, J. A. Castro-Mondragon, A. Khan et al., "JASPAR 2020: update of the open-access database of transcription factor binding profiles," *Nucleic Acids Research*, vol. 48, no. D1, pp. D87–d92, 2020.

[51] L. Wang, Y. Cao, B. Gorshkov et al., "Ablation of endothelial _Pfkfb3_ protects mice from acute lung injury in LPS- induced endotoxemia," *Pharmacological Research*, vol. 146, p. 104292, 2019.

[52] X. Zhang, K. Zhang, and Y. Zhang, "Pigment epithelium-derived factor facilitates NLRP3 inflammasome activation through downregulating cytidine monophosphate kinase 2: a potential treatment strategy for missed abortion," *International Journal of Molecular Medicine*, vol. 45, no. 5, pp. 1436–1446, 2020.

[53] A. Correia-Branco, E. Keating, and F. Martel, "Involvement of mTOR, JNK and PI3K in the negative effect of ethanol and metformin on the human first-trimester extravillous trophoblast HTR-8/SVneo cell line," *European Journal of Pharmacology*, vol. 833, pp. 16–24, 2018.

[54] C. S. Han, M. A. Herrin, M. C. Pitruzzello et al., "Glucose and metformin modulate human first trimester trophoblast function: a model and potential therapy for diabetes-associated

uteroplacental insufficiency," *American Journal of Reproductive Immunology*, vol. 73, no. 4, pp. 362–371, 2015.

[55] J. Hu, J. Zhang, and B. Zhu, "Protective effect of metformin on a rat model of lipopolysaccharide-induced preeclampsia," *Fundamental & Clinical Pharmacology*, vol. 33, no. 6, pp. 649–658, 2019.

[56] H. W. Yung, F. Colleoni, E. Dommett et al., "Noncanonical mitochondrial unfolded protein response impairs placental oxidative phosphorylation in early-onset preeclampsia," *Proceedings of the National Academy of Sciences of the United States of America*, vol. 116, no. 36, pp. 18109–18118, 2019.

[57] S. Muralimanoharan, A. Maloyan, J. Mele, C. Guo, L. G. Myatt, and L. Myatt, "miR-210 modulates mitochondrial respiration in placenta with preeclampsia," *Placenta*, vol. 33, no. 10, pp. 816–823, 2012.

[58] S. Haché, L. Takser, F. LeBellego et al., "Alteration of calcium homeostasis in primary preeclamptic syncytiotrophoblasts: effect on calcium exchange in placenta," *Journal of Cellular and Molecular Medicine*, vol. 15, no. 3, pp. 654–667, 2011.

[59] R. O. Bahado-Singh, R. Akolekar, R. Mandal et al., "Metabolomics and first-trimester prediction of early-onset preeclampsia," *The Journal of Maternal-Fetal & Neonatal Medicine : the official journal of the European Association of Perinatal Medicine, the Federation of Asia and Oceania Perinatal Societies, the International Society of Perinatal Obstet*, vol. 25, no. 10, pp. 1840–1847, 2012.

[60] R. O. Bahado-Singh, A. Syngelaki, R. Mandal et al., "Metabolomic determination of pathogenesis of late-onset preeclampsia," *The Journal of Maternal-Fetal & Neonatal Medicine : the official journal of the European Association of Perinatal Medicine, the Federation of Asia and Oceania Perinatal Societies, the International Society of Perinatal Obstet*, vol. 30, no. 6, pp. 658–664, 2017.

[61] L. C. Sánchez-Aranguren, C. T. Espinosa-González, L. M. González-Ortiz et al., "Soluble Fms-like tyrosine kinase-1 alters cellular metabolism and mitochondrial bioenergetics in preeclampsia," *Frontiers in Physiology*, vol. 9, 2018.

[62] E. Sato, Y. Tsunokuni, M. Kaneko et al.et al., "Metabolomics of a mouse model of preeclampsia induced by overexpressing soluble fms-like tyrosine kinase 1," *Biochemical and Biophysical Research Communications*, vol. 527, no. 4, pp. 1064–1071, 2020.

[63] K. Y. F. Tsai, B. Tullis, J. Mejia, P. R. Reynolds, and J. A. Arroyo, "Regulation of trophoblast cell invasion by pyruvate kinase isozyme M2 (PKM2)," *Placenta*, vol. 103, pp. 24–32, 2021.

[64] R. Singh, V. Dubey, D. Wolfson et al., "Quantitative assessment of morphology and sub-cellular changes in macrophages and trophoblasts during inflammation," *Biomedical Optics Express*, vol. 11, no. 7, pp. 3733–3752, 2020.

[65] Y. Wang, H. An, T. Liu et al., "Metformin improves mitochondrial respiratory activity through activation of AMPK," *Cell Reports*, vol. 29, no. 6, pp. 1511–1523.e5, 2019.

[66] S. Q. Wang, S. X. Cui, and X. J. Qu, "Metformin inhibited colitis and colitis-associated cancer (CAC) through protecting mitochondrial structures of colorectal epithelial cells in mice," *Cancer Biology & Therapy*, vol. 20, no. 3, pp. 338–348, 2019.

[67] Z. Z. La Hu, Q. Xia, Z. Liu et al., "Metformin attenuates hepatoma cell proliferation by decreasing glycolytic flux through the HIF-1α/PFKFB3/PFK1 pathway," *Life Sciences*, vol. 239, p. 116966, 2019.

[68] X. Liu, Y. Zhao, E. Zhang, H. Yan, N. Lv, and Z. Cai, "The synergistic effect of PFK15 with metformin exerts anti-myeloma activity via PFKFB3," *Biochemical and Biophysical Research Communications*, vol. 515, no. 2, pp. 332–338, 2019.

[69] T. Yamamoto, N. Takano, K. Ishiwata et al., "Reduced methylation of PFKFB3 in cancer cells shunts glucose towards the pentose phosphate pathway," *Nature Communications*, vol. 5, no. 1, 2014.

[70] L. L. Chen, Y. F. Liao, T. S. Zeng, F. Yu, H. Q. Li, and Y. Feng, "Effects of metformin plus gliclazide compared with metformin alone on circulating endothelial progenitor cell in type 2 diabetic patients," *Endocrine*, vol. 38, no. 2, pp. 266–275, 2010.

[71] L. Ali, J. G. Schnitzler, and J. Kroon, "Metabolism: the road to inflammation and atherosclerosis," *Current Opinion in Lipidology*, vol. 29, no. 6, pp. 474–480, 2018.

[72] O. M. Finucane, J. Sugrue, A. Rubio-Araiz, M. V. Guillot-Sestier, and M. A. Lynch, "The NLRP3 inflammasome modulates glycolysis by increasing PFKFB3 in an IL-1β-dependent manner in macrophages," *Scientific Reports*, vol. 9, no. 1, p. 4034, 2019.

[73] X. Peng, T. Yang, G. Liu, H. Liu, Y. Peng, and L. He, "Piperine ameliorated lupus nephritis by targeting AMPK-mediated activation of NLRP3 inflammasome," *International Immunopharmacology*, vol. 65, pp. 448–457, 2018.

[74] F. Yang, Y. Qin, Y. Wang et al., "Metformin inhibits the NLRP3 inflammasome via AMPK/mTOR-dependent effects in diabetic cardiomyopathy," *International Journal of Biological Sciences*, vol. 15, no. 5, pp. 1010–1019, 2019.

[75] Z. Zheng, Y. Bian, Y. Zhang, G. Ren, and G. Li, "Metformin activates AMPK/SIRT1/NF-κB pathway and induces mitochondrial dysfunction to drive caspase3/GSDME-mediated cancer cell pyroptosis," *Cell Cycle (Georgetown, Tex)*, vol. 19, no. 10, pp. 1089–1104, 2020.

[76] C. Juliana, T. Fernandes-Alnemri, S. Kang, A. Farias, F. Qin, and E. S. Alnemri, "Non-transcriptional Priming and Deubiquitination Regulate NLRP3 Inflammasome Activation," *The Journal of Biological Chemistry*, vol. 287, no. 43, pp. 36617–36622, 2012.

[77] S. Han, T. B. Lear, J. A. Jerome et al., "Lipopolysaccharide Primes the NALP3 Inflammasome by Inhibiting Its Ubiquitination and Degradation Mediated by the SCF^{FBXL2} E3 Ligase," *The Journal of Biological Chemistry*, vol. 290, no. 29, pp. 18124–18133, 2015.

Hindawi
Oxidative Medicine and Cellular Longevity
Volume 2021, Article ID 7914829, 13 pages
https://doi.org/10.1155/2021/7914829

Research Article

ASC Speck Formation after Inflammasome Activation in Primary Human Keratinocytes

Nikola Smatlik,[1] **Stefan Karl Drexler**,[2] **Marc Burian**,[3] **Martin Röcken**,[1] **and Amir Sadegh Yazdi**[1,3]

[1]*Department of Dermatology, University Hospital Tübingen, 72076 Tübingen, Germany*
[2]*Department of Biochemistry, University of Lausanne, Switzerland*
[3]*Department of Dermatology and Allergology, University Hospital RWTH Aachen, 52074 Aachen, Germany*

Correspondence should be addressed to Nikola Smatlik; nikolasmatlik@gmail.com

Received 6 August 2021; Accepted 4 October 2021; Published 5 November 2021

Academic Editor: Juyi Li

Chronic UV irradiation results in many changes in the skin, including hyperplasia, changes in dermal structures, and alteration of pigmentation. Exposure to UVB leads to cutaneous damage, which results in inflammation characterized by increased NF-κB activation and the induction of inflammatory cytokines, such as tumor necrosis factor (TNF), interleukin- (IL-) 1, or IL-8. IL-1 secretion is the result of inflammasome activation which is besides apoptosis, a result of acute UVB treatment. Inflammasomes are cytosolic protein complexes whose formation results in the activation of proinflammatory caspase-1. Key substrates of caspase-1 are IL-1β and IL-18, and the cytosolic protein gasdermin D (GSDMD), which is involved in inflammatory cell death. Here, we demonstrate that UVB-induced inflammasome activation leads to the formation of ASC specks. Our findings show that UVB provokes ASC speck formation in human primary keratinocytes prior to cell death, and that specks are, opposed to the perinuclear cytosolic localization in myeloid cells, formed in the nucleus. Additionally, we showed by RNAi that NLRP1 and not NLRP3 is the major inflammasome responsible for UVB sensing in primary human keratinocytes. Formation of ASC specks indicates inflammasome assembly and activation as their formation in hPKs depends on the presence of NLRP1 and partially on NLRP3. Nuclear ASC specks are not specific for NLRP1/NLRP3 inflammasome activation, as the activation of the AIM2 inflammasome by cytosolic DNA results in ASC specks too. These nuclear ASC specks putatively link cell death to inflammasome activation, possibly by binding of IFI16 (gamma-interferon-inducible protein) to ASC. ASC can interact upon UVB sensing via IFI16 with p53, linking cell death to ASC speck formation.

1. Introduction

Human skin is constantly exposed to ultraviolet (UV) irradiation. Chronic UV irradiation results in many changes in the skin, including epidermal hyperplasia, elastic fiber fragmentation, and alteration of pigmentation [1]. There are three types of UV light (200-400 nm): UVA, UVB, and UVC, with UVA (314-400 nm) and UVB (280-315 nm) responsible for damage and inflammation in the skin. UVA penetrates through the epidermis into the dermis, and it is weakly absorbed by DNA and protein. In contrast, UVB is absorbed by DNA and protein and therefore impacts the epidermis [2]. Due to its effects on DNA, UVB is a potent inducer of apoptosis while UVA is a potent inducer of reactive oxygen species (ROS). UVB-induced apoptosis is a complex mechanism that includes different signaling pathways: apoptosis induced by direct DNA damage, death receptor-mediated apoptosis, and apoptosis via the formation of reactive oxygen species (ROS) [3].

In human keratinocytes, UVB additionally induces the activation of inflammatory caspases, such as caspase-4 [4] and caspase-1 [5]. These are activated by inflammasomes. Inflammasomes are protein complexes located in the cytosol [6]. Upon stimulation, inflammasome complexes assemble to process the cleavage of caspase-1, which activates the proinflammatory cytokines interleukin IL-1β and IL-18.

In keratinocytes, both the NLRP1 and NLRP3 inflammasomes seem to be important for UVB-induced caspase-1

activation [7]. Substrates of caspase-1 are not only cytokines but also gasdermin D (GSDMD) [8, 9]. Cleaved GSDMD translocates from the cytosol to the cell membrane where it forms pores, which induce pyroptotic cell death and permit the release of IL-1β and IL-18 into the extracellular space [10]. Pyroptosis and apoptosis are both caspase-mediated types of cell death. In contrast to apoptosis, membrane damage or cell membrane rupture is an early event in pyroptosis, leading to the release of danger-associated molecules from damaged cells [11]. Their release leads to a pronounced inflammatory response. It was shown before that UVB radiation can induce inflammasome-dependent IL-1 activation and secretion via GSDMD cleavage [5].

To be activated, inflammasomes form complexes of a nucleotide oligomerization domain- (NOD-) like receptor (NLR) and the adaptor protein ASC (apoptosis-associated speck-like protein) containing a caspase recruitment domain (CARD), which recruits pro-caspase-1 to the complex [11–13].

Upon oligomerization, the helical fibrillar assembly of ASC via pyrin domain (PYD)-PYD interactions [11, 14] forms large structures called ASC specks [15–17] which can be visualized in fluorescent microscopy.

This study is aimed at deciphering whether UVB-induced inflammasome activation and cell death can be separated or whether inflammasome activation ultimately results in apoptosis or pyroptosis. By visualizing ASC aggregates, we claim that nuclear ASC speck formation might putatively be linked to apoptosis and cell death.

2. Materials and Methods

2.1. Cell Culture of Primary Human Keratinocytes. Primary human keratinocytes were isolated from human foreskins. In brief, the epidermis was separated from the dermis using Dispase II solution (Roche, Basel, Switzerland). Then, the epidermis was cut into small pieces and incubated in trypsin/EDTA solution (Biochrom, Berlin, Germany). Cells were filtrated using Millipore cell culture filters 100 μm (Sigma-Aldrich, Darmstadt, Germany), centrifuged and resuspended in CnT-PR cell culture media (CELLnTEC Advanced Cell Systems, Bern, Switzerland), and cultivated until they reached 100% confluency.

2.2. Transfection of Primary Human Keratinocytes. Cells were seeded on 12-well plates (Greiner Bio-One GmbH, Frickenhausen, Germany) until they reached 60-70% of confluency. Then, cells were transfected in the Opti-MEM (1x) reduced serum media (Gibco, Thermo Fisher Scientific, Karlsruhe Germany), with siGENOME Human NLRP1 siRNA (10 μM) and siGENOME Human NLRP3 siRNA (10 μM) (Dharmacon, Lafayette, CO 80266 USA), using Lipofectamine RNAiMax reagent (Thermo Fisher Scientific, Karlsruhe, Germany); single guide RNA (sgRNA) (New England Biolabs GmbH, Frankfurt am Main, Germany) was transfected as control.

After 24 hours, transfected keratinocytes without differentiation with $CaCl_2$ (in experiments requiring transfection, differentiation with $CaCl_2$ has been done 24 hours before UV irradiation) were irradiated with UVB (50 mJ/cm^2) using a Medisun® Psori-Kamm (Schulze & Böhm, Brühl, Germany), followed by a 4-hour or 8-hour incubation.

2.3. Treatment with Chemical Inhibitors. To block caspase activation, cells were treated with 20 μM zVAD-FMK pan-caspase inhibitor (InvivoGen, San Diego, USA) for 1 hour prior to UVB irradiation. MCC950 (InvivoGen, San Diego, USA) is a specific inhibitor of NLRP3 activation and was used at 5 μM 1 hour before irradiation.

2.4. ASC Speck Staining. Cells were fixed using 2% formaldehyde. Permeabilization was on cell membrane to enable antibody binding to the ASC protein, which has been made using 0.5% Triton X-100 (Carl Roth GmbH, Karlsruhe, Germany) which was used for permeabilization, 1-3% normal donkey serum (Jackson ImmunoResearch, Hamburg, Germany), and AURION BSA-c (AURION 6709 PD Wageningen, The Netherlands) for blocking. For staining, anti-ASC, rabbit pAb (AL177), antibody (Adipogen AG, Liestal, Switzerland), 1 : 200 diluted in washing buffer containing Dulbecco's phosphate-buffered saline (Sigma-Aldrich, Darmstadt, Germany), and Tween 20 (Sigma-Aldrich, Darmstadt, Germany) were applied to the slide, followed by a Cy3 F $(ab)_2$ donkey-anti rabbit IgG secondary antibody 1 : 200 (Jackson ImmunoResearch, Hamburg, Germany). To be able to better localize the ASC staining, the actin cytoskeleton was stained with Alexa Fluor™ 488 phalloidin (Thermo Fisher Scientific, Karlsruhe, Germany) and the nuclei with DAPI (4′,6-diamidine-2′-phenylindole dihydrochloride) (Sigma-Aldrich, Darmstadt, Germany). Pictures were taken using a Zeiss LSM 800 confocal laser scanning microscope with Zeiss ZEN 2.3 (blue edition) Software (Carl Zeiss Microscopy GmbH, Jena, Germany), using 43x magnification.

2.5. AIM2 Inflammasome Activation via Double-Stranded DNA Analogue Poly(dA:dT). Cells were seeded on 8-chamber polystyrene slides (Corning Incorporated, NY 14831, USA) (for ASC staining), until they reached 60-70% confluency. Then, cells were transfected in the Opti-MEM (1x) reduced serum media (Gibco, Thermo Fisher Scientific, Karlsruhe, Germany), with 5 μg/ml poly(dA:dT) naked double-stranded B-DNA (InvivoGen, San Diego, USA) for 24 h, using Lipofectamine RNAiMax reagent (Thermo Fisher Scientific, Karlsruhe, Germany). Opti-MEM media were used as a negative control.

2.6. ASC siRNA Knockdown. Transient transfection of siRNA (Ambion, USA) was performed using the DNA-calcium phosphate precipitation method. HaCaT cells were incubated for 24 h before transfection, and knockdown was evaluated 24 h, 48 h, and 72 h after transfection. Most efficient knockdown was achieved 72 h after transfection at which time point cells were stimulated with 50 mJ/cm^2 UVB.

2.7. Immunoprecipitation. HaCaT cells were resuspended in lysis buffer (50 mM Tris, pH 7.8, 50 mM NaCl, 0.1% (vol/vol) Nonidet-P40, 5 mM EDTA, and 10% (vol/vol) glycerol). Endogenous ASC was immunoprecipitated, and

Table 1: Oligonucleotide primers and LightCycler hybridization probes.

Target gene	Accession no.	Primer	Sequence	Purpose
		ACTIN F	AGCCTCGCCTTTGCCGA	qPCR
β-Actin	P60709	ACTIN R	CTGGTGCCTGGGGCG	qPCR
		ACTIN TM	6FAM-CCGCCGCCCGTCCACACCCGCC—BBQ	Hybridization probe
		NLRP1 F	CACTTTATATGGGCTGTCGTTACA	qPCR
		NLRP1 S	GGGTCTGGTTCAGGGATGC	qPCR
NLRP1	Q9C000	NLRP1 A	CCAACGTAGAACTCCGAGAACA	Hybridization probe
		NLRP1 R	CTCATCTTTCTTGTCTTTCACTTGC	
		NLRP1 P	6FAM-CTCCAGGGCTTCGATAGCAGAGCT—BBQ	
		NLRP3 F	CACTTCTGACCTCCAGCCA	qPCR
		NLRP3 S	CAACAATGACCTGGGCGA	qPCR
NLRP3	Q1JQ87	NLRP3 A	TCTTCTTGAAGTGTTTCTAACGCA	Hybridization probe
		NLRP3 R	AGGCTCAAAGACGACGGT	
		NLRP3	6FAM-CTGAAACAGCAGAGCTGCCTCCTG—BBQ	

the interaction of ASC with IFI16 and p53 was assessed by immunoblot.

2.8. Nuclear and Cytoplasmic Fractionation. HaCaT cells were harvested, washed in PBS, and lysed in a buffer containing 10 mM HEPES, 1.5 mM $MgCl_2$, 300 mM sucrose, 0.5% NP-40, 10 mM KCl, 0.5 mM DTT, and complete protease inhibitor cocktail (Roche, Basel, Switzerland). Cells were spun down at 9000 rpm for 45 s, and the supernatant was collected as a cytosolic fraction. The remaining pellet was washed in the previously described lysis buffer before being resuspended in a buffer containing 20 mM HEPES, 100 mM NaCl, 0.2 mM EDTA, 20% glycerol, 100 mM KCl, 0.5 mM DTT, and complete protease inhibitor cocktail. The resuspended pellet was frozen/thawed 3 times and sonicated for 10 s. The cell suspension was spun down at 13000 rpm for 10 min, and the supernatant was collected as nuclear fraction.

2.9. RNA Isolation and Gene Expression Analysis. Total RNA was isolated using peqGOLD Total RNA Kit Sline (VWR, Erlangen, Germany), and reverse transcription (Maxima First Strand cDNA Synthesis Kit for RT-qPCR, Thermo Fisher Scientific, Waltham, Massachusetts) was performed according to the manufacturer's instructions.

To determine gene expression, quantitative real-time PCR (Roche LightCycler 480 system) was performed using the LightCycler 480 instrument (Roche, Basel, Switzerland). The expression of the specified genes was calculated relative to the expression of the housekeeping gene β-actin. Primer and probe sequences are listed in Table 1.

2.10. Cytokine Analysis. Human IL-1α and IL-1β secretion was measured in cell-free supernatants using R&D ELISA kits (Minneapolis, Canada) (Human IL-1 beta/IL-1F2 DuoSet ELISA, Human IL-1α DuoSet ELISA) according to the manufacturer's instructions using a EMax Endpoint ELISA Microplate Reader (Molecular Devices, LLC, San Jose, CA 95134, USA).

2.11. FAM FLICA Active Caspase-1 Staining. Keratinocytes were seeded on 8-chamber polystyrene slides (Corning Incorporated, NY 14831, USA) and were differentiated using 1.2 mM $CaCl_2$ overnight. Active caspase-1 was visualized using FAM FLICA Caspase-1 Kit (Bio-Rad Laboratories GmbH, D-85622 Feldkirchen, Germany). Hoechst was performed using 0.5% Hoechst reagent followed by propidium iodide (PI) staining (0.5% PI). Then, cells were fixed using fixative solution diluted 1 : 10 in apoptosis wash buffer. Pictures were taken using a Zeiss LSM 800 confocal laser scanning microscope with Zeiss ZEN 2.3 (blue edition) Software (Carl Zeiss Microscopy GmbH, Jena, Germany).

2.12. LDH Cell Viability Assay. Primary human keratinocytes were seeded on a 96-well plate until 100% of confluency; then, cells were differentiated using 1.2 mM $CaCl_2$ overnight. LDH assay was performed using LDH assay kit (Thermo Fisher Scientific, Karlsruhe, Germany), according to the manufacturer's instructions.

2.13. Statistics. For statistical analyses, one-way ANOVA and Student's t-test have been used. Statistics has been done in GraphPad Prism 8 and Origin 8 software.

3. Results

3.1. Exposure to UVB Leads to Inflammasome Activation and to the Formation of ASC "Specks" in hPKs. To confirm that UVB activates the inflammasome in primary human keratinocytes, primary keratinocytes were exposed to UVB and IL-1 secretion was measured in the supernatants. Here, we observed a significant increase in IL-1α release after exposure to UVB (Figure 1(a)).

In myeloid cells, inflammasome formation can be visualized using ASC speck formation in fluorescence microscopy. To check for the formation of these ASC multimers, primary human keratinocytes were irradiated with UVB (50 mJ/cm^2). Cells in the negative control group were left in the medium without UVB irradiation for 4 h and 8 hours

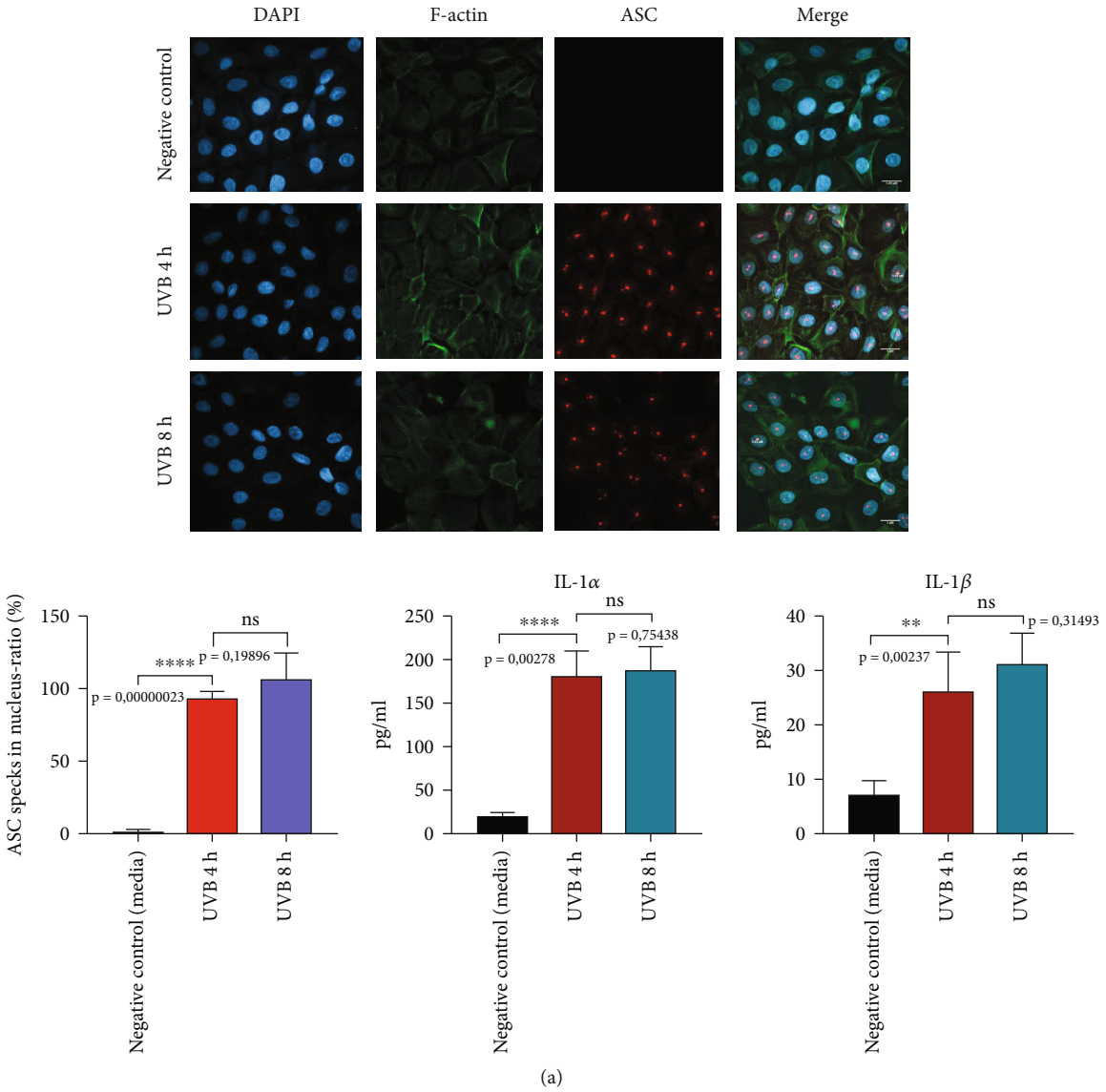

(a)

Figure 1: Continued.

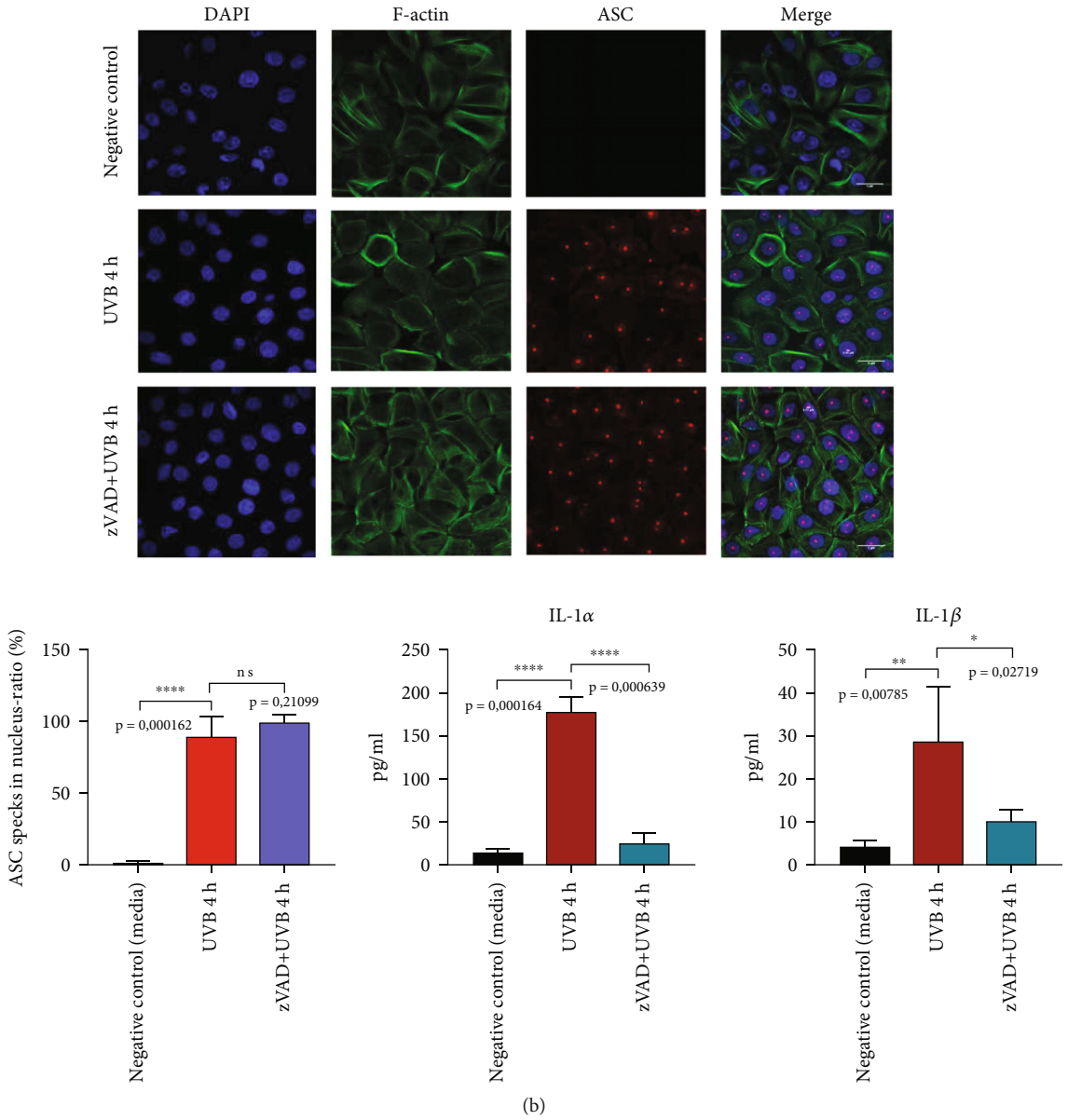

Figure 1: (a) UVB irradiation leads to the formation of ASC specks in primary human keratinocytes. Primary human keratinocytes were irradiated with UVB (50 mJ/cm^2). Exposure to UVB light leads to the formation of nuclear ASC "specks". (b) zVAD does not inhibit ASC "speck" formation, but suppresses IL-1 secretion. Keratinocytes were treated with 20 μM zVAD for 1 h and were irradiated with UVB (50 mJ/cm^2). ASC (red), F-actin (green), and DAPI (dark blue). IL-1α and IL-1β were measured in cell-free supernatants using ELISA. Data represent at least 3 independent experiments and are presented as the means ± SD. Statistics: one-way ANOVA statistical test. Symbols for P values used in the figures. $^*P < 0.05$, $^{**}P < 0.01$, $^{***}P < 0.001$, and $^{****}P < 0.0001$. NS: not significant. Magnification: ×43.

(Supplementary Figure 1). UVB irradiation leads to translocation of cytoplasmatic ASC protein to the nucleus and formation of nuclear ASC specks in hPKs. In the negative control, cells were not irradiated with UVB, and because of that, there is no formation of nuclear ASC "specks" that could be detected by anti-ASC (AL177) antibody. Anti-ASC (AL177) antibody also recognizes cytosolic ASC specks, but in negative control, there were no treatments sufficient to induce formation of cytosolic ASC aggregates. After 4 hours, the formation of ASC "specks" was observed with no significant difference in the number of "specks" 8 hours after UVB light exposure (Figure 1(a)).

To elucidate if the formation of ASC specks depends on caspase activation, hPKs were incubated with the pan-caspase inhibitor zVAD-FMK diluted in DMSO prior to UVB treatment. Negative control cells were treated with DMSO as a solvent for zVAD-FMK. As expected, zVAD did not block ASC "speck" formation (Figure 1(b)).

The formation of the inflammasome complex occurs prior to caspase activation. As zVAD blocks caspase activation, inflammasome complexes are still formed; however, they are not able to activate inflammasomes. Therefore, ASC speck formation is not influenced, while IL-1 secretion is reduced upon zVAD treatment (Figure 1(b)).

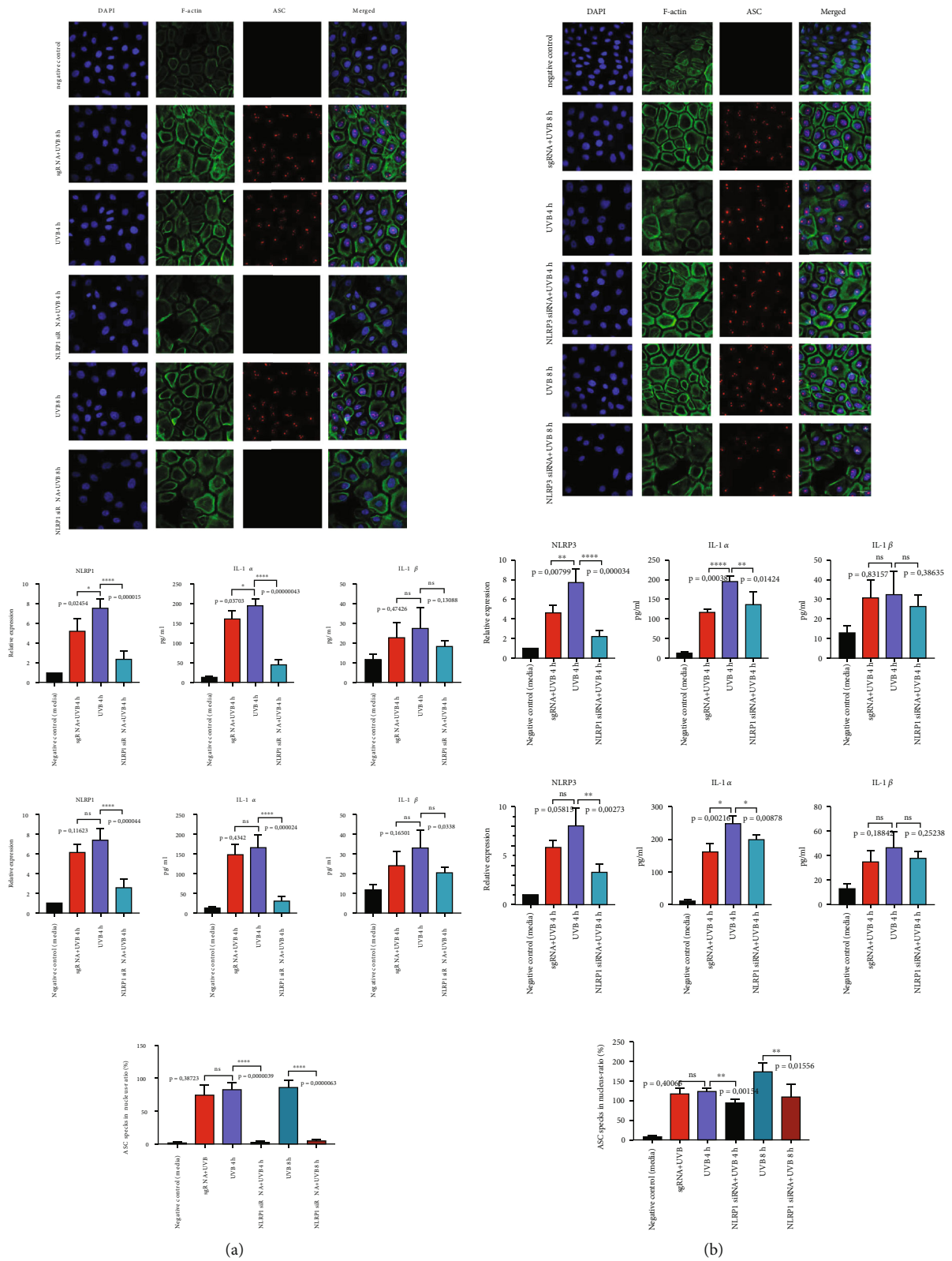

FIGURE 2: (a) NLRP1 is the most important inflammasome in primary human keratinocytes responsible for UVB sensing. Cells were transfected with NLRP1 and NLRP3 siRNA and were irradiated with UVB (50 mJ/cm^2) for 14 s. NLRP1 siRNA completely blocked the formation of ASC aggregates. ASC (red), F-actin (green), and DAPI (blue). (b) NLRP3 is dispensable for UVB-induced ASC "specks" in hPKs. IL-1α and IL-1β were measured in cell-free supernatants by ELISA. Data represent at least 3 independent experiments and are presented as the means ± SD. Statistics: one-way ANOVA statistical test. Symbols for P values used in the figures. $^*P < 0.05$, $^{**}P < 0.01$, $^{***}P < 0.001$, and $^{****}P < 0.0001$. NS: not significant. Magnification: ×43.

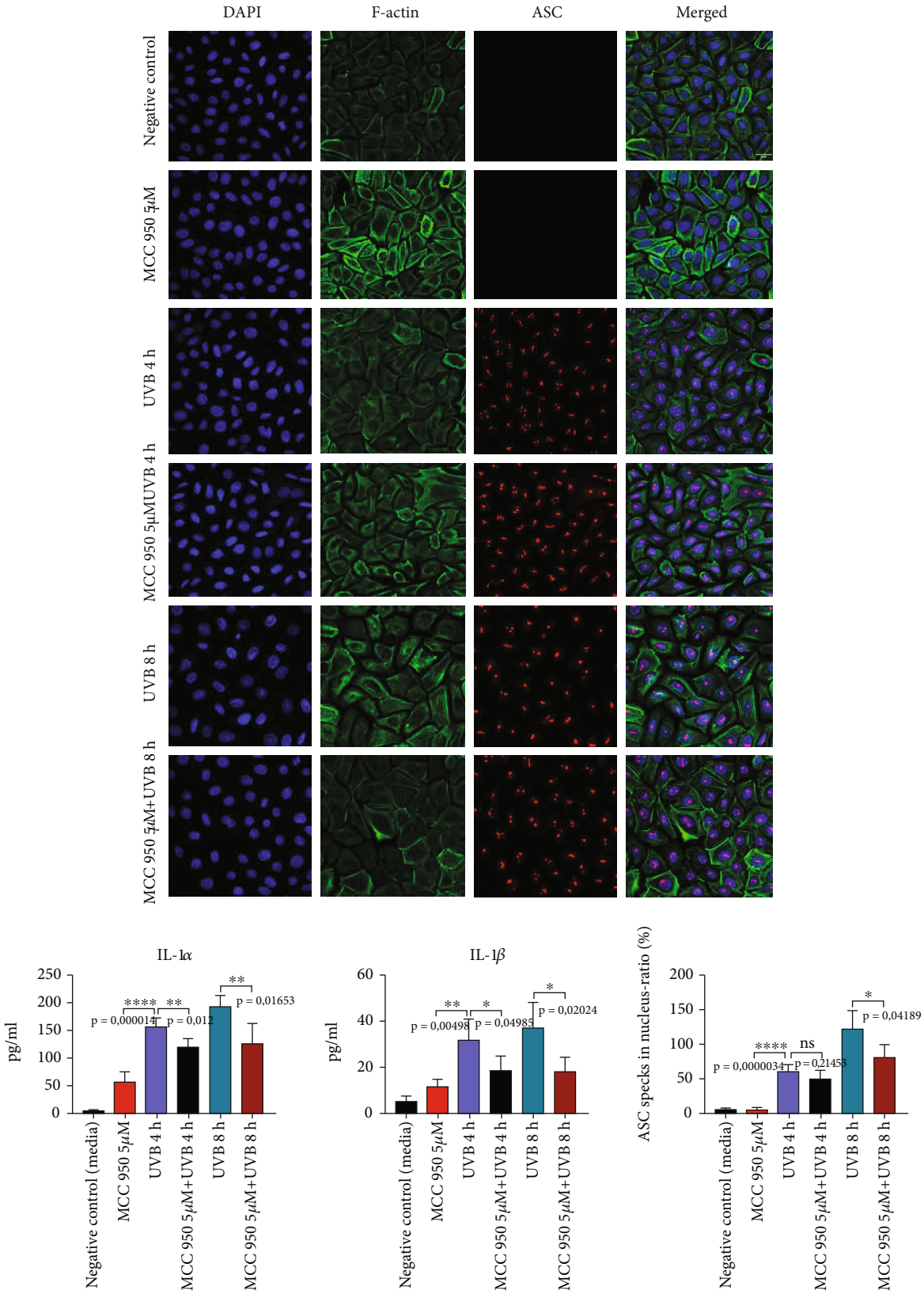

FIGURE 3: Pharmacological blocking of NLRP3 via MCC950 does not suppress UVB-induced ASC speck formation and IL-1 secretion. Cells were treated with 5 μM MCC950 for 1 h prior to UVB treatment (50 mJ/cm^2). IL-1α and IL-1β were measured in cell-free supernatants using ELISA. Data represent at least 3 independent experiments and are presented as the means ± SD. Statistics: one-way ANOVA statistical test. Symbols for P values used in the figures. $^*P < 0.05$, $^{**}P < 0.01$, $^{***}P < 0.001$, and $^{****}P < 0.0001$. NS: not significant. Magnification: ×43.

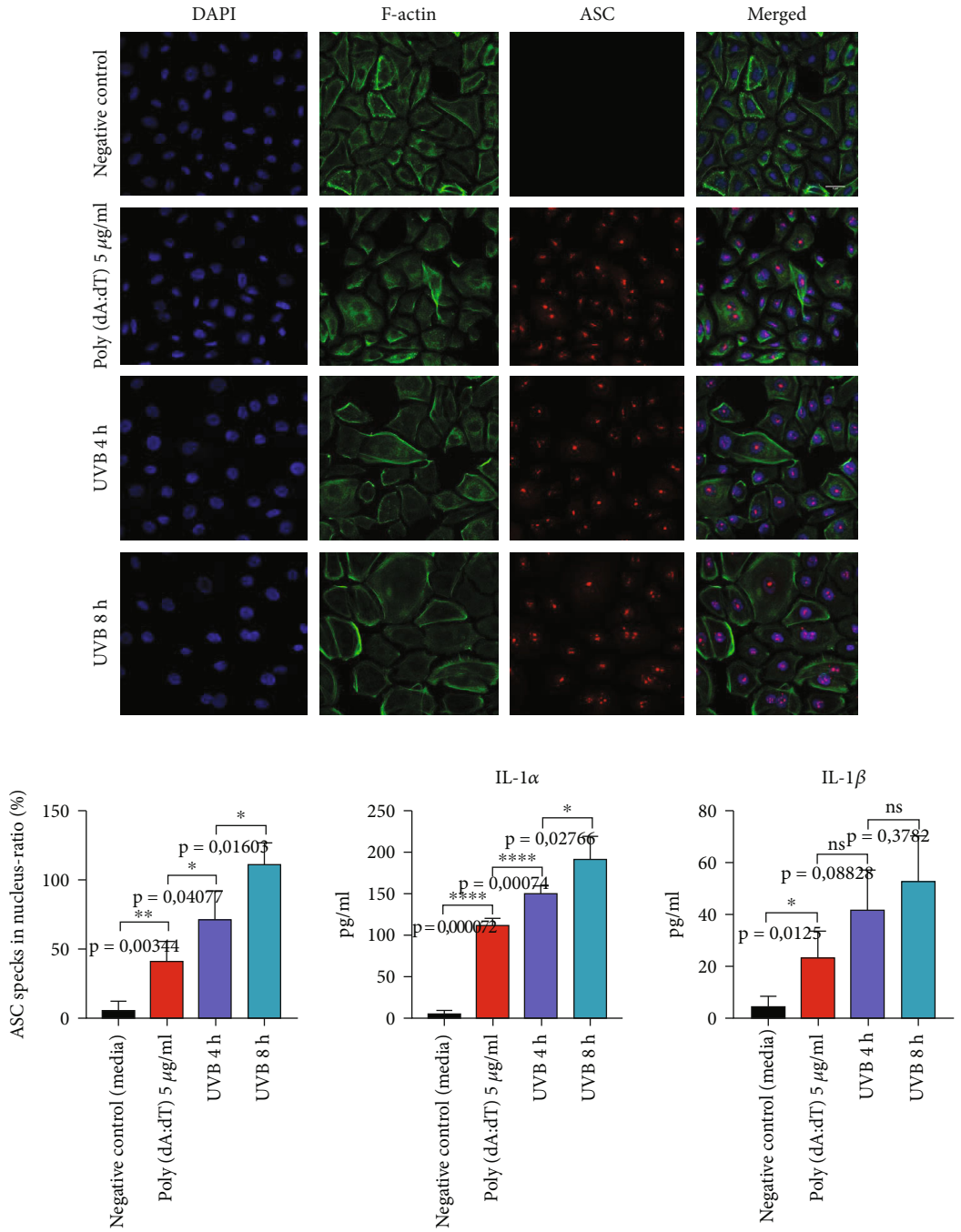

FIGURE 4: Poly(dA:dT) leads to AIM2 inflammasome and ASC "speck" formation. Human keratinocytes were transfected with poly(dA:dT) using Lipofectamine RNAiMax reagent, incubated for 24 h, or were irradiated with UVB (50 mJ/cm^2). Anti-ASC, rabbit pAb (AL177), antibody (red), F-actin (green), and DAPI (blue). IL-1α and IL-1β were measured in cell-free supernatants using ELISA. Data represent at least 3 independent experiments and are presented as the means ± SD. Statistics: one-way ANOVA statistical test. Symbols for P values used in the figures. $^*P < 0.05$, $^{**}P < 0.01$, $^{***}P < 0.001$, and $^{****}P < 0.0001$. NS: not significant. Magnification: ×43.

As it is still not clear whether the NLRP1 or the NLPR3 inflammasome is the major inflammasome in hPKs [5, 18], we wanted to decipher which of the two inflammasomes is more important for UVB sensing. First, we transfected hPKs with NLRP1 siRNA or NLRP3 siRNA to specifically silence the respective NLR. 24 hours after transfection, the knockdown efficiency was evaluated by qRT-PCR and UVB irradiation (50 mJ/cm^2) was performed.

Again, 4 and 8 hours after UV exposure, ASC "speck" formation occurred. In the absence of NLRP1, ASC was not able to form speck-like aggregates (Figure 2(a)), while the silencing of NLRP3 did not impair the presence of ASC "specks" in the nucleus (Figure 2(b)). The presence of ASC specks partially correlates with IL-1 secretion. In the absence of NLRP1 and of ASC specks, IL-1α secretion is strongly diminished (Figure 2(a)), while siNLRP3 does not

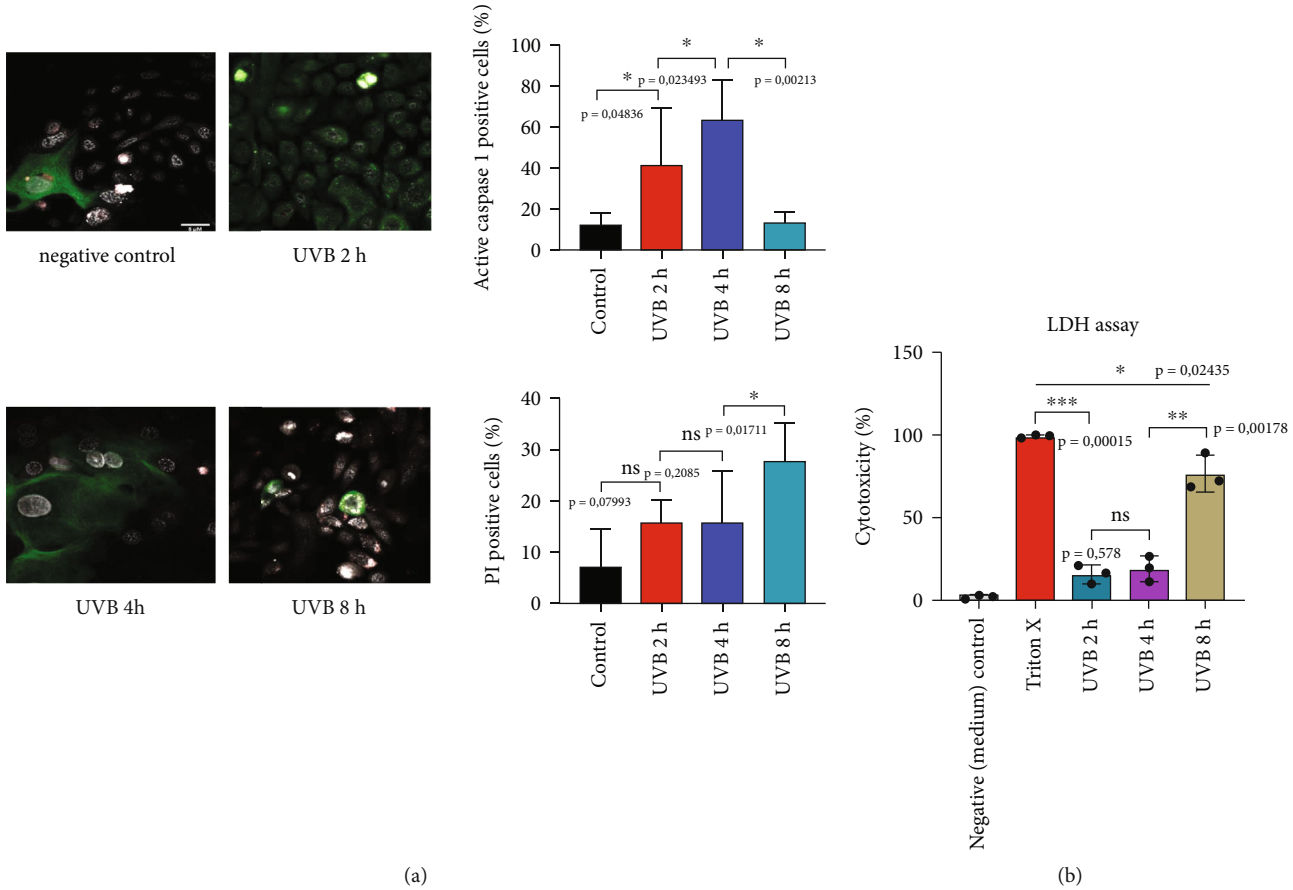

Figure 5: (a) UVB irradiation causes cell death in primary human keratinocytes. hPKs were irradiated with UVB (50 mJ/cm^2). To detect active caspase-1, FAM FLICA staining (green) was done. Propidium iodide (PI) staining (red) was performed to detect dying cells. (b) LDH cell death assay. Data represent at least 3 independent experiments and are presented as the means ± SD. Statistics: one-way ANOVA statistical test. Symbols for P values used in the figures. $^*P < 0.05$, $^{**}P < 0.01$, and $^{***}P < 0.001$. NS: not significant. Magnification: ×43.

alter ASC speck, but significantly reduced IL-1α secretion. IL-1β secretion was not affected after NLRP1 and NLRP3 silencing and was close to the background, because hPKs mostly secrete IL-1α (Figure 2(b)).

Additionally, NLRP3 was blocked pharmacologically by MCC950, a small molecule that specifically prevents NLRP3 oligomerization. Neither the UVB-induced formation of ASC "specks" nor the secretion of IL-1α was suppressed after MCC 950 treatment, suggesting that NLRP1 and not NLRP3 were needed for UVB-induced inflammasome activation in human primary keratinocytes (Figure 3).

AIM2 senses dsDNA via its C-terminal dsDNA-binding HIN-200 domain. The AIM2 inflammasome can recognize intracellular dsDNA. Upon activation, AIM2 binds and recruits the adaptor protein ASC and caspase-1 [19]. A relevant role of AIM2 in keratinocytes was demonstrated during human papillomavirus (HPV) infection [20] and in psoriasis [10].

Next, we aimed to investigate if the activation of the AIM2 inflammasome via transfected poly(dA:dT) leads to ASC "speck" formation and IL-1 secretion. hPKs were transfected with poly(dA:dT) using Lipofectamine RNAiMax reagent, incubated for 24 h, or were irradiated with UVB light (50 mJ/cm^2). ASC "specks" were observed both after exposure to UVB and to a lesser extent after poly(dA:dT) transfection. Measurement of secreted IL-1α also confirms the ASC "speck" staining pattern, showing that the activation of AIM2 leads to IL-1α and IL-1β secretion, but weaker than UVB (Figure 4).

Both NLRP1/NLRP3 activation via UVB and AIM2 stimulation of intracellular dsDNA lead to the formation of ASC "specks" in hPKs. ASC is also involved in apoptosis; therefore, we investigated next whether UVB irradiation leads to apoptosis. The caspase FLICA kit detected active caspase-1 in whole living cells. FLICA is cell permeable and can efficiently diffuse into cells. Cells were also stained with propidium iodide, to identify DNA of dying cells.

Caspase activation is visible starting 2 hours after exposure to UVB with the peak of activity 4 hours after UVB irradiation.

As expected, most PI-positive cells were observed 8 hours after UVB exposure; therefore, we used that time point in those and in the previous experiments. This indicates that inflammasome activation and ASC speck formation ultimately

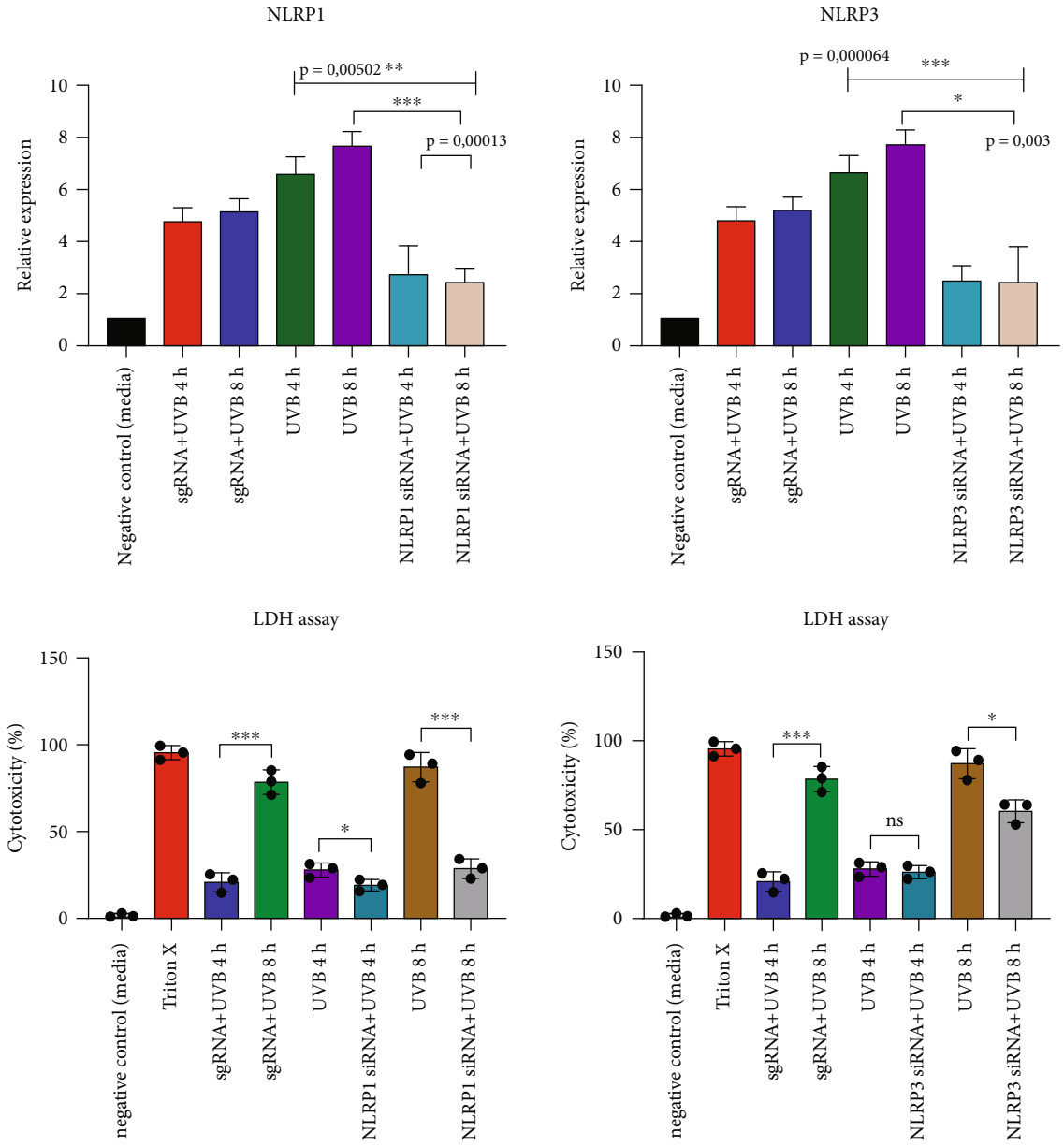

Figure 6: NLRP1 inflammasome blocking protects from cell death: hPKs were transfected with NLRP1 and NLRP3 siRNA and were irradiated with UVB (50 mJ/cm^2). The absence of NLRP1 and partially of NLPR3 protected from cell death resulting in a reduction of LDH release. Data represent at least 3 independent experiments and are presented as the means ± SD. Statistics: one-way ANOVA statistical test. Symbols for P values used in the figures. $^*P < 0.05$, $^{**}P < 0.01$, and $^{***}P < 0.001$. NS: not significant.

result in cell death in human primary keratinocytes. UVB exposure first leads to inflammasome assembly and finally to cell death in hPKs (Figure 5(a)).

To support FLICA stainings, we additionally performed LDH assay. LDH leakage from dying cells increases over time, correlating with the FAM FLICA results (Figure 5(b)).

To investigate which type of inflammasome NLRP1 or NLPR3 in hPKs leads to cell death via formation of ASC aggregates, NLRP1 or NLRP3 were silenced by siRNA. As described above, after 4 h, no significant amounts of LDH were released, while cell death occurred 8 h after exposure to UVB (Figure 5). Cells without functional NLRP1 inflammasome were protected from LDH release, showing that NLRP1 inflammasome activation is crucial for both inflammasome activation and at later time point apoptotic cell death in human hPKs (Figure 6).

IFI16 is a resident nuclear protein and is involved in sensing of the danger signals [21]. IFI16 is part of the large BRCA1-associated genome surveillance (BASC) DDR complex and it is involved in BRCA1-mediated apoptosis and inflammation [22, 23]. UVB irradiation leads to redistribution of IFI16 from the nucleus to the cytoplasm in later time points (16 h) and further into the supernatants of the cells [24]. Additionally, Rao et al. and Kerur et al. demonstrated that ASC could interact with IFI16 to form IFI16-ASC complexes that could recruit pro-caspase-1 [17, 25].

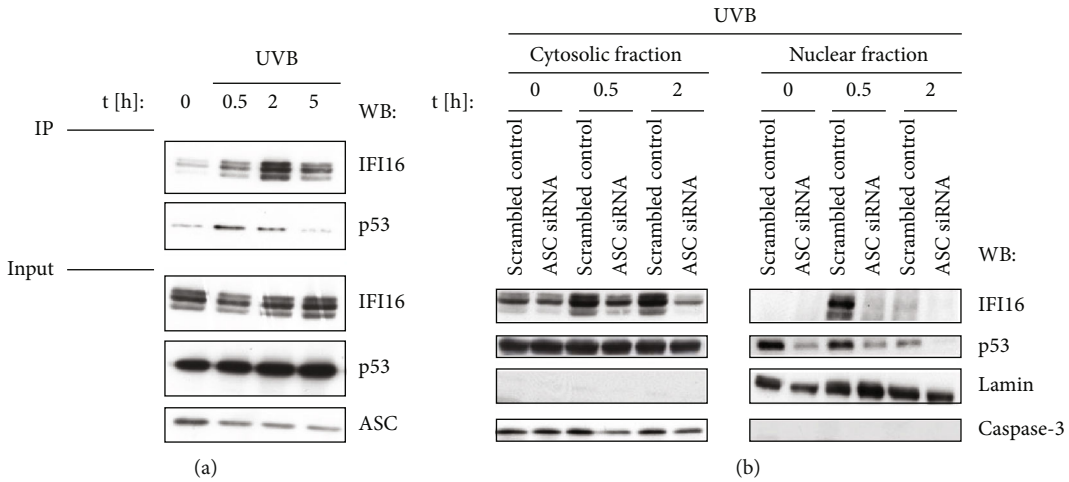

Figure 7: (a) IFI16 interacts with ASC after UVB sensing in HaCaT cells. HaCaT cells were irradiated with UVB. After 0.5 h, 2 h, and 5 h, the interaction of ASC with IFI16 was observed using immunoprecipitation. ASC interacts with IFI16 following UVB radiation with the maximum interaction occurring 2 hours after stimulation. (b) p53 and IFI16 translocation to the nucleus was impaired in ASC knockdown HaCaT cells. Cells were knocked down with ASC and then irradiated with UVB. The translocation of p53 and IFI16 was absent in HaCaT cells that have been knocked down with ASC.

Furthermore, IFI16 is necessary for p53, which is a binding partner of ASC [16]. To confirm these observations, immunoprecipitation of endogenous ASC in HaCaT cells was performed (Figure 7(a)).

ASC transiently interacted with IFI16 following UVB radiation with a maximum interaction occurring 2 hours after stimulation (Figure 7(a)). Interestingly, the time-dependent interaction of p53 with ASC followed the pattern of IFI16, possibly suggesting IFI16 dependency (Figure 7(a)). This data supports a recent report which also demonstrated the interaction of ASC with IFI16 [26]. Based on these data, we hypothesized that ASC regulates p53 and thus is involved in apoptosis via activation of IFI16.

To investigate whether the decrease in p53 phosphorylation has functional consequences, we measured the nuclear translocation of p53 and IFI16 following UVB radiation. Indeed, p53 as well as IFI16 translocation to the nucleus was impaired in ASC knockdown HaCaT cells (Figure 7(b)).

4. Discussion

Exposure to UV light is harmful to the skin, which leads to skin inflammation and increases the risk of epithelial and melanocytic skin cancer. However, UVB is also used therapeutically, as it is a potent inducer of apoptosis. Keratinocytes are particularly affected by UV exposure, which leads to inflammation [7, 27]. One of the key inflammatory complexes involved in immune responses to UV are inflammasomes. Their activation results in the activation of proinflammatory caspases and prior to caspase activation is the formation of ASC aggregates that are a prerequisite for caspase-1 activation.

Here, we confirm the findings from Fenini et al. that UVB exposure induces inflammasome activation in human primary keratinocytes [18]. We are the first to show that this can be visualized by the nuclear formation of ASC "specks."

The localization of those specks differs from findings in myeloid cells where ASC "specks" are located in the perinuclear area upon activation and are only in resting conditions observed in the nucleus [28].

Our data are confirmed by Kuri et al. where ASC "specks" are also located in the nucleus of zebrafish keratinocytes [29].

Therefore, myeloid cells and keratinocytes might act differently.

As a further difference between myeloid cells and epithelial cells, in myeloid cells, NLRP3 is the key inflammasome, while we and others [18] demonstrate that NLRP1 dominates over NLRP3 in keratinocytes. NLRP1 carries a CARD domain, and therefore, ASC is not directly needed to recruit a CARD domain for caspase binding in the cytosol.

However, the presence of nuclear ASC specks demands the presence of NLRP1, while zVAD as pan-caspase inhibitor blocks IL-1 secretion, but not ASC speck formation. Confirming that the occurrence of nuclear ASC specks is mediated by inflammasome formation, AIM2 activation by transfected poly(dA:dT) also results in nuclear ASC speck formation.

NLRP1 is not only crucial for inflammasome activation but also for cell death, as hPKs silenced for NLRP1 secreted IL-1 at earlier time points and showed improved survival at later time points upon UVB treatment. This might be due to the link between inflammatory and apoptotic caspases, as NLRP1 was described both as an inflammasome forming protein and also as a key mediator of apoptosis in cancer cells [19], similar to the tumor suppressor ASC [21].

The presence of nuclear ASC was previously observed by Kerur et al. [25] in HMVEC cells. These nonmyeloid endothelial cells react upon infection with Kaposi's sarcoma virus first with nuclear ASC aggregates.

Similar to our findings, the presence of nuclear ASC correlated with inflammasome activation, as in their setting,

caspase-1 cleavage occurred at the same time as the nuclear ASC aggregates formed.

Therefore, similar to the expression of ASC isoforms [30], differences between ASC localization might exist between myeloid cells and resident cells, such as endothelial cells or keratinocytes.

Possibly, DNA damage induced by UVB or transfected DNA implies the formation of nuclear ASC specks. They are only present if an inflammatory response is initiated via NLRP1 activation.

Although the formation of ASC "specks" in the nucleus in primary human keratinocytes is a rather an early event, it could also be involved in the induction of cell death.

As early as 2 h after UVB irradiation, FAM FLICA staining visualized caspase activity with its peak in activity after 4 h correlating with IL-1α secretion. IFI16 is a part of the large BRCA1-DDR complex that plays an important role in apoptosis [1]. UVB irradiation leads to IFI16 redistribution from the nucleus to the cytoplasm in later time points (16 h) [24]. ASC interacts with IFI16 to form an IFI16-ASC complex that can recruit pro-caspase-1 [19, 25].

IFI16 might also be necessary for p53 regulation, which is a binding partner of ASC [16]. Binding of p53 to ASC leads to apoptosis after UVB sensing in human keratinocytes.

To support our findings that the formation of ASC "specks" may putatively lead to apoptosis, we observed p53 interacting with ASC and IFI16 after UVB exposure in HaCaT cells. Our findings support previous reports that ASC is a binding partner of p53 [16] that additionally interacts with IFI16 [19]. We clearly observed that ASC interacts with both p53 and IFI16 after UVB irradiation in keratinocytes and that the nuclear presence of IFI16 is absent when ASC is knocked down.

5. Conclusions

The NLRP1 inflammasome plays an important role in UVB sensing in primary human keratinocytes. UVB leads to inflammasome assembly, caspase-1 recruitment, and IL-1 secretion. UVB induces nuclear ASC "speck" formation in primary human keratinocytes.

These findings are opposite to myeloid cells, where ASC "specks" localize in the perinuclear area, but are similar to the findings in zebrafish keratinocytes and in endothelial cells.

The formation of ASC "specks" indicates inflammasome assembly and activation as their formation in hPKs depends on the presence of NLRP1 and partially on NLRP3. Moreover, we found that the formation of ASC "specks" may putatively lead to apoptosis, as ASC interacts via IFI16 with p53 after UVB sensing. Blocking of NLRP1 may have a protective role in primary human keratinocytes exposed to UVB light.

Data Availability

Data shown in this manuscript are available on request. Please contact the corresponding author Nikola Smatlik.

Conflicts of Interest

The authors report no conflict of interest.

Acknowledgments

We wish to thank Mrs. Birgit Fehrenbacher and the staff of the electron microscopy facility at the Department of Dermatology, University Hospital Tübingen, for great assistance and expertise in the staining experiments. This work was supported by the Deutsche Forschungsgemeinschaft (DFG) Sonderforschungsbereich (SFB) Transregio (TRR) 156, project B06 (to MR and ASY) and DFG-YA-182/4-1.

Supplementary Materials

Supplementary Figure 1: UVB light leads to inflammasome activation, followed by ASC "speck" formation and IL-1α secretion in the time-dependent manner. Human keratinocytes had been irradiated with UVB light (50 mJ/cm^2). ASC specks have been stained 30 min, 1 h, 2 h, 4 h, and 8 h after UV irradiation using anti-ASC, rabbit pAb (AL177), antibody (red), F-actin (green), and DAPI (blue). IL-1α and IL-1β have been measured in cell-free supernatants using ELISA. Data represent at least 3 independent experiments and are presented as the means ± SD. Statistics: one-way ANOVA statistical test. Symbols for P values used in the figures. $^{*}P < 0.05$, $^{**}P < 0.01$, $^{***}P < 0.001$, and $^{****}P < 0.0001$. NS: not significant. Magnification: ×43. *(Supplementary Materials)*

References

[1] F. Daniels Jr., D. Brophy, and W. C. Lobitz Jr., "Histochemical responses of human skin following ultraviolet irradiation[1]," *The Journal of Investigative Dermatology*, vol. 37, no. 5, pp. 351–357, 1961.

[2] M. Bijl and C. G. M. Kallenberg, "Ultraviolet light and cutaneous lupus," *Lupus*, vol. 15, no. 11, pp. 724–727, 2006.

[3] E. Reefman, P. C. Limburg, C. G. M. Kallenberg, and M. Bijl, "Apoptosis in human skin: role in pathogenesis of various diseases and relevance for therapy," *Annals of the New York Academy of Sciences*, vol. 1051, no. 1, pp. 52–63, 2005.

[4] V. V. Singh, N. Kerur, V. Bottero et al., "Kaposi's sarcoma-associated herpesvirus latency in endothelial and B cells activates gamma interferon-inducible protein 16-mediated inflammasome," *Journal of Virology*, vol. 8, pp. 4417–4431, 2013.

[5] L. Feldmeyer, M. Keller, G. Niklaus, D. Hohl, S. Werner, and H. Dietmar Beer, "The inflammasome mediates UVB-induced activation and secretion of interleukin-1β by keratinocytes," *Current Biology*, vol. 17, no. 13, pp. 1140–1145, 2007.

[6] J. Chavarría-Smith and R. E. Vance, "The NLRP1 inflammasomes," *Immunological Reviews*, vol. 1, pp. 22–34, 2015.

[7] M. Ichihashi, M. Ueda, A. Budiyanto et al., "UV-induced skin damage," *Toxicology*, vol. 189, no. 1-2, pp. 21–39, 2003.

[8] X. Liu, Z. Zhang, J. Ruan et al., "Inflammasome-activated gasdermin D causes pyroptosis by forming membrane pores," *Nature*, vol. 7610, pp. 153–158, 2016.

[9] S. Nagata and M. Tanaka, "Programmed cell death and the immune system," *Nature Reviews. Immunology*, vol. 5, pp. 333–340, 2017.

[10] Y. Dombrowski, M. Peric, S. Koglin et al., "Cytosolic DNA triggers inflammasome activation in keratinocytes in psoriatic lesions," *Science translational medicine*, vol. 3, no. 82, p. 82ra38, 2011.

[11] A. Lu, V. G. Magupalli, J. Ruan et al., "Unified polymerization mechanism for the assembly of ASC-dependent inflammasomes," *Cell*, vol. 6, pp. 1193–1206, 2014.

[12] A. C. Ogilvie, C. E. Hack, J. Wagstaff, G. J. van Mierlo, and etal, "IL-1 beta does not cause neutrophil degranulation but does lead to IL-6, IL-8, and nitrite/nitrate release when used in patients with cancer," *Journal of Immunology*, vol. 156, pp. 389–394, 1996.

[13] G. Sollberger, G. E. Strittmatter, M. Kistowska, L. E. French, and H. Dietmar Beer, "Caspase-4 is required for activation of inflammasome," *Journal of Immunology*, vol. 4, pp. 1992–2000, 2012.

[14] M. Magna and D. S. Pisetsky, "The role of cell death in the pathogenesis of SLE: is pyroptosis the missing link?," *Scandinavian Journal of Immunology*, vol. 3, pp. 218–224, 2015.

[15] B. S. Franklin, L. Bossaller, D. De Nardo et al., "Adaptor ASC has extracellular and 'prionoid' activities that propagate inflammation," *Nature immunology*, vol. 8, pp. 727–737, 2014.

[16] T. Ohtsuka, H. Ryu, Y. A. Minamishima et al., "ASC is a Bax adaptor and regulates the p53-Bax mitochondrial apoptosis pathway," *Nature Cell Biology*, vol. 2, pp. 121–128, 2004.

[17] P. H. Rao, S. Zhao, Y. J. Zhao et al., "Coamplification of Myc/Pvt1 and homozygous deletion of Nlrp1 locus are frequent genetics changes in mouse osteosarcoma," *Gene Chromosome and Cancer*, vol. 12, pp. 796–808, 2015.

[18] G. Fenini, S. Grossi, E. Contassot et al., "Genome editing of human primary keratinocytes by CRISPR/Cas9 reveals an essential role of the NLRP1 inflammasome in UVB sensing," *The Journal of Investigative Dermatology*, vol. 12, pp. 2644–2652, 2018.

[19] T. Bürckstümmer, C. Baumann, S. Blüml et al., "An orthogonal proteomic-genomic screen identifies AIM2 as a cytoplasmic DNA sensor for inflammasome," *Nature Immunology*, vol. 3, pp. 266–272, 2009.

[20] M. Reinholz, Y. Kawakami, S. Salzer et al., "HPV16 activates the AIM2 inflammasome in keratinocytes," *Archives of Dermatological Research*, vol. 8, pp. 723–732, 2013.

[21] S. K. Drexler, L. Bonsignore, M. Masin et al., "Tissue-specific opposing functions of the inflammasome adaptor ASC in the regulation of epithelial skin carcinogenesis," *Proceedings of the National Academy of Sciences of the United States of America*, vol. 45, pp. 18384–18389, 2012.

[22] J. A. Aglipay, S. W. Lee, S. Okada et al., "A member of the pyrin family, IFI16, is a novel BRCA1-associated protein involved in the p53-mediated apoptosis pathway," *Oncogene*, vol. 22, no. 55, pp. 8931–8938, 2003.

[23] D. Dutta, S. Dutta, M. V. Veettil et al., "BRCA1 regulates IFI16 mediated nuclear innate sensing of herpes viral DNA and subsequent induction of the innate inflammasome and interferon-β responses," *Plos Pathogens*, vol. 11, no. 6, article e1005030, 2015.

[24] S. Costa, C. Borgogna, M. Mondini et al., "Redistribution of the nuclear protein IFI16 into the cytoplasm of ultraviolet B-exposed keratinocytes as a mechanism of autoantigen processing," *The British Journal of Dermatology*, vol. 164, pp. 282–290, 2011.

[25] N. Kerur, M. V. Veettil, N. Sharma-Walia et al., "IFI16 acts as a nuclear pathogen sensor to induce the inflammasome in response to Kaposi sarcoma-associated herpesvirus infection," *Cell Host & Microbe*, vol. 9, no. 5, pp. 363–375, 2011.

[26] F. I. Schmidt, A. Lu, J. W. Chen et al., "A single domain antibody fragment that recognizes the adaptor ASC defines the role of ASC domains in inflammasome assembly," *The Journal of Experimental Medicine*, vol. 5, pp. 771–790, 2016.

[27] G. J. Gludsdale, G. W. Dandie, and H. K. Muller, "Ultraviolet light induced injury: immunological and inflammatory effects," *Immunology and Cell Biology*, vol. 79, no. 6, pp. 547–568, 2001.

[28] N. B. Bryan, A. Dorfleutner, Y. Rojanasakul, and C. Stehlik, "Activation of inflammasomes requires intracellular redistribution of the apoptotic speck-like protein containing a caspase recruitment domain," *Journal of Immunology*, vol. 5, pp. 3173–3182, 2009.

[29] P. Kuri, N. L. Schieber, T. Thumberger, J. Wittbrodt, Y. Schwab, and M. Leptin, "Dynamics of in vivo ASC speck formation," *The Journal of Cell Biology*, vol. 9, pp. 2891–2909, 2017.

[30] N. B. Bryan, A. Dorfleutner, S. J. Kramer, C. Yun, Y. Rojanasakul, and C. Stehlik, "Differential splicing of the apoptosis-associated speck like protein containing a caspase recruitment domain (ASC) regulates inflammasomes," *Journal of Inflammation*, vol. 7, no. 1, 2010.